# UNDERSTANDING THE ROLE OF T CELL MEDIATED IMMUNE RESPONSES IN CANCER IMMUNOTHERAPIES

by

Prathyusha Konda

Submitted in partial fulfilment of the requirements

for the degree of Doctor of Philosophy

at

Dalhousie University

Halifax, Nova Scotia

April 2022

## DEDICATION

I arrived for my Ph.D. in Canada as a 21-year-old naive south Indian girl who had never walked inside an airport or boarded a flight before that day, with a great passion for science but little knowledge and life experience. It's been a little over six years since then, and my journey in this foreign country has culminated in preparing this document. There have been so many people who have helped me over the years, and I'd like to take this opportunity to thank them all here.

First and foremost, my parents and brother, who have been my staunchest supporters and constants throughout my life. Thank you for bearing with me and supporting me when I decided to go on this adventure as a first-generation Ph.D. student, even when you didn't understand a word I said. My mother genuinely embodies the persona of a strong working woman, continually seeking to better herself and thrive amid chaos. My father, who is extremely hard working and caring, has instilled the same character in me. My brother, for being my partner in crime and putting up with my antics. Thank you for all the love, for being my role models, for letting me believe that there are no limits in life and that I can shoot for the stars.

My friends in the USA, Europe, Japan, and India, who loved and supported me from across the globe during my program, thank you so much. I know the time difference was no fun! Special thanks to Vatsav for suggesting that I read Dr. Patrick Lee's reovirus publication, which prompted my email to Patrick and the rest of this journey. My friends in Halifax, thank you for the laughs and support both inside and outside the lab. You made the whole process and my stay in Canada memorable. Thank you to all my former teachers and supervisors, who shaped me into the student I am today and introduced me to the exciting world of research. Many thanks to Dr. Shashi Gujar, my Ph.D. advisor, who has been supporting me since my first day in Canada when he picked me up from the airport till now. **Finally, to everyone who helped my mental health over the years - Thank you for being there; it meant a lot more than words can ever express.**

## TABLE OF CONTENTS

# LIST OF TABLES

# LIST OF FIGURES

# ABSTRACT

The field of cancer immunotherapy has been transformed over the last decade, with a significant emphasis on T cell-based therapies due to their ability to attack cancer cells specifically. However, despite substantial progress in the development of T cell-based cancer immunotherapies, a large proportion of patients do not respond favorably, particularly in ‘cold’ tumors, which are typically categorized by a lack of tumor antigens, and defective antigen-presenting cell (APC) and T cell priming, activation, or infiltration. Methods for characterizing and modulating tumor microenvironments (TME) could help develop future immunotherapies. The current thesis investigates two avenues of research: developing new methods for detecting tumor antigens and developing novel therapeutics to make tumors ‘hot’ and boost anticancer immunity.

The first project focuses on discovering class I major histocompatibility complex (MHC-I)-bound tumor antigens that govern the specificity and activation of CD8+ T cells. Traditional methods using mass spectrometry (LC-MS/MS) based MHC-peptide identification suffer from inflated search spaces, leading to limited efficiency and poor statistical power in peptide mapping and identification. The current thesis addresses these shortcomings by employing a targeted database search strategy and developing an accompanying tool, SpectMHC, which is based on previously predicted MHC-I peptides. This unique technique improved the identification rates and statistical power of MHC-I peptides in human and mouse models in an MS-based peptide discovery platform.

The later projects focus on utilizing immunogenic cell death (ICD) of cancer, a regulatory form of cell death characterized by enhanced antigenicity and adjuvanticity, to modulate the TME and initiate specific anticancer immune responses mediated by APCs and T cells. We created novel photodynamic therapies that target cancer cells directly via cytotoxic and indirectly via inflammatory responses, induction of the hallmarks of ICD, and activation of dendritic cells resulting in protective anticancer immunity. This research resulted in the development of promising immunogenic photodynamic therapies for the treatment of melanoma, which have the potential to be translated from bench to bedside. Overall, the current thesis presents novel strategies for understanding and inducing T cell-mediated anticancer immune responses.

## LIST OF ABBREVIATIONS USED

| | |
|---|---|
| 1O2 | Singlet oxygen |
| 3IL | Triplet intraligand |
| 3ILCT | Triplet intraligand charge transfer |
| 3MLCT | Triplet metal-to-ligand charge transfer |
| 4-HT | 4-hydroxytamoxifen |
| aa | Amino acid |
| Ab | Antibody |
| ACG | Advanced gain control |
| ACK | Ammonium-chloride-potassium |
| ACT | Adoptive cell transfer |
| AGER | Advanced glycosylation end-product-specific receptor |
| AKT | Protein kinase B |
| ALL | B cell lymphoblastic leukemia |
| APC | Antigen presenting cell |
| ATP | Adenosine triphosphate |
| BCC | Basal cell carcinoma |
| BCG | Bacillus calmette–guérin |
| BMDC | Bone marrow derived dendritic cell |
| Ca2+ | Calcium ion |
| CALR | Calreticulin |

| | |
|---|---|
| CAR | Chimeric antigen receptor |
| CCAC | Canadian Council on Animal Care |
| CDKN2A | Cyclin-dependent kinase inhibitor 2A |
| cGAS | Cyclin GMP-AMP synthase |
| CID | Collision-induced dissociation |
| CNS | Central nervous system |
| CRC | Colorectal carcinoma |
| CTL | Cytotoxic T lymphocyte |
| CTLA-4 | Cytotoxic T lymphocyte antigen 4 |
| DAMPs | Damage-associated molecular patterns |
| DB | Database |
| DC | Dendritic cell |
| DLI | Drug-light-interval |
| DMEM | Dulbecco’s modified Eagle medium |
| ECM | Extracellular matrix |
| ER | Endoplasmic reticulum |
| FasL | Fas ligand |
| FBS | Fetal bovine serum |
| FDA | Food and Drug Administration |
| FDR | False discovery rate |
| G-CSF | Granulocyte colony-stimulating factor |

| | |
|---|---|
| GM-CSF | Granulocyte-macrophage colony-stimulating factor |
| HBV | Hepatitis B |
| HLA | Human leukocyte antigen |
| HMGB1 | High mobility group box 1 |
| HPPH | 2-[1-hexyloxyethyl]-2-devinyl pyropheophorbide-a |
| HPV | Human papillomavirus |
| HR | Hazard ratio |
| HSP | Heat shock proteins |
| HSV | Herpes simplex virus |
| ICD | Immunogenic cell death |
| ICI | Immune checkpoint inhibitors |
| iDAMPs | Inhibitory damps |
| IFN | Interferon |
| IFNAR | Interferon alpha receptor |
| IFNBR | Interferon beta receptor |
| IL | Intraligand |
| IM | Invasive margin |
| IP | Immuno-precipitation |
| IP | Intraperitoneal |
| ISC | Intersystem crossing |
| ISG | Interferon-stimulated genes |

| | |
|---|---|
| l | Liter |
| LC-MS/MS | Liquid chromatography tandem mass spectrometry |
| LRP1 | LDL-receptor-related protein 1 |
| mAb | Monoclonal antibody |
| MAPK | Mitogen-activated protein kinase |
| MC | Metal-centered |
| MFI | Mean fluorescence intensity |
| MHC | Major histocompatibility complex |
| ml | Milli liter |
| MLCT | Metal-to-ligand charge transfer |
| MM | Multiple myeloma |
| MS | Mass spectrometry |
| MTD | Maximum tolerated dose |
| NAC | N-acetyl-L-cysteine |
| NDV | Newcastle disease virus |
| NGS | Next generation sequencing |
| NIR | Near-infrared |
| NK | Natural killer |
| nm | Nano meter |
| NMIBC | Non-muscle invasive bladder cancer |
| NO | Nitric oxide |

| | |
|---|---|
| Nrf2 | Nuclear factor erythroid 2-related factor |
| NT | Nontreated |
| OV | Oncolytic viruses |
| P2RX7 | Purinergic receptor P2X 7 |
| P2RY2 | Purinergic receptor P2Y2 |
| p53/ TP53 | Tumor protein 53 |
| PBMC | Peripheral blood mononuclear cells |
| PD-1 | Programmed cell death 1 |
| PDT | Photodynamic therapy |
| PEP | Posterior error probabilities |
| PI | Photoindices |
| PLC | Peptide loading complex |
| PMEL | Premelanosome protein |
| PRR | Pattern-recognition receptors |
| PS | Photosensitizer |
| PSM | Peptide spectral match |
| PTEN | Phosphatase and tensin homolog |
| qRT-PCR | Quantitative real-time polymerase chain reaction |
| RBC | Red blood cell |
| ROS | Reactive oxygen species |
| Ru | Ruthenium |

| | |
|---|---|
| SC | Subcutaneous |
| scRNA-seq | Single-cell RNA sequencing |
| STING | Signal transducer stimulator of IFN response cgamp interactor 1 |
| TAA | Tumor associated antigen |
| TAM | Tumor-associated macrophages |
| TAP | Transporter associated with antigen processing |
| TAPBPR | TAP binding protein-related protein |
| TC | Tumor core |
| TCGA | The cancer genome atlas |
| TCR | T cell receptor |
| TERT | Telomerase reverse transcriptase |
| TFA | Trifluoroacetic acid |
| Th | T helper |
| Th17 | T helper 17 |
| TIL | Tumor infiltrating lymphocytes |
| TM | Transition metal |
| TME | Tumor microenvironment |
| TME | Tumor microenvironment |
| TNFa | Tumor necrosis factor |
| Treg | Regulatory t cell |
| TSA | Tumor specific antigen |

| | |
|---|---|
| T-VEC | Talimogene laherparepvec |
| ul | Microliter |
| um | Micro meter |
| UPR | Unfolded protein response |
| UVR | Ultraviolet radiation |
| V | Variable |
| VIN | Vulva intraepithelial neoplasia |
| WT | Wild type |
| WT1 | Wilm’s tumor protein |

# ACKNOWLEDGEMENTS

*“It truly took a village.”*

First and foremost, I want to thank my Ph.D. supervisor, Dr. Shashi Gujar, for his open doors, scientific support, motivation, and, most importantly, for his support of my mental health. I will be eternally grateful for his encouragement and kindness over the years. I'd also like to thank Dr. Patrick Lee, my former supervisor, for welcoming me into the lab and giving me this opportunity.

I am deeply thankful to my amazing committee members, Dr. Brent Johnston, Dr. Daniel Gaston, and Dr. Paola Marcato, who were always available to help me and provided constructive feedback during committee meetings, which significantly impacted my academic growth. Thank you so much, Dr. Gaston, for your willingness to discuss and help with my silly bioinformatics questions.

Dr. Patrick Murphy, former lab member, my first collaborator, and co-author - I can undoubtedly say that our work together as Pat-Prat team was THE BEST part of my Ph.D. Forever grateful for his guidance in the lab and our productive, fun, and memorable collaborations.

I'd also like to thank our collaborators, Dr. Stefan Stevanoic, Dr. Steven Gygi, and Dr. Alehandro Cohen, for their assistance with mass spectrometry work, and Dr. Sherri McFarland and her team for synthesizing the amazing photosensitizers used in this thesis. Special thanks to Angelita Alcos and Nadia Farbestein, who helped me with animal handling.

Many thanks to Dr. Valerie Chappe for fostering my leadership activities outside the lab, during my time as FMGSS President, and while building the Peer Support Network. Thank you for being so kind and accessible to the student body.

Finally, I'd like to thank Marsha Scott-Meldrum, our former graduate studies secretary, who provided behind-the-scenes support with paperwork during my program.

# CHAPTER 1: INTRODUCTION

## 1.1. CANCER & IMMUNE SYSTEM

The idea that the immune system can control cancers and can be harnessed to attack cancers dates back to the nineteenth century.[1,2] Drs. Wilhelm Busch and Friedrich Fehleisen were the first to report the epidemiological association between spontaneous tumor regression in cancer patients following the development of erysipelas, a skin infection caused by *Streptococcus pyogenes*.[1] Decades later, in 1891, American surgeon Dr. William Coley noticed that sarcoma patients with erysipelas had a better clinical outcome than those without erysipelas. To verify this connection, Coley treated his cancer patients with mixtures of live and heat-inactivated *S. pyogenes* and *Serratia marcescens*, which were termed as 'Coley's toxins.' He demonstrated that these toxins had potent immunostimulatory properties and caused tumor regression in sarcoma, lymphoma, and testicular carcinomas.[1,2] However, due to issues with reproducibility and a lack of scientific rigor, the findings were disregarded at that time.[1,2] These discoveries were confirmed more than 50 years later, in 1959, when Lloyd J Old showed the antitumor effects of Bacillus Calmette-Guerin (BCG) in a mouse model,[3] which was followed by the demonstration of clinical efficacy of BCG against bladder cancer in 1976.[4] These observations shifted the focus of therapeutics from tumor-centric towards tumor and immune system-centric. They formed the basis of the current cancer immunotherapies designed to harness the immune system against cancer.

During this period, several other observations were made about the connection between the immune system and cancer. Most notably, in 1909, Dr. Paul Ehrlich hypothesized that the immune system spontaneously inhibited the formation of tumors in the body; however, this was not tested due to lack of understanding of the immune

system and unavailability of appropriate study models at that time.[1,2] In the mid-20th century, Drs. Lewis Thomas and MacFarlane Burnet coined the term “immunological surveillance” and suggested that lymphocytes eliminate tumors by detecting the tumor-specific neo-antigens.[5,6] Immunosurveillance is the ability of the immune system to continually scan the body for threats and evoke an immune response when a threat is detected. These hypotheses were supported by robust experimental data from Schreiber, Dunn, Old, and colleagues at the end of the twentieth century[7–10], eventually solidifying the concepts of cancer immunosurveillance and cancer immunoediting.

### *1.1.1. Cancer immunoediting*

Cancers are characterized by several hallmarks associated with genetic, cellular, and metabolic alterations, along with their ability to evade immunosurveillance.[11] These alterations result in mutated cellular proteins, abnormally expressed normal proteins, or genes encoding viral proteins, all of which contribute to the generation of tumor antigens. Tumor antigens assist the immune system in differentiating malignant cells from normal cells, playing a significant part in cancer immunosurveillance. Tumor antigens are explained in more detail in section **1.3.4**. Investigations from the Schreiber group in 2001 demonstrated that lymphocytes protect against carcinogen-induced tumors and that this process also leads to the immunoselection of tumor cells that are better capable of surviving in an immunocompetent host.[8–10,12] This suggested that the immune system not only controlled tumor quantity but also tumor quality (immunogenicity) and that immunity had both tumor inhibitory and tumor-promoting effects on developing tumors. Such interactions between cancer cells and immune cells are known as “cancer immunoediting,” and the process is comprised of three phases: Elimination, Equilibrium, and Escape.[8–10,12]

The elimination phase of cancer immunoediting consists of active immunosurveillance of malignancies followed by their eradication.[8–10,12] If the immune system fails to eliminate the tumor, the surviving tumor cells enter an equilibrium phase. Here, surviving tumor cells that are less immunogenic than the ones that were cleared maintain a dormant or latent phase, wherein the selective pressure from the immune system results in the development of cells resistant to immune surveillance and attack.[8–10,12] Finally, in the escape phase, tumor cells that have successfully adapted to the immunological pressures and have acquired immune resistance or evasion mechanisms that mediate progression into clinically manifested disease.[8–10,12] Tumor elimination is an essential phase of cancer immunoediting that involves several critical molecules and cells. Many immunotherapeutics designed to destroy cancer boost this aspect of cancer-immune interactions.

### *1.1.2. Cancer immunity cycle*

To achieve complete tumor elimination by the immune system, a series of steps mainly involving dendritic cells (DCs) and T lymphocytes at different anatomical sites are necessary. These steps are collectively termed the “cancer immunity cycle” by Chen & Mellman [**Figure 1.1**].[13] The process is initiated by the release of tumor antigens generated through oncogenesis; this is considered **step 1**.[13] These tumor antigens are captured through phagocytosis by immature dendritic cells that are recruited to the tumor site. The captured antigens are processed, and the antigenic peptides are presented on dendritic cells via major histocompatibility complex (MHC) class I and MHC class II molecules (**step 2**).[13] The activated and matured dendritic cells migrate to lymph nodes and present these tumor antigens to T cells, thereby priming and activating antigen-specific effector T cells (**step 3**).[13] The activated effector T cells migrate and infiltrate the tumor stroma (**steps 4** & **5**). Here, they recognize and bind to cancer cells through

the interactions between T cell receptor (TCR) and the antigen bound to MHC-I on cancer cells, eventually killing the target cells (**step 6**).[13] T cell-mediated killing of cancer cells results in the release of more cancer antigens (**step 1**) and reactivation of this cancer immunity cycle, thereby enhancing the response to eliminate remaining cancer cells [**Figure 1.1**].[13] The activation (step 3) and infiltration (step 5) of T cells in the cancer immunity cycle are often considered rate-limiting steps.

While dendritic cells and T cells are the main players of this cancer immunity cycle, virtually every subset of immune cells has been implicated in the context of anticancer immune responses.[14–20] The current thesis will focus primarily on the DC-CD8+ T cell axis; however, the significance of other immune cells in treatment-induced anticancer immunity has been detailed in section **1.6.3.4**. Additionally, as mentioned above, clinically manifested tumors overcome the elimination phase and are in the immune escape phase. Therefore, an intact cancer immunity cycle is often absent in human cancers. These discoveries led to the development of several cancer immunotherapies to target cancer immune evasion and restore cancer immunity, which are discussed in section **1.4**.

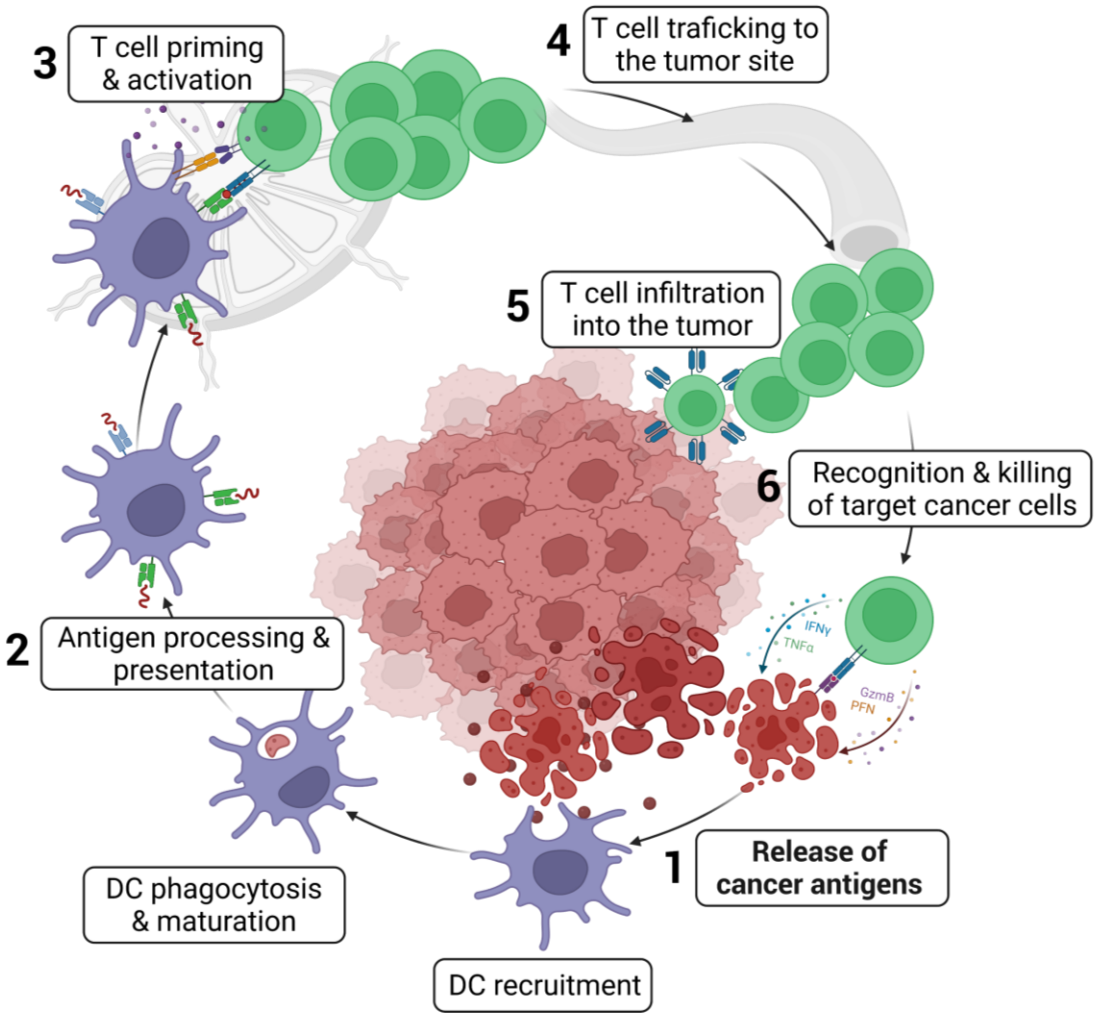


**Figure 1.1.** Cancer immunity cycle.

The cancer immunity cycle can be divided into several parts, beginning with the 1. Release of antigens from the cancer cell, 2. Antigen processing and presentation by mature DCs, 3. T cell priming and activation by DCs in the lymph node, 4. T cell trafficking and 5. Infiltration into the tumor site, 6. Recognition and killing of target cancer cells release more antigens and self propagate the cycle. DC: Dendritic cell. Figure made using Biorender.

## 1.2. T CELLS IN CANCER IMMUNITY

CD8+ T lymphocytes are effector cells that can specifically target and kill the cancer cells, hence playing an essential role in the cancer immunity cycle. Due to their specific tumor-killing properties, CD8+ T cells have become the central focus of cancer immunotherapies in recent decades.[21] Apart from CD8+ T cells, T lymphocytes constitute CD4+ T cells- T helper (Th) cells and regulatory T cells (Tregs), MAIT cells, NKT cells, γδ-T cells, with multiple subsets amongst each cell type.[22,23] This section will focus on the significance of CD8+ cytotoxic T lymphocytes (CTLs), which are the key effector cells in the cancer immunity cycle.

### *1.2.1. Prognostic significance*

T cell infiltration at the tumor site, step 5 in the cancer immunity cycle, has been associated with favorable prognosis and response in several tumors.[24] One of the earliest studies dating back to 1989 has shown that higher densities of tumor-infiltrating lymphocytes (TILs) in stage I cutaneous melanoma was a predictor of better overall survival in these patients.[25] Many subsequent studies have strongly supported these conclusions in melanoma.[24] In epithelial ovarian cancer patients with a complete clinical response, the five-year overall survival of individuals with TILs was 73.9%.[26] In contrast, it was only 11.9% in those whose tumors contained no T cells.[26] Furthermore, the presence of TILs was independently associated with delayed recurrence or delayed mortality in all ovarian cancer patients.[26] In breast cancer patients, higher TIL concentration predicted responsiveness to neoadjuvant treatment and was also associated with a survival advantage in HER2-positive and triple-negative breast cancers.[27] Furthermore, microsatellite-unstable colorectal carcinomas (CRCs) with high immunogenicity and frequent lymphocyte infiltration are associated with the best prognosis and have a low chance of metastatic spread.[28,29] Similarly, TIL infiltration has

been correlated with positive prognostic outcomes in several cancers such as bladder cancer, prostate cancer, pancreatic cancer, and lung cancer.[30–35]

Recently, the cancer genome atlas (TCGA) has performed an extensive genomic and histological analysis of the immune landscape of over 10,000 tumor samples from 30 solid tumor types, which revealed similar conclusions.[36] Cancers with interferon-gamma dominant and inflammatory subsets with high TIL density scores correlated with best overall survival.[36] On the other hand, cancer subsets characterized by lymphocyte depleted signature and low TIL densities are associated with the worst prognosis.[36] Tumors with higher immunogenicity (mutational burden & neoantigen load) displayed higher content of CD8 T cells as compared to tumors with a lower mutational burden.[36] Along with lymphocyte expression signature, many unique T cell receptor clonotypes were also strongly correlated with improved overall survival.[36]

It has also been shown that TILs can recognize tumor-specific antigens, and the presence of functional T cells is associated with a better prognosis. For instance, functional analyses of specific CTL clones isolated from TILs of a lung carcinoma patient with prolonged survival indicated that these cells could recognize a tumor-specific antigen and initiate cytotoxic activity against the autologous tumor cell line.[37] Further characterization of these clones revealed a CD3+ CD8+ CD4- CD28- phenotype. These clones identified *in vitro* were also selectively expanded *in vivo* and were present in higher concentrations at the tumor site than peripheral blood.[37] Adoptive transfer of these T cells into immunocompromised mice transplanted with autologous tumor cells generated anticancer immune responses against the tumor.[37] In a study of T cells purified from lymph nodes of advanced-stage head and neck cancer patients, patients whose T cells responded poorly to CD3 activation exhibited a higher incidence of recurring malignancy.[38] Similar research in melanoma identified tumor antigen-specific

TILs with cytotoxic capacities against autologous tumors. The adoptive transfer of such antigen-specific TILs into cancer patients is positively correlated with tumor regression.[39–45]

The spatial organization of T cells in the tumor microenvironment is also associated with the prognosis of patients.[46] In over a decade-long global collaborative effort, the density and compartmentalization of CD3+ T cells, CD8+ T cells, CD45R+ memory cells, and T cell cytotoxic molecules (granzyme B) were analyzed in more than 4,000 colorectal cancer patients.[29,46–48] They studied the distribution in the tumor core (TC) that is the center of the tumor and at the invasive margin (IM). These analyses revealed a strong correlation between the density of immune cell populations in the TC and IM tumor locations and the patients' clinical outcomes regarding disease-free survival and overall survival.[29,46–48] Furthermore, combining the TC and IM cell densities substantially increased the variation in the clinical outcome between groups of patients with a high immune cell density in both tumor regions against patients with a low immune density in both areas.[29,46–48] Subsequent evaluation of individuals with clinically localized CRCs revealed that only 4.8 percent of those with a significant CD8+ T cell infiltration relapsed five years after diagnosis, whereas 75 percent of those with a low CD8+ immune infiltrate relapsed, and 72.5 percent died.[29,46–48] These findings resulted in the development of the “Immunoscore” to assess the infiltration of CD3+ and CD8+ T cells in the TC and IM regions, which is now part of clinical diagnostics for the classification of cancers.[29,46–48] Immunoscore is considered a better prognostic predictor than the assessment of microsatellite instability or the traditional tumor, node, metastasis classification system.[29,46–48] Positive prognostic value of immunoscore has since been validated in more than 16 other cancer types including hepatocellular carcinoma, head

and neck cancer, ovarian cancer, melanoma and breast cancers.[49] Overall, T cells play an important role in determining the clinical outcome of cancers.

### *1.2.2. Activation of effector T cells in the cancer immunity cycle*

T cells generated in the thymus leave the thymus and enter the circulation as naïve T cells or antigen-inexperienced T cells.[22] When these naïve T cells encounter an APC expressing an antigen to which they can bind with high affinity, they start an activation program and produce effector functions.[22] The activation of T cells requires three major signals [**Figure 1.2**]: signal 1 is provided by T cell receptor (TCR) engagement with MHC-antigen complex, signal 2 involves interactions with co-stimulatory molecules, and signal 3 is provided by cytokines.[22,50–53]

#### 1.2.2.1. Signal 1: TCR-MHC activation

CD8+ T lymphocytes bind to MHC-I molecules on the surface of antigen-presenting cells and target cancer cells, which are loaded with antigenic peptide fragments formed by proteasomal degradation of cytoplasmic proteins, as explained in section **1.3**. Upon efficient binding of the TCR and CD8 with the specific MHC-antigen complex, the T cell activation signal transduction begins through the intracellular domain of the TCR-CD3 complex.[22,50–53] However, to achieve effector mechanisms of T cells, the TCR-MHC activation signal must be followed by a crucial co-stimulatory signal.

#### 1.2.2.2. Signal 2: CD28 co-stimulatory signal

T cell co-stimulation signals are provided by APCs (DCs, macrophages and B cells); however, dendritic cells are the best activators of T cells.[22,50,51] Co-stimulation of T cells is mediated through interactions of CD28 receptors on CD8+ T cells with CD80 and CD86 on APCs.[22,50–53] CD80 and CD86 are upregulated on mature DCs and usually absent on cancer cells; therefore, cancer cells cannot provide the signal 2 to activate T

cells.[22,50–53] This co-stimulatory signal is essential for T cell activation, and the presence of only signal 1 and absence of signal 2 leads to T cell anergy (unresponsive state of T cells) and apoptosis.[22,50–53] The CD28 mediated signal activation increases T cell proliferation and survival and enhances the TCR response to antigen, reducing the stimulation threshold.[22,50–53] T cells activated by signal 1 and signal 2 release cytokines, which act as signal 3 and play an essential role in determining the outcome of T cell effector activity.[22,52–54]

#### 1.2.2.3. Signal 3: Cytokines

Cytokines secreted by activated APCs and T cells bind to specific cytokine receptors on T cells and enhance the proliferation as well as the survival of T cells. IL-2 is one of the major cytokines involved in this function.[22,52–54] Activation of signal transduction through signals 1 and 2 induces transcription of genes IL-2 and the corresponding receptor IL-2R.[22,52–54] Additionally, they also enhance the stability of IL-2 mRNA and result in the production of IL-2 by the activated T cells.[22,52–54] These secreted IL-2 binds to the IL-2R on T cells and increases proliferation and survival.[22,52–54]

#### 1.2.2.4. Effector T cell-mediated target cell killing

After infiltrating the tumor site, fully primed and activated T cells can recognize specific cancer cells by binding to the MHC-I-peptide on the cancer cell and forming an immunological synapse. This interaction initiates a cascade of events by T cells, such as the release of perforins that cause pore formation on the target-cell membrane allowing for diffusion of granules containing cytotoxic molecules (granzymes and granulysin) to kill the cancer cells.[50,55] Furthermore, Fas ligand (FasL) expressed on CD8+ T lymphocytes can interact with Fas receptors on target cells, activating death pathways and releasing cytochrome c in the cancer cells.[50,55] Finally, activated CD8+ T

lymphocytes can kill cancer cells indirectly by releasing cytokines such as tumor necrosis factor-alpha (TNFα) and interferon-gamma (IFNγ), which attach to respective receptors on tumor cells and can stimulate apoptotic pathways.[55–57] Interferon-gamma released by activated CD8+ T cells also increases the expression of MHC-I on cancer cells, thereby making them more susceptible to CD8 T cell-mediated killing.[55–57] Activated T cells have the potential to target and destroy cancer cells in this manner and so play an important role in the cancer immunity cycle.

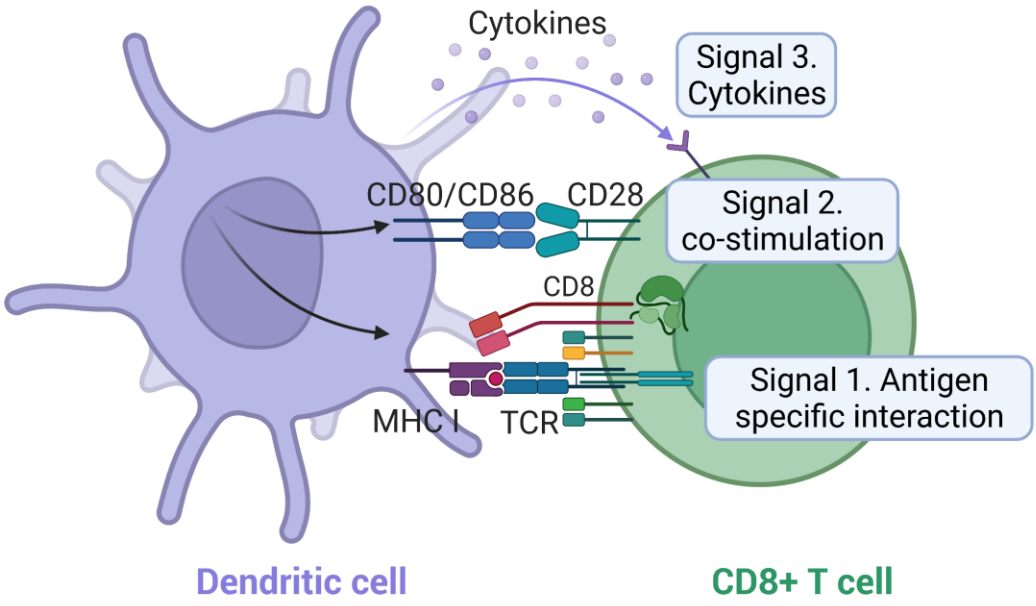


**Figure 1.2.** Signals required for T cell activation.

T cell activation requires three signals. 1. Antigen presentation in the context of MHC-I, recognized by antigen-specific TCR. 2. Co-stimulation upon binding of CD28 on T cells with CD80 or CD81 on DCs. 3. Cytokine signals from DCs. TCR: T cell receptor, MHC: Major histocompatibility complex, DC: Dendritic cell. Figure made using Biorender.

## 1.3. ANTIGEN PROCESSING AND PRESENTATION IN CANCER IMMUNITY

The earliest phases in the cancer immunity cycle that entail the processing and presentation of tumor antigens form the basis for T cell activation signal 1 and dictate the specificity of resultant T cell responses. Tumor antigens are peptides derived from abnormally expressed cellular proteins resulting from tumorigenesis.[58,59] The generation of these peptides from native proteins is referred to as antigen processing, and their display on the cell surface is referred to as antigen presentation.[58,59] Antigenic peptides (also referred to as ligands) are typically processed and presented through either MHC class I or MHC class II pathways, associated with different sources of antigenic peptides.[60]

MHC class I and II molecules are membrane-bound glycoproteins with structural and functional similarities [**Figure 1.3**].[60] These membrane-bound glycoproteins act as highly specialized antigen-presenting molecules, with binding grooves that form stable complexes with peptide ligands, allowing them to be displayed on the cell surface for TCR interaction.[60] MHC class I complexes are found on the surface of all nucleated cells, but MHC class II complexes are predominantly found on the surface of antigen-presenting cells.[60] MHC class I molecules bind peptides typically 8–11 amino acids (aa) long and derived from endogenous proteins. On the other hand, MHC class II molecules bind peptides that are several amino acids longer (9–25 aa) and derived from exogenous, transmembrane, and cytosolic proteins.[60] Peptides presented by the MHC-I complexes activate CD8+ T cells, whereas peptides presented by the MHC-II complexes activate CD4+ T cells.[60] However, some exogenous peptides can be presented by MHC class I molecules via cross-presentation in dendritic cells.[60] The current thesis focuses on MHC class I peptides, and so, this section will discuss the MHC-I mediated antigen processing and presentation pathway.

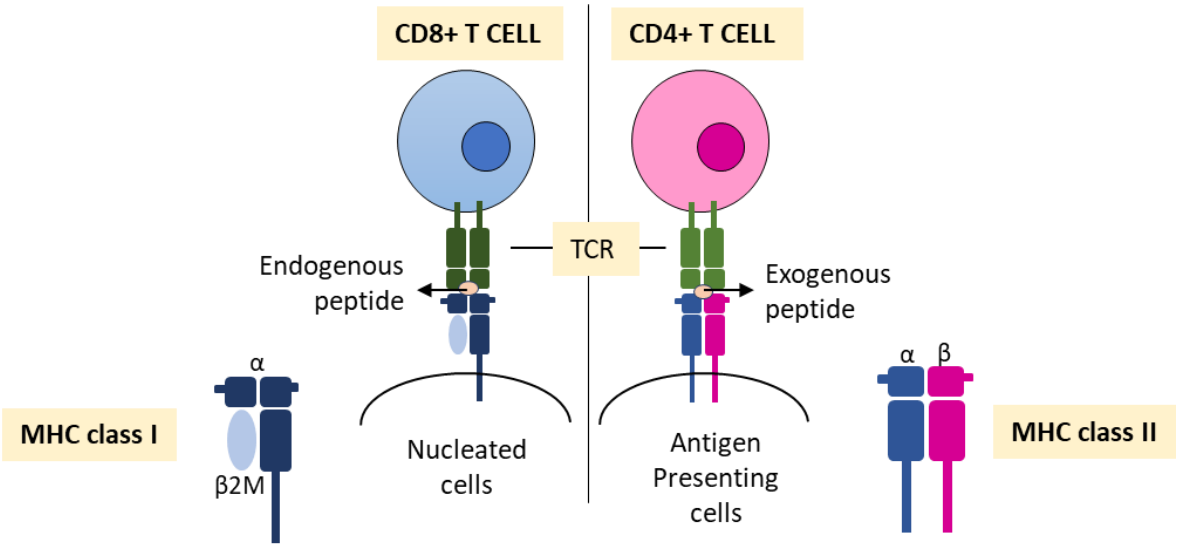


**Figure 1.3.** Overview of MHC class I and MHC class II antigen presentation to T cells

MHC class I molecules can be found in all nucleated cells, whereas MHC class II molecules can only be found in antigen-presenting cells. Endogenous peptides are presented to TCRs on CD8+ T cells by MHC class I molecules, whereas exogenous peptides are presented to TCRs on CD4+ T cells by MHC class II molecules. MHC: Major histocompatibility complex, TCR: T cell receptor.

### *1.3.1. MHC-I complex structure and polymorphism*

MHC class I molecules are made up of a heavy chain (α chain) and β2-microglobulin [**Figure 1.4**].[22,23] The α chain consists of three external domains (α1, α2, and α3), a transmembrane domain, and a cytoplasmic domain. The β2-microglobulin is non-covalently bound to the α chain at α3 and does not contain any transmembrane domain.[22,23] The α3 domain is highly conserved among MHC-I molecules and contains sequence motifs to strongly interact with CD8 on T cells.[22,23] The proper folding and

expression of all these molecules are essential for the stability of the MHC complex.[22,23] The antigen-binding groove is formed within the α chain between α1 and α2. The peptide is bound within this antigen-binding groove, which is pinched off at the termini and hence preferentially binds peptides of 8–10 amino acids in length.[22,23] Pockets within an MHC molecule's antigen-binding groove dictate the position of the peptide within the groove and its peptide-binding preferences, which are shaped by MHC polymorphisms.[22,23,61]

MHC molecules are polygenic and polymorphic; that is, they contain different genes as well as variants of each gene, with more than 6000 variants differing by up to 20 amino acids being identified so far.[60,61] Variants of MHC molecules are called MHC alleles and a particular combination of MHC alleles is known as a haplotype.[60,61] The MHC polymorphism also implies that the amino acids that line the pockets of the MHC peptide-binding groove are distinct; consequently, the peptide residues binding these pockets are also different.[60,61] These properties of MHC broaden the range of peptides presented to T cells in each individual and a population as a whole, even when derived from the same protein.[60,61]

The variation in MHC alleles is accompanied by a diverse repertoire of TCRs ($10^{15}$–$10^{21}$ potential TCRs per individual), accommodating the wide variety of MHC antigens while maintaining specificity.[62–64] This means that every T cell clone will have a unique TCR capable of binding to a limited range of target MHC-peptide complexes.[62–64] This is also known as MHC-TCR restriction, wherein the specific MHC molecule and its allele determine the interaction with a TCR.[62–64] Accordingly, a T cell that recognizes a particular peptide on one MHC molecule may not recognize the same peptide on a different MHC. The highly polymorphic nature of the MHC complex has functional consequences and determines the specificity of T cell activation.[62–64]

MHC is referred to as human leukocyte antigen (HLA) in humans. The HLA class I heavy chains are encoded by three genes on chromosome 6: HLA-A, HLA-B, and HLA-C, resulting in 6 different HLA class I molecules per individual.[60,61] The mouse counterparts of these MHC genes include H2-K, H2-D, and H2-L. Several differences between the three HLA loci have been reported.[60,61] HLA-A and HLA-B are usually expressed at higher levels than HLC-C.[60,61] HLA-A and HLA-C bind more efficiently to the peptide loading complex than HLA-B.[60,61] HLA-B is loaded with peptides and transported to the cell surface faster than HLA-A and HLA-C.[60,61] Additionally, all HLA-B complexes are shown to be almost always loaded with peptides, whereas only a portion of HLA-A and HLA-C are loaded.[60,61]

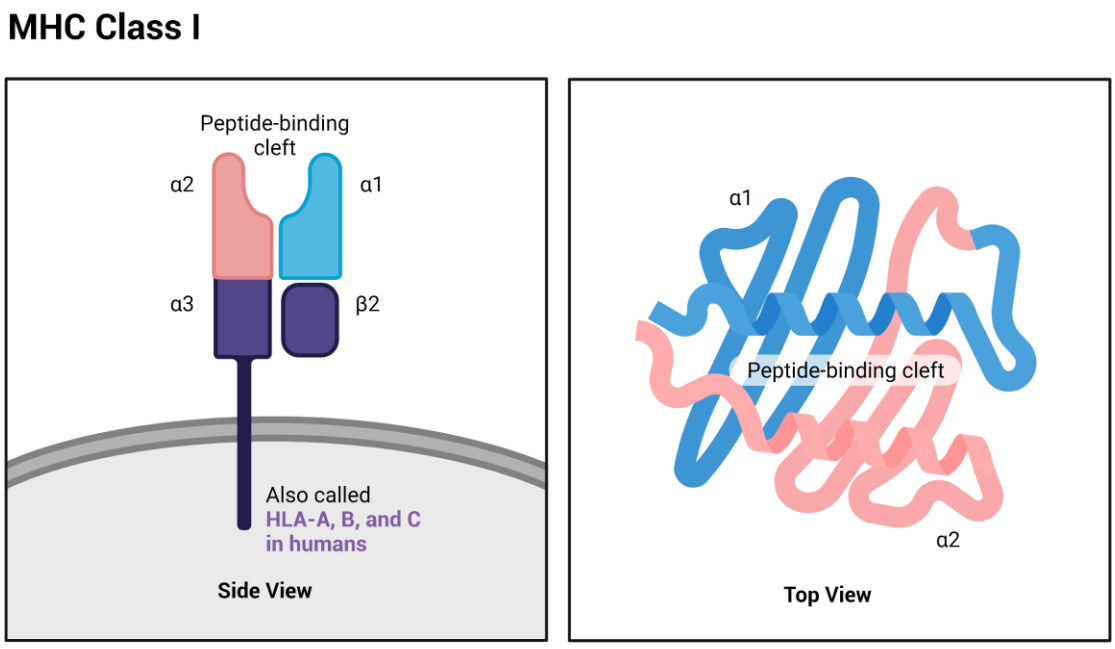


**Figure 1.4.** MHC class I molecule structure

MHC class I molecules are composed of two polypeptide chains, one membrane-spanning α chain (heavy chain), and one β chain (light chain or β2-microglobulin), linked noncovalently through the interaction of β2 and the α3 domains. The α1 and α2 domains

fold together to create a peptide binding cleft. HLA: Human leukocyte antigen, MHC: Major histocompatibility complex. Figure made using Biorender.

### *1.3.2. MHC-I mediated antigen processing and presentation pathway*

The processing and presentation of MHC-I peptides is a multi-step process that begins in the cytoplasm [**Figure 1.5**]. In general, 26S proteasomal degradation generates protein fragments from ubiquitinated, aberrant, or misfolded proteins.[59,60,65,66] The constitutively expressed 26S proteasome has a barrel-like structure with two outer alpha rings and two inner beta rings.[59,60,65,66] Upon exposure to inflammatory cytokines, the beta subunits of the proteasome are replaced by its variants, resulting in the formation of an immunoproteasome complex with distinct structure and cleavage site specificity, that contributes to the generation of unique MHC-I peptides.[59,60,65,66] The MHC-I peptides generated by the immunoproteasome are also referred to as the immunopeptidome or MHC ligandome. The immunoproteasome cleaves proteins into peptides ranging in length from 2 to 26 amino acids, with C-terminus anchor residues unique to the MHC-I binding groove and extended N-terminus residues, and releases them into the cytosol.[59,60,65,66] These peptides are transported into the endoplasmic reticulum (ER) via a transmembrane pore formed by the transporter associated with antigen processing (TAP) heterodimer consisting of TAP1 and TAP2.[59,60,65,66] TAP primarily translocates peptides with 9-16 aa residues most efficiently; however, peptides with up to 30 aa residues may also be translocated with less efficiency.[59,60,65,66]

Upon entering the ER, peptides are loaded onto nascent MHC-I molecules by a multi-subunit complex called the peptide loading complex (PLC).[59,60,65,66] TAP is one of the core components of the PLC and serves as a docking site for Tapasin, which aids in the recruitment of MHC-I complexes to the PLC.[59,60,65,66] Tapasin is linked to the

proteins ERp57, calreticulin, and calnexin, which regulate the folding and oxidation of newly generated MHC-I molecules.[59,60,65,66] ERAP1 and ERAP2 further process peptides that enter the ER to the appropriate length by cutting the N-terminal ends before being loaded into the groove of the MHC-I molecule.[59,60,65,66] Here, an additional chaperone TAP binding protein-related protein (TAPBPR) assists with the quality control of loaded peptides and stabilizes the structure of MHC-I and peptide complex.[59,60,65,66] Upon achieving a stable MHC-I-peptide complex with high affinity, TABPR is released, and the MHC-I-peptide complex is transported to the cell surface via the Golgi apparatus.[59,60,65,66] These MHC-I-peptides are then presented to T lymphocytes, initiating signal 1 of the T cell activation cascade in T cells with specific TCRs.

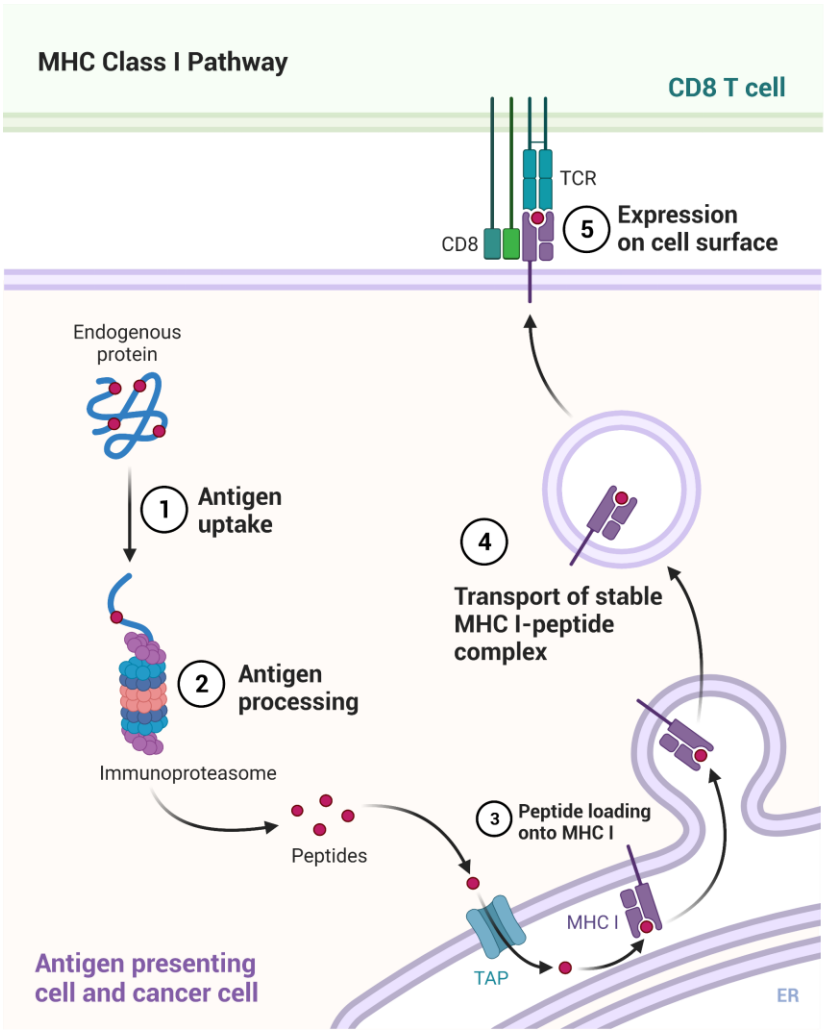


**Figure 1.5.** MHC-I antigen processing and presentation pathway

Immunoproteasome in the cytosol processes endogenous proteins into peptides, which are then transported into the ER by TAP for further processing. In the ER, these processed peptides are subsequently loaded onto MHC I molecules and transported to the cell surface, where they are presented to CD8 T cells. MHC: Major histocompatibility complex, ER: Endoplasmic reticulum, TAP: Transporter associated with Antigen Processing. Figure made using Biorender.

### *1.3.3. Cross presentation by dendritic cells*

In the setting of cancer immunity, where dendritic cells might acquire antigens from external sources such as dying cancer cells, it is inefficient for these antigens to be processed and presented to only CD4+ T cells by MHC-II complexes without activating cytotoxic CD8+ T cells via MHC-I complexes. As an exception in these circumstances, DCs have evolved an efficient antigen processing and presentation system capable of presenting exogenous peptides via MHC-I molecules. This process is referred to as cross-presentation.[67,68]

Exogenous antigens taken up by dendritic cells via phagocytosis, macropinocytosis, or receptor-mediated endocytosis are shown to be efficiently cross-presented.[67] Two mechanisms of cross-presentation have been implicated in DCs, which could form different types of MHC-I peptides.[67,68] One mechanism involves the phagosome to cytosol pathway, wherein phagocytosed exogenous antigens are transported into the cytosol via phagosomes.[67,68] Upon translocation into the cytosol, the antigens can be processed and presented by the traditional MHC-I pathway involving proteasome, TAP, and PLC, as previously described.[67,68] Here, antigens can also be processed within the cytosol using the proteasome as in the traditional pathway and re-transported into the phagosomes, where the peptides are loaded onto MHC-I complexes via TAP and PLC.[67,68] Alternatively, antigens can be processed through a vacuolar pathway, in which proteins are catabolized into peptides within the endocytic compartments and loaded on MHC-I molecules in these vesicles. [67,68] This pathway occurs independent of proteasome, TAP, and without the antigens encountering cytosol.[67] While both processes are reported, the proteasome-dependent cytosol pathway seems to occur predominantly within DCs.[67,68] Certainly, efficient antigen presentation to induce cancer immunity would require DCs presenting identical peptides

as observed on the target tumor cells to activate T cells. This would necessitate the use of phagosome-to-cytosol pathway, which would generate similar peptides in both DCs as well as cancer cells.

### *1.3.4. Tumor antigens*

Tumor antigens are peptide molecules present in tumor cells that can help immune cells distinguish between self and non-self and provide the specificity for T cell responses. For an antigen to elicit effective cytotoxic T cell responses, it must be a) immunogenic, that is, it can generate an immune response, b) tumor-specific, that is, different from normal antigens so T cells can discriminate between tumor cells and normal cells, and c) expressed in sufficient quantities on tumor cells.[69] Malignant cells display antigens that can induce an immune response against the host. These antigens can be divided into three main categories: 1. Tumor specific antigens or neoantigens, 2. Tumor-associated antigens, and 3. Viral antigens.[70]

Cancers can display increased antigenicity due to accelerated mutation rates frequently associated with tumorigenesis and evolution.[13] Such mutations can affect the protein sequences and confirmation, like non-synonymous point mutations or frameshift mutations.[69,70] These antigens generated from mutated proteins are known as ‘neoantigens’ or ‘tumor-specific antigens (TSA)’ and typically have poor structural homology with self-antigens, allowing them to prime T cell responses.[71–73] Some self-antigens expressed by cancer cells can also initiate T cell responses and are termed as ‘tumor-associated antigens (TAA)’ due to their presence in normal cells and lack of specificity to the tumor cell.[71–73] TAAs are most commonly obtained from cell-specific or tissue differentiation antigens such as CD19, CD20, premelanosome protein (PMEL), Melan-A; tissue restricted proteins such as cancer/ testis antigens as well as proteins expressed in abnormally high levels in cancer cells compared to healthy cells such as

ERBB2 (also known as HER2) and Wilm's tumor protein (WT1).[74–77] TAAs typically generate weaker anticancer immunity than TSAs as they are covered by central or peripheral tolerance mechanisms. Yet, due to leaky tolerance and in the presence of strong adjuvants, they continue to play an important role in cancers with low mutation burdens.[75,78–81]

Finally, viral antigens are derived from viruses known to cause cancers, such as human papillomavirus, Epstein-Barr virus, and Merkel cell polyomavirus.[82–85] These antigens are often highly immunogenic due to their foreign origin; however, they may not be tumor-specific and may not be produced at later stages of tumor development.[66,75] Recent studies have identified additional sources of peptides, including those arising from dysregulated RNA editing,[86] a posttranscriptional mechanism that causes sequence variations in proteins. Additionally, proteasome-generated spliced peptides[87–89] in which peptide fragments from different or same protein can be spliced and ligated into unique non-contiguous sequences; and cryptic peptides derived from the translation of non-coding genome or non-canonical translation of protein-coding genes are also reported.[90] Cryptic peptides provide a new promise for therapeutic utility as they constitute a considerably larger genetic pool than conventional canonical peptides. The presence of tumor antigens varies greatly between cancer types and hosts due to MHC restriction.

### *1.3.5. Detecting MHC-I tumor antigens*

Detecting MHC-I peptides (or ligands) has been of great interest due to their unique role in the cancer immunity cycle by providing and determining the specificity for T cell responses. As a result, significant developments have been made in identifying these peptides. **Chapter 3** of this thesis discusses one such method to improve the efficiency

of MHC-I ligand identification. This section will provide a brief background of the most employed techniques.

### 1.3.5.1. Mass spectrometry-based immunopeptidomics

The development of mass spectrometry (MS) technologies for isolating and identifying peptides has greatly aided in the discovery of MHC peptides, collectively referred to as the immunopeptidome or MHC ligandome. The development of a method in 1987 for isolating MHC-I ligands from surface-attached proteins using mild acid elution was a significant step forward in these discoveries.[91] Since then, the technology has progressed, and immunoaffinity purification is now the most used method for isolating immunopeptidomes [**Figure 1.6**].[92,93]

Briefly, a lysate of cells or homogenized tissue is incubated with MHC-specific antibodies.[92–95] Typically, pan-HLA antibodies are used for human samples, but allele-specific antibodies are also available.The MHC-complexes are purified by immunoaffinity purification and eluted from this mixture while non-specifically bound substances are removed.[92–95] The eluted peptides are then separated using liquid chromatography and directly injected into a mass spectrometer.[92–95] The mass spectrometer measures the mass of the peptide fragments and outputs spectra, which can be matched against a reference database containing mouse or human protein sequences [**Figure 1.6**].[92–95]

Currently, MS is the only unbiased approach for examining the quality and quantity of repertoire of MHC peptides naturally presented in cells.[92–95] The entire MS-based discovery workflow enriches the peptide pool to MHC or HLA-specific peptides, offering a reliable assessment of the immunopeptidome, with up to 95% of recovered peptides exhibiting typical length distribution and binding motifs of MHC peptides.[94,96] Although tumor-associated antigens[97–105] are the most commonly discovered peptide

pool utilizing this method, some studies have demonstrated efficacy in identifying neoantigens[105,106] as well. Another appealing aspect of utilizing MS for peptide identification is that it is currently the only approach capable of identifying peptides with post-translational modifications such as phosphorylation[107–109] or glycosylation.[110,111]

Despite the numerous advantages, this approach has several computational, technical, and analytical restrictions. The sample material required to perform this technique is very high, ranging from $5x10^7$ to $1x10^9$ cells per sample, preventing it from being applied to minimally available clinical samples.[92–95] While the quality of the peptide output may be high, the quantity of peptides identified is often low, even with large sample size. This method does not discover lowly abundant peptides.[92–95] These drawbacks are attributed to various technical factors, such as peptide loss during different stages of sample processing or computational restrictions.[92–95] One such limitation associated with MS-based immunopeptidome research has been addressed in Chapter 3 of this thesis. Nonetheless, MS-based immunopeptidomics has remained the finest quantitative technique available and has sparked great interest in biotechnology and pharmaceutical companies for the development of personalized cancer therapeutics.[112]

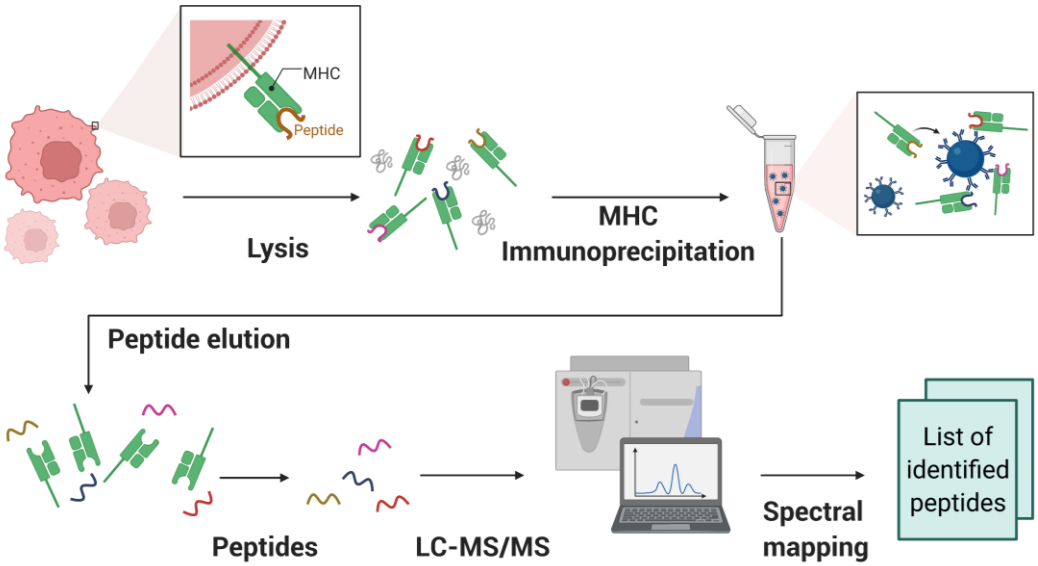


**Figure 1.6.** Mass spectrometry-based MHC peptide identification.

Top, MHC complexes are extracted from cell lysates by immunoprecipitation using MHC-specific antibodies. Bottom, Peptides are eluted from the isolated MHC complexes and analyzed using LC-MS/MS. Resultant MS spectra are mapped against a database to identify and generate the list of peptides. MHC: Major histocompatibility complex, LC-MS/MS: Liquid chromatography-tandem mass spectrometry, MS: Mass spectrometry. Figure made using Biorender.

### 1.3.5.2. Genomics and *in silico* predictions

The advent of next-generation sequencing (NGS) technologies and machine learning resulted in the rapid development of high throughput identification of MHC-I ligands.[113,114] Whole exome sequencing, whole-genome sequencing, and RNA

sequencing are commonly employed to generate sequence information on coding regions of DNA, coding and non-coding regions of DNA, or the RNA transcriptome, respectively. Whole exome sequencing is most commonly used to assess the mutations and the resultant neoantigens.[115] While RNA sequencing can offer mutation information, it is mostly used to acquire transcriptomic signatures of genes, indicating that they are turned on and can be a more effective strategy than DNA sequencing alone.[116] This method also allows identification of differentially expressed genes, thereby aiding the discovery of tumor-associated antigens. Finally, whole-genome sequencing provides a unique opportunity to characterize the noncoding regions consequently identifying cryptic peptides.[116] Upon collecting sequence information of mutated or abnormally expressed genes, they are translated into protein sequences which are then utilized to predict potential MHC-I ligands.[117]

Bioinformatics and *in silico* models of MHC-I peptides have advanced dramatically during the last decade, evolving into neural network-based prediction algorithms.[118–122] Over the years, experimental identification and analysis of peptides have provided critical information on peptide sequence, preferences of amino acid composition, stability, or half-life of complexes, all of which are utilized for training and constructing neural network models.[118–122] Prediction algorithms are either based on the structural information of peptide-MHC-I complexes, which has suffered greatly due to inaccurate predictions, or on sequence-based information, which is the most employed method and has produced efficient and accurate models for various MHC alleles.[118–122] Sequence-based models can predict the sequences of prospective MHC ligands and their affinity for the MHC molecule.[118–122] Numerous peptide prediction algorithms have been created, but the most common ones include NetMHC and SYFPEITHI.[123,124]

NetMHC[123,124] is used in Chapter 3 of this thesis and utilizes protein sequence and MHC allele information as inputs to generate a list of potential MHC ligands.

While this method of integrating genome sequencing with prediction algorithms may provide a more extensive mapping of peptides than the traditional mass spectrometry, there are two key issues. 1) This approach relies on prediction algorithms that contain inherent biases due to the different datasets used to train the neural network model. As a result, caution must be exercised when using this approach to discover unique peptides with distinct characteristics from the previously reported ones, such as cryptic peptides. 2) The presence of DNA or RNA sequence in cells is not representative of the presence of protein or relevant peptides and hence necessitates quantitative assessment in later stages.

Regardless of the technique utilized, both approaches only identify peptides that are bound to MHC complexes or have the capacity to bind the MHC molecules. The binding of a peptide to the MHC complex does not imply that it is immunogenic; therefore, experimental procedures must be used to validate relevant targets. Identifying these immunogenic antigens is essential to understand the molecular signature that defines the T cell specificity and to develop cancer immunotherapies such as cancer vaccines, discussed in section **1.4.3**. Overall, both antigen processing and presentation pathways as well as expression of MHC-peptide complexes play essential roles in cancer immunity and are associated with better immune responses and prognosis in multiple cancers.[125–130]

## 1.4. ENHANCING ANTICANCER IMMUNE RESPONSES

As the previous sections emphasized, recognition of cancer cells by the immune system is essential to mount productive anticancer immune responses and eliminate tumors. Despite evidence of immune infiltration at the tumor site in some tumors, the TILs and

the cancer immunity cycle are often dysfunctional, and the immune system fails to destroy the tumor. This is because clinically manifested tumors have evolved a variety of strategies to escape recognition by the immune system and disrupt the cancer immunity cycle, including **1**) evasion of recognition by T cells by reduced immunogenicity and loss of MHC-I antigen processing and presentation due to downregulated MHC-I molecules or defective antigen processing pathways, **2**) preventing T cell infiltration & function at the tumor site by forming abnormal blood vessels and fostering an immunosuppressive microenvironment, **3**) defective immune sensing pathways thereby evading T cell-mediated cancer cell killing, and 4) selective loss of targeted antigens.[131–133] As a result, one of the primary goals of cancer immunotherapies is to reverse these immune evasion mechanisms and restart the cancer immunity cycle. This section will briefly overview some of the major cancer immunotherapies developed to achieve these goals.

### *1.4.1. Immune checkpoint inhibitors*

Immune checkpoint molecules are co-inhibitory signaling molecules expressed on activated T cells that help regulate T cell hyperactivation, immune tolerance, and avoid autoimmunity.[134] However, cancer cells exploit these signaling mechanisms to cause T cell dysfunction and promote tumor survival. The monoclonal antibodies (mAb) which block the interactions of immune checkpoint molecules are called immune checkpoint inhibitors (ICIs). Programmed cell death 1 (PD-1) and Cytotoxic T lymphocyte antigen 4 (CTLA-4) are well studied in cancer immunity and are widely used targets for ICIs. Drs. James P. Allison and Tasuku Honjo were awarded the 2018 Nobel Prize in Physiology or Medicine for their respective research leading to these breakthroughs.[135]

The discovery of CD28-mediated T cell co-stimulation prompted the investigation for new immune regulators, which resulted in the discovery of CTLA4, a receptor on T cells with structural and biochemical similarities to CD28.[136–138] Unlike CD28, which is

highly expressed on conventional T cells, CTLA4 is expressed at a low basal level but significantly increases following antigen stimulation.[139] CTLA4 binds to the same ligands as CD28 (CD80 and CD86) but with a 20-fold higher affinity, outcompeting CD28, and inhibiting T cell activation.[140,141] CTLA4 activation in T cells also increases T cell mobility and decreases contact time with APCs, inhibiting the development of stable immunological conjugates between T cells and APCs.[142] CTLA-4 signals are effective during the priming phase of T cells and primarily occur in lymphatic tissues.[21,139]

PD-1 was initially discovered on T cells as a molecule involved in programmed cell death,[143] but later research revealed that it, like CTLA4, has coinhibitory functions.[144,145] PD-1 is expressed on T cells upon antigen stimulation and binds to its ligands PD-L1 and PD-L2, expressed on APCs or cancer cells.[146–149] These interactions of PD-1 with its ligands are referred to as the PD-1 axis. In contrast to CTLA-4, the PD-1 axis is active during the T cell effector phase, occurs mainly in peripheral tissues, and leads to T cell exhaustion.[149] Tumor cells increase the expression of PD-1 ligands to escape immune surveillance.[150,151] While both PD-1 and CTLA-4 have similar regulatory and inhibitory actions, they occur at different biological locations and times during the cancer immunity cycle and complement one another.

Preclinical findings[152] revealing that inhibiting CTLA-4 with antibodies might promote effective antitumor immune responses and lead to tumor regression inspired a new era of cancer therapeutics by using antibodies to release immune cell brakes to enhance anticancer immune responses.[153] Following clinical studies and efficacy assessments, ipilimumab, a CTLA-4 mAb, was approved by the U.S. Food and Drug Administration (FDA) as the first ICI for treating non-resectable stage III/IV melanoma due to its potential to boost T-cell activation and elicit long-lasting responses.[154–156] Similarly, blocking PD-1 or PD-L1 has been shown to enhance the cytotoxic ability of T

cells and induce tumor regression and has achieved remarkable clinical outcomes.[150,157] Consequently, the mAbs blocking the PD-1 axis (pembrolizumab and nivolumab) have been approved for various cancers such as melanoma, non-small cell lung carcinoma, head and neck squamous cell carcinoma, Hodgkin lymphoma, colorectal cancer, and urothelial carcinoma, amongst others.[158–161] Overall, PD-1 blockade has demonstrated a better and wider clinical utility than CTLA-4 blockade. In a clinical trial comparing pembrolizumab to ipilimumab, the former outperformed the latter in progression-free survival and overall survival while causing less high-grade toxicity in patients with advanced melanoma.[162–164] Moreover, combination ICI therapies targeting both CTLA-4 and PD-1 axis have demonstrated better clinical outcomes than either treatment alone, although associated with high toxicity.[155,165,166]

### *1.4.2. Adoptive T cell transfer therapy*

Adoptive cell transfer (ACT) therapy uses autologous or allogenic T cells, which are expanded *ex vivo* and reinfused into patients to target cancers. The initial demonstrations of the utility of this therapy involved TILs expanded *ex vivo* with IL-2 and reinfused along with large amounts of IL-2.[167] Later, this approach was combined with lymphodepletion prior to TIL transfer in melanoma, resulting in complete tumor regression in 20 out of 93 patients with 19 patients in complete remission three years after treatment.[168] While the initial successes drove the clinical utility of ACTs, due to the difficulty in obtaining effector antitumor T cells from the tumors, especially as many cancers lack TILs and the laborious isolation and expansion methods, alternative approaches, including genetically modified T cells were developed.[169]

Chimeric antigen receptor (CAR) T cell therapy utilizes T cells obtained from peripheral blood that are genetically modified to express immunoglobulin chains with intracellular signaling domains and antigen-binding domains to recognize specific

antigens or molecules expressed on the surface of cancer cells.[170] The advantage of using CAR T cells is that they bypass the MHC restriction of conventional T cells, therefore overcoming cancer evasion of T cell recognition by lack of MHC molecules or defects in antigen processing and presentation pathways.[170] Several developments in this field have resulted in multiple generations of CAR T cells with great clinical utility.[170]

Most notably, CAR T cells developed to target CD19, which is expressed by B cells, have demonstrated tremendous success in B cell malignancies, with objective and complete response rates of 82% and 54%, respectively, in patients with refractory large B cell lymphoma.[171] Similarly, CAR T cell therapy led to tumor remission in all treated B cell lymphoblastic leukemia (ALL) patients, with long-term complete remission in 83% of patients with a median follow-up of 29 months.[172,173] As a result of these successes, CAR T cells were approved to treat diffuse large B cell lymphoma and B cell ALL. Most recently, it was shown that CD19-directed CAR T cell therapy in patients with chronic lymphocytic leukemia led to decade-long remissions and persistent CAR T cells identified ten years post-treatment.[174] While CAR T cells have shown enormous potential in leukemias and lymphomas, they have had limited success in solid tumors due to poor infiltration.[175–177] Furthermore, this therapy generates a range of side effects, the most serious of which being cytokine release syndrome and neurotoxicity.[170] Various efforts have been made to prevent or mitigate these toxicities, including modification of CAR T cells and combination of CAR T cells with other therapies.[178,179]

### *1.4.3. Cancer vaccines*

Vaccines traditionally used for infectious diseases have become attractive therapeutic approaches for cancer due to their ability to induce antigen-specific immune responses. Two types of cancer vaccines are employed clinically, prophylactic or preventive cancer

vaccines and therapeutic cancer vaccines.[180] Preventive vaccines include vaccines against cancer-causing viruses such as hepatitis B (HBV) in liver malignancies and human papillomavirus (HPV) in cervical and HPV positive oral cancers.[180] These vaccines have been clinicaly successful in preventing the infection by oncogenic viruses and reducing the incidence of their associated cancers.[180–184] Therapeutic vaccines are vaccines administered upon cancer incidence to expose the immune system to cancer antigens, initiate the cancer immunity cycle, and eliminate cancer cells.[185]

Historically, therapeutic vaccines were created by combining autologous cancer cells from patients with viruses such as Newcastle disease virus (NDV) or adjuvants to stimulate cancer-specific immune responses in metastatic T lymphoma and metastatic melanoma.[186,187] These resulted in the activation of anticancer immune responses, prolonged survival in mice, and reduced metastatic tumor burden.[186,187] Such early studies prompted the clinical investigations of autologous vaccines for various cancers, leading to FDA approval of Sipuleucel-T for prostate cancer.[188] Despite some successes, the clinical translation has been challenging, mainly due to limitations with obtaining tumor specimens, poor immunogenicity, and long and inconsistent production processes.[21,189,190] Similarly, allogeneic vaccinations, which utilize established human cancer cell lines were developed.[190] While these vaccines could provide a limitless supply for tumor antigens and produce reliable outcomes, they have been ineffective mainly due to the extensive intratumoral heterogeneity, misrepresentation of tumor antigens compared to autologous tumors, and non-effective allo-HLA-specific immune responses.[185,191] These challenges inspired the development of newer approaches for generating personalized cancer vaccines.

As mentioned in section **1.3.5**., the recent evolution of mass spectrometry and next-generation sequencing technologies shifted our ability to detect tumor mutations,

aberrantly expressed genes, and the corresponding TAAs or TSAs. This allowed the exploration of personalized peptide-based vaccinations, wherein multiple mutated peptides with high affinity to HLA molecules are administered along with adjuvants.[192,193] A phase I clinical trial in patients with metastatic melanoma showed that the vaccination with multi-peptide based vaccine targeting up to 20 neoantigens resulted in induction of polyfunctional CD4+ and CD8+ T cells, which could identify the autologous tumor and differentiate between the mutated and wildtype antigens.[194] Four out of six patients were disease-free at 25 months post-vaccination, and the remaining two patients showed complete regression upon additional treatment with ICI.[194] Long term evaluation of these patients showed persistence of neoantigen-specific T cell responses exhibiting memory phenotype and epitope spreading, with all six individuals surviving four years following vaccination.[195] Phase I clinical trials in glioblastoma patients with TSA peptide vaccines or a combination of TAA and TSA peptides resulted in increased TILs and induction of CD4+ and CD8+ T cell responses, with enriched CD8+ memory phenotypes.[196,197] Similar study with personalized RNA vaccine showed induction of T cell infiltration and antigen-specific T cells, which could kill autologous melanoma tumor cells.[198] While the clinical investigations of such personalized cancer vaccines are still in the beginning stages, these findings provide a promising future for their therapeutic applications.

### *1.4.4. Oncolytic viruses*

The historical development of cancer immunotherapies began with observations of therapeutic prognosis associated with acute infections of cancers, as outlined in section **1.1**. Those early findings led to the development of oncolytic viruses (OVs), which can selectively infect and replicate in malignant cells while leaving normal cells unharmed.[199] OVs destroy cancer cells through direct oncolysis, vascular collapse, and

inducing antitumor immune responses.[199,200] OVs have been shown, in preclinical models, to reverse cancer immune evasion strategies and induce the cancer immunity cycle by inducing antigen processing and presentation, expression of MHC molecules on cancer cells, release of tumor antigens by direct cell killing, and creating an inflammatory response which increases immune cell infiltration at the tumor site.[201–204] Due to these multimodal strategies, OVs have emerged as an effective therapeutic option against multiple cancers.[205]

Various viruses, including adenovirus, herpes simplex virus (HSV), measles virus, reovirus, and Newcastle disease viruses, have been utilized as OVs, either in their naturally occurring form or by genetically engineering them to selectively target tumor cells and enhance immune responses by expressing tumor-specific molecules or immunomodulating factors.[205,206] Several promising preclinical studies led to clinical investigations that resulted in the FDA approval of the first OV, Talimogene laherparepvec (T-VEC), an attenuated HSV-1 expressing granulocyte-macrophage colony-stimulating factor (GM-CSF) for the treatment of unresectable recurrent melanoma.[207] In patients bearing stage III and IV unresectable metastatic melanoma, treatment with T-VEC resulted in a durable response rate of 16.3% and an objective response rate of 31.5% compared to 2.1% and 6.4%, respectively, in patients treated with GM-CSF alone.[208] A recent retrospective study based on data from 10 melanoma centers in 3 countries showed an overall response rate of 63.7%, with 43.2% of treated individuals showing a complete response.[209] Despite promising preclinical findings, many OVs fail to demonstrate robust antitumor activities in clinical investigations due to limitations in viral delivery and penetration of the tumor site, off-target infections, resistance in the TME, and antiviral immune responses that clear the virus.[210,211]

## 1.5. IMMUNOGENIC CELL DEATH OF CANCER

Beyond the cancer immunotherapies outlined in section **1.4.**, inducing immunogenic cell death (ICD) of cancer has recently been identified as one way to overturn tumor immune evasion and generate effective cancer immunity. Cell death is a physiological process that occurs regularly and is essential to maintain whole-body homeostatic function.[80,212] This process of steady-state turnover of healthy tissues includes the death of 50-70 billion cells daily, is tolerogenic, and results in non-inflammatory clearance of dead cells by phagocytic cells [**Figure 1.7**].[80,212] While this physiological cell death is an immunologically silent event, in the context of pathologies such as cancer and infections, other mechanism of cell death can trigger immunostimulatory events leading to activation of the adaptive arm of the immune system. In this context, a successful cell death-induced immune response can not only clear the cancer cells or the pathogen but also generate long-term immunity against them. This form of immunostimulatory cell death is termed 'immunogenic cell death'.[80,212] ICD is a regulated form of cell death that occurs with certain cancer therapies or infections and is characterized by a precise series of molecular events involving changes in cell surface molecules and the release of soluble mediators, which interact with and activate immune cells [**Figure 1.7**].[80,212]

Originally realized in the context of certain chemotherapeutics, the discovery of ICD has transformed our understanding of cancer therapeutics.[80,212] Chemotherapies are historically thought to be highly cytotoxic and immunosuppressive therapies; however, the discovery of ICD in the past decade led to a reassessment of the impact of these chemotherapies. Studies have shown that certain chemotherapeutics, not all, have the potential to induce ICD and associated antitumor immune responses.[80,212] Similarly, several other therapies and pathological events have been characterized for their ICD

inducing capabilities, leading to the identification of different forms of ICD, each characterized by a unique set of hallmarks.[80,212]

Broadly, immunogenicity in the context of ICD depends on the combination of antigenicity and adjuvanticity of the dying cancer cells, which influence host immune cells to induce antigen-specific immune responses.[80,212] This section will discuss antigenicity and adjuvanticity, focusing on established hallmarks of ICD, in vivo validation of ICD, ICD-mediated anticancer immune responses, and clinical relevance of ICD.

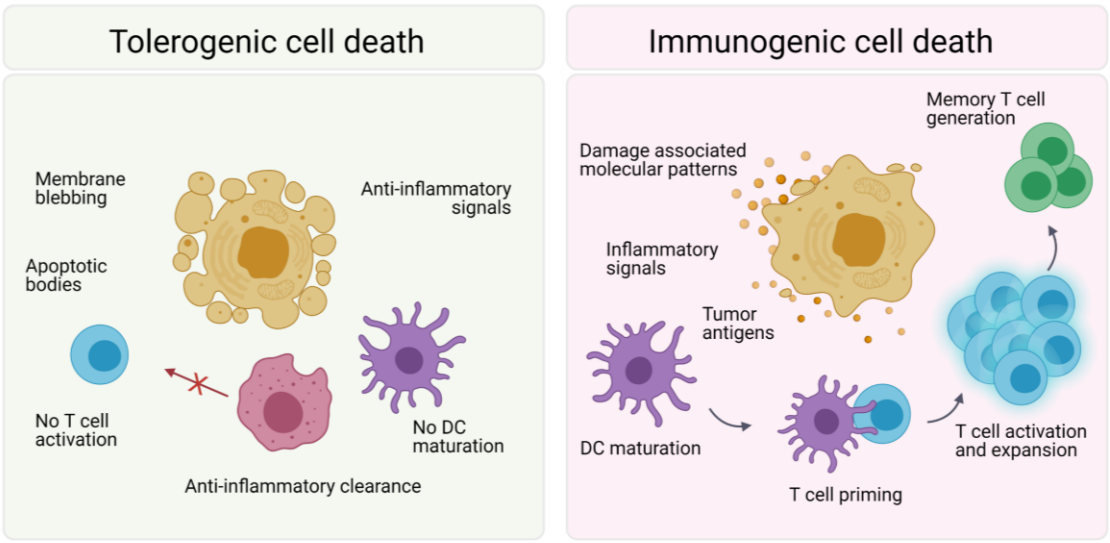


**Figure 1.7.** Tolerogenic vs. immunogenic cell death.

Left, Tolerogenic cell death causes membrane blebbing, apoptotic bodies, and anti-inflammatory signals that result in anti-inflammatory clearance of dead cells by phagocytic cells without activating the immune response. Right, Immunogenic cell death, on the other hand, causes the production of DAMPs and tumor antigens, which produce an inflammatory milieu and drive immune cell infiltration and activation, culminating in

the development of long-lasting immunity. DC: Dendritic cell, DAMPs: Damage associated molecular patterns. Figure made using Biorender.

### *1.5.1. Antigenicity*

Antigenicity is conferred by the expression and presentation of MHC or HLA antigens, which are not covered by central tolerance and can elicit T cell response. These antigens can be derived from internal proteins formed from carcinogenesis or external sources such as viral proteins involved in carcinogenesis, which are deemed foreign and hence capable of inducing antigen-specific immune responses.[212] The different types of tumor antigens and their sources are explained in section **1.3.4**.

Cancer antigens from dying cells associated with enhanced adjuvanticity (section **1.4.2**) are phagocytosed by DCs, processed, and cross-presented to T cells to activate antigen-specific immune responses. While most ICD inducers are expected to have little effect on antigenicity, studies have demonstrated the ability of some to boost antigenicity. These include treatments that can induce mutations, modulate the proteosome processing machinery, reactivate endogenous retroviruses, and/or induce expression of TSAs or TAAs, such as radiation therapies, DNA damage response inhibitors, oncolytic viruses, HDAC inhibitors, photodynamic therapies (PDT), and epigenetic regulators.[213–227] For example, treating patients with ICD-inducing 5-Aminolevulinic acid (ALA)-PDT increased the reactivity towards basal cell carcinoma-associated tumor antigen and increased systemic immune responses compared to the cohort with surgical removal.[226,228] Similarly, we recently showed that oncolytic reovirus could induce the processing and presentation of immunogenic TAAs in mouse ovarian cancer and sarcoma models, thereby modulating the antigenicity.[224,225] On the contrary, a recent study from the Kroemer group showed that treatment with autophagy and

polyploidization resulted in the induction of ICD adjuvanticity but had no effect on cancer cell antigenicity.[229] Regardless of whether ICD inducers contribute to modifying existing antigenicity, antigens released from dying cells in the presence of significant adjuvanticity contribute to the generation of anticancer immunity and immunological memory.[229] Furthermore, ICD can induce MHC expression and antigen processing and presentation pathways in cancer cells.[230–234]

### *1.5.2. Adjuvanticity (Damage associated molecular patterns)*

Stressed and dying cells initiate a cascade of intracellular responses that mediate ICD, relaying danger signals in an attempt to maintain the systemic homeostasis.[235] Investigation of these events following the cell death induced by cancer treatments identified several molecular and metabolic signals, whose critical role in immunogenicity of ICD has been established by mechanistic studies.[80,212] These danger signals from dying cells are collectively termed damage-associated molecular patterns (DAMPs) and contribute to the adjuvanticity of ICD. DAMPs are endogenous molecules with predominantly non-immunological functions under normal conditions that acquire immunomodulatory properties when exposed or secreted by dying cells.[236–240]

DAMPs elicited by ICD are spatiotemporally regulated [**Figure 1.8**] and are detected by various pattern-recognition receptors (PRR) of innate and adaptive immune cells, creating a proinflammatory state and driving therapeutically relevant anticancer immunity.[80,212,241] While DAMPs are present in most cells, their spatiotemporal exposure/ release kinetics and intensity of exposure or release are regulated by the intracellular stress responses caused by ICD inducers, which determines the outcome of anticancer immunity.[80,212] Many DAMPs associated with ICD have been discovered over the years, with considerable variation depending on ICD inducers and cell types.[212] Of these, the most significant DAMPs, also known as hallmarks of ICD, include 1. ER

stress and exposure of ER chaperones such as Calreticulin (CALR), 2. Release of Adenosine triphosphate (ATP), 3. Release of High mobility group box 1 (HMGB1), and 4. Viral mimicry associated type I IFN signaling.[80]

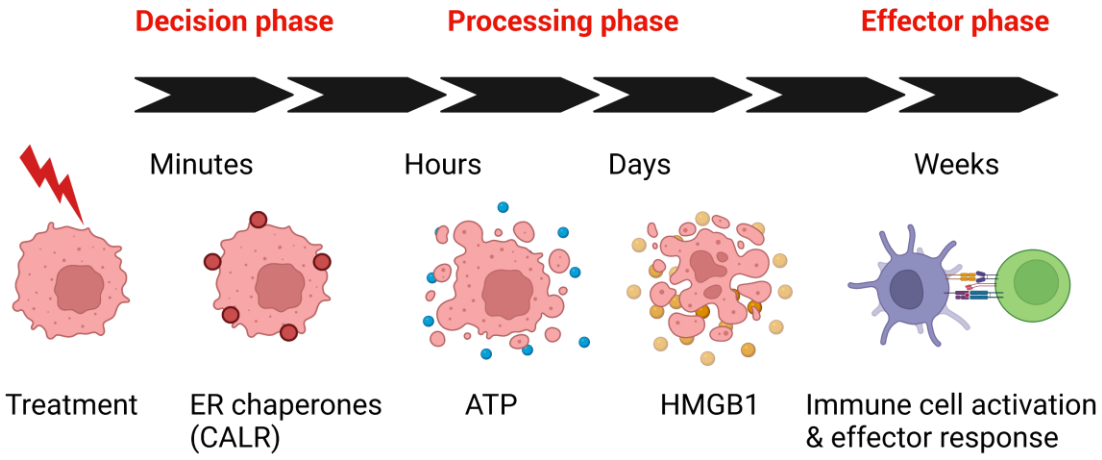


**Figure 1.8.** Spatiotemporal DAMPs secretion upon ICD.

ICD involves the spatiotemporal regulation of the decision and processing phases, eventually leading to the effector phase of immune system activation. The figure depicts the order of hallmark DAMPs induced during the process. ICD: Immunogenic cell death, DAMPs: Damage associated molecular patterns, ER: Endoplasmic reticulum, CALR: Calreticulin, ATP: Adenosine triphosphate, HMGB1: High mobility group box 1. Figure made using Biorender.

### 1.5.2.1. ER chaperones: calreticulin and heat shock proteins

Calreticulin is an endoplasmic reticulum chaperone protein involved in various cellular homeostatic processes. In a normal state, it functions as a calcium ion ($Ca^{2+}$) buffer and

supports $Ca^{2+}$-dependent processes, as well as facilitating proper protein folding and preventing premature export of misfolded proteins from the ER to the Golgi apparatus.[242] In response to ICD mediated ER stress and unfolded protein response (UPR), CALR is transported from ER to the cell surface membranes of dying cells, where it acts as an 'eat-me' signal for APCs.[242,243] In some cases, such as photodynamic therapy and chemotherapeutics, therapy-induced ER stress-CALR exposure and dependent on the formation of reactive oxygen species (ROS).[244–247]

Surface translocation of CALR usually occurs before the exposure of phosphatidylserine on the outer leaflet of the plasma membrane and is temporally essential for cell death to be perceived as immunogenic.[244,245] While phosphatidylserine also acts as an eat-me signal, in the absence of CALR, it mediates tolerogenic clearance of apoptotic cells.[248,249] CALR on the cell surface binds to LDL-receptor-related protein 1 (LRP1, also known as CD91), an ER chaperone-sensing PRR expressed by APCs such as DCs.[244] The CALR-LRP1 interaction causes the engulfment of dying cancer cells and associated antigens by DCs, resulting in the initiation of antigen-specific cancer immunity cycle.[212] Hence, CALR exposure is considered a pre-apoptotic event and the first step in the ICD initiation process.

Calreticulin exposure is one of the key features of ICD, and its involvement in many types of ICD has been demonstrated, as preventing CALR surface exposure abrogates ICD.[212] Similarly, despite identical cell death and molecular processes, cisplatin fails to induce UPR and CALR translocation, whereas oxaliplatin does. [250] As a result, cisplatin-treated cells fail to produce anticancer immune responses, but oxaliplatin-treated cells do so effectively.[250] In this context, combining cisplatin with a UPR inducer such as thapsigargin or tunicamycin effectively restores CALR translocation and immunogenicity of cisplatin-elicited cell death, supporting its role in

ICD.[251] Furthermore, recombinant CALR surface adsorption restored the prophylactic power of CALR-depleted cells and induced ICD *in vivo*, showing the importance of its activity at the cell surface.[243,252]

CALR has also been linked to several immunological and immunostimulatory roles aside from its involvement as a pro-phagocytic molecule in ICD. CALR plays a critical role in the antigen presentation pathway by stabilizing the MHC-I peptide loading complex.[253] CALR maintains steady-state levels of TAPBP and MHC-I heavy chains while retrieving sub-optimally formed MHC class I from post-ER compartments.[254,255] High levels of CALR have been associated with T cell anticancer immunity and enhanced NK cell effector capabilities against AML, which rely on CD11c+ $CD14^{high}$ myeloid cells expressing maturation markers.[256] CALR expression on AML cells activated the host type I IFN pathway required for the CALR-mediated survival and anticancer immunity.[256,257]

Other ER chaperones, such as heat shock proteins HSP70 and HSP90, are also reported in ICD. HSP70 and HSP90 are engaged in cytoprotective tasks intracellularly, but upon ICD induced ER stress, they translocate to the cell surface, where they interact with LRP1 and act as eat-me signals for DCs.[212] One of the earliest studies linking HSPs and ICD emerged from the observation that induction of HSPs in response to cell death was associated with increased tumor immunogenicity of dying cells and tumor clearance *in vivo*.[258] Later studies have identified exposure of HSPs in different forms of ICD such as hypericin-based PDT, chemotherapy, and radiation therapy.[259–263] Blocking HSP70 and HSP90 hindered DC activation and lowered the anticancer effectiveness of treatment-induced ICD in different animal models.[259,260,263] HSPs have a variety of immunomodulatory roles, including APC activation, maturation, and phagocytosis, as well as the activation and induction of NK and CD8+ T cell responses.[264–270] While

HSP70/90 exposure has been identified in some cases of ICD, its necessity in the process has not been well characterized and is hence considered a ‘bystander’ and not a major hallmark.

### 1.5.2.2. Adenosine triphosphate

Adenosine triphosphate is a key molecule involved in the bioenergetic metabolism of all cellular compartments in the body and is often referred to as the energy currency of the cell.[271] While ATP serves many physiological functions inside a cell, ATP secreted extracellularly functions as a potent signal transducer.[241,271] Extracellular ATP availability and function are balanced by degradation by cells via Ecto-ATPases.[241,271] ATP release from dying cancer cells has been identified as one of the major hallmarks in the context of a variety of ICD inducers.[80,212,272,273]

ATP secretion can occur via various mechanisms.[274] An autophagy-dependent pathway has been shown to be the main player in most instances of ICD.[275,276] Pharmacological or genetic interventions aimed at lowering or activating autophagy in cancer cells have been associated with decreased or enhanced ATP secretion.[275,277–279] In a few treatments, such as hypericin-based PDT, an autophagy in-dependent ATP secretion mechanism has been reported.[280]

In the extracellular milieu, ATP mediates two main functions: 1. It acts as a “find me” signal, facilitating the recruitment of myeloid cells and DC precursors to the sites of ICD via the purinergic receptor P2Y2 (P2RY2).[281,282] 2. It induces proinflammatory effects by activating the NLRP3-dependent CASP1 inflammasome in DCs, resulting in IL-1β and IL-18 secretion upon binding to the purinergic receptor P2X 7 (P2RX7).[283] ATP released by dying cancer cells recruits DC precursors to the site of ICD, that mature upon ATP-driven inflammasome activation, then recruit and prime adaptive immune cells

such as CD8+ T cells and IL-17 producing γδ-T cells, which are required for optimal anticancer immune responses.[212,284] Therefore, ATP release upon ICD facilitates the link between the innate and adaptive arms of the immune system and associated responses. These effects of ATP are essential for effective activation of tumor-specific immune responses in ICD as demonstrated by studies in *P2ry2*$^{-/-}$[281], *P2rx7*$^{-/-}$[285], *CASP1*$^{-/-}$[285], and *Nlrp3*$^{-/-}$[285] mice, which could not mount adaptive immune responses. Furthermore, early recruitment of myeloid precursors into the TME is prevented in the absence of ATP secretion, presence of purinergic receptor inhibitors, or ATP degrading molecules such as CD39.[286,287] Extracellular ATP has also been demonstrated to deplete immunosuppressive P2RX7+ M2-like TAMs in the TME by inducing pyroptosis and promoting T cell-mediated antitumor immunity.[288]

### 1.5.2.3. High mobility group box 1

High mobility group box 1 is a nonhistone chromatin-binding protein ubiquitously found in the nucleus of all cells. Under steady-state, it is involved in a variety of nuclear processes such as gene transcription, DNA repair, and the stabilization of nucleoprotein complexes.[212,289] Upon ICD, HMGB1 is secreted into the extracellular space, similar to ATP, where it functions as a pro-inflammatory molecule.[290] Release of HMGB1 requires permeabilization of both nuclear and plasma membranes, resulting in the transport of HMGB1 from the nucleus to the cytoplasm and eventually into the extracellular environment.[212] As a result, this is classified as a post-mortem event that occurs during the later stages of ICD.

The immunomodulatory potential of extracellular HMGB1 seems to be largely dependent on its redox state, with the reduced form facilitating potent pro-inflammatory activities.[291,292] HMGB1 can bind to multiple PRRs expressed on myeloid cells such as

TLR4, TLR2, and advanced glycosylation end-product-specific receptors (AGER, also called RAGE).[212,291] In the context of ICD, knockout studies have revealed that only HMGB1-TLR4 signaling via the MYD88 immune signal transduction adaptor is required for cell death to be perceived as immunogenic.[293]

HMGB1 mediated TLR4 stimulation of DCs is essential for DC activation and maturation by enhancing phagocytic, antigen processing, and presentation pathways resulting in anticancer immune responses.[212] In cancer cells with low or RNAi-depleted HMGB1, TLR4 agonist administration rescued the ICD-mediated anticancer immune response.[294] This also suggests that TLR4 stimulation without the ligand (HMGB1) may be sufficient to activate DCs. HMGB1 also synergizes with ATP to induce IL-1β release by DCs, and antibody blockade of HMGB1 in this context inhibited IL-1β production by DCs.[285] In addition to these functions, HMGB1 can interact with CXCL12 and recruit immune cells to sites of inflammation.[295] Overall, HMGB1-TLR4 axis-mediated DC activation is critical for ICD-elicited immunogenicity.

#### 1.5.2.4. Type I interferon signaling

Interferons (IFNs), a family of cytokines, have long been utilized to treat a variety of cancers even before their mechanism of action was discovered.[296,297] Activation of type I IFN mediated signaling pathways by microbial ligands has been extensively studied.[298–300] In the last decade, studies have confirmed the role of type I IFNs (IFNα/ IFNβ) in the context of cancer therapy mediated ICD, where endogenous or exogenous nucleic acids from dying cancer cells induce IFN signaling in a viral mimicking pattern.[241,301–303]

ICD-mediated IFN signaling is initiated by activation of endosomal TLR3 via RNA[303,304] or cyclin GMP-AMP synthase (cGAS) / signal transducer stimulator of IFN

response cGAMP interactor 1 (STING or STING1) via cellular DNA.[305–307] IFNs bind to IFNα or IFNβ receptors (IFNAR/ IFNBR) on cancer cells and trigger autocrine and paracrine signals leading to the production of a cascade of interferon-stimulated genes (ISGs) such as CXCL10 and IFIT1.[303] Dying cancer cells showed reduced immunogenicity *in vivo* when *Tlr3*, *Ifnar1*, *Ifnar2* genes were absent or when IFNAR1-neutralizing antibody was present.[303] In this model, the addition of exogenous type I IFNs or recombinant CXCL10 restored the immunogenicity of ICD, confirming the importance of the signaling cascade.[303] Furthermore, nucleic acids derived from dying cancer cells can mediate immunostimulatory effects in DCs by activating type I IFN production.[308,309] Exogenous addition of type I IFN rescued the DC cross-presentation in cGAS/ STING deficient DCs, indicating the relevance of cGAS/ STING signaling for ICD-mediated immune responses.[309] Additionally, degradation of nucleic acids has been shown to diminish immunogenicity of ICD mediated by DCs and T cells.[310,311]

Acute and robust type I IFN responses mediate potent immunostimulatory effects by interacting with homodimeric or heterodimeric receptors on diverse immune cells.[296,298,312,313] Following the engulfment of dying cancer cells, IFNs boost DC activation and survival, as well as antigen cross-presentation, leading to CD8 T cell cross-priming.[80,212,296,314] IFNs also enhance the cytotoxic functions of CD8 T cells and NK cells.[315,316] Moreover, type I IFNs stimulate the secretion of pro-inflammatory mediators by macrophages and inhibit immunosuppressive Tregs.[317,318] CXCL10, produced via IFN signaling, acts as a chemoattractant for T cells and neutrophils alone or in conjunction with CXCL1 and CCL2 and has been linked to neutrophil-mediated cancer immunity with some inducers of ICD.[303,319]

While the above-reported hallmarks have been identified in various scenarios and forms of ICD, not one of them or a combination of them is sufficient to induce ICD.

Ultimately, these hallmarks work in cohesion with the antigenicity of ICD to induce anticancer immunity. This concept is explained in the next section, 1.4.3.

In conclusion, antigenicity and spatiotemporally regulated adjuvanticity (DAMPs) of ICD-induced dying cancer cells interact with and initiate a cascade of innate and adaptive immune responses: 1. ‘find me signal’ ATP initiates DC recruitment and activation at the site of ICD via interactions with P2RX7 and P2RY2, 2. ‘eat me signals’ CALR/ HSP70/ HSP90 trigger cancer cell phagocytosis and antigen uptake by DCs via interactions with LRP1, 3. HMGB1, ATP, and type I IFNs promote DC maturation and cross-presentation via interactions with TLR4 and IFNAR, respectively, and 4. facilitate recruitment and activation of T cells via CXCL10 and other cytokines. Together, these events result in the initiation of the cancer immunity cycle and long-lasting antigen-specific immune responses [**Figure 1.9**].

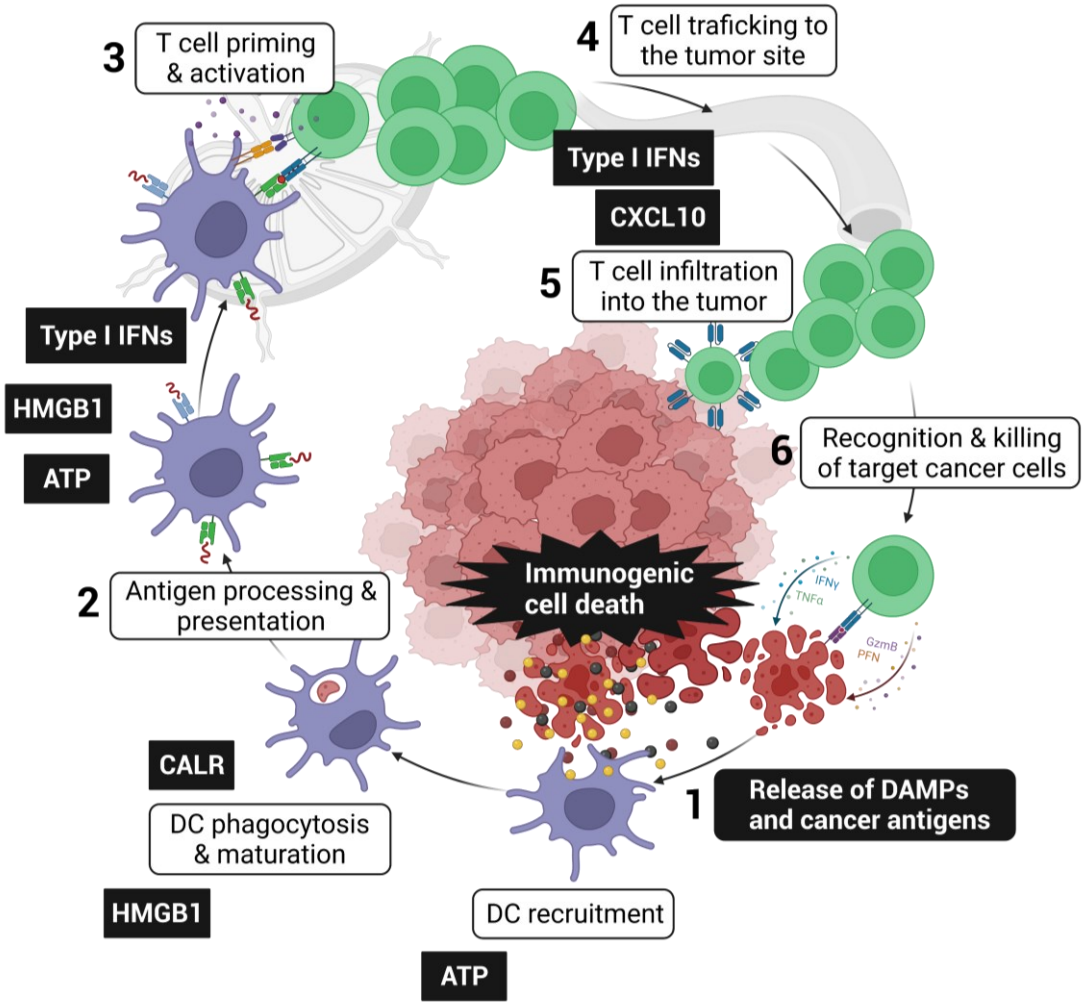


**Figure 1.9.** Immunogenic cell death and cancer immunity cycle.

Cancer cells emit various DAMPs in response to ICD inducers, which interact with immune cells and promote distinct stages of the cancer immunity cycle. The primary events connected with ICD are illustrated in black boxes, whereas the events in the cancer immunity cycle are depicted in white boxes, demonstrating their coordination. ICD: Immunogenic cell death, DAMPs: Damage associated molecular patterns, CALR: Calreticulin, ATP: Adenosine triphosphate, HMGB1: High mobility group box 1, IFNs: Interferons, DC: Dendritic cell. Figure made using Biorender.

### *1.5.3. Gold standard approach to validate ICD*

Both antigenicity and adjuvanticity, as previously stated, are critical components of ICD-mediated anticancer immune responses, and several hallmarks have been identified in the context of ICD. Assessing these *in vitro* hallmarks will provide crucial information at the molecular level, allowing researchers to perform large-scale therapeutic screens, uncover prognostic or predictive markers, devise multimodal regimens, and improve therapy success. However, none of the discovered DAMPs, alone or in combination, can predict the immunogenicity of cell death *in vivo*, implying that there are unknown ICD-related DAMPs and molecular events that need to be investigated. For example, cardiac glycoside digoxin generated signature DAMPs in mouse MCA205 fibrosarcoma cells *in vitro* but had a poor impact against tumor growth suppression *in vivo*.[320] In the same model, combining digoxin with a non-ICD producing chemotherapeutic enhanced treatment efficacy relative to either treatment alone, demonstrating that factors other than DAMPs influence *in vivo* efficacy.[320] Thus, biochemical analysis of different hallmarks is insufficient to identify whether a treatment promotes ICD. Furthermore, because ICD ultimately results in anticancer immunity that also includes antigenicity, *in vivo* vaccination experiments in immunocompetent models are used to determine the immunogenicity of cell death.

Briefly, cancer cells treated with a cancer agent are injected into immunocompetent syngeneic mice.[321] These vaccinated mice are then challenged with living cancer cells of the same kind.[321] If the treatment agent of choice is an ICD inducer, the dying cells would be immunogenic, and vaccination with these cells would activate immune responses against the cancer antigens.[321] As a result, the immune system can recognize, fight, and eliminate tumor cells when challenged, resulting in tumor-free mice.[321] On the other hand, if the therapeutic agent of choice is not an ICD

inducer; the vaccination with dying cells will fail to generate an efficient immune response, and animals will develop tumors when challenged.[321] The absence of tumor growth and the percentage of tumor-free mice in these experiments provide a reliable estimate of immunogenicity.[321]

Recent studies (including ours in Chapter 5) have confirmed the importance of performing *in vivo* vaccination experiments to identify bonafide ICD. Mouse G69 bladder cancer cells treated with gemcitabine released all hallmark DAMPs but failed to induce protection *in vivo*.[322] In this study, the authors detected an inhibitory DAMP that, when blocked, rescued gemcitabine's *in vivo* ICD properties. Therefore, as we discover more immunostimulatory or inhibitory DAMPs involved in different immunological pathways, it is essential to perform vaccination experiments to validate ICD. This is especially important when testing novel therapies, the distinctive ICD hallmarks of which may be unknown. However, this technique has a limitation; it cannot be used to verify ICD in human cancer models, which will continue to rely on *in vitro* hallmark identifications until better humanized mouse models are developed.

### *1.5.4. Clinical relevance of ICD*

Consistent with effects in preclinical models, a vast amount of clinical literature suggests the importance of various DAMPs in determining the disease outcome. Treatment with ICD-inducing oxaliplatin improved the overall as well as progression-free survival in colorectal cancer patients with normal TLR4 but not in patients with loss-of-function TLR4 (NCT00126256).[232,323] There was no difference in patients who did not get chemotherapy, irrespective of their TLR4 status. Loss-of-function polymorphisms in TLR4 have also been associated with unfavorable disease outcomes in breast cancer, melanoma, and head and neck squamous cell carcinoma patients.[241,293,324–326] Similarly, the absence of HMGB1 staining in anthracycline-treated breast cancer tumors was

correlated with poor overall and progression-free survival in these patients,[327] highlighting the importance of the HMGB1-TLR4 axis in cancer prognosis. Low levels of calreticulin have been associated with advanced disease stages in urothelial carcinoma patients.[328] In contrast, higher expression was associated with improved disease outcomes in multiple cancers such as colorectal cancer, glioblastoma, neuroblastoma, ovarian cancer, osteosarcoma, AML, and non-small cell lung carcinoma.[252,329–335] Furthermore, high CALR levels were correlated with several parameters of anticancer immunity such as intratumoral infiltration by DCs, memory T cells, antigen-specific T cells, NK cells, and CD4+ Th1 cells, in different cancer models.[256,329,332,333,335,336] Likewise, loss of function polymorphisms in P2RX7, the receptor of ATP, have been associated with poor clinical outcomes in a variety of malignancies.[271,285,337–340] Bortezomib, a proteasome inhibitor, has recently been demonstrated to induce ICD in human and animal models of multiple myeloma (MM). Moreover, bortezomib enhanced transcriptional expression of the "ICD signature," which consists of 90 immune-related genes, has been linked to a better clinical outcome in MM patients.[341,342] It is worth noting that 57 of the 90 genes were classified as interferon-stimulated, showing that bortezomib activated ICD via type-I IFN response in MM cells.[341,342] These findings point to the importance of DAMPs and related pathways in determining the clinical outcome of cancer patients.

Although there is abundant evidence for the function of ICD and related immunological responses in preclinical models and correlative evidence of the role of DAMPs in determining clinical prognosis in some malignancies, the mechanistic contribution of ICD processes in a clinical setting remains unclear. The relationship between ICD induction and treatment efficacy in clinical settings has been difficult to establish for various reasons. For instance, DAMP identification using expression levels

in the tissues does not necessarily correlate with secretion, as demonstrated in preclinical models of ICD in a spatiotemporal manner.[241,343] Similarly, lack of understanding of clinically applicable systemic biomarkers; ICD's reliance on various host factors such as intact signaling pathways, the absence of immune evasion mechanisms, TME, and the functional status of immune cells; the relevance of different DAMPs in different therapies; and restrictions on the availability of tumor samples for follow up studies - all contribute to the difficulties in understanding ICD clinically.[241,343] Nevertheless, there is a growing interest in filling these knowledge gaps. Hundreds of clinical trials are now focused on studying the induction of ICD by cancer therapies such as chemotherapies and radiation therapies, either alone or in combination with other immunotherapeutic strategies.[232,343,344] Importantly, many clinical reports have indicated that ICD-induction by immunogenic chemotherapies sensitizes tumors to combination therapy with checkpoint inhibitors,[345] supporting the clinical significance of ICD and paving the way to optimize and design better combination therapies with ICD inducers.

## 1.6. PHOTODYNAMIC THERAPY OF CANCER

Given the evolution of cancer therapeutic strategies from tumor-centric to immune-focused, the ideal therapy is one that can destroy the malignant cells while also generating protective antitumor responses. Photodynamic therapy provides a desirable option due to its ability to destroy cancers by implementing dual functionalities.[346] PDT is a minimally invasive clinically approved therapeutic modality, which utilizes a light activatable chemical compound known as photosensitizer (PS), light, and molecular oxygen.[347–349] The photochemical reaction between these three usually harmless components results in the generation of molecules such as reactive oxygen species, that can kill the cancer cells [**Figure 1.10**]. While the precise mechanism of activation and action varies, the general principle of PDT is that illumination of the PS leads to

absorption of a photon that promotes the PS to its excited singlet state, which is energetically unstable. The PS returns to its ground state from this unstable and usually short-lived state by converting energy into heat or fluorescence.[347–349] Alternatively, PS from a singlet state can transition to a longer-lived, more stable triplet state. While returning to the ground state, PS transfers its energy to create chemically reactive species, such as superoxide anion radicals, which is considered a type I reaction, or singlet oxygen, considered a type II reaction.[347–349] The products of type I and type II reactions, singlet oxygen and superoxide anions, initiate a cascade of biochemical events that lead to oxidative damage and death of cells, contributing to PDT's therapeutic potential.[347–349] In general, type II reactions are most commonly observed.

References to therapeutic usage of light and PDT were made thousands of years ago in ancient Egyptian, Chinese and Indian literature.[347,350] The idea of using PDT for treatment considered the modern era of PDT began over a century ago, with the discovery of cell death triggered by a combination of chemicals and light that varied depending on the amount of exposure to light. The first PS used in humans was haematoporphyrin, a mixture of porphyrins derived from haemoglobin.[347,350] The purified haematoporphyrin derivative, Photofrin (also known as Porfimer sodium), accumulated in tumors and reduced tumor growth in preclinical and clinical studies. These findings resulted in the first clinical approval of PDT for the treatment of bladder cancer, in Canada, in 1993, followed by approval from the food and drug administration (FDA) in 1995.[349,351]

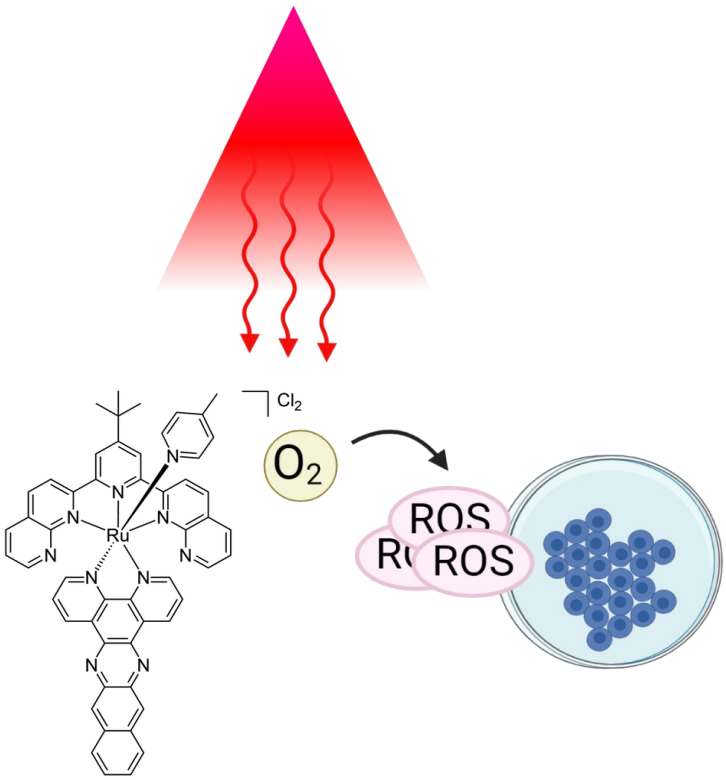


**Figure 1.10.** Photodynamic therapy reaction.

Photodynamic reaction involves the interaction of photosensitizer with a light of a specific wavelength in the presence of molecular oxygen and results in the formation of reactive oxygen species (ROS). Figure made using Biorender.

### *1.6.1. Photosensitizers*

Photosensitizers are mainly classified into three generations based on their evolution. Photofrin is considered a first-generation PS that has been most widely studied. Despite this and the clinical approval, it failed to become a mainline treatment due to concerns such as the requirement of high doses of PS to achieve therapeutic efficacy, prolonged

skin phototoxicity, poor tissue selectivity, and compromised bladder function.[346,352–354] Furthermore, the compound only absorbs shorter wavelength visible light, resulting in limited tissue penetration and the inability to target deeper tumors. These limitations prompted the development of second-generation PSs intended to overcome the shortcomings of the first generation. These included purer porphyrins such as porphyrins, chlorins, pheophorbides, phthalocyanines, and so on.[346,352–357] The goal was to improve PS purity, tumor selectivity, minimize the overall drug dosage and side effects, and absorb longer wavelengths. The challenges in simultaneously achieving better tumor selectivity, limiting off-site tissue damage, and optimal photophysical and photochemical properties resulted in the third generation of PSs. Third generation PSs are modified versions of second-generation PSs, that can target tumors either actively (PSs attached to molecules such ligands or antibodies that preferentially bind to tumor surface receptors) or passively (modified delivery systems - PSs loaded into nanoparticles or liposomes that can penetrate the leaky vasculature) to improve selectivity to malignant tissue.[346,358–360] The goal behind these is to control the localization of PSs while retaining their photophysical properties.

#### 1.6.1.1. Ideal photosensitizer

The evolution of PSs has been aimed at developing an ideal PS with desired characteristics[346,352,353,361] such as 1. Effective singlet oxygen production, 2. Preferential tumor accumulation and rapid systemic clearance, 3. No dark toxicity, 4. A broad range of activation wavelength, 5. Chemically stable structure, 6. Ease of solubility in clinically applicable injectable formulations, and 7. Easy and reproducible synthesis process. To date, no PS has been created with all desired characteristics, and even if one does, it would not be applicable against a wide range of cancers and tumor phenotypes. While

most photosensitizer development has been centered around organic molecules or porphyrins, there is an emerging interest in utilizing transition metal complexes for PSs due to their superior properties.[352,353]

### 1.6.1.2. Transition metal complexes

The success of metal complexes such as cisplatin and its derivatives in cancer treatment led the path for the exploration of other transition metal (TM) complexes.[362] Due to their appealing photophysical-photochemical properties, several TM complexes such as ruthenium (II) complexes, osmium (II), iridium(III) complexes, and polymetallic complexes have been proposed as prospective PSs. TM PSs can absorb light efficiently in both the visible range as well as near-infrared (NIR) ranges, giving them a wide activation range and thus applicability.[346,361,363,364] Upon excitation, TM PSs can efficiently (close to 100%) yield triplet excited states, providing more time for interaction with molecular oxygen, leading to high yields of singlet oxygen generation.[346,361] TM complexes also offer a large number of excited-state electronic configurations, allowing them to be exploited as dual-action agents in both oxygen-dependent as well as oxygen-independent cytotoxic reactions.[346,365,366] In contrast to many organic PSs, TM complexes have high photostability, allowing for prolonged recycling of the PS and, as a result, reduction in overall PS dosage needed to achieve the desired cytotoxicity.[353,361,367] Many TM PSs have been reported to have high photoindices (PI = light toxicity/ dark toxicity), demonstrating minimal toxicity without light illumination.[361] Furthermore, TM complexes are relatively easy to synthesize, allowing for the ability to fine-tune their properties as required.[346,353,361,368] Among the several TM PSs reported, ruthenium (Ru) II complexes have been most extensively studied in PDT. Notably, a Ru (II)-PS based PDT (TLD1433), developed by our collaborator, Dr. Sherri McFarland, is

currently undergoing phase IIb clinical trials for use in non-muscle-invasive bladder cancer, indicating a promising future for TM complexes in PDT.[369] Chapters 4 and 5 of this thesis discuss the development and immunological characterization of novel Ru (II) TM complexes for PDT of melanoma.

### *1.6.2. Light source*

The efficacy of PDT reaction also depends on the properties of the light source used to activate the PS. In a clinical setting, this necessitates the light's ability to penetrate skin and tissue and activate the PS at the tumor site [**Figure 1.11**].[346,352–354] The wavelength of light also dictates tissue penetration, with shorter wavelengths targeting surface-level tissues and longer wavelengths targeting deeper tissues. Most of the first- and second-generation PSs are designed to be activated by shorter wavelengths, restricting their usage.[346,352–354] Light penetration into tissues is a complex process that is often hampered by tissue heterogeneity, which influences light absorption and scatter. For instance, the efficacy of shorter visible wavelengths can be limited due to absorption by endogenous chromophores such as haemoglobin.[346,352–354] On the other hand, water can absorb longer wavelengths, and wavelengths beyond 850nm fail to activate PSs to triplet state to generate singlet oxygen efficiently. Noting these limitations, the "phototherapeutic window" or optimal wavelengths for tissue penetration and PS activation are considered to be between 600nm and 850nm.[346,352–354] It was recently recommended that the optimal wavelength should change based on the location of the tumor, as using longer wavelengths for superficial cancers is unnecessary and undesired.[346]

Various light sources such as lamps, LEDs, lasers, incandescent bulbs have been utilized in PDT, with varying applications and degrees of efficiency. Lasers are widely used and desired for clinical application of PDT, as they are powerful and can be

coupled with optical fibers and diffusing tips to illuminate deeper tumors interstitially.[346,352–354] In addition to wavelength and light source, PDT efficacy is also determined by the application and dosage of light, such as light fluence (total energy of exposed light across irradiated area, J/cm2), light fluence rate (energy per second across irradiated area, W/cm2), light exposure time, and light delivery method (single or fractionated). It has been shown that high fluence rates can deplete oxygen levels in the TME rapidly, limiting the reach of PDT.[346,352–354] Lower fluence rates, on the other hand, have been demonstrated to be more effective and to promote tumor cell-specific apoptosis.[352,353] Some studies showed the effectiveness of combining high and low PDT doses to achieve a superior outcome.[370] However, the optimal dose regimens are case-dependent, reliant on the tumor characteristics, and therefore important to investigate.

Finally, the optimum PS and PDT regimen is dependent on a number of parameters, including tumor characteristics and clinical requirements. Furthermore, most PS development has been centered on a PS-centric model, focused only on PS properties. Recently, a tumor-centric-PS development paradigm based on clinical criteria for PS and PDT regimen development was proposed, which is implemented in Chapters 4 and 5.[371]

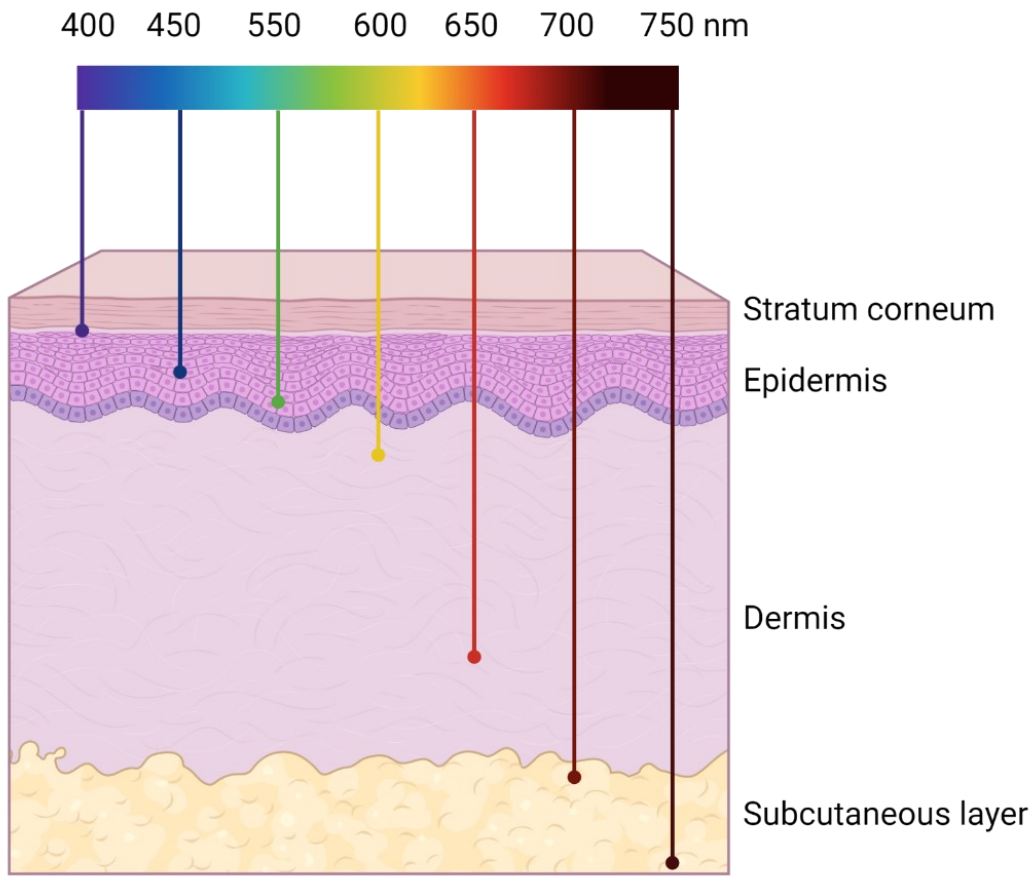


**Figure 1.11.** Tissue penetration by lights of different wavelengths.

The depth of tissue penetration increases as the wavelength increases, with blue light targeting the skin's surface and red or near-infrared wavelengths reaching deeper into the dermis and subcutaneous layers. Figure made using Biorender.

### *1.6.3. PDT mediated anticancer responses*

PDT-mediated tumor destruction can occur through three main mechanisms. First, the localization and activation of the PS in tumor tissues result in ROS production and direct cell death of malignant cells at the site of PDT. Alternatively, PS can localize in the tumor

vasculature and destroy the endothelial cells, limiting the delivery of nutrients and oxygen to the tumor cells. Finally, PDT can indirectly eliminate the tumors by stimulating inflammatory responses and activating the immune system against tumor cells.

### 1.6.3.1. Cytotoxicity

Much of the cytotoxicity caused by PDT is mediated by the production of reactive oxygen species and their interactions with various biomolecules. In general, the phototoxic effects of PDT are not tumor-selective, and the PSs are taken up by both normal and malignant cells. The major cytotoxic ROS formed from the photodynamic reaction of PS and oxygen, singlet oxygen ($^1O_2$), has a short life of less than 0.05 μs in cells and can diffuse less than 0.02 μm from the site of production.[352,372,373] Therefore, the targets of PDT reaction are highly dependent on the site of PS activation.

PDT-mediated cell death is a complex cellular process dependent on the PDT regimen and PS characteristics, which determine the localization of PS into organelles such as mitochondria, Golgi apparatus, endoplasmic reticulum, lysosomes, or plasma membrane.[374,375] While PDT promotes cell death through various pathways, apoptosis, necrosis, and autophagy are the main mechanisms.[373] PS localization in mitochondria, has been shown to promote apoptosis in the targeted cell by photodamage to Bcl2, resulting in mitochondrial membrane permeabilization and release of pro-apoptotic molecules such as cytochrome c.[376–380] Alternatively, PS localization to the plasma membrane has been associated with loss of membrane integrity and induction of necrotic cell death.[381] The PS localization to different organelles can be controlled by the PS incubation protocols. For instance, incubating Photofrin for longer vs. shorter periods (24 vs. 1 hour) shifted its localization from cytoplasm to plasma membrane, altering the cell death pathway from apoptotic to necrotic.[382] This phenomenon has

been confirmed with other PSs.[381,383–385] It is also shown that high-dose PDT, either through high PS concentration or high light dose, can result in necrosis due to extensive damage to the cell.[386–389] In addition, PDT also induces cell death via autophagy in the event of impaired apoptosis.[390,391] Low dosages of PDT have been shown to induce protective autophagy, whereas higher doses result in autophagic cell death.[392] PS localization also influences autophagy; PS localization to mitochondria and ER is shown to induce prosurvival autophagy, whereas lysosomal targeted PS inhibits autophagy.[392–394] Recent studies have indicated that PDT-mediated cell death can also occur through necroptosis, ferroptosis, and pyroptosis pathways.[395–397]

Similar to the subcellular localization, the site of PS localization and ROS generation within the tumor microenvironment determines the cells that are being damaged. Within the tumor, the PS can localize to the tumor parenchyma consisting of malignant cells or the stroma consisting of structural proteins, connective tissue cells, and inflammatory cells. Since the interactions between tumor cells and stromal cells are essential for tumor cell growth, motility and invasiveness, tumor stroma is also an important target for cancer therapies.[398,399] PDT has been shown to affect the tumor stromal cells in addition to the tumor cells, which is believed to play a major role in the efficacy of PDT.[400] PDT can destroy stromal fibroblasts, alter the tumor extracellular matrix (ECM), thereby inhibiting tumor progression while improving therapeutic outcome.[401–404] PDT also induces damage to structural proteins such as integrins disrupting the tumor-stromal signaling.[405] Furthermore, upon localization to tumor ECM, PDT-generated ROS can alter ECM composition by inducing hyaluronic acid degradation, cross-linking in the collagen matrix, inactivating the matrix-residing growth factors, and inhibiting cancer cell migration.[406,407] PDT-mediated damage to tumor vasculature is explained in 1.5.3.2.

PDT-mediated ROS also causes oxidative stress and damage to different biomolecules, initiating various adaptive stress responses to repair the damage and maintain cellular homeostasis. The activated survival pathways include integrated stress response, which is mediated by eIF2α phosphorylation and results in unfolded protein response and ER stress as well as antioxidant stress response, which results in nuclear factor erythroid 2-related factor (Nrf2) mediated clearance of oxidized biomolecules.[373,385] While these stress mechanisms target homeostasis and recovery, prolonged oxidative stress resulting from PDT leads to inevitable cell death via multiple cell death pathways, as described above.[373,385] PDT-mediated oxidative stress also results in immunogenic cell death, explained in section **1.6.3.3**.

### 1.6.3.2. Vascular damage

In addition to the direct destruction of tumor cells, PDT can effectively target tumor blood vessels. PSs localized and activated in the tumor vasculature cause vascular collapse and inhibit the formation of new blood vessels, thereby restricting nutrient and oxygen supply and reducing tumor proliferation. Vascular-targeted PDT regimens include shorter intervals between PS administration and light activation (also referred to as drug-light-interval, DLI), allowing the PS to localize in the tumor vasculature and are shown to be effective therapeutic regimens with various PSs.[372,408] Intravascular PDT damages endothelial cells resulting in thrombosis and release of clotting factors which can activate platelets.[409–411] These activated platelets can induce vasoconstriction, further reducing the blood flow to the tumor and resulting in tissue hypoxia, nutrient deprivation, and tumor destruction.[372,412] The therapeutic effect of PSs such as HPD is largely due to the disrupted blood flow.[410]

A decrease in tumor oxygen levels or an increase in tumor hypoxia has been demonstrated to be a critical factor in vascular-targeted PDT with various PSs such as redaporfin, padeliporfin, and verteporfin.[413–418] Measurement of tissue oxygen levels during and after conventional cellular PDT (180 min DLI) vs. vascular-targeted short DLI PDT (5-30 min DLI) with verteporfin resulted in a significant reduction of pO2 in both regimens.[413] However, the reduction was transient, and oxygen levels recovered quickly upon cellular PDT compared to vascular PDT, wherein the hypoxic environment was maintained for an extended period.[413] Furthermore, no apparent vascular damage was observed with 180 min DLI. Tissue reoxygenation promoted tumor growth and lowered the therapeutic outcome of PDT, which was overcome by destroying the vasculature.[413] Therefore, prolonged and robust hypoxia has been associated with better therapeutic outcomes in PDT.[418]

Interestingly, the treatment efficacy was also impacted by altering the tissue selectivity of verteporfin to tumor microvasculature vs. normal blood vessels utilizing 30 min vs. 5 min DLI.[413] While tissue selectivity of verteporfin improved with 30 min DLI, maximum PDT efficacy was achieved with 5 min DLI, which eliminated the tumor vasculature as well as a margin of normal tissue. This is consistent with the observation that tumor cures with PDT are improved by establishing circulation-free zones around the tumor, thereby inhibiting the re-supply of nutrients to residual tumor cells that survived the PDT.[372] Current PDT protocols utilizing verteporfin favor a DLI of 15 min, which leads to complete blocking of blood flow in the neovasculature.[372,419]

As a result, vascular targeted PDTs have received a lot of attention, with many groups focusing on this approach to increase the therapeutic efficacy of PDT. Furthermore, combining cellular PDT with vascular PDT has been shown to further improve the efficacy by targeting both tumor vasculature as well as the tumor

parenchyma.[408,416] Anti-angiogenic therapeutics have a significant role in the clinical treatment of cancers; therefore, this property of PDT is regarded as an important factor in determining its efficacy.[420]

### 1.6.3.3. Immunogenic cell death

The role of danger signaling and local inflammatory reactions in PDT has been explored since the 1990s, long before ICD was conceptualized.[421] Early studies noted the induction of heat shock proteins upon PDT-mediated oxidative stress in multiple *in vitro* and *in vivo* models and implicated in PDT-induced cell death.[421–425] Co-culture of PDT-treated cancer cells expressing HSPs with immature dendritic cells resulted in efficient engulfment of dying cancer cells by DCs as well as functional maturation of DCs.[426,427] Given these initial observations and the importance of ROS and oxidative stress in PDT-mediated anticancer responses, the relevance of ICD in PDT has been ponderedsince the idea of ICD was first proposed.[428]

Not surprisingly, ICD has been implicated in various PSs, with a recent surge of investigations in this field. Many PSs from first, second, and third generations have been demonstrated to induce ICD to varying degrees in different models; however, the precise mechanism of induction varies.[429] For example, ICD-mediated activation of CALR is followed by co-translocation of ER protein 57 following Rose Bengal Acetate therapy, while this occurs independently of ERp57 during hypericin-based PDT.[244,261,430] Additionally, hypericin-based PDT induction of CALR is demonstrated to occur independently of eIF2α phosphorylation, which is considered a pre-requisite for chemotherapy-induced ICD.[244,261,431] Unlike chemotherapy, ATP secretion by hypericin-based PDT mediated ICD is independent of autophagy.[275,280]

The effects of PS localization and PDT dosage on ICD induction have also been evaluated. Recent studies have demonstrated that PSs localizing to ER resulted in significant upregulation of ICD DAMPs and induced efficient immune responses against mouse colorectal, melanoma, and glioma tumor models.[246,396] Considering the significant role of ER stress in ICD, PSs localizing to the ER can be expected to induce efficient ICD. On the other hand, the immunogenicity of PSs that localize to lysosomes in a mouse fibrosarcoma model has been associated with DAMP emission, DC maturation, and reduced tumor growth.[432] Furthermore, redaporfin, which localizes to both ER and Golgi apparatus, has been demonstrated to induce efficient ICD in mouse lung cancer cells.[433] The inhibition of Golgi function pharmacologically greatly lowered the outcome of redaporfin-based PDT, demonstrating its significance in the process.[433] Given the discrepancies between different PSs, the role of PS localization on ICD remains unclear. Nonetheless, efforts to design ER-targeted PDTs continue.[429,434,435] In addition to localization, PDT-dosage dependency in ICD has been evaluated. PDT-mediated ICD, similar to cytotoxicity, may also be dose dependent, with lower doses providing more pronounced benefits from ICD than higher doses, as demonstrated in mouse squamous cell carcinoma and melanoma models.[436,437]

ICD plays a significant role in PDT-mediated anticancer responses, and PDT-induced ICD vaccines' potential has been explored. However, ICD upon PDT is also a developing area with many unknowns, and requires more studies to understand fully. Chapters 5 and 6 in this thesis focus on exploring the role of ICD in transition metal complexes.

### 1.6.3.4. Anticancer immune responses

Photodynamic therapy was initially thought to be a local cytotoxic treatment that only affected cancer cells and vasculature. However, studies in the last two decades have demonstrated that PDT can induce local and systemic inflammatory responses, resulting in the activation of both innate and adaptive arms of anticancer immune responses.

**Innate immune responses & inflammation**

PDT generated cell death of resident cancer and stromal cells has been shown to induce proinflammatory cytokines such as IL-6, IL-1β, and TNFα, mediated by the activation of transcription factors including NFkB and AP1.[438–444] IL-6 has been identified as an important proinflammatory cytokine in PDT-mediated antitumor immune responses.[445] Porfimer sodium and related photosensitizers have been shown to increase the expression of IL-6 in both mouse tumors and serum.[441,444,446,447] Vascular-targeted PDT with redaporfin led to a significant increase in IL-6 levels in the peripheral blood.[448] IL-6 is also thought to be involved in complement production and neutrophil migration; however, pre-existing IL-6 induction through surgery has been shown to have no or negative effect on PDT-mediated immunity.[445,449,450]

Similarly, increased IL-1β is linked to the expression of endothelial adhesion molecules, neutrophil recruitment, and the number of circulating neutrophils.[451,452] TNFα production by PDT-treated macrophages has been linked to direct cytolytic and anti-vascular actions.[443] Urinary cytokines IL-1β and TNFα were detected in bladder cancer patients who had PDT with the highest light fluences.[453] Furthermore, after Photofrin-based PDT, factors such as granulocyte colony-stimulating factor (G-CSF), IL-10, histamine, and leukotrienes were released.[439,451] Together, these inflammatory mediators play an important role in activating and recruiting various immune cells to the PDT-treated region.

### Neutrophils:

Massive local and systemic neutrophilia has been observed during PDT with several PSs and is one of the significant manifestations of PDT-mediated acute inflammation.[439,454–459] Photodamage to tumor vascular endothelial cells causes structural changes and upregulates the expression of adhesion molecules such as E-selectin and ICAM1, which are required for neutrophil adhesion, and chemokine MIP2, which mediates neutrophil migration to the tumor site.[439,444,454,458,460] High neutrophil infiltration at the tumor site has been observed within 5 minutes post-PDT and lasted for 24 hours.[457,460–462] An increase in peripheral neutrophils is shown to be dependent on the complement system, which is also increased upon PDT.[446,462–465] Administration of blocking antibodies that inhibit C3a and C5a, which promote vascular permeability, fully eliminated PDT-induced neutrophilia.[457,460,462,464] In addition to neutrophil infiltration at the irradiated tumor site, PDT treatment also results in neutrophil migration and accumulation in the tumor-draining lymph nodes via secretion of IL-1β and IL-17 by the T helper 17 (Th17) cells.[454,456]

Several investigations have demonstrated that neutrophilia is important for the success of PDT treatment. Strong and early activation of neutrophils at the irradiated tumor site has been associated with better tumor cures following Photofrin-based PDT.[459,466] Likewise, blocking local or systemic neutrophilia in mice through CXCR2 knock out, selective immunodepletion, or anti-neutrophil sera resulted in significantly decreased PDT efficacy and antitumor CD8+ T cell infiltration at the tumor site in various PS and PDT regimens.[454–456,458,459,467,468] Clinically, peripheral neutrophils were significantly increased in esophageal squamous cell carcinoma patients treated with Photofrin-PDT.[469] Thus, PDT-induced local and systemic neutrophilia contributes to the prolonged efficacy of PDT and activation of adaptive immune responses.

### Macrophages:

Tumor-associated macrophages (TAMs) are another important player in PDT-mediated antitumor immunity. The tumor microenvironment is typically composed of M2 macrophages, which have an immunosuppressive phenotype and promote tumor metastasis and angiogenesis.[470,471] It was shown in multiple models that PSs accumulate at higher levels in these phagocytic M2 macrophages, which were eliminated upon light irradiation.[443,472–478] Additionally, this elimination of M2 macrophages followed the infiltration and activation of immunostimulatory M1 macrophages into the TME.[461,472,473,479] PDT-induced release of HSP70 from tumor cells was shown to activate macrophages through interactions with TLR2/ TLR4 and release proinflammatory cytokines such as IL-6, IL-12, nitric oxide (NO), and TNFα at the tumor site.[425] Furthermore, PDT treatment increased the expression of complement receptor C3aR on monocytes *in vivo*. Co-culture of treatment-naïve macrophages with PDT treated cancer cells *ex vivo* resulted in elevated expression of C3aR on macrophages, which can enable them to phagocytose tumor cells opsonized with C3 after PDT.[446,462–465] Increase in macrophage infiltration at the irradiated site was also observed in clinical samples from basal cell carcinoma patients treated with ALA-PDT.[480] Therefore, photodynamic therapy can shift the M1/M2 balance in the TME from immunosuppressive towards an immunostimulatory environment.

### Natural killer cells:

Natural killer (NK) cells are innate effector cells capable of destroying cancer cells. Unlike cytotoxic T lymphocytes, NK cells are not antigen-specific and function by identifying the missing self-receptor, the MHC class I molecule, on the surface of cells.[481–483] MHC I molecules on normal cells interact with inhibitory receptors on NK cells, thereby preventing NK cells from attacking them. As cancer cells tend to

downregulate MHC I molecules to escape T cell-mediated cytotoxicity, these cells are detected and destroyed by NK cells.[481–483] Additionally, NK cells can also interact with cancer cells through their activation receptors and corresponding ligands, leading to their activation. The outcome of NK cell effector activity appears to be determined by the balance of inhibitory and activation receptor engagement.[481–483]

PDT with 2-[1-hexyloxyethyl]-2-devinyl pyropheophorbide-a (HPPH) resulted in upregulation of non-classical MHC class I molecules, NKG2DL in human colon carcinoma cells *in vitro* and mouse colon carcinoma cells *in vivo,* respectively.[484] These molecules function as ligands for the NKG2D activation receptor on NK cells and are involved in NK cell-mediated immunity. As a result, HPPH-PDT treated cancer cells were more sensitive to NK cell-mediated cytotoxicity *ex vivo*.[484] No difference was noticed in classical MHC class I or antigen presentation pathway associated molecules upon HPPH-PDT. Similarly, hematoporphyrin-PDT enhanced the expression of NKG2D ligands such as MICA/B and ULBP family proteins in human gastric and lung cancer cells, increasing their sensitivity to NK cell-mediated cytotoxicity.[485] Furthermore, blocking NKG2D using monoclonal antibodies prevented NK cells from destroying cancer cells.[485]

Several studies have reported that NK cell activity is important for overall PDT efficacy. In a mouse breast cancer model, depleting NK cells reduced overall PDT efficacy and associated CD8 T cell immunity in local and metastatic tumors following Photofrin or benzophenothiazine-PDT.[486–488] Additionally, PDT in combination with NK-based adoptive immunotherapy resulted in improved tumor control in multiple tumor models.[489] Clinical photodynamic therapy of patients with head and neck cancer enhanced the frequencies of NK cells in the peripheral blood.[490] Overall, these studies highlight the potential role of NK cell-mediated immunity in PDT.

## Adaptive immune responses

One of the earliest observations indicating the significance of adaptive immunity upon PDT was made in 1994, when a group demonstrated that immunocompetent mice cured of fibrosarcoma by PDT could resist a rechallenge of tumor cells, unlike immunosuppressed mice or mice cured through surgery.[491] The efficacy of PDT on EMT6 breast tumors in *scid* mice was enhanced upon adoptive transfer of splenocytes from PDT-cured immunocompetent mice.[488] This impact was not observed when splenocytes from X-ray cured immunocompetent animals were transferred to *scid* mice. Furthermore, transfer of T cells from naïve immunocompetent mice to tumor-bearing immunocompromised mice prior to PDT increased PDT efficacy in *scid* mice, suggesting a specific role of T cells in PDT-mediated antitumor immunity.[492] PDT cure rates were also higher in immunocompetent mice than immunocompromised animals in different models of PDT.[486,492–495] Over the years, numerous investigations have confirmed the role of T cells and adaptive immune responses in PDT-mediated antitumor immunity.

Targeted depletion or deletion investigations identified subsets of T cells implicated in PDT-induced adaptive immune responses. Transfer of splenocytes depleted of CD8+ or CD4+ T cells from PDT-generated EMT6 breast tumor primed mice into *scid* mice before PDT revealed that CD8+ T cells are the primary immune effectors. In this model, CD4+ T helper cells serve a supportive role in conferring the curative outcome to PDT.[488] Antibody-mediated depletion of CD8+ T cells in immunocompetent mice prior to PDT reduced the efficacy of PDT, confirming the importance of CTLs for PDT outcome.[487] T cells obtained from PDT-cured tumor-free mice were able to specifically lyse antigen-positive cancer cells, demonstrating the generation of CD8+ T cell responses.[494]

The function of CD4+ T helper cells in PDT remains unclear. Kabingu et al. showed that antibody-based depletion of CD4+ T cells before PDT did not affect the PDT outcome on distant tumors in an EMT6 metastatic lung tumor model.[486] In a local EMT6 tumor model, anti-CD4 antibody inhibited tumor growth in both treated as well as untreated mice, leaving the precise role of CD4+ cells in PDT mediated immunity ambiguous.[487] In contrast, in a different model of PDT, administration of CD4 or CD25 or a combination of both antibodies to immunocompetent EMT6 tumor-bearing mice immediately after PDT lowered the cure rates.[468] Similarly, in a CT26 colon cancer model, adoptive transfer of CD4+ T cells from vascular PDT-cured animals to naïve recipients resulted in protection from subsequent challenges with viable cells of the same kind.[493] Restimulation of these CD4+ cells revealed induction of IFNγ, confirming their Th1 phenotype. Moreover, an increase of Th17 cells and the corresponding cytokine IL-17A was observed in tumor-draining lymph nodes of colon cancer tumor-bearing mice following PDT treatment.[454] Together, these findings suggest a vital role for cytotoxic T cells and a varied role for T helper cells, which is likely dependent on the PS, PDT regimen, and tumor models.

Unlike T lymphocytes, the role of humoral immune responses involving B lymphocytes following PDT has not been well characterized. To date, only one preclinical study has demonstrated the link between humoral responses and PDT.[493] Novel tumor antigen-specific antibodies were detected in the sera of PDT treated mice but not in the untreated control group in a vascular PDT treated CT26 model.[493] IgG binding assays demonstrated stronger binding to PDT-treated tumors compared to untreated tumors.[493] Furthermore, serum transfer from PDT-treated mice to naive mice protected the latter group from a subsequent challenge with intravenously injected CT26

cells, thereby preventing lung metastasis. Together, these data indicate the activation of humoral immunity following vascular PDT.

Various models have reported the generation of systemic immunity and immunological memory upon PDT.[370,486,493–495] Canti et al.[491] showed that immunocompetent MS-2 fibrosarcoma tumor-bearing mice cured by PDT resisted rechallenge with cancer cells of the same kind. However, when these mice were challenged with leukemia cancer cells L1210 or P388, they succumbed to the disease, indicating the specificity of PDT-generated immunological memory against MS-2 fibrosarcoma.[491] Similarly, *scid* mice engrafted with splenocytes sensitized by PDT to Meth-A sarcomas had no therapeutic benefit when challenged with EMT6 breast cancer cells.[488] In an experimental model of lung metastasis, where mice were injected with EMT6 cells both subcutaneously and intravenously, local PDT treatment of primary tumor resulted in ablation of the local tumor as well as a significant reduction of lung metastasis compared to untreated mice.[486] In mice bearing EMT6 tumors on contralateral flanks, local PDT treatment of one tumor resulted in increased CD8+ T cell infiltration in the distant tumor, confirming the generation of systemic responses.[486] Likewise, in a CT26 tumor model, local administration of vascular PDT protected the mice from subsequent challenge with intravenously injected CT26 cells by inducing a systemic memory immune response.[493,495] PDT treatment of tumors on only one contralateral flank of a CT26 two tumor model (mice with same tumors on both flanks) resulted in significant regression of tumor growth in a distant untreated tumor in all mice and a complete, permanent regression noticed in 7 out of 9 mice.[494] In this study, PDT cured mice also resisted a rechallenge in an antigen-specific manner, wherein mice inoculated with antigen-negative CT26 cells developed tumors.

Few clinical studies have reported the generation of adaptive immune responses. In basal cell carcinoma (BCC) patients treated with ALA-PDT, increased CD4+ and CD8+ T lymphocyte infiltration was detected at the irradiated tumor site and lasted for at least 72 hours.[480] In vulva intraepithelial neoplasia (VIN) patients treated with ALA-PDT, enhanced CD8+ T cell infiltration was observed in PDT responders but not in nonresponders, who also displayed loss of HLA class I.[496] Peripheral blood leukocytes isolated from PDT-treated BCC patients showed increased antigen recognition and cytolytic activity against tumor cells.[226] Moreover, spontaneous remission of distant tumors outside of the local ALA-PDT or Fotolon-PDT treated area has been reported in multiple cases of BCC and angiosarcoma.[226,497] Biopsies of these untreated tumors revealed infiltration of CD8+ T cells.[226] Also, Tregs isolated from patients with esophageal squamous cell carcinoma before and after Photofrin-PDT showed a reduced suppressive capacity after PDT.[469]

Overall, PDT-mediated multimodal anticancer responses consist of direct cytotoxicity, vascular damage, and the development of anticancer immune responses involving various innate and adaptive immune mediators. Accordingly, the outcome of PDT is determined by multiple factors, and the contribution of each may depend on the treatment regimen and tumor model.

## 1.7. MELANOMA

### *1.7.1. Biological origin*

Melanoma is a highly aggressive form of skin cancer that arises from the malignant transformation of melanocytes. Melanocytes are melanin-forming cells derived from the neural crest cells of neuroectodermal origin that migrate and dwell throughout the body

and are responsible for pigmentation and photoprotection.[498–501] Melanoma can occur anywhere on the body, independent of anatomical location or kind of tissue or organ, due to the vast distribution of melanocytes. Melanocytes reside in the basal layer of the skin epidermis and hair follicles and are regulated by epidermal keratinocytes.[498–501] When exposed to ultraviolet radiation (UVR), keratinocytes secrete factors that promote melanocyte proliferation, differentiation, and survival, resulting in the production of melanin and subsequent protection from the damaging effects of UVR.[498–501] Upon extensive and irreversible damage, melanocytes escape the regulation by keratinocytes, resulting in disrupted growth regulation and intracellular signaling, and develop into naevi (common moles), which can later advance to melanoma.[498–501] Cutaneous melanoma is the most common form of melanoma, followed by relatively rare cases of non-cutaneous melanomas such as acral, mucosal, conjunctival, and uveal melanomas.[502] This section will focus on cutaneous melanoma.

### *1.7.2. Mutational and genetic landscape*

Melanomas have high somatic mutation loads of more than 10 mutations per megabase, which is attributed to the mutagenic effects of UVR as well as indirect effects from the formation of ROS.[503–506] These include UVR hallmark mutations such as the G to T transition induced by ultraviolet A radiation (9%) and the C to T transition generated by ultraviolet B radiation (46%).[503–505] The rate of mutations in melanomas varies significantly between persons and kinds of melanoma. For example, melanomas of the head, neck, and upper extremities have a high mutation burden. In contrast, melanomas of the lower extremities have an intermediate burden, and melanomas of the acral, uveal, and mucosal areas have the lowest mutation burden.[507] BRAF mutations are the most common and represent 50% of melanomas, followed by NRAS and NF1, which are identified in around 25% and 15% of melanomas, respectively.[504,508] Other common

mutations include those in telomerase reverse transcriptase (TERT) promoter, and tumor suppressors cyclin-dependent kinase inhibitor 2A (CDKN2A), phosphatase and tensin homolog (PTEN), and tumor protein 53 (p53 or TP53).[504,508–511]

BRAF V600E mutation accounts for 74 to 86 percent of all BRAF mutations and is linked to skin with moderate sun exposure rather than chronic sun exposure.[507,512,513] BRAF V600K mutations are present in people over the age of 65 and account for 10 to 30 percent of all BRAF mutations.[513] BRAF V600E mutations are primarily associated with the formation of benign naevi, and their progression into intermediate and malignant melanoma lesions involves BRAF V600K or other mutations such as those in NRAS and TERT promoter.[502–504,514] Further mutations, including the ones related to CDKN2A, are exclusively linked to invasive melanomas, and advanced metastatic melanomas harbor additional mutations in genes associated with tumor suppressor proteins PTEN and p53.[502,514]

Malignant transformation of melanoma is caused by a series of genetic events that result in constitutive activation of oncogenic signaling pathways. Mitogen-activated protein kinase (MAPK) pathway, protein kinase B (AKT) pathway, cell-cycle regulation process, and pigmentation-related pathway are some of the key processes involved in this transition.[515] Disrupted MAPK signaling is most commonly identified in melanomas. Mutations in BRAF, NRAS, and NF1 cause constitutive activation of RAS, MEK, Raf, and ERK, leading to hyperactivation of MAPK signaling pathway and rapid tumor cell proliferation.[516–523] Targeted BRAF/ MEK inhibitors are clinically approved for the treatment of melanoma.[502] Another essential characteristic of melanoma development is uncontrolled cell cycle regulation, which is initiated by mutations in CDKN2A, Cyclin D1, and CDK4 genes that impair the function of downstream tumor suppressors, RB1 and p53.[524–527] Combination of AKT3 activation and deletion or loss of PTEN function

results in dysregulated activation of AKT pathway and subsequent tumor cell survival and development.[528,529] Finally, mutations in various pigmentation process-related genes impair the UV-protective capabilities of melanocytes and have been implicated in sporadic melanoma cases, which are caused by UVR and account for nearly 90% of all melanomas.[515,530]

### *1.7.3. Epidemiology and diagnosis*

Melanoma occupies around 1.7% of global primary malignant cancers and accounts for about 55,000 cancer deaths annually.[502] Melanoma incidence varies greatly worldwide, with New Zealand and Australia having the highest occurrences, followed by North America, with incidence rates of 35.8, 34.9, and 13.8 per 100,000 individuals, respectively.[502] UVR exposure, family or personal history of cutaneous melanoma, indoor tanning, phenotypic traits such as pale skin, hair, eye colors, a predisposition to freckle, and immunosuppression are the strongest proven risk factors for melanoma.[502] Current accepted characteristics that prompt clinical screening or surveillance include the presence of melanocytic naevi, dysplastic naevi, and family history of melanoma.[502] Gene mutations alone account for only a small proportion of melanoma cases, and genetic testing, while commercially available, is not recommended for initial screening due to lack of evidence of clinical benefit.[502,531]

The current guidelines for diagnosis and assessment of the clinical stage of melanoma are based on histopathology classification and rely on three major factors: tumor thickness with or without ulceration (T stage), regional metastasis in the lymph nodes (N stage), and distant metastasis (M stage).[502,532] Broadly, tumors are classified into stage 1 if T >1–2 mm thickness with no ulceration, no lymph node, and no distant metastasis.[502,532] Stage 2 classified tumors have up to 4mm thickness with or without ulceration, no N and M; or no tumor thickness, but the presence of micro or macro

metastasis in one lymph node without M.[502,532] Stage 3 tumors include those with up to 4mm thickness with lymph node metastasis but no distant metastasis.[502,532] All tumors with any T and N, with distant metastasis to skin or lung or non-central nervous system (CNS) or CNS sites, are classified as stage 4.[502,532]

While melanoma is often easier to detect and diagnose in its early stages than other cancers, it is also more prone to metastasize to other parts of the body, with 5% to 15% of individuals with thin stage 1A melanoma (1mm thickness) developing metastasis.[533,534] The 5-year survival rate for localized (stage I and II) melanoma is 98 percent; however, when cancer has metastasized to regional or distant sites, this lowers to 63 to 66% or 10 to 15%, respectively.[534–536] The 5-year survival rate for advanced metastatic melanoma varies depending on the location of metastasis, with lung metastasis having a prognosis of 15 to 17 percent and visceral metastasis having a prognosis of less than 10 percent, with a median survival of less than 1 year.[534] Melanoma incidence has been rising significantly globally, with the estimated likelihood of a Caucasian developing melanoma increasing from 1 in 1500 individuals in 1935 to 1 in 50 in 2011.[534]

### *1.7.4. Clinical management*

Surgery remains the primary treatment modality for primary cutaneous melanoma, with or without radiation.[532,537,538] For early stages, 0 to IIA, wide excision of primary tumors with variable safety margins is performed depending on tumor thickness.[502,532,537,538] In case of isolated lymph node metastasis, lymph node dissection is performed along with surgical removal of the primary tumor.[532,537,538] This could be combined with radiation therapy in high-risk cases with multiple lymph node metastases or distant brain metastases.[532,537,538]

In high-risk resectable tumors with stages, II-B, II-C, III, and IV, a combination of surgery and adjuvant therapies with targeted therapies BRAF/MEK inhibitors or immunotherapies including IL-2, IFNα, ICIs, and TVEC are used.[532,537,538] For local recurrent tumors (stage II), surgery in combination with IL-2 or IFNα is recommended.[537,538] Surgery combined with systemic therapy with BRAF/MEK inhibitors or ICIs is recommended for stage III and IV tumors.[537–539] Stage III BRAF wild-type (WT) tumors are treated with ICI monotherapy nivolumab or pembrolizumab. In contrast, in the case of stage III BRAF mutant tumors, either ICIs or BRAF/MEK combination targeted therapy with dabrafenib and trametinib are recommended.[537–539] TVEC may be recommended as an alternative if there are accessible and injectable lesions, but ICIs are more commonly used.[539] For stage IV unresectable BRAF WT melanomas, either monotherapy nivolumab or pembrolizumab or combination with ipilimumab and nivolumab are recommended.[537–539] In case of stage IV BRAF MUT tumors, monotherapy or combination ICIs or combination BRAF/MEK inhibitors (dabrafenib/trametinib, encorafenib/binimetinib, or vemurafenib/cobimetinib) are recommended.[537–539] Since the introduction of targeted therapies and ICIs, the use of chemotherapies has been discouraged.[537–539] The treatment guidelines vary in different countries, depending on the approval and availability of therapeutic options. The above mentioned are in North America, according to the American society of clinical oncology and Canadian cancer society.

While recent improvements in immunotherapies using ICIs have greatly enhanced the possibility for stage IV melanoma management, the treatment only benefits a small subset of patients. For example, about 60% of patients acquire primary resistance to ICIs, while 20 to 30% of early responders develop secondary resistance.[502] Nonetheless, the clinical success of ICIs has offered prospective therapy

alternatives for stage IV melanomas, for whom there were previously no viable options.[537]

### *1.7.5. Mouse models of melanoma*

Mouse models of cancers, despite the variation from human diseases, have become an essential part of cancer research. The work in this thesis utilizes two models of melanoma that have some similarities to the human disease, a syngeneic B16F10 tumor model and a genetically engineered $BRaf^{CA}$, $Pten^{loxP}$, Tyr::$CreER^{T2}$ (B6.Cg-Tg(Tyr-cre/ERT2)13Bos $Braf^{tm1Mmcm}$ $Pten^{tm1Hwu}$/BosJ) tumor model.

B16F10 tumor model is the most used mouse melanoma model and is the primary model used in this thesis. B16F0 is a cell line harvested and established in the 1950s from melanin-producing melanoma cells from the posterior of ears of C57BL/6 mice.[540,541] From this, B16F10 was established by inoculating B16F0 into mice and selecting for a line with the capacity to form lung colonies *in vivo* upon 10 cycles of *in vivo* inoculation and *in vitro* culture.[540,541] Currently, B16F10 cells are commonly injected into C57BL/6 mice, either subcutaneously to generate a localized tumor with minimal metastatic potential or intravenously to establish a distant metastasis in the lungs.[542] In this thesis, the B16F10 cell line is utilized for *in vitro* work and the localized tumor model for *in vivo* work. Genetically, B16F10 cells encode CDKN2A mutations commonly implicated in human melanomas, but not the BRAF or PTEN mutations.[541] These cells express TAAs associated with tyrosinase and gp100 proteins but fail to display them due to lack of MHC-I, similar to human melanomas.[540–542] They also express checkpoint molecule PD-L1 and have been utilized for preclinical testing of ICIs.[541] These features make them poorly immunogenic in terms of activation of T cell responses. Overall, B16F10 is an aggressive model of melanoma that forms tumors within 5 to 10 days of inoculation with overall survival of 3-4 weeks.[540–542] This model is also associated with

the formation of ulcerations, a characteristic of human melanomas, as early as 10 to 14 days post-inoculation.[540–542] Due to the rapid escalation of disease, it only provides a short window to test therapeutics.

A secondary *in vivo* tumor model used in this thesis is a genetically engineered mouse model that encodes the most frequently found BRAF V600E and PTEN mutations, expressed upon induction of Cre recombinase by topical application of 4-hydroxytamoxifen (4-HT).[543,544] This model generates tumors within 3-4 weeks of 4-HT application and is highly metastatic and aggressive, with metastasis identified in many distant sites, which is also noticed without 4-HT application in about 70% of mice due to leaky expression of mutated BRAF and PTEN.[543,544] Spread of melanoma to regional draining lymph nodes is observed in 100% mice and to lungs in some instances.[544] This model also provides a close resemblance to human disease. In general, these tumors remain resistant to treatment with mice in which drug treatment is ceased subsequently develop malignant melanoma.[543–545] Treatment of melanoma bearing mice with MEK1/2 inhibitor PD325901 or mTorc1 inhibitor rapamycin resulted in inhibition of tumor growth but showed little or no effect on tumor regression.[543,545]

## 1.8. THESIS OVERVIEW

I focus on two aspects of the cancer immunity cycle in this thesis. First, the goal of Chapter 3 is to provide a novel approach for overcoming the limitations of conventional mass spectrometry-based MHC-I peptide detection. Then, in Chapters 4 and 5, we create novel transition metal complexes for PDT of melanoma that can produce clinically desired direct cytotoxicity as well as indirect anticancer immune responses.

**Chapter 3: MHC-I Ligand Discovery Using Targeted Database Searches of Mass Spectrometry Data: Implications for T-Cell Immunotherapies.**

Recent developments in mass spectrometry have allowed for the accurate identification of MHC peptides, providing a better understanding of T cell-mediated immune responses. The standard experimental workflow for MHC-I peptide identification involves immunoprecipitation of MHC-bound peptides with anti-MHC-I antibodies, followed by peptide elution, purification, and LC-MS/MS analysis, involving MS spectral searches against reference proteome. The LC-MS/MS search techniques for MHC-I peptide discovery have been developed and optimized from well-established proteomics approaches, which account for enzyme cleavage sites. However, MHC-I peptide generation does not follow the same rules and lacks enzyme-specific residues. This lack of enzyme specificity means the MS/MS spectra are compared against the entire human or mouse proteome for every possible 8-11 aa peptide match. For example, the potential number of matches for a 9 aa MHC-I peptide from mouse GAPDH protein, which is 333 aa long, is a total of 325 peptides. This creates large search spaces to be explored for spectral matching, which decreases statistical power in assigning false-positive peptides and ultimately reduces the number of peptide identifications in an experiment.

*I hypothesized that employing a tailored database produced by predicted and potential MHC-I peptides would significantly limit the search space and enhance peptide*

*identifications from LC-MS/MS data.* I developed an algorithm named '*SpectMHC'* for generating targeted databases for LC-MS/MS searches and demonstrated the superior performance of this approach in detecting MHC-I peptides in mice and human models compared to traditional searches.

**Chapter 4: Near-infrared absorbing Ru (II) complexes act as immunoprotective photodynamic therapy (PDT) agents against aggressive melanoma.** (and)

**Chapter 5: Photodynamic therapy of melanoma with new, structurally similar, NIR-absorbing ruthenium (II) complexes promotes tumor growth control via distinct hallmarks of immunogenic cell death.**

Despite recent advances in targeted therapies and immunotherapies, there is no cure for high-risk invasive melanomas. Furthermore, due to primary and secondary resistance to these therapies, the survival benefit is only observed in a small proportion of patients. Therefore, new approaches that act both locally and systemically, without developing resistance are highly desired. While PDT is not currently utilized as a treatment option for melanoma, it could be a great strategy because it 1. can induce direct tumor cytotoxicity, stimulate antitumor immunity and generate long term protection, 2. can be used as an adjuvant in combination with surgery or radiation, without compromising the other therapies, 3. has no off-site or systemic toxicity due to the specific activation of compounds at the local tumor site, and so, 4. can improve quality of life in palliative care. However, traditional organic PSs currently approved for clinical usage do not offer the full potential of PDT due to limitations such as lower activation wavelengths that allow them to treat only surface-level tumors, poor chemical stabilities, heavy reliance on oxygen and other limitations outlined in section **1.5.2**. Furthermore, existing PSs are less effective for treating pigmented melanomas because light penetration and PS functions are limited by the cryoprotective qualities of melanocytes and melanin.

*I hypothesized that transition metal complexes with superior photophysical and photochemical properties might be leveraged to overcome existing limitations and develop a platform for designing immunotherapeutic PDTs for melanoma treatment.* To accomplish this, we developed several novel Ruthenium (II) based PSs in collaboration with photochemist Dr. Sherri McFarland at the University of Texas Arlington. I investigated these novel compounds in mouse models of aggressive melanoma for their 1. direct cytotoxicity, 2. inflammatory and immunogenic cell death causing capabilities, and 3. therapeutic potential by employing *in vitro*, *ex vivo*, and *in vivo* experimental techniques. The work reported in these two chapters is the first to characterize the immunostimulatory potential of transition metal complexes.

# CHAPTER 2: MATERIALS AND METHODS

## 2.1. CELL LINES & CELL CULTURE

EL4 cells were originally purchased from ATCC and were maintained in Dulbecco's modified Eagle medium (DMEM, Invitrogen catalog no 11965), containing 10% FBS (Invitrogen catalog no 12484) and 5% antibiotic/antimycotic penicillin, streptomycin, and Amphotericin B (Invitrogen catalog no 12484). Cells were grown in T75 flasks to a density of $2 \times 10^6$ cells/mL before subculturing or harvesting for experiments. B16F10 cells (ATCC CRL-6475) were cultured at 37°C, 5% $CO_2$ in DMEM medium (Invitrogen catalog no 11965) supplemented with 10% fetal bovine serum (Invitrogen catalog no 12484), 1% sodium pyruvate (Invitrogen catalog no 11360), 1% non-essential amino acids (Invitrogen catalog no 11140) and 1% antibiotic-antimycotic penicillin, streptomycin, and Amphotericin B (Invitrogen catalog no 15240). Cells were grown in 10- or 15-mm cell culture dishes (Corning) and subcultured on alternative days. Cell culture supernatants were tested for mycoplasma monthly using Mycoalert detection kit as per manufacturer's instructions (Lonza catalog no LT07-118).

## 2.2. MOUSE MHC-I AND HUMAN HLA PEPTIDE DATABASE

Mouse and human FASTA (a txt format file that begins with a single-line description followed by lines of sequence data) databases were downloaded from UniProtKB (mouse, December 2015; human, February 2015), containing all mouse or human proteins, including isoforms and variants. Then, using an offline version of NetMHC (version 4.0)[124], allotype-specific mouse or human binding affinities were predicted for all 8-, 9-, 10-, and 11-mer peptides for 2 mouse allotypes (H-2 Db and H-2 Kb) and 14 human allotypes (A*01, A*02, A*03, A*11, A*24, A*29, A*32, B*07, B*08, B*27, B*35, B*39, B*44, and B*51). All peptides with NetMHC-predicted binding affinities ≤ 2% rank

(binding threshold recommended by NetMHC algorithm) for each allotype were then compiled into a new FASTA database. All database manipulations were performed using Python and R scripts.

## 2.3. ANTIBODY-BASED MHC-I PULL DOWN

An aliquot of $8 \times 10^8$ EL4 cells was pelleted and used for MHC-I peptide immunoprecipitation as previously described.[546] In brief, cells were lysed in PBS containing 0.4% CHAPS and mini-complete protease inhibitor tablets (Roche, Indianapolis, IN). Antibodies were produced in-house from hybridoma clones B22.249 (H-2 Db-specific) and Y3 (H-2 Kb-specific). MHC-I proteins were precipitated from the cell lysate using 2 mg of each antibody coupled to 80 mg of CNBr-activated Sepharose 4B resin (Uppsala, Sweden). Incubations were performed overnight at 4°C in 10 mL glass tubes. Bound MHC-I proteins and peptides were washed with 40 mL of PBS, then 30 mL of Milli-Q water, and then peptides eluted eight times with 200 µL of 0.2% trifluoroacetic acid (TFA). Eluates were filtered through 3 kDa molecular weight cutoff filters (Millipore, Cork, Ireland); then, the filtrate was lyophilized and desalted using Stage-tips.[547]

## 2.4. MASS SPECTROMETRY – LIGANDOME

Lyophilized peptides were solubilized in 12 µL of 1% formic acid and analyzed by LC–MS/MS. For each antibody eluate, an aliquot of 1 µL of peptides was injected onto a 75 µm × 30 cm column (New Objective, Woburn, MA) self-packed with 4 µm, 90 Å, Proteo C18 material (Phenomenex, Torrance, CA). Online chromatography was performed using a Dionex Ultimate 3000 UHPLC (Thermo-Scientific, San Jose, CA) at a flow rate of 300 nL/min. Peptides were separated and eluted into the mass spectrometer using a gradient of 3 to 35% acetonitrile (0.1% formic acid) over 65 minutes, followed by 5 minutes at 95% acetonitrile (0.1% formic acid). MS was performed using an Orbitrap

Velos Pro (Thermo-Scientific, San Jose, CA), which was operated in a data-dependent mode. Survey scans (MS1) were performed using the Orbitrap over a scan range of 350–650 m/z and resolution setting of 60 000. A lock mass of 445.12003 m/z was used to achieve internal mass calibration as previously described.[548] On the basis of MS1 scans, MS2 scans were performed using the ion trap, selecting the top 10 most intense precursor (MS1) ions for fragmentation by collision-induced dissociation (CID) at 35% collision energy with a precursor isolation window of 2 m/z. MS2 scans were only collected on peptides with charge states of 2+ or 3+ with a minimum MS1 intensity of 50 counts. Advanced gain control (AGC) settings were $5 \times 10^5$ for Orbitrap scans and $2 \times 10^5$ for ion trap scans.

## 2.5. DATABASE SEARCHING AND COMPARISONS

Mouse and human database searches were performed using either Sequest or Mascot implemented with Proteome Discoverer 1.4 (Thermo Scientific catalog no OPTON-30810). The parent ion (MS1) tolerance was 5 ppm, and fragment ion tolerance was 0.5 Da. Spectra for each immunoprecipitation (IP) were searched against either the parent database (Parent-DB) or the MHC-targeted database (MHC-DB or HLA-DB). Spectra were searched against Parent-DB using no enzyme specificity but searched against MHC-DB or HLA-DB using no cleavage restriction. Peptide false discovery rate (FDR) was controlled using Percolator.[549] All peptides with “medium” (5% FDR) or “high” (1% FDR) confidence were reported in the final data sets. Peptide and Peptide Spectral Match (PSM) analyses comparing results for the different antibody eluates and database searches were performed using R. Mouse MS (.raw) files have been deposited to Chorus, https://chorusproject.org, ID#1098.

## 2.6. PDT LIGHT DEVICES

For all *in vitro* experiments, briefly, confluent plate of B16F10 cells were trypsinized, seeded into plates and incubated for 3 hours at 37°C before adding the photosensitizer at respective concentrations. The plates were covered in aluminum foil to protect from light and were incubated at 37°C, 5% $CO_2$ for 16 hours upon which PDT treatment plates were exposed to a 630 nm light (Prizmatix LED, UHP-T-LED-630) or 733 nm laser (2 W, CivilLaser; (9–10 $mW^{-2}$) coupled to a 600 µm optical fiber with a 2 mm flat-cut diffuser (Medlight, FD1) to achieve the required light dosage.

## 2.7. ALAMAR BLUE CELL VIABILITY ASSAY

B16F10 cells were seeded in 96 well plates at a density of 4000 cells per well in 75 µl DMEM complete media and were mixed twice (up, down, left, right tilting) in the biosafety cabinet before placing inside the incubator for 1–3 hours. During the incubation, PDT compound dilutions were prepared in sterile 0.8 ml 96-deep well plates (Greiner BioOne, 780261) using PBS as solvent. Dilutions were prepared in serial across 9 concentrations ranging from 300–$1\times10^{-3}$ µM. Covered deep-well plates were incubated for 0.5–1 h before final dispensing 25 µl per well into B16F10 seeded plates. All sample and control wells total 100 µl per well at this point. The biosafety cabinet's lights were kept off while dispensing compounds. Following dark (sham) or light treatments (630 nm or 733 nm, 16-hour drug-to-light interval, DLI), plates are further incubated for 48 hours before final viability measurements. At this point, 10 µl per well of 0.3 mM sterile filtered resazurin (commercially known as alamar blue) in 0.2 M phosphate buffer (pH = 7.4) is dispensed across all well plates. Resazurin-treated plates were incubated for 3 hours before reading fluorometrically on a Molecular Devices SpectraMax M2 or M3 (30 s shake, bottom-read, λexc 530 nm, long-pass 570 nm, λem 620 nm).

## 2.8. FLOW CYTOMETRY QUANTIFICATION OF CELL DEATH

Cell death was assessed by Annexin V (Biolegend catalog no 640905) and 7AAD (eBioscience catalog no 00-6993) staining. A total of 5 x $10^5$ B16F10 cells were plated per well in 12-well plates and treated with EC50 (dose effective in producing 50% of the maximal response identified using alamar blue assay) of PDT compound and 25 J/$cm^2$ of 630 nm light. Untreated, PS only, or light treatment only controls were included for every compound. Briefly, cells were collected, washed in PBS, pelleted, and resuspended in an incubation buffer (10mM HEPES/NaOH (pH 7.4), 140mm NaCl, and 5mM CaCl2) at 0.5-1x$10^6$ cells/ml. Annexin V (5µl) followed by 7AAD (5µl) was added to the cell suspension, and samples were incubated in the dark for 15 minutes at room temperature. Samples were subsequently analyzed on a BD FACSCanto II flow cytometer using BD FACSDiva and FCS 6 software.

## 2.9. CALRETICULIN SURFACE LOCALIZATION

A total of 5x$10^5$ B16F10 cells were plated in 12-well plates and treated with EC50 of LL364 and 25 J/$cm^2$ of 630 nm light. For Calreticulin staining, cells were collected by trypsinization 4 hours post-treatment, washed twice in cold PBS, incubated for 45 minutes with the rabbit anti-Calreticulin primary antibody (Abcam catalog no ab2907), diluted in cold blocking buffer (1% fetal bovine serum in PBS), followed by washing and incubation with the Alexa Fluor 647-conjugated secondary antibody (Invitrogen catalog no A-21246) in a blocking buffer (for 30 minutes). Cells were washed twice with PBS and fixed in 2% paraformaldehyde in PBS for 10 minutes. Each sample was then analyzed on BD FACSCanto II to identify cell surface Calreticulin.

## 2.10. CELLULAR REACTIVE OXYGEN SPECIES ANALYSIS

A total of 5x$10^5$ B16F10 cells were plated in 12-well plates and treated with EC50 of LL364 and 25 J/$cm^2$ of 630 nm light. For measuring reactive oxygen species, cells were

collected by trypsinization 4 hours post-treatment, washed twice in cold PBS, incubated with CM-H2DCFDA (Molecular Probes catalog no. C6827, 1 μmol/L) for total ROS or MitoSOX to measure mitochondrial ROS (Molecular Probes catalog no. M36008) for 30 minutes at 37°C in PBS before analysis on the BD FACSCanto II.

## 2.11. HMGB1 ELISA

A total of $5x10^5$ B16F10 cells were plated in 12-well plates and treated with EC50 LL364 and 25J/$cm^2$ of 630 nm light. Supernatant samples were collected 24 hours post-treatment and immediately assessed for HMGB1 levels by enzyme-linked immunosorbent assay according to the manufacturer's instructions (IBL International, ST51011) on SpectraMax M2 (Molecular Devices).

## 2.12. DETECTION OF ATP SECRETION

A total of $5x10^5$ B16F10 cells were plated in 12-well plates and treated with EC50 LL364 and 25J/$cm^2$ of 630 nm light. Supernatant samples were collected 12 hours post-treatment, and ATP concentrations were measured by means of an ATP Determination Kit (Invitrogen catalog no A22066), according to the manufacturer's protocol on SpectraMax M2.

## 2.13. REAL-TIME QPCR

RNA extractions were conducted using standard TRIzol methodology as per manufacturer's guidelines (Invitrogen catalog nos 15596026 & 12183025). Extracted RNA was quantified via A260/A280 absorption reading obtained using spectra drop microvolume microplate RNA quantification setting on Spectramax M2 (Molecular Devices), diluted to a total of 2 μg, and synthesized into cDNA using SuperScript II Reverse Transcriptase (Invitrogen catalog no 18064014). The Bio-Rad CFX96 PCR machine was used for qPCR, using ssoadvanced universal sybr green supermix (Bio-

Rad catalog no 1725274) according to the manufacturer's instructions for amplification and quantification. Gene-specific primers for murine HSP90, HSPA1B, CXCL10, TNFα, IL6, IFNβ, IFIT1, TLR3, H2D, TAP1, β2M, GAPDH were custom synthesized and purchased from Invitrogen. All primers were validated using serially diluted cDNA and confirmed to have an efficiency of >95%. RT-qPCR reaction was performed using cycle setting 95$^{o}$C-30 sec, (95$^{o}$C-10 sec, 60$^{o}$C-30 sec) x 39 cycles, 65$^{o}$C-05 sec, 95$^{o}$C-05 sec. The data from the qPCR were collected and analyzed using Livak and Schmittgen's $2^{-\Delta\Delta CT}$ method. The fold change was calculated by first normalizing the cycle threshold of the indicated gene against GAPDH, followed by a comparison against the control untreated sample.

## 2.14. MICE

*In vivo* experimental procedures were approved by the Dalhousie University Animal Ethics Committee in accordance with the regulations/guidelines from the Canadian Council on Animal Care (CCAC). Female and male C57BL/6 mice were purchased from Charles River Laboratory (Strain Code #027). Transgenic BRaf$^{CA}$, Pten$^{loxP}$, Tyr::CreER$^{T2}$ mice were purchased from The Jackson Laboratory (Strain Code #013590).

## 2.15. BONE MARROW-DERIVED DENDRITIC CELL CULTURE

Bone marrow cells were harvested from the femurs and tibias of euthanized 6-8-week-old C57BL/6 mice and flushed using a 26G needle attached to a syringe containing complete RPMI 1640 media. Harvested single-cell suspensions were strained through 40-70 µm cell strainers and treated with red blood cell -lysing ammonium-chloride-potassium buffer (150mM NH4Cl, 10mM KHCO3, 0.1mM Na2EDTA) for 5 minutes. Lysing buffer was neutralized with RPMI 1640 complete media, cells were pelleted and resuspended in fresh complete RPMI 1640 media containing 20ng/mL GMCSF for 7-10 days. Media was supplemented with fresh GMCSF-containing RPMI media on day 3

post culture and resuspended in fresh media on days 6 and 9. Suspension cells were used for the indicated experiments.

## 2.16. DENDRITIC CELL PHAGOCYTOSIS AND FUNCTIONAL CHARACTERIZATION EXPERIMENTS

5-(and 6)-Carboxyfluorescein diacetate succinimidyl ester (CFSE, Biolegend, 423801) labelled B16F10 cells were treated with determined EC50 of PDT compounds and 25 J cm-2 of 630 nm irradiation for phagocytosis experiments. Cells were collected 4 hours post-PDT and co-cultured with harvested bone marrow derived dendritic cells (BMDCs) at 1:1 or 1:5 ratio for 2 hours at 37°C. After co-culture, cells were washed and incubated with anti-mouse CD16/ CD32 (BioXCell, BE0307) for 30 minutes, followed by labeling with CD11c-APC/Cy7 (Biolegend, 117323) for 30 minutes. Cells were acquired on BD FACS Canto II or BD FACS Celesta. For functional characterization, harvested BMDCs were cultured in PDT-treated B16F10 conditioned media (50% of total volume and 50% base DC media as described above) for 24 hours at 37°C. LPS treated sample (50 ng/mL LPS, 24 hrs) was used as a positive control. Cells were collected in TRIzol (Thermo, 15596026) post-activation with appropriate conditioned medium treatment for qRT-PCR analysis.

## 2.17. IN VIVO VACCINATION EXPERIMENT

A total of $5\times10^5$ B16F10 cells per well in a 6-well plate were treated with the determined EC50 of PDT compounds and 50 J $cm^{-2}$ of 630 nm irradiation. For the vaccination, 4- and 12-hour post-treatment cells were combined, and $5\times10^5$ cells in 100 µl PBS were injected subcutaneously into the left flank of male and female C57BL/6 mice. One week after vaccination, mice were challenged with $1\times10^5$ untreated B16F10 cells in 100 µl PBS into the right flank. Tumor sizes were measured using a digital vernier caliper, and volumes were calculated using the formula pi x (length x width x height)/3.[550]

## 2.18. IN VIVO PDT EXPERIMENT

C57BL/6 female mice were subcutaneously inoculated in the right flank with $1x10^5$ B16F10 cells in 100 µl PBS. Spontaneous tumors formed on transgenic $BRaf^{CA}$, $Pten^{loxP}$, $Tyr::CreER^{T2}$ mice were utilized. Upon palpable tumor formation, tumors were injected with ML18H01 PS at a dose of 20 mg/kg (maximum tolerated dose, MTD determined at 50 mg/kg) in 100 µl PBS. A drug light interval of 4 hours was implemented, and tumors were illuminated with a 733 nm laser to deliver a dose of fluence=150 J $cm^{-2}$ at irradiance=172.4 mW $cm^{-2}$, for roughly 15 minutes per mouse. Mice were covered with a blanket with only the tumor site exposed during this procedure.

## 2.19. DATA ANALYSIS & STATISTICS

Flow cytometry data were analyzed using FCS Express 6 software. Mean fluorescence intensity values were reported after subtracting the background fluorescence of respective treatments. qRT-PCR analysis was done using Bio-Rad CFX Manager software. All statistical analyses were performed in GraphPad Prism 7. Hazard ratios were calculated with the Mantel-Haenszel method using GraphPad Prism 7. The hazard ratios represent the hazard rate of the unvaccinated group over the vaccinated group. One-way ANOVA coupled with Bonferroni post-test or Student's t-test was performed, and significance is listed as follows: * = $p < 0.05$, ** = $p < 0.01$, *** = $p < 0.001$, **** = $p < 0.0001$. All experiments represent data from a minimum of n=3 experiments. Data is represented as mean +/- standard deviation.

## 2.20. CODE AVAILABILITY

We have made SpectMHC available on GitHub: https://github.com/Prathyusha-konda/SpectMHC. This semicommand-line-based tool is customized to be used with preinstalled stand-alone NetMHC packages in Darwin (Mac) and Linux platforms. The tool takes an input protein FASTA database and outputs predicted MHC-binding

peptides using NetMHC 4.0, NetMHC 3.4, or NetMHCpan. The instructions to utilize the code are available in the readme file found in the above GitHub folder.

**Table 2.1.** List of qRT-PCR primers

| Gene name | Forward primer | Reverse primer |
|---|---|---|
| CXCL10 | GTTGAGATCATTGCCACGATGAAA | CTGCTGTCCATCCATCGCA |
| IFNβ | GTCCGAGCAGAGATCTTCAGG | GAGTCCGCCTCTGATGCTTA |
| HSP90 | CTCCAATTCATCGGACGCTCT | AAGTCGGCCTTGGTCATTCC |
| HSPA1B | CAGGACCCACCATCGAGGA | ACAGTAATCGGTGCCCAAGC |
| TLR3 | TCCTGCTGGAAAACTGGATGG | AGCCTGAAAGTGAAACTCGCT |
| β2M | ATGCTATCCAGAAAACCCCTCA | TTTCAATGTGAGGCGGGTGG |
| IL6 | TCTCTGCAAGAGACTTCCATCC | TTGTGAAGTAGGGAAGGCCG |
| IFIT1 | ACCATGGGAGAGAATGCTGATG | TTGTGCATCCCCAATGGGTT |
| TNFα | TGTTGCCTCCTCTTTTGCTT | TGGTCACCAAATCAGCGTTA |
| TAP1 | CCACGAGTGTCTCGGGAAT | ATGAGACAAGGTTGCCGCT |
| H2D | GAGTGAGCCTGAGGAACCTG | AGCCAGACATCTGCTGGAGT |
| GAPDH | TGGCAAAGTGGAGATTGTTG | AAGATGGTGATGGGCTTCCC |
| CD40 | TGTCATCTGTGAAAAGGTGGTC | ACTGGAGCAGCGGTGTTATG |
| CD80 | GCAGGATACACCACTCCTCAA | AAAGACGAATCAGCAGCACAA |
| CD83 | CGCAGCTCTCCTATGCAGTG | GTGTTTTGGATCGTCAGGGAATA |

| Gene name | Forward primer | Reverse primer |
|---|---|---|
| CD86 | TGTTTCCGTGGAGACGCAAG | TTGAGCCTTTGTAAATGGGCA |
| CTLA4 | AGAACCATGCCCGGATTCTG | CATCTTGCTCAAAGAAACAGCAG |
| IcosL | TAAAGTGTCCCTGTTTTGTGTCC | ATTGCACCGACTTCAGTCTCT |
| IL12β | TGGTTTGCCATCGTTTTGCTG | ACAGGTGAGGTTCACTGTTTCT |
| Arg1 | CTCCAAGCCAAAGTCCTTAGAG | AGGAGCTGTCATTAGGGACATC |
| PD-L1 | CCTCGCCTGCAGATAGTTCC | AGCCGTGATAGTAAACGCCC |
| Tim3 | TCAGGTCTTACCCTCAACTGTG | GGCATTCTTACCAACCTCAAACA |

# CHAPTER 3: MHC-I LIGAND DISCOVERY USING TARGETED DATABASE SEARCHES OF MASS SPECTROMETRY DATA: IMPLICATIONS FOR T-CELL IMMUNOTHERAPIES

This work is published in:

Murphy JP*, **Konda P***, Kowalewski DJ, Schuster H, Clements D, Kim Y, Cohen AM, Sharif T, Nielsen M, Stevanovic S, Lee PW, Gujar S. MHC-I ligand discovery using targeted database searches of mass spectrometry data: implications for T-cell immunotherapies. ***Journal of Proteome Research***. 2017 Apr 7;16(4):1806-16.

* contributed equally

## CONTRIBUTIONS:

J.P.M. and **P.K.** designed the study, carried out the experimentation, collected and analyzed data, and prepared the manuscript. **P.K.** wrote the code for *SpectMHC* tool used for database compilation. A.M.C. helped with MS instrumentation. M.N. provided bioinformatics support. T.S. S.S, H.S, D.J.K, D.C, Y.K, and P.W.L. provided input. S.G. assisted with study design, writing, and critical review of the manuscript.

**Details of PK's contributions:**

- Sections 3.3.1, 3.3.2., 3.3.4. were written by **P.K**.
- **P.K.** wrote the code for *SpectMHC* tool and developed the computational pipeline for MS data analysis. **J.P.M.** performed MHC-I immunopeptidome experiment**.**
- Data analysis and generation of graphs related to Figures 3.1., 3.2., 3.3., 3.5. (A and B), supplementary 3.1., 3.2., 3.3., 3.4., and 3.7. (A) were performed by **P.K.** In general, both first authors involved in the decision-making processes for all figures.
- Sections 3.3.5., 3.1. (abstract), 3.2. (introduction), and 3.4. (discussion) were written together by **P.K. and J.P.M.**

## 3.1. ABSTRACT

Class I major histocompatibility complex bound peptide ligands dictate the activation and specificity of CD8+ T cells and thus are important for devising T-cell immunotherapies. In recent times, advances in mass spectrometry have enabled the precise identification of these MHC-I peptides, wherein MS spectra are compared against a reference proteome. Unfortunately, matching these spectra to reference proteome databases is hindered by inflated search spaces attributed to a lack of enzyme restriction in the searches, limiting the efficiency with which MHC ligands are discovered. Here we offer a solution to this problem whereby we developed a targeted database search approach and accompanying tool SpectMHC, that is based on a priori-predicted MHC-I peptides. We first validated the approach using MS data from two different allotype-specific immunoprecipitates for the C57BL/6 mouse background. We then developed allotype-specific HLA databases to search previously published MS data sets of human peripheral blood mononuclear cells (PBMCs). This targeted search strategy improved peptide identifications for both mouse and human ligandomes by greater than 2-fold and is superior to traditional “no enzyme” searches of reference proteomes. Our targeted database search promises to uncover otherwise missed novel T-cell epitopes of therapeutic potential.

## 3.2. INTRODUCTION

Antigen-specific activation of CD8+ T-cells is initiated when a specific T-cell receptor recognizes its cognate peptide epitopes presented through class I major histocompatibility complexes (MHC-I) on antigen-presenting cells. These MHC-bound peptides, collectively known as the MHC-I ligandome, are usually 8–11 amino acids long and are derived from intracellular-cleaved "self" or foreign proteins.[89] MHC-I molecules, termed Human Leukocyte Antigens (HLA) in humans, are highly polymorphic, particularly in the human population, and the peptides bound are highly dependent on an individual's HLA allotype. Surveying the MHC-I ligandome in both a context- and allotype-specific manner is of the utmost importance in understanding how the adaptive immune response is regulated in pathogen infection and cancer. Furthermore, precise MHC-I peptide identification from mass spectrometry (MS) data is especially important in designing therapeutic targets that could be used to formulate personalized CD8+ T-cell-based therapies such as vaccines against infectious diseases.[551] Additionally, for vaccine-based cancer immunotherapies, MS-enabled identification of tumor-associated MHC-I ligands or those containing neo-antigens is crucial.[13,552]

Identifying MHC-I ligands by MS remains difficult due to low peptide abundance, but advancements in MS sensitivity are revolutionizing the process. Currently, the main experimental approach is to perform immuno-precipitation (IP) of MHC-I proteins, followed by peptide elution, purification, and analysis by LC–MS/MS.[553] For mouse models, well-characterized MHC-I allotype-specific antibodies can be employed in the IP because allelic diversity in mice is low. In contrast, human allelic diversity is high but pan-HLA-specific antibodies such as the W6/32 antibody are well established.[554] Spectra from the antibody eluates are then scored against a protein database using search algorithms such as Mascot and filtered to a certain false discovery rate (FDR).

Following the database searches, it is common for a large portion of the collected spectra to not be assigned a peptide identification. Recently, this has been partially attributed to unforeseen proteasomally spliced peptides nonexistent in the database searches.[89] In the past, other types of nonstandard MHC-I peptides have also been reported that may explain missing spectral assignments in database searches such as noncanonical reading frames[555] and nonclassical peptide cleavage.[556] However, another common problem that complicates spectral assignments in all MHC ligandome analyses to date is the inability to narrow the number of potential spectral matches by specifying a proteolytic enzyme cleavage specificity, as would be implemented when searching shotgun proteomics data. As a result, vast search spaces are explored during database searches of MHC-I IP MS data because the composition of peptide assignments tested is not representative of the sample. As such, statistical power is low when estimating FDRs for MS/MS spectra. It has been proposed for proteomics studies that search space sizes could be reduced by limiting them to only those peptides likely to be present in the sample.[557,558] This strategy would improve FDR estimations and increase the number of peptides identified from shotgun MS data. We therefore questioned whether the search spaces for MHC-I IP MS database searches could be limited solely to predicted MHC-I ligands for the allotypes of the sample to improve identification rates.

Various MHC-I peptide prediction tools are available to implement the MHC-peptide database search approach.[559–562] Most predictors are trained on existing MHC-I binding assay data and output lists of potential MHC-I peptides from protein sequences.[563] One such tool, NetMHC,[560] uses neural networks trained on large data sets of MHC-I peptide binding affinity values and predicts probable MHC-I ligands for queried proteins. Executing NetMHC in mouse models is practical because few allotypes

exist among mouse MHC-I proteins. Although polymorphism of human alleles is high, performing HLA predictions is now becoming feasible as peptide-binding data sets are being collected on more allotypes.[564]

Here we developed a targeted database search strategy using NetMHC predictions to compile peptide databases to search MHC-I IP MS data. The approach leads to greatly improved numbers of MHC class I peptide identifications from both murine and human IPs. To implement the targeted searches, we made an accompanying Python-based tool, SpectMHC, available to the immunology community. On the basis of a reference proteome, SpectMHC compiles targeted MHC-I peptide FASTA databases to be used for searching MHC-I IP MS data and is available on GitHub: https://github.com/Prathyusha-konda/SpectMHC. It is worth noting that our approach not only is applicable to current and future MHC ligand discovery efforts but also can be used retrospectively; when we applied it to already published MHC ligandome data sets, MHC ligands were detected that otherwise went unreported.

## 3.3. RESULTS

### *3.3.1. Generation of targeted MHC-I databases.*

Improving MHC peptide ligand identification and measurement by MS is important because MHC-I peptides are not produced from easily predictable enzymatic cleavage sites. This leads to all peptides within a specific precursor ion tolerance being tested, resulting in large search spaces that most likely result in inflated FDR statistics and low specificity. It has been proposed that the assignment of spectra from shotgun MS experiments can be improved by tailoring the search database to those peptides likely to be in the sample.[557,565] Even in the proteomics field, recent attempts have been made to narrow search spaces to improve protein identifications from peptide digests by, for

example, using databases formed from spectral libraries of previously identified peptides[558] or from RNASeq data collected from the samples.[566] In these cases, the targeted searches resulted in databases that more accurately reflected the samples analyzed and increased the number of identified peptides. We thus anticipated that this targeted strategy could be employed to reduce the complexity of databases used for MHC-I IP MS searches. Searches against a targeted MHC-I peptide database could then be implemented in which the MHC prediction tool replaces enzymatic cleavage specificity. Such a strategy allows the use of a no cleavage search, whereby spectra are only tested against full database entries and not to non-MHC peptides residing in the sequences therein. This is exemplified by the predicted MHC peptide, FQALNAEKL from the mouse protein kinase ATR [**Figure 3.1.A**], where instead of the many matches to the full protein when using a no enzyme search, a no cleavage search of the targeted database results in fewer potential matches to unlikely spectral assignments.

We began with a simple mouse model for which the MHC-I peptides could be easily predicted due to their low MHC-I allelic polymorphism. The commonly used C57BL/6 laboratory mouse strain carries the well-characterized H-2 Db and H-2 Kb mouse MHC-I allotypes, for which hybridomas producing allele-specific antibodies exist. To generate a targeted MHC-I database, we used a “parent” reference database containing 56 479 mouse UniProtKB protein sequences (Parent-DB). Although many other tools are available such as SYFPEITHI[562] and IEDB,[561] we have employed NetMHC for peptide predictions because it has high allotype coverage. Furthermore, in situations where the HLA alleles in question are not covered by NetMHC 4.0, the pan-allotype-specific NetMHCpan 3.0 predictor performs very well.[123] Using NetMHC (offline, version 4.0), we predicted the H-2 Db and H-2 Kb binding affinities for all possible 8-, 9-, 10-, and 11-mer peptides for each protein in the parent database [**Figure**

**3.1.B**]. Rather than a specific nM affinity cutoff, a % rank cutoff in NetMHC has recently been shown to be more versatile across different allotypes, whereby the top 2% ranking predicted MHC peptides show high specificity.[123] Therefore, all 8- to 11-mer peptides were filtered to ≤2% NetMHC rank. This vastly smaller list of peptides was compiled into a targeted, MHC-I peptide database (MHC-DB) [**Figure 3.1.B**]. The MHC-DB is composed of 1 458 851 entries of which H-2 Db peptides were 38% 8- to 9-mers whereas H-2 Kb peptides were 67% 8- to 9-mers [as illustrated in **Figure 3.1.C**]. The MHC-DB contained only 1% of the 8- to 11-mers in the Parent-DB [**Figure 3.1.B**]; thus the potential peptide identifications in the search space decreased by ~2 orders of magnitude. It is clear that MHC-I searches against this database would successfully limit the search space to a small fraction of the mouse proteome. Using the database for searching MS data also replaces the need for an enzymatic cleavage specificity because it is inherently built into the database prediction step. The targeted database allows for a novel, simplified search strategy for MHC-I database searches to increase ligand identification. Because it would be of interest to others, we offer a supporting tool (*SpectMHC*) to make searchable targeted MHC-I FASTA databases.

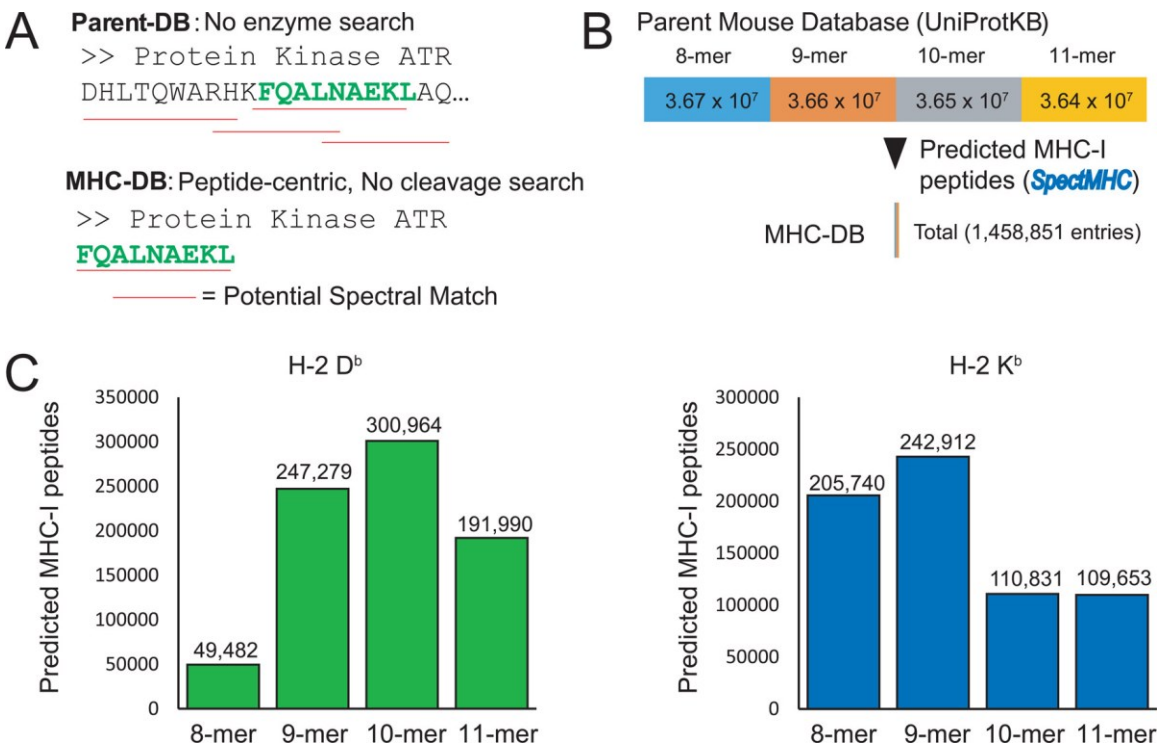


**Figure 3.1.** Predicting MHC-I peptides for the full mouse proteome.

(A) Targeted MHC-I search (MHC-DB), performed with no cleavage specificity, limits potential spectral matches and decreases the search space compared with a reference proteome (Parent-DB) search. (B) Beginning with a reference database of mouse proteins, a targeted MHC-I- database (MHC-DB) solely containing predicted sequences was formed (NetMHC ≤ 2% rank) using SpectMHC. The MHC-DB contained peptides from the H-2 Db and H-2 Kb mouse alleles. Shown are the numbers of 8- to 11-mer peptide sequences in the parent database and the total NetMHC-predicted peptides (H-2 Db and H-2 Kb). (C) Distribution of the total NetMHC-predicted (≤2% rank) mouse MHC-I peptides (by 8- to 11-mers) for the H-2 Db and H-2 Kb allotypes used to create the MHC-DB.

### *3.3.2. Targeted MHC-I peptide database searches increase identification rates for MHC-I ligands.*

With the mouse MHC-I peptide FASTA database in hand, we then empirically tested the targeted MHC-I database search strategy. As a model, we used the EL4 mouse cell line (C57BL/6 background) and performed allotype-specific MHC-IP experiments using established protocols.[546] Specificity was enabled using antibodies specific to the H-2 Db (B22.249 hybridoma[567]) or H-2 Kb (Y3 hybridoma[568]) mouse allotypes [**Figure 3.2.A**]. Following antibody-based MHC molecule elution and peptide separation, peptide mass spectra were generated using shotgun LC–MS/MS. An issue with limiting the search space only to MHC-I peptides is that non-MHC peptides may be falsely matched to MHC-I peptides because non-MHC matches are not present. To test this, we intentionally did not separate NetMHC-predicted H-2 Db and H-2 Kb predictions. This strategy allowed us to assess whether non-MHC peptides would be matched to the MHC-DB because correct peptide matches from each IP should reflect the specificity of the antibody used. Alternatively, if peptide matches to the MHC-DB search were incorrect, then new peptide assignments should be equally distributed among H-2 Db and H-2 Kb peptides independent of the antibody.

To estimate false discovery rates for peptide identification, commercial software implementations of tools such as Percolator[569] are common and use reversed or shuffled versions of the peptides as decoy databases. Using the MHC-I peptide-targeted approach, a decoy database of reversed peptides can be formed either before or after NetMHC prediction. Reversing proteins before predicting requires an additional round of NetMHC prediction and requires specifying target and decoy databases during the search, which in most commercial database search tools is not yet implementable. Before implementing our searches with commercial software (Proteome Discoverer) we

manually assessed the target decoy strategy, comparing Sequest search PSMs where the decoy was formed by (1) reversing proteins in the Parent-DB then predicting by NetMHC (Reverse then Predict) or (2) reversing the NetMHC-predicted peptides (Predict then Reverse). We observed the overall distribution (by Sequest XCorr) of target and decoy hits (PSMs) to be similar by both strategies for both the B22.249 and Y3 IPs [**Supplementary Figure 3.1.A**]. Furthermore, in our 2-antibody model both approaches accurately returned target PSMs of the correct antibody (H-2 Db to B22.249 and H-2 Kb to Y3), whereas decoy PSMs were equally represented by the correct or incorrect allele-matching PSMs [**Supplementary Figure 3.1.B**]. Manual estimation of the FDR as previously described[570] showed only minor differences in the total number of unique peptides from each target decoy strategy, and antibody allotype was conserved at 5% [**Supplementary Figure 3.1.C**] and 1% FDR [**Supplementary Figure 3.1.D**]. As such, the approach could be implemented using a single forward NetMHC-predicted database, which allowed implementing Percolator in Proteome Discoverer whereby reversed MHC peptides served as the decoy database.

To assess the EL4 MHC-I IP for the study, we first performed database searches against Parent DB using both Sequest and Mascot with no enzyme as the search specificity, with both 5% and 1% Percolator[569] FDR thresholds. Using Sequest/Percolator at 1% FDR, a total of 1537 unique peptides were identified between the B22.249 and Y3 antibody IPs. Using Mascot/Percolator at 1% FDR, a total of 995 unique peptides were identified between the B22.249 and Y3 antibody IPs. Of these, only 8.9% (150) and 12.6% (126) of the Sequest and Mascot searches, respectively, were not considered MHC-I peptides using a 2% NetMHC rank cutoff [**Figure 3.2.B**]. Furthermore, the IPs were allotype-specific, in that MHC-I peptides identified from the Sequest Parent-DB search were 97% (845/868) H-2 Db-specific and 90% (668/742) H-2

Kb-specific (as revealed by a 2% NetMHC rank cutoff) for the B22.249 and Y3 IPs, respectively (1% FDR) [**Figure 3.2.B**]. MHC-I peptides identified from the Mascot Parent-DB search were 98% (471/482) H-2 Db-specific and 88% (370/422) H-2 Kb-specific for B22.249 and Y3 IPs, respectively (1% FDR) [**Figure 3.2.B**]. At 5% Percolator FDR, a total of 2238 and 1942 peptides were identified by Sequest and Mascot searches, respectively, of which 250 (11%) and 252 (13%) were not considered MHC-I peptides by NetMHC (2% rank cutoff), respectively [**Supplementary Figure 3.2.A**]. Interestingly, even at this much less stringent FDR (5%), antibody specificity was similarly maintained as it was at 1% FDR. MHC-I peptides identified from the Sequest Parent-DB search were 97% (1062/1092) H-2 Db-specific and 89% (894/1008) H-2 Kb-specific (as revealed by a 2% NetMHC rank cutoff) for B22.249 and Y3 IPs, respectively [**Supplementary Figure 3.2.B**]. MHC-I peptides identified from the Mascot Parent-DB search were 98% (911/934) H-2 Db-specific and 88% (747/850) H-2 Kb-specific (as revealed by a 2% NetMHC rank cutoff) for B22.249 and Y3 IPs, respectively [**Supplementary Figure 3.2.B**]. Next, to test the targeted search approach, we performed Sequest and Mascot searches to match the MHC-IP spectra using no cleavage search specificity against the MHC-DB. These searches resulted in drastic improvements in unique MHC-I peptide identifications compared with the Parent-DB, specifically for the Mascot results: 3.9 and 3.6 fold for the B22.249 and Y3 IPs, respectively, and 3.7 fold across the total unique H-2 Db and H-2 Kb peptides identified [1% FDR in **Figure 3.2.C**, 5% FDR in **Supplementary Figure 3.2.B**]. Importantly, we find that Mascot searches with no cleavage also resulted in higher numbers of unique peptides compared with Sequest searches with no cleavage [**Figure 3.2.C, Supplementary Figure 3.2.B**]. Matching non-MHC peptides to the MHC-DB was not evident based on maintenance of allotype-specificity, whereby 96 and 91% of the

peptides identified from the Sequest MHC-DB searches matched the appropriate antibody for the B22.249 (H-2 Db-specific) and Y3 (H-2 Kb-specific) IPs, respectively [**Figure 3.2.C**]. For the Mascot searches, 90 and 84% of the peptides identified matched the appropriate antibody for the B22.249 and Y3 IPs, respectively [**Figure 3.2.C**]. As such, these peptides are assumed to be correct, and using the targeted search approach was successful. Accordingly, maintenance of allotype-specificity was also observed at 5% FDR for both Sequest and Mascot [**Supplementary Figure 3.2.B**]. We also created MHC-DBs using 1, 5, and 10% rank as NetMHC cutoffs, and a few additional peptides were identified with increased % rank cutoffs [**Supplementary Figure 3.3.A,B**]. Further support of these MHC-I peptide assignments is evident from the distribution of binding affinities; 85 and 84% of Mascot MHC-DB search peptides were considered strong binders (NetMHC ≤ 0.5% rank) for the B22.249 H-2 Db and Y3 H-2 Kb peptides, respectively [**Supplementary Figure 3.4.A**]. These data are particularly supportive because the % rank for MHC-DB peptides (≤2%) of all lengths was distributed relatively evenly [**Supplementary Figure 3.4.B**]. Taken together, these data show the potential for targeted database searches (particularly Mascot) in solving the “no enzyme” problem for MHC-I peptide identifications.

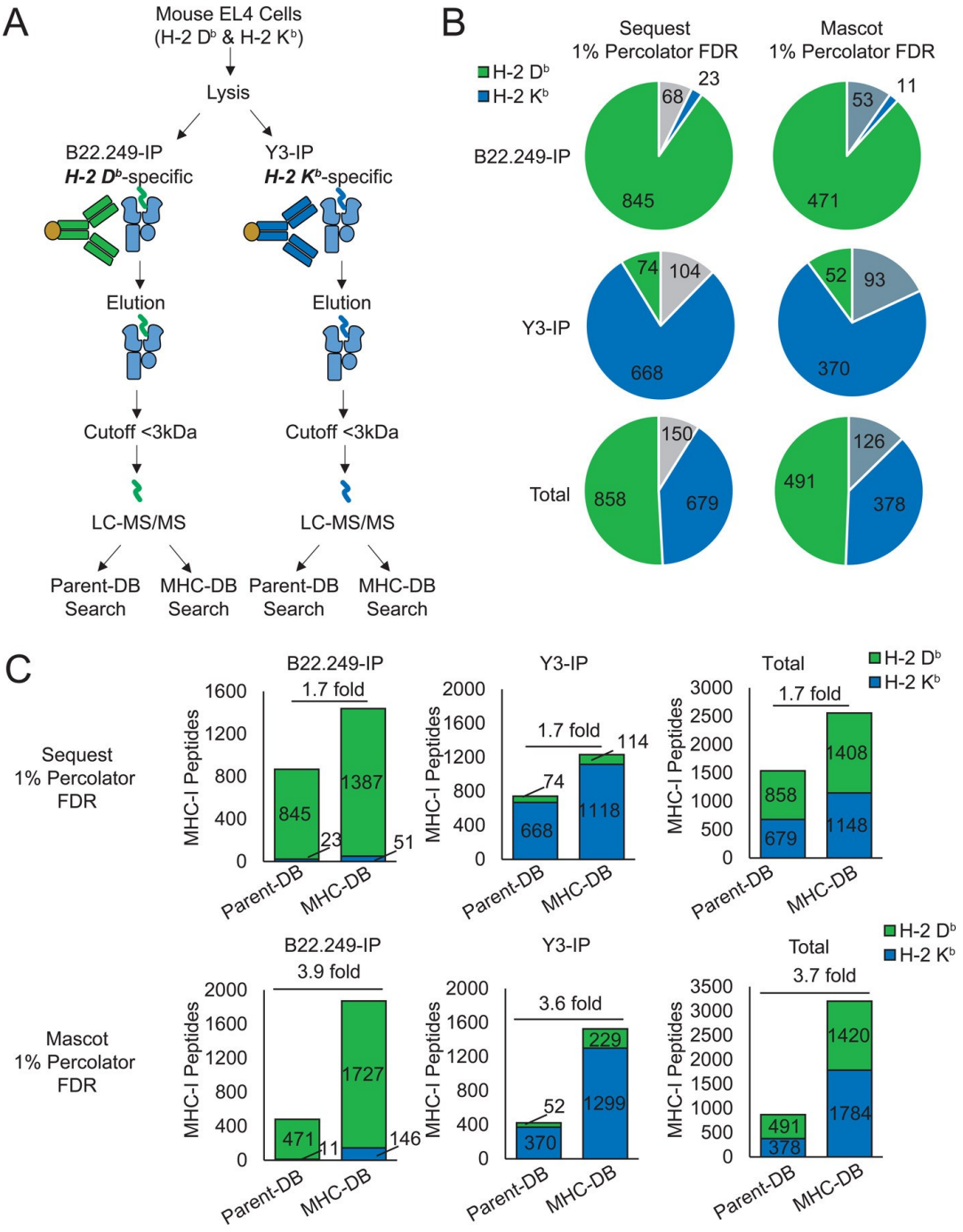


**Figure 3.2.** Targeted MHC-I peptide database search increases MHC ligandome identifications.

(A) Schematic for an allotype-specific, two-antibody experiment to assess the MHC-DB search. H-2 Db and H-2 Kb-specific antibodies (B22.249 and Y3, respectively) were

used to immuno-precipitate MHC-I proteins from mouse EL4 cells (carrying the H-2 Db and H-2 Kb allotypes), followed by elution of peptides, separation from MHC-I proteins by a cutoff filter, and analysis by LC–MS/MS. Spectra were assigned using Sequest and Mascot and false discovery rates (FDRs) determined using Percolator with either the Parent-DB or MHC-DB. (B) Parent-DB search results for mouse EL4 cells at 1% FDR, showing purity and allotype specificity of the B22.249 and Y3 antibodies. Shown separately for each allele-specific IP (and the total of both) are the number of unique peptides considered H-2 Db binders (NetMHC ≤ 2% rank for H-2 Db), H-2 Kb binders (NetMHC ≤ 2% rank for H-2 Kb), or nonbinders (NetMHC > 2% rank, gray). (C) Comparison of the MHC-I peptides (NetMHC ≤ 2% rank) identified using the targeted MHC-DB search approach with both Sequest and Mascot compared to the no enzyme Parent-DB search (1% FDR).

### *3.3.3. Increased MHC-I ligand identifications are due to enhanced statistical power.*

In previous studies where the search space was reduced, increased numbers of identified peptides were mostly attributed to better statistical power when performing FDR estimation.[565] Poor statistical power and sensitivity is especially a concern for searching MS data from MHC-I IPs using no enzyme restriction. In such searches, the likelihood of getting a high-scoring incorrect match to a peptide not likely present in the sample is higher than with enzyme-restricted databases. As a result, false-positive estimates appear higher and fewer matches meet a required cutoff. In our mouse data, we examined our Mascot search results, which showed the greatest boost in performance, and we observed that when peptides identified in both the Parent-DB and MHC-DB search types are compared, 99.3 and 94.1% of Percolator q values (FDR

estimates) are lower for the MHC-DB search than the Parent-DB search for the B22.249 and Y3 IPs, respectively [**Figure 3.3.A**]. Percolator posterior error probabilities (PEPs), similar metrics to q values, showed similar decreases [**Supplementary Figure 3.5.A**]. Furthermore, across all identified peptides, Percolator q values and PEP were also distributed lower in the MHC-DB search [**Figure 3.3.B, Supplementary Figure 3.5.B**]. Performing the MHC-DB search thus improves statistical power for MHC IP searches, which, taken together with the aforementioned maintenance of allotype specificity, suggests that the approach is sensitive but also accurate. Furthermore, by performing the MHC-DB search, we were able to assign MS/MS spectra with lower Mascot ions scores [1% FDR in **Figure 3.3.C**, 5% FDR in **Supplementary Figure 3.6**], which often occur when measuring peptides of low abundance such as MHC-I peptides. Interestingly, the approach also rescued the identification of many high Mascot-scoring spectra because they were identified only in the MHC-DB search [exemplified in **Figure 3.4**]. As such, a mechanistic explanation for the improved peptide identification rates is the higher sensitivity occurring from decreasing the search space size to more accurately represent the sample.

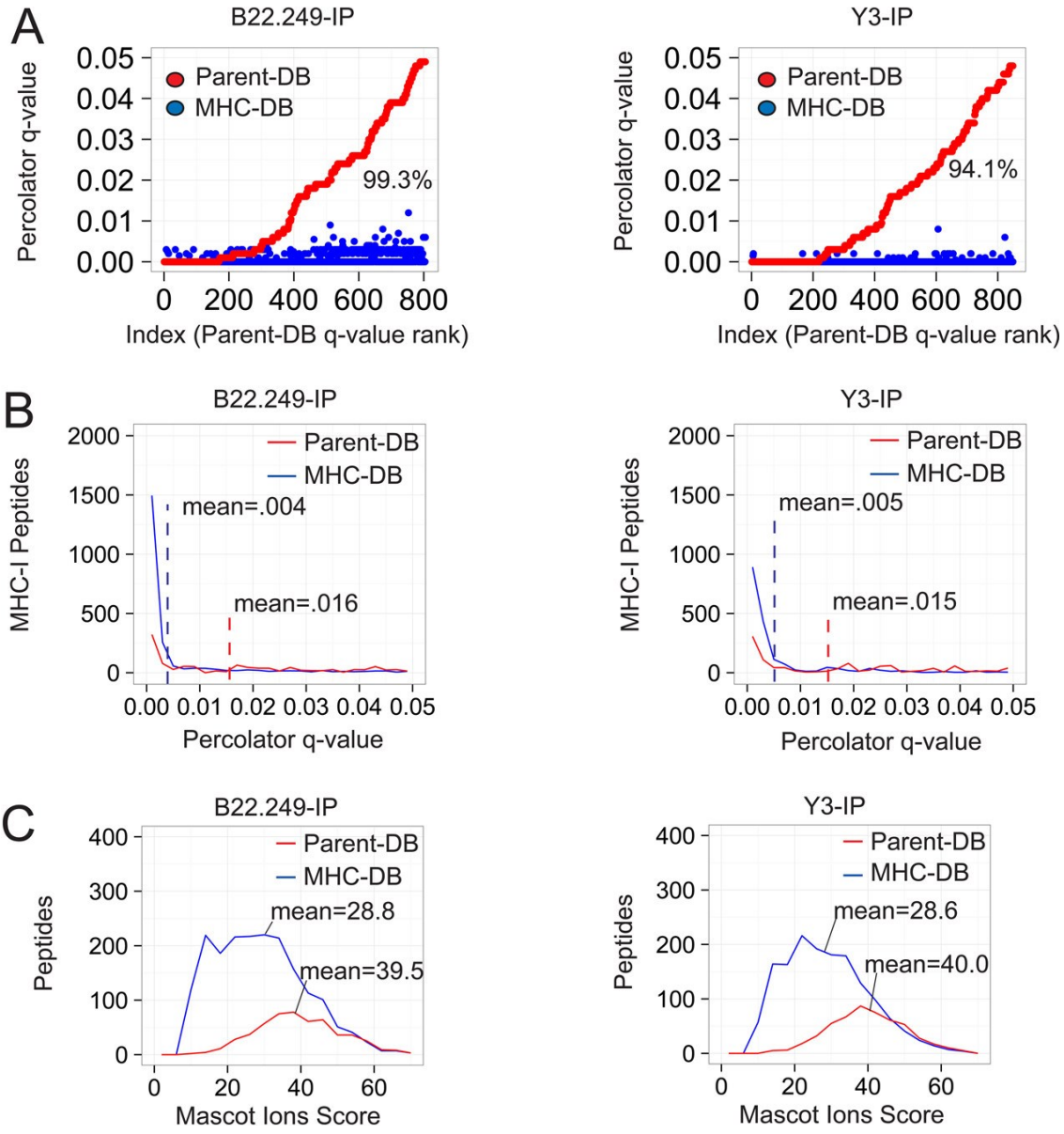


**Figure 3.3.** Effect of a targeted MHC database on search statistics.

(A) Percolator q values for each peptide identified in both search types are plotted in numerical order according to their Parent-DB q values. Percentages are the peptides for which the q value of the MHC-DB search was less than the Parent-DB search. (B) Distribution of the Percolator q values (shown up to 5% FDR) for each MHC-IP search result, comparing Parent-DB and MHC-DB search types. (C) Distribution and mean

values of Mascot ions scores among identified peptides (1% FDR) for the Parent-DB and MHC-DB search types for the B22.249 and Y3 IPs.

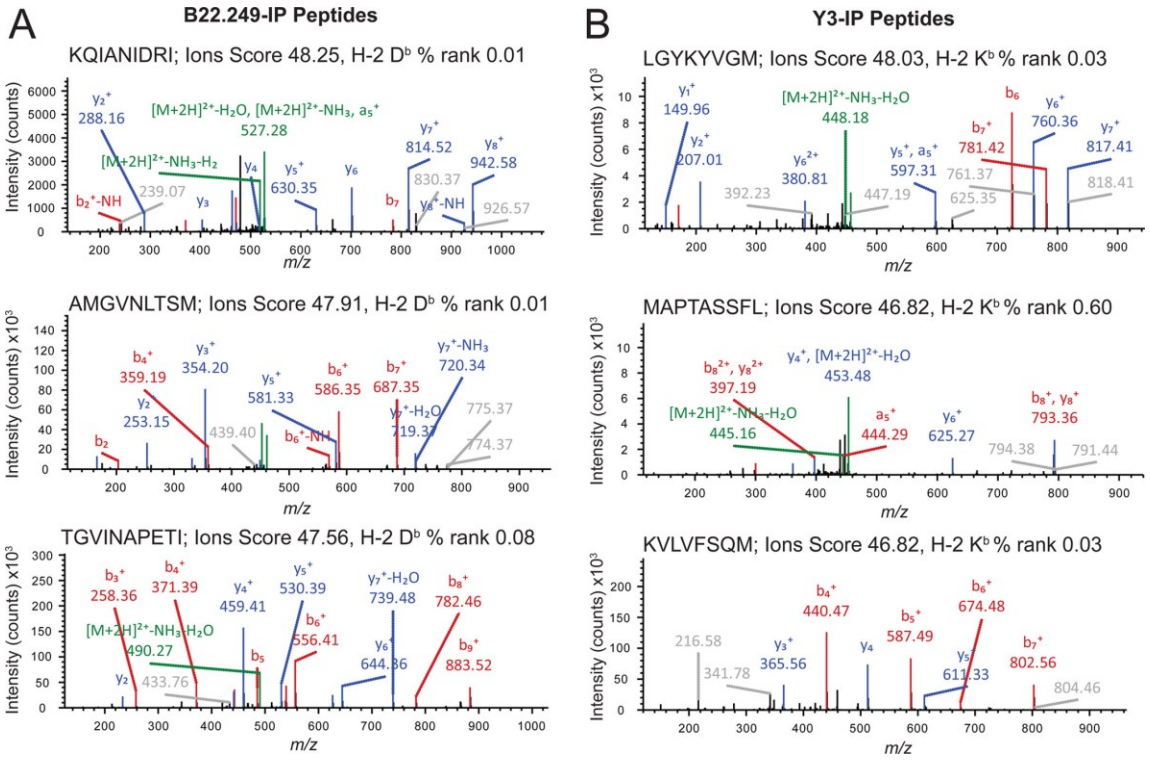


**Figure 3.4.** Examples of spectra assigned by only the MHC-DB search.

Shown are several MS/MS spectra with high Mascot ions scores from the (A) B22.249 and (B) Y3 IPs that were not assigned to a peptide in the Parent-DB searches but assigned to peptides in the MHC-DB searches. Such peptides were mostly allotype-specific (B22.249 peptides were ≤2% NetMHC rank for the H-2 Db allele; Y3 peptides were ≤2% NetMHC rank for the H-2 Kb allele).

### *3.3.4. HLA-specific database searches improve statistical power and peptide identifications in human HLA-IP searches.*

Having established the MHC-DB search approach in a mouse model, we next assessed the use of the targeted approach in human-derived samples. To test this approach, we retrieved eight MS/MS raw data files from recently published HLA ligandome data collected from peripheral blood mononuclear cells (PBMCs) of healthy donors.[571,572] We thus compiled targeted HLA databases for searching human HLA ligandome data based on the HLA-A and HLA-B allotypes of the patients. As in the mouse experiments, we began with a human reference proteome (Parent-DB) and used NetMHC to predict allotype-specific HLA peptides (NetMHC ≤ 2% rank), forming a targeted HLA database for each patient allotype (HLA-DB). Using a 2% rank cutoff, the representation of predicted 8- to 11-mer peptides was similar to that of the mouse databases [**Supplementary Figure 3.7.A**]. The Parent-DB search showed that most identified peptides were HLA binders (as revealed by a NetMHC rank ≤2%) [**Supplementary Figure 3.7.B**]. Depending on the patient sample, Mascot searching against the HLA-DB resulted in 1.2- to 2.3-fold increases in HLA peptides compared with the Parent-DB (at 1% FDR) [**Figure 3.5.A, Supplementary Data 3.2**]. As in the mouse experiments, peptide identification increases could also be attributed to better statistical power estimation because Percolator q values were again lower for the HLA-DB search than for the Parent-DB search for all PBMC samples [**Figure 3.5.B**]. Using the HLA-DB searches also enabled the identification of peptides with lower Mascot ions scores on average [**Figure 3.5.C**]. The success of the targeted approach to increase HLA peptide identification in human samples is important because they may bear a host of important immunotherapeutic antigens.

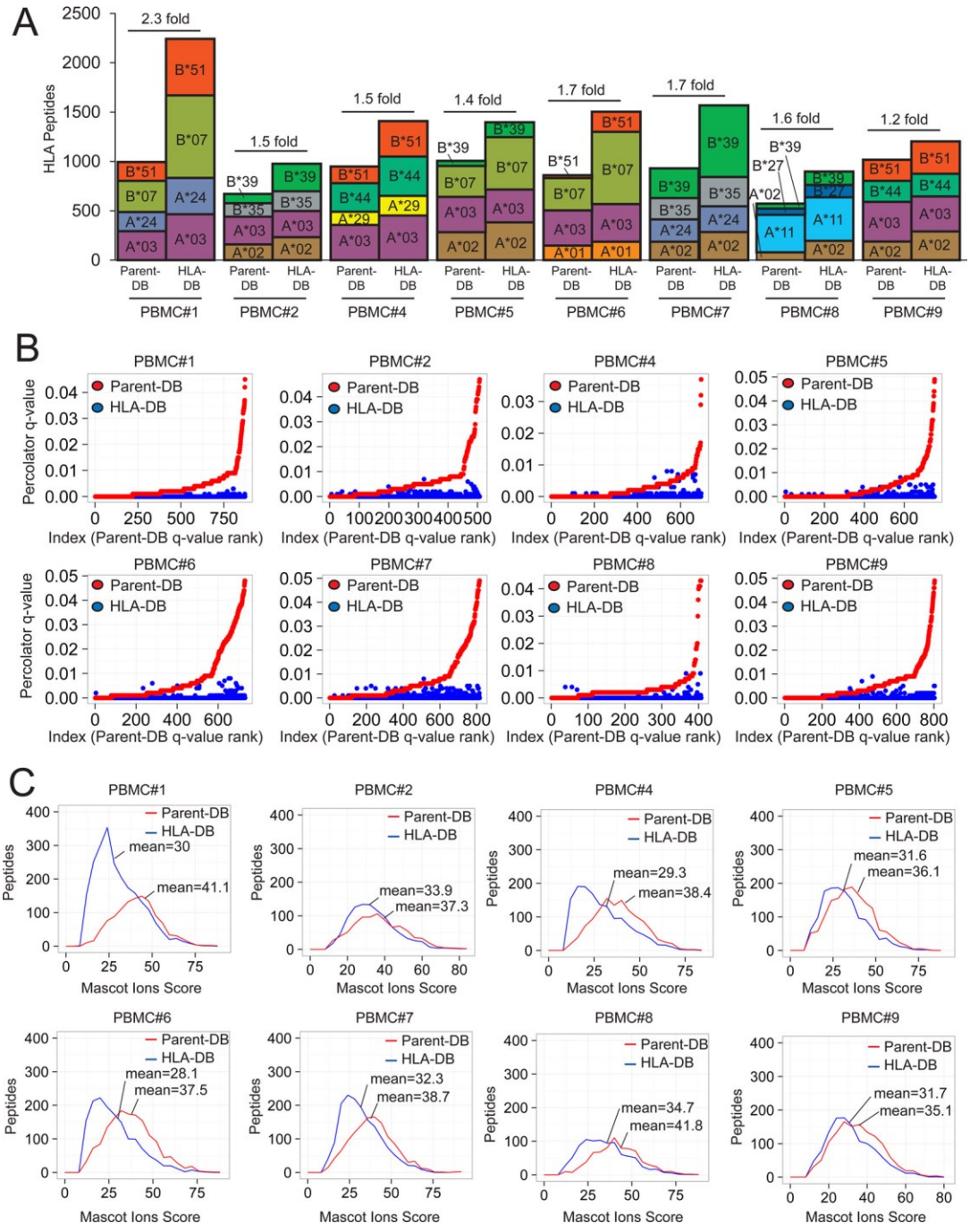


**Figure 3.5.** Targeted HLA database searches increase peptide identifications in human PBMC class I HLA ligandome data.

Publically available human class I HLA ligandome raw data were retrieved and reanalyzed using searches based on allotype-specific targeted HLA databases. For each

PBMC, HLA peptides were predicted from a human reference proteome database (Parent-DB) using NetMHC (≤2% rank) based on the patient allotype as stated in the publication. [572] A patient-specific targeted HLA database search was performed and compared to the reference database (Parent-DB) using Mascot and Percolator. (A) Peptide identification increases (1% FDR) for each PBMC data set comparing the targeted HLA database (HLA-DB) to the reference (Parent-DB) search. (B) For each PBMC ligandome search, Percolator q values (up to 5% FDR) are shown for peptides (all allotypes) identified using both the Parent-DB and HLA-DB search. Peptides are plotted in numerical order according to their q value in the Parent-DB search. Each PBMC number matches to that in the previously reported data set (Orbitrap data only). [572] (C) Distribution and mean values of Mascot ions scores among identified peptides (1% FDR) for the Parent-DB and HLA-DB search types for human PBMC ligandome data sets.

### *3.3.5. MHC-I peptides assigned with the targeted databases are not contaminant peptides.*

Arguably, a potential pitfall of performing the MHC-targeted database search is that spectra identified as non-MHC-binding peptides (most likely contaminant peptides) could be falsely assigned as MHC-I peptides. The occurrence of these contaminant assignments can be discerned by performing a standard no enzyme search against the reference database. Examination of the PSM overlap between the Parent-DB and MHC-DB searches shows that few PSMs are solely identified by the Parent-DB [**Supplementary Figure 3.8**]. In this regard, we found that only 12/118 of B22.249 and 8/180 of those Y3 peptide spectrum matches (PSMs) considered nonbinders in the Parent-DB searches were reassigned as binders by the MHC-DB search (at 1% FDR)

[**Figure 3.6.A**]. In the human data, of the nonbinder PSMs from the Parent-DB search, again few were reassigned to HLA-binding peptides in the HLA-DB search [**Figure 3.6.B**]. These PSMs can be flagged for removal during routine practice of the targeted approach, and overall, the strategy still leads to a net increase in confident MHC-I or HLA peptide assignments. It is not known how much of this net increase comes at the cost of true MHC/HLA peptides not predicted by NetMHC, but true binders should be further interrogated by validation methods, iteratively improving the prediction tools. Such may be the case for HLA-C allotypes, which were not available from the PBMC data and are more poorly studied. Taken together with the maintenance of allotype specificity in the mouse experiment, these data also support the notion that non-MHC-I binders will not match the MHC-DB. We therefore propose that the targeted approach is a superior option for identifying MHC-I ligands from MS data as a result of its enhanced statistical power and will reveal otherwise unidentified ligands. The targeted approach could also bolster patient-specific immunotherapies because it is conceivable that targeted databases could be based on patient sequence data, improving the likelihood of detecting, for example, neoantigen peptides in cancer.[573]

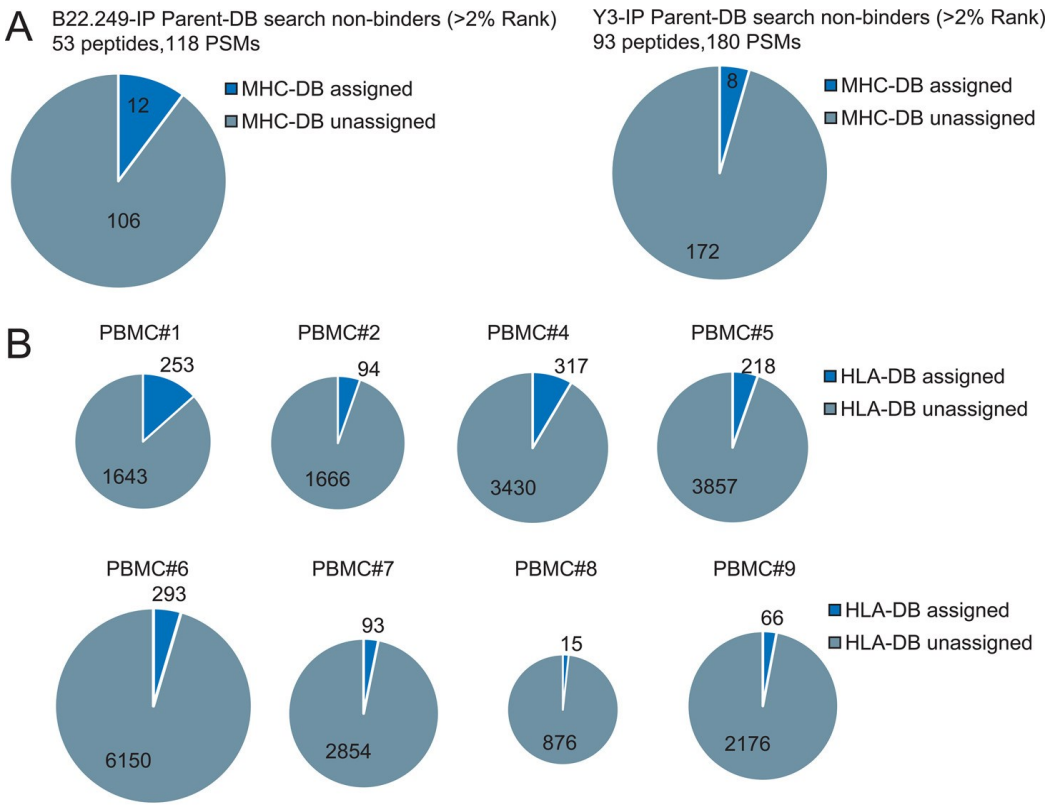


**Figure 3.6.** Most contaminant peptides are not assigned to MHC peptides.

(A) Fraction of PSMs identified as nonbinders (NetMHC > 2% rank) in the Parent-DB search that are reassigned as a binder by the MHC-DB search (1% FDR). (B) Fraction of PSMs from each human PBMC ligandome identified as nonbinders (NetMHC > 2% rank) in the Parent-DB search that are reassigned as a binder by the HLA-DB search (1% FDR).

## 3.4. DISCUSSION

MHC ligandomes hold information on therapeutic targets essential for understanding antigen-specific, T-cell-mediated immunity. Exciting recent developments in antitumor immunotherapy involving T-cell-based therapeutics, including PD-1 and CTLA4 immune

checkpoint inhibitors, have led to a renewed importance for MHC-I ligand identification,[75] with their potential for use as peptide vaccines. Database search strategies for identifying MHC ligand mass spectra from LC–MS/MS experiments were initially intended to be employed by matching spectra to predictable protein fragments cleaved by proteolytic enzymes.[574] This leads to a lack of enzymatic cleavage specificity in the search and is one of the many potential reasons why the success rate in assigning peptide identifications to ligand mass spectra data is low. Here, by compiling databases limited to predicted MHC-I peptides, we have greatly reduced the spectral search space. This approach essentially replaces the proteolytic peptides with predicted MHC-I ligands so that search strategies can be implemented as originally intended. As mentioned, unassigned spectra in MHC-I ligand studies could result from IP of nonclassical ligands that our approach does not consider such as those proteasomally spliced,[89] which have recently been introduced as being widespread. Furthermore, it is not known to what extent proteasomal splicing, peptide bulging, or post-translational modifications play in the ability of peptides to be predicted by NetMHC. It is worth noting that many newly discovered proteasomally spliced peptides were not considered binders by NetMHC[89] but might be better predicted as more is known about them. Although novel peptide motifs missed as part of our predictive approach can be recovered by performing a complementary nontargeted search, caution should be taken in combining iterative searches unless a global FDR is properly considered.[575] Future approaches should address how to combine such searches. Overall, however, the targeted approach is effective for most scenarios, and as pan-allotype prediction tools are improving over time,[576] targeted database searches will only improve. Furthermore, advances in MS speed and sensitivity, alongside better MHC-I IP methodologies, will result in the acquisition of even greater numbers of quality spectra. Finally, this novel targeted

database search approach could be extended to other non-MHC-based investigations, such as using motif-targeted databases composed of known kinase phosphorylation motifs, thus improving phospho-peptide identification rates. We ultimately suggest that the targeted database search for MHC-I peptide identification is an essential step forward in the ever-expanding field of MHC ligand analysis.

## 3.5. CONFLICT OF INTEREST

The authors declare no competing financial interest.

Mouse MS (.raw) files have been deposited to Chorus, https://chorusproject.org, ID#1098.

## 3.6. ACKNOWLEDGEMENTS

We acknowledge Drs. Steve Gygi and Brian Erickson (Harvard Medical School) for providing feedback on the manuscript. We further acknowledge Dr. Dan Gaston (Nova Scotia Health Authority) for bioinformatics advice. This work was supported by grants from the Canadian Cancer Society Research Institute (CCSRI), Canadian Institutes of Health Research (CIHR), and Terry Fox Research Institute (TFRI) to S.G. and P.W.L.. J.P.M. is supported through the Cancer Research Training Program (CRTP) of BHCRI. P.K. is supported by Nova Scotia Graduate Scholarships during this work.

## 3.7. SUPPLEMENTARY FIGURES

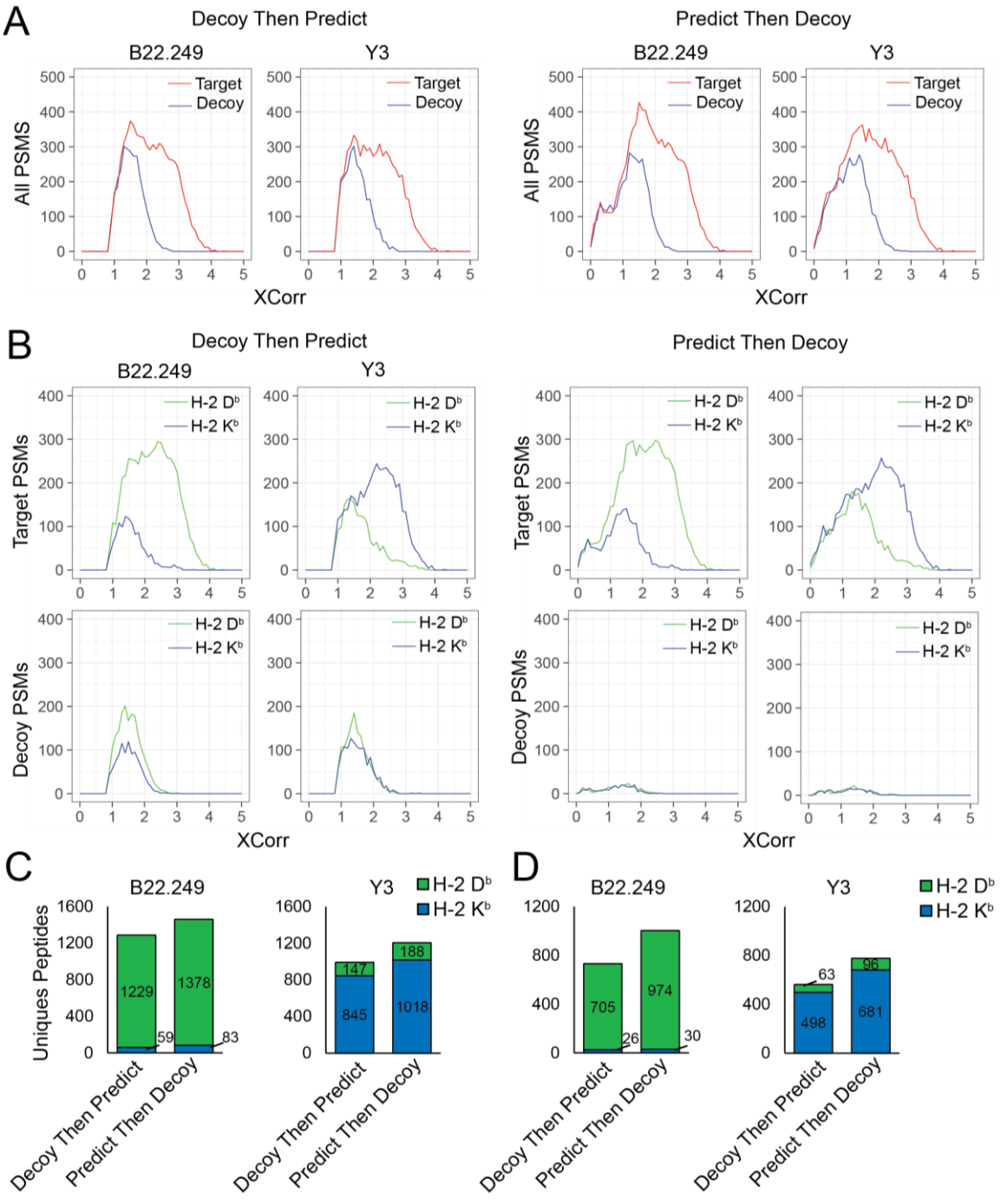


**Supplementary Figure 3.1.** Decoy database comparisons.

(A) Distribution of all target and decoy PSMs for MHC IPs from mouse EL4 cells (by Sequest XCorr) where MHC-DB decoy databases formed by either reversing all mouse proteins in Parent-DB then predicting by NetMHC (Decoy Then Predict) or by reversing the NetMHC-predicted peptides (Predict Then Decoy). (B) Distribution of H-2 Db and H-2 Kb –specific decoy and target PSMs for each allotype-specific IP, comparing the "Decoy Then Predict" and "Predict Then Decoy" strategies. (C) Total unique peptides for each allotype-specific IP, comparing the "Decoy Then Predict" and "Predict Then Decoy" strategies at 5% FDR. (D) Same as C, at 1% FDR.

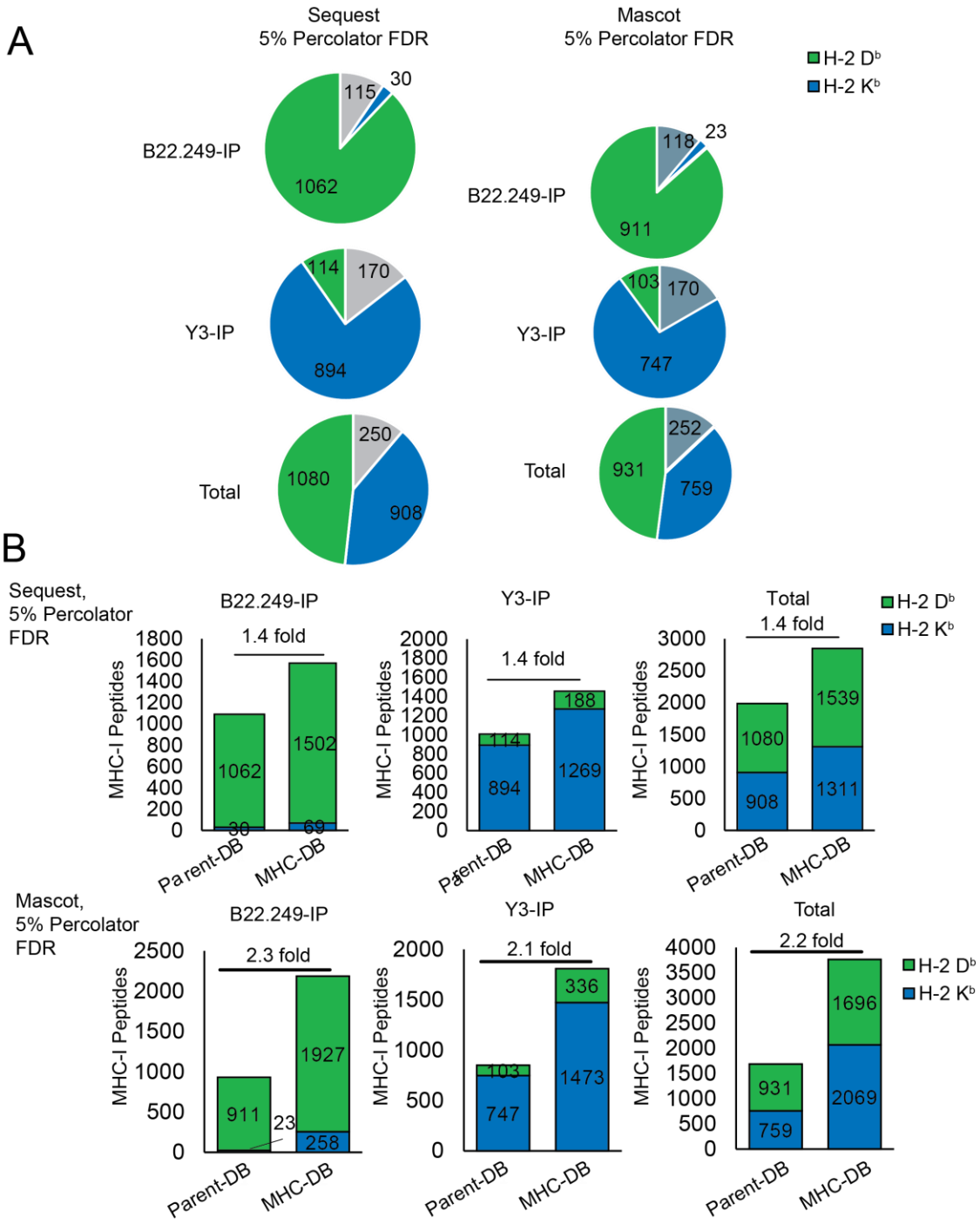


**Supplementary Figure 3.2.** Search results at 5% FDR.

(A) Parent-DB search results (Sequest and Mascot) for mouse EL4 cells at 5% FDR, showing purity and allotype specificity of the B22.249 and Y3 antibodies. Shown

separately for each allele-specific IP (and the total of both) are the number of unique peptides considered H-2 Db (NetMHC < 2% rank for H-2 Db), H-2 Kb (NetMHC < 2% rank for H-2 Kb) binders, or nonbinders (NetMHC > 2% rank, grey). (B) Allotype-specific increases in MHC-I peptides (NetMHC < 2% rank) achieved with the Sequest and Mascot MHC-DB searches (5% FDR).

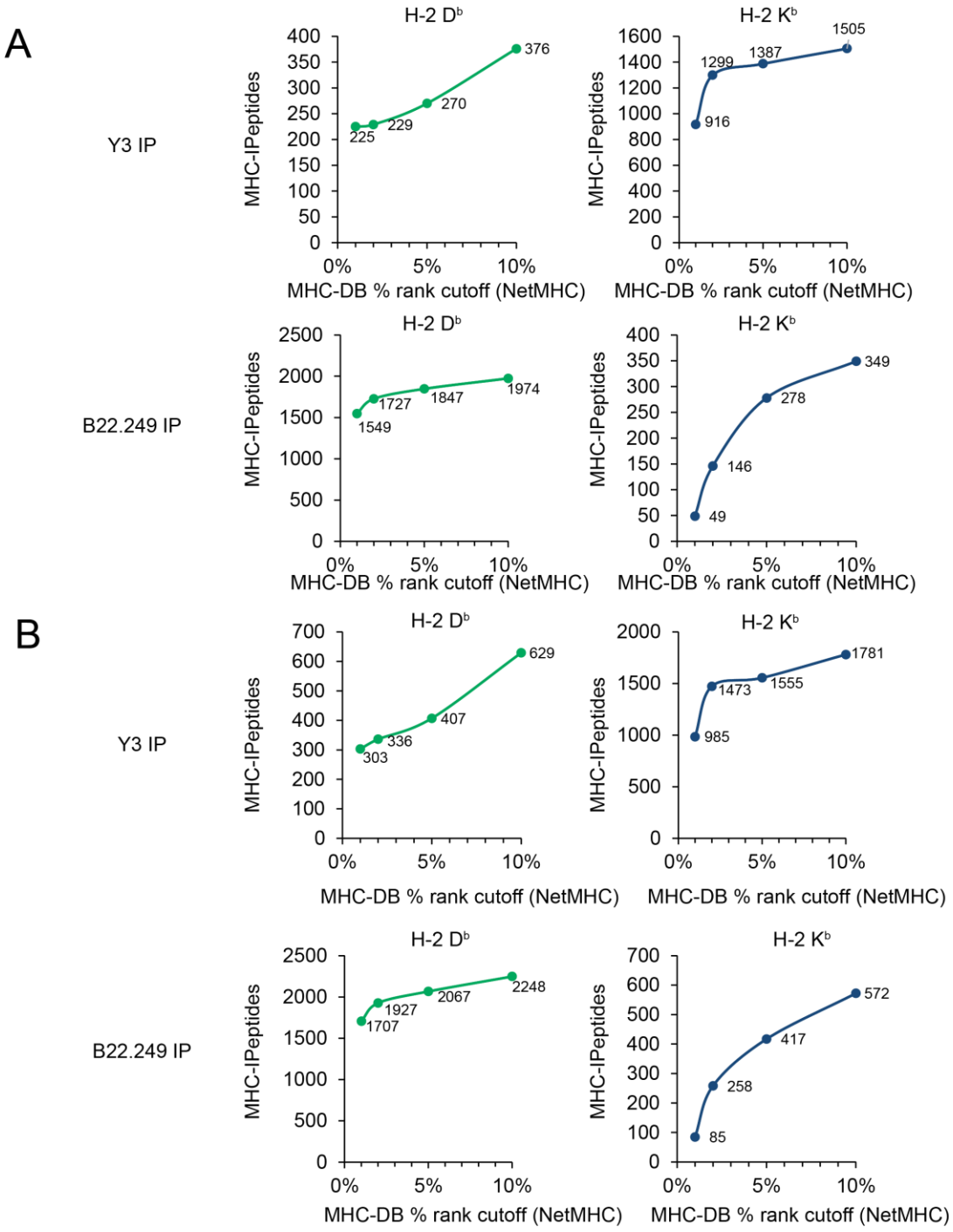


**Supplementary Figure 3.3.** Search results by NetMHC % rank cutoff.

(A) Total unique H-2 Db and H-2 Kb peptides for each allotype specific IP identified by varying the % rank cutoff (1%, 2%, 5% and 10%) used to create the mouse MHC-DB.

Peptides were identified using Mascot searches at 1% Percolator FDR (B) Same as (A), but using Mascot searches at 5% Percolator FDR.

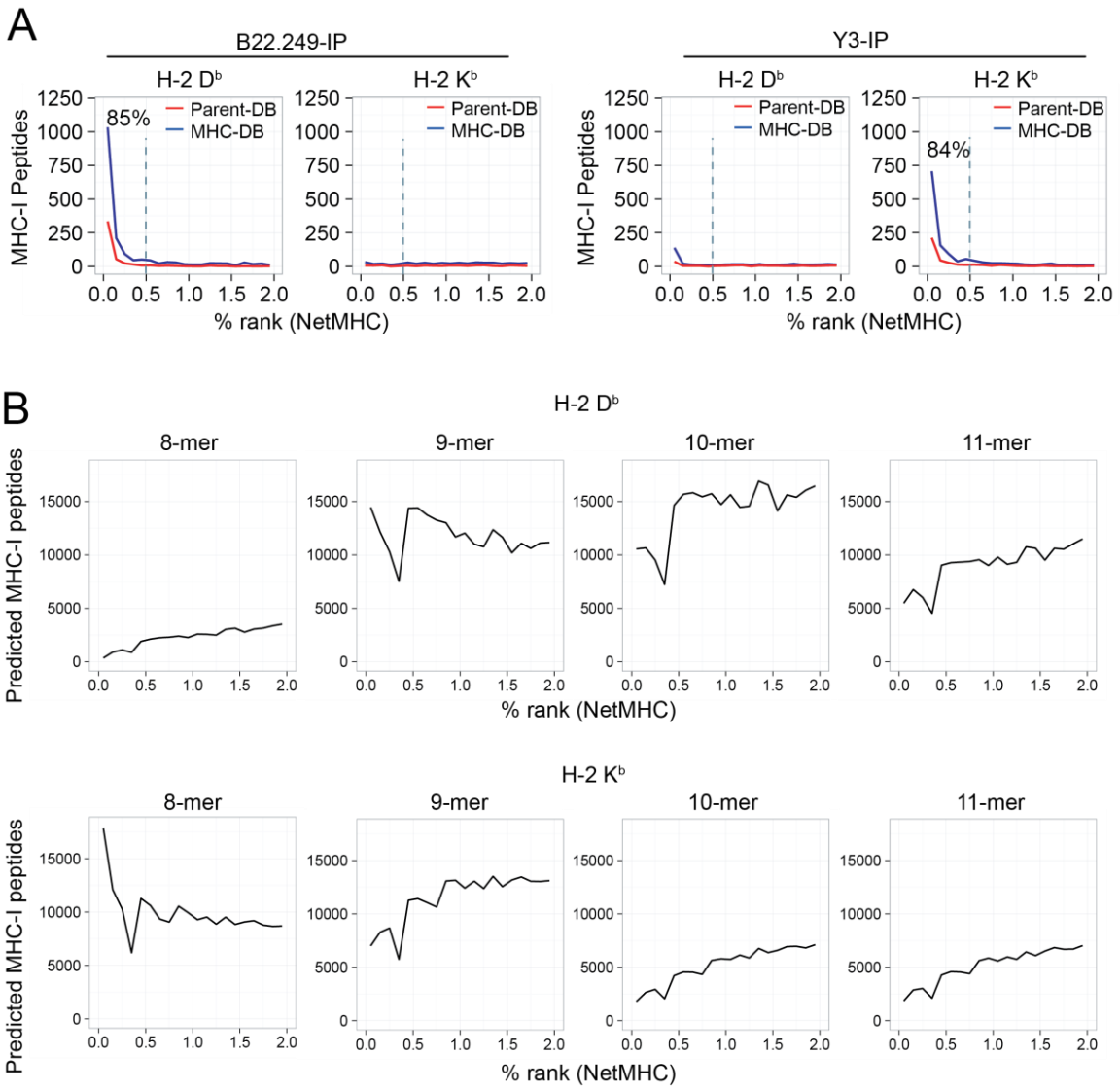


**Supplementary Figure 3.4.** Predicted and Identified NetMHC % ranks.

(A) Shown are the distributions, across peptide lengths, of the NetMHC % rank values for all predicted H-2 Db and H-2 Kb peptides in the MHC-DB. (B) Distribution of NetMHC % ranks for the unique H-2 Db and H-2 Kb peptides for each allotype-specific IP based on Mascot searches at 1% Percolator FDR.

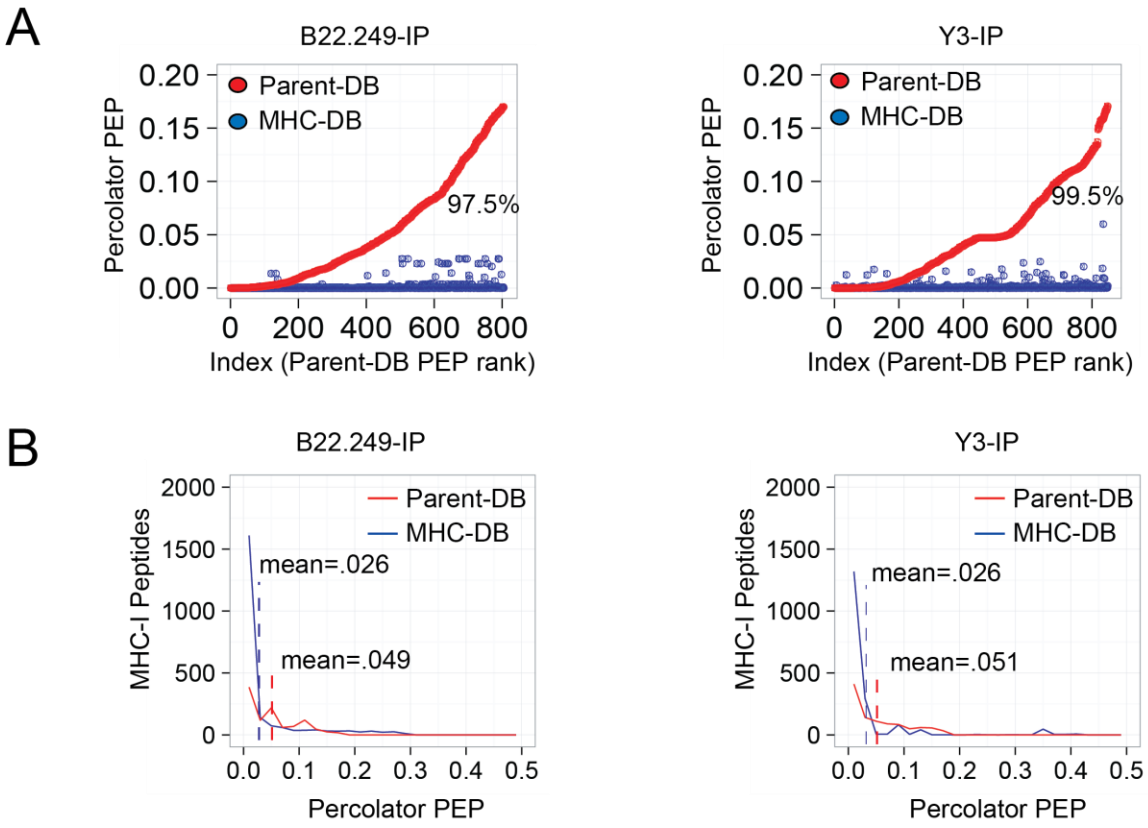


**Supplementary Figure 3.5.** Percolator PEP statistics.

(A) Percolator PEP for each peptide identified in Mascot searches of both Parent-DB and MHC-DB search types are plotted in numerical order according to their q-value in the Parent-DB search. Percentages are the peptides for which the PEP of the MHC-DB search was less than that of the Parent-DB search. (B) As in A, the distribution and mean values of the PEP for each MHC-I IP search result, comparing Parent-DB and MHC-DB search types.

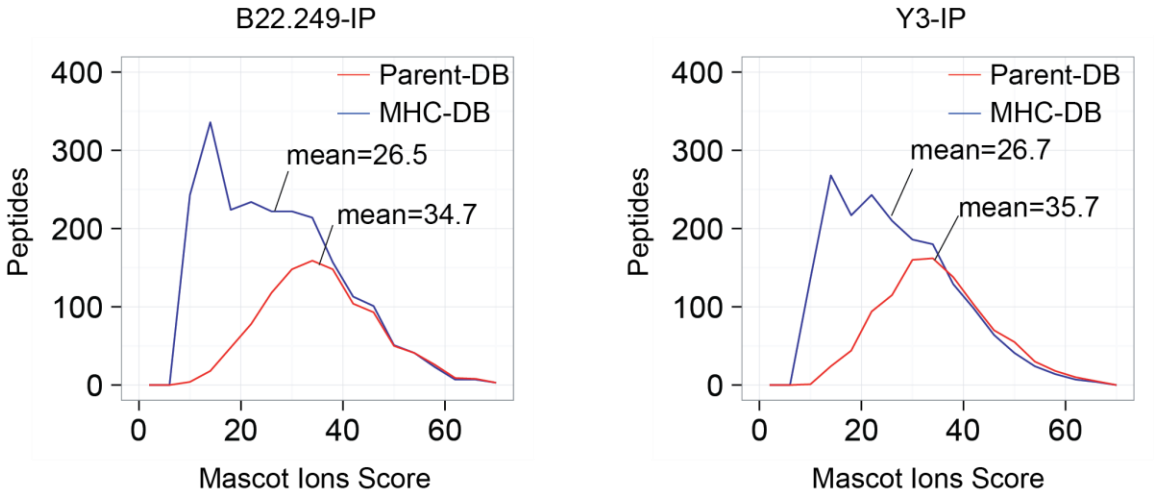


**Supplementary Figure 3.6.** Mascot ions score distributions.

Distribution and mean values of Mascot ions scores among identified peptides (5% FDR) for the Parent-DB and MHC-DB search types for the B22.249 and Y3 IPs.

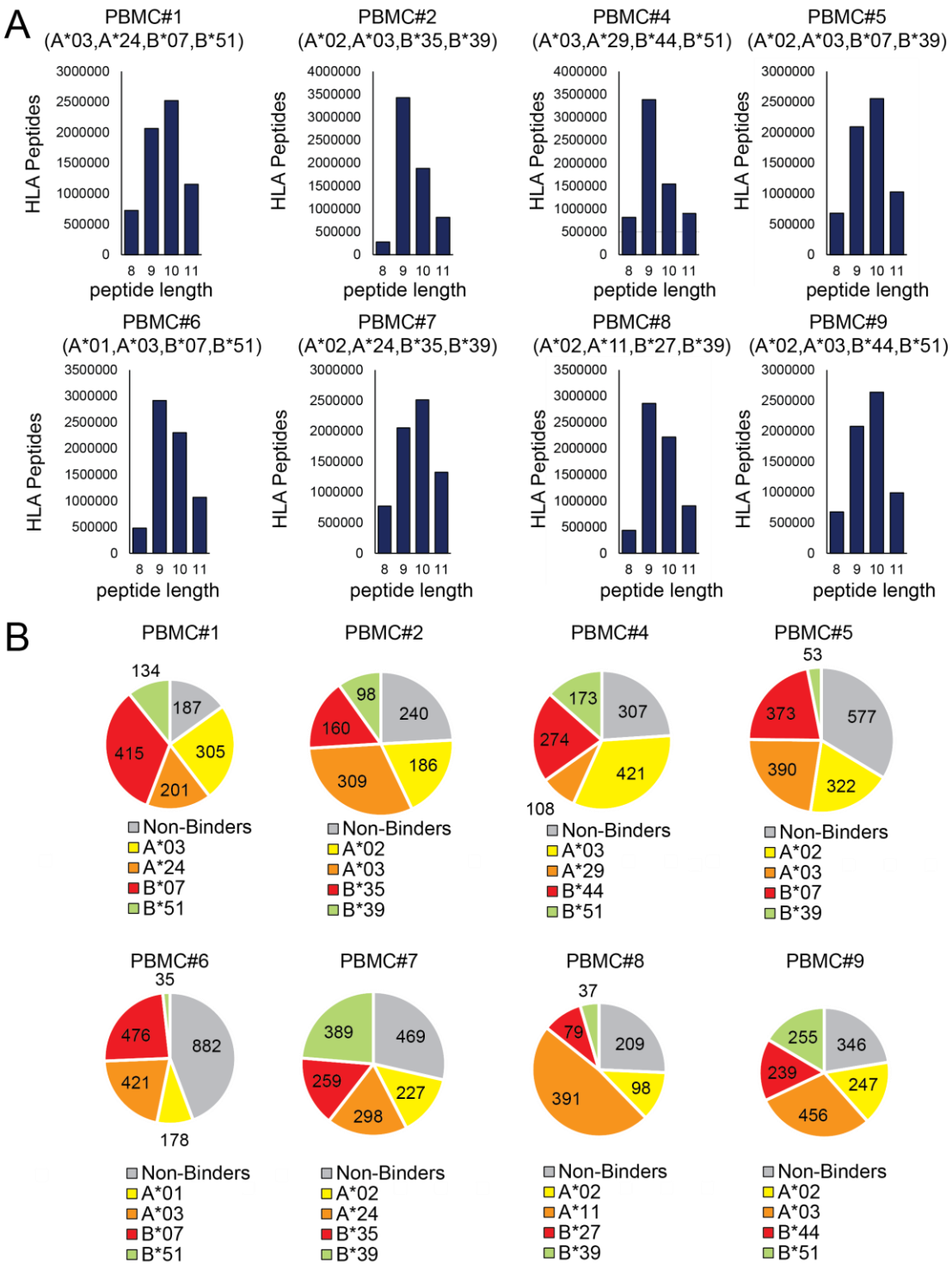


**Supplementary Figure 3.7.** Predicted and Identified HLA peptides.

(A) NetMHC-predicted peptides for eight PBMC HLA IP datasets based on the patient allotype. Shown for each PBMC is the total number of predicted peptides (< 2% rank) by peptide length. (B) Identified peptides (Mascot, 1% FDR) from published PBMC ligandome datasets using a reference human proteome database (Parent-DB) showing the purity and peptide distribution among alleles for each patient allotype. Based on NetMHC, peptides were considered binders to the patient allotypes (< 2% rank for a specific allele) or non-binders (> 2% rank).

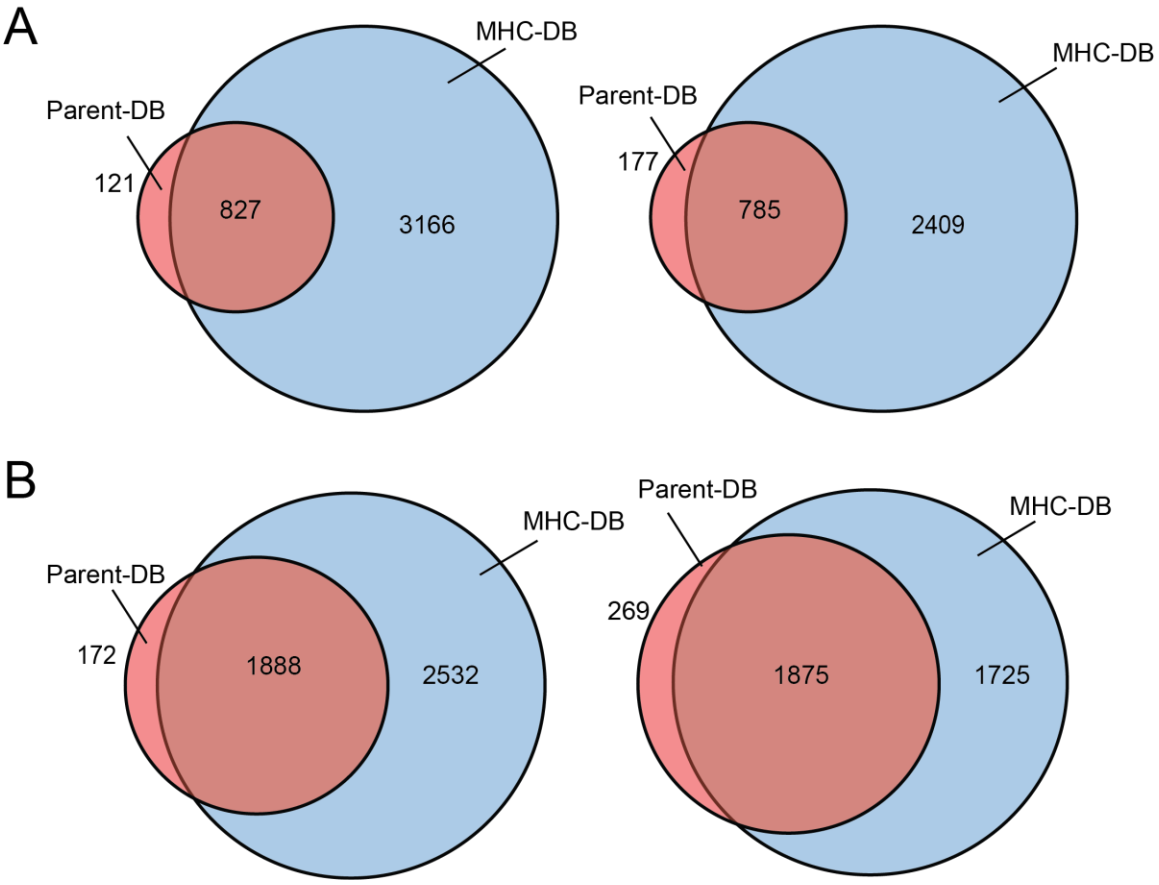


**Supplementary Figure 3.8.** Database overlap.

Overlap of PSMs identified in the Parent-DB and MHC-DB for each mouse IP using searches by Mascot at (A) 1% FDR and (B) 5% FDR.

## 3.8. SUMMARY OF CHAPTER 3

We developed a new workflow for MHC-I ligandome-associated MS spectral searches and a computational solution to one of the main non-enzymatic search problems encountered with LC-MS/MS-based MHC-I ligandome. Implementing a targeted search strategy through our SpectMHC pipeline not only overcomes the constraints of non-enzymatic searches but also improves MHC-I ligand identification in mouse and human samples by more than two-fold. Furthermore, compared to the parent reference database technique, the targeted database search strategy reduced false discovery rates and effectively discovered MHC-I ligands with low ion mass scores. By overcoming such fundamental limitations with MS, our targeted search strategy has the potential to find previously unidentified MHC-I ligands, including therapeutically important T cell epitopes involved in the cancer immunity cycle. The following chapters seek to enhance the entire cancer immunity cycle by stimulating immunogenic cell death for therapeutic development. We develop and investigate the efficacy of novel, clinically desired near-infrared activated photodynamic therapies with unique chemical properties that attack melanoma in two ways: directly by cytotoxicity and indirectly by activating anticancer immune responses, yielding excellent therapeutic responses.

# CHAPTER 4: NEAR-INFRARED ABSORBING RU(II) COMPLEXES ACT AS IMMUNOPROTECTIVE PHOTODYNAMIC THERAPY (PDT) AGENTS AGAINST AGGRESSIVE MELANOMA

This work is published in:

Lifshits LM*, Roque III JA*, **Konda P***, Monro S, Cole HD, von Dohlen D, Kim S, Deep G, Thummel RP, Cameron CG, Gujar S, McFarland SA. Near-infrared absorbing Ru (II) complexes act as immunoprotective photodynamic therapy (PDT) agents against aggressive melanoma. ***Chemical science***. 2020;11(43):11740-62.

* contributed equally

## CONTRIBUTIONS:

**P.K.** designed the cellular assays and immunology study, carried out the experimentation, collected and analyzed data, and prepared the immunology section of the manuscript. L.M.L., J.A.R., S.M., H.D.C., D.V.D., S.K., R.P.T. designed and performed experiments for the chemistry part of the study. M.N. provided bioinformatics support for chemistry part of the study. G.D. performed the MTD study for the lead photosensitizer. S.G., S.A.M., and C.G.C., assisted with study design, writing, and critical review of the manuscript.

**Details of PK's contributions:**

- Sections 4.3.2, 4.3.3., 4.3.4., 4.3.5., 4.3.6., and 4.3.7. were written by **P.K**.
- Experimental work, data analysis, and generation of graphs related to Figures 4.10., 4.11., 4.12., 4.13., 4.14., 4.15., supplementary 4.1., and supplementary 4.2. were performed by **P.K.**
- Immunology parts in Sections 4.1. (abstract), 4.2. (introduction), and 4.4. (discussion) were written by **P.K.**

## 4.1. ABSTRACT

Mounting evidence over the past 20 years suggests that photodynamic therapy (PDT), an anticancer modality known mostly as a local treatment, has the capacity to invoke a systemic antitumor immune response, leading to protection against tumor recurrence. For aggressive cancers such as melanoma, where chemotherapy and radiotherapy are ineffective, immunomodulating PDT as an adjuvant to surgery is of interest. Towards the development of specialized photosensitizers (PS) for treating pigmented melanomas, nine new near-infrared (NIR) absorbing PSs based on a Ru(II) tris-heteroleptic scaffold [Ru(NNN)(NN)(L)]Cln, were explored. Compounds 2, 6, and 9 exhibited high potency toward melanoma cells, with visible EC50 values as low as 0.292–0.602 μM and phototherapeutic indices (PIs) as high as 156–360. Single-micromolar phototoxicity was obtained with NIR-light (733 nm) with PIs up to 71. The common feature of these lead NIR PSs was an accessible low-energy triplet intraligand (3IL) excited state for high singlet oxygen (1O2) quantum yields (69–93%), which was only possible when the photosensitizing 3IL states were lower in energy than the lowest triplet metal-to-ligand charge transfer (3MLCT) excited states that typically govern Ru(II) polypyridyl photophysics. PDT treatment with compound **2** elicited a pro-inflammatory response alongside immunogenic cell death in mouse B16F10 melanoma cells and proved safe for *in vivo* administration (maximum tolerated dose=50 mg kg−1). Male and female mice vaccinated with B16F10 cells that were PDT-treated with compound **2** and challenged with live B16F10 cells exhibited 80 and 50% protection from tumor growth, respectively, leading to significantly improved survival and excellent hazard ratios of ≤0.2.

## 4.2. INTRODUCTION

Photodynamic therapy (PDT) is an approved anticancer modality where light is used to activate an otherwise nontoxic photosensitizer (PS) to generate cytotoxic reactive oxygen species (ROS) through energy (Type II) or electron (Type I) transfer. Type II formation of $^1O_2$ is thought to be the major contributor to the antitumor photodynamic effect, arising from three synergistic mechanisms: direct cytotoxicity toward tumor cells, damage to tumor vasculature, and induction of an inflammatory response that can stimulate systemic antitumor immunity.[346–349,352,371,577–583] PDT is delivered in two stages: local or systemic administration of a PS, followed by light delivery to the site of the primary tumor. The light can be delivered virtually anywhere in the body with today's flexible fiber optic devices, and interstitial PDT (i-PDT) techniques can even be used to physically implant the fibers directly inside tumors.[584] The overall PDT response is determined by the PDT regimen, which includes the PS dose as well as the light treatment (wavelength, fluence, and irradiance),[370,455] and can be tuned to enhance local or systemic effects.[370]

The most recent preclinical and clinical studies have shown that, apart from its direct tumor-destroying capacity, PDT can perform immunomodulatory functions. Specifically, PDT stimulates both innate and adaptive immune responses, destroying distant untreated tumor cells (at either primary or metastatic sites) and leading to the development of antitumor immunity that can prevent cancer recurrence.[455,585,440,467,586–594] Such therapy-induced antitumor immunological benefits form the foundation of modern-day cancer immunotherapies. Thus, local PDT has much unrealized promise, and has the potential to be an important adjuvant in multimodal cancer therapy.

Porfimir sodium (Photofrin), a mixture of oligomeric tetrapyrrolic macrocycles that is activated with 630-nm light, was the first approved PS for cancer therapy and remains the gold standard in many PDT applications.[348,595,350,596,597] Most second- and third-generation PSs are also based on tetrapyrrole macrocycles (porphyrins, chlorins, bacteriochlorins, and phthalocyanines),[583,356,598,599,357,355] but are single compounds aimed at increasing water solubility, reducing prolonged photosensitivity, and/or improving other properties. Related systems have also been prepared that involve coordination of a central metal ion (e.g., $Sn^{IV}$, $Lu^{III}$, $Al^{III}$, $Pd^{II}$) to the tetrapyrrole framework to enhance their photophysical and biological properties.[396,600–603] Only a handful of these next-generation PSs have been approved for clinical use or have advanced to clinical trials.[346]

In a marked departure from these tetrapyrrole macrocycles and their metallated counterparts, we and others have focused on coordination complexes of Ru(II) as light-responsive prodrugs.[600,604–616] Ru(II) has long been at the forefront for many light-based applications due to the rich photophysical and photochemical characteristics of many of its complexes.[583,346,617–619,364,620–627,361] A wealth of photophysical studies on a variety of Ru(II) polypyridyl complexes over more than several decades has made it possible to tune the excited state dynamics of these systems using rational design principles.[346,628–634] In many systems, the photophysical properties are set by the lowest-energy metal-to-ligand charge transfer (MLCT) excited state. However, judicious choice of ligand combinations around Ru(II) can also lead to accessible excited states that involve predominantly the metal (metal-centered, MC) or one of its ligands (intraligand, IL), each of which has its own characteristic excited state reactivity that can be tailored according to the desired response.

The success of this approach has been demonstrated by our own TLD1433, which is the first Ru(II) PS to advance to human clinical trials.[346] TLD1433 completed a Phase 1b study for treating non-muscle invasive bladder cancer (NMIBC) with PDT in 2018 and proceeded to a Phase 2 study that is currently underway (ClinicalTrials.gov identifiers NCT03053635, NCT03945162). TLD1433 is a Ru(II) polypyridyl complex that incorporates a polarizable π-expansive ligand having a triplet intraligand charge transfer ($^3$ILCT) state energy that is lower than that of the $^3$MLCT state. This results in a prolonged excited state lifetime due to the significant organic $^3\pi\pi^*$ character of the $^3$ILCT state that slows competitive intersystem crossing (ISC) back to the ground state. Prolonged triplet state lifetimes are generally longer than 10 μs[633] in the absence of excited state quenchers such as oxygen and tend to promote extremely high $^1O_2$ quantum yields.[635–641]

While many Ru(II) complexes sensitize $^1O_2$ most efficiently with activation in the 400–500 nm wavelength range, we have observed that Ru(II) complexes with π-expansive ligands and lowest-energy $^3$IL or $^3$ILCT states can produce $^1O_2$ (and photocytotoxic effects) with 630 nm light despite molar extinction coefficients that are vanishingly small in the red spectral region.[346,639,642] In order to increase the efficiency of this process by increasing molar extinction coefficients and extending the absorption window into the near-infrared (NIR), we have combined π-expanded tridentate ligands with Ru(II) to produce lower-energy MLCT states. These NNN ligands are referred to as chromophoric ligands herein and their π-expansion orthogonal to the direction of the M-N bond is the key feature for extending the absorption window into the NIR. The PDT-active ligand that installs the low-energy $^3$IL state for efficient $^1O_2$ sensitization is also π-expansive, but extending conjugation along the M-N bond has little effect on the MLCT energy. The challenge in creating NIR-absorbing PSs with high $^1O_2$ quantum yields lies

in lowering the energy of the $^1$MLCT state without lowering the energy of the $^3$MLCT state below that of the $^3$IL state. For this we chose the benzo[*i*]dipyrido[3,2-*a*:2′,3′-*c*]phenazine (dppn) ligand due to its exceptionally low-energy $^3$IL state, estimated at 1.33 eV.[636,643]

Our primary reason for extending the absorption window for Ru(II) complexes that use PDT-active $^3$IL (or $^3$ILCT) states was to develop Ru(II)-based NIR PSs for melanoma PDT. Melanoma cells contain melanin, a pigment that is well-adapted for detoxifying ROS[644,645] and that can absorb and attenuate visible light,[646] including the red wavelengths often used for PDT. Although PDT has produced some encouraging results both *in vitro* and *in vivo*[645,647] and in a few isolated clinical cases for melanoma,[644,645,648] pigmented melanomas have proven more resistant to PDT[649] than their amelanotic counterparts.[644,645,650] To improve PDT effectiveness against some of the most aggressive melanomas, we set out to design Ru(II) NIR PSs with high $^1O_2$ quantum yields that could also generate an antitumor immunological response. The longer-term vision is that these NIR PSs may provide immunotherapeutic benefit in optimized PDT regimens delivered alongside surgery.

This study systematically explores combinations of ligands types and Ru(II) with the goal being to achieve NIR PDT effects with a chemically well-defined PS that is stable in the absence of light and has a high $^1O_2$ quantum yield. The core metal-containing scaffold [**Figure 4.1**] was inspired by a family of Ru(II) complexes designed as catalysts for water oxidation,[651] where the tridentate 2,2′-(4-(*tert*-butyl)pyridine-2,6-diyl)bis(1,8-naphthyridine) (tpbn) ligand was coordinated to Ru(II) to form robust catalysts with NIR absorption out to approximately 800 nm. We envisioned that this scaffold could be combined with π-expansive PDT-active ligands such as dppn to build

PSs for PDT applications that might benefit from the use of NIR light. Herein, we report the results from our structure-activity (SAR) study and identify a novel Ru(II)-based PS platform for achieving PDT with longer wavelengths of light. We also demonstrate that this PDT effect has the potential to create antitumor immunotherapeutic effects *in vitro* and *in vivo*.

## 4.3. RESULTS

### *4.3.1. Chemical synthesis and characterization of compounds*

### Synthesis and characterization of compounds

The inspiration for the NIR Ru(II) scaffold used in our design was the tpbn-bearing Ru(II) complex $[Ru(tpbn)(4\text{-pic})_2(H_2O)](PF_6)_2$ [**Figure 4.1**] that was reported by Thummel and coworkers in 2005.[651] Although designed as a water oxidation catalyst for applications in artificial photosynthesis, $[Ru(tpbn)(4\text{-pic})_2(H_2O)](PF_6)_2$ exhibited several key properties that were attractive for PDT. The catalyst was redox active, relatively robust, and absorbed light panchromatically from the UV into the NIR, extending to 800 nm. In addition, substituents on the axial pyridine ligands had a profound influence on the low-energy $^1$MLCT transitions. The switch from electron withdrawing to electron donating groups at the para positions red-shifted the longest wavelength absorption maxima by almost 100 nm. In the present study, we adapted this structure to incorporate a bidentate ligand in the place of the aqua and one of the pyridyl ligands in order to install a π-expansive ligand with a low-energy $^3$IL state for effective $^1O_2$ sensitization.

The target complexes [**1**–**9**, **Figure 4.2**] of the type $[Ru(NNN)(NN)(L)]Cl_n$ were selected for examining SARs with regard to NIR absorption, $^1O_2$ quantum yields, and *in vitro* PDT effects. Given that the Ru(II) family was designed to have low-energy MLCT states for NIR absorption and that $^1O_2$ generation is most efficient when the $^3$IL state is

below the $^3$MLCT, the dppn ligand was used as the PDT ligand due to its low-energy $^3$IL state lying near 1.33 eV.[640,642,652] We hypothesized that there would be a minimum $^3$MLCT-$^3$IL energy gap required for effective $^3$IL population that would limit how far into the NIR the absorption could be shifted while still maintaining high $^1O_2$ quantum yields and good photocytotoxicity.

To demonstrate that the energy of the $^3$IL state must be below that of the $^3$MLCT state for activity, the reference compounds **7** and **8**, with 1,10-phenanthroline (phen) in place of dppn, were included since the $^3$IL state of phen is much higher than the $^3$MLCT state but the coordination geometry between phen and dppn remains similar. To probe the $^3$MLCT-$^3$IL energy gap limit by changing the MLCT energy, the chromophoric NNN and the axial (monodentate L) ligands were varied in complexes containing dppn. The NNN ligand tpbbn was used to lower the MLCT states due to its more expanded π-system with distal benzo groups fused to each napthyridine of tpbn. Cl as the axial ligand was also used to lower the MLCT energy. The expectation was that the NIR absorption would red-shift in the following order as a consequence of lowering the MLCT energies: Cl combined with tpbbn (**3**) > Cl combined with tpbn (**1**), 4-pic combined with tpbbn (**4**) > 4-pic combined with tpbn (**2**).

Simple variation to the central pyridine ring of the chromophoric ligand and the axial pyridyl ligands of compound **2** were also explored to determine whether these positions could be used to fine-tune existing properties. Compound **6** contained 2,6-di(1,8-naphthyridin-2-yl)pyridine (dnp) as the chromophoric ligand, which lacked the *t*-Bu group of the tpbn ligand in **2**, and **9** contained 4-methoxypyridine (4-mp) in place of 4-pic in **2**. The corresponding chloro complexes (**5** and **1**, respectively), were also examined given that **1**, **3**, **5** and **7** were synthesized as precursors to the pyridyl complexes.

Whereas the pyridyl complexes have an overall charge of +2, the Ru(II) complexes with chloro in the axial position have an overall charge of +1. Complexes **1**, **3**, **5** and **7** and were thus expected to be less water soluble and potentially labile.

Complexes of the formula [Ru(NNN)(NN)(Cl)]Cl **1**, **3**, **5**, **7** were synthesized following a 2-step procedure, similar to what was reported by Thummel and coworkers.[651] $RuCl_3 \bullet 3H_2O$ was refluxed with the NNN chromophoric ligand (tpbn, tpbbn, or dnp) to give the corresponding $[Ru(NNN)](Cl)_3$ species *in situ*, which was then combined (without isolation or purification) with the bidentate NN ligand (dppn or phen) in the presence of TEA to give the [Ru(NNN)(NN)(Cl)]Cl complexes **1**, **3**, **5**, **7** which were purified on neutral alumina to afford the desired products in 30–48% yield. Complexes **1** and **5** were also prepared using microwave irradiation to shorten total reaction time and gave similar yields. Although not tested, it is anticipated that **3** and **7** could also be prepared in much shorter reaction times with microwave irradiation.

The $[Ru(NNN)(NN)(4\text{-pic})]Cl_2$ complexes **2**, **4**, **6**, **8** were synthesized from the corresponding [Ru(NNN)(NN)(Cl)]Cl complexes **1**, **3**, **5**, **7** following a two-step procedure. First, [Ru(NNN)(NN)(Cl)]Cl was refluxed with $AgNO_3$ to facilitate removal of the axial chloride ligand following a modified literature procedure.[653] An excess of 4-pic was then added and the reaction mixture was refluxed to give $[Ru(NNN)(NN)(4\text{-pic})]Cl_2$. Complexes **2**, **4**, **6**, **8** were purified on neutral alumina, affording final products in 66–81% yield. Complexes **2, 6** and **8** were also prepared using microwave irradiation to shorten reaction times significantly. In this case, $AgNO_3$ was not required. It is anticipated that **4** could also be prepared in this manner. Complex **9** was synthesized from complex **1** in a similar approach as for **2**, except 4-mp was used in place of 4-pic and was likewise successfully prepared using microwave irradiation.

Complexes **1**–**9** were characterized by high resolution $ESI^+$ mass spectrometry [Appendix Figures S29–S37], 1D $^1H$ NMR and 2D $^1H$–$^1H$ COSY NMR spectra [Appendix Figures S1–S28], and HPLC [Appendix Figures S38–S46]. The molecular ion peaks matching the calculated $[M\text{-}Cl]^+$ peaks were observed for [Ru(NNN)(NN)(Cl)]Cl complexes **1**, **3**, **5**, **7**. Likewise, molecular ion peaks matching the calculated $[M\text{-}2Cl]^{2+}$ peaks were observed for $[Ru(NNN)(NN)(4\text{-pic})]Cl_2$ complexes **2**, **4**, **6**, **8** and for $[Ru(tpbn)(dppn)(4\text{-mp})]Cl_2$ complex **9**, confirming the correct molecular masses of the complexes. Observed molecular ions exhibited isotopic patterns characteristic of mononuclear Ru(II)-containing complexes, with separation of 1 m/z between the peaks for $M^+$ ions and 0.5 m/z between the peaks for $M^{2+}$ ions.

To confirm structures, the 1D $^1H$ NMR and 2D $^1H$–$^1H$ COSY NMR spectra of complexes **1**–**9** [Appendix Figures S1–S28] were closely analyzed and all hydrogens assigned. Assignments were made based on connectivity observed by 2D $^1H$–$^1H$ COSY NMR, coupling constants observed in 1D $^1H$ NMR spectra, and precedent assignments of similar systems reported in the literature s.[654,655] The process of assigning the signals in each $^1H$ NMR spectrum for complexes **1**–**9** is described in detail in the Supporting Information.

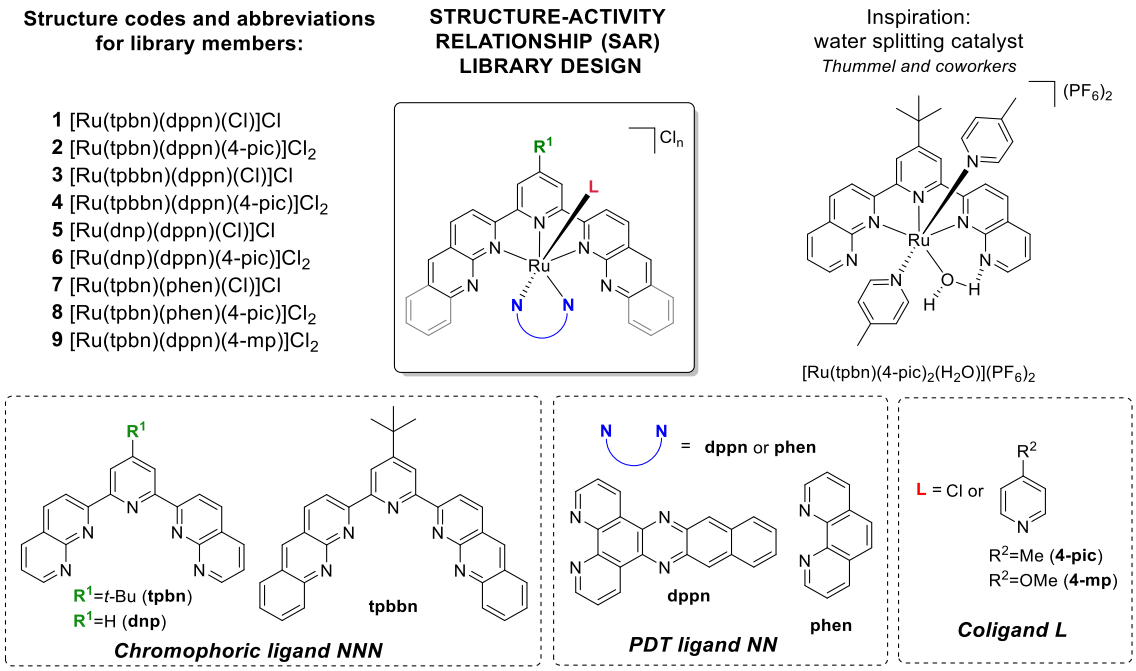


**Figure 4.1.** Library design for Ru(II) complexes investigated in this study.

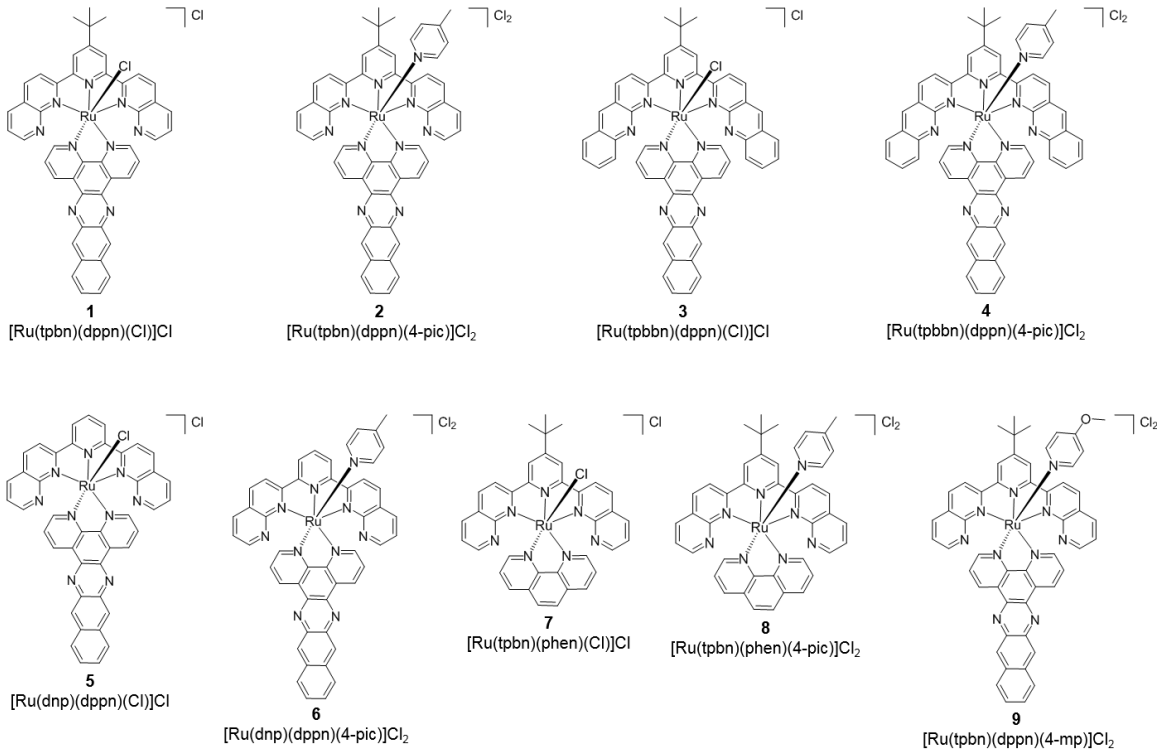


**Figure 4.2.** Molecular structures of Ru(II) complexes 1–9.

## Photophysical Characterization

Absorption properties

The compounds within the series were panchromatic absorbers from the UV into the NIR, with the NIR cut-off determined by the ligand combinations in a predictable manner. Generally, the electronic transitions in these complexes could be grouped into three or four wavelength regions [**Figure 4.3**]. Below 400 nm, ligand-localized $^{1}\pi\pi^{*}$ transitions involving the polypyridyl groups of the NNN, NN, and N ligands gave rise to intense, sharp bands with large molar extinction coefficients ($10^{4}$–$10^{5}$ $M^{-1}$ $cm^{-1}$).[628,632,656,657]

Spectra for compounds containing the dppn ligand included additional ligand-localized $^1\pi\pi^*$ bands ($\varepsilon \approx 10^4$ $M^{-1}$ $cm^{-1}$) with characteristic fine structure between 370–430 nm contributed by transitions typical of azaaromatics.[640] Much broader and less intense bands ($\varepsilon \approx 10^3$–$10^4$ $M^{-1}$ $cm^{-1}$) due to $^1$MLCT transitions involving Ru(d$\pi$) orbitals and ligand $\pi^*$ orbitals of the polypyridyl groups appeared between 400–650 nm.[628,632,658–660] The longer wavelength $^1$MLCT bands ($\varepsilon \leq 10^3$ $M^{-1}$ $cm^{-1}$) that occurred beyond 650 and into the NIR were assigned to Ru(d$\pi$)→$\pi^*$ transitions involving increased $\pi$-delocalization onto the distal polypyridyl groups of the NNN chromophoric ligands.[661–664]

The longest wavelength absorption maxima in the NIR was dictated by the ligand combinations around Ru(II) and ranged from 715 to 903 nm. Generally, chloro as the monodentate ligand and tpbbn as the NNN chromophoric ligand produced the largest bathochromic shifts of the NIR $^1$MLCT transitions, while pyridyl as the monodentate ligand and tpbn as the NNN chromophoric ligand resulted in the smallest shifts. The largest red-shifts result from an increase in the energies of the Ru(d$\pi$) orbitals (due to the weak-field chloro monodentate ligand) and a concomitant decrease in the energies of the ligand-based $\pi^*$ orbitals (with more extended $\pi$-conjugation in the tpbbn chromophoric ligand) as exemplified by **3** having the longest NIR absorption maximum in the series at 903 nm and **2** having the shortest at 715 nm.

Combining the chloro ligand with the smaller chromophoric tpbn ligand (**1**, **7**) or 4-pic with the larger chromophoric tpbbn ligand (**4**) resulted in NIR maxima (805–820 and 785 nm, respectively) that were intermediate between these two extremes. Minor changes to the substituents on the central pyridyl ring of the smaller chromophoric ligand, e.g., dnp, (**1** vs. **5**, **2** vs. **6**) or on the monodentate pyridyl ligand (**2** vs. **9**) produced only minor shifts in these bands. Likewise, the bidendate NN ligand in this

series (dppn or phen) had little influence on these maxima (**1** vs. **7**, **2** vs. **8**) despite dppn being much more π-extended compared to phen, supporting the notion that the π* orbitals involved in the NIR MLCT transitions of complexes containing dppn involve only the proximal portion of this ligand.

Together, the absorption studies highlight that the ([Ru(NNN)(NN)(L)]$Cl_n$ scaffold selected for this investigation represents a reliable system for tunable NIR absorption, where local maxima can be shifted over 200 nm in the NIR, from 700 to 900 nm. Course tuning (50–100 nm) was achieved by controlling (i) whether L was a weaker- or stronger-field ligand, and (ii) the degree of π-expansion for the NNN chromophoric ligand. Fine-tuning (<20 nm) was demonstrated through substituent modifications to the tpbn and 4-pic ligands of **2** [**Figure 4.4**]. The pyridyl complexes combined with the smaller chromophoric tpbn ligand (**2**, **4**, **6**, **8**, and **9**) exhibited better solubility and did not undergo ligand dissociation during the course of the absorption measurements (as was observed for the chloro complexes). Therefore, these complexes were preferred for additional spectroscopic and biological studies. Their higher-energy NIR MLCT transitions could also be advantageous for maximizing $^1O_2$ sensitization. Nevertheless, the chloro and tpbbn complexes (**1**, **3**, **5**, and **7**) were included in some of the subsequent studies to better understand the activities of the favored compounds.

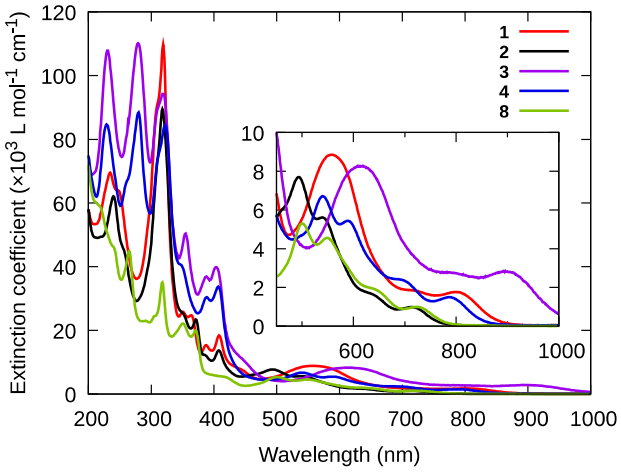


**Figure 4.3.** Steady-state UV-vis absorption spectra of compounds **1**–**4** and **8** (20 μM in MeCN).

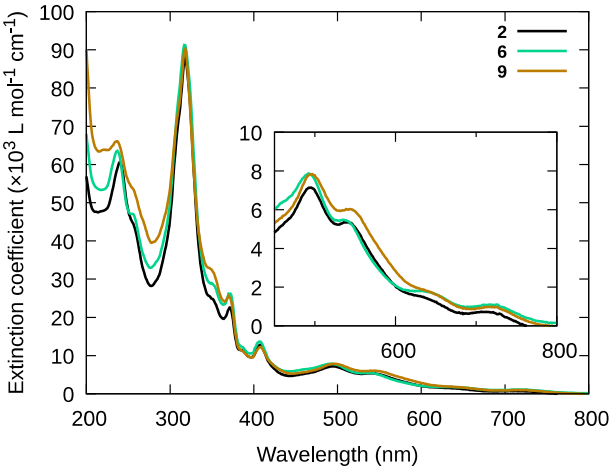


**Figure 4.4.** Steady-state UV-vis absorption spectra of selected compounds.

Steady-state UV-vis absorption spectra of compounds **2**, **6**, and **9** (20 μM in MeCN). Compound **2** is **ML18H01**.

Transient absorption spectroscopy

The excited states of the pyridyl complexes (**2**, **4**, **6**, **8**–**9**) were interrogated by transient absorption (TA) spectroscopy using a 355 nm excitation pulse [**Figure 4.5**]. The TA profiles are differential spectra derived from positive signals (arising from excited state absorption) that are superimposed on negative signals (arising from the ground state bleach). They offer an opportunity to extract information on lowest-energy excited state configurations and lifetimes. Compounds combining the tpbn chromophoric (NNN) ligand with dppn produced the characteristic spectral signature of the dppn-based $^3$IL excited state with a maximum near 550 nm,[(636)] while compounds **4** and **8** did not. The excited state decays for **4** and **8** were dominated by signals with lifetimes on the order of tens of nanoseconds (attributed to $^3$MLCT relaxation), while **2**, **6**, and **9** decayed biexponentially with a short component that was similar to that observed for **4** and **8** (assigned as $^3$MLCT relaxation) but also a longer component that reflected contributions from the dppn-based $^3$IL state.

While the longer lifetimes were on the order of hundreds of nanoseconds and shorter than the microsecond $^3$IL lifetimes in Ru(II) diimine complexes such as $[Ru(bpy)_2(dppn)]^{2+}$, the intense and broad transient with a maximum near 550 nm in the TA spectra displayed the characteristic signature of the dppn-based $^3$IL excited state.[(636)] These shorter lifetimes for the $^3$IL state in **2**, **6**, and **9** were attributed to substantial mixing with the much lower-energy $^3$MLCT states in these systems. The absence of this signature in **8**, which lacked the dppn ligand and thus a low-energy $^3$IL state, provided further support of this assignment. The lack of the $^3$IL signature in the TA spectrum of **4**, which does incorporate the dppn ligand, was attributed to a much lower-energy $^3$MLCT state afforded by the more π-extended tpbbn chromophoric ligand. This lower energy was reflected in an $^3$MLCT lifetime for **4** that was twice as short as the corresponding

$^3$MLCT decay for the other pyridyl-based complexes. Together, the TA data suggests that the Ru(II) complexes containing the tpbn chromophoric ligand and dppn lead to effective population of $^3$IL states within this family. It was anticipated that these longer-lived $^3$IL states would be better poised to sensitize $^1O_2$.

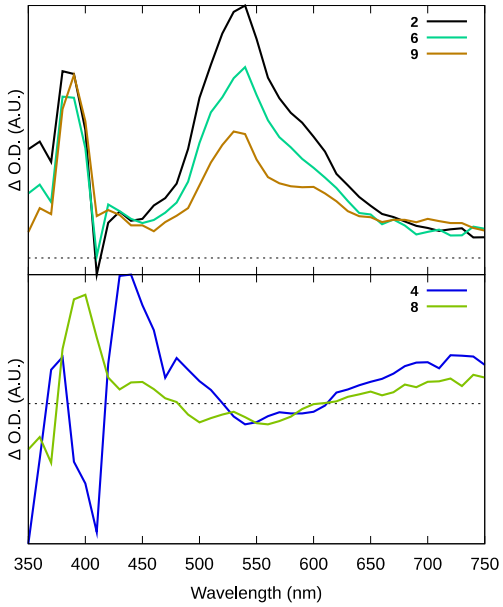


**Figure 4.5.** Transient absorption (TA) spectra collected for selected compounds. Using $\lambda_{ex}$=355 nm (*t*=0, 20 ns integration), 20 μM in degassed MeCN. Compound **2** is **ML18H01**.

Singlet oxygen quantum yields

The $^1O_2$ quantum yields ($\Phi_\Delta$) for the complexes were calculated relative to $[Ru(bpy)_3](PF_6)_2$ by direct measurement of $^1O_2$ phosphorescence in acetonitrile with excitation at 630 nm and 753 nm (Table 4.). These excitation wavelengths were chosen

based on those used clinically for Photofrin (630 nm) and TOOKAD Soluble (753 nm) [**Table 4.1**]. Values for $\Phi_{\Delta}$ were also determined using the maxima from excitation scans collected at $\lambda_{em}$=1270 nm (if different from the two clinical wavelengths). Despite the chloro ligand being somewhat labile in MeCN, the $^1O_2$ quantum yields are included for these complexes (only initial scans with fresh solutions were used in order to limit error due to sample degradation during the measurement). All of the chloro complexes (**1**, **3**, **5**, and **7**) were poor $^1O_2$ generators, with $\Phi_{\Delta}$ values less than 10%, with the exception of **5**, where the value for $\Phi_{\Delta}$ was 28% using the excitation maximum at 464 nm but <10% at the clinical wavelengths.

Complexes containing the tpbn, or related dnp, chromophoric ligand combined with dppn and a pyridyl-based monodentate ligand (**2**, **6**, **9**) gave the largest $^1O_2$ quantum yields. Compound **2**, derived from 4-pic, was the most efficient producer of $^1O_2$ ($\Phi_{\Delta}$=93% with $\lambda_{ex\ max}$=630 nm and 86% with $\lambda_{ex}$=753 nm). The $[Ru(NNN)(dppn)(N)]^{2+}$ scaffold tolerated changes to either the 4-position of the central pyridine (**6**) or monodentate pyridine-based ligand (**9**) with only a slight loss of efficiency for $^1O_2$ production, with the exception **6** exhibiting a wavelength dependence and suffering a loss in efficiency at 753 nm ($\Phi_{\Delta}$=0.34) compared to 630 nm ($\Phi_{\Delta}$=0.77).

By contrast, the pyridyl-based complexes derived from the π-expanded tpbbn ligand (**4**) or lacking the dppn ligand (**8**) were poor $^1O_2$ generators, with values of $\Phi_{\Delta}$ near 10% or less using the longer (clinical) wavelengths and only slightly higher when excited at their excitation maxima (14 and 17%, respectively). These were also the two pyridyl complexes that lacked the dppn-based $^3$IL transient in their TA spectra and exhibited only the shorter $^3$MLCT lifetime.

Complexes **2**, **6**, and **9** were the complexes that had the largest $^1O_2$ quantum yields, displayed the characteristic $^3$IL signature, and had the longest excited state lifetimes. These observations suggest that the presence of the longer-lived excited state lifetime exhibited by **2**, **6**, and **9** is correlated with larger quantum yields for $^1O_2$ sensitization. Thus, we assign efficient $^1O_2$ production to the accessible $^3$IL state identified in TA spectra for the Ru(II) complexes containing tpbn, dppn, and a pyridyl-based monodentate ligand. We anticipated that such complexes based on this scaffold, with accessible and longer-lived $^3$IL states, would be most active for PDT.

**Table 4.1.** Spectroscopic data and singlet oxygen quantum yields ($\Phi_\Delta$) for ruthenium complexes 1–9.

| **Compound** | **$\lambda_{abs}$ / nm (log ($\varepsilon$ / $M^{-1}$ $cm^{-1}$))** | **$\tau_{TA}$ / ns ($\lambda\tau_{1\rightarrow}\tau_n$ / nm)** | **$\Phi_\Delta$ ($\lambda_{ex}$ / nm)** |
|---|---|---|---|
| **1** | 234 (4.76), 318 (4.94), 365 (4.31), 409 (4.18), 560 (3.87), 805[a] (3.18) | n.d. | 0.04[b] (630), 0.02 (753) |
| **2 (ML18H01)** | 240 (4.79), 318 (4.95), 371 (4.37), 406 (4.12), 493 (3.88), 540 (3.75), 636 (3.22), 715[a] (2.98) | 59 ns, 564 ns (380)<br>59 ns, 563 ns (540) | 0.93[b] (630), 0.86 (753) |
| **3** | 230 (4.91), 278 (4.92), 319 (4.85), 354 (4.58), 402 (4.48), 610 (3.80), 903[a] (3.31) | n.d. | 0.05[b] (464),<br>0.01 (630), 0.03 (753) |

| Compound | $\lambda_{abs}$ / nm (log ($\varepsilon$ / $M^{-1}$ $cm^{-1}$)) | $\tau_{TA}$ / ns ($\lambda\tau_{1\rightarrow}\tau_n$ / nm) | $\Phi_\Delta$ ($\lambda_{ex}$ / nm) |
|---|---|---|---|
| **4** | 229 (4.93), 279 (4.95), 322 (4.93), 350 (4.60), 386 (4.48), 406 (4.53), 540 (3.83), 785[a] (3.18) | 36 ns (380)<br>30 ns (410)<br>33 ns (440)<br>29 ns (540) | 0.14[b] (455),<br>0.09 (630), 0.03 (753) |
| **5** | 233 (4.47), 250 (4.43), 318 (4.66), 366 (4.04), 405 (3.91), 436 (3.63), 813[a] (2.85) | n.d. | 0.28[b] (464),<br>0.09 (630), 0.07 (753) |
| **6** | 237 (4.80), 255 (4.66), 318 (4.95), 371 (4.41), 408 (4.13), 493 (3.89), 725[a] (3.02) | 120 ns, 334–367 ns (380)<br>81 ns, 340–411 ns (540) | 0.77 (630),<br>0.82[b] (640),<br>0.34 (753) |
| **7** | 224 (4.65), 266 (4.53), 319 (4.37), 364 (4.18), 406 (3.71), 553 (3.67), 821[a] (3.12) | n.d. | 0.06[b] (455),<br>0.04 (630), 0.05 (753) |
| **8** | 264 (4.74), 318 (4.63), 350 (4.44), 370 (4.39), 416 (3.83), 501 (3.82), 725[a] (3.08) | 62 ns (400)<br>62 ns (560) | 0.17[b] (455),<br>0.10 (630), 0.10 (753) |

| Compound | $\lambda_{abs}$ / nm (log ($\varepsilon$ / $M^{-1}$ $cm^{-1}$)) | $\tau_{TA}$ / ns ($\lambda\tau_{1\rightarrow}\tau_n$ / nm) | $\Phi_\Delta$ ($\lambda_{ex}$ / nm) |
|---|---|---|---|
| **9** | 237 (4.91), 318 (5.09), 370 (4.48), 406 (4.25), 498 (4.00), 725[a] (3.12) | 67–79 ns, 358–384 ns (390) 357–361 ns (530) | 0.69 (630), 0.75[b] (632), 0.69 (753) |

Longest wavelength absorption maximum, [b]maximum singlet oxygen quantum yield

## Photobiological studies

Cellular assays

The dark and light cytotoxicities for **1**–**9** were measured in three melanoma lines growing as 2D adherent monolayers. The cell lines were chosen to represent different sexes (male human SKMEL28 vs. female human A375) and species (murine B16F10 vs. human SKMEL28 and A375) since our *in vivo* work would use a murine line. They also differ in their pigmentation (melanotic B16F10), aggressiveness, and melanosome stages.[665,666] Briefly, cells growing in log phase were seeded, dosed with compound (1 nM–300 μM), and then incubated for 48 h before cell viability was determined using the resazurin assay for cytotoxicity. To determine photocytotoxicity, an analogous set of plates were prepared but were irradiated 16–19 h after compound addition. Dose-response curves were prepared from both dark and light conditions and analyzed to provide dark and light $EC_{50}$ values, the effective concentration to reduce relative viability by 50%. Phototherapeutic indices (PIs), or the light-induced amplification of cytotoxicity, were calculated as the ratios of the dark $EC_{50}$ values to the light $EC_{50}$ values.

Specialized treatment protocols (hypoxia, light dosimetry, immunology, etc.) are described as they are discussed.

Across the family, compounds with +1 charge (i.e., those containing the anionic chloro monodentate ligand) aggregated in aqueous solutions of high ionic strength. The chloro compounds were labile at room temperature in some coordinating solvents, did not display the desirable $^3$IL signature in the TA spectra, and had low $^1O_2$ quantum yields. By contrast, compounds with +2 charge (i.e., those containing the neutral pyridine-based monodentate ligand) were readily water-soluble and stable in coordinating solvents under ambient conditions. Family members with substituted pyridines (4-pic, 4-mp) combined with dppn as the bidentate ligand exhibited the desired $^3$IL TA signature and had the highest $^1O_2$ quantum yields. Therefore, we focused on the substituted pyridine-based compounds (**2**, **6**, **9**) as the most suitable members for photobiological studies, but compared to their chloro counterparts and other reference compounds when appropriate.

Dark cytotoxicity

The dark cytotoxicities for the nine compounds in all three cell lines are illustrated in the activity plots shown in **Figure 4.6** (black filled circles) and tabulated in Table S4–S6. The dark $EC_{50}$ values ranged from 15 to 256 μM in the SKMEL28 cell line, with compound **1** being the most cytotoxic and **7** being the least (both chloro compounds). The range for the pyridine-based counterparts was smaller, from approximately 50 to 130 μM where **4** was the most cytotoxic and **8** the least. The dark cytotoxicity in both chloro and pyridine compounds roughly paralleled lipophilicity for soluble compounds [Appendix Figure S48].

Using compound **2** as a reference point because it had the highest $^1O_2$ quantum yield ($\Phi_\Delta$=0.93) and potential as a phototherapeutic lead, we were interested in comparing dark cytotoxicity in terms of SARs for **2** and its close relatives. Replacing 4-pic in **2** with the anionic chloro ligand as in **1** reduced the charge on the Ru(II) compound from +2 to +1 and increased the dark toxicity by seven-fold. Expanding the chromophoric ligand in **2** by fusing two additional benzene rings as in **4** doubled the dark cytotoxicity. Removal of the t-Bu group of the central pyridine ring of the chromophoric ligand in **2** as in **6**, replacing dppn with phen as in **8**, or changing 4-pic to 4-mp as in **9** had only a modest effect. Replacing dppn for phen in **8** decreased dark toxicity whereas the other two modifications in **6** and **9** slightly increased toxicity. A closer look at lipophilicities within this comparison group (Fig. S48, Table S1), reveals a significant correlation between dark cytotoxicity and lipophilicity in SKMEL28. Correlation in either A375 or B16F10, however, was not significant. The general trends are the same for A375 and B16F10 but with subtle distinctions. Changing the pyridine ligand as in **9** relative to **2** brings their dark toxicities within error of each other in the additional lines. Instead of doubling the toxicity, the expanded chromophore in compound **4** only slightly increased toxicity from **2** (51.1 vs. 62.6 μM) in A375. Additionally, compounds with dppn are more cytotoxic in A375 than either SKMEL28 or B16F10 while those with phen (**7**, **8**) are much less cytotoxic.

Generally, compounds with the lowest dark cytotoxicity (largest $EC_{50}$ values) are most desirable as phototherapeutic compounds. Excluding the chloro compounds, which had other undesirable properties, the pyridine-based compounds **2**, **6**, **8**, and **9** were the least dark toxic toward all three melanoma cell lines (dark $EC_{50}$ values ≥ 46.3 μM) with their magnitude and order of toxicity not deviating significantly between the lines. Of these, **2**, **6**, and **9** had the largest $^1O_2$ quantum yields (and displayed the characteristic

$^3$IL TA signature for dppn) and thus might be expected to exhibit the widest phototherapeutic margins.

Photocytotoxicity

The photocytotoxicities of the compounds in the series were assessed using 100 J cm$^{-2}$ doses of broadband visible (400–700 nm, 19 mW cm$^{-2}$), green (523 nm, 18.5 mW cm$^{-2}$), red (633 nm, 20 mW cm$^{-2}$) and NIR (733 nm, 9 mW cm$^{-2}$) light. The spectral output of the applied light sources are shown in Appendix Figure S49. Comparisons of the photocytotoxicity values are shown in **Figure 4.6**.

With light activation, the cytotoxicities exerted by the compounds increased by as much as 360-fold. The extent of light amplification depended on the wavelength(s) used and the particular compound, with shorter wavelengths (e.g., visible irradiation containing significant contributions from the bluer wavelengths) generally producing greater light-related cytotoxicity. Light of any wavelength had very little effect on the cytotoxicity of compound **8**, which contained phen as the bidentate ligand instead of dppn, and confirmed that both the high $^1O_2$ quantum yield and long $^3$IL state lifetime imparted by the dppn ligand were crucial for generating phototoxic effects.

Compounds **2**, **6**, and **9**, having the highest $^1O_2$ quantum yields and the characteristic $^3$IL state signature in their TA spectra, were the most phototoxic compounds in the series across all light treatments and all cell lines. Light $EC_{50}$ values toward the SKMEL28 cell line ranged from 0.292 μM to 0.602 μM with broadband visible light, from 0.407 μM to 0.720 μM with 523-nm green light, from 0.798 μM to 1.52 μM with 633-nm red light, and from 1.29 μM to 1.56 μM with 733-nm NIR light. The order of potency toward SKMEL28 generally was **2**>**6**>**9**, but with a few discrepancies in the trend depending on wavelength. The A375 and B16F10 melanoma cell lines proved to

be slightly more resistant, but compounds **2**, **6**, and **9** were still the most photocytotoxic. In both B16F10 and A375 the order of potency reversed with **9**>**6**>**2** being the general trend. Interestingly, the wavelength-dependence for photocytotoxicity appeared to be different across the three cell lines and also between compounds. For example, compound **2** in A375 and B16F10 exhibited almost no difference in its $EC_{50}$ values between the visible and 733 nm NIR treatments. For comparison, the difference between the visible and NIR $EC_{50}$ values for **2** in SKMEL28 was 5-fold.

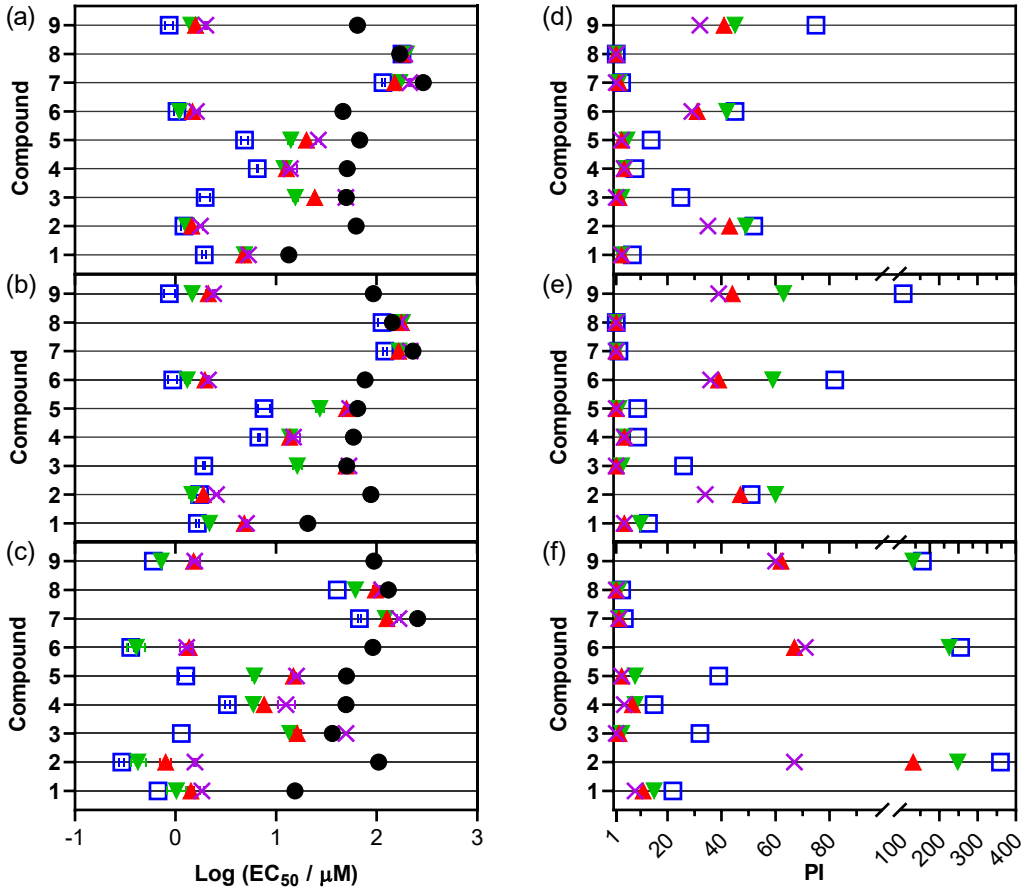


**Figure 4.6.** *In vitro* cytotoxicity and photocytotoxicity dose-response.

Parameters in A375 (a, d), B16F10 (b, e), and SKMEL28 (c, f) melanoma cell lines with compounds **1**–**9**. Treatments include dark (0 J $cm^{-2}$; black circles) and 100 J $cm^{-2}$ doses of 733 nm (purple cross), 633 nm (red triangle), 523 nm (green inverted triangle), and visible (peak maxima ~450 nm; open blue square). Plots a–c show Log ($EC_{50}$ ± SEM) and d–f show PI, where PI is the ratio of dark to light $EC_{50}$ values. All linear-scale values are listed in the SI. Compound **2** is **ML18H01**.

Phototherapeutic Indices (PIs)

The structural variations that led to lower dark cytotoxicities also resulted in the best photocytotoxicity profiles with all wavelengths in all three cell lines. Therefore, the PIs, which are the true measure of light-induced cytotoxicity, were the largest for these three compounds as well. Across all cell lines, the order of PI potency for **2**, **6**, and **9** varied based on wavelength. Their PI values in SKMEL28 ranged from 156 to 360 with visible light, 131 to 248 with 523 nm light, 62 to 132 with 633 nm light, and 60 to 71 with 733 nm light treatments. The general order of compound potency by PI for **2**, **6**, and **9** largely followed their light $EC_{50}$ values. In the more resistant lines, PIs were attenuated by 50% or more. For example, in the most resistant line A375, values ranged from 52 to 75 with visible light and 29 to 35 with 733 nm light, with both 523 and 633 nm falling between these two ranges. The attenuated activity in A375 and B16F10 could be due to a combination of their greater endogenous defenses against ROS, differences in melanosome stages and overall pigmentation, and/or greater aggressiveness compared to SKMEL28.[665,666]

Although the PI values were somewhat attenuated at 733 nm compared to the other light treatments, the fact that **2**, **6**, and **9** had sizeable PIs with NIR light means that

we can now push the activation of Ru(II) systems beyond the red/far-red wavelengths (630–670 nm) that had been the limit for single-photon PDT with Ru(II) polypyridyl complexes. Our orthogonal strategy for accessing the NIR window with polypyridyl complexes has been to combine Os(II) with π-expanded ligands and was described by us for $[Os(biq)_2(NN)]Cl_2$ in 2017. We used a high fluence at 808 nm (600 J $cm^{-2}$) to achieve PI values between 6 and 12 in human U87 glioblastoma and HT1376 bladder cancer cell lines.[667] While these compounds were NIR active, certain characteristics limited their utility and suited them as model systems for later generations. More recently, we have reported an Os(II) complex ($[Os(phen)_2(IP\text{-}4T)]Cl_2$, where IP-4T is imidazo[4,5-*f*][1,10]phenanthroline appended with quaterthiophene) with a submicromolar light $EC_{50}$ value and PI of 77 at 733 nm.[668] Our choice of 733 nm for the present Ru(II) series is still within the PDT window and produces greater activity than that reported for the $[Os(biq)_2(NN)]Cl_2$ examples (71 vs. 12) with 800 nm activation [**Figure 4.8**] and is of similar activity to our recently reported ($[Os(phen)_2(IP\text{-}4T)]Cl_2$. To our knowledge, the present series gives the largest NIR PIs (60–71) for Ru-based photosensitizers without the use of special measures such as two photon absorption[361] or upconverting nanoparticles.[669]

The PI values of the nine compounds investigated were significantly correlated to their $^1O_2$ quantum yields, demonstrating the potential role of ROS as the mediator for cell death. **Figure 4.7** shows the correlation of $^1O_2$ quantum yield and PI in the SKMEL28 cell line using 630 nm, the clinically approved wavelength used for Photofrin. Two clusters were apparent: (i) compounds with the lowest $^1O_2$ quantum yields that had the smallest PI values, and (ii) compounds with the highest $^1O_2$ quantum yields that also had the largest PI values.

To confirm the critical role of oxygen in the observed photoactivity, we screened the family under low oxygen tension using SKMEL28 cells (where the compounds exhibited the largest PI values under normoxia). $[Ru(bpy)_2(dppn)]Cl_2$ was included as an internal control for oxygen-dependence because it has a comparably high $^1O_2$ quantum yield ($\Phi_\Delta$ = 0.75 in MeCN), similar to compounds **2**, **6**, and **9**, but is not photoactive in 1% hypoxia ($O_2$).[636,638,640,670] Regardless of the light treatment, the compounds lost almost all of their photocytotoxicity toward SKMEL28 cells (PIs ≤ 3) at 1% oxygen (Table S7). Although not tested, a similar loss of activity would be expected in the more resistant cell lines. This absolute dependence on molecular oxygen suggests that these compounds exert their photocytotoxic effects through ROS-based mechanisms.

While the pyridyl complexes such as **2**, **6**, and **9** were completely stable to ligand dissociation at 37 °C for extended periods of time in the absence of a light trigger, 100 J $cm^{-2}$ doses of broadband visible (400–700 nm, 19 mW $cm^{-2}$), green (523 nm, 18.5 mW $cm^{-2}$), red (633 nm, 20 mW $cm^{-2}$) and NIR (733 nm, 9 mW $cm^{-2}$) light resulted in changes to the UV-Vis and HPLC spectra of the complexes that were consistent with dissociation of the monodentate pyridyl ligand to form the aquated product and free ligand as well as oxidation[642] of the dppn ligand. The quantum yields for these competing photochemical pathways were not determined, but the amount of photoproduct formed was related qualitatively to photon energy where visible light resulted in the most photoproduct and NIR the least. The photosubstitution pathway (where light causes one of the three ligands to dissociate from the Ru complex), which might be expected to lead to oxygen independent photocytotoxicity, did not yield any photocytotoxic effects in hypoxia. Likewise, the PIs were highly correlated to $^1O_2$ quantum yields. These observations point toward a very minor role, if any, for the photosubstitution pathway.

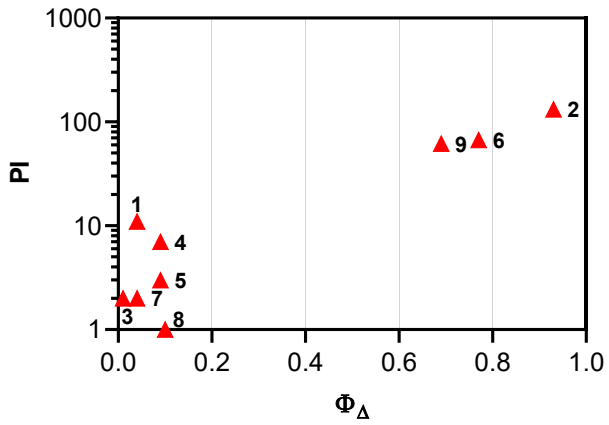


**Figure 4.7.** Correlation plot of PI and $\Phi_\Delta$ for SKMEL28 cells using 633 nm excitation or illumination, respectively.

Compound **2** is **ML18H01**.

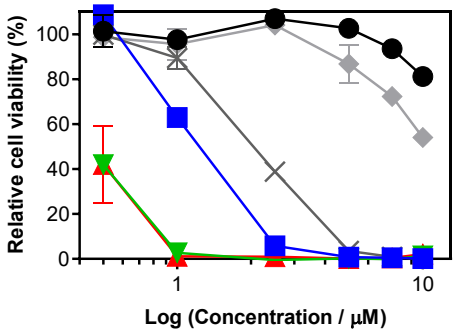


**Figure 4.8.** Panchromatic PDT example of compound **2** in SKMEL28 cells at high irradiance from 455–810 nm using the ML8500 platform.

Values shown are in duplicate and are the mean ± standard deviation (SD). Treatments include dark (black circle, 0 J $cm^{-2}$), 455 nm (blue square, 25 J $cm^{-2}$, 100 mW $cm^{-2}$), 525 nm (green inverse triangle, 100 J $cm^{-2}$, 300 mW $cm^{-2}$), 630 nm (red triangle, 200 J $cm^{-2}$, 300 mW $cm^{-2}$), 753 nm (grey X, 200 J $cm^{-2}$, 300 mW $cm^{-2}$), 810 nm (grey diamond, 400

J $cm^{-2}$, 400 mW $cm^{-2}$). Light-only controls are available in Figure S50. Compound **2** is **ML18H01**.

Validation

Given the variability that can result in cellular assays across laboratories using different assay methods, cells of different passage number, and culture conditions, we assayed the top three compounds in two different cell lines (B16F10 and SKMEL28) across two additional laboratories (Dalhousie University and Acadia University) by two different researchers (Konda and Monro) using slightly different assay conditions (noted in experimental). The dark cytotoxicities were greater at both Dalhousie and Acadia Universities, likely due to a longer (1-day) total incubation period. Compounds **2** and **6** were similar in their dark $EC_{50}$ values while **9** had 2- to 3-fold greater toxicity in SKMEL28 and B16F10, respectively. While the PIs were smaller when **2**, **6**, and **9** were tested elsewhere, they were still active. Visible PIs were comparable for all three compounds in SKMEL28 cells. Discrepancies arose for 630 nm treatments regarding compound **9** with a two-fold smaller PI at Dalhousie University in B16F10 and two-fold greater PI values for compounds **6** and **9** at Acadia University in SKMEL28. In light of these efforts, compounds **2**, **6**, and **9** remained strong candidates for further photobiological study.

Photocytotoxicity at higher light doses

The light sources used in the standard dose-response assay described previously are limited in the irradiances that can be delivered to an entire microplate. In order to control the irradiance more precisely and to explore higher fluences and irradiances, we performed photocytotoxicity experiments using the Modulight illumination system

(ML8500, Modulight Inc.) which has the unique feature of well-by-well illumination using different light conditions. In **Figure 4.8** compound **2** is highlighted for its panchromatic activity in SKMEL28 from 455 to 810 nm. Higher fluences were required with longer wavelengths (namely, 753 and 810 nm), and 976 nm was ineffective regardless of the fluence (data not shown). The high fluences and irradiances used in these light treatments did not cause any loss in cell viability in the absence of compound [Appendix Figure S50]. All light treatments with **2** reduced cell viability by ≥60% down to 2.5 μM except for 810 nm, where lower activity correlated with photon energy as described earlier [**Figure 4.6**]. The most potent effects were obtained with 455 to 630 nm ($EC_{50}$=0.5 to 1 μM), followed by 753 nm ($EC_{50}$=2.02 μM), and lastly 810 nm with roughly 10 to 20% viability reduction compared to dark controls between 2.5 and 10 μM. Compounds **6** and **9** followed similar trends. Compound **2** maintained its potency at the higher irradiances, where PDT effects can be reduced due to PDT-induced oxygen depletion in more advanced tissue or 3D models.[671–673]

Photocytotoxicity at lower light doses

The effects of lower fluence and irradiance were examined with the light sources used in **Figure 4.6** (visible, 523 nm, 633 nm, and 733 nm). For all three compounds and light treatments [Appendix Figure S51–54], photocytotoxicity could be maintained at lower fluence or irradiance. Fluences 1/20 to 1/2 of that used for the data shown in **Figure 4.6** (5 to 50 J $cm^{-2}$ vs. 100 J $cm^{-2}$) yielded single micromolar activity [**Figure 4.9**]. Notably, the Modulight's 20 nm longer 753 nm treatment [**Figure 4.8**] provided comparable cell kill, between 1–5 μM, as the 733-nm condition in **Figure 4.9**. For added perspective, treatment times were the same or up to ten times longer in **Figure 4.9** compared to the high fluence and high irradiance applied in the 753 nm treatment in **Figure 4.8**. The

question arose whether the compound activity would improve at low irradiance as reported in some PDT examples.[672,674]

The contrast in activities between the three leads **2**, **6**, and **9** became clearer at 10 J $cm^{-2}$ with varying irradiance between 2–10 mW $cm^{-2}$ [Appendix Figure S53–S54]. At this low fluence, a stronger wavelength dependence was observed with increasing potency in the order of 733 nm < 633 nm < 523 nm ≤ vis. In general, increased irradiance resulted in increased activity for these leads in SKMEL28. We only tested their irradiance dependence across a small range, however, and further study is required to probe how far this dependence extends, whether it increases asymptotically or plateaus below the maximum tested values of 100–400 mW $cm^{-2}$. This is only a limited example of the compound behavior, since other models (e.g., tissue, *ex vivo*) would require their own dosimetry optimizations.

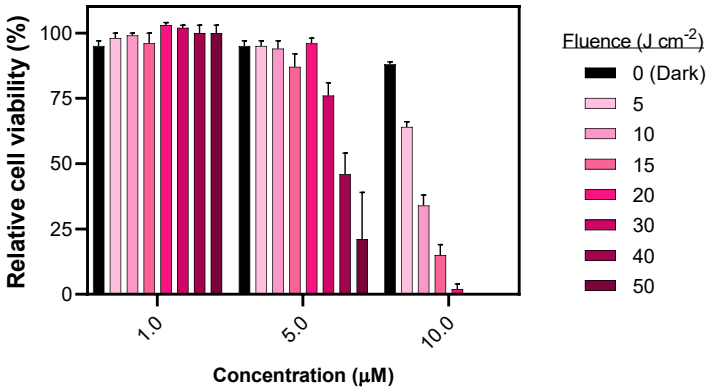


**Figure 4.9.** Fluence dependence (±SD) of compound **2** against SKMEL28 cells.

SKMEL28 cells with compound 2 and 733 nm treatment at 10 mW $cm^{-2}$ with fluences ranging from 0–50 J $cm^{-2}$. Compound **2** is **ML18H01**.

Maximum tolerated dose (MTD)

Compound **2** was chosen for additional longer-term studies. In preparation, its safety profile in mice was determined according to the metric of maximum tolerated dose (MTD) in a dose-escalation study using intraperitoneal injection (IP). Observable toxicity was only apparent at the higher doses 75–100 mg $kg^{-1}$. The MTD was determined to be 50 mg $kg^{-1}$ and acceptable for *in vivo* immunological experiments. Moving forward, compound **2** will be referred to as **ML18H01**.

### *4.3.2. ML18H01-PDT leads to cytotoxicity of B16F10 mouse melanoma cell line in vitro.*

It is becoming more evident in the realm of cancer research that there is an urgent need to develop therapies that do not simply kill cancer cells but also induce an immunological response against the tumor to confer long term protection and prevent relapse. Given the importance of the immunological response in melanoma, **ML18H01** (compound **2)** was selected for further investigation of its immunological potential as a PDT agent. The B16F10 mouse melanoma cell line was used for *in vitro* characterization since this is the cell line that would be used for subsequent *in vivo* immunological studies in a syngeneic mouse model. In this cell line, the $EC_{50}$ and $PI_{630}$ values for **ML18H01** activated by clinically approved 630 nm light were approximately 1.40 μM and 37, respectively, using a fluence of 100 J $cm^{-2}$ and irradiance of 22.8 mW $cm^{-2}$. Cell death analysis (with Annexin-V/7AAD staining by flow cytometry), using this $EC_{50}$ value but with a fluence of 25 or 50 J $cm^{-2}$ (22.8 mW $cm^{-2}$), revealed the existence of pre-apoptotic (Annexin-V +ve/ 7AAD −ve)$^{(675)}$ and post-apoptotic (Annexin-V +ve/ 7AAD +ve)$^{(675)}$ populations alongside some smaller fraction of live B16F10 cells [**Figure 4.10 A-B**] where **ML18H01** in the absence of light treatment showed no dark cytotoxicity. Therefore, 1.40 μM was

determined to be a suitable concentration to use for the subsequent immunological experiments, which require some fraction of live and pre-apoptotic cells for analysis.

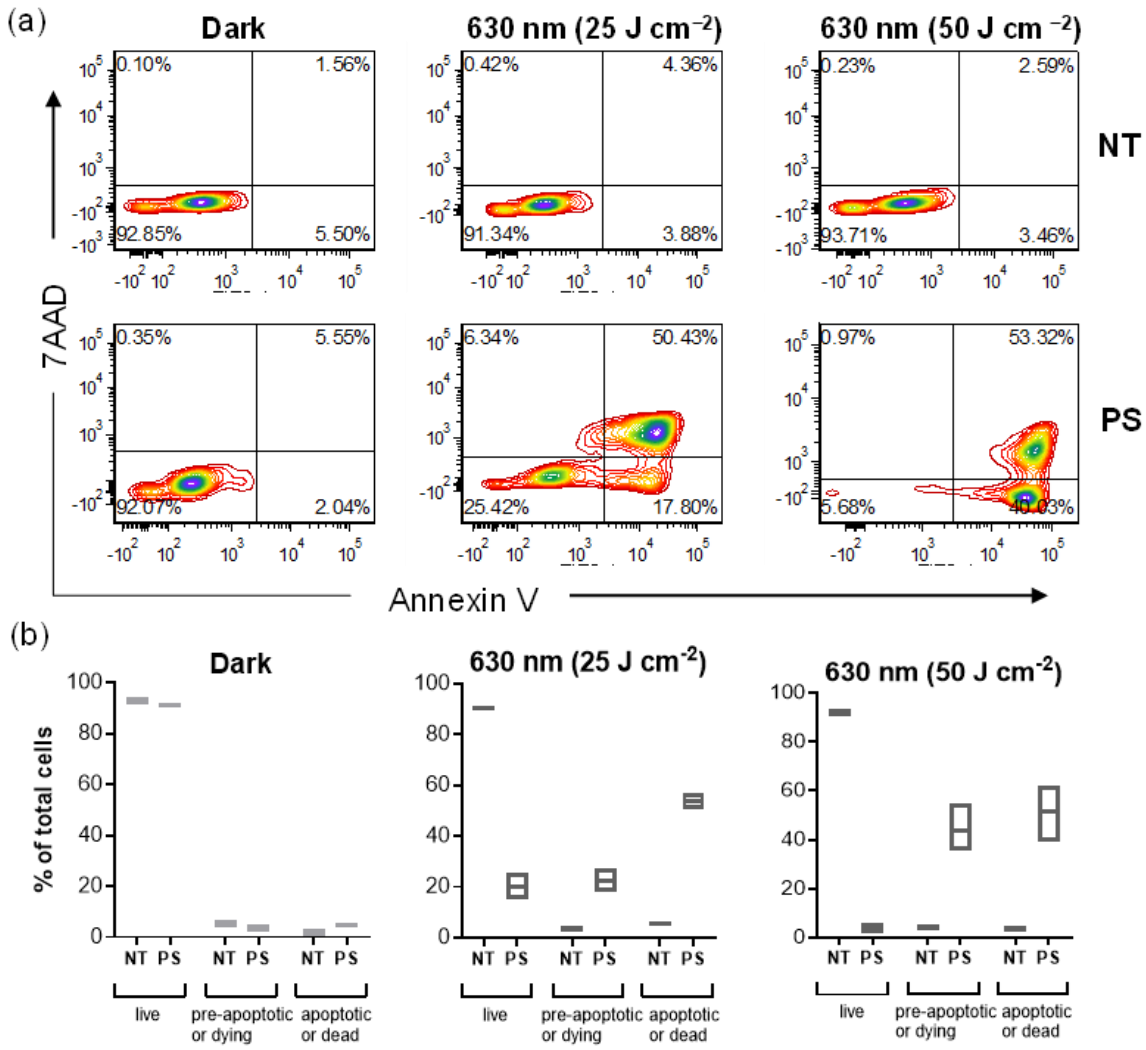


**Figure 4.10. ML18H01**-PDT induces cell death in B16F10 melanoma cell line.

(a–b) *In vitro* cell death analysis using Annexin V – 7AAD flow cytometry assay. Contour plots are depicted in (a) where the lower left quadrant represents live cells, lower right represents pre-apoptotic cells, upper left represents necrotic cells, and upper right represents apoptotic or dead cells. Top panel of c is non-treated (NT) and bottom panel

is PS-treated (PS). Corresponding data to (a) is represented as box plots in (b). Compound **2** is **ML18H01**. Experiment n=3.

### *4.3.3. ML18H01-PDT initiates pro-inflammatory immune response.*

Cancers harbor a suppressive milieu in which the antitumor actions of the immune response are dampened via various immune evasion strategies. Thus, therapies which overturn such cancer-associated immunosuppression can induce clinically desired antitumor immunity. In this context, the effect of **ML18H01**-PDT on the expression of various immunological markers known to be involved in inflammatory processes in B16F10 melanoma cells was examined. As revealed by quantitative real-time polymerase chain reaction (qRT-PCR) analysis, **ML18H01**-PDT upregulated the gene expression of several type I interferon pathway molecules IFNβ, IFIT1, and TLR3; [**Figure 4.11.A**],[303,676,677] proinflammatory cytokines [IL6, TNFα, and CXCL10; **Figure 4.11.B**],[303,676,677] and molecules involved in antigen presentation [TAP1, β2M, and H2D; **Figure 4.11.C**][677,678] in the B16F10 melanoma cell line. While some of these markers were also upregulated with only light treatment in the absence of the compound, the level was significantly lower compared to treatment with compound **ML18H01**-PDT. These results indicate that **ML18H01**-PDT promotes a strong pro-inflammatory immune response in the B16F10 melanoma cell line, which is a prerequisite to the initiation of innate and adaptive antitumor immunity.

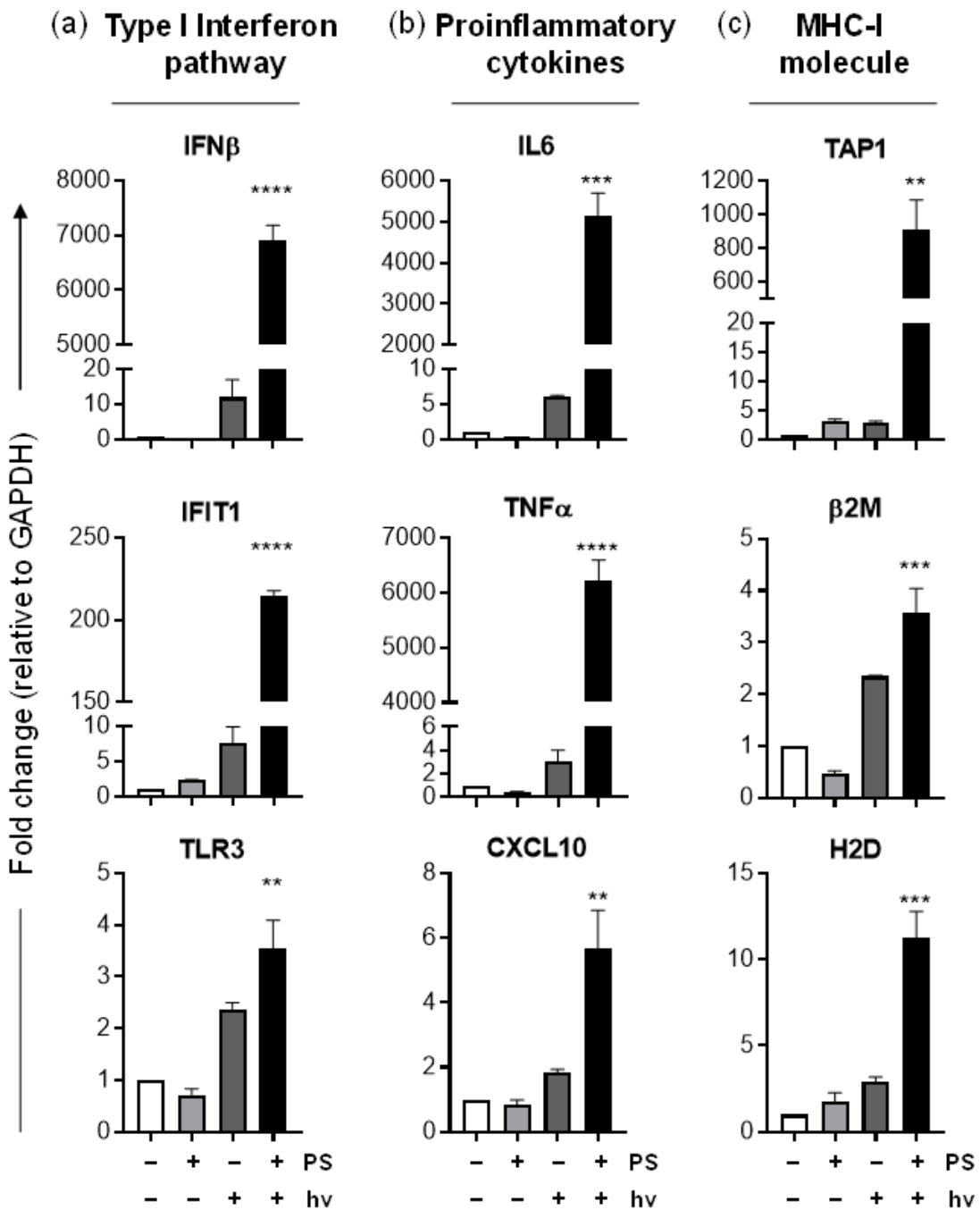


**Figure 4.11. ML18H01**-PDT stimulates multiple immunological pathways *in vitro*.

qRT-PCR analysis of B16F10 cells untreated, treated only with **ML18H01**, only light or treated with both ML18H01 and light (2-PDT), for genes associated with (a) type 1 interferon pathway (IFNβ, IFIT1, TLR3); (b) proinflammatory cytokines (IL6, TNFα,

CXCL10); (c) antigen presentation – MHC-I molecule (TAP1, β2M, H2D). Fold changes represented relative to untreated samples and normalized to control gene, GAPDH. Compound 2 is **ML18H01**. Anova statistical test was performed. Experiment n=3.

### *4.3.4. ML18H01-PDT induces immunogenic cell death in B16F10 melanoma cells in vitro.*

The process of therapy-driven generation of antitumor immunity is often preceded by 'immunogenic' death of cancer cells. Considering the pro-inflammatory effects of **ML18H01**-PDT, we then explored whether the photocytotoxicity by **ML18H01**-PDT involved any immunological mechanisms with a focus on the process of immunogenic cell death (ICD) through a multifaceted analysis of diverse immunological parameters. First, ROS induction as well as endoplasmic reticulum (ER) stress-induced ER chaperone expression[679–684] was examined following **ML18H01**-PDT. Flow cytometry analysis captured the induction of ROS molecules at both the cellular and mitochondrial level [**Figure 4.12.A**], and qRT-PCR analysis revealed an increase in the gene expression of ER chaperones HSP90 and HSPA1B [**Figure 4.12.B**]. As such, inhibiting ROS during **ML18H01**-PDT using ROS inhibitor, N-acetyl-L-cysteine (NAC), reduced cell death in B16F10 cells [**Supp Figure 4.1.A**], indicating the role of ROS in PDT mediated cell death. Together, these data showed that **ML18H01**-PDT induced ROS and cell stress, key hallmarks of ICD in cancer cells.

Other important ICD hallmarks were also assessed, including damage-associated molecular patterns (DAMPs) such as the translocation of ER chaperone calreticulin (CALR) to the plasma membrane, secretion of adenosine triphosphate (ATP), and release of high mobility group box 1 protein (HMGB1) extracellularly.[677] The effect

of **ML18H01**-PDT on CALR, HMGB1 and ATP$^{(677)}$ in B16F10 cells was tested at various time points, with those time points producing optimal expression of ICD marker highlighted in **Figure 4.12**. Flow cytometry analysis of B16F10 cells 4 h post- **ML18H01**-PDT showed a significant increase in surface calreticulin expression compared to nontreated (NT) cells or cells treated with PS or light only [**Figure 4.12.C**] alongside extracellular release of ATP 12 h post-treatment [**Figure 4.12.D**]. A significant increase in extracellular HMGB1 was also detected in the supernatant collected from the cells 24 h post **ML18H01**-PDT [**Figure 4.12.E**]. These results suggest that **ML18H01**-PDT-treated B16F10 cells trigger DAMPs associated with ICD. Furthermore, addition of ROS inhibitor, NAC, inhibits the upregulation of CALR by **ML18H01**-PDT, confirming the role of ROS in **ML18H01**-PDT mediated CALR induction [**Supp Figure 4.1.B**]. Together, these analyses demonstrate that compound **ML18H01**-PDT-induced photocytotoxicity in B16F10 melanoma cells is accompanied by ICD.

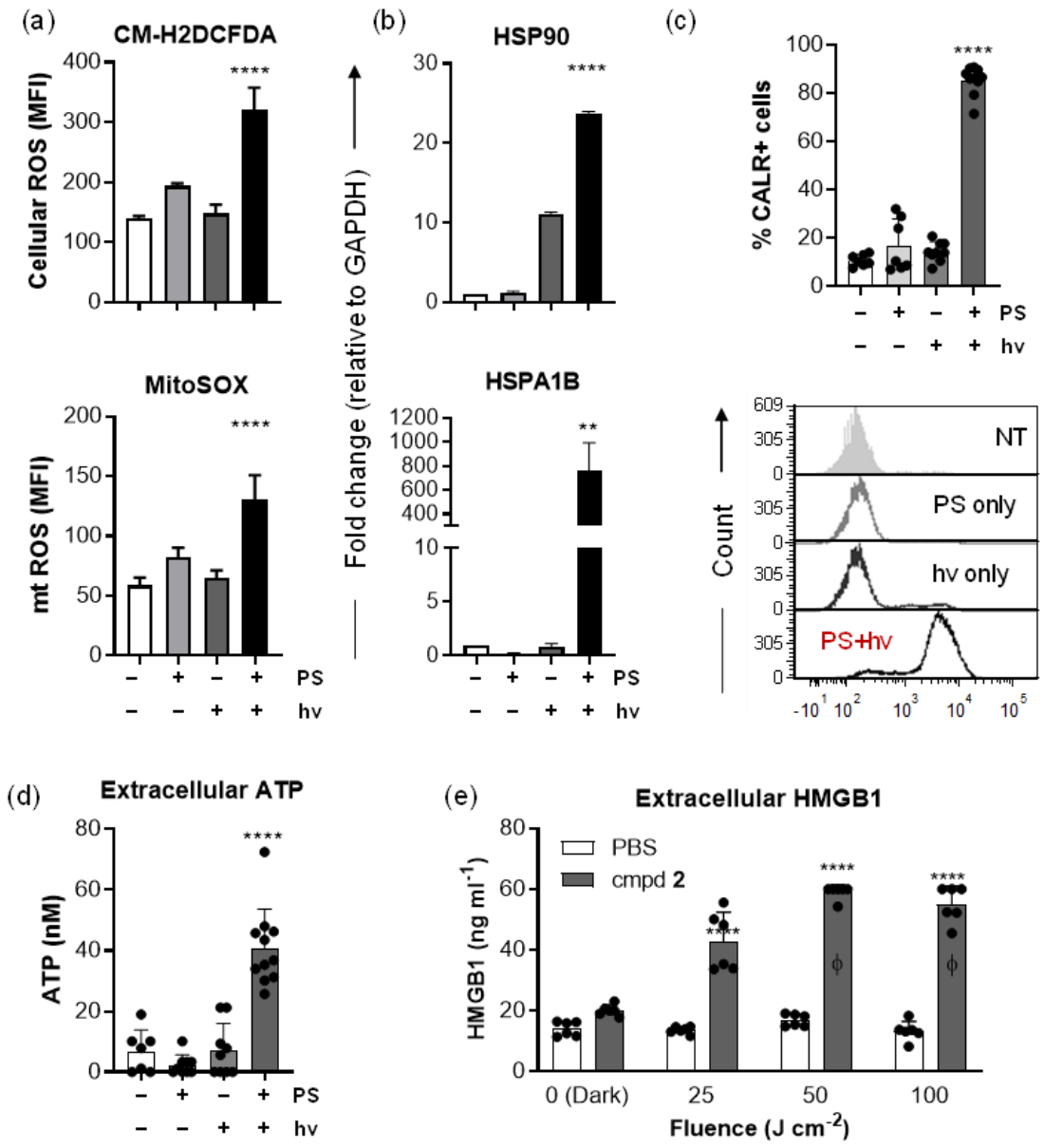


**Figure 4.12. ML18H01**-PDT induces immunogenic cell death in B16F10 melanoma model *in vitro*.

(a) Mean fluorescence intensity of ROS analysis with flow cytometry 4 h post **ML18H01**-PDT for cellular ROS (CM-H2DCFDA) and mitochondrial ROS (MitoSOX). (b) qRT-PCR analysis of ER chaperones HSP90 and HSPA1B 12 h post- **ML18H01**-PDT in B16F10 cells *in vitro*. (c) Analysis of surface expression of ER chaperone Calreticulin using flow

cytometry 4 h post- **ML18H01**-PDT in B16F10 cells *in vitro*. Representative histograms associated with the bar graph (c, bottom). (d) Extracellular ATP analysis 12-h post-**ML18H01**-PDT in B16F10 cells *in vitro*. (e) Analysis of HMGB1 release from B16F10 cells *in vitro* 24 h post- **ML18H01**-PDT. Treatment conditions represent no treatment, PS only, light only, PS and light (**ML18H01**-PDT). Φ=sample beyond upper limit of detection, >60 ng mL−1. Compound **2** is **ML18H01**. Anova statistical test was performed for a-d. Student's t test with respective control was performed for e. Experiment n>=3.

### *4.3.5. ML18H01-PDT treated B16F10 cells activate dendritic cells and lead to DC-mediated phagocytosis of dying cells.*

ICD-mediated anticancer immune responses are initiated by the recognition and phagocytosis of dying cancer cells by antigen-presenting cells such as dendritic cells via the interactions with phagocytic CALR signals. Given the induction of CALR upon **ML18H01**-PDT, we investigated the functional consequence of this event and the ability of DCs to phagocytose **ML18H01**-PDT treated cancer cells. Co-culture of GM-CSF differentiated mouse bone marrow-derived dendritic cells (BMDCs) with live versus **ML18H01**-PDT treated B16F10 cells resulted in phagocytosis of exclusively the PDT-treated cells [**Figure 4.13.A**]. Furthermore, the rate of phagocytosis also increased from 40% to 80% by increasing BMDCs: cancer cell ratio from 1:1 to 1:10 [**Figure 4.13.A**]. This data indicates the capacity of PDT-treated dying cancer cells to induce phagocytosis by BMDCs.

Immunogenic cell death, in addition to phagocytosis, stimulates functional activation of DCs *in vivo*. To investigate this and the effect of ICD-mediated secreted DAMPs *ex vivo*, we cultured BMDCs in **ML18H01**-PDT treated B16F10 culture supernatant and assessed them for immunogenic and tolerogenic markers using qRT-

PCR. We noticed an increase in mRNA expression levels of immunogenic or activation markers CD80,[685,686] CD83,[687] and CD40,[688] with no change in CD86,[685] IL12β,[689,690] or IcosL[691] [**Figure 4.13.B**]. Furthermore, analysis of tolerogenic markers revealed no significant induction of any of the investigated markers - PDL1,[692,693] TIM3,[694] CTLA4,[695,696] and Arg[697] [**Figure 4.13.B**]. This data suggests that conditioned media from **ML18H01**-PDT treated ICD undergoing B16F10 cells can specifically induce DC functional markers. Overall, these findings reveal the potential of **ML18H01**-PDT treated dying cancer cells to trigger DC phagocytosis and activation.

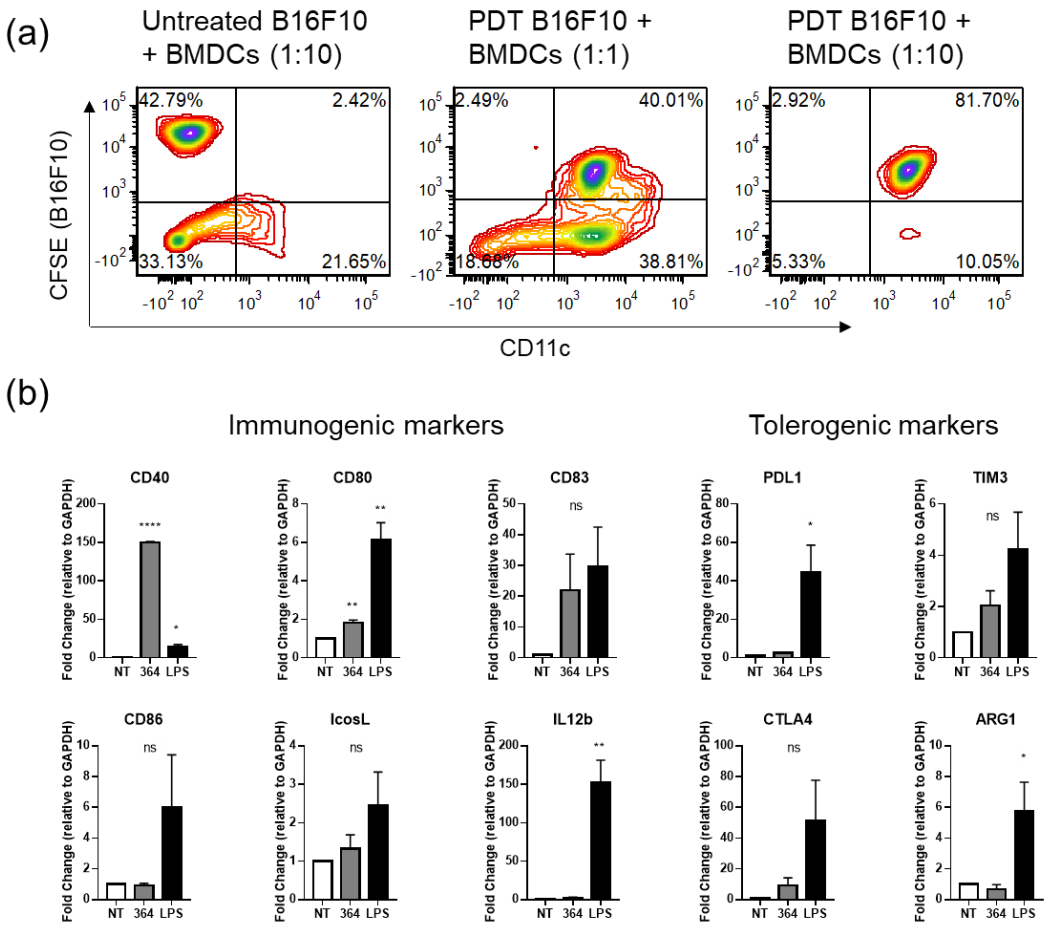

**Figure 4.13.** Phagocytosis and functional state of BMDCs co-cultured with **ML18H01**-PDT treated B16F10 cells.

(a) *Ex vivo* DC phagocytosis assay. Contour plots depicting uptake of CFSE labelled untreated (left) or treated (middle, right) B16F10 cells by CD11c+ DCs. CD11c+ CFSE+ population in the upper right quadrant indicates the percentage of phagocytosed cells. A co-culture ratio of 1:1 (middle) and 1:10 (right) of BMDC: cancer cells are represented. (b) Expression analysis of genes associated with immunogenic (CD40, CD80, CD83, CD86, IcosL, IL12b) and regulatory (PDL1, TIM3, CTLA4, ARG1) markers in DCs. Bar graphs represent fold changes relative to untreated samples and normalized to the control gene, GAPDH. LPS (40ng/ml, 24hrs) treated sample was used as a positive control. Student's t test was performed for statistical analysis. Experiment n=3.

### *4.3.6. Effects of vaccination with ML18H01-PDT treated B16F10 cells on melanoma progression in vivo.*

The therapeutic relevance of **ML18H01**-PDT induced ICD *in vitro* was examined *in vivo* with an immuno-competent, syngeneic B16F10 tumor model. The gold standard approach to evaluate the therapeutic and anticancer potential ICD consists of vaccination with the *in vitro*-treated, ICD-undergoing, cancer cells that is followed by a challenge with the live cancer cells of the same antigenic origin.[677] B16F10 cells were treated with **ML18H01**-PDT and ICD-undergoing cells collected at 4 h and 16 h post-**ML18H01**-PDT were combined for the vaccination. Either PBS- or **ML18H01**-PDT-treated B16F10 cells were injected subcutaneously (SC) into the left flank of C57BL/6 female and male mice. The mice were then challenged 7 days later with untreated B16F10 cells by injection into the right flank. These mice were assessed for tumor growth and survival [**Figure 4.14.A**].

Female and male C57BL/6 mice that received the vaccination showed either no tumor growth or reduced tumor growth as compared to unvaccinated mice [**Figure 4.14.B–D**]. This analysis showed either delayed or no tumor growth with 80% protection from tumor growth in female mice and 55% protection in male mice. Survival studies revealed a significant improvement of tumor-free survival in vaccinated female and male mice as compared to unvaccinated mice [**Figure 4.14.C-D**]. Hazard ratios, which estimate treatment risk, were strongly favorable with values of 0.1 for females and 0.2 for males, denoting low risk for mice treated with the **ML18H01**-PDT vaccine. Given that the vaccination and challenge injections were done on bilateral flanks, this data indicates an abscopal effect and generation of systemic immunity. Together, these data confirm the induction of ICD with **ML18H01**-PDT in the B16F10 syngeneic mouse melanoma model and also highlight differences in the PDT-induced antitumor response based on the sex of the mice.

It is becoming increasingly apparent that biological sex determines the progression and therapeutic outcomes in several cancers.[698] In the context of melanoma, men have a higher incidence as well as mutation burden compared to women[699,700] It has also been noted that men and women show varied responses and outcomes to cancer therapies like checkpoint blockade therapy.[701–708] In congruence, we observed that the percentage of melanoma tumor-free mice following vaccination was greater in female mice and that tumor survival rates were also higher for this cohort.

While tumor growth itself was comparable in unvaccinated female and male mice, differences in tumor development and survival in the vaccinated groups suggest that there may be variations in immune responses elicited by female and male mice toward B16F10 melanoma. Sex-dependent biases in immune responses to both self-

antigens and foreign antigens have previously been documented in both animal models as well as in humans, with an overall higher innate and adaptive immune responses in women as compared to men.[698,709,710] In the context of C57BL/6 mice, female mice display superior tumor- specific $CD8^+$ T cell responses against B16F10 melanoma in response to checkpoint inhibitor therapy compared to male mice.[702] Similar sex-biased differences have also been reported in pro-inflammatory and anti-inflammatory cytokines associated with various stages of B16F10 melanoma development in female and male C57BL/6 mice.[711] We believe that similar variations in tumor-specific immune responses are responsible for the sex-based differences observed in our study, but further characterization is required to outline the underlying differences in sex-biased immune parameters for **ML18H01**-PDT.

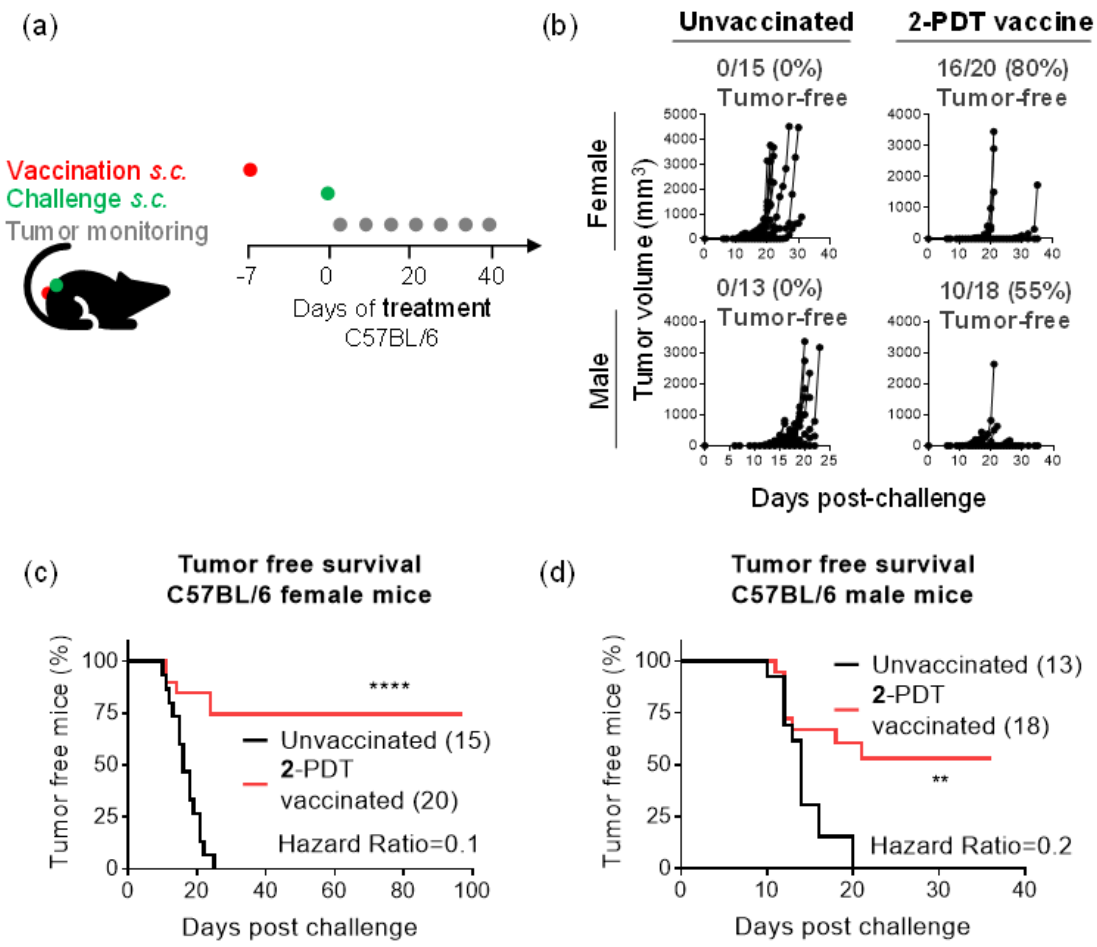


**Figure 4.14. ML18H01**-PDT induced immunogenic cell death confers protection against rechallenge *in vivo* in B16F10 mouse melanoma model.

(a) Schematic representation of the *in vivo* mouse experiment. C57BL/6NCrl mice were injected with PBS or compound **ML18H01**-PDT treated B16F10 cells (vaccination) and challenged with untreated B16F10 cells 7 days post-vaccination on the opposite flank and monitored for tumor growth and survival. (b) Tumor growth curves for unvaccinated and vaccinated female and male mice. Each line represents one mouse. (c–d) Tumor free survival curves of unvaccinated and vaccinated C57BL/6NCrl female (c) and male mice (d). Mantel cox statistical analysis was performed on survival curves.

### *4.3.7. Assessment of the therapeutic effect of ML18H01-PDT on tumor growth in melanoma models.*

Given the superior ICD-inducing and immunomodulating properties of **ML18H01**-PDT on B16F10 melanoma cells, we investigated its therapeutic efficacy in mouse melanoma models. Female C57BL/6 mice were inoculated with B16F10 melanoma cells and divided into control (PBS only) or PDT-treatment groups. Animals in the PDT-treatment group received a single dose PDT with **ML18H01** PS (20 mg/kg per mouse, MTD=50 mg/kg) with a 4 hr drug-light interval (DLI) between PS injection and light administration [**Figure 4.15.A**]. In contrast, animals in the control group received PBS injections and no light. A total of 150 J/cm$^2$ of light fluence from a NIR 733nm laser was administered at an irradiance of 172.4 mW/cm$^2$, for a total time of 15 min per mouse. Animals were monitored for tumor growth, signs of inflammation, and necrosis at the site of treatment. Treatment of B16F10 tumor-bearing C57BL/6 mice with NIR activated **ML18H01**-PDT resulted in a significant reduction in tumor growth in treated mice compared to the untreated group [**Figure 4.15.B**]. In addition, tumor volume analyses on ten days post-**ML18H01**-PDT revealed substantial differences between treated and untreated mice, with extremely low or no tumor volumes recorded in the treated group [**Figure 4.15.C**]. We confirmed the therapeutic efficacy of **ML18H01**-PDT in another mouse model-transgenic BRaf$^{CA}$, Pten$^{loxP}$, Tyr::CreER$^{T2}$ melanoma model. For this, we used mice bearing two spontaneous tumors, one of which was treated with PDT as described above, and the other tumor was left untreated. Similar to the syngeneic model, **ML18H01**-PDT resulted in the reduction of tumor volumes in the transgenic model [**Supp figure 4.2**]. Furthermore, necrotic damage at the tumor site, commonly noticed in human melanomas as well as upon PDT treatments, was cured in some **ML18H01**-PDT treated mice, as demonstrated in **Figure 4.15.D**. Together, these findings suggest that,

in addition to the superior ICD inducing properties, **ML18H01**-PDT has therapeutic efficacy against melanoma.

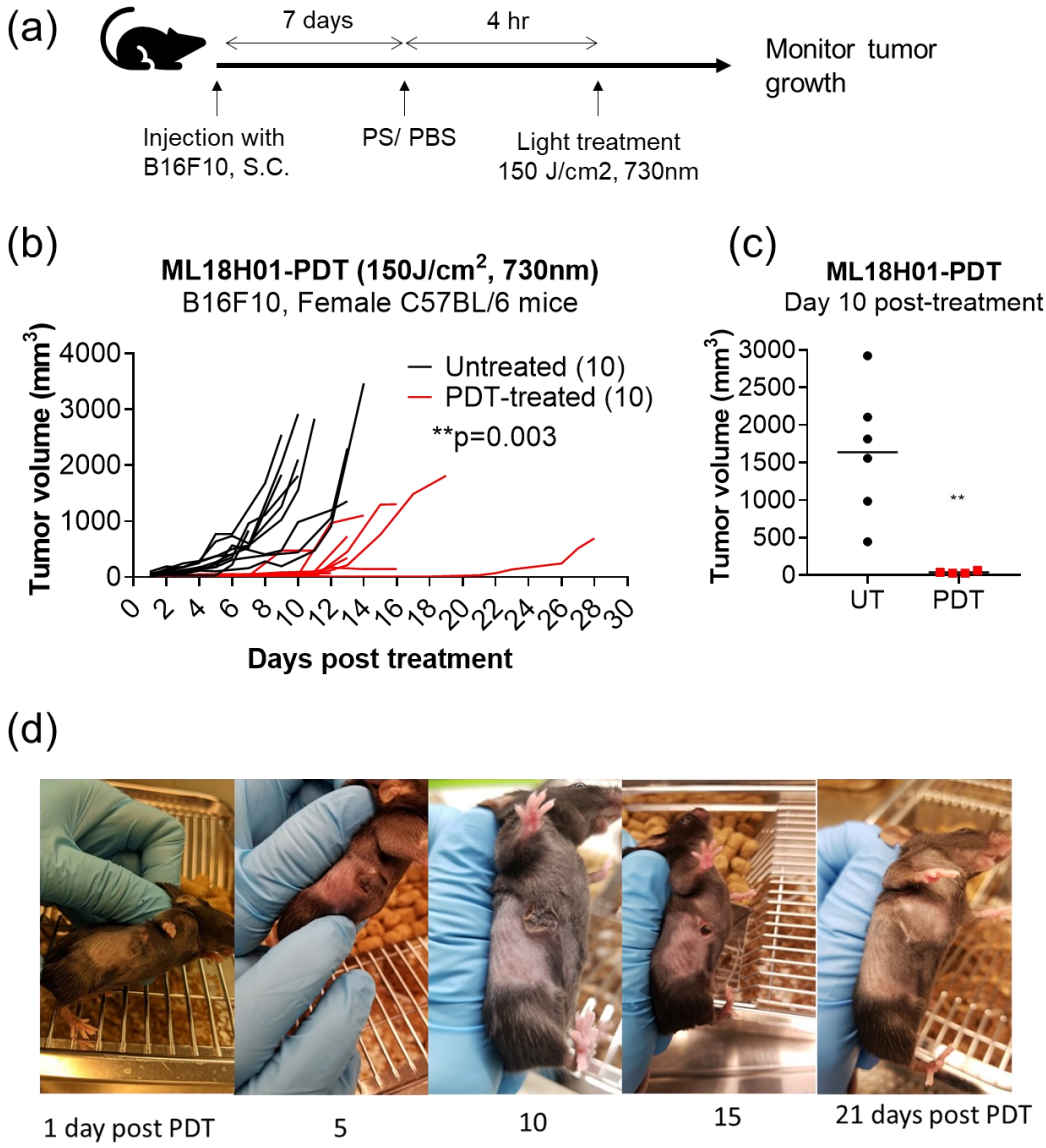


**Figure 4.15. ML18H01**-PDT reduced tumor growth and tumor volumes in the B16F10 tumor model.

(a) Schematic representation of evaluation of PDT therapeutic efficacy in B16F10 tumor-bearing mice. (b) Tumor growth curves for ML18H01-PDT treated and untreated tumor-

bearing mice. (c) Comparison of tumor volumes 10 days post-PDT. (d) Depiction of clearance of necrotic damage and cured tumor in a representative mouse.

## 4.4. DISCUSSION

This multi-dimensional study defines the SARs for achieving the requisite photophysical properties to elicit PDT effects with NIR-absorbing Ru(II)-based PSs. All of the investigated compounds exhibited NIR absorption beyond 700 nm, which was tunable over 200 nm. Combining the tpbbn chromophoric ligand with the chloro axial ligand (**3**) led to the longest NIR absorption ($\lambda_{max}$=900 nm) that extended past 1000 nm. The smaller chromophoric tpbn ligand combined with the axial chloro ligand (**1**, **5**, **7**) or the combination of the larger tpbbn ligand and the pyridyl monodentate ligand (**4**) blue-shifted the NIR maximum to 790–800 nm, and the smaller tpbn ligand combined with the pyridyl axial ligand (**2**, **6**, **9**) resulted in $\lambda_{max}$ near 720 nm. The identity of the bidentate ligand (phen versus dppn) had little impact on the NIR absorption profiles of otherwise identical complexes.

The absorption studies underscored that the pyridyl complexes combined with the smaller chromophoric tpbn ligand (**2**, **6**, **9**) had higher stabilities and better aqueous solubilities. Structural modifications to the axial monodentate pyridyl ligand or the central pyridyl group of the tpbn chromophoric ligand were well tolerated and did not substantially impact the energies or relative molar extinction coefficients of the major electronic transitions observed for this sub-family. Therefore, $R_1$ and $R_2$ represent convenient handles for fine-tuning the chemical, biological, and photophysical properties of this new structure class while maintaining NIR absorption.

Compared to the rest of the compounds, **2**, **6**, and **9** had the largest $^1O_2$ quantum yields by a wide margin. A detailed photophysical investigation revealed that these were

the only compounds with accessible $^3$IL states. Given that the NIR absorption is set by the energies of the MLCT states and that $^1O_2$ is generated most effectively from $^3$IL states, there exists a fundamental limit with regard to how much the MLCT state energies can be lowered without compromising the PDT effect. In other words, the $^3$MLCT state cannot be lower in energy than the $^3$IL state, which explains why the $^1O_2$ quantum yields for **2**, **6**, and **9** were largest and also suggests that in the present system, the $^3$MLCT-$^3$IL energy gap, estimated at 0.22 eV, is sufficient for $^3$IL population. This assertion was also corroborated in the *in vitro* cellular studies where **2**, **6**, and **9** gave the largest PI values, regardless of the wavelengths of light used in the investigated melanoma cell lines. Importantly, wavelengths longer than 700 nm yielded photocytotoxic effects with single-digit micromolar $EC_{50}$ values.

These compounds lost activity in hypoxia, pointing toward PDT (e.g., ROS) as the source of photocytotoxicity. Given the immunostimulatory potential of PDT and the importance of the immune response for melanoma outcomes, compound **2** (**ML18H01**) was selected for further investigation in this context. Treatment of B16F10 melanoma cells with **ML18H01**-PDT stimulated immunological responses and resulted in a significant upregulation of several immune-associated genes from the type 1 interferon pathway, proinflammatory cytokines, and the antigen-presentation pathway. **ML18H01**-PDT also induced both mitochondrial and cellular ROS alongside a significant upregulation of ER chaperones HSP90 and HSPA1B gene expression, translocation of calreticulin to the plasma membrane, and secretion of ATP and HMGB1 into the extracellular media. **ML18H01**-PDT induced cell death and CALR exposure are in part regulated by ROS induction. Moreover, co-culture of dendritic cells with **ML18H01**-PDT treated dying cancer cells enhanced DC phagocytosis and promoted DC activation

markers. These results confirmed that compound **ML18H01**-PDT induces bonafide ICD markers in B16F10 cells, facilitates their uptake and activation of DCs.

The immunogenicity of **ML18H01**-PDT was also confirmed in a syngeneic mouse model *in vivo*. Vaccination with **ML18H01**-PDT treated B16F10 cells conferred protection against tumor growth upon challenge with live B16F10 cells, statistically improving tumor-free survival in female and male vaccinated mice as compared to the unvaccinated group. These results also indicate the generation of systemic immunity as revealed from the abscopal effect. The percentage of melanoma tumor-free mice following vaccination as well as overall survival rates were greater for females, underscoring that tumor-specific immune responses may be responsible for the sex-based differences that have been observed clinically with regard to melanoma incidence, mutation burden, and response to therapy. Additional studies to delineate the therapeutic potential of NIR activated **ML18H01**-PDT demonstrated significantly reduced tumor volumes and tumor growth upon PDT in syngeneic and transgenic mouse melanoma models.

Overall, this study shows that **ML18H01**-PDT (with clinically approved red light and NIR light) destroys melanoma cells directly as well as indirectly by ICD-mediated generation of anti-tumor immune responses, resulting in clinically desired outcomes against aggressive mouse melanomas.

## 4.5. CONFLICT OF INTEREST

S. A. M. has a potential research conflict of interest due to a financial interest with Theralase Technologies, Inc. and PhotoDynamic, Inc. A management plan has been created to preserve objectivity in research in accordance with UTA policy.

## 4.6. ACKNOWLEDGEMENTS

S. A. M., C. G. C., S. G., R. P. T., and G. D. thank the National Cancer Institute (NCI) of the National Institutes of Health (NIH) (Award R01CA222227) for support. The content in this article is solely the responsibility of the authors and does not necessarily represent the official views of the National Institutes of Health. S. A. M. also thanks Dr Daniel Todd as UNCG's Triad Mass Spectrometry Facility manager and his assistants Jennifer Simpson and Diane Wallace. S. A. M. likewise thanks Dr Franklin Moy for his experimental support and instrument maintenance as UNCG's NMR facility manager. P. K. thanks Angelita Alcos and Nadia Farbstein for providing experimental support with animal handling. P. K. was supported by Killam Doctoral Fellowship, Research Nova Scotia – Scotia Scholar Award, and Nova Scotia Graduate Student Fellowship.

## 4.7. SUPPLEMENTARY FIGURES

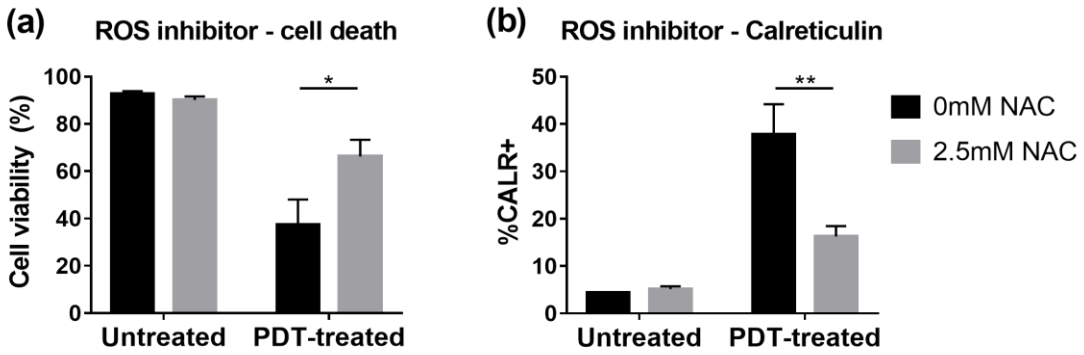


**Supplementary Figure 4.1.** Effect of ROS inhibition on **ML18H01**-PDT induced cell death and calreticulin.

Culture of **ML18H01**-PDT treated B16F10 cells with and without ROS inhibitor N-acetyl-l-cysteine (NAC). (a) Alamar blue cell viability analysis of untreated or **ML18H01**-PDT treated B16F10 cells with and without ROS inhibition. (b) Flow cytometry-based analysis of surface calreticulin expression in untreated or **ML18H01**-PDT treated B16F10 cells with and without ROS inhibition.

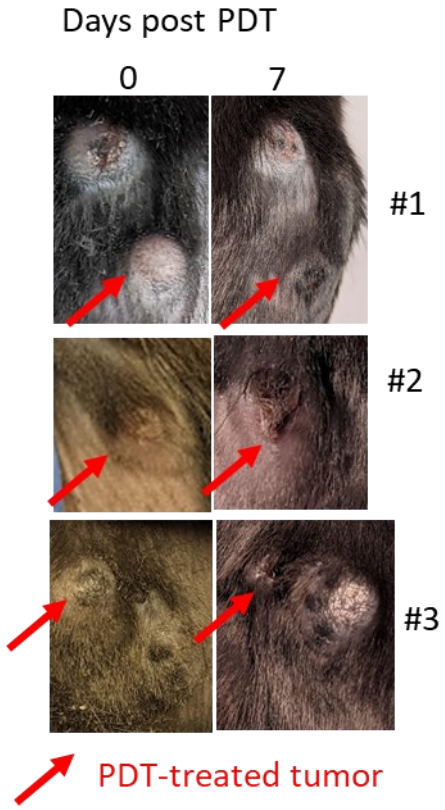


**Supplementary Figure 4.2. ML18H01**-PDT on transgenic $Braf^{CA}Pten^{loxP}Tyr::CreER^{T2}$ mouse model.

PDT-treated tumors are highlighted with red arrows.

## 4.8. SUMMARY OF CHAPTER 4

This chapter reported the development of nine ruthenium coordination complexes with different ligand combinations to identify an optimal to achieve desired photophysical and PDT efficacies. The compounds produced varying energetics and absorption kinetics. **ML18H01** (also referred to as compound **2**) was selected for *in vitro* and *in vivo* studies based on its high quantum yield, efficient near-infrared wavelength absorption, and photocytotoxic effects. *In vitro* studies revealed the potent cytotoxic effects of **ML18H01**-PDT on B16F10 mouse melanoma cells, mediated by the generation of reactive oxygen species, implicated in both cytotoxicity and immunogenic cell death. Additionally, we observed significantly upregulated expression of genes encoding components of type 1 interferon pathway, proinflammatory cytokines, and antigen-presentation machinery upon **ML18H01**-PDT. Moreover, **ML18H01**-PDT promoted immunogenic cell death in B16F10 cells, as evidenced by the upregulation of HSP90, HSPA1B, surface translocation of CALR, ATP secretion, and HMGB1 release. Furthermore, **ML18H01**-PDT enabled DCs to phagocytose dying B16F10 cells and induced functional markers in DCs, indicating activation. Vaccination with **ML18H01**-PDT induced dying cancer cells resulted in protection against tumor challenge with live B16F10 cells in a sex-biased manner, confirming ICD and demonstrating efficient cancer immunity development. Finally, the therapeutic potential of ML18H01-PDT was evaluated in two mouse melanoma models: a syngeneic B16F10 model and a transgenic model, both of which demonstrated reduced tumor growth upon treatment. Overall, we demonstrate the clinical utility of our lead compound for the treatment of melanoma. The following chapter investigates two additional Ru-PDTs with similar chemical structures and cytotoxic potential but different immunostimulatory mechanisms.

# CHAPTER 5: PHOTODYNAMIC THERAPY OF MELANOMA WITH NEW, STRUCTURALLY SIMILAR, NIR-ABSORBING RUTHENIUM (II) COMPLEXES PROMOTES TUMOR GROWTH CONTROL VIA DISTINCT HALLMARKS OF IMMUNOGENIC CELL DEATH

This work is published in:

**Konda P***, Roque III JA*, Lifshits LM*, Alcos A, Azzam E, Shi G, Cameron CG, McFarland SA, Gujar S. Photodynamic therapy of melanoma with new, structurally similar, NIR-absorbing ruthenium (II) complexes promotes tumor growth control via distinct hallmarks of immunogenic cell death. ***American Journal of Cancer Research***. 2022;12(1):210.

* contributed equally

## CONTRIBUTIONS:

**P.K.** designed the immunology study (along with S.G.), carried out the experimentation, collected and analyzed data, and prepared the immunology section of the manuscript (All sections excluding 5.3.1 and Figure 5.1.). A.A. assisted with animal experiments. E.A. and G.S. helped with the qRT-PCR experiment (Figure 5.3.B-C, n=1). L.M.L., J.A.R., C.G.C., and S.A.M. designed and performed experiments for the chemistry part of the study (5.3.1 and Figure 5.1). S.G., and S.A.M., assisted with writing and critical review of the manuscript.

**Details of PK's contributions:**

- All sections excluding 5.3.1.were written by **P.K**.
- Experimental work, data analysis, and generation of graphs related to Figures 5.2., 5.3., 5.4., 5.5., and 5.6. were performed by **P.K.**

## 5.1. ABSTRACT

Cancer therapies that generate T cell-based anti-cancer immune responses are critical for clinical success and are favored over traditional therapies. One way to elicit T cell immune responses and generate long-lasting anti-cancer immunity is through induction of immunogenic cell death (ICD), a form of regulated cell death that promotes antigenicity and adjuvanticity within dying cells. Therefore, research in the last decade has focused on developing cancer therapies which stimulate ICD. Herein, we report novel photodynamic therapy (PDT) compounds with immunomodulatory and ICD inducing properties. PDT is a clinically approved, minimally invasive anti-cancer treatment option and has been extensively investigated for its tumor-destroying properties, lower side effects, and immune activation capabilities. In this study, we explore two structurally related ruthenium compounds, ML19B01 and ML19B02, that can be activated with near infrared light to elicit superior cytotoxic properties. In addition to their direct cell killing abilities, we investigated the effect of our PSs on immunological pathways upon activation. PDT treatment with ML19B01 and ML19B02 induced differential expression of reactive oxygen species, proinflammatory response-mediating genes, and heat shock proteins. Dying melanoma cells induced by ML19B01-PDT and ML19B02-PDT contained ICD hallmarks such as calreticulin, ATP, and HMGB1, initiated activation of antigen presenting cells, and were efficiently phagocytosed by bone marrow-derived dendritic cells. Most importantly, despite the distinct profiles of ICD hallmark inducing capacities, vaccination with both PDT-induced dying cancer cells established anti-tumor immunity that protected mice against subsequent challenge with melanoma cells.

## 5.2. INTRODUCTION

Cancer immunotherapies hold tremendous promise in clinics due to their ability to harness the patient's own immune system to attack tumor cells.[712] Several immunotherapies have been developed by targeting different phases of the cancer-immunity cycle, such as immune checkpoint inhibitors, adoptive T cell transfer therapies, and cancer vaccines.[14,21,713,714] T cell-based immunotherapies have become a central focus for generating durable anti-cancer immune responses, due to their capacity for recognizing and eradicating malignant cells through cancer-specific antigen-directed cytotoxicity.[21] Furthermore, T cell infiltration in the tumor microenvironment (TME) has been correlated with control of tumor progression and is deemed a critical factor in the efficacy of immunotherapies.[21,715–717] Professional antigen presenting cells (APCs) such as dendritic cells (DCs) play a crucial role in the initiation of these T cell-based immune responses by presenting tumor antigens to T cells thereby activating them.[718] Consequently, therapeutic interventions that promote the DC-T cell-based anti-cancer immunity are highly desired.

In this context, immunogenic cell death (ICD) has garnered attention in recent times, as this form of regulated cell death can activate DCs, induce anti-tumor T cell responses, and generate beneficial long-lasting immunity.[212,241,719] ICD encompasses diverse 'hallmarks' that ultimately involve two major aspects of anti-tumor T cell response: antigenicity and adjuvanticity. Dying cells undergoing ICD provide access to cancer antigens, which contributes to the antigenicity aspect of ICD.[80,272] In addition, danger-associated molecular patterns (DAMPs) are emitted spatiotemporally and function as adjuvants in ICD mediated anti-tumor immunity. These DAMPs promote the recruitment and activation of APCs such as DCs by binding to specific pattern recognition receptors (PRRs) on their surface.[718,720,721] Activated DCs engulf dying

cancer cells, process cancer antigens, and participate in cross-presentation of antigenic peptides to CD8+ T cells, hence activating them and initiating the anti-tumor immune response.[718,722–725] Numerous preclinical and clinical studies suggest the prognostic and predictive value for DAMPs and associated processes in cancer treatment prognosis.[726] Together, ICD facilitates overturning the TME by recruiting immune cells to the tumor site and converting “cold” tumors to “hot”. Therefore, the development of next generation anti-cancer modalities with ICD-inducing properties can improve the clinical outcomes for cancers. Recent efforts have focused on evaluating previously approved chemotherapeutics and developing new agents and therapies with ICD-inducing capabilities.[727]

Photodynamic therapy (PDT) is a clinically approved anti-cancer modality that can be used alone or as an adjuvant delivered alongside surgery or other therapies.[421] PDT employs a light-responsive prodrug, known as a photosensitizer (PS), to sensitize cytotoxic reactive oxygen species (ROS) that directly destroy tumors and tumor vasculature.[412,728–731] The PDT reaction is confined to regions where the PS, light, and oxygen overlap in space and time, thus providing tumor selectivity and fewer side effects compared to conventional therapies. Besides its cytotoxic properties, studies have shown that PDT-induced oxidative stress effectively initiates an inflammatory response and causes the infiltration of immune cells at the treatment site.[385,730,732] The acute inflammatory response from PDT is also implicated in the development of adaptive anti-tumor immune responses.[733–735] Recently, PDT has been investigated for its ability to produce ICD and anti-tumor immune responses,[261,428,736] and approaches to improve ICD-inducing capabilities of PDT are being developed.[246,435] Here, we report the discovery of new ICD-inducing, near infrared (NIR) absorbing ruthenium-based PSs as PDT agents for targeting aggressive melanoma.[737,738]

**ML19B01** and **ML19B02** are tris heteroleptic Ru(II) complexes containing a chromophoric ligand to shift the absorption into the NIR and a PDT ligand for sensitizing singlet oxygen. Activation of the PS in the NIR window is advantageous for deeper tissue penetration and thus treating a wider tumor margin and may be especially important for highly pigmented melanomas where melanin can effectively compete for light absorption of the shorter wavelengths. PDT generally employs red light and designing new PSs that can be activated with longer wavelength NIR light while maintaining potent photocytotoxic effects has been a major challenge to the field of PS design for PDT. Herein, we not only overcome this hurdle but also demonstrate that both PSs have similar cytotoxic potential but differ in their ICD hallmark-promoting capacities. Additionally, both PDT treatments induce the release of DAMPs *in vitro* and treated cells are efficiently phagocytosed by bone marrow-derived dendritic cells (BMDCs). Using dying cancer cells as tumor vaccination modalities, we demonstrate that the PSs delay tumor growth and improve tumor-free survival in the highly aggressive B16F10 mouse melanoma model.

## 5.3. RESULTS

### *5.3.1. Synthesis and characterization of ruthenium compounds.*

Ruthenium compound **ML18H01** was reported previously (chapter 4).[737] Compounds **ML19B01** and **ML19B02** were synthesized in 63% and 47% yields, respectively, following a synthetic protocol that we recently described for the synthesis of analogous Ru(II) complexes.[737] Briefly, intermediate [Ru(tpbn)(dppn)(Cl)]Cl[737] was treated with an excess of monodentate pyridine ligand (4-phenylpyridine or 4-dimethylaminopyridine) and subjected to microwave irradiation while heating at 140–150°C. Compounds **ML19B01** and **ML19B02** were purified using flash column chromatography on alumina

and size-exclusion chromatography on Sephadex® LH-20. After purification, the molecular structures of isolated compounds were confirmed with 1D and 2D $^{1}$H NMR and high-resolution mass spectrometry, and their purities were confirmed by HPLC analysis.

*NMR assignments:* The assignments of the $^{1}$H NMR signals of Ru(II) complexes **ML19B01** and **ML19B02** were made based on correlations observed by $^{1}$H–$^{1}$H COSY NMR, based on the values of observed *J*-values, and based on our previously reported assignments of related complexes. Hydrogens from the **tpbn** ligand (**3**, **3′**, **4′**, **5′**, **6′**, **7′**, and **4-tBu**) and hydrogens from the dppn ligand (**a**, **b**, **c**, **d**, **e**, **f**, **g**, **h**, **i**, **j**, **k**, **l**) were assigned as we previously described for analogous Ru(II) complexes [737]. Hydrogens from the monodentate pyridine ligands (4-phenylpyridine and 4-dimethylaminopyridine) were assigned similarly as we previously described for the hydrogens of 4-picoline ligand.[737] In the monodentate pyridine ligands, the signal for hydrogen **2″** was the most downfield shifted due to its *ortho*-position relative to the nitrogen. In **ML19B01**, the next most downfield signal appeared as a doublet of doublets and was assigned to hydrogen **6″** due to the best fit for this multiplicity. Hydrogen **3″** is expected to be a clear doublet with a *J*-value matching the *J*-value of a doublet corresponding to **2″**, hydrogen **7″** is expected to be a doublet of doublets with two close *J*-values, and hydrogen **8″** is expected to be a triplet of doublets with a small $J_2$-value, but these three signals (**3″**, **7″**, and **8″**) fully overlapped so fine splitting was obscured. In **ML19B02**, hydrogen **3″** was assigned based on its $^{1}$H–$^{1}$H correlation to **2″**.

The electronic absorption spectra of the compounds are shown in Figure 1, and the local absorption maxima and extinction coefficients at those peak maxima are tabulated in Table 2. The shorter wavelength, sharper peaks (<425 nm) can be ascribed to ππ* $^{1}$IL transitions on the ligands and vary in intensity. The dominant peak at

approximately 318 nm is diagnostic of the tpbn ligand. Weaker absorptions in the longer wavelength region occur near 540, 635, and 720 nm, corresponding to $^1$MLCT transitions. The longest wavelength absorption is assigned as the spin-allowed singlet Ru(dπ)→tpbn(π*) transition, in accordance with our earlier findings,[737] and is unusually long for a Ru(II) polypyridyl-type complex.[739] The three MLCT peaks observed for **ML19B02**, having the dimethylaminopyridine monodentate ligand, are bathochromically shifted by around 0.07, 0.10, and 0.05 eV, respectively, compared to the other two complexes. This is consistent with a higher Ru(dπ) energy due to the increased electron density on the metal by this electron-donating monodentate ligand. The result is a red shift of the longest wavelength $^1$MLCT absorption bands. We have observed this shift in NIR absorption energy previously for analogous chloro complexes. The data indicate that the two new photosensitizers, like **ML18H01**, are panchromatic light absorbers from the ultraviolet to the visible region as well as the NIR [**Figure 5.1**]. The [Ru(tpbn)(dppn)(L)]$Cl_2$ construct is a robust scaffold for generating NIR absorption well past 700 nm and extending all the way out to 800 nm. Further, the scaffold not only tolerates changes to the monodentate ligand L without compromising its NIR absorption but can be fine-tuned by minor substituent changes to this ligand in order to improve its NIR absorption characteristics.

**Table 5.1.** Absorption peak maxima (nm) and corresponding molar extinction coefficients (log ε)

| COMPOUND | $\lambda_{abs}$/nm ($\log_{10}(\varepsilon/M^{-1}\ cm^{-1})$) |
|---|---|
| **ML18H01** | 240 (4.79), 318 (4.95), 371 (4.37), 408 (4.14), 494 (3.89), 540 (3.75), 634 (3.22), 716 (2.99) |
| **ML19B01** | 240 (4.93) 318 (5.08), 371 (4.56), 408 (4.34), 492 (4.01), 542 (3.88), 639 (3.33), 710 (3.07) |
| **ML19B02** | 240 (4.98), 319 (5.19), 408 (4.37), 502 (4.01), 558 (3.93), 671 (3.41), 736 (3.20) |

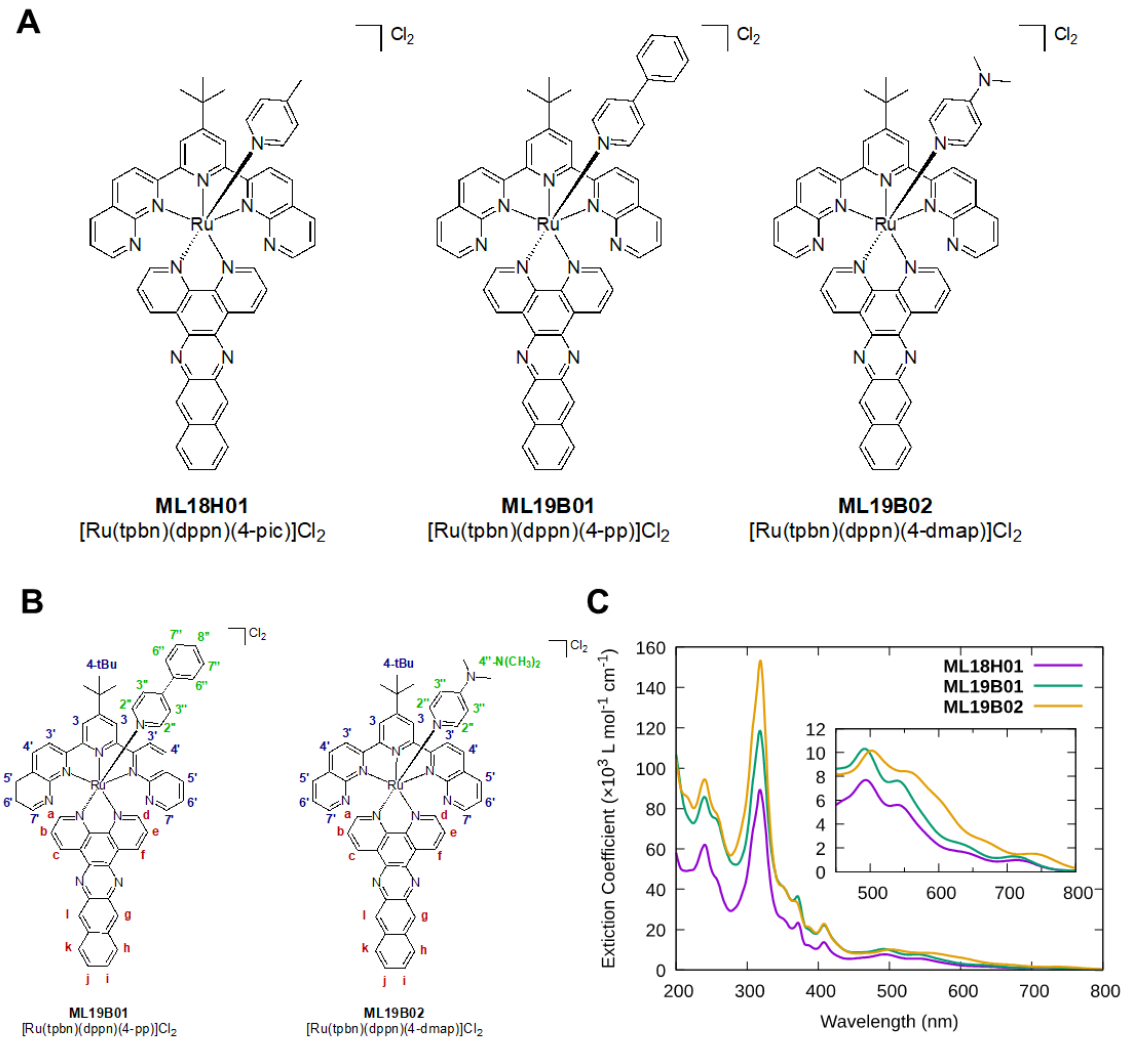


**Figure 5.1.** Structures and spectral profiles of the compounds investigated in this study**.**

**A**. Molecular structures of the two NIR-absorbing and PDT-active ruthenium compounds of this study and the parent complex **ML18H01**. **B**. Hydrogen labeling for the purpose of assigning the one and two-dimensional NMR spectra. **C**. UV-Vis-NIR absorption spectra of the NIR-absorbing and PDT-active ruthenium compounds.

### *5.3.2. ML19B01-PDT and ML19B02-PDT induce cell death in melanoma cells.*

Next, to understand the anti-cancer potential of **ML19B01** and **ML19B02** PSs**,** we first analyzed their capacity to induce cell death in B16F10 mouse melanoma cells upon activation with 630 nm red light or 730 nm NIR light. The shorter wavelength was selected because it is the wavelength used for clinically approved Photofrin-PDT, and 730 nm was used as the NIR wavelength because it is the longest wavelength that produced a PDT effect for our previously reported **ML18H01.**[737] Briefly, B16F10 cells were treated with increasing concentrations of the PS, incubated in the dark for 16 h, and then irradiated for a total fluence of 100 J $cm^{-2}$ at an irradiance of 22.8 mW $cm^{-2}$ [**Figure 5.2.A**]. An analogous set of controls were included that were treated in the same manner; except they did not receive a light treatment but instead were incubated in the dark throughout the experiment. The alamar blue cell viability assay revealed that **ML19B01** and **ML19B02** did not induce cell death in concentrations of up to 50 μM in dark conditions. Irradiation of PS-treated cells with 630 nm red light resulted in cell death [**Figure 5.2.B**] wherein **ML19B01** and **ML19B02**-PDT had $EC_{50}$ values of 1.14 μM and 2.19 μM, respectively. **ML19B01** and **ML19B02** showed a similar $EC_{50}$ profile (1.59 μM and 2.51 μM, respectively) with 730 nm NIR light, confirming activation and cell death at both wavelengths. Further analysis was performed with 630 nm as the clinically approved wavelength for PDT with Photofrin. Cell death analysis with Annexin V/ 7AAD flow cytometry using cells treated with **ML19B01** and **ML19B02** at their respective $EC_{50}$ values and irradiated with a fluence of 25 J $cm^{-2}$ revealed similar cell death characteristics for both the PSs, as represented by percentages of pre-apoptotic and apoptotic cell populations [**Figure 5.2.D**]. The data confirmed that little cell death

occurred in the absence of the light treatment. Therefore, the 630nm $EC_{50}$ values were used for subsequent immunological analysis for both the PSs.

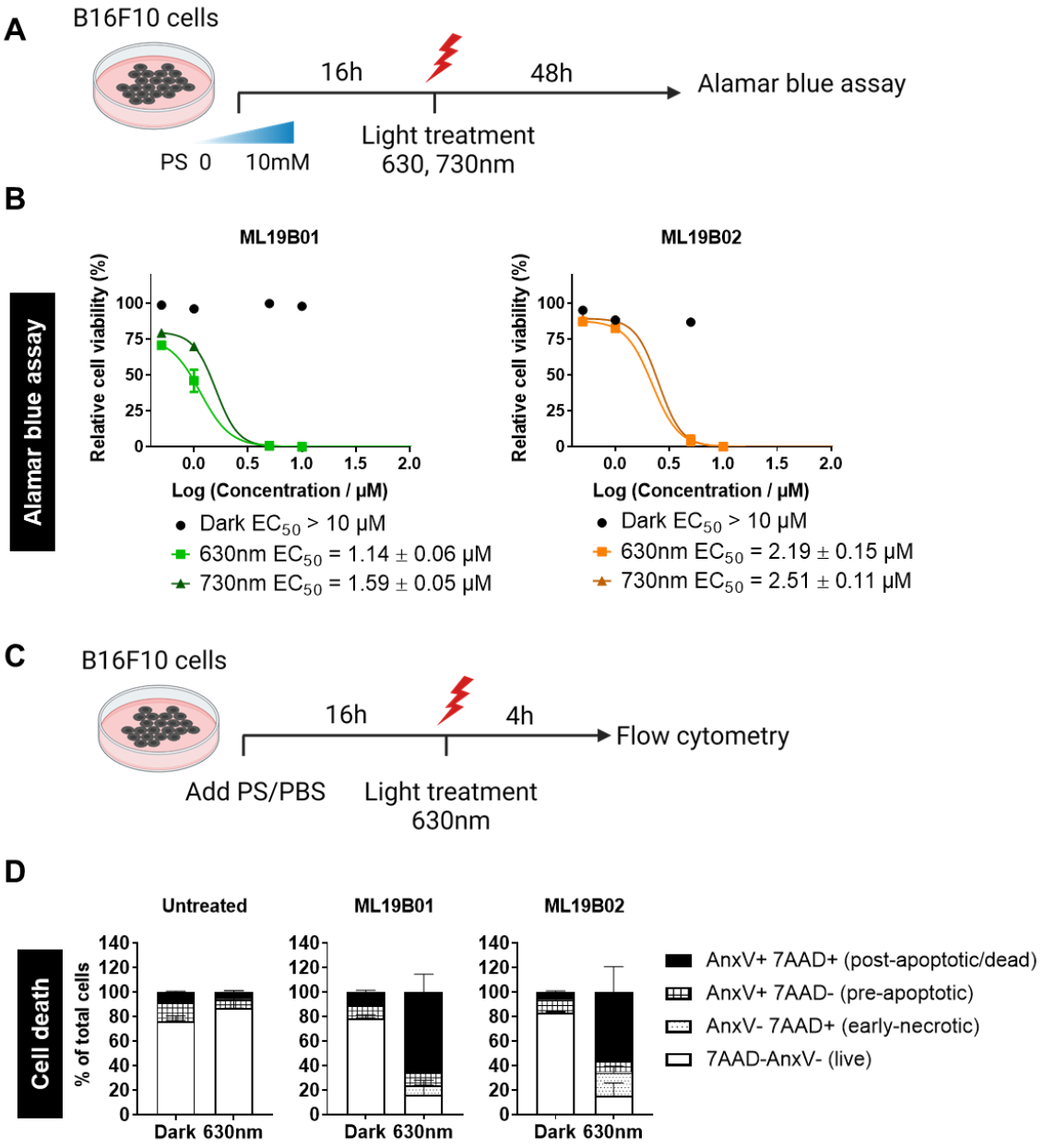


**Figure 5.2.** Cell death analysis in B16F10 cells treated with **ML19B01**-PDT or **ML19B02**-PDT.

**A**. Schematic representation of alamar blue cell viability assay. **B**. Cell viability graphs indicating respective EC50 values for different conditions. Treatments include both PSs or PBS with and without light treatment (630 nm and 730 nm). **C**. Schematic representation of the experimental strategy for cell death analysis via flow cytometry. **D**. Bar plots indicating the percentages of cell death in different phases. Percentages of pre-apoptotic (7AAD- Annexin V+), post-apoptotic (7AAD+ Annexin V+), early necrotic (7AAD+ Annexin V-) and live (7AAD- Annexin V-) cell populations are plotted.

### *5.3.3. ML19B01-PDT and ML19B02-PDT produce distinct immunomodulatory responses.*

Recent studies have revealed the potential for PDT-induced oxidative stress to result in an inflammatory response.[385] We previously designed one such Ru(II) PS, **ML18H01**, which efficiently induced multiple proinflammatory pathways that can overturn the immunosuppressive TME in cancers.[737] To this end, we examined the immunomodulatory effects of **ML19B01**- and **ML19B02**-PDT in B16F10 melanoma cells. Treatment of B16F10 cells with **ML19B01** and **ML19B02** at their respective $EC_{50}$ values, followed by irradiation (630 nm, 25 J $cm^{-2}$, 22.8 mW $cm^{-2}$) resulted in differential modulation of immunological pathways. **ML19B01**-PDT resulted in superior induction of heat shock proteins (HSPs), HSP70, and HSP90 whereas **ML19B02** did not result in a significant induction [**Figure 5.3.B**]. While both PSs resulted in induction of proinflammatory cytokines CXCL10,[80] IL6,[80,447] TNFα,[80] and the type 1 interferon (T1 IFN) pathway[80,314] associated gene IFIT1, the magnitude of expression was higher upon **ML19B02**-PDT as compared to **ML19B01**-PDT [**Figures 5.3.C, D**]. Neither PS altered the expression of other genes related to the T1 IFN pathway, (IFNβ, TLR3) or those associated with the MHC-I molecule[132,740] (H2D, β2M, TAP1) [Supplementary Figure

5.1.]. Additionally, **ML19B01** and **ML19B02** under the dark condition did not affect the expression of any of the genes tested [**Figure 5.3.B, C, D**]. Together these results demonstrate the differential immunomodulatory capacities of **ML19B01** and **ML19B02**-PDT.

PDT-induced cell death is usually characterized by an oxidative stress response and generation of ROS, both of which are implicated in ICD.[80,212] Moreover, HSPs function as molecular chaperones in response to ICD induced oxidative stress.[212,428,741] Therefore, we studied the generation of ROS with **ML19B01**- and **ML19B02**-PDT using B16F10 cells. Treatment with both **ML19B01**-PDT and **ML19B02**-PDT resulted in an increase in cellular ROS expression, quantified by flow cytometry staining with DCFDA, however, a higher increase was observed with **ML19B01**-PDT [**Figure 5.3.E**]. Flow cytometry staining with Mitosox revealed an increase in mitochondrial ROS with only **ML19B01**-PDT and not in **ML19B02**-PDT [**Figure 5.3.E**]. These observations demonstrate the differential regulation of ROS upon treatment with **ML19B01** and **ML19B02**-PDT.

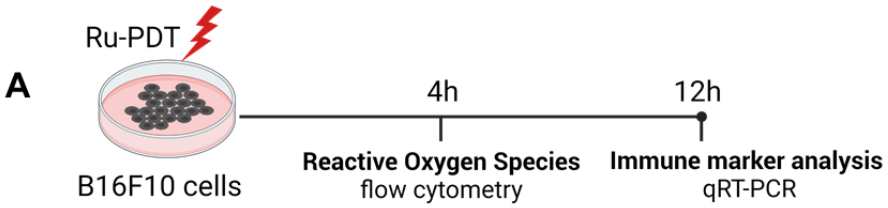
A
Ru-PDT
B16F10 cells
4h
12h
Reactive Oxygen Species
flow cytometry
Immune marker analysis
qRT-PCR

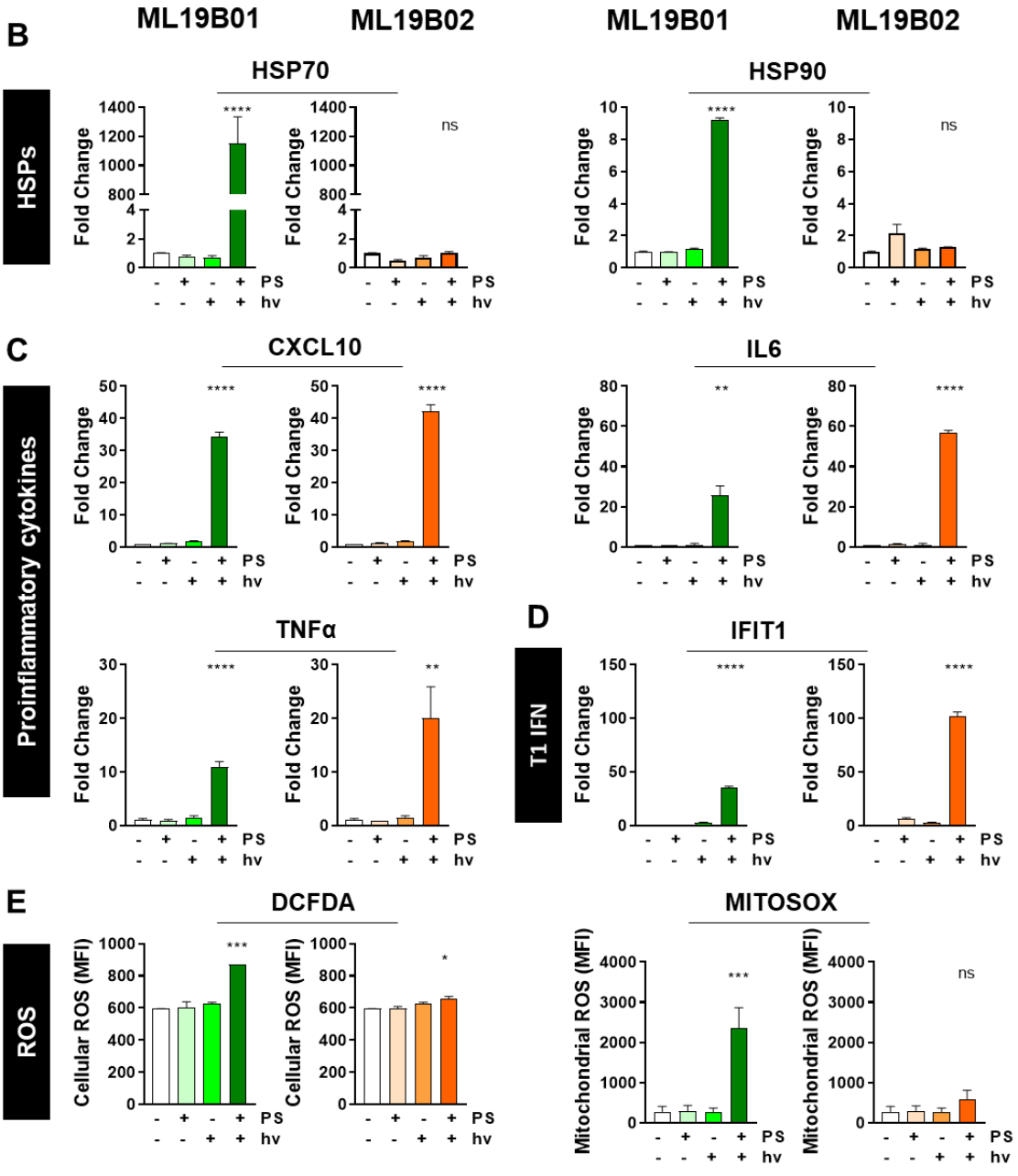
B
ML19B01
ML19B02
ML19B01
ML19B02
HSPs
HSP70
HSP90
Fold Change
ns
PS
hv
C
Proinflammatory cytokines
CXCL10
IL6
TNFα
D
T1 IFN
IFIT1
E
ROS
DCFDA
MITOSOX
Cellular ROS (MFI)
Mitochondrial ROS (MFI)

**Figure 5.3. ML19B01** and **ML19B02**-PDT induce differential modulation of immunological pathways.

**A**. Schematic representation of the experimental strategy for immune marker analysis and ROS analysis upon PDT treatment. **B-D**. qRT-PCR analysis of PDT treated B16F10 cells for genes associated with **B**) heat shock proteins, HSP90 and HSP70. **C**) Proinflammatory cytokines, CXCL10, IL6, TNFα. **D**) Type 1 interferon pathway associated gene IFIT1. Fold changes are relative to untreated samples and normalized to the control gene, GAPDH. **E**. Mean fluorescence intensities for ROS, analyzed by flow cytometry for cellular ROS (DCFDA) and mitochondrial ROS (MitoSOX). PS: compound. hv: light treatment. Anova statistical analysis was performed. Experiment n=3.

### *5.3.4. Cell death by ML19B01-PDT and ML19B02-PDT is associated with the emission of DAMPs.*

ICD has been recognized as one of the promising ways to reverse cancer cell immune evasion and the immunosuppressive TME.[241] Considering the potential immunomodulatory capacity of **ML19B01**- and **ML19B02**-PDT [**Figure 5.3**] and the roles of HSPs as well as ROS in ICD, we then explored whether the cell death associated with **ML19B01**- and **ML19B02**-PDT resulted in the emission of DAMPs. Here, we investigated the major ICD hallmarks,[80] calreticulin (CALR) surface translocation,[243] ATP secretion,[244] and HMGB1 release,[294] (which play an important role in anti-tumor immunity due to interactions with the innate immune system) in B16F10 cells treated with **ML19B01**- and **ML19B02**-PDT [**Figure 5.4.A**]. Surface CALR in ICD stimulates the uptake of dead-cell-associated antigens by DCs, ATP facilitates the recruitment of APCs and their activation, and HMGB1 promotes the activation of DCs and antigen presentation by DCs to T cells.[80,212] Flow cytometry analysis of B16F10 cells revealed a

significant increase in surface CALR expression upon **ML19B01**-PDT [**Figure 5.4.B**]. While **ML19B02**-PDT resulted in a statistically significant increase in CALR expression, it is much lower compared to **ML19B01**-PDT. Additionally, **ML19B01**- and **ML19B02**-PDT treatment increased the extracellular secretion of ATP [**Figure 5.4.C**] as well as HMGB1 [**Figure 5.4.D**] in the culture supernatants of B16F10 cells. Together, these data revealed the distinct ICD hallmark-inducing capacity of **ML19B01**- and **ML19B02**-PDT in mouse melanoma cells *in vitro*.

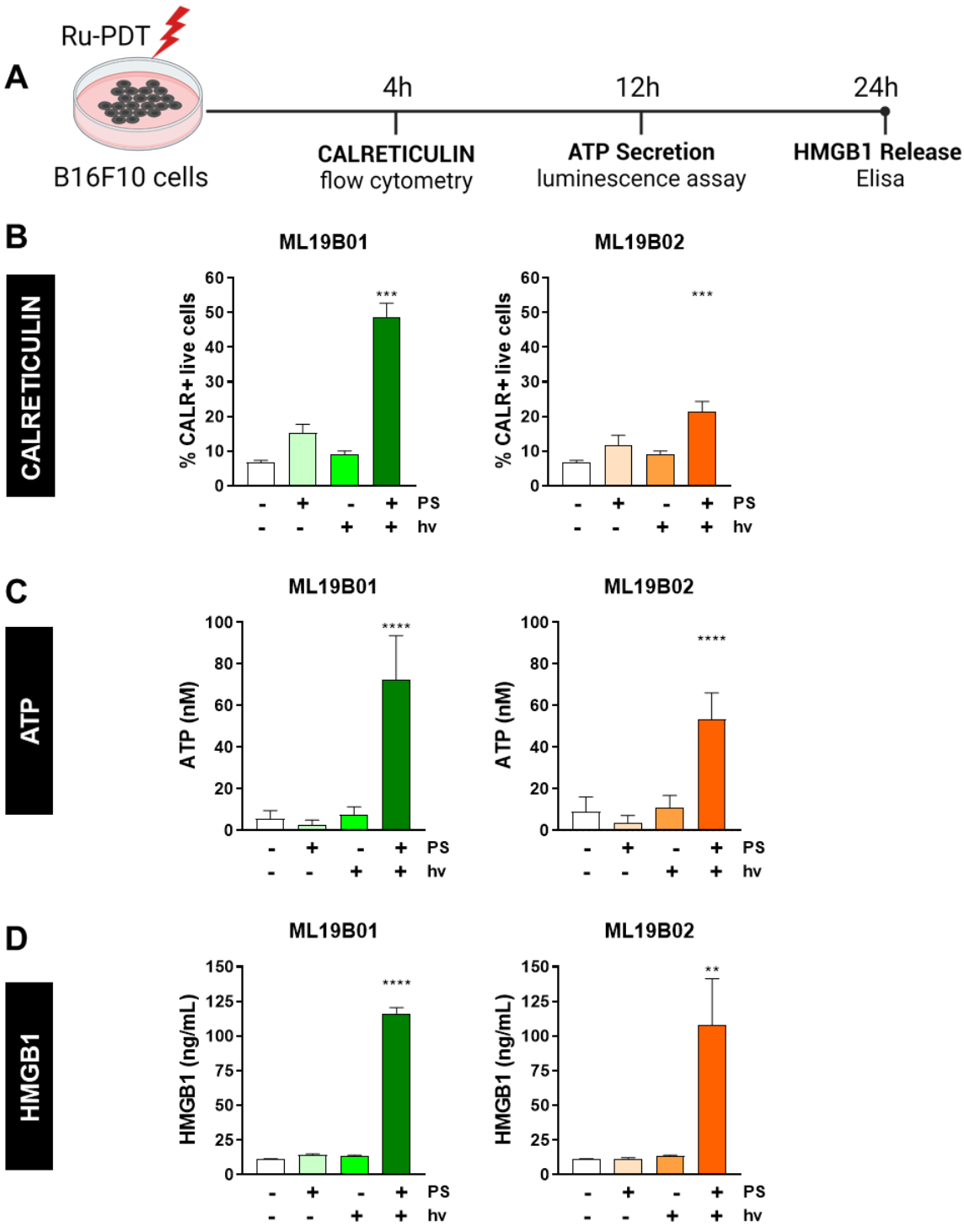


**Figure 5.4.** Cell death generated by **ML19B01** and **ML19B02**-PDT induces hallmarks of immunogenic cell death in B16F10 cells.

**A**. Schematic representation of the experimental strategy for analysis of surface CALR expression, ATP secretion, and HMGB1 release upon PDT treatment of B16F10 cells. **B**. Flow cytometry analysis of surface expression of CALR in B16F10 cells *in vitro*. **C**. Extracellular ATP analysis in B16F10 cells *in vitro*. **D**. Analysis of HMGB1 release in supernatant samples of PDT treated B16F10 cells. PS: compound. hv: light treatment. Anova statistical analysis was performed. Experiment n=3 for ATP and HMGB1 and n=5 for CALR.

### *5.3.5. ML19B01- and ML19B02-PDT treated cancer cells are phagocytosed by and induce functional markers in BMDCs.*

DCs, professional antigen presenting cells, play an important role in antigen presentation and priming of CD8+ T cells.[718] As such, successful activation and maturation of DCs have been identified as essential for initiation of the anti-tumor immune responses during ICD.[721] Here, we used GM-CSF differentiated DCs from mouse bone marrow[742] to assess *in vitro* phagocytosis of B16F10 cells treated with **ML19B01**- and **ML19B02**-PDT [**Figure 5.5.A**]. Co-culture of live vs. PDT-treated cells resulted in phagocytosis of only PDT-treated cells [**Figure 5.5.B**]. **ML19B01**-PDT treated cells were phagocytosed better than **ML19B02**-PDT treated B16F10 cells. The rate of phagocytosis also increased with an increase of BMDCs: cancer cell ratio from 1:1 to 1:5. This data shows that dying cancer cells upon PDT-treatment are being phagocytosed by DCs.

Next, we evaluated the immunomodulatory effects of DAMPs released upon PDT-treatment on BMDC maturation, by treating the BMDCs with culture supernatant from **ML19B01**- or **ML19B02**-PDT treated B16F10 cells [**Figure 5.5.C**]. Analysis of mRNA expression of immunogenic or activation markers of DCs revealed an increase in expression of CD40,[688] CD80,[685,686] CD83,[687] and IL12β[689,690] upon culture with PDT-

treated supernatants. Both **ML19B01**- and **ML19B02**-PDT-treated conditioned media increased the expression of these markers but by different magnitudes [**Figure 5.5.D**]. In addition to the immunogenic markers, we assessed the expression of several regulatory markers in BMDCs treated with conditioned media from PDT-treated B16F10 cells. Here, we identified an increase in expression of inhibitory PDL1[(692,693)] as well as CTLA4[(695,696)] in BMDCs cultured in **ML19B01**- and **ML19B02**-PDT treated B16F10 supernatants. There was no effect on additional immunogenic marker CD86,[(685)] and regulatory markers TIM3[(694)] and Arg1[(697)]. This data shows that conditioned media from PDT-treated B16F10 cells promotes the expression of immunogenic as well as regulatory markers on DCs.

Collectively, these results indicate that along with the secretion of immunogenic DAMPs, the **ML19B01**- and **ML19B02**-PDT-compromised cells are efficiently engulfed by BMDCs, and **ML19B01**- and **ML19B02**-PDT increases the expression of DC functional markers.

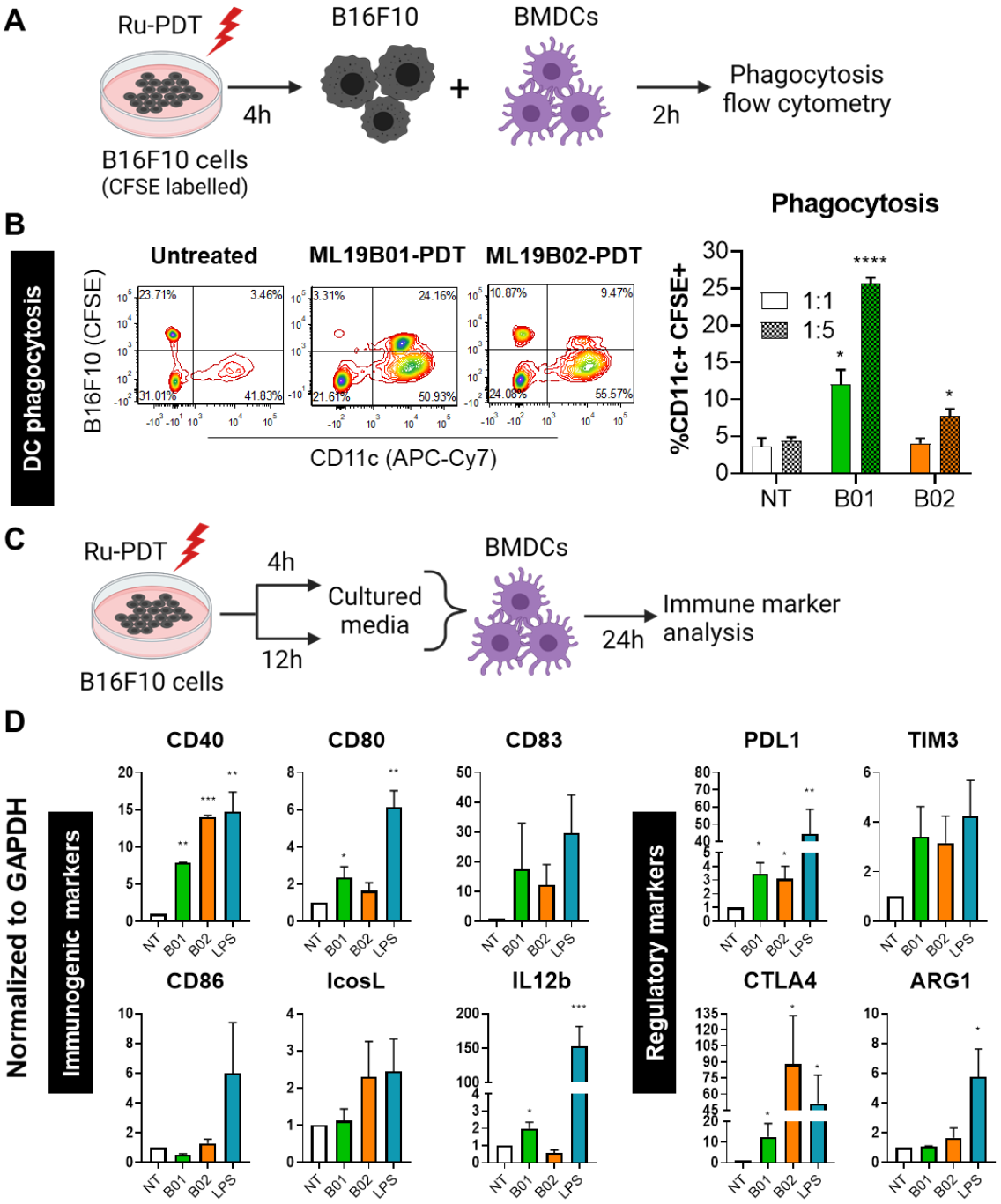


**Figure 5.5. ML19B01** and **ML19B02**-PDT treated cells are engulfed by BMDCs and induce BMDC functional markers.

**A**. A schematic representation of the workflow for BMDC phagocytosis experiment. **B**. Contour plots depicting uptake of CFSE labelled B16F10 cells by CD11c+ cells. CD11c+ CFSE+ population in the upper right quadrant indicates the percentage of phagocytosed cells. Representative contour plots represent 1:5 ratio of BMDC: cancer cells. Corresponding bar plot on the right-side depicting percentage CD11c+ CFSE+ cells with 1:1 and 1:5 ratio of BMDC: cancer cells. **C**. A schematic representation of the experimental strategy for immune marker analysis in DCs upon incubation with PDT-treated conditioned media. **D**. qRT-PCR analysis of immunogenic markers CD40, CD80, CD83, CD86, IcosL, IL12b and regulatory markers PDL1, TIM3, CTLA4, ARG1. Fold changes are relative to untreated samples and normalized to the control gene, GAPDH. LPS treated sample was used as a positive control. Experiment n=3. Student's t test was performed respective to the control, NT.

### *5.3.6. Vaccination with ML19B01-PDT and ML19B02-PDT-treated cancer cells results in delay of tumor growth and enhanced survival.*

To evaluate the therapeutic potential of ICD induced by our PSs, we performed the gold standard ICD confirmation experiment.[80,321] First, mouse B16F10 melanoma cells were treated *in vitro* at concentrations corresponding to the $EC_{50}$ values of **ML19B01**- or **ML19B02**-PDT, and dying cells were collected 4 and 12 h post-treatment and injected into the left flank of C57BL/6 mice for vaccination [**Figure 5.6.A**]. These mice were then challenged with untreated B16F10 cells on the right flank 7 days post-vaccination and assessed for tumor growth and tumor-free survival. Mice vaccinated with **ML19B01**- and **ML19B02**-PDT treated dying cancer cells displayed improved tumor-free survival and delay in tumor growth compared to unvaccinated control mice [**Figure 5.6.B**]. Despite the differential ICD-inducing capacities, the *in vivo* anti-tumor effects imparted by

**ML19B01**- and **ML19B02**-PDT were comparable and statistically indistinguishable. This data shows that vaccination with B16F10 cells treated with **ML19B01-** and **ML19B02-**PDT produced similar protection against tumor challenge.

The influence of sex differences on cancer incidence, mortality, and treatment outcomes has become increasingly evident in the past decade.[743,744] To understand the impact of sex on the outcome of ICD-induced anti-tumor protection against melanoma, we performed the vaccination experiment in both female and male mice. Comparison between male and female C57BL/6 mice showed equivalent tumor-free survival. However, vaccinated female mice demonstrated statistically superior tumor growth control as compared to vaccinated male mice [**Figure 5.6.B, C**]. Together, these results indicate the induction of beneficial anti-tumor protection in C57BL/6 mice upon vaccination with **ML19B01** and **ML19B02**-PDT treated B16F10 cells in a sex-biased manner.

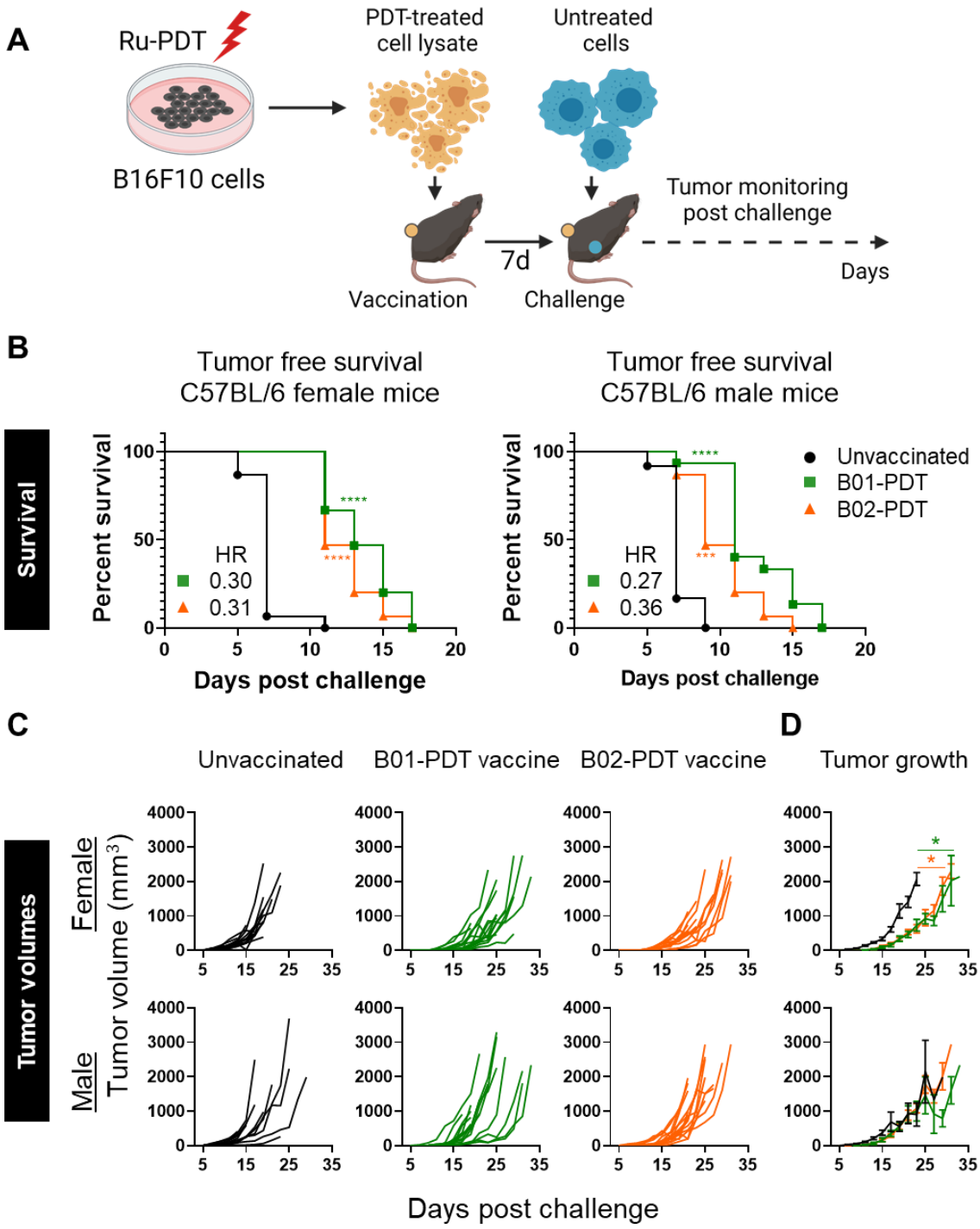


**Figure 5.6.** Immunization with **ML19B01** and **ML19B02**-PDT treated cancer cells prolongs tumor-free survival and delays tumor growth in the B16F10 mouse melanoma model.

**A**. Schematic representation of the workflow for the *in vivo* vaccination experiment. Male and female C57BL/6 mice were first immunized with PDT-treated cells on the left flank, challenged 7 days later with untreated live cells on the right flank, and monitored for tumor growth and survival. **B**. Tumor-free survival graphs in male and female mice vaccinated with ML19B01 or ML19B02-PDT treated B16F10 cells. Hazard ratio (HR) values are indicated within the graphs. **C**. Tumor growth comparison for unvaccinated vs. vaccinated male and female mice, individual groups as well as combined mean tumor growth graphs. Each group represents data from 15 mice, except for the unvaccinated male group, which has 13 mice. Statistical analysis was performed using Mantel-cox test for survival curves and paired t-test for tumor growth graphs.

## 5.4. DISCUSSION

In our quest to develop effective immunostimulatory PDT as adjuvant therapy for the most aggressive melanomas, we recently reported Ru-based coordination complexes designed to absorb and be activated with NIR light to achieve potent cytotoxicity in melanoma cells.[737,738] In our previous study, we used coordination chemistry as a powerful tool to rapidly generate a library of Ru-based PSs with ideal properties for melanoma PDT. Importantly, we established structure-activity relationships to develop the relevant photophysical models for optimizing NIR PDT effects toward melanoma cells and identified several lead Ru(II) PSs. We further explored the immunomodulating properties of PDT with lead **ML18H01**. The structural scaffold of **ML18H01** allows for variation of a monodentate pyridyl-based ligand without compromising the attractive features of NIR absorption and PDT potency. Modifications at this position provide a convenient handle for fine-tuning biological activity, and our current study with **ML19B01** and **ML19B02** as next-generation NIR Ru PSs illustrates that the favorable bulk PDT

properties are retained while the *in vitro* immunological signatures can be varied. In the longer term, optimization of these signatures through structural variation may prove useful for directing anti-tumor responses *in vivo*, with the goal being to maximize immunoprotective effects in melanoma treatment.

Recent studies, both preclinical and clinical, have demonstrated the ability of PDT to initiate innate and adaptive immune responses against tumors. In this context, ICD of cancer cells is considered a promising way to activate the anti-tumor T cell and DC-based immune responses and achieve ultimate tumor cell clearance. We evaluated the immunological consequences in the context of **ML19B01**- and **ML19B02**-PDT-associated cytotoxicity in the B16F10 melanoma model. By analyzing qRT-PCR based gene expression, we found that the two PSs differentially modulate proinflammatory markers and heat shock proteins, both of which play a key role in PDT-associated anti-tumor immunity. While **ML19B01**-PDT led to a significant increase in HSP90 and HSP70, **ML19B02**-PDT produced a higher increase in proinflammatory cytokines IL6, TNFα, and CXCL10 compared to **ML19B01**-PDT. Light treatment alone or PS in the dark condition did not affect the expression of these genes, confirming that the increase only occurred when the PS was activated by light. Interestingly, analysis of ROS revealed that **ML19B01**-PDT induces higher cellular as well as mitochondrial ROS as compared to **ML19B02**-PDT. HSPs and ROS are both involved in PDT-mediated oxidative stress, and are also implicated in ICD; here, HSPs act as eat me signals,[745] and ROS is involved in the unfolded protein response-mediated exposure of endoplasmic reticulon chaperone CALR to the cell surface.[212,280]

Several hallmarks or signatures of ICD have been discovered in the context of different therapies.[80,241] For PDT, where ICD is not completely characterized, CALR surface expression, ATP secretion, and HMGB1 release are suggested as core

hallmarks.[212] CALR exposure in dying cells is a crucial “eat me” signal during ICD and facilitates the recognition of dying cancer cells by phagocytic cells such as DCs.[212] Along similar lines with HSP and ROS expression, surface translocation of CALR was higher upon **ML19B01**-PDT treatment than **ML19B02**-PDT in B16F10 melanoma cells. After CALR exposure, late-stage dying cells secrete ATP and HMGB1 molecules extracellularly, both of which can interact with PRRs on DCs and activate them *in vivo*. Studies on ATP secretion and HMGB1 release showed a similar increase of both hallmarks with **ML19B01**- as well as **ML19B02**-PDT. Together, these findings reveal the immunomodulatory and ICD hallmark-inducing potential for **ML19B01**- as well as **ML19B02**-PDT.

Since DAMPs interact with DCs, which play a crucial role in stimulating anti-tumor immune responses, we sought to identify the capacity of PDT-treated dying cancer cells to be phagocytosed. Phagocytosis of cancer cells is a key event which leads to the processing of antigens and eventually, the presentation of antigen by DCs to T cells, therefore impacting the anti-cancer immunity. Both **ML19B01** and **ML19B02**-PDT treated B16F10 cells were engulfed by BMDCs in a dose-dependent manner, with **ML19B01**-PDT treated cells resulting in higher phagocytosis. Because CALR plays an important role in DC phagocytosis,[746–748] this data agrees with our observation wherein **ML19B01**-PDT induced higher surface CALR than **ML19B02**-PDT. Despite the differences in levels of phagocytosis, culture media from both **ML19B01**- and **ML19B02**-PDT treated cells was able to upregulate the expression of immunogenic markers in BMDCs. It is possible that while the ER chaperones HSPs and CALR were differentially regulated by **ML19B01**- and **ML19B02**-PDT, leading to a difference in phagocytosis, other DAMPs which were comparable between both groups were able to compensate for the difference in BMDC stimulation. Both **ML19B01**- and **ML19B02**-PDT increased the

expression of CD40, CD80, and CD83 genes, all associated with activation of BMDCs, but to different extents. Interestingly, we also noted the upregulation of inhibitory genes upon treatment with conditioned media from both compounds. Conditioned media from **ML19B01** and **ML19B02**-PDT treated B16F10 cells increased the expression of PDL1 and CTLA4 genes, both identified as regulatory markers of DC maturation.

While *in vitro* release of DAMPs provides an indication of ICD, ultimately, their ability to trigger anti-tumor immune responses *in vivo* is the end goal. To validate the ICD *in vivo* and furthermore, to understand whether the differences in levels of some ICD hallmarks *in vitro* translates to the response *in vivo*, we performed the gold standard vaccination experiments in immunocompetent C57BL/6 mice.[321] Of note, to understand the possible sex-biased immune responses in the ICD mediated response, we performed this experiment with both male and female C57BL/6 mice. Vaccination of mice with dying B16F10 cancer cells from **ML19B01**- or **ML19B02**-PDT treatment resulted in a delay in tumor growth and overall improvement in tumor-free survival as compared to unvaccinated mice, upon challenge with live B16F10 cells. Additionally, both **ML19B01**-PDT, as well as **ML19B02**-PDT treated cells provided comparable protection from tumor growth.

Although both male and female mice showed improved tumor-free survival upon vaccination with PDT-treated cells, the control of tumor growth was greater and statistically significant in female mice compared to male mice, indicating a better anti-tumor immune response in female mice. This agrees with our previous findings with **ML18H01**-PDT, where we found sex-biased differences in the vaccination efficacy of Ru(II) PDT-treated cells in female and male mice. Moreover, preclinical and clinical data in melanoma provides evidence for sex-biased differences in immune responses, tumor development as well as response to therapies, particularly immunotherapies.[744,749–752]

However, neither group was fully protected against tumor growth, and mice vaccinated with either **ML19B01**- or **ML19B02**-treated cancer cells eventually formed tumors.

There could be two explanations behind this observation. While we noticed efficient induction of immunostimulatory DAMPs, studies have associated the hindrance of ICD with inhibitory DAMPs (iDAMPs), which could play a role in the context of our treatment.[746,753] A recent study identified prostaglandin E2 as an inhibitory molecule released in response to gemcitabine treatment and blocking this iDAMP reversed the outcome of gemcitabine-induced ICD.[322,754] Some ICD associated DAMPs are shown to have dual roles, both immunogenic as well as immune-inhibitory or suppressive, depending on their mutations, epigenetic modifications, dose, mode, time of release, and interactions in the TME.[449,753,755–757] Additionally, our findings from the *in vitro* BMDC experiments identified upregulation of inhibitory genes PDL1 and CTLA4 in BMDCs exposed to conditioned media from PDT-treated cells, suggesting that PDT with **ML19B01** and **ML19B02** triggers the release of these important regulatory molecules. A similar increase of these checkpoint molecules *in vivo* upon vaccination can result in inefficient stimulation of DC activation, maturation, and T cell activation.[692,758–761] By exploiting these observations, we hope to design combination therapies with checkpoint inhibitors or by blocking iDAMPs to improve the efficacy of these treatments.[762] However, considering the highly aggressive and poorly immunogenic nature of B16F10 melanoma, the extent of protection observed from our study was notable. Moreover, our study confirms yet again, the importance of performing *in vivo* vaccination to validate the concept of ICD. Overall, we report two novel ruthenium compounds with cytotoxic as well as immunomodulatory capacities for PDT of metastatic melanoma.

## 5.5. CONFLICT OF INTEREST

S. A. M. has a potential research conflict of interest due to a financial interest with Theralase Technologies, Inc. and PhotoDynamic, Inc. A management plan has been created to preserve objectivity in research in accordance with UTA policy.

## 5.6. ACKNOWLEDGEMENTS

S. G. and S. A. M. thank the National Cancer Institute (NCI) of the National Institutes of Health (NIH) (Award R01CA222227) for support. The content in this article is solely the responsibility of the authors and does not necessarily represent the official views of the National Institutes of Health. P.K. was supported by Killam Predoctoral Fellowship, Research Nova Scotia – Scotia Scholar Award, and Nova Scotia Graduate Student Fellowship. S. G. and P.K. note that the schematic figures were created with https://www.BioRender.com.

## 5.7. SUPPLEMENTARY FIGURES

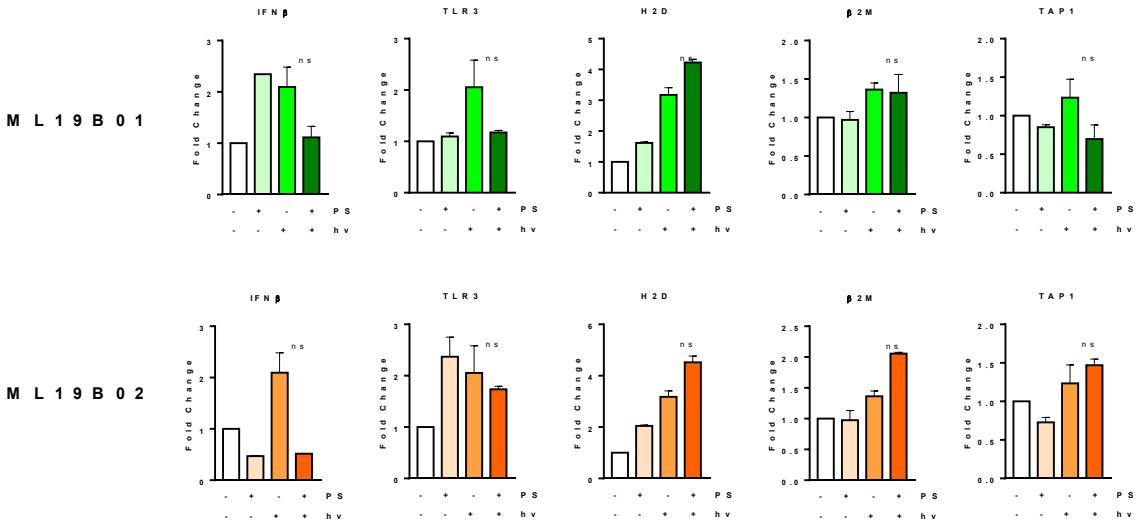


**Supplementary Figure 5.1**. Analysis of Type I interferon and MHC-I molecule associated genes upon **ML19B01**- and **ML19B02**-PDT.

Analysis of **ML19B01**- and **ML19B02**-PDT treated B16F10 cells using qRT-PCR for genes associated with interferon beta (IFNβ), toll like receptor 3 (TLR3), MHC-I molecule genes (H2D, β2M, TAP1). PS: compound, hv: light treatment. Anova statistical analysis was performed. Experiment n=3.

## 5.8. SUMMARY OF CHAPTER 5

We developed two new ruthenium compounds, **ML19B01** and **ML19B02**, by modifying the ligands in the core structure of **ML18H01**, reported in Chapter 4. The modifications retained the PDT features of the compounds but varied in their immunostimulatory properties. Following NIR activation, both compounds demonstrated similar activation characteristics and potent cytotoxicity against B16F10 cells with single-digit EC50s. **ML19B01** was effective at inducing heat shock proteins and reactive oxygen species *in vitro*. While both compounds increased proinflammatory cytokines, **ML19B02**-PDT resulted in a more significant increase in associated genes. ICD evaluations revealed that **ML19B01**-PDT greatly increased surface calreticulin induction than **ML19B02**-PDT, but both had a similar effect on ATP and HMGB1 secretion. Overall, *in vitro* analyses revealed varied capacities of both PSs, with **ML19B01**-PDT preferentially upregulating the ROS-ER chaperone axis of ICD. Phagocytosis assays with DCs revealed substantially higher phagocytosis of **ML19B01**-PDT killed B16F10 cells than **ML19B02**-PDT destroyed cells. Interestingly, conditioned media from **ML19B01** and **ML19B02**-PDT treated B16F10 resulted in the upregulation of activation and inhibitory markers in DCs. Vaccination with **ML19B01** and **ML19B02**-PDT treated cells improved tumor-free survival and reduced tumor growth upon challenge with live B16F10 cells. Intriguingly, neither PSs generated complete protection against tumor growth, which could be related to the inhibitory markers identified in DCs and other as-yet-unidentified immunosuppressive mechanisms [see section **6.2.2**]. Overall, we report two structurally related Ru compounds with similar cytotoxicity profiles but distinct immunostimulatory actions, with potential therapeutic benefits in combination with other therapies [see section **6.2.3**].

# CHAPTER 6: DISCUSSION

## 6.1. SUMMARY & SIGNIFICANCE OF CENTRAL FINDINGS

Since establishing the concepts of cancer immunoediting and the cancer immunity cycle, there has been a surge in research to better understand these processes and harness them to improve the therapeutic landscape. MHC-I bound peptides play an essential role in the CD8 T cell-driven cancer immunity cycle by providing specificity for anticancer immune responses. As a result, identifying these peptides is critical for understanding and regulating T cell responses against cancer. While recent developments in mass spectrometry have provided a new avenue for MHC-I peptide discovery, they also present unique challenges.

Traditionally, MS/MS spectra for eluted MHC-I peptides are compared to a reference proteome database that lacks enzymatic digestion specificity. This results in inflated search spaces and hampered ability to perform false discovery rate correction, reducing the number of identified peptides. We address this issue in this report by establishing a targeted database search technique and an associated tool, *SpectMHC*, which is based on previously predicted MHC-I peptides. When compared to a standard "no-enzyme" search of reference proteomes, our tailored search method enhanced peptide identifications by more than two-fold for both mouse and human MHC-I ligands. These peptides' false discovery rate assessments revealed that increased MHC-I ligand identifications are associated with improved statistical power.

Furthermore, MS detection of peptides with low ion scores is challenging with lowly abundant peptides like MHC-I ligands. By performing targeted searches, we were able to assign MS/MS spectra with lower ion scores, increasing the sensitivity of MHC-I ligand detection. As a result, this strategy has the potential to uncover otherwise missed

MHC-I ligands, including those harboring novel T cell epitopes with therapeutic potential [**Figure 6.1.1**].

Such technical and computational advances are especially important in the ever-changing field of MHC-ligand discovery, as sensitive and accurate identifications will improve our understanding of T cell epitopes and allow us to design better therapeutics, such as cancer vaccines. This approach offers a wide range of applications for identifying TAAs and TSAs and can also be used in other fields such as infectious diseases and autoimmune diseases. There is a strong interest in this work among researchers interested in studying the MHC-I peptide landscape (cited 41 times) and hence adopting the approach for use in various biological models. Furthermore, the publication associated with this work was selected as an Editor's Choice Article by the American Chemical Society in 2017, and I was invited to write two book chapters on using the tool and approach. Overall, this study has piqued the interest of the mass spectrometry and immunology communities and has provided a non-laborious, budget-free solution for overcoming existing limitations and improving MHC-I ligand identifications from valuable preclinical and clinical samples.

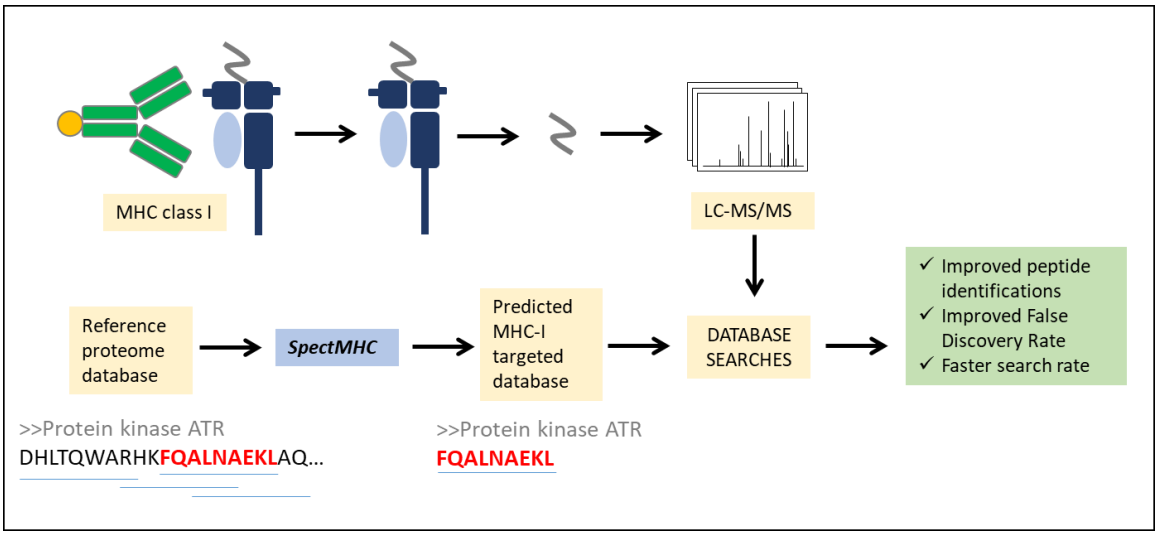


**Figure 6.1.1.** Overview of *SpectMHC*-based MHC-I ligand discovery.

Immunoprecipitation is used to isolate MHC-I bound peptides from cell lysates, which are then identified using LC-MS/MS techniques. The resulting MS spectra are compared to a targeted database developed using the *SpectMHC* technique. This MHC-I-specific database was created using a reference proteome as input and utilizing neural network methods to identify potential MHC-I ligands. The comparison of MS/MS spectra to the targeted database results in enhanced peptide identifications, lower false discovery rates, and a faster overall search rate.

**The above figure was previously published in:**

**Konda P**, Murphy JP, Gujar S. Improving MHC-I ligand identification by incorporating targeted searches of mass spectrometry data. In Bioinformatics for cancer immunotherapy 2020 (pp. 161-171). Humana, New York, NY.

The subsequent chapters of the thesis focus on the development of novel immunogenic photodynamic therapies to enhance the cancer immunity cycle. We used ruthenium coordination complexes designed to achieve the desired chemical and photophysical properties (section **1.6.1.1**) and to shift the photosensitizer's light absorption window into the near-infrared region. In mouse melanoma models, NIR activation of these complexes resulted in potent cytotoxicity, immunogenic cell death, and immunostimulatory events. NIR-activated Ru complexes efficiently generated cellular and mitochondrial ROS, which have been implicated in PDT-induced cytotoxicity and are known mediators of hypericin PDT-induced ICD. Ru-PDT significantly increased the expression of genes encoding components of the type 1 interferon pathway, proinflammatory cytokines, heat shock proteins, and antigen-presentation machinery, all of which are involved in different stages of cancer immunity. Ru-PDT also induced spatiotemporal immunogenic cell death in mouse melanoma cells via calreticulin translocation mediated by ROS, ATP secretion, and HMGB1 release. These Ru PDT-treated dying melanoma cancer cells enabled DCs to uptake dead and dying cancer cells and induced DC activation markers.

Furthermore, *in vivo* vaccination and treatment effectiveness tests confirmed the clinical utility of these Ru complexes. Vaccination with Ru-PDT-treated B16F10 cells offered protection by causing either reduced or delayed tumor growth when challenged with untreated B16F10 cells and led to improved tumor-free survival in vaccinated mice compared to the unvaccinated group. Since the vaccination and challenge were performed on the mice's opposite flanks, the tumor-inhibiting effects of Ru PDT-based vaccines also suggested the generation of systemic anticancer immunity, which caused the abscopal effect. Interestingly, female mice had more remarkable tumor-free survival and protection from tumor development after vaccination than male mice, suggesting

sex-biased differences. Finally, NIR-activated Ru-PDT of melanoma tumor-bearing mice resulted in tumor growth reduction and control in syngeneic and transgenic aggressive melanoma models. In summary, our findings reveal that Ru PDT causes a two-pronged attack on melanoma cells, eliciting direct cytotoxicity as well as immunogenic cell death and protective antitumor immunity [**Figure 6.1.2**].

These findings demonstrate for the first time that transition metal complexes have immunostimulatory and immunogenic cell death-inducing properties, as well as clinical relevance for melanoma treatment. This is especially significant since metal complexes for therapeutic PDT are an emerging concept in the field. Our findings help promote the development of such therapies, which are far superior to traditional PSs. Moreover, PDT has traditionally been regarded as a local therapy used to treat superficial lesions. Our findings support the use of PDT for generating systemic antitumor responses, as evidenced by the abscopal effect in ICD vaccination experiments. We provided the *in vivo* characterization of the top three Ru-compounds evaluated for cytotoxic and immunostimulatory properties out of 11 compounds tested. Despite having identical structure and cytotoxic properties, each of these three compounds demonstrated a distinct immunostimulatory and ICD profile, both *in vitro* and *in vivo*. This indicates the intricate molecular mechanisms that underlie each compound that are undetermined by their chemical properties, emphasizing the need for detailed immunological characterizations. A similar finding was reported in 2009 between chemotherapies cisplatin and oxaliplatin, which have identical cytotoxicity but induce different DAMPs.[250] To date, most ICD investigations have been conducted in either male or female mouse models. Our data is the first to show that ICD-vaccination provides sex-biased protection, which has therapeutic implications. These findings are in

congruence with previous observations that male and female melanoma patients have distinct susceptibilities to immunotherapies, resulting in biased clinical outcomes.

Many novel methodologies have been utilized in the project's development. **1)** We used novel transition metal complexes, which are gaining popularity in the field of PDT. Because of their superior activation characteristics even in highly pigmented and hypoxic tumor regions, which most current PDT compounds are not capable of targeting, these are far superior to their traditional counterparts currently utilized in clinics/or clinical trials.[346] This property is important because melanoma cancers are highly pigmented, and most cancers are hypoxic, making them difficult to target.

**2)** These Ru compounds can be activated by a wide variety of light wavelengths, from blue light to near-infrared light, enabling them to target both surface and deeper cancers.[346,737,738,763] This type of activation property, particularly in the NIR region, is uncommon in PDT yet critical for targeting invasive cancers.

**3)** We employed tumor-focused optimization of compounds as well as therapeutic regimens. Most PSs and PDT regimens are developed with no specific cancer in mind, with the goal of broad applicability. While this is theoretically appealing, in practice, each malignancy has different clinical factors and provides unique challenges. Therefore, this project focused on melanoma as a target cancer, and all *in vitro* and *in vivo* regimens are optimized accordingly.

**4)** Unlike conventional evaluation practices that rely exclusively on PDT's tumor or vascular ablation properties, we adopted an integrated strategy that included assessing immunomodulatory capabilities in addition to cell killing. This required a step-by-step evaluation of PSs. PSs with high *in vitro* cytotoxicity were chosen for further testing of their immunostimulatory characteristics. The immunostimulant PSs were then tested for *in vitro* ICD inducing properties before being prioritized for *ex vivo* DC phagocytosis and

maturation studies, as well as *in vivo* ICD vaccination experiments. Furthermore, we investigated sex as a variable in our *in vivo* ICD assessment, which has only recently gained prominence in cancer therapies. Finally, compounds with the best *in vivo* ICD characteristics were shortlisted for *in vivo* therapeutic evaluation in two distinct mouse melanoma models.

There is a great deal of interest in this strategy to prioritize PDT treatment because of the recognition of the role of ICD and immunological responses in PDT-mediated anticancer responses, and there has been a recent surge in such investigations [**Figure 6.1.3**]. Overall, this work generated many significant findings and approaches, and it has been well recognized by the research community, with 22 citations in the 14 months since the publication of Chapter 4.

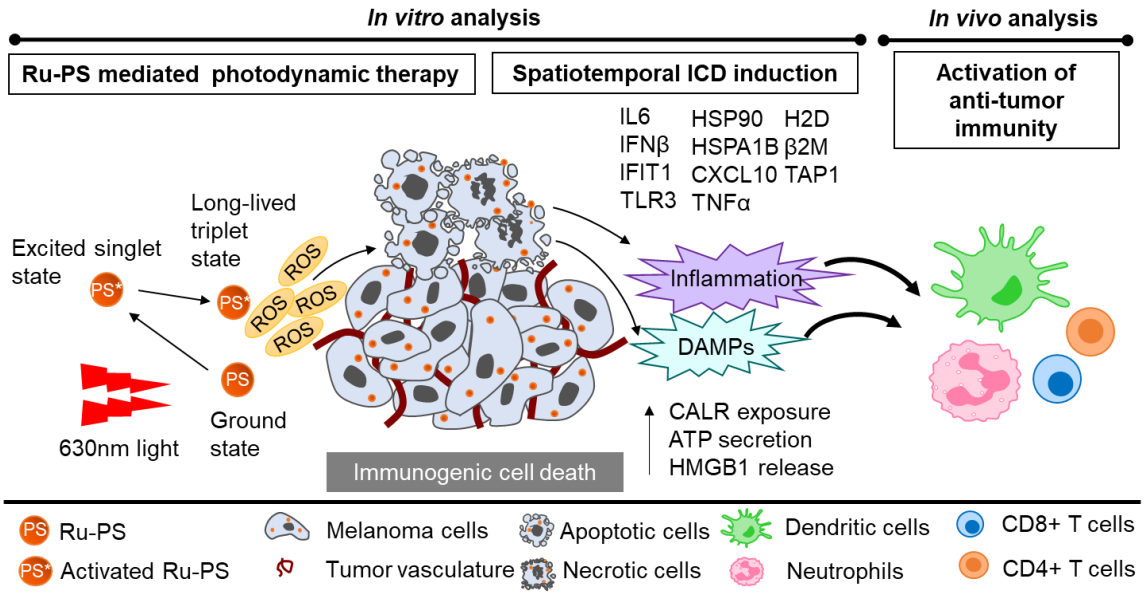


**Figure 6.1.2.** Proposed model for anticancer properties of Ru-based PDT

The Ru PS absorbs photons from a light source, initially forming the short-lived excited singlet state that undergoes a change in electron spin to produce the long-lived and lower-energy triplet state. The triplet state PS produces reactive oxygen species (ROS), leading to melanoma cell death. Ru PS-based PDT also induces molecules associated with inflammatory pathways and damage-associated molecular patterns (DAMPs) characteristic of immunogenic cell death. *In vivo* vaccination of mice with Ru PDT-treated melanoma cells develops antigen-specific antitumor immunity protective against melanoma growth and confirms the induction of ICD and anticancer immunity. IL6: Interleukin 6; IFNβ: Interferon Beta; IFIT1: Interferon Induced Protein With Tetratricopeptide Repeats 1; TLR3: Toll-Like Receptor 3; HSP90: Heat Shock Protein 90; HSPA1B: Heat Shock Protein Family A (Hsp70) Member 1B; CXCL10: C-X-C Motif Chemokine Ligand 10; TNFα: Tumor Necrosis Factor-Alpha; H2D: H-2 class I histocompatibility antigen, D chain; β2M: Beta-2-Microglobulin; TAP1: Transporter

associated with Antigen Processing 1; CALR: Calreticulin; ATP: Adenosine triphosphate; HMGB1: High Mobility Group Box 1.

**The above figure was previously published in:**

**Konda P**, Lifshits LM, Roque III JA, Cole HD, Cameron CG, McFarland SA, Gujar S. Discovery of immunogenic cell death-inducing ruthenium-based photosensitizers for anticancer photodynamic therapy. Oncoimmunology. 2021 Jan 1;10(1):1863626.

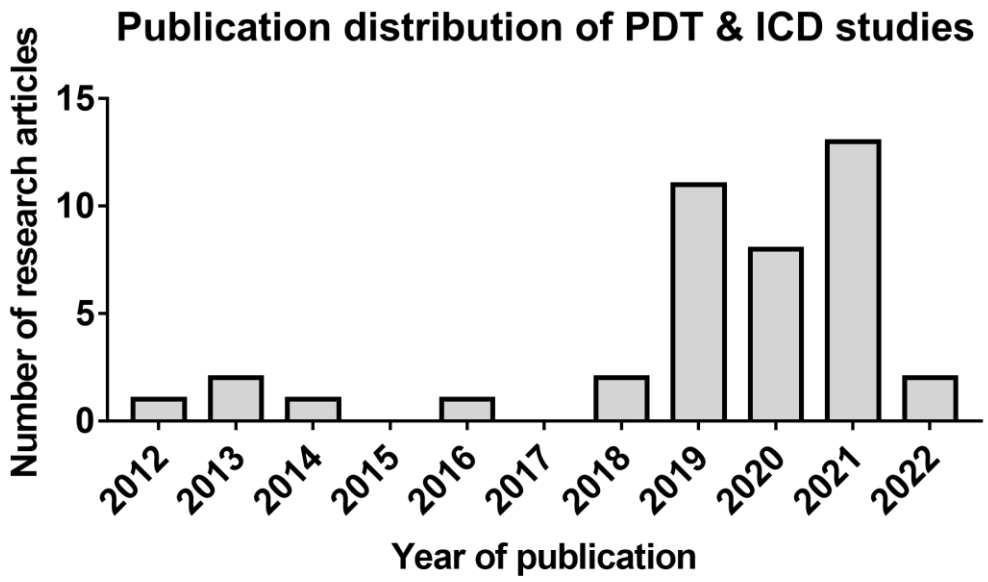


**Figure 6.1.3.** Publication distribution of PDT and ICD studies.

The graph depicts the recent spike (3 years) in publications investigating ICD in relation to PDT, indicating the recognition of its role in PDT-mediated anticancer treatments. Plotted data was collected from PubMed on February 1st, 2022, using the search term 'PDT+Cancer+ICD[Title/Abstract]' and excluding review articles.

## 6.2. FUTURE DIRECTIONS

"*The biggest impediment to scientific discovery is a limited budget.*" – *Prathyusha Konda*

Our one-of-a-kind, novel, and unexplored transition metal complex platform for PDT of melanoma offers infinitesimal opportunities for scientific investigations. Based on current knowledge in the field and the findings from the reported work, I propose the following future directions, which I believe will improve our fundamental understanding of PDT (particularly Ru PDT) as well as their therapeutic efficacy for clinical translation.

### *6.2.1. Integrated genomics, mass spectrometry, and immunological approaches to assess PDT-induced antigenicity and antigen-specific responses in melanoma*

The studies presented in Chapters 4 and 5 show that Ru-PDT can elicit immunogenic cell death, DC phagocytosis and maturation, and protective antitumor immunity. Because CD8 T cells are the primary effectors in ICD,[212] activated/ matured DCs could activate these CD8 T cell responses, which have yet to be characterized in our system. Investigating CD8 T cells, particularly antigen-specific T cells would help us better understand the immunological responses elicited by Ru-PDT. To examine such antigen-specific responses, it is crucial to know the specific antigens induced by PDT that may be contributing to cancer immunity. Furthermore, while our investigation revealed that PDT-induced ICD produces adjuvanticity, the effect of the resulting ICD on antigenicity is unknown. To investigate such PDT-induced antigenicity, I suggest an integrated genomics and mass spectrometry strategy that effectively merges my work from chapter 3 with chapters 4 and 5.

The workflow [**Figure 6.2.1**] would involve the collection of PDT-treated tumors from male and female melanoma-bearing mice, along with their untreated counterparts. Utilizing a syngeneic B16F10 model will allow the transplantation of WT tumor cells into

GFP mice, or GFP inserted B16F10 cells into WT C57BL/6 mice, aiding the sorting of the cancer cell population from the TME. These samples can be processed for genomics as well as immunopeptidomics using mass spectrometry as described in Chapter 3. Utilizing whole-exome and RNA sequencing data from these samples as the reference in the *SpectMHC* approach to generate targeted MHC databases would enable the global assessment of TAAs and TSAs.[764] Combining this with whole-genome sequencing rather than whole-exome sequencing would also account for non-canonical and cryptic peptides, which have been discovered in melanoma tumors.[765,766] Distinguishing the peptides that are elevated in PDT-treated tumors compared to untreated tumors would provide insights on PDT-induced antigenicity and help us comprehend PDT's potential to modify the antigenic landscape of cancer cells.

Functional validation using *ex vivo* experiments is required to dissect specific T cell responses against these antigens. T cell activation and proliferation studies that include co-culture of splenocytes obtained from PDT-treated mice with the synthesized antigens followed by evaluation of proliferation and production of cytokines such as IFNγ and TNFα would aid in identifying functionally relevant peptides. Peptides that elicit T cell activation might subsequently be employed to create antigen-specific tetramers or pentamers capable of detecting antigen-specific T cells. Combining such tetramers with additional activation and inhibitory markers for flow cytometry techniques would reveal the phenotypes of these antigen-specific cells at the tumor site as well as lymphoid organs. Indeed, our lab and others have previously reported the significance of therapy-induced antigenicity and antigen-specific immune responses in cancer.[224,225,767–770]

Overall, this research would help us better understand the influence of PDT on antigenicity and provide new insights into Ru-PDT-mediated antigen-specific immune

responses. The functionally verified tumor antigens can also be used to guide the development of peptide-based vaccines [**Figure 6.2.1**].[771]

**Note:** In the long term, it would be interesting to compare the relevance of peptides discovered by mass spectrometry to those not found by mass spectrometry but are detected via transcriptomics. Given the inherent limitations of mass spectrometry techniques [refer section **1.3.5.1.**] for identifying lowly abundant TSAs and cryptic peptides, this investigation could help us determine whether or not this methodology has diagnostic value.

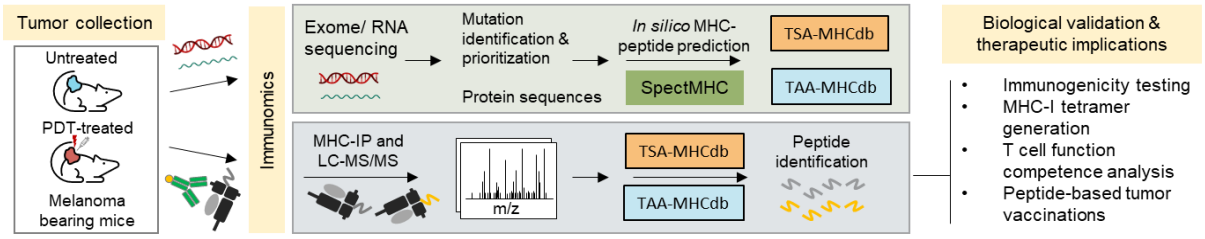


**Figure 6.2.1**. Integrated omics approaches to dissect PDT-induced antigen-specific CD8 T cells.

Tumors from untreated and PDT-treated melanoma-bearing mice will be collected and processed using the immunomics pipeline indicated above. Exome/RNA-sequencing on tumors will be performed to identify and prioritize mutations present at the DNA and transcript levels. RNA-seq data will be analyzed to determine dysregulated genes after PDT treatment. Selected mutations (altered protein sequences) and normal protein sequences will be used to construct MHC-specific targeted databases using *SpectMHC* pipeline. Tumor samples from untreated and PDT-treated mice will be processed through LC-MS/MS-based MHC ligand discovery per our previously published technique. The LC-MS/MS spectra will be compared to the targeted databases created in the previous step – Tumor specific antigen MHC database (TSA-MHCdb) and Tumor-

associated antigen MHC database (TAA-MHCdb). Immunogenicity of identified MHC-I peptides will be tested using T cell activation and proliferation assays. Peptides with high immunogenicity can be utilized to synthesize MHC-I tetramers, which can identify antigen-specific T cells and investigate their functional competence. Furthermore, peptides with high immunological activity can be evaluated as peptide-based tumor vaccines, either alone or in combination with other immunotherapies.

### *6.2.2. Global profiling of PDT-induced TME using single-cell technologies*

Cancer cells, blood vessels, extracellular matrix, immune cells, and signaling molecules interact and regulate each other in the tumor microenvironment, influencing sensitivity or resistance to therapy. As a result, I believe that a comprehensive knowledge of TME modulation upon PDT can help us better understand the mechanisms of action of the therapies and design better combination therapies.[772] While a few targeted studies found some immune populations pertinent for a couple of organic PSs (mainly Photofrin and ALA-PDT, section **1.6.3.4**), a global unbiased investigation is yet to be conducted on any PS. Furthermore, because of the unique nature of PSs and different mechanisms of action, discoveries from other PSs may not be relevant to Ru-PSs. Recent advances in single-cell isolation, indexing, and sequencing technologies have fundamentally altered our ability to conduct high dimension analysis.[773] Therefore, to characterize the TME after Ru-PDT, I propose utilizing single-cell sequencing technologies, specifically single-cell RNA sequencing (scRNA-seq), due to the broad applicability and generation of significantly higher data dimensions than traditional flow cytometry technologies. However, this data would still need to be validated using traditional approaches such as flow cytometry or histological analyses.

The workflow [**Figure 6.2.2**] for this study would include collecting tumors from PDT-treated and untreated melanoma tumor-bearing mice, dissociating the tumors into individual cells, and then sequencing and analyzing using scRNA-seq platforms. For the purpose of this section, it is ideal to use the cells without any further manipulations such as sorting or selecting for specific subsets. As such, this can be applied for both B16F10 and transgenic tumor models. This investigation can address a variety of questions from the perspectives of both cancer and the surrounding immune components.

**1)** The first and most important application is the characterization of immune cells and their phenotypes. While the current thesis focuses on the CD8 T cell and DC axis, anticancer immune responses encompass nearly every type of immune cell, with a positive or negative association to therapeutic outcomes. Single-cell transcriptomics can provide a global landscape of various immune cells as well as their subsets and functional phenotypes.[774,775] This will not only help us understand the various players involved in Ru-PDT-mediated anticancer immune responses but also identify immunosuppressive elements, which are important for understanding responsive vs. resistant mechanisms against the treatment. This information can further guide combination therapies with other cancer immunotherapies. Moreover, combining scRNA-seq with TCR sequencing would allow us to track specific clones of T cells relevant to treatment-induced cancer immunity.[774]

**2)** Molecular & immunogenic signatures in cancer. This part would require combining with other single-cell technologies such as single-cell proteomics. While our research and others have observed ICD induction, the complete range of PDT-induced ICD characteristics, as well as the mechanisms underlying such induction, remain unknown. As previously stated, each treatment appears to have a distinct ICD signature; thus, a comprehensive analysis could provide insights into such questions. Furthermore, we will

be able to discover cancer biomarkers, which will allow us to better predict the outcome of PDT and develop new combination targeted therapies. In the long run, researching the basic mechanisms of actions can help us comprehend the differences in outcomes between different PSs.

**3)** The heterogeneity of cancer cells before and after therapy. Tumor heterogeneity remains a clinical challenge due to its contribution to therapy resistance and poor prognosis.[776,777] Therefore, scRNA-seq based investigations will assist us to understand the evolution of melanoma, the emergence of resistant clones, and their transcriptional states and aid in the development of prospective combinations.[778]

**4)** Exploration of stromal components of the TME. Tumor stroma has been linked to promoting tumor growth, metastasis, and therapeutic resistance; hence, assessing the stromal landscape can assist us in inhibiting such processes.[779–782]

Understanding the diversity of TME and the associated phenotypes will help us understand how cancer cells, immune cells, and other components co-evolve during therapy and will guide future therapeutic combinations [**Figure 6.2.2**]. Moreover, such approaches could discover unique populations of cell types in the TME at both preclinical and clinical levels. While single-cell technologies are currently expensive, I believe that the clinical utility will soon become a viable option with the exponential advances in processing and analysis pipelines as seen in the previous decade.

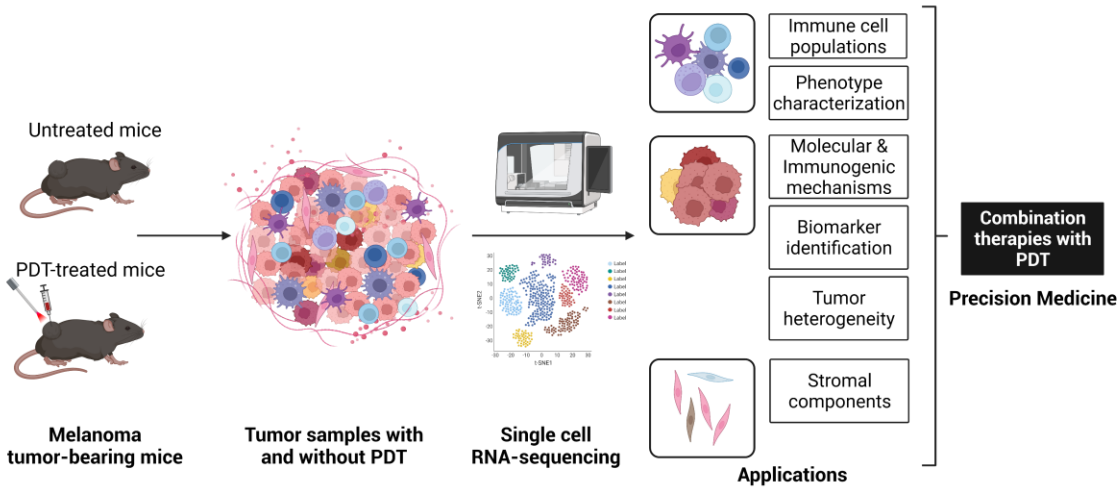


**Figure 6.2.2.** Elucidation of PDT-induced tumor microenvironment using single-cell technologies.

Tumors from untreated and PDT-treated melanoma-bearing mice will be collected and processed through a single-cell RNA-sequencing pipeline. As shown above, the resulting data can be analyzed to better understand various facets of the TME involving immune cells, heterogeneous tumor cells, and stromal components. In addition, the findings of this study can be used to guide the development of effective PDT-based combination treatments.

### *6.2.3. Combination Immunotherapies with PDT*

The ultimate goal of this project is to develop immunogenic photodynamic therapies with high clinical potential in order to progress from preclinical to clinical investigations. As such, our focus is to improve the antitumor efficacy of our novel Ru-PDTs and optimize therapeutic regimens that yield excellent outcomes for melanoma patients. The

development of combination therapies in recent years has dramatically changed the landscape of clinical oncology. Combination therapies seek to improve and broaden the therapeutic outcome by combining synergistic treatments that target different aspects of cancer, thereby potentiating each other.

While checkpoint inhibitors have unquestionably improved therapeutic outcomes for malignant melanomas, their efficacy as monotherapy is limited.[537] PDT could be an excellent option for combination therapy with ICIs due to its ability to induce immunogenic cell death and recruit and activate immune cells, especially T cells, to the tumor site. Furthermore, our analyses of DCs treated with culture supernatants from ML19B01 and ML19B02 PDT-treated melanoma cells revealed an increase in the expression of checkpoints PDL1 and CTLA4 (Chapter 5). Since the ICD vaccinations with cells treated with ML19B01 and ML19B02 PSs did not offer complete protection, it is possible that Ru-PDT efficacy is limited due to the induction of these checkpoint molecules in the TME, which may suppress T cell responses and lead to T cell exhaustion. Consequently, combining PDT with checkpoint inhibitors may provide a synergistic therapeutic approach in which PDT induces anticancer responses that lead to immune cell infiltration and ICIs reverse T cell inhibition and restore the antitumor potential of the PDT-induced T cell response. Overall, such a combination could also improve the cures of melanoma in preclinical and clinical models.

The workflow to demonstrate the efficacy of such combination therapy would start with a flow cytometry-based screening of the TME for key checkpoint molecules after PDT treatment. Following the identification of a specific target, such as PDL, PD1, LAG3, or CTLA4, a treatment regimen containing PDT and the appropriate ICI can be evaluated on melanoma tumor-bearing mice. Recent studies showed that combining PDT based on nanoparticles loaded with second-generation PSs and ICIs targeting

CTLA4 or PDL1 improved treatment outcomes in colorectal cancer models.[783,784] Thus, a similar strategy using our Ru-PSs could improve melanoma therapeutic efficacy. Furthermore, global evaluations like the one recommended in section **6.2.2**. will guide other relevant combination therapies that could be investigated. Employing such synergistic and guided combinations could enhance the therapeutic outcome from PDT and provide a segue into clinical translation of our novel therapies for melanoma.

# BIBLIOGRAPHY


1. Oiseth SJ, Aziz MS. Cancer immunotherapy: a brief review of the history, possibilities, and challenges ahead. J Cancer Metastasis Treat. 2017 Oct 31;3:250–61. https://doi.org/10.20517/2394-4722.2017.41

2. Dobosz P, Dzieciątkowski T. The Intriguing History of Cancer Immunotherapy. Front Immunol. 2019;10:2965. https://doi.org/10.3389/fimmu.2019.02965

3. Old LJ, Clarke DA, Benacerraf B. Effect of Bacillus Calmette-Guerin infection on transplanted tumours in the mouse. Nature. 1959 Jul 25;184(Suppl 5):291–2. https://doi.org/10.1038/184291a0

4. Morales A, Eidinger D, Bruce AW. Intracavitary Bacillus Calmette-Guerin in the treatment of superficial bladder tumors. J Urol. 1976 Aug;116(2):180–3. https://doi.org/10.1016/s0022-5347(17)58737-6

5. Burnet FM. Immunological surveillance in neoplasia. Transplant Rev. 1971;7:3–25. https://doi.org/10.1111/j.1600-065x.1971.tb00461.x

6. Thomas L. On immunosurveillance in human cancer. Yale J Biol Med. 1982 Aug;55(3–4):329–33.

7. Shankaran V, Ikeda H, Bruce AT, White JM, Swanson PE, Old LJ, et al. IFNgamma and lymphocytes prevent primary tumour development and shape tumour immunogenicity. Nature. 2001 Apr 26;410(6832):1107–11. https://doi.org/10.1038/35074122

8. Schreiber RD, Old LJ, Smyth MJ. Cancer immunoediting: integrating immunity's roles in cancer suppression and promotion. Science. 2011 Mar 25;331(6024):1565–70. https://doi.org/10.1126/science.1203486

9. Vesely MD, Kershaw MH, Schreiber RD, Smyth MJ. Natural innate and adaptive immunity to cancer. Annu Rev Immunol. 2011;29:235–71. https://doi.org/10.1146/annurev-immunol-031210-101324

10. Dunn GP, Old LJ, Schreiber RD. The three Es of cancer immunoediting. Annu Rev Immunol. 2004;22:329–60. https://doi.org/10.1146/annurev.immunol.22.012703.104803

11. Hanahan D. Hallmarks of Cancer: New Dimensions. Cancer Discov. 2022 Jan;12(1):31–46. https://doi.org/10.1158/2159-8290.CD-21-1059

12. Kim R, Emi M, Tanabe K. Cancer immunoediting from immune surveillance to immune escape. Immunology. 2007 May;121(1):1–14. https://doi.org/10.1111/j.1365-2567.2007.02587.x

13. Chen DS, Mellman I. Oncology meets immunology: the cancer-immunity cycle. Immunity. 2013 Jul 25;39(1):1–10. https://doi.org/10.1016/j.immuni.2013.07.012

14. Zhang Y, Zhang Z. The history and advances in cancer immunotherapy: understanding the characteristics of tumor-infiltrating immune cells and their therapeutic implications. Cell Mol Immunol. 2020 Aug;17(8):807–21. https://doi.org/10.1038/s41423-020-0488-6

15. Huntington ND, Cursons J, Rautela J. The cancer-natural killer cell immunity cycle. Nat Rev Cancer. 2020 Aug;20(8):437–54. https://doi.org/10.1038/s41568-020-0272-z

16. Largeot A, Pagano G, Gonder S, Moussay E, Paggetti J. The B-side of Cancer Immunity: The Underrated Tune. Cells. 2019 May 13;8(5):E449. https://doi.org/10.3390/cells8050449

17. Bald T, Pedde A-M, Corvino D, Böttcher JP. The role of NK cell as central communicators in cancer immunity. Adv Immunol. 2020;147:61–88. https://doi.org/10.1016/bs.ai.2020.06.002

18. Tay RE, Richardson EK, Toh HC. Revisiting the role of CD4+ T cells in cancer immunotherapy-new insights into old paradigms. Cancer Gene Ther. 2021 Feb;28(1–2):5–17. https://doi.org/10.1038/s41417-020-0183-x

19. Jaillon S, Ponzetta A, Di Mitri D, Santoni A, Bonecchi R, Mantovani A. Neutrophil diversity and plasticity in tumour progression and therapy. Nat Rev Cancer. 2020 Sep;20(9):485–503. https://doi.org/10.1038/s41568-020-0281-y

20. Faget J, Peters S, Quantin X, Meylan E, Bonnefoy N. Neutrophils in the era of immune checkpoint blockade. J Immunother Cancer. 2021 Jul;9(7):e002242. https://doi.org/10.1136/jitc-2020-002242

21. Waldman AD, Fritz JM, Lenardo MJ. A guide to cancer immunotherapy: from T cell basic science to clinical practice. Nat Rev Immunol. 2020 Nov;20(11):651–68. https://doi.org/10.1038/s41577-020-0306-5

22. Kuby Immunology 8th Edition | Jenni Punt | Macmillan Learning [Internet]. [cited 2022 Jan 20]. Available from: https://store.macmillanlearning.com/ca/product/Kuby-Immunology/p/1464189781

23. Jr CAJ, Travers P, Walport M, Shlomchik MJ, Jr CAJ, Travers P, et al. Janeway's Immunobiology. 5th ed. Garland Science; 2001.

24. Fridman WH, Pagès F, Sautès-Fridman C, Galon J. The immune contexture in human tumours: impact on clinical outcome. Nat Rev Cancer. 2012 Mar 15;12(4):298–306. https://doi.org/10.1038/nrc3245

25. Clark WH, Elder DE, Guerry D, Braitman LE, Trock BJ, Schultz D, et al. Model predicting survival in stage I melanoma based on tumor progression. J Natl Cancer Inst. 1989 Dec 20;81(24):1893–904. https://doi.org/10.1093/jnci/81.24.1893

26. Zhang L, Conejo-Garcia JR, Katsaros D, Gimotty PA, Massobrio M, Regnani G, et al. Intratumoral T cells, recurrence, and survival in epithelial ovarian cancer. N Engl J Med. 2003 Jan 16;348(3):203–13. https://doi.org/10.1056/NEJMoa020177

27. Denkert C, von Minckwitz G, Darb-Esfahani S, Lederer B, Heppner BI, Weber KE, et al. Tumour-infiltrating lymphocytes and prognosis in different subtypes of breast cancer: a pooled analysis of 3771 patients treated with neoadjuvant therapy. Lancet Oncol. 2018 Jan;19(1):40–50. https://doi.org/10.1016/S1470-2045(17)30904-X

28. Bindea G, Mlecnik B, Tosolini M, Kirilovsky A, Waldner M, Obenauf AC, et al. Spatiotemporal dynamics of intratumoral immune cells reveal the immune landscape in human cancer. Immunity. 2013 Oct 17;39(4):782–95. https://doi.org/10.1016/j.immuni.2013.10.003

29. Mlecnik B, Bindea G, Angell HK, Maby P, Angelova M, Tougeron D, et al. Integrative Analyses of Colorectal Cancer Show Immunoscore Is a Stronger Predictor of Patient Survival Than Microsatellite Instability. Immunity. 2016 Mar 15;44(3):698–711. https://doi.org/10.1016/j.immuni.2016.02.025

30. Schalper KA, Brown J, Carvajal-Hausdorf D, McLaughlin J, Velcheti V, Syrigos KN, et al. Objective measurement and clinical significance of TILs in non-small cell lung cancer. J Natl Cancer Inst. 2015 Mar;107(3):dju435. https://doi.org/10.1093/jnci/dju435

31. Ding W, Xu X, Qian Y, Xue W, Wang Y, Du J, et al. Prognostic value of tumor-infiltrating lymphocytes in hepatocellular carcinoma: A meta-analysis. Medicine (Baltimore). 2018 Dec;97(50):e13301. https://doi.org/10.1097/MD.0000000000013301

32. Fridman WH, Galon J, Pagès F, Tartour E, Sautès-Fridman C, Kroemer G. Prognostic and predictive impact of intra- and peritumoral immune infiltrates. Cancer Res. 2011 Sep 1;71(17):5601–5. https://doi.org/10.1158/0008-5472.CAN-11-1316

33. Sharma P, Shen Y, Wen S, Yamada S, Jungbluth AA, Gnjatic S, et al. CD8 tumor-infiltrating lymphocytes are predictive of survival in muscle-invasive urothelial carcinoma. Proc Natl Acad Sci U S A. 2007 Mar 6;104(10):3967–72. https://doi.org/10.1073/pnas.0611618104

34. Kärjä V, Aaltomaa S, Lipponen P, Isotalo T, Talja M, Mokka R. Tumour-infiltrating lymphocytes: A prognostic factor of PSA-free survival in patients with local prostate carcinoma treated by radical prostatectomy. Anticancer Res. 2005 Dec;25(6C):4435–8.

35. Fukunaga A, Miyamoto M, Cho Y, Murakami S, Kawarada Y, Oshikiri T, et al. CD8+ tumor-infiltrating lymphocytes together with CD4+ tumor-infiltrating lymphocytes and dendritic cells improve the prognosis of patients with pancreatic adenocarcinoma. Pancreas. 2004 Jan;28(1):e26-31. https://doi.org/10.1097/00006676-200401000-00023

36. Thorsson V, Gibbs DL, Brown SD, Wolf D, Bortone DS, Ou Yang T-H, et al. The Immune Landscape of Cancer. Immunity. 2018 Apr 17;48(4):812-830.e14. https://doi.org/10.1016/j.immuni.2018.03.023

37. Mami-Chouaib F, Echchakir H, Dorothée G, Vergnon I, Chouaib S. Antitumor cytotoxic T-lymphocyte response in human lung carcinoma: identification of a tumor-associated antigen. Immunol Rev. 2002 Oct;188:114–21. https://doi.org/10.1034/j.1600-065x.2002.18810.x

38. Shibuya TY, Nugyen N, McLaren CE, Li K-T, Wei W-Z, Kim S, et al. Clinical significance of poor CD3 response in head and neck cancer. Clin Cancer Res Off J Am Assoc Cancer Res. 2002 Mar;8(3):745–51.

39. Mackensen A, Ferradini L, Carcelain G, Triebel F, Faure F, Viel S, et al. Evidence for in situ amplification of cytotoxic T-lymphocytes with antitumor activity in a human regressive melanoma. Cancer Res. 1993 Aug 1;53(15):3569–73.

40. van Rooij N, van Buuren MM, Philips D, Velds A, Toebes M, Heemskerk B, et al. Tumor exome analysis reveals neoantigen-specific T-cell reactivity in an ipilimumab-responsive melanoma. J Clin Oncol Off J Am Soc Clin Oncol. 2013 Nov 10;31(32):e439-442. https://doi.org/10.1200/JCO.2012.47.7521

41. Robbins PF, Lu Y-C, El-Gamil M, Li YF, Gross C, Gartner J, et al. Mining exomic sequencing data to identify mutated antigens recognized by adoptively transferred tumor-reactive T cells. Nat Med. 2013 Jun;19(6):747–52. https://doi.org/10.1038/nm.3161

42. Dudley ME, Wunderlich JR, Robbins PF, Yang JC, Hwu P, Schwartzentruber DJ, et al. Cancer regression and autoimmunity in patients after clonal repopulation with antitumor lymphocytes. Science. 2002 Oct 25;298(5594):850–4. https://doi.org/10.1126/science.1076514

43. Dudley ME, Yang JC, Sherry R, Hughes MS, Royal R, Kammula U, et al. Adoptive cell therapy for patients with metastatic melanoma: evaluation of intensive myeloablative chemoradiation preparative regimens. J Clin Oncol Off J Am Soc Clin Oncol. 2008 Nov 10;26(32):5233–9. https://doi.org/10.1200/JCO.2008.16.5449

44. Besser MJ, Shapira-Frommer R, Treves AJ, Zippel D, Itzhaki O, Hershkovitz L, et al. Clinical responses in a phase II study using adoptive transfer of short-term cultured tumor infiltration lymphocytes in metastatic melanoma patients. Clin Cancer Res Off J Am Assoc Cancer Res. 2010 May 1;16(9):2646–55. https://doi.org/10.1158/1078-0432.CCR-10-0041

45. Verdegaal EME, de Miranda NFCC, Visser M, Harryvan T, van Buuren MM, Andersen RS, et al. Neoantigen landscape dynamics during human melanoma-T cell interactions. Nature. 2016 Aug 4;536(7614):91–5. https://doi.org/10.1038/nature18945

46. Galon J, Costes A, Sanchez-Cabo F, Kirilovsky A, Mlecnik B, Lagorce-Pagès C, et al. Type, density, and location of immune cells within human colorectal tumors predict clinical outcome. Science. 2006 Sep 29;313(5795):1960–4. https://doi.org/10.1126/science.1129139

47. Galon J, Mlecnik B, Bindea G, Angell HK, Berger A, Lagorce C, et al. Towards the introduction of the “Immunoscore” in the classification of malignant tumours. J Pathol. 2014 Jan;232(2):199–209. https://doi.org/10.1002/path.4287

48. Kirilovsky A, Marliot F, El Sissy C, Haicheur N, Galon J, Pagès F. Rational bases for the use of the Immunoscore in routine clinical settings as a prognostic and predictive biomarker in cancer patients. Int Immunol. 2016 Aug;28(8):373–82. https://doi.org/10.1093/intimm/dxw021

49. Fridman WH, Zitvogel L, Sautès-Fridman C, Kroemer G. The immune contexture in cancer prognosis and treatment. Nat Rev Clin Oncol. 2017 Dec;14(12):717–34. https://doi.org/10.1038/nrclinonc.2017.101

50. Raskov H, Orhan A, Christensen JP, Gögenur I. Cytotoxic CD8+ T cells in cancer and cancer immunotherapy. Br J Cancer. 2021 Jan;124(2):359–67. https://doi.org/10.1038/s41416-020-01048-4

51. Tai Y, Wang Q, Korner H, Zhang L, Wei W. Molecular Mechanisms of T Cells Activation by Dendritic Cells in Autoimmune Diseases. Front Pharmacol. 2018;9:642. https://doi.org/10.3389/fphar.2018.00642

52. Mak TW, Saunders ME. 14 - T Cell Activation. In: Mak TW, Saunders ME, editors. The Immune Response [Internet]. Burlington: Academic Press; 2006 [cited 2022 Jan 21]. p. 373–401. Available from: https://www.sciencedirect.com/science/article/pii/B9780120884513500168https://doi.org/10.1016/B978-012088451-3.50016-8

53. Peterson EJ, Maltzman JS. 12 - T-Cell Activation and Tolerance. In: Rich RR, Fleisher TA, Shearer WT, Schroeder HW, Frew AJ, Weyand CM, editors. Clinical Immunology (Fifth Edition) [Internet]. London: Elsevier; 2019 [cited 2022 Jan 21]. p. 183-196.e1. Available from: https://www.sciencedirect.com/science/article/pii/B9780702068966000120https://doi.org/10.1016/B978-0-7020-6896-6.00012-0

54. Curtsinger JM, Mescher MF. Inflammatory cytokines as a third signal for T cell activation. Curr Opin Immunol. 2010 Jun;22(3):333–40. https://doi.org/10.1016/j.coi.2010.02.013

55. Martínez-Lostao L, Anel A, Pardo J. How Do Cytotoxic Lymphocytes Kill Cancer Cells? Clin Cancer Res Off J Am Assoc Cancer Res. 2015 Nov 15;21(22):5047–56. https://doi.org/10.1158/1078-0432.CCR-15-0685

56. Propper DJ, Chao D, Braybrooke JP, Bahl P, Thavasu P, Balkwill F, et al. Low-dose IFN-gamma induces tumor MHC expression in metastatic malignant melanoma. Clin Cancer Res Off J Am Assoc Cancer Res. 2003 Jan;9(1):84–92.

57. Zhang S, Kohli K, Black RG, Yao L, Spadinger SM, He Q, et al. Systemic Interferon-γ Increases MHC Class I Expression and T-cell Infiltration in Cold Tumors: Results of a Phase 0 Clinical Trial. Cancer Immunol Res. 2019 Aug;7(8):1237–43. https://doi.org/10.1158/2326-6066.CIR-18-0940

58. Leko V, Rosenberg SA. Identifying and Targeting Human Tumor Antigens for T Cell-Based Immunotherapy of Solid Tumors. Cancer Cell. 2020 Oct 12;38(4):454–72. https://doi.org/10.1016/j.ccell.2020.07.013

59. Lee MY, Jeon JW, Sievers C, Allen CT. Antigen processing and presentation in cancer immunotherapy. J Immunother Cancer. 2020 Aug;8(2):e001111. https://doi.org/10.1136/jitc-2020-001111

60. Neefjes J, Jongsma MLM, Paul P, Bakke O. Towards a systems understanding of MHC class I and MHC class II antigen presentation. Nat Rev Immunol. 2011 Nov 11;11(12):823–36. https://doi.org/10.1038/nri3084

61. Charles A Janeway J, Travers P, Walport M, Shlomchik MJ. The major histocompatibility complex and its functions. Immunobiol Immune Syst Health Dis 5th Ed [Internet]. 2001 [cited 2022 Jan 22]; Available from: https://www.ncbi.nlm.nih.gov/books/NBK27156/

62. Larché M. Determining MHC restriction of T-cell responses. Methods Mol Med. 2008;138:57–72. https://doi.org/10.1007/978-1-59745-366-0_6

63. Zareie P, Farenc C, La Gruta NL. MHC Restriction: Where Are We Now? Viral Immunol. 2020 Apr;33(3):179–87. https://doi.org/10.1089/vim.2019.0195

64. La Gruta NL, Gras S, Daley SR, Thomas PG, Rossjohn J. Understanding the drivers of MHC restriction of T cell receptors. Nat Rev Immunol. 2018 Jul;18(7):467–78. https://doi.org/10.1038/s41577-018-0007-5

65. Hewitt EW. The MHC class I antigen presentation pathway: strategies for viral immune evasion. Immunology. 2003 Oct;110(2):163–9. https://doi.org/10.1046/j.1365-2567.2003.01738.x

66. Mpakali A, Stratikos E. The Role of Antigen Processing and Presentation in Cancer and the Efficacy of Immune Checkpoint Inhibitor Immunotherapy. Cancers. 2021 Jan 4;13(1):E134. https://doi.org/10.3390/cancers13010134

67. Cruz FM, Colbert JD, Merino E, Kriegsman BA, Rock KL. The Biology and Underlying Mechanisms of Cross-Presentation of Exogenous Antigens on MHC-I Molecules. Annu Rev Immunol. 2017 Apr 26;35:149–76. https://doi.org/10.1146/annurev-immunol-041015-055254

68. Joffre OP, Segura E, Savina A, Amigorena S. Cross-presentation by dendritic cells. Nat Rev Immunol. 2012 Jul 13;12(8):557–69. https://doi.org/10.1038/nri3254

69. Blankenstein T, Coulie PG, Gilboa E, Jaffee EM. The determinants of tumour immunogenicity. Nat Rev Cancer. 2012 Mar 1;12(4):307–13. https://doi.org/10.1038/nrc3246

70. Ilyas S, Yang JC. Landscape of Tumor Antigens in T Cell Immunotherapy. J Immunol Baltim Md 1950. 2015 Dec 1;195(11):5117–22. https://doi.org/10.4049/jimmunol.1501657

71. Minati R, Perreault C, Thibault P. A Roadmap Toward the Definition of Actionable Tumor-Specific Antigens. Front Immunol. 2020;11:583287. https://doi.org/10.3389/fimmu.2020.583287

72. Jhunjhunwala S, Hammer C, Delamarre L. Antigen presentation in cancer: insights into tumour immunogenicity and immune evasion. Nat Rev Cancer. 2021 May;21(5):298–312. https://doi.org/10.1038/s41568-021-00339-z

73. Smith CC, Selitsky SR, Chai S, Armistead PM, Vincent BG, Serody JS. Alternative tumour-specific antigens. Nat Rev Cancer. 2019 Aug;19(8):465–78. https://doi.org/10.1038/s41568-019-0162-4

74. Bezu L, Kepp O, Cerrato G, Pol J, Fucikova J, Spisek R, et al. Trial watch: Peptide-based vaccines in anticancer therapy. Oncoimmunology. 2018;7(12):e1511506. https://doi.org/10.1080/2162402X.2018.1511506

75. Coulie PG, Van den Eynde BJ, van der Bruggen P, Boon T. Tumour antigens recognized by T lymphocytes: at the core of cancer immunotherapy. Nat Rev Cancer. 2014 Feb;14(2):135–46. https://doi.org/10.1038/nrc3670

76. Kirkin AF, Dzhandzhugazyan KN, Guldberg P, Fang JJ, Andersen RS, Dahl C, et al. Adoptive cancer immunotherapy using DNA-demethylated T helper cells as antigen-presenting cells. Nat Commun. 2018 Mar 6;9(1):785. https://doi.org/10.1038/s41467-018-03217-9

77. Simpson AJG, Caballero OL, Jungbluth A, Chen Y-T, Old LJ. Cancer/testis antigens, gametogenesis and cancer. Nat Rev Cancer. 2005 Aug;5(8):615–25. https://doi.org/10.1038/nrc1669

78. Gilboa E. The makings of a tumor rejection antigen. Immunity. 1999 Sep;11(3):263–70. https://doi.org/10.1016/s1074-7613(00)80101-6

79. Stone JD, Harris DT, Kranz DM. TCR affinity for p/MHC formed by tumor antigens that are self-proteins: impact on efficacy and toxicity. Curr Opin Immunol. 2015 Apr;33:16–22. https://doi.org/10.1016/j.coi.2015.01.003

80. Galluzzi L, Vitale I, Warren S, Adjemian S, Agostinis P, Martinez AB, et al. Consensus guidelines for the definition, detection and interpretation of immunogenic cell death. J Immunother Cancer. 2020 Mar;8(1). https://doi.org/10.1136/jitc-2019-000337

81. Schuster H, Peper JK, Bösmüller H-C, Röhle K, Backert L, Bilich T, et al. The immunopeptidomic landscape of ovarian carcinomas. Proc Natl Acad Sci U S A. 2017 Nov 14;114(46):E9942–51. https://doi.org/10.1073/pnas.1707658114

82. Long HM, Parsonage G, Fox CP, Lee SP. Immunotherapy for Epstein-Barr virus-associated malignancies. Drug News Perspect. 2010 May;23(4):221–8. https://doi.org/10.1358/dnp.2010.23.4.1439500

83. van der Burg SH, Melief CJM. Therapeutic vaccination against human papilloma virus induced malignancies. Curr Opin Immunol. 2011 Apr;23(2):252–7. https://doi.org/10.1016/j.coi.2010.12.010

84. Fujita Y, Rooney CM, Heslop HE. Adoptive cellular immunotherapy for viral diseases. Bone Marrow Transplant. 2008 Jan;41(2):193–8. https://doi.org/10.1038/sj.bmt.1705906

85. Ramos JC, Lossos IS. Newly emerging therapies targeting viral-related lymphomas. Curr Oncol Rep. 2011 Oct;13(5):416–26. https://doi.org/10.1007/s11912-011-0186-8

86. Zhang M, Fritsche J, Roszik J, Williams LJ, Peng X, Chiu Y, et al. RNA editing derived epitopes function as cancer antigens to elicit immune responses. Nat Commun. 2018 Sep 25;9(1):3919. https://doi.org/10.1038/s41467-018-06405-9

87. Mylonas R, Beer I, Iseli C, Chong C, Pak H-S, Gfeller D, et al. Estimating the Contribution of Proteasomal Spliced Peptides to the HLA-I Ligandome. Mol Cell Proteomics MCP. 2018 Dec;17(12):2347–57. https://doi.org/10.1074/mcp.RA118.000877

88. Hanada K-I, Yewdell JW, Yang JC. Immune recognition of a human renal cancer antigen through post-translational protein splicing. Nature. 2004 Jan 15;427(6971):252–6. https://doi.org/10.1038/nature02240

89. Liepe J, Marino F, Sidney J, Jeko A, Bunting DE, Sette A, et al. A large fraction of HLA class I ligands are proteasome-generated spliced peptides. Science. 2016 Oct 21;354(6310):354–8. https://doi.org/10.1126/science.aaf4384

90. Chong C, Müller M, Pak H, Harnett D, Huber F, Grun D, et al. Integrated proteogenomic deep sequencing and analytics accurately identify non-canonical peptides in tumor immunopeptidomes. Nat Commun. 2020 Mar 10;11(1):1293. https://doi.org/10.1038/s41467-020-14968-9

91. Sugawara S, Abo T, Kumagai K. A simple method to eliminate the antigenicity of surface class I MHC molecules from the membrane of viable cells by acid treatment at pH 3. J Immunol Methods. 1987 Jun 26;100(1–2):83–90. https://doi.org/10.1016/0022-1759(87)90175-x

92. Kuznetsov A, Voronina A, Govorun V, Arapidi G. Critical Review of Existing MHC I Immunopeptidome Isolation Methods. Mol Basel Switz. 2020 Nov 19;25(22):E5409. https://doi.org/10.3390/molecules25225409

93. Chong C, Coukos G, Bassani-Sternberg M. Identification of tumor antigens with immunopeptidomics. Nat Biotechnol. 2021 Oct 11; https://doi.org/10.1038/s41587-021-01038-8

94. Bassani-Sternberg M, Coukos G. Mass spectrometry-based antigen discovery for cancer immunotherapy. Curr Opin Immunol. 2016 Aug;41:9–17. https://doi.org/10.1016/j.coi.2016.04.005

95. Purcell AW, Ramarathinam SH, Ternette N. Mass spectrometry-based identification of MHC-bound peptides for immunopeptidomics. Nat Protoc. 2019 Jun;14(6):1687–707. https://doi.org/10.1038/s41596-019-0133-y

96. Bassani-Sternberg M, Pletscher-Frankild S, Jensen LJ, Mann M. Mass spectrometry of human leukocyte antigen class I peptidomes reveals strong effects of protein abundance and turnover on antigen presentation. Mol Cell Proteomics MCP. 2015 Mar;14(3):658–73. https://doi.org/10.1074/mcp.M114.042812

97. Pritchard AL, Hastie ML, Neller M, Gorman JJ, Schmidt CW, Hayward NK. Exploration of peptides bound to MHC class I molecules in melanoma. Pigment Cell Melanoma Res. 2015 May;28(3):281–94. https://doi.org/10.1111/pcmr.12357

98. Jarmalavicius S, Welte Y, Walden P. High immunogenicity of the human leukocyte antigen peptidomes of melanoma tumor cells. J Biol Chem. 2012 Sep 28;287(40):33401–11. https://doi.org/10.1074/jbc.M112.358903

99. Dutoit V, Herold-Mende C, Hilf N, Schoor O, Beckhove P, Bucher J, et al. Exploiting the glioblastoma peptidome to discover novel tumour-associated antigens for immunotherapy. Brain J Neurol. 2012 Apr;135(Pt 4):1042–54. https://doi.org/10.1093/brain/aws042

100. Krämer BF, Schoor O, Krüger T, Reichle C, Müller M, Weinschenk T, et al. MAGED4-expression in renal cell carcinoma and identification of an HLA-A*25-restricted MHC class I ligand from solid tumor tissue. Cancer Biol Ther. 2005 Sep;4(9):943–8. https://doi.org/10.4161/cbt.4.9.1907

101. Walter S, Weinschenk T, Stenzl A, Zdrojowy R, Pluzanska A, Szczylik C, et al. Multipeptide immune response to cancer vaccine IMA901 after single-dose cyclophosphamide associates with longer patient survival. Nat Med. 2012 Aug;18(8):1254–61. https://doi.org/10.1038/nm.2883

102. Ramakrishna V, Ross MM, Petersson M, Gatlin CC, Lyons CE, Miller CL, et al. Naturally occurring peptides associated with HLA-A2 in ovarian cancer cell lines identified by mass spectrometry are targets of HLA-A2-restricted cytotoxic T cells. Int Immunol. 2003 Jun;15(6):751–63. https://doi.org/10.1093/intimm/dxg074

103. Berlin C, Kowalewski DJ, Schuster H, Mirza N, Walz S, Handel M, et al. Mapping the HLA ligandome landscape of acute myeloid leukemia: a targeted approach toward peptide-based immunotherapy. Leukemia. 2015 Mar;29(3):647–59. https://doi.org/10.1038/leu.2014.233

104. Abelin JG, Keskin DB, Sarkizova S, Hartigan CR, Zhang W, Sidney J, et al. Mass Spectrometry Profiling of HLA-Associated Peptidomes in Mono-allelic Cells Enables More Accurate Epitope Prediction. Immunity. 2017 Feb 21;46(2):315–26. https://doi.org/10.1016/j.immuni.2017.02.007

105. Sarkizova S, Klaeger S, Le PM, Li LW, Oliveira G, Keshishian H, et al. A large peptidome dataset improves HLA class I epitope prediction across most of the human population. Nat Biotechnol. 2020 Feb;38(2):199–209. https://doi.org/10.1038/s41587-019-0322-9

106. Bassani-Sternberg M, Bräunlein E, Klar R, Engleitner T, Sinitcyn P, Audehm S, et al. Direct identification of clinically relevant neoepitopes presented on native human melanoma tissue by mass spectrometry. Nat Commun. 2016 Nov 21;7:13404. https://doi.org/10.1038/ncomms13404

107. Mommen GPM, Frese CK, Meiring HD, van Gaans-van den Brink J, de Jong APJM, van Els CACM, et al. Expanding the detectable HLA peptide repertoire using electron-transfer/higher-energy collision dissociation (EThcD). Proc Natl Acad Sci U S A. 2014 Mar 25;111(12):4507–12. https://doi.org/10.1073/pnas.1321458111

108. Marcilla M, Alpízar A, Lombardía M, Ramos-Fernandez A, Ramos M, Albar JP. Increased diversity of the HLA-B40 ligandome by the presentation of peptides phosphorylated at their main anchor residue. Mol Cell Proteomics MCP. 2014 Feb;13(2):462–74. https://doi.org/10.1074/mcp.M113.034314

109. Abelin JG, Trantham PD, Penny SA, Patterson AM, Ward ST, Hildebrand WH, et al. Complementary IMAC enrichment methods for HLA-associated phosphopeptide identification by mass spectrometry. Nat Protoc. 2015 Sep;10(9):1308–18. https://doi.org/10.1038/nprot.2015.086

110. Ostankovitch M, Altrich-Vanlith M, Robila V, Engelhard VH. N-glycosylation enhances presentation of a MHC class I-restricted epitope from tyrosinase. J Immunol Baltim Md 1950. 2009 Apr 15;182(8):4830–5. https://doi.org/10.4049/jimmunol.0802902

111. Marino F, Bern M, Mommen GPM, Leney AC, van Gaans-van den Brink JAM, Bonvin AMJJ, et al. Extended O-GlcNAc on HLA Class-I-Bound Peptides. J Am Chem Soc. 2015 Sep 2;137(34):10922–5. https://doi.org/10.1021/jacs.5b06586

112. Bouchie A, DeFrancesco L. Nature Biotechnology's academic spinouts of 2015. Nat Biotechnol. 2016 May 6;34(5):484–92. https://doi.org/10.1038/nbt.3564

113. Zhou C, Zhu C, Liu Q. Toward in silico Identification of Tumor Neoantigens in Immunotherapy. Trends Mol Med. 2019 Nov;25(11):980–92. https://doi.org/10.1016/j.molmed.2019.08.001

114. Richters MM, Xia H, Campbell KM, Gillanders WE, Griffith OL, Griffith M. Best practices for bioinformatic characterization of neoantigens for clinical utility. Genome Med. 2019 Aug 28;11(1):56. https://doi.org/10.1186/s13073-019-0666-2

115. Li L, Goedegebuure P, Mardis ER, Ellis MJC, Zhang X, Herndon JM, et al. Cancer genome sequencing and its implications for personalized cancer vaccines. Cancers. 2011 Nov 25;3(4):4191–211. https://doi.org/10.3390/cancers3044191

116. Rogers Y-H, Zhang C. Chapter 2 - Genomic Technologies in Medicine and Health: Past, Present, and Future. In: Kumar D, Antonarakis S, editors. Medical and Health Genomics [Internet]. Oxford: Academic Press; 2016 [cited 2022 Jan 23]. p. 15–28. Available from: https://www.sciencedirect.com/science/article/pii/B9780124201965000022https://doi.org/10.1016/B978-0-12-420196-5.00002-2

117. Khodadoust MS, Alizadeh AA. Tumor antigen discovery through translation of the cancer genome. Immunol Res. 2014 May;58(2–3):292–9. https://doi.org/10.1007/s12026-014-8505-4

118. Peters B, Nielsen M, Sette A. T Cell Epitope Predictions. Annu Rev Immunol. 2020;38(1):123–45. https://doi.org/10.1146/annurev-immunol-082119-124838

119. Sidney J, Peters B, Sette A. Epitope prediction and identification- adaptive T cell responses in humans. Semin Immunol. 2020 Aug;50:101418. https://doi.org/10.1016/j.smim.2020.101418

120. Backert L, Kohlbacher O. Immunoinformatics and epitope prediction in the age of genomic medicine. Genome Med. 2015 Nov 20;7:119. https://doi.org/10.1186/s13073-015-0245-0

121. Lundegaard C, Lund O, Buus S, Nielsen M. Major histocompatibility complex class I binding predictions as a tool in epitope discovery. Immunology. 2010 Jul;130(3):309–18. https://doi.org/10.1111/j.1365-2567.2010.03300.x

122. Soria-Guerra RE, Nieto-Gomez R, Govea-Alonso DO, Rosales-Mendoza S. An overview of bioinformatics tools for epitope prediction: implications on vaccine development. J Biomed Inform. 2015 Feb;53:405–14. https://doi.org/10.1016/j.jbi.2014.11.003

123. Nielsen M, Andreatta M. NetMHCpan-3.0; improved prediction of binding to MHC class I molecules integrating information from multiple receptor and peptide length datasets. Genome Med. 2016 Mar 30;8(1):33. https://doi.org/10.1186/s13073-016-0288-x

124. Reynisson B, Alvarez B, Paul S, Peters B, Nielsen M. NetMHCpan-4.1 and NetMHCIIpan-4.0: improved predictions of MHC antigen presentation by concurrent motif deconvolution and integration of MS MHC eluted ligand data. Nucleic Acids Res. 2020 Jul 2;48(W1):W449–54. https://doi.org/10.1093/nar/gkaa379

125. Chowell D, Morris LGT, Grigg CM, Weber JK, Samstein RM, Makarov V, et al. Patient HLA class I genotype influences cancer response to checkpoint blockade immunotherapy. Science. 2018 Feb 2;359(6375):582–7. https://doi.org/10.1126/science.aao4572

126. Albitar M, Johnson M, Do KA, Day A, Jilani I, Pierce S, et al. Levels of soluble HLA-I and beta2M in patients with acute myeloid leukemia and advanced myelodysplastic syndrome: association with clinical behavior and outcome of induction therapy. Leukemia. 2007 Mar;21(3):480–8. https://doi.org/10.1038/sj.leu.2404506

127. Thompson JC, Davis C, Deshpande C, Hwang W-T, Jeffries S, Huang A, et al. Gene signature of antigen processing and presentation machinery predicts response to checkpoint blockade in non-small cell lung cancer (NSCLC) and melanoma. J Immunother Cancer. 2020 Oct;8(2):e000974. https://doi.org/10.1136/jitc-2020-000974

128. Wang S, He Z, Wang X, Li H, Liu X-S. Antigen presentation and tumor immunogenicity in cancer immunotherapy response prediction. eLife. 2019 Nov 26;8:e49020. https://doi.org/10.7554/eLife.49020

129. Schaafsma E, Fugle CM, Wang X, Cheng C. Pan-cancer association of HLA gene expression with cancer prognosis and immunotherapy efficacy. Br J Cancer. 2021 Aug;125(3):422–32. https://doi.org/10.1038/s41416-021-01400-2

130. Goeppert B, Frauenschuh L, Zucknick M, Roessler S, Mehrabi A, Hafezi M, et al. Major histocompatibility complex class I expression impacts on patient survival and type and density of immune cells in biliary tract cancer. Br J Cancer. 2015 Nov 3;113(9):1343–9. https://doi.org/10.1038/bjc.2015.337

131. Spranger S, Gajewski TF. Mechanisms of Tumor Cell–Intrinsic Immune Evasion. Annu Rev Cancer Biol. 2018;2(1):213–28. https://doi.org/10.1146/annurev-cancerbio-030617-050606

132. Dhatchinamoorthy K, Colbert JD, Rock KL. Cancer Immune Evasion Through Loss of MHC Class I Antigen Presentation. Front Immunol. 2021;12:636568. https://doi.org/10.3389/fimmu.2021.636568

133. Beatty GL, Gladney WL. Immune escape mechanisms as a guide for cancer immunotherapy. Clin Cancer Res Off J Am Assoc Cancer Res. 2015 Feb 15;21(4):687–92. https://doi.org/10.1158/1078-0432.CCR-14-1860

134. Pardoll DM. The blockade of immune checkpoints in cancer immunotherapy. Nat Rev Cancer. 2012 Mar 22;12(4):252–64. https://doi.org/10.1038/nrc3239

135. Ballas ZK. The 2018 Nobel Prize in Physiology or Medicine: An exemplar of bench to bedside in immunology. J Allergy Clin Immunol. 2018 Dec;142(6):1752–3. https://doi.org/10.1016/j.jaci.2018.10.021

136. Brunet JF, Denizot F, Luciani MF, Roux-Dosseto M, Suzan M, Mattei MG, et al. A new member of the immunoglobulin superfamily--CTLA-4. Nature. 1987 Jul 16;328(6127):267–70. https://doi.org/10.1038/328267a0

137. Dariavach P, Mattéi MG, Golstein P, Lefranc MP. Human Ig superfamily CTLA-4 gene: chromosomal localization and identity of protein sequence between murine and human CTLA-4 cytoplasmic domains. Eur J Immunol. 1988 Dec;18(12):1901–5. https://doi.org/10.1002/eji.1830181206

138. Harper K, Balzano C, Rouvier E, Mattéi MG, Luciani MF, Golstein P. CTLA-4 and CD28 activated lymphocyte molecules are closely related in both mouse and human as to sequence, message expression, gene structure, and chromosomal location. J Immunol Baltim Md 1950. 1991 Aug 1;147(3):1037–44.

139. Korman AJ, Garrett-Thomson SC, Lonberg N. The foundations of immune checkpoint blockade and the ipilimumab approval decennial. Nat Rev Drug Discov. 2021 Dec 22; https://doi.org/10.1038/s41573-021-00345-8

140. Linsley PS, Greene JL, Brady W, Bajorath J, Ledbetter JA, Peach R. Human B7-1 (CD80) and B7-2 (CD86) bind with similar avidities but distinct kinetics to CD28 and CTLA-4 receptors. Immunity. 1994 Dec;1(9):793–801. https://doi.org/10.1016/s1074-7613(94)80021-9

141. Pentcheva-Hoang T, Egen JG, Wojnoonski K, Allison JP. B7-1 and B7-2 selectively recruit CTLA-4 and CD28 to the immunological synapse. Immunity. 2004 Sep;21(3):401–13. https://doi.org/10.1016/j.immuni.2004.06.017

142. Schneider H, Downey J, Smith A, Zinselmeyer BH, Rush C, Brewer JM, et al. Reversal of the TCR stop signal by CTLA-4. Science. 2006 Sep 29;313(5795):1972–5. https://doi.org/10.1126/science.1131078

143. Ishida Y, Agata Y, Shibahara K, Honjo T. Induced expression of PD-1, a novel member of the immunoglobulin gene superfamily, upon programmed cell death. EMBO J. 1992 Nov;11(11):3887–95.

144. Agata Y, Kawasaki A, Nishimura H, Ishida Y, Tsubata T, Yagita H, et al. Expression of the PD-1 antigen on the surface of stimulated mouse T and B lymphocytes. Int Immunol. 1996 May;8(5):765–72. https://doi.org/10.1093/intimm/8.5.765

145. Nishimura H, Nose M, Hiai H, Minato N, Honjo T. Development of lupus-like autoimmune diseases by disruption of the PD-1 gene encoding an ITIM motif-carrying immunoreceptor. Immunity. 1999 Aug;11(2):141–51. https://doi.org/10.1016/s1074-7613(00)80089-8

146. Freeman GJ, Long AJ, Iwai Y, Bourque K, Chernova T, Nishimura H, et al. Engagement of the PD-1 immunoinhibitory receptor by a novel B7 family member leads to negative regulation of lymphocyte activation. J Exp Med. 2000 Oct 2;192(7):1027–34. https://doi.org/10.1084/jem.192.7.1027

147. Latchman Y, Wood CR, Chernova T, Chaudhary D, Borde M, Chernova I, et al. PD-L2 is a second ligand for PD-1 and inhibits T cell activation. Nat Immunol. 2001 Mar;2(3):261–8. https://doi.org/10.1038/85330

148. Keir ME, Butte MJ, Freeman GJ, Sharpe AH. PD-1 and its ligands in tolerance and immunity. Annu Rev Immunol. 2008;26:677–704. https://doi.org/10.1146/annurev.immunol.26.021607.090331

149. Francisco LM, Sage PT, Sharpe AH. The PD-1 pathway in tolerance and autoimmunity. Immunol Rev. 2010 Jul;236:219–42. https://doi.org/10.1111/j.1600-065X.2010.00923.x

150. Iwai Y, Ishida M, Tanaka Y, Okazaki T, Honjo T, Minato N. Involvement of PD-L1 on tumor cells in the escape from host immune system and tumor immunotherapy by PD-L1 blockade. Proc Natl Acad Sci U S A. 2002 Sep 17;99(19):12293–7. https://doi.org/10.1073/pnas.192461099

151. Willimsky G, Blankenstein T. Sporadic immunogenic tumours avoid destruction by inducing T-cell tolerance. Nature. 2005 Sep 1;437(7055):141–6. https://doi.org/10.1038/nature03954

152. Leach DR, Krummel MF, Allison JP. Enhancement of antitumor immunity by CTLA-4 blockade. Science. 1996 Mar 22;271(5256):1734–6. https://doi.org/10.1126/science.271.5256.1734

153. Pardoll D. Releasing the brakes on antitumor immune response. Science. 1996 Mar 22;271(5256):1691. https://doi.org/10.1126/science.271.5256.1691

154. Hodi FS, O'Day SJ, McDermott DF, Weber RW, Sosman JA, Haanen JB, et al. Improved survival with ipilimumab in patients with metastatic melanoma. N Engl J Med. 2010 Aug 19;363(8):711–23. https://doi.org/10.1056/NEJMoa1003466

155. Hellmann MD, Ciuleanu T-E, Pluzanski A, Lee JS, Otterson GA, Audigier-Valette C, et al. Nivolumab plus Ipilimumab in Lung Cancer with a High Tumor Mutational Burden. N Engl J Med. 2018 May 31;378(22):2093–104. https://doi.org/10.1056/NEJMoa1801946

156. Ledford H. Melanoma drug wins US approval. Nature. 2011 Mar 31;471(7340):561. https://doi.org/10.1038/471561a

157. Hirano F, Kaneko K, Tamura H, Dong H, Wang S, Ichikawa M, et al. Blockade of B7-H1 and PD-1 by monoclonal antibodies potentiates cancer therapeutic immunity. Cancer Res. 2005 Feb 1;65(3):1089–96.

158. Hargadon KM, Johnson CE, Williams CJ. Immune checkpoint blockade therapy for cancer: An overview of FDA-approved immune checkpoint inhibitors. Int Immunopharmacol. 2018 Sep;62:29–39. https://doi.org/10.1016/j.intimp.2018.06.001

159. Brahmer JR, Drake CG, Wollner I, Powderly JD, Picus J, Sharfman WH, et al. Phase I study of single-agent anti-programmed death-1 (MDX-1106) in refractory solid tumors: safety, clinical activity, pharmacodynamics, and immunologic correlates. J Clin Oncol Off J Am Soc Clin Oncol. 2010 Jul 1;28(19):3167–75. https://doi.org/10.1200/JCO.2009.26.7609

160. Gong J, Chehrazi-Raffle A, Reddi S, Salgia R. Development of PD-1 and PD-L1 inhibitors as a form of cancer immunotherapy: a comprehensive review of registration trials and future considerations. J Immunother Cancer. 2018 Jan 23;6(1):8. https://doi.org/10.1186/s40425-018-0316-z

161. Weber JS, D'Angelo SP, Minor D, Hodi FS, Gutzmer R, Neyns B, et al. Nivolumab versus chemotherapy in patients with advanced melanoma who progressed after anti-CTLA-4 treatment (CheckMate 037): a randomised, controlled, open-label, phase 3 trial. Lancet Oncol. 2015 Apr;16(4):375–84. https://doi.org/10.1016/S1470-2045(15)70076-8

162. Robert C, Schachter J, Long GV, Arance A, Grob JJ, Mortier L, et al. Pembrolizumab versus Ipilimumab in Advanced Melanoma. N Engl J Med. 2015 Jun 25;372(26):2521–32. https://doi.org/10.1056/NEJMoa1503093

163. Schachter J, Ribas A, Long GV, Arance A, Grob J-J, Mortier L, et al. Pembrolizumab versus ipilimumab for advanced melanoma: final overall survival results of a multicentre, randomised, open-label phase 3 study (KEYNOTE-006). Lancet Lond Engl. 2017 Oct 21;390(10105):1853–62. https://doi.org/10.1016/S0140-6736(17)31601-X

164. Weber J, Mandala M, Del Vecchio M, Gogas HJ, Arance AM, Cowey CL, et al. Adjuvant Nivolumab versus Ipilimumab in Resected Stage III or IV Melanoma. N Engl J Med. 2017 Nov 9;377(19):1824–35. https://doi.org/10.1056/NEJMoa1709030

165. Overman MJ, Lonardi S, Wong KYM, Lenz H-J, Gelsomino F, Aglietta M, et al. Durable Clinical Benefit With Nivolumab Plus Ipilimumab in DNA Mismatch Repair-Deficient/Microsatellite Instability-High Metastatic Colorectal Cancer. J Clin Oncol Off J Am Soc Clin Oncol. 2018 Mar 10;36(8):773–9. https://doi.org/10.1200/JCO.2017.76.9901

166. Motzer RJ, Penkov K, Haanen J, Rini B, Albiges L, Campbell MT, et al. Avelumab plus Axitinib versus Sunitinib for Advanced Renal-Cell Carcinoma. N Engl J Med. 2019 Mar 21;380(12):1103–15. https://doi.org/10.1056/NEJMoa1816047

167. Rosenberg SA, Packard BS, Aebersold PM, Solomon D, Topalian SL, Toy ST, et al. Use of tumor-infiltrating lymphocytes and interleukin-2 in the immunotherapy of patients with metastatic melanoma. A preliminary report. N Engl J Med. 1988 Dec 22;319(25):1676–80. https://doi.org/10.1056/NEJM198812223192527

168. Rosenberg SA, Yang JC, Sherry RM, Kammula US, Hughes MS, Phan GQ, et al. Durable complete responses in heavily pretreated patients with metastatic melanoma using T-cell transfer immunotherapy. Clin Cancer Res Off J Am Assoc Cancer Res. 2011 Jul 1;17(13):4550–7. https://doi.org/10.1158/1078-0432.CCR-11-0116

169. Perica K, Varela JC, Oelke M, Schneck J. Adoptive T cell immunotherapy for cancer. Rambam Maimonides Med J. 2015 Jan;6(1):e0004. https://doi.org/10.5041/RMMJ.10179

170. Labanieh L, Majzner RG, Mackall CL. Programming CAR-T cells to kill cancer. Nat Biomed Eng. 2018 Jun;2(6):377–91. https://doi.org/10.1038/s41551-018-0235-9

171. Neelapu SS, Locke FL, Bartlett NL, Lekakis LJ, Miklos DB, Jacobson CA, et al. Axicabtagene Ciloleucel CAR T-Cell Therapy in Refractory Large B-Cell Lymphoma. N Engl J Med. 2017 Dec 28;377(26):2531–44. https://doi.org/10.1056/NEJMoa1707447

172. Brentjens RJ, Davila ML, Riviere I, Park J, Wang X, Cowell LG, et al. CD19-targeted T cells rapidly induce molecular remissions in adults with chemotherapy-refractory acute lymphoblastic leukemia. Sci Transl Med. 2013 Mar 20;5(177):177ra38. https://doi.org/10.1126/scitranslmed.3005930

173. Park JH, Rivière I, Gonen M, Wang X, Sénéchal B, Curran KJ, et al. Long-Term Follow-up of CD19 CAR Therapy in Acute Lymphoblastic Leukemia. N Engl J Med. 2018 Feb 1;378(5):449–59. https://doi.org/10.1056/NEJMoa1709919

174. Melenhorst JJ, Chen GM, Wang M, Porter DL, Chen C, Collins MA, et al. Decade-long leukaemia remissions with persistence of CD4+ CAR T cells. Nature. 2022 Feb 2; https://doi.org/10.1038/s41586-021-04390-6

175. Beatty GL, Haas AR, Maus MV, Torigian DA, Soulen MC, Plesa G, et al. Mesothelin-specific chimeric antigen receptor mRNA-engineered T cells induce anti-tumor activity in solid malignancies. Cancer Immunol Res. 2014 Feb;2(2):112–20. https://doi.org/10.1158/2326-6066.CIR-13-0170

176. Kershaw MH, Westwood JA, Parker LL, Wang G, Eshhar Z, Mavroukakis SA, et al. A phase I study on adoptive immunotherapy using gene-modified T cells for ovarian cancer. Clin Cancer Res Off J Am Assoc Cancer Res. 2006 Oct 15;12(20 Pt 1):6106–15. https://doi.org/10.1158/1078-0432.CCR-06-1183

177. Park JR, Digiusto DL, Slovak M, Wright C, Naranjo A, Wagner J, et al. Adoptive transfer of chimeric antigen receptor re-directed cytolytic T lymphocyte clones in patients with neuroblastoma. Mol Ther J Am Soc Gene Ther. 2007 Apr;15(4):825–33. https://doi.org/10.1038/sj.mt.6300104

178. Milone MC, Xu J, Chen S-J, Collins MA, Zhou J, Powell DJ, et al. Engineering enhanced CAR T-cells for improved cancer therapy. Nat Cancer. 2021 Aug;2(8):780–93. https://doi.org/10.1038/s43018-021-00241-5

179. Wagner DL, Fritsche E, Pulsipher MA, Ahmed N, Hamieh M, Hegde M, et al. Immunogenicity of CAR T cells in cancer therapy. Nat Rev Clin Oncol. 2021 Jun;18(6):379–93. https://doi.org/10.1038/s41571-021-00476-2

180. Finn OJ. The dawn of vaccines for cancer prevention. Nat Rev Immunol. 2018 Mar;18(3):183–94. https://doi.org/10.1038/nri.2017.140

181. Chang M-H, You S-L, Chen C-J, Liu C-J, Lai M-W, Wu T-C, et al. Long-term Effects of Hepatitis B Immunization of Infants in Preventing Liver Cancer. Gastroenterology. 2016 Sep;151(3):472-480.e1. https://doi.org/10.1053/j.gastro.2016.05.048

182. Guo T, Eisele DW, Fakhry C. The potential impact of prophylactic human papillomavirus vaccination on oropharyngeal cancer. Cancer. 2016 Aug 1;122(15):2313–23. https://doi.org/10.1002/cncr.29992

183. Kenter GG, Welters MJP, Valentijn ARPM, Lowik MJG, Berends-van der Meer DMA, Vloon APG, et al. Vaccination against HPV-16 oncoproteins for vulvar intraepithelial neoplasia. N Engl J Med. 2009 Nov 5;361(19):1838–47. https://doi.org/10.1056/NEJMoa0810097

184. Finn OJ, Edwards RP. Human papillomavirus vaccine for cancer prevention. N Engl J Med. 2009 Nov 5;361(19):1899–901. https://doi.org/10.1056/NEJMe0907480

185. Saxena M, van der Burg SH, Melief CJM, Bhardwaj N. Therapeutic cancer vaccines. Nat Rev Cancer. 2021 Jun;21(6):360–78. https://doi.org/10.1038/s41568-021-00346-0

186. Heicappell R, Schirrmacher V, von Hoegen P, Ahlert T, Appelhans B. Prevention of metastatic spread by postoperative immunotherapy with virally modified autologous tumor cells. I. Parameters for optimal therapeutic effects. Int J Cancer. 1986 Apr 15;37(4):569–77. https://doi.org/10.1002/ijc.2910370416

187. Plaksin D, Porgador A, Vadai E, Feldman M, Schirrmacher V, Eisenbach L. Effective anti-metastatic melanoma vaccination with tumor cells transfected with MHC genes and/or infected with Newcastle disease virus (NDV). Int J Cancer. 1994 Dec 15;59(6):796–801. https://doi.org/10.1002/ijc.2910590615

188. Kantoff PW, Higano CS, Shore ND, Berger ER, Small EJ, Penson DF, et al. Sipuleucel-T immunotherapy for castration-resistant prostate cancer. N Engl J Med. 2010 Jul 29;363(5):411–22. https://doi.org/10.1056/NEJMoa1001294

189. Sondak VK, Sabel MS, Mulé JJ. Allogeneic and autologous melanoma vaccines: where have we been and where are we going? Clin Cancer Res Off J Am Assoc Cancer Res. 2006 Apr 1;12(7 Pt 2):2337s–41s. https://doi.org/10.1158/1078-0432.CCR-05-2555

190. Guo C, Manjili MH, Subjeck JR, Sarkar D, Fisher PB, Wang X-Y. Therapeutic cancer vaccines: past, present, and future. Adv Cancer Res. 2013;119:421–75. https://doi.org/10.1016/B978-0-12-407190-2.00007-1

191. Srivatsan S, Patel JM, Bozeman EN, Imasuen IE, He S, Daniels D, et al. Allogeneic tumor cell vaccines: the promise and limitations in clinical trials. Hum Vaccines Immunother. 2014;10(1):52–63. https://doi.org/10.4161/hv.26568

192. Hu Z, Ott PA, Wu CJ. Towards personalized, tumour-specific, therapeutic vaccines for cancer. Nat Rev Immunol. 2018 Mar;18(3):168–82. https://doi.org/10.1038/nri.2017.131

193. Blass E, Ott PA. Advances in the development of personalized neoantigen-based therapeutic cancer vaccines. Nat Rev Clin Oncol. 2021 Apr;18(4):215–29. https://doi.org/10.1038/s41571-020-00460-2

194. Ott PA, Hu Z, Keskin DB, Shukla SA, Sun J, Bozym DJ, et al. An immunogenic personal neoantigen vaccine for patients with melanoma. Nature. 2017 Jul 13;547(7662):217–21. https://doi.org/10.1038/nature22991

195. Hu Z, Leet DE, Allesøe RL, Oliveira G, Li S, Luoma AM, et al. Personal neoantigen vaccines induce persistent memory T cell responses and epitope spreading in patients with melanoma. Nat Med. 2021 Mar;27(3):515–25. https://doi.org/10.1038/s41591-020-01206-4

196. Keskin DB, Anandappa AJ, Sun J, Tirosh I, Mathewson ND, Li S, et al. Neoantigen vaccine generates intratumoral T cell responses in phase Ib glioblastoma trial. Nature. 2019 Jan;565(7738):234–9. https://doi.org/10.1038/s41586-018-0792-9

197. Hilf N, Kuttruff-Coqui S, Frenzel K, Bukur V, Stevanović S, Gouttefangeas C, et al. Actively personalized vaccination trial for newly diagnosed glioblastoma. Nature. 2019 Jan;565(7738):240–5. https://doi.org/10.1038/s41586-018-0810-y

198. Sahin U, Derhovanessian E, Miller M, Kloke B-P, Simon P, Löwer M, et al. Personalized RNA mutanome vaccines mobilize poly-specific therapeutic immunity against cancer. Nature. 2017 Jul 13;547(7662):222–6. https://doi.org/10.1038/nature23003

199. Russell SJ, Peng K-W, Bell JC. Oncolytic virotherapy. Nat Biotechnol. 2012 Jul 10;30(7):658–70. https://doi.org/10.1038/nbt.2287

200. Pikor LA, Bell JC, Diallo J-S. Oncolytic Viruses: Exploiting Cancer's Deal with the Devil. Trends Cancer. 2015 Dec;1(4):266–77. https://doi.org/10.1016/j.trecan.2015.10.004

201. Marelli G, Howells A, Lemoine NR, Wang Y. Oncolytic Viral Therapy and the Immune System: A Double-Edged Sword Against Cancer. Front Immunol. 2018;9:866. https://doi.org/10.3389/fimmu.2018.00866

202. Gujar S, Pol JG, Kroemer G. Heating it up: Oncolytic viruses make tumors "hot" and suitable for checkpoint blockade immunotherapies. Oncoimmunology. 2018;7(8):e1442169. https://doi.org/10.1080/2162402X.2018.1442169

203. Zhang B, Wang X, Cheng P. Remodeling of Tumor Immune Microenvironment by Oncolytic Viruses. Front Oncol. 2020;10:561372. https://doi.org/10.3389/fonc.2020.561372

204. Achard C, Surendran A, Wedge M-E, Ungerechts G, Bell J, Ilkow CS. Lighting a Fire in the Tumor Microenvironment Using Oncolytic Immunotherapy. EBioMedicine. 2018 May;31:17–24. https://doi.org/10.1016/j.ebiom.2018.04.020

205. Kaufman HL, Kohlhapp FJ, Zloza A. Oncolytic viruses: a new class of immunotherapy drugs. Nat Rev Drug Discov. 2016 Aug 30;15(9):660. https://doi.org/10.1038/nrd.2016.178

206. Russell L, Peng K-W. The emerging role of oncolytic virus therapy against cancer. Chin Clin Oncol. 2018 Apr;7(2):16. https://doi.org/10.21037/cco.2018.04.04

207. Ferrucci PF, Pala L, Conforti F, Cocorocchio E. Talimogene Laherparepvec (T-VEC): An Intralesional Cancer Immunotherapy for Advanced Melanoma. Cancers. 2021 Mar 18;13(6):1383. https://doi.org/10.3390/cancers13061383

208. Andtbacka RHI, Collichio F, Harrington KJ, Middleton MR, Downey G, Öhrling K, et al. Final analyses of OPTiM: a randomized phase III trial of talimogene laherparepvec versus granulocyte-macrophage colony-stimulating factor in unresectable stage III-IV melanoma. J Immunother Cancer. 2019 Jun 6;7(1):145. https://doi.org/10.1186/s40425-019-0623-z

209. Ressler JM, Karasek M, Koch L, Silmbrod R, Mangana J, Latifyan S, et al. Real-life use of talimogene laherparepvec (T-VEC) in melanoma patients in centers in Austria, Switzerland and Germany. J Immunother Cancer. 2021 Feb;9(2):e001701. https://doi.org/10.1136/jitc-2020-001701

210. Martinez-Quintanilla J, Seah I, Chua M, Shah K. Oncolytic viruses: overcoming translational challenges. J Clin Invest. 2019 Mar 4;129(4):1407–18. https://doi.org/10.1172/JCI122287

211. Goradel NH, Baker AT, Arashkia A, Ebrahimi N, Ghorghanlu S, Negahdari B. Oncolytic virotherapy: Challenges and solutions. Curr Probl Cancer. 2021 Feb;45(1):100639. https://doi.org/10.1016/j.currproblcancer.2020.100639

212. Galluzzi L, Buqué A, Kepp O, Zitvogel L, Kroemer G. Immunogenic cell death in cancer and infectious disease. Nat Rev Immunol. 2017;17(2):97–111. https://doi.org/10.1038/nri.2016.107

213. Twyman-Saint Victor C, Rech AJ, Maity A, Rengan R, Pauken KE, Stelekati E, et al. Radiation and dual checkpoint blockade activate non-redundant immune mechanisms in cancer. Nature. 2015 Apr 16;520(7547):373–7. https://doi.org/10.1038/nature14292

214. Lhuillier C, Rudqvist N-P, Elemento O, Formenti SC, Demaria S. Radiation therapy and anti-tumor immunity: exposing immunogenic mutations to the immune system. Genome Med. 2019 Jun 20;11(1):40. https://doi.org/10.1186/s13073-019-0653-7

215. Goel S, DeCristo MJ, Watt AC, BrinJones H, Sceneay J, Li BB, et al. CDK4/6 inhibition triggers anti-tumour immunity. Nature. 2017 Aug 24;548(7668):471–5. https://doi.org/10.1038/nature23465

216. Roulois D, Loo Yau H, Singhania R, Wang Y, Danesh A, Shen SY, et al. DNA-Demethylating Agents Target Colorectal Cancer Cells by Inducing Viral Mimicry by Endogenous Transcripts. Cell. 2015 Aug 27;162(5):961–73. https://doi.org/10.1016/j.cell.2015.07.056

217. Petrizzo A, Ragone C, Cavalluzzo B, Mauriello A, Manolio C, Tagliamonte M, et al. Human Endogenous Retrovirus Reactivation: Implications for Cancer Immunotherapy. Cancers. 2021 Apr 21;13(9):1999. https://doi.org/10.3390/cancers13091999

218. Dillon MT, Bergerhoff KF, Pedersen M, Whittock H, Crespo-Rodriguez E, Patin EC, et al. ATR Inhibition Potentiates the Radiation-induced Inflammatory Tumor Microenvironment. Clin Cancer Res Off J Am Assoc Cancer Res. 2019 Jun 1;25(11):3392–403. https://doi.org/10.1158/1078-0432.CCR-18-1821

219. Chabanon RM, Muirhead G, Krastev DB, Adam J, Morel D, Garrido M, et al. PARP inhibition enhances tumor cell-intrinsic immunity in ERCC1-deficient non-small cell lung cancer. J Clin Invest. 2019 Mar 1;129(3):1211–28. https://doi.org/10.1172/JCI123319

220. Briere D, Sudhakar N, Woods DM, Hallin J, Engstrom LD, Aranda R, et al. The class I/IV HDAC inhibitor mocetinostat increases tumor antigen presentation, decreases immune suppressive cell types and augments checkpoint inhibitor therapy. Cancer Immunol Immunother CII. 2018 Mar;67(3):381–92. https://doi.org/10.1007/s00262-017-2091-y

221. Woller N, Gürlevik E, Fleischmann-Mundt B, Schumacher A, Knocke S, Kloos AM, et al. Viral Infection of Tumors Overcomes Resistance to PD-1-immunotherapy by Broadening Neoantigenome-directed T-cell Responses. Mol Ther J Am Soc Gene Ther. 2015 Oct;23(10):1630–40. https://doi.org/10.1038/mt.2015.115

222. Segovia C, San José-Enériz E, Munera-Maravilla E, Martínez-Fernández M, Garate L, Miranda E, et al. Inhibition of a G9a/DNMT network triggers immune-mediated bladder cancer regression. Nat Med. 2019 Jul;25(7):1073–81. https://doi.org/10.1038/s41591-019-0499-y

223. Weber J, Salgaller M, Samid D, Johnson B, Herlyn M, Lassam N, et al. Expression of the MAGE-1 tumor antigen is up-regulated by the demethylating agent 5-aza-2'-deoxycytidine. Cancer Res. 1994 Apr 1;54(7):1766–71.

224. Murphy JP, Kim Y, Clements DR, Konda P, Schuster H, Kowalewski DJ, et al. Therapy-Induced MHC I Ligands Shape Neo-Antitumor CD8 T Cell Responses during Oncolytic Virus-Based Cancer Immunotherapy. J Proteome Res. 2019 Jun 7;18(6):2666–75. https://doi.org/10.1021/acs.jproteome.9b00173

225. Kim Y, Konda P, Murphy JP, Paulo JA, Stevanovic S, Gygi SP, et al. Immune checkpoint blockade augments changes within oncolytic virus-induced cancer MHC-I peptidome, creating novel antitumor CD8 T cell reactivities. Mol Cell Proteomics. 2021;Under Revisions.

226. Kabingu E, Oseroff AR, Wilding GE, Gollnick SO. Enhanced systemic immune reactivity to a Basal cell carcinoma associated antigen following photodynamic therapy. Clin Cancer Res Off J Am Assoc Cancer Res. 2009 Jul 1;15(13):4460–6. https://doi.org/10.1158/1078-0432.CCR-09-0400

227. Bonaventura P, Alcazer V, Mutez V, Tonon L, Martin J, Chuvin N, et al. Identification of shared tumor epitopes from endogenous retroviruses inducing high-avidity cytotoxic T cells for cancer immunotherapy. Sci Adv. 2022 Jan 28;8(4):eabj3671. https://doi.org/10.1126/sciadv.abj3671

228. Ji J, Fan Z, Zhou F, Wang X, Shi L, Zhang H, et al. Improvement of DC vaccine with ALA-PDT induced immunogenic apoptotic cells for skin squamous cell carcinoma. Oncotarget. 2015 Jul 10;6(19):17135–46. https://doi.org/10.18632/oncotarget.3529

229. Bloy N, Garcia P, Laumont CM, Pitt JM, Sistigu A, Stoll G, et al. Immunogenic stress and death of cancer cells: Contribution of antigenicity vs adjuvanticity to immunosurveillance. Immunol Rev. 2017 Nov;280(1):165–74. https://doi.org/10.1111/imr.12582

230. Liu WM, Fowler DW, Smith P, Dalgleish AG. Pre-treatment with chemotherapy can enhance the antigenicity and immunogenicity of tumours by promoting adaptive immune responses. Br J Cancer. 2010 Jan 5;102(1):115–23. https://doi.org/10.1038/sj.bjc.6605465

231. Frey B, Rubner Y, Kulzer L, Werthmöller N, Weiss E-M, Fietkau R, et al. Antitumor immune responses induced by ionizing irradiation and further immune stimulation. Cancer Immunol Immunother CII. 2014 Jan;63(1):29–36. https://doi.org/10.1007/s00262-013-1474-y

232. Fabian KP, Wolfson B, Hodge JW. From Immunogenic Cell Death to Immunogenic Modulation: Select Chemotherapy Regimens Induce a Spectrum of Immune-Enhancing Activities in the Tumor Microenvironment. Front Oncol. 2021;11:728018. https://doi.org/10.3389/fonc.2021.728018

233. Chiriva-Internati M, Grizzi F, Pinkston J, Morrow KJ, D'Cunha N, Frezza EE, et al. Gamma-radiation upregulates MHC class I/II and ICAM-I molecules in multiple myeloma cell lines and primary tumors. In Vitro Cell Dev Biol Anim. 2006 Apr;42(3–4):89–95. https://doi.org/10.1290/0508054.1

234. Sharma A, Bode B, Studer G, Moch H, Okoniewski M, Knuth A, et al. Radiotherapy of human sarcoma promotes an intratumoral immune effector signature. Clin Cancer Res Off J Am Assoc Cancer Res. 2013 Sep 1;19(17):4843–53. https://doi.org/10.1158/1078-0432.CCR-13-0352

235. Galluzzi L, Yamazaki T, Kroemer G. Linking cellular stress responses to systemic homeostasis. Nat Rev Mol Cell Biol. 2018 Nov;19(11):731–45. https://doi.org/10.1038/s41580-018-0068-0

236. Garg AD, Martin S, Golab J, Agostinis P. Danger signalling during cancer cell death: origins, plasticity and regulation. Cell Death Differ. 2014 Jan;21(1):26–38. https://doi.org/10.1038/cdd.2013.48

237. Garg AD, Dudek AM, Agostinis P. Cancer immunogenicity, danger signals, and DAMPs: what, when, and how? BioFactors Oxf Engl. 2013 Aug;39(4):355–67. https://doi.org/10.1002/biof.1125

238. Rubartelli A, Lotze MT. Inside, outside, upside down: damage-associated molecular-pattern molecules (DAMPs) and redox. Trends Immunol. 2007 Oct;28(10):429–36. https://doi.org/10.1016/j.it.2007.08.004

239. Bianchi ME. DAMPs, PAMPs and alarmins: all we need to know about danger. J Leukoc Biol. 2007 Jan;81(1):1–5. https://doi.org/10.1189/jlb.0306164

240. Matzinger P. Tolerance, danger, and the extended family. Annu Rev Immunol. 1994;12:991–1045. https://doi.org/10.1146/annurev.iy.12.040194.005015

241. Fucikova J, Kepp O, Kasikova L, Petroni G, Yamazaki T, Liu P, et al. Detection of immunogenic cell death and its relevance for cancer therapy. Cell Death Dis. 2020 Nov 26;11(11):1013. https://doi.org/10.1038/s41419-020-03221-2

242. Fucikova J, Spisek R, Kroemer G, Galluzzi L. Calreticulin and cancer. Cell Res. 2021 Jan;31(1):5–16. https://doi.org/10.1038/s41422-020-0383-9

243. Obeid M, Tesniere A, Ghiringhelli F, Fimia GM, Apetoh L, Perfettini J-L, et al. Calreticulin exposure dictates the immunogenicity of cancer cell death. Nat Med. 2007 Jan;13(1):54–61. https://doi.org/10.1038/nm1523

244. Garg AD, Krysko DV, Verfaillie T, Kaczmarek A, Ferreira GB, Marysael T, et al. A novel pathway combining calreticulin exposure and ATP secretion in immunogenic cancer cell death. EMBO J. 2012 Mar 7;31(5):1062–79. https://doi.org/10.1038/emboj.2011.497

245. Panaretakis T, Kepp O, Brockmeier U, Tesniere A, Bjorklund A-C, Chapman DC, et al. Mechanisms of pre-apoptotic calreticulin exposure in immunogenic cell death. EMBO J. 2009 Mar 4;28(5):578–90. https://doi.org/10.1038/emboj.2009.1

246. Li W, Yang J, Luo L, Jiang M, Qin B, Yin H, et al. Targeting photodynamic and photothermal therapy to the endoplasmic reticulum enhances immunogenic cancer cell death. Nat Commun. 2019 Jul 26;10(1):3349. https://doi.org/10.1038/s41467-019-11269-8

247. Li C, Zhang Y, Yan S, Zhang G, Wei W, Qi Z, et al. Alternol triggers immunogenic cell death via reactive oxygen species generation. Oncoimmunology. 2021;10(1):1952539. https://doi.org/10.1080/2162402X.2021.1952539

248. Fadok VA, Bratton DL, Rose DM, Pearson A, Ezekewitz RA, Henson PM. A receptor for phosphatidylserine-specific clearance of apoptotic cells. Nature. 2000 May 4;405(6782):85–90. https://doi.org/10.1038/35011084

249. Segawa K, Kurata S, Yanagihashi Y, Brummelkamp TR, Matsuda F, Nagata S. Caspase-mediated cleavage of phospholipid flippase for apoptotic phosphatidylserine exposure. Science. 2014 Jun 6;344(6188):1164–8. https://doi.org/10.1126/science.1252809

250. Tesniere A, Schlemmer F, Boige V, Kepp O, Martins I, Ghiringhelli F, et al. Immunogenic death of colon cancer cells treated with oxaliplatin. Oncogene. 2010 Jan 28;29(4):482–91. https://doi.org/10.1038/onc.2009.356

251. Martins I, Kepp O, Schlemmer F, Adjemian S, Tailler M, Shen S, et al. Restoration of the immunogenicity of cisplatin-induced cancer cell death by endoplasmic reticulum stress. Oncogene. 2011 Mar 10;30(10):1147–58. https://doi.org/10.1038/onc.2010.500

252. Garg AD, Elsen S, Krysko DV, Vandenabeele P, de Witte P, Agostinis P. Resistance to anticancer vaccination effect is controlled by a cancer cell-autonomous phenotype that disrupts immunogenic phagocytic removal. Oncotarget. 2015 Sep 29;6(29):26841–60. https://doi.org/10.18632/oncotarget.4754

253. Sadasivan B, Lehner PJ, Ortmann B, Spies T, Cresswell P. Roles for calreticulin and a novel glycoprotein, tapasin, in the interaction of MHC class I molecules with TAP. Immunity. 1996 Aug;5(2):103–14. https://doi.org/10.1016/s1074-7613(00)80487-2

254. Gao B, Adhikari R, Howarth M, Nakamura K, Gold MC, Hill AB, et al. Assembly and antigen-presenting function of MHC class I molecules in cells lacking the ER chaperone calreticulin. Immunity. 2002 Jan;16(1):99–109. https://doi.org/10.1016/s1074-7613(01)00260-6

255. Howe C, Garstka M, Al-Balushi M, Ghanem E, Antoniou AN, Fritzsche S, et al. Calreticulin-dependent recycling in the early secretory pathway mediates optimal peptide loading of MHC class I molecules. EMBO J. 2009 Dec 2;28(23):3730–44. https://doi.org/10.1038/emboj.2009.296

256. Truxova I, Kasikova L, Salek C, Hensler M, Lysak D, Holicek P, et al. Calreticulin exposure on malignant blasts correlates with improved natural killer cell-mediated cytotoxicity in acute myeloid leukemia patients. Haematologica. 2020 Jul;105(7):1868–78. https://doi.org/10.3324/haematol.2019.223933

257. Chen X, Fosco D, Kline DE, Kline J. Calreticulin promotes immunity and type I interferon-dependent survival in mice with acute myeloid leukemia. Oncoimmunology. 2017;6(4):e1278332. https://doi.org/10.1080/2162402X.2016.1278332

258. Melcher A, Todryk S, Hardwick N, Ford M, Jacobson M, Vile RG. Tumor immunogenicity is determined by the mechanism of cell death via induction of heat shock protein expression. Nat Med. 1998 May;4(5):581–7. https://doi.org/10.1038/nm0598-581

259. Cirone M, Di Renzo L, Lotti LV, Conte V, Trivedi P, Santarelli R, et al. Primary effusion lymphoma cell death induced by bortezomib and AG 490 activates dendritic cells through CD91. PloS One. 2012;7(3):e31732. https://doi.org/10.1371/journal.pone.0031732

260. Zunino B, Rubio-Patiño C, Villa E, Meynet O, Proics E, Cornille A, et al. Hyperthermic intraperitoneal chemotherapy leads to an anticancer immune response via exposure of cell surface heat shock protein 90. Oncogene. 2016 Jan 14;35(2):261–8. https://doi.org/10.1038/onc.2015.82

261. Garg AD, Krysko DV, Vandenabeele P, Agostinis P. Hypericin-based photodynamic therapy induces surface exposure of damage-associated molecular patterns like HSP70 and calreticulin. Cancer Immunol Immunother CII. 2012 Feb;61(2):215–21. https://doi.org/10.1007/s00262-011-1184-2

262. Brusa D, Migliore E, Garetto S, Simone M, Matera L. Immunogenicity of 56 degrees C and UVC-treated prostate cancer is associated with release of HSP70 and HMGB1 from necrotic cells. The Prostate. 2009 Sep 1;69(12):1343–52. https://doi.org/10.1002/pros.20981

263. Spisek R, Charalambous A, Mazumder A, Vesole DH, Jagannath S, Dhodapkar MV. Bortezomib enhances dendritic cell (DC)-mediated induction of immunity to human myeloma via exposure of cell surface heat shock protein 90 on dying tumor cells: therapeutic implications. Blood. 2007 Jun 1;109(11):4839–45. https://doi.org/10.1182/blood-2006-10-054221

264. Wang R, Town T, Gokarn V, Flavell RA, Chandawarkar RY. HSP70 enhances macrophage phagocytosis by interaction with lipid raft-associated TLR-7 and upregulating p38 MAPK and PI3K pathways. J Surg Res. 2006 Nov;136(1):58–69. https://doi.org/10.1016/j.jss.2006.06.003

265. Lauber K, Brix N, Ernst A, Hennel R, Krombach J, Anders H, et al. Targeting the heat shock response in combination with radiotherapy: Sensitizing cancer cells to irradiation-induced cell death and heating up their immunogenicity. Cancer Lett. 2015 Nov 28;368(2):209–29. https://doi.org/10.1016/j.canlet.2015.02.047

266. Spisek R, Dhodapkar MV. Towards a better way to die with chemotherapy: role of heat shock protein exposure on dying tumor cells. Cell Cycle Georget Tex. 2007 Aug 15;6(16):1962–5. https://doi.org/10.4161/cc.6.16.4601

267. Udono H, Srivastava PK. Comparison of tumor-specific immunogenicities of stress-induced proteins gp96, hsp90, and hsp70. J Immunol Baltim Md 1950. 1994 Jun 1;152(11):5398–403.

268. Schild H, Arnold-Schild D, Lammert E, Rammensee HG. Stress proteins and immunity mediated by cytotoxic T lymphocytes. Curr Opin Immunol. 1999 Feb;11(1):109–13. https://doi.org/10.1016/s0952-7915(99)80019-3

269. Vega VL, Rodríguez-Silva M, Frey T, Gehrmann M, Diaz JC, Steinem C, et al. Hsp70 translocates into the plasma membrane after stress and is released into the extracellular environment in a membrane-associated form that activates macrophages. J Immunol Baltim Md 1950. 2008 Mar 15;180(6):4299–307. https://doi.org/10.4049/jimmunol.180.6.4299

270. Multhoff G, Mizzen L, Winchester CC, Milner CM, Wenk S, Eissner G, et al. Heat shock protein 70 (Hsp70) stimulates proliferation and cytolytic activity of natural killer cells. Exp Hematol. 1999 Nov;27(11):1627–36. https://doi.org/10.1016/s0301-472x(99)00104-6

271. Kepp O, Bezu L, Yamazaki T, Di Virgilio F, Smyth MJ, Kroemer G, et al. ATP and cancer immunosurveillance. EMBO J. 2021 Jul 1;40(13):e108130. https://doi.org/10.15252/embj.2021108130

272. Kepp O, Senovilla L, Vitale I, Vacchelli E, Adjemian S, Agostinis P, et al. Consensus guidelines for the detection of immunogenic cell death. Oncoimmunology. 2014 Oct;3(9):e955691. https://doi.org/10.4161/21624011.2014.955691

273. Martins I, Tesniere A, Kepp O, Michaud M, Schlemmer F, Senovilla L, et al. Chemotherapy induces ATP release from tumor cells. Cell Cycle Georget Tex. 2009 Nov 15;8(22):3723–8. https://doi.org/10.4161/cc.8.22.10026

274. Martins I, Wang Y, Michaud M, Ma Y, Sukkurwala AQ, Shen S, et al. Molecular mechanisms of ATP secretion during immunogenic cell death. Cell Death Differ. 2014 Jan;21(1):79–91. https://doi.org/10.1038/cdd.2013.75

275. Michaud M, Martins I, Sukkurwala AQ, Adjemian S, Ma Y, Pellegatti P, et al. Autophagy-dependent anticancer immune responses induced by chemotherapeutic agents in mice. Science. 2011 Dec 16;334(6062):1573–7. https://doi.org/10.1126/science.1208347

276. Wang Y, Martins I, Ma Y, Kepp O, Galluzzi L, Kroemer G. Autophagy-dependent ATP release from dying cells via lysosomal exocytosis. Autophagy. 2013 Oct;9(10):1624–5. https://doi.org/10.4161/auto.25873

277. Pietrocola F, Pol J, Vacchelli E, Rao S, Enot DP, Baracco EE, et al. Caloric Restriction Mimetics Enhance Anticancer Immunosurveillance. Cancer Cell. 2016 Jul 11;30(1):147–60. https://doi.org/10.1016/j.ccell.2016.05.016

278. Wang Y, Xie W, Humeau J, Chen G, Liu P, Pol J, et al. Autophagy induction by thiostrepton improves the efficacy of immunogenic chemotherapy. J Immunother Cancer. 2020 Mar;8(1):e000462. https://doi.org/10.1136/jitc-2019-000462

279. Ko A, Kanehisa A, Martins I, Senovilla L, Chargari C, Dugue D, et al. Autophagy inhibition radiosensitizes in vitro, yet reduces radioresponses in vivo due to deficient immunogenic signalling. Cell Death Differ. 2014 Jan;21(1):92–9. https://doi.org/10.1038/cdd.2013.124

280. Garg AD, Dudek AM, Ferreira GB, Verfaillie T, Vandenabeele P, Krysko DV, et al. ROS-induced autophagy in cancer cells assists in evasion from determinants of immunogenic cell death. Autophagy. 2013 Sep;9(9):1292–307. https://doi.org/10.4161/auto.25399

281. Elliott MR, Chekeni FB, Trampont PC, Lazarowski ER, Kadl A, Walk SF, et al. Nucleotides released by apoptotic cells act as a find-me signal to promote phagocytic clearance. Nature. 2009 Sep 10;461(7261):282–6. https://doi.org/10.1038/nature08296

282. Chekeni FB, Elliott MR, Sandilos JK, Walk SF, Kinchen JM, Lazarowski ER, et al. Pannexin 1 channels mediate “find-me” signal release and membrane permeability during apoptosis. Nature. 2010 Oct 14;467(7317):863–7. https://doi.org/10.1038/nature09413

283. Perregaux DG, McNiff P, Laliberte R, Conklyn M, Gabel CA. ATP acts as an agonist to promote stimulus-induced secretion of IL-1 beta and IL-18 in human blood. J Immunol Baltim Md 1950. 2000 Oct 15;165(8):4615–23. https://doi.org/10.4049/jimmunol.165.8.4615

284. Ma Y, Aymeric L, Locher C, Mattarollo SR, Delahaye NF, Pereira P, et al. Contribution of IL-17-producing gamma delta T cells to the efficacy of anticancer chemotherapy. J Exp Med. 2011 Mar 14;208(3):491–503. https://doi.org/10.1084/jem.20100269

285. Ghiringhelli F, Apetoh L, Tesniere A, Aymeric L, Ma Y, Ortiz C, et al. Activation of the NLRP3 inflammasome in dendritic cells induces IL-1beta-dependent adaptive immunity against tumors. Nat Med. 2009 Oct;15(10):1170–8. https://doi.org/10.1038/nm.2028

286. Michaud M, Sukkurwala AQ, Martins I, Shen S, Zitvogel L, Kroemer G. Subversion of the chemotherapy-induced anticancer immune response by the ecto-ATPase CD39. Oncoimmunology. 2012 May 1;1(3):393–5. https://doi.org/10.4161/onci.19070

287. Ma Y, Adjemian S, Mattarollo SR, Yamazaki T, Aymeric L, Yang H, et al. Anticancer chemotherapy-induced intratumoral recruitment and differentiation of antigen-presenting cells. Immunity. 2013 Apr 18;38(4):729–41. https://doi.org/10.1016/j.immuni.2013.03.003

288. Bidula S, Dhuna K, Helliwell R, Stokes L. Positive allosteric modulation of P2X7 promotes apoptotic cell death over lytic cell death responses in macrophages. Cell Death Dis. 2019 Nov 25;10(12):882. https://doi.org/10.1038/s41419-019-2110-3

289. Bell CW, Jiang W, Reich CF, Pisetsky DS. The extracellular release of HMGB1 during apoptotic cell death. Am J Physiol Cell Physiol. 2006 Dec;291(6):C1318-1325. https://doi.org/10.1152/ajpcell.00616.2005

290. Yang H, Wang H, Czura CJ, Tracey KJ. The cytokine activity of HMGB1. J Leukoc Biol. 2005 Jul;78(1):1–8. https://doi.org/10.1189/jlb.1104648

291. Kwak MS, Kim HS, Lee B, Kim YH, Son M, Shin J-S. Immunological Significance of HMGB1 Post-Translational Modification and Redox Biology. Front Immunol. 2020;11:1189. https://doi.org/10.3389/fimmu.2020.01189

292. Venereau E, Casalgrandi M, Schiraldi M, Antoine DJ, Cattaneo A, De Marchis F, et al. Mutually exclusive redox forms of HMGB1 promote cell recruitment or proinflammatory cytokine release. J Exp Med. 2012 Aug 27;209(9):1519–28. https://doi.org/10.1084/jem.20120189

293. Apetoh L, Ghiringhelli F, Tesniere A, Obeid M, Ortiz C, Criollo A, et al. Toll-like receptor 4-dependent contribution of the immune system to anticancer chemotherapy and radiotherapy. Nat Med. 2007 Sep;13(9):1050–9. https://doi.org/10.1038/nm1622

294. Yamazaki T, Hannani D, Poirier-Colame V, Ladoire S, Locher C, Sistigu A, et al. Defective immunogenic cell death of HMGB1-deficient tumors: compensatory therapy with TLR4 agonists. Cell Death Differ. 2014 Jan;21(1):69–78. https://doi.org/10.1038/cdd.2013.72

295. Schiraldi M, Raucci A, Muñoz LM, Livoti E, Celona B, Venereau E, et al. HMGB1 promotes recruitment of inflammatory cells to damaged tissues by forming a complex with CXCL12 and signaling via CXCR4. J Exp Med. 2012 Mar 12;209(3):551–63. https://doi.org/10.1084/jem.20111739

296. Borden EC. Interferons α and β in cancer: therapeutic opportunities from new insights. Nat Rev Drug Discov. 2019 Mar;18(3):219–34. https://doi.org/10.1038/s41573-018-0011-2

297. Asadzadeh Z, Safarzadeh E, Safaei S, Baradaran A, Mohammadi A, Hajiasgharzadeh K, et al. Current Approaches for Combination Therapy of Cancer: The Role of Immunogenic Cell Death. Cancers. 2020 Apr 23;12(4):E1047. https://doi.org/10.3390/cancers12041047

298. McNab F, Mayer-Barber K, Sher A, Wack A, O'Garra A. Type I interferons in infectious disease. Nat Rev Immunol. 2015 Feb;15(2):87–103. https://doi.org/10.1038/nri3787

299. Ivashkiv LB, Donlin LT. Regulation of type I interferon responses. Nat Rev Immunol. 2014 Jan;14(1):36–49. https://doi.org/10.1038/nri3581

300. Murira A, Lamarre A. Type-I Interferon Responses: From Friend to Foe in the Battle against Chronic Viral Infection. Front Immunol. 2016;7:609. https://doi.org/10.3389/fimmu.2016.00609

301. Vacchelli E, Sistigu A, Yamazaki T, Vitale I, Zitvogel L, Kroemer G. Autocrine signaling of type 1 interferons in successful anticancer chemotherapy. Oncoimmunology. 2015 Aug;4(8):e988042. https://doi.org/10.4161/2162402X.2014.988042

302. Rodriguez-Ruiz ME, Buqué A, Hensler M, Chen J, Bloy N, Petroni G, et al. Apoptotic caspases inhibit abscopal responses to radiation and identify a new prognostic biomarker for breast cancer patients. Oncoimmunology. 2019;8(11):e1655964. https://doi.org/10.1080/2162402X.2019.1655964

303. Sistigu A, Yamazaki T, Vacchelli E, Chaba K, Enot DP, Adam J, et al. Cancer cell-autonomous contribution of type I interferon signaling to the efficacy of chemotherapy. Nat Med. 2014 Nov;20(11):1301–9. https://doi.org/10.1038/nm.3708

304. Medler T, Patel JM, Alice A, Baird JR, Hu H-M, Gough MJ. Activating the Nucleic Acid-Sensing Machinery for Anticancer Immunity. Int Rev Cell Mol Biol. 2019;344:173–214. https://doi.org/10.1016/bs.ircmb.2018.08.006

305. Yamazaki T, Kirchmair A, Sato A, Buqué A, Rybstein M, Petroni G, et al. Mitochondrial DNA drives abscopal responses to radiation that are inhibited by autophagy. Nat Immunol. 2020 Oct;21(10):1160–71. https://doi.org/10.1038/s41590-020-0751-0

306. Hopfner K-P, Hornung V. Molecular mechanisms and cellular functions of cGAS-STING signalling. Nat Rev Mol Cell Biol. 2020 Sep;21(9):501–21. https://doi.org/10.1038/s41580-020-0244-x

307. McLaughlin M, Patin EC, Pedersen M, Wilkins A, Dillon MT, Melcher AA, et al. Inflammatory microenvironment remodelling by tumour cells after radiotherapy. Nat Rev Cancer. 2020 Apr;20(4):203–17. https://doi.org/10.1038/s41568-020-0246-1

308. Diamond JM, Vanpouille-Box C, Spada S, Rudqvist N-P, Chapman JR, Ueberheide BM, et al. Exosomes Shuttle TREX1-Sensitive IFN-Stimulatory dsDNA from Irradiated Cancer Cells to DCs. Cancer Immunol Res. 2018 Aug;6(8):910–20. https://doi.org/10.1158/2326-6066.CIR-17-0581

309. Deng L, Liang H, Xu M, Yang X, Burnette B, Arina A, et al. STING-Dependent Cytosolic DNA Sensing Promotes Radiation-Induced Type I Interferon-Dependent Antitumor Immunity in Immunogenic Tumors. Immunity. 2014 Nov 20;41(5):843–52. https://doi.org/10.1016/j.immuni.2014.10.019

310. Vanpouille-Box C, Alard A, Aryankalayil MJ, Sarfraz Y, Diamond JM, Schneider RJ, et al. DNA exonuclease Trex1 regulates radiotherapy-induced tumour immunogenicity. Nat Commun. 2017 Jun 9;8:15618. https://doi.org/10.1038/ncomms15618

311. Yamazaki T, Galluzzi L. TREX1 Cuts Down on Cancer Immunogenicity. Trends Cell Biol. 2017 Aug;27(8):543–5. https://doi.org/10.1016/j.tcb.2017.06.001

312. Motwani M, Pesiridis S, Fitzgerald KA. DNA sensing by the cGAS-STING pathway in health and disease. Nat Rev Genet. 2019 Nov;20(11):657–74. https://doi.org/10.1038/s41576-019-0151-1

313. Kawasaki T, Kawai T. Discrimination Between Self and Non-Self-Nucleic Acids by the Innate Immune System. Int Rev Cell Mol Biol. 2019;344:1–30. https://doi.org/10.1016/bs.ircmb.2018.08.004

314. Lamberti MJ, Mentucci FM, Roselli E, Araya P, Rivarola VA, Rumie Vittar NB, et al. Photodynamic Modulation of Type 1 Interferon Pathway on Melanoma Cells Promotes Dendritic Cell Activation. Front Immunol. 2019;10:2614. https://doi.org/10.3389/fimmu.2019.02614

315. Oh JH, Kim MJ, Choi SJ, Ban YH, Lee HK, Shin E-C, et al. Sustained Type I Interferon Reinforces NK Cell-Mediated Cancer Immunosurveillance during Chronic Virus Infection. Cancer Immunol Res. 2019 Apr;7(4):584–99. https://doi.org/10.1158/2326-6066.CIR-18-0403

316. Bek S, Stritzke F, Wintges A, Nedelko T, Böhmer DFR, Fischer JC, et al. Targeting intrinsic RIG-I signaling turns melanoma cells into type I interferon-releasing cellular antitumor vaccines. Oncoimmunology. 2019;8(4):e1570779. https://doi.org/10.1080/2162402X.2019.1570779

317. Müller E, Christopoulos PF, Halder S, Lunde A, Beraki K, Speth M, et al. Toll-Like Receptor Ligands and Interferon-γ Synergize for Induction of Antitumor M1 Macrophages. Front Immunol. 2017;8:1383. https://doi.org/10.3389/fimmu.2017.01383

318. Gangaplara A, Martens C, Dahlstrom E, Metidji A, Gokhale AS, Glass DD, et al. Type I interferon signaling attenuates regulatory T cell function in viral infection and in the tumor microenvironment. PLoS Pathog. 2018 Apr;14(4):e1006985. https://doi.org/10.1371/journal.ppat.1006985

319. Garg AD, Vandenberk L, Fang S, Fasche T, Van Eygen S, Maes J, et al. Pathogen response-like recruitment and activation of neutrophils by sterile immunogenic dying cells drives neutrophil-mediated residual cell killing. Cell Death Differ. 2017 May;24(5):832–43. https://doi.org/10.1038/cdd.2017.15

320. Menger L, Vacchelli E, Adjemian S, Martins I, Ma Y, Shen S, et al. Cardiac glycosides exert anticancer effects by inducing immunogenic cell death. Sci Transl Med. 2012 Jul 18;4(143):143ra99. https://doi.org/10.1126/scitranslmed.3003807

321. Humeau J, Lévesque S, Kroemer G, Pol JG. Gold Standard Assessment of Immunogenic Cell Death in Oncological Mouse Models. Methods Mol Biol Clifton NJ. 2019;1884:297–315. https://doi.org/10.1007/978-1-4939-8885-3_21

322. Hayashi K, Nikolos F, Lee YC, Jain A, Tsouko E, Gao H, et al. Tipping the immunostimulatory and inhibitory DAMP balance to harness immunogenic cell death. Nat Commun. 2020 Dec 7;11(1):6299. https://doi.org/10.1038/s41467-020-19970-9

323. Gustave Roussy, Cancer Campus, Grand Paris. Randomized Trial of Treatment Strategy for Chemotherapy in Colorectal Cancer, FFCD 2000-05 [Internet]. clinicaltrials.gov; 2015 Aug [cited 2021 Dec 22]. Report No.: NCT00126256. Available from: https://clinicaltrials.gov/ct2/show/NCT00126256

324. Bergmann C, Bachmann HS, Bankfalvi A, Lotfi R, Pütter C, Wild CA, et al. Toll-like receptor 4 single-nucleotide polymorphisms Asp299Gly and Thr399Ile in head and neck squamous cell carcinomas. J Transl Med. 2011 Aug 21;9:139. https://doi.org/10.1186/1479-5876-9-139

325. Tittarelli A, González FE, Pereda C, Mora G, Muñoz L, Saffie C, et al. Toll-like receptor 4 gene polymorphism influences dendritic cell in vitro function and clinical outcomes in vaccinated melanoma patients. Cancer Immunol Immunother CII. 2012 Nov;61(11):2067–77. https://doi.org/10.1007/s00262-012-1268-7

326. Sprooten J, Ceusters J, Coosemans A, Agostinis P, De Vleeschouwer S, Zitvogel L, et al. Trial watch: dendritic cell vaccination for cancer immunotherapy. Oncoimmunology. 2019;8(11):e1638212. https://doi.org/10.1080/2162402X.2019.1638212

327. Ladoire S, Enot D, Andre F, Zitvogel L, Kroemer G. Immunogenic cell death-related biomarkers: Impact on the survival of breast cancer patients after adjuvant chemotherapy. Oncoimmunology. 2016 Feb;5(2):e1082706. https://doi.org/10.1080/2162402X.2015.1082706

328. Cathro HP, Smolkin ME, Theodorescu D, Jo VY, Ferrone S, Frierson HF. Relationship between HLA class I antigen processing machinery component expression and the clinicopathologic characteristics of bladder carcinomas. Cancer Immunol Immunother CII. 2010 Mar;59(3):465–72. https://doi.org/10.1007/s00262-009-0765-9

329. Kasikova L, Hensler M, Truxova I, Skapa P, Laco J, Belicova L, et al. Calreticulin exposure correlates with robust adaptive antitumor immunity and favorable prognosis in ovarian carcinoma patients. J Immunother Cancer. 2019 Nov 20;7(1):312. https://doi.org/10.1186/s40425-019-0781-z

330. Muth C, Rubner Y, Semrau S, Rühle P-F, Frey B, Strnad A, et al. Primary glioblastoma multiforme tumors and recurrence : Comparative analysis of the danger signals HMGB1, HSP70, and calreticulin. Strahlenther Onkol Organ Dtsch Rontgengesellschaft Al. 2016 Mar;192(3):146–55. https://doi.org/10.1007/s00066-015-0926-z

331. Zhang X-H, Zhang Y, Xie W-P, Sun D-S, Zhang Y-K, Hao Y-K, et al. Expression and significance of calreticulin in human osteosarcoma. Cancer Biomark Sect Dis Markers. 2017;18(4):405–11. https://doi.org/10.3233/CBM-160266

332. Schardt JA, Weber D, Eyholzer M, Mueller BU, Pabst T. Activation of the unfolded protein response is associated with favorable prognosis in acute myeloid leukemia. Clin Cancer Res Off J Am Assoc Cancer Res. 2009 Jun 1;15(11):3834–41. https://doi.org/10.1158/1078-0432.CCR-08-2870

333. Fucikova J, Becht E, Iribarren K, Goc J, Remark R, Damotte D, et al. Calreticulin Expression in Human Non-Small Cell Lung Cancers Correlates with Increased Accumulation of Antitumor Immune Cells and Favorable Prognosis. Cancer Res. 2016 Apr 1;76(7):1746–56. https://doi.org/10.1158/0008-5472.CAN-15-1142

334. Hsu WM, Hsieh FJ, Jeng YM, Kuo ML, Chen CN, Lai DM, et al. Calreticulin expression in neuroblastoma--a novel independent prognostic factor. Ann Oncol Off J Eur Soc Med Oncol. 2005 Feb;16(2):314–21. https://doi.org/10.1093/annonc/mdi062

335. Peng R-Q, Chen Y-B, Ding Y, Zhang R, Zhang X, Yu X-J, et al. Expression of calreticulin is associated with infiltration of T-cells in stage IIIB colon cancer. World J Gastroenterol. 2010 May 21;16(19):2428–34. https://doi.org/10.3748/wjg.v16.i19.2428

336. Fucikova J, Truxova I, Hensler M, Becht E, Kasikova L, Moserova I, et al. Calreticulin exposure by malignant blasts correlates with robust anticancer immunity and improved clinical outcome in AML patients. Blood. 2016 Dec 29;128(26):3113–24. https://doi.org/10.1182/blood-2016-08-731737

337. Dardano A, Falzoni S, Caraccio N, Polini A, Tognini S, Solini A, et al. 1513A>C polymorphism in the P2X7 receptor gene in patients with papillary thyroid cancer: correlation with histological variants and clinical parameters. J Clin Endocrinol Metab. 2009 Feb;94(2):695–8. https://doi.org/10.1210/jc.2008-1322

338. Thunberg U, Tobin G, Johnson A, Söderberg O, Padyukov L, Hultdin M, et al. Polymorphism in the P2X7 receptor gene and survival in chronic lymphocytic leukaemia. Lancet Lond Engl. 2002 Dec 14;360(9349):1935–9. https://doi.org/10.1016/S0140-6736(02)11917-9

339. Wiley JS, Dao-Ung LP, Gu BJ, Sluyter R, Shemon AN, Li C, et al. A loss-of-function polymorphic mutation in the cytolytic P2X7 receptor gene and chronic lymphocytic leukaemia: a molecular study. Lancet Lond Engl. 2002 Mar 30;359(9312):1114–9. https://doi.org/10.1016/S0140-6736(02)08156-4

340. Zhang LY, Ibbotson RE, Orchard JA, Gardiner AC, Seear RV, Chase AJ, et al. P2X7 polymorphism and chronic lymphocytic leukaemia: lack of correlation with incidence, survival and abnormalities of chromosome 12. Leukemia. 2003 Nov;17(11):2097–100. https://doi.org/10.1038/sj.leu.2403125

341. Gulla A, Morelli E, Samur MK, Botta C, Hideshima T, Bianchi G, et al. Bortezomib induces anti-multiple myeloma immune response mediated by cGAS/STING pathway activation. Blood Cancer Discov. 2021 Sep;2(5):468–83. https://doi.org/10.1158/2643-3230.bcd-21-0047

342. Zitvogel L, Kroemer G. Bortezomib Induces Immunogenic Cell Death in Multiple Myeloma. Blood Cancer Discov. 2021 Sep;2(5):405–7. https://doi.org/10.1158/2643-3230.BCD-21-0059

343. Rapoport BL, Anderson R. Realizing the Clinical Potential of Immunogenic Cell Death in Cancer Chemotherapy and Radiotherapy. Int J Mol Sci. 2019 Feb 22;20(4):E959. https://doi.org/10.3390/ijms20040959

344. Garg AD, More S, Rufo N, Mece O, Sassano ML, Agostinis P, et al. Trial watch: Immunogenic cell death induction by anticancer chemotherapeutics. Oncoimmunology. 2017;6(12):e1386829. https://doi.org/10.1080/2162402X.2017.1386829

345. Kepp O, Zitvogel L, Kroemer G. Clinical evidence that immunogenic cell death sensitizes to PD-1/PD-L1 blockade. Oncoimmunology. 2019;8(10):e1637188. https://doi.org/10.1080/2162402X.2019.1637188

346. Monro S, Colón KL, Yin H, Roque J, Konda P, Gujar S, et al. Transition Metal Complexes and Photodynamic Therapy from a Tumor-Centered Approach: Challenges, Opportunities, and Highlights from the Development of TLD1433. Chem Rev. 2019 Jan 23;119(2):797–828. https://doi.org/10.1021/acs.chemrev.8b00211

347. Kostron H, Hasan T, Royal Society of Chemistry (Great Britain), editors. Photodynamic medicine: from bench to clinic. Cambridge: Royal Society of Chemistry; 2016. 650 p. (Comprehensive series in photochmistry and photobiology).

348. Hamblin MR, Huang Y-Y, editors. Handbook of photomedicine. Boca Raton, FL: CRC Press; 2014. 854 p.

349. Henderson BW, Dougherty TJ, editors. Photodynamic therapy: basic principles and clinical applications. New York: Dekker; 1992. 459 p.

350. Abdel-Kader MH. History of Photodynamic Therapy. In: Abdel-Kader MH, editor. Photodynamic Therapy [Internet]. Berlin, Heidelberg: Springer Berlin Heidelberg; 2014 [cited 2020 Jun 22]. p. 3–22. Available from: http://link.springer.com/10.1007/978-3-642-39629-8_1https://doi.org/10.1007/978-3-642-39629-8_1

351. Usuda J, Kato H, Okunaka T, Furukawa K, Tsutsui H, Yamada K, et al. Photodynamic therapy (PDT) for lung cancers. J Thorac Oncol Off Publ Int Assoc Study Lung Cancer. 2006 Jun;1(5):489–93.

352. van Straten D, Mashayekhi V, de Bruijn H, Oliveira S, Robinson D. Oncologic Photodynamic Therapy: Basic Principles, Current Clinical Status and Future Directions. Cancers. 2017 Feb 18;9(12):19. https://doi.org/10.3390/cancers9020019

353. Correia JH, Rodrigues JA, Pimenta S, Dong T, Yang Z. Photodynamic Therapy Review: Principles, Photosensitizers, Applications, and Future Directions. Pharmaceutics. 2021 Aug 25;13(9):1332. https://doi.org/10.3390/pharmaceutics13091332

354. Gunaydin G, Gedik ME, Ayan S. Photodynamic Therapy for the Treatment and Diagnosis of Cancer-A Review of the Current Clinical Status. Front Chem. 2021;9:686303. https://doi.org/10.3389/fchem.2021.686303

355. Zhang J, Jiang C, Figueiró Longo JP, Azevedo RB, Zhang H, Muehlmann LA. An updated overview on the development of new photosensitizers for anticancer photodynamic therapy. Acta Pharm Sin B. 2018 Mar;8(2):137–46. https://doi.org/10.1016/j.apsb.2017.09.003

356. Sternberg ED, Dolphin D. Second Generation Photodynamic Agents: A Review. J Clin Laser Med Surg. 1993 Oct;11(5):233–41. https://doi.org/10.1089/clm.1993.11.233

357. Kataoka H, Nishie H, Hayashi N, Tanaka M, Nomoto A, Yano S, et al. New photodynamic therapy with next-generation photosensitizers. Ann Transl Med. 2017 Apr;5(8):183–183. https://doi.org/10.21037/atm.2017.03.59

358. Nakamura Y, Mochida A, Choyke PL, Kobayashi H. Nanodrug Delivery: Is the Enhanced Permeability and Retention Effect Sufficient for Curing Cancer? Bioconjug Chem. 2016 Oct 19;27(10):2225–38. https://doi.org/10.1021/acs.bioconjchem.6b00437

359. Jung HS, Lee J-H, Kim K, Koo S, Verwilst P, Sessler JL, et al. A Mitochondria-Targeted Cryptocyanine-Based Photothermogenic Photosensitizer. J Am Chem Soc. 2017 Jul 26;139(29):9972–8. https://doi.org/10.1021/jacs.7b04263

360. Lv W, Zhang Z, Zhang KY, Yang H, Liu S, Xu A, et al. A Mitochondria-Targeted Photosensitizer Showing Improved Photodynamic Therapy Effects Under Hypoxia. Angew Chem Int Ed Engl. 2016 Aug 16;55(34):9947–51. https://doi.org/10.1002/anie.201604130

361. McKenzie LK, Bryant HE, Weinstein JA. Transition metal complexes as photosensitisers in one- and two-photon photodynamic therapy. Coord Chem Rev. 2019 Jan;379:2–29. https://doi.org/10.1016/j.ccr.2018.03.020

362. Zhang P, Sadler PJ. Advances in the design of organometallic anticancer complexes. J Organomet Chem. 2017 Jun 15;839:5–14. https://doi.org/10.1016/j.jorganchem.2017.03.038

363. Tucker JW, Stephenson CRJ. Shining light on photoredox catalysis: theory and synthetic applications. J Org Chem. 2012 Feb 17;77(4):1617–22. https://doi.org/10.1021/jo202538x

364. Prier CK, Rankic DA, MacMillan DWC. Visible Light Photoredox Catalysis with Transition Metal Complexes: Applications in Organic Synthesis. Chem Rev. 2013 Jul 10;113(7):5322–63. https://doi.org/10.1021/cr300503r

365. Knoll JD, Albani BA, Turro C. Excited state investigation of a new Ru(II) complex for dual reactivity with low energy light. Chem Commun Camb Engl. 2015 May 25;51(42):8777–80. https://doi.org/10.1039/c5cc01865j

366. Knoll JD, Albani BA, Turro C. New Ru(II) Complexes for Dual Photoreactivity: Ligand Exchange and 1O2 Generation. Acc Chem Res. 2015 Aug;48(8):2280–7. https://doi.org/10.1021/acs.accounts.5b00227

367. Zhao Q, Huang C, Li F. Phosphorescent heavy-metal complexes for bioimaging. Chem Soc Rev. 2011 May;40(5):2508–24. https://doi.org/10.1039/c0cs00114g

368. Mari C, Pierroz V, Ferrari S, Gasser G. Combination of Ru(ii) complexes and light: new frontiers in cancer therapy. Chem Sci. 2015 May 1;6(5):2660–86. https://doi.org/10.1039/c4sc03759f

369. Phase IIb 180-day results – McFarland Labs – The University of Texas at Arlington [Internet]. [cited 2021 Dec 28]. Available from: https://mcfarlandlabs.uta.edu/2021/02/01/phase-iib-180-day-results/

370. Shams M, Owczarczak B, Manderscheid-Kern P, Bellnier DA, Gollnick SO. Development of photodynamic therapy regimens that control primary tumor growth and inhibit secondary disease. Cancer Immunol Immunother CII. 2015 Mar;64(3):287–97. https://doi.org/10.1007/s00262-014-1633-9

371. Plaetzer K, Krammer B, Berlanda J, Berr F, Kiesslich T. Photophysics and photochemistry of photodynamic therapy: fundamental aspects. Lasers Med Sci. 2009 Mar;24(2):259–68. https://doi.org/10.1007/s10103-008-0539-1

372. Dąbrowski JM, Arnaut LG. Photodynamic therapy (PDT) of cancer: from local to systemic treatment. Photochem Photobiol Sci Off J Eur Photochem Assoc Eur Soc Photobiol. 2015 Oct;14(10):1765–80. https://doi.org/10.1039/c5pp00132c

373. Kessel D, Oleinick NL. Cell Death Pathways Associated with Photodynamic Therapy: An Update. Photochem Photobiol. 2018 Mar;94(2):213–8. https://doi.org/10.1111/php.12857

374. Kessel D. Subcellular Targeting as a Determinant of the Efficacy of Photodynamic Therapy. Photochem Photobiol. 2017 Mar;93(2):609–12. https://doi.org/10.1111/php.12692

375. Kessel D. Subcellular targets for photodynamic therapy: implications for initiation of apoptosis and autophagy. J Natl Compr Cancer Netw JNCCN. 2012 Oct 1;10 Suppl 2:S56-59. https://doi.org/10.6004/jnccn.2012.0177

376. Buytaert E, Dewaele M, Agostinis P. Molecular effectors of multiple cell death pathways initiated by photodynamic therapy. Biochim Biophys Acta. 2007 Sep;1776(1):86–107. https://doi.org/10.1016/j.bbcan.2007.07.001

377. Kessel D, Castelli M. Evidence that bcl-2 is the target of three photosensitizers that induce a rapid apoptotic response. Photochem Photobiol. 2001 Aug;74(2):318–22. https://doi.org/10.1562/0031-8655(2001)074<0318:etbitt>2.0.co;2

378. Xue LY, Chiu SM, Oleinick NL. Photochemical destruction of the Bcl-2 oncoprotein during photodynamic therapy with the phthalocyanine photosensitizer Pc 4. Oncogene. 2001 Jun 7;20(26):3420–7. https://doi.org/10.1038/sj.onc.1204441

379. Usuda J, Chiu S, Murphy ES, Lam M, Nieminen A-L, Oleinick NL. Domain-dependent photodamage to Bcl-2. A membrane anchorage region is needed to form the target of phthalocyanine photosensitization. J Biol Chem. 2003 Jan 17;278(3):2021–9. https://doi.org/10.1074/jbc.M205219200

380. Reiners JJ, Caruso JA, Mathieu P, Chelladurai B, Yin X-M, Kessel D. Release of cytochrome c and activation of pro-caspase-9 following lysosomal photodamage involves Bid cleavage. Cell Death Differ. 2002 Sep;9(9):934–44. https://doi.org/10.1038/sj.cdd.4401048

381. Thompson SA, Aggarwal A, Singh S, Adam AP, Tome JPC, Drain CM. Compromising the plasma membrane as a secondary target in photodynamic therapy-induced necrosis. Bioorg Med Chem. 2018 Oct 1;26(18):5224–8. https://doi.org/10.1016/j.bmc.2018.09.026

382. Dellinger M. Apoptosis or necrosis following Photofrin photosensitization: influence of the incubation protocol. Photochem Photobiol. 1996 Jul;64(1):182–7. https://doi.org/10.1111/j.1751-1097.1996.tb02440.x

383. Hsieh Y-J, Wu C-C, Chang C-J, Yu J-S. Subcellular localization of Photofrin determines the death phenotype of human epidermoid carcinoma A431 cells triggered by photodynamic therapy: when plasma membranes are the main targets. J Cell Physiol. 2003 Mar;194(3):363–75. https://doi.org/10.1002/jcp.10273

384. Fabris C, Valduga G, Miotto G, Borsetto L, Jori G, Garbisa S, et al. Photosensitization with zinc (II) phthalocyanine as a switch in the decision between apoptosis and necrosis. Cancer Res. 2001 Oct 15;61(20):7495–500.

385. Donohoe C, Senge MO, Arnaut LG, Gomes-da-Silva LC. Cell death in photodynamic therapy: From oxidative stress to anti-tumor immunity. Biochim Biophys Acta Rev Cancer. 2019 Dec;1872(2):188308. https://doi.org/10.1016/j.bbcan.2019.07.003

386. Pucelik B, Arnaut LG, Stochel G, Dąbrowski JM. Design of Pluronic-Based Formulation for Enhanced Redaporfin-Photodynamic Therapy against Pigmented Melanoma. ACS Appl Mater Interfaces. 2016 Aug 31;8(34):22039–55. https://doi.org/10.1021/acsami.6b07031

387. Luo W, Liu R-S, Zhu J-G, Li Y-C, Liu H-C. Subcellular location and photodynamic therapeutic effect of chlorin e6 in the human tongue squamous cell cancer Tca8113 cell line. Oncol Lett. 2015 Feb;9(2):551–6. https://doi.org/10.3892/ol.2014.2720

388. Plaetzer K, Kiesslich T, Krammer B, Hammerl P. Characterization of the cell death modes and the associated changes in cellular energy supply in response to AlPcS4-PDT. Photochem Photobiol Sci Off J Eur Photochem Assoc Eur Soc Photobiol. 2002 Mar;1(3):172–7. https://doi.org/10.1039/b108816e

389. Miki Y, Akimoto J, Hiranuma M, Fujiwara Y. Effect of talaporfin sodium-mediated photodynamic therapy on cell death modalities in human glioblastoma T98G cells. J Toxicol Sci. 2014;39(6):821–7. https://doi.org/10.2131/jts.39.821

390. Xue L, Chiu S, Azizuddin K, Joseph S, Oleinick NL. The death of human cancer cells following photodynamic therapy: apoptosis competence is necessary for Bcl-2 protection but not for induction of autophagy. Photochem Photobiol. 2007 Oct;83(5):1016–23. https://doi.org/10.1111/j.1751-1097.2007.00159.x

391. Kessel D, Oleinick NL. Initiation of autophagy by photodynamic therapy. Methods Enzymol. 2009;453:1–16. https://doi.org/10.1016/S0076-6879(08)04001-9

392. Inguscio V, Panzarini E, Dini L. Autophagy Contributes to the Death/Survival Balance in Cancer PhotoDynamic Therapy. Cells. 2012 Aug 3;1(3):464–91. https://doi.org/10.3390/cells1030464

393. Kessel D, Reiners JJ. Apoptosis and autophagy after mitochondrial or endoplasmic reticulum photodamage. Photochem Photobiol. 2007 Oct;83(5):1024–8. https://doi.org/10.1111/j.1751-1097.2007.00088.x

394. Kessel DH, Price M, Reiners JJ. ATG7 deficiency suppresses apoptosis and cell death induced by lysosomal photodamage. Autophagy. 2012 Sep;8(9):1333–41. https://doi.org/10.4161/auto.20792

395. Turubanova VD, Mishchenko TA, Balalaeva IV, Efimova I, Peskova NN, Klapshina LG, et al. Novel porphyrazine-based photodynamic anti-cancer therapy induces immunogenic cell death. Sci Rep. 2021 Mar 30;11(1):7205. https://doi.org/10.1038/s41598-021-86354-4

396. Turubanova VD, Balalaeva IV, Mishchenko TA, Catanzaro E, Alzeibak R, Peskova NN, et al. Immunogenic cell death induced by a new photodynamic therapy based on photosens and photodithazine. J Immunother Cancer. 2019 Dec;7(1):350. https://doi.org/10.1186/s40425-019-0826-3

397. Li L, Song D, Qi L, Jiang M, Wu Y, Gan J, et al. Photodynamic therapy induces human esophageal carcinoma cell pyroptosis by targeting the PKM2/caspase-8/caspase-3/GSDME axis. Cancer Lett. 2021 Nov 1;520:143–59. https://doi.org/10.1016/j.canlet.2021.07.014

398. Hofmeister V, Schrama D, Becker JC. Anti-cancer therapies targeting the tumor stroma. Cancer Immunol Immunother CII. 2008 Jan;57(1):1–17. https://doi.org/10.1007/s00262-007-0365-5

399. Desgrosellier JS, Cheresh DA. Integrins in cancer: biological implications and therapeutic opportunities. Nat Rev Cancer. 2010 Jan;10(1):9–22. https://doi.org/10.1038/nrc2748

400. Peng Q, Nesland JM. Effects of photodynamic therapy on tumor stroma. Ultrastruct Pathol. 2004 Dec;28(5–6):333–40. https://doi.org/10.1080/01913120490515586

401. Li S, Wang P, Zhang G, Ji J, Lv T, Wang X, et al. The effect of ALA-PDT on reversing the activation of cancer-associated fibroblasts in cutaneous squamous cell carcinoma. Photodiagnosis Photodyn Ther. 2019 Sep;27:234–40. https://doi.org/10.1016/j.pdpdt.2019.05.043

402. Celli JP. Stromal interactions as regulators of tumor growth and therapeutic response: A potential target for photodynamic therapy? Isr J Chem. 2012 Sep;52(8–9):757–66. https://doi.org/10.1002/ijch.201200013

403. Lu J, Roy B, Anderson M, Leggett CL, Levy MJ, Pogue B, et al. Verteporfin- and sodium porfimer-mediated photodynamic therapy enhances pancreatic cancer cell death without activating stromal cells in the microenvironment. J Biomed Opt. 2019 Nov;24(11):1–11. https://doi.org/10.1117/1.JBO.24.11.118001

404. Karimnia V, Rizvi I, Slack FJ, Celli JP. Photodestruction of Stromal Fibroblasts Enhances Tumor Response to PDT in 3D Pancreatic Cancer Coculture Models. Photochem Photobiol. 2021 Mar;97(2):416–26. https://doi.org/10.1111/php.13339

405. Margaron P, Sorrenti R, Levy JG. Photodynamic therapy inhibits cell adhesion without altering integrin expression. Biochim Biophys Acta. 1997 Dec 12;1359(3):200–10. https://doi.org/10.1016/s0167-4889(97)00115-8

406. Shen HR, Spikes JD, Kopeceková P, Kopecek J. Photodynamic crosslinking of proteins. I. Model studies using histidine- and lysine-containing N-(2-hydroxypropyl)methacrylamide copolymers. J Photochem Photobiol B. 1996 Jul;34(2–3):203–10. https://doi.org/10.1016/1011-1344(96)07286-7

407. Milla Sanabria L, Rodríguez ME, Cogno IS, Rumie Vittar NB, Pansa MF, Lamberti MJ, et al. Direct and indirect photodynamic therapy effects on the cellular and molecular components of the tumor microenvironment. Biochim Biophys Acta. 2013 Jan;1835(1):36–45. https://doi.org/10.1016/j.bbcan.2012.10.001

408. Chen B, Pogue BW, Hoopes PJ, Hasan T. Vascular and cellular targeting for photodynamic therapy. Crit Rev Eukaryot Gene Expr. 2006;16(4):279–305. https://doi.org/10.1615/critreveukargeneexpr.v16.i4.10

409. Nelson JS, Liaw LH, Berns MW. Tumor destruction in photodynamic therapy. Photochem Photobiol. 1987 Nov;46(5):829–35. https://doi.org/10.1111/j.1751-1097.1987.tb04855.x

410. Star WM, Marijnissen HP, van den Berg-Blok AE, Versteeg JA, Franken KA, Reinhold HS. Destruction of rat mammary tumor and normal tissue microcirculation by hematoporphyrin derivative photoradiation observed in vivo in sandwich observation chambers. Cancer Res. 1986 May;46(5):2532–40.

411. Fingar VH, Wieman TJ, Haydon PS. The effects of thrombocytopenia on vessel stasis and macromolecular leakage after photodynamic therapy using photofrin. Photochem Photobiol. 1997 Oct;66(4):513–7. https://doi.org/10.1111/j.1751-1097.1997.tb03182.x

412. van Straten D, Mashayekhi V, de Bruijn HS, Oliveira S, Robinson DJ. Oncologic Photodynamic Therapy: Basic Principles, Current Clinical Status and Future Directions. Cancers. 2017 Feb 18;9(2):E19. https://doi.org/10.3390/cancers9020019

413. Fingar VH, Kik PK, Haydon PS, Cerrito PB, Tseng M, Abang E, et al. Analysis of acute vascular damage after photodynamic therapy using benzoporphyrin derivative (BPD). Br J Cancer. 1999 Apr;79(11–12):1702–8. https://doi.org/10.1038/sj.bjc.6690271

414. Trachtenberg J, Weersink RA, Davidson SRH, Haider MA, Bogaards A, Gertner MR, et al. Vascular-targeted photodynamic therapy (padoporfin, WST09) for recurrent prostate cancer after failure of external beam radiotherapy: a study of escalating light doses. BJU Int. 2008 Aug 5;102(5):556–62. https://doi.org/10.1111/j.1464-410X.2008.07753.x

415. Zilberstein J, Schreiber S, Bloemers MC, Bendel P, Neeman M, Schechtman E, et al. Antivascular treatment of solid melanoma tumors with bacteriochlorophyll-serine-based photodynamic therapy. Photochem Photobiol. 2001 Mar;73(3):257–66. https://doi.org/10.1562/0031-8655(2001)073<0257:atosmt>2.0.co;2

416. Chen B, Pogue BW, Hoopes PJ, Hasan T. Combining vascular and cellular targeting regimens enhances the efficacy of photodynamic therapy. Int J Radiat Oncol Biol Phys. 2005 Mar 15;61(4):1216–26. https://doi.org/10.1016/j.ijrobp.2004.08.006

417. Kavanagh BD, Coffey BE, Needham D, Hochmuth RM, Dewhirst MW. The effect of flunarizine on erythrocyte suspension viscosity under conditions of extreme hypoxia, low pH, and lactate treatment. Br J Cancer. 1993 Apr;67(4):734–41. https://doi.org/10.1038/bjc.1993.134

418. Krzykawska-Serda M, Dąbrowski JM, Arnaut LG, Szczygieł M, Urbańska K, Stochel G, et al. The role of strong hypoxia in tumors after treatment in the outcome of bacteriochlorin-based photodynamic therapy. Free Radic Biol Med. 2014 Aug;73:239–51. https://doi.org/10.1016/j.freeradbiomed.2014.05.003

419. Kurohane K, Tominaga A, Sato K, North JR, Namba Y, Oku N. Photodynamic therapy targeted to tumor-induced angiogenic vessels. Cancer Lett. 2001 Jun 10;167(1):49–56. https://doi.org/10.1016/s0304-3835(01)00475-x

420. Al-Husein B, Abdalla M, Trepte M, Deremer DL, Somanath PR. Antiangiogenic therapy for cancer: an update. Pharmacotherapy. 2012 Dec;32(12):1095–111. https://doi.org/10.1002/phar.1147

421. Dougherty TJ, Gomer CJ, Henderson BW, Jori G, Kessel D, Korbelik M, et al. Photodynamic therapy. J Natl Cancer Inst. 1998 Jun 17;90(12):889–905. https://doi.org/10.1093/jnci/90.12.889

422. Gomer CJ, Ryter SW, Ferrario A, Rucker N, Wong S, Fisher AM. Photodynamic therapy-mediated oxidative stress can induce expression of heat shock proteins. Cancer Res. 1996 May 15;56(10):2355–60.

423. Luna MC, Ferrario A, Wong S, Fisher AM, Gomer CJ. Photodynamic therapy-mediated oxidative stress as a molecular switch for the temporal expression of genes ligated to the human heat shock promoter. Cancer Res. 2000 Mar 15;60(6):1637–44.

424. Blank M, Mandel M, Keisari Y, Meruelo D, Lavie G. Enhanced ubiquitinylation of heat shock protein 90 as a potential mechanism for mitotic cell death in cancer cells induced with hypericin. Cancer Res. 2003 Dec 1;63(23):8241–7.

425. Korbelik M, Sun J, Cecic I. Photodynamic therapy-induced cell surface expression and release of heat shock proteins: relevance for tumor response. Cancer Res. 2005 Feb 1;65(3):1018–26.

426. Jalili A, Makowski M, Switaj T, Nowis D, Wilczynski GM, Wilczek E, et al. Effective photoimmunotherapy of murine colon carcinoma induced by the combination of photodynamic therapy and dendritic cells. Clin Cancer Res Off J Am Assoc Cancer Res. 2004 Jul 1;10(13):4498–508. https://doi.org/10.1158/1078-0432.CCR-04-0367

427. Etminan N, Peters C, Lakbir D, Bünemann E, Börger V, Sabel MC, et al. Heat-shock protein 70-dependent dendritic cell activation by 5-aminolevulinic acid-mediated photodynamic treatment of human glioblastoma spheroids in vitro. Br J Cancer. 2011 Sep 27;105(7):961–9. https://doi.org/10.1038/bjc.2011.327

428. Panzarini E, Inguscio V, Dini L. Immunogenic cell death: can it be exploited in PhotoDynamic Therapy for cancer? BioMed Res Int. 2013;2013:482160. https://doi.org/10.1155/2013/482160

429. Alzeibak R, Mishchenko TA, Shilyagina NY, Balalaeva IV, Vedunova MV, Krysko DV. Targeting immunogenic cancer cell death by photodynamic therapy: past, present and future. J Immunother Cancer. 2021 Jan;9(1):e001926. https://doi.org/10.1136/jitc-2020-001926

430. Panzarini E, Inguscio V, Fimia GM, Dini L. Rose Bengal acetate photodynamic therapy (RBAc-PDT) induces exposure and release of Damage-Associated Molecular Patterns (DAMPs) in human HeLa cells. PloS One. 2014;9(8):e105778. https://doi.org/10.1371/journal.pone.0105778

431. Bezu L, Sauvat A, Humeau J, Leduc M, Kepp O, Kroemer G. eIF2α phosphorylation: A hallmark of immunogenic cell death. Oncoimmunology. 2018;7(6):e1431089. https://doi.org/10.1080/2162402X.2018.1431089

432. Turubanova VD, Balalaeva IV, Mishchenko TA, Catanzaro E, Alzeibak R, Peskova NN, et al. Immunogenic cell death induced by a new photodynamic therapy based on photosens and photodithazine. J Immunother Cancer. 2019 Dec;7(1):350. https://doi.org/10.1186/s40425-019-0826-3

433. Gomes-da-Silva LC, Zhao L, Bezu L, Zhou H, Sauvat A, Liu P, et al. Photodynamic therapy with redaporfin targets the endoplasmic reticulum and Golgi apparatus. EMBO J. 2018 Jul 2;37(13):e98354. https://doi.org/10.15252/embj.201798354

434. Garg AD, Agostinis P. ER stress, autophagy and immunogenic cell death in photodynamic therapy-induced anti-cancer immune responses. Photochem Photobiol Sci Off J Eur Photochem Assoc Eur Soc Photobiol. 2014 Mar;13(3):474–87. https://doi.org/10.1039/c3pp50333j

435. Deng H, Zhou Z, Yang W, Lin L-S, Wang S, Niu G, et al. Endoplasmic Reticulum Targeting to Amplify Immunogenic Cell Death for Cancer Immunotherapy. Nano Lett. 2020 Mar 11;20(3):1928–33. https://doi.org/10.1021/acs.nanolett.9b05210

436. Morais JAV, Almeida LR, Rodrigues MC, Azevedo RB, Muehlmann LA. The induction of immunogenic cell death by photodynamic therapy in B16F10 cells in vitro is effected by the concentration of the photosensitizer. Photodiagnosis Photodyn Ther. 2021 Sep;35:102392. https://doi.org/10.1016/j.pdpdt.2021.102392

437. Doix B, Trempolec N, Riant O, Feron O. Low Photosensitizer Dose and Early Radiotherapy Enhance Antitumor Immune Response of Photodynamic Therapy-Based Dendritic Cell Vaccination. Front Oncol. 2019;9:811. https://doi.org/10.3389/fonc.2019.00811

438. Matroule J-Y, Volanti C, Piette J. NF-kappaB in photodynamic therapy: discrepancies of a master regulator. Photochem Photobiol. 2006 Oct;82(5):1241–6. https://doi.org/10.1562/2006-03-30-IR-862

439. Cecic I, Korbelik M. Mediators of peripheral blood neutrophilia induced by photodynamic therapy of solid tumors. Cancer Lett. 2002 Sep 8;183(1):43–51. https://doi.org/10.1016/s0304-3835(02)00092-7

440. Castano AP, Mroz P, Hamblin MR. Photodynamic therapy and anti-tumour immunity. Nat Rev Cancer. 2006 Jul;6(7):535–45. https://doi.org/10.1038/nrc1894

441. Gollnick SO, Liu X, Owczarczak B, Musser DA, Henderson BW. Altered expression of interleukin 6 and interleukin 10 as a result of photodynamic therapy in vivo. Cancer Res. 1997 Sep 15;57(18):3904–9.

442. Kick G, Messer G, Goetz A, Plewig G, Kind P. Photodynamic therapy induces expression of interleukin 6 by activation of AP-1 but not NF-kappa B DNA binding. Cancer Res. 1995 Jun 1;55(11):2373–9.

443. Evans S, Matthews W, Perry R, Fraker D, Norton J, Pass HI. Effect of photodynamic therapy on tumor necrosis factor production by murine macrophages. J Natl Cancer Inst. 1990 Jan 3;82(1):34–9. https://doi.org/10.1093/jnci/82.1.34

444. Gollnick SO, Evans SS, Baumann H, Owczarczak B, Maier P, Vaughan L, et al. Role of cytokines in photodynamic therapy-induced local and systemic inflammation. Br J Cancer. 2003 Jun 2;88(11):1772–9. https://doi.org/10.1038/sj.bjc.6600864

445. Jones SA. Directing transition from innate to acquired immunity: defining a role for IL-6. J Immunol Baltim Md 1950. 2005 Sep 15;175(6):3463–8. https://doi.org/10.4049/jimmunol.175.6.3463

446. Korbelik M, Cooper PD. Potentiation of photodynamic therapy of cancer by complement: the effect of gamma-inulin. Br J Cancer. 2007 Jan 15;96(1):67–72. https://doi.org/10.1038/sj.bjc.6603508

447. Wei L-H, Baumann H, Tracy E, Wang Y, Hutson A, Rose-John S, et al. Interleukin-6 trans signalling enhances photodynamic therapy by modulating cell cycling. Br J Cancer. 2007 Dec 3;97(11):1513–22. https://doi.org/10.1038/sj.bjc.6604073

448. Lobo ACS, Gomes-da-Silva LC, Rodrigues-Santos P, Cabrita A, Santos-Rosa M, Arnaut LG. Immune Responses after Vascular Photodynamic Therapy with Redaporfin. J Clin Med. 2019 Dec 31;9(1):E104. https://doi.org/10.3390/jcm9010104

449. Brackett CM, Owczarczak B, Ramsey K, Maier PG, Gollnick SO. IL-6 potentiates tumor resistance to photodynamic therapy (PDT). Lasers Surg Med. 2011 Sep;43(7):676–85. https://doi.org/10.1002/lsm.21107

450. Davis RW, Papasavvas E, Klampatsa A, Putt M, Montaner LJ, Culligan MJ, et al. A preclinical model to investigate the role of surgically-induced inflammation in tumor responses to intraoperative photodynamic therapy. Lasers Surg Med. 2018 Jul;50(5):440–50. https://doi.org/10.1002/lsm.22934

451. de Vree WJ, Essers MC, Koster JF, Sluiter W. Role of interleukin 1 and granulocyte colony-stimulating factor in photofrin-based photodynamic therapy of rat rhabdomyosarcoma tumors. Cancer Res. 1997 Jul 1;57(13):2555–8.

452. Wang X, Feuerstein GZ, Gu JL, Lysko PG, Yue TL. Interleukin-1 beta induces expression of adhesion molecules in human vascular smooth muscle cells and enhances adhesion of leukocytes to smooth muscle cells. Atherosclerosis. 1995 May;115(1):89–98. https://doi.org/10.1016/0021-9150(94)05503-b

453. Nseyo UO, Whalen RK, Duncan MR, Berman B, Lundahl SL. Urinary cytokines following photodynamic therapy for bladder cancer. A preliminary report. Urology. 1990 Aug;36(2):167–71. https://doi.org/10.1016/0090-4295(90)80220-h

454. Brackett CM, Muhitch JB, Evans SS, Gollnick SO. IL-17 promotes neutrophil entry into tumor-draining lymph nodes following induction of sterile inflammation. J Immunol Baltim Md 1950. 2013 Oct 15;191(8):4348–57. https://doi.org/10.4049/jimmunol.1103621

455. Henderson BW, Gollnick SO, Snyder JW, Busch TM, Kousis PC, Cheney RT, et al. Choice of oxygen-conserving treatment regimen determines the inflammatory response and outcome of photodynamic therapy of tumors. Cancer Res. 2004 Mar 15;64(6):2120–6.

456. Kousis PC, Henderson BW, Maier PG, Gollnick SO. Photodynamic therapy enhancement of antitumor immunity is regulated by neutrophils. Cancer Res. 2007 Nov 1;67(21):10501–10. https://doi.org/10.1158/0008-5472.CAN-07-1778

457. Korbelik M, Cecic I, Merchant S, Sun J. Acute phase response induction by cancer treatment with photodynamic therapy. Int J Cancer. 2008 Mar 15;122(6):1411–7. https://doi.org/10.1002/ijc.23248

458. Sun J, Cecic I, Parkins CS, Korbelik M. Neutrophils as inflammatory and immune effectors in photodynamic therapy-treated mouse SCCVII tumours. Photochem Photobiol Sci Off J Eur Photochem Assoc Eur Soc Photobiol. 2002 Sep;1(9):690–5. https://doi.org/10.1039/b204254a

459. de Vree WJ, Essers MC, de Bruijn HS, Star WM, Koster JF, Sluiter W. Evidence for an important role of neutrophils in the efficacy of photodynamic therapy in vivo. Cancer Res. 1996 Jul 1;56(13):2908–11.

460. Cecic I, Parkins CS, Korbelik M. Induction of systemic neutrophil response in mice by photodynamic therapy of solid tumors. Photochem Photobiol. 2001 Nov;74(5):712–20. https://doi.org/10.1562/0031-8655(2001)074<0712:iosnri>2.0.co;2

461. Krosl G, Korbelik M, Dougherty GJ. Induction of immune cell infiltration into murine SCCVII tumour by photofrin-based photodynamic therapy. Br J Cancer. 1995 Mar;71(3):549–55. https://doi.org/10.1038/bjc.1995.108

462. Cecic I, Sun J, Korbelik M. Role of complement anaphylatoxin C3a in photodynamic therapy-elicited engagement of host neutrophils and other immune cells. Photochem Photobiol. 2006 Apr;82(2):558–62. https://doi.org/10.1562/2005-09-09-RA-681

463. Cecic I, Korbelik M. Deposition of complement proteins on cells treated by photodynamic therapy in vitro. J Environ Pathol Toxicol Oncol Off Organ Int Soc Environ Toxicol Cancer. 2006;25(1–2):189–203. https://doi.org/10.1615/jenvironpatholtoxicoloncol.v25.i1-2.110

464. Cecic I, Serrano K, Gyongyossy-Issa M, Korbelik M. Characteristics of complement activation in mice bearing Lewis lung carcinomas treated by photodynamic therapy. Cancer Lett. 2005 Jul 28;225(2):215–23. https://doi.org/10.1016/j.canlet.2004.11.059

465. Stott B, Korbelik M. Activation of complement C3, C5, and C9 genes in tumors treated by photodynamic therapy. Cancer Immunol Immunother CII. 2007 May;56(5):649–58. https://doi.org/10.1007/s00262-006-0221-z

466. Davis RW, Snyder E, Miller J, Carter S, Houser C, Klampatsa A, et al. Luminol Chemiluminescence Reports Photodynamic Therapy-Generated Neutrophil Activity In Vivo and Serves as a Biomarker of Therapeutic Efficacy. Photochem Photobiol. 2019 Jan;95(1):430–8. https://doi.org/10.1111/php.13040

467. Gollnick SO, Brackett CM. Enhancement of anti-tumor immunity by photodynamic therapy. Immunol Res. 2010 Mar;46(1–3):216–26. https://doi.org/10.1007/s12026-009-8119-4

468. Korbelik M, Cecic I. Contribution of myeloid and lymphoid host cells to the curative outcome of mouse sarcoma treatment by photodynamic therapy. Cancer Lett. 1999 Mar 22;137(1):91–8. https://doi.org/10.1016/s0304-3835(98)00349-8

469. Reginato E, Lindenmann J, Langner C, Schweintzger N, Bambach I, Smolle-Jüttner F, et al. Photodynamic therapy downregulates the function of regulatory T cells in patients with esophageal squamous cell carcinoma. Photochem Photobiol Sci Off J Eur Photochem Assoc Eur Soc Photobiol. 2014 Sep;13(9):1281–9. https://doi.org/10.1039/c4pp00186a

470. Murray PJ, Wynn TA. Protective and pathogenic functions of macrophage subsets. Nat Rev Immunol. 2011 Oct 14;11(11):723–37. https://doi.org/10.1038/nri3073

471. Hao N-B, Lü M-H, Fan Y-H, Cao Y-L, Zhang Z-R, Yang S-M. Macrophages in tumor microenvironments and the progression of tumors. Clin Dev Immunol. 2012;2012:948098. https://doi.org/10.1155/2012/948098

472. Korbelik M, Hamblin MR. The impact of macrophage-cancer cell interaction on the efficacy of photodynamic therapy. Photochem Photobiol Sci Off J Eur Photochem Assoc Eur Soc Photobiol. 2015 Aug;14(8):1403–9. https://doi.org/10.1039/c4pp00451e

473. Ai X, Hu M, Wang Z, Lyu L, Zhang W, Li J, et al. Enhanced Cellular Ablation by Attenuating Hypoxia Status and Reprogramming Tumor-Associated Macrophages via NIR Light-Responsive Upconversion Nanocrystals. Bioconjug Chem. 2018 Apr 18;29(4):928–38. https://doi.org/10.1021/acs.bioconjchem.8b00068

474. Hamblin MR, Newman EL. On the mechanism of the tumour-localising effect in photodynamic therapy. J Photochem Photobiol B. 1994 Apr;23(1):3–8. https://doi.org/10.1016/s1011-1344(94)80018-9

475. Steubing RW, Yeturu S, Tuccillo A, Sun CH, Berns MW. Activation of macrophages by Photofrin II during photodynamic therapy. J Photochem Photobiol B. 1991 Jul;10(1–2):133–45. https://doi.org/10.1016/1011-1344(91)80218-7

476. Song S, Zhou F, Chen WR, Xing D. Direct imaging of macrophage activation during PDT treatment. In: Tenth International Conference on Photonics and Imaging in Biology and Medicine (PIBM 2011) [Internet]. SPIE; 2012 [cited 2022 Jan 9]. p. 159–68. Available from: https://www.spiedigitallibrary.org/conference-proceedings-of-spie/8329/83290M/Direct-imaging-of-macrophage-activation-during-PDT-treatment/10.1117/12.919005.fullhttps://doi.org/10.1117/12.919005

477. Hayashi N, Kataoka H, Yano S, Tanaka M, Moriwaki K, Akashi H, et al. A novel photodynamic therapy targeting cancer cells and tumor-associated macrophages. Mol Cancer Ther. 2015 Feb;14(2):452–60. https://doi.org/10.1158/1535-7163.MCT-14-0348

478. Kawczyk-Krupka A, Czuba Z, Szliszka E, Król W, Sieroń A. The role of photosensitized macrophages in photodynamic therapy. Oncol Rep. 2011 Jul;26(1):275–80. https://doi.org/10.3892/or.2011.1262

479. Zhu Z, Scalfi-Happ C, Ryabova A, Gräfe S, Wiehe A, Peter R-U, et al. Photodynamic activity of Temoporfin nanoparticles induces a shift to the M1-like phenotype in M2-polarized macrophages. J Photochem Photobiol B. 2018 Aug;185:215–22. https://doi.org/10.1016/j.jphotobiol.2018.06.015

480. Prignano F, Lotti T, Spallanzani A, Berti S, de Giorgi V, Moretti S. Sequential effects of photodynamic treatment of basal cell carcinoma. J Cutan Pathol. 2009 Apr;36(4):409–16. https://doi.org/10.1111/j.1600-0560.2008.01063.x

481. Wu J, Lanier LL. Natural killer cells and cancer. Adv Cancer Res. 2003;90:127–56. https://doi.org/10.1016/s0065-230x(03)90004-2

482. Vivier E, Tomasello E, Baratin M, Walzer T, Ugolini S. Functions of natural killer cells. Nat Immunol. 2008 May;9(5):503–10. https://doi.org/10.1038/ni1582

483. Long EO, Kim HS, Liu D, Peterson ME, Rajagopalan S. Controlling natural killer cell responses: integration of signals for activation and inhibition. Annu Rev Immunol. 2013;31:227–58. https://doi.org/10.1146/annurev-immunol-020711-075005

484. Belicha-Villanueva A, Riddell J, Bangia N, Gollnick SO. The effect of photodynamic therapy on tumor cell expression of major histocompatibility complex (MHC) class I and MHC class I-related molecules. Lasers Surg Med. 2012 Jan;44(1):60–8. https://doi.org/10.1002/lsm.21160

485. Park M-J, Bae J-H, Chung JS, Kim S-H, Kang C-D. Induction of NKG2D ligands and increased sensitivity of tumor cells to NK cell-mediated cytotoxicity by hematoporphyrin-based photodynamic therapy. Immunol Invest. 2011;40(4):367–82. https://doi.org/10.3109/08820139.2010.551435

486. Kabingu E, Vaughan L, Owczarczak B, Ramsey KD, Gollnick SO. CD8+ T cell-mediated control of distant tumours following local photodynamic therapy is independent of CD4+ T cells and dependent on natural killer cells. Br J Cancer. 2007 Jun 18;96(12):1839–48. https://doi.org/10.1038/sj.bjc.6603792

487. Hendrzak-Henion JA, Knisely TL, Cincotta L, Cincotta E, Cincotta AH. Role of the immune system in mediating the antitumor effect of benzophenothiazine photodynamic therapy. Photochem Photobiol. 1999 May;69(5):575–81.

488. Korbelik M, Dougherty GJ. Photodynamic therapy-mediated immune response against subcutaneous mouse tumors. Cancer Res. 1999 Apr 15;59(8):1941–6.

489. Korbelik M, Sun J. Cancer treatment by photodynamic therapy combined with adoptive immunotherapy using genetically altered natural killer cell line. Int J Cancer. 2001 Jul 15;93(2):269–74. https://doi.org/10.1002/ijc.1326

490. Theodoraki MN, Lorenz K, Lotfi R, Fürst D, Tsamadou C, Jaekle S, et al. Influence of photodynamic therapy on peripheral immune cell populations and cytokine concentrations in head and neck cancer. Photodiagnosis Photodyn Ther. 2017 Sep;19:194–201. https://doi.org/10.1016/j.pdpdt.2017.05.015

491. Canti G, Lattuada D, Nicolin A, Taroni P, Valentini G, Cubeddu R. Antitumor immunity induced by photodynamic therapy with aluminum disulfonated phthalocyanines and laser light. Anticancer Drugs. 1994 Aug;5(4):443–7. https://doi.org/10.1097/00001813-199408000-00009

492. Korbelik M, Krosl G, Krosl J, Dougherty GJ. The role of host lymphoid populations in the response of mouse EMT6 tumor to photodynamic therapy. Cancer Res. 1996 Dec 15;56(24):5647–52.

493. Preise D, Oren R, Glinert I, Kalchenko V, Jung S, Scherz A, et al. Systemic antitumor protection by vascular-targeted photodynamic therapy involves cellular and humoral immunity. Cancer Immunol Immunother CII. 2009 Jan;58(1):71–84. https://doi.org/10.1007/s00262-008-0527-0

494. Mroz P, Szokalska A, Wu MX, Hamblin MR. Photodynamic therapy of tumors can lead to development of systemic antigen-specific immune response. PloS One. 2010 Dec 14;5(12):e15194. https://doi.org/10.1371/journal.pone.0015194

495. Rocha LB, Gomes-da-Silva LC, Dąbrowski JM, Arnaut LG. Elimination of primary tumours and control of metastasis with rationally designed bacteriochlorin photodynamic therapy regimens. Eur J Cancer Oxf Engl 1990. 2015 Sep;51(13):1822–30. https://doi.org/10.1016/j.ejca.2015.06.002

496. Abdel-Hady ES, Martin-Hirsch P, Duggan-Keen M, Stern PL, Moore JV, Corbitt G, et al. Immunological and viral factors associated with the response of vulval intraepithelial neoplasia to photodynamic therapy. Cancer Res. 2001 Jan 1;61(1):192–6.

497. Thong PS-P, Ong K-W, Goh NS-G, Kho K-W, Manivasager V, Bhuvaneswari R, et al. Photodynamic-therapy-activated immune response against distant untreated tumours in recurrent angiosarcoma. Lancet Oncol. 2007 Oct;8(10):950–2. https://doi.org/10.1016/S1470-2045(07)70318-2

498. Slominski A, Tobin DJ, Shibahara S, Wortsman J. Melanin pigmentation in mammalian skin and its hormonal regulation. Physiol Rev. 2004 Oct;84(4):1155–228. https://doi.org/10.1152/physrev.00044.2003

499. Gray-Schopfer V, Wellbrock C, Marais R. Melanoma biology and new targeted therapy. Nature. 2007 Feb 22;445(7130):851–7. https://doi.org/10.1038/nature05661

500. Lin JY, Fisher DE. Melanocyte biology and skin pigmentation. Nature. 2007 Feb 22;445(7130):843–50. https://doi.org/10.1038/nature05660

501. Lo JA, Fisher DE. The melanoma revolution: from UV carcinogenesis to a new era in therapeutics. Science. 2014 Nov 21;346(6212):945–9. https://doi.org/10.1126/science.1253735

502. Schadendorf D, van Akkooi ACJ, Berking C, Griewank KG, Gutzmer R, Hauschild A, et al. Melanoma. Lancet Lond Engl. 2018 Sep 15;392(10151):971–84. https://doi.org/10.1016/S0140-6736(18)31559-9

503. Hodis E, Watson IR, Kryukov GV, Arold ST, Imielinski M, Theurillat J-P, et al. A landscape of driver mutations in melanoma. Cell. 2012 Jul 20;150(2):251–63. https://doi.org/10.1016/j.cell.2012.06.024

504. Cancer Genome Atlas Network. Genomic Classification of Cutaneous Melanoma. Cell. 2015 Jun 18;161(7):1681–96. https://doi.org/10.1016/j.cell.2015.05.044

505. Bastian BC. The molecular pathology of melanoma: an integrated taxonomy of melanocytic neoplasia. Annu Rev Pathol. 2014;9:239–71. https://doi.org/10.1146/annurev-pathol-012513-104658

506. Mitra D, Luo X, Morgan A, Wang J, Hoang MP, Lo J, et al. An ultraviolet-radiation-independent pathway to melanoma carcinogenesis in the red hair/fair skin background. Nature. 2012 Nov 15;491(7424):449–53. https://doi.org/10.1038/nature11624

507. Curtin JA, Fridlyand J, Kageshita T, Patel HN, Busam KJ, Kutzner H, et al. Distinct sets of genetic alterations in melanoma. N Engl J Med. 2005 Nov 17;353(20):2135–47. https://doi.org/10.1056/NEJMoa050092

508. Hayward NK, Wilmott JS, Waddell N, Johansson PA, Field MA, Nones K, et al. Whole-genome landscapes of major melanoma subtypes. Nature. 2017 May 11;545(7653):175–80. https://doi.org/10.1038/nature22071

509. Huang FW, Hodis E, Xu MJ, Kryukov GV, Chin L, Garraway LA. Highly recurrent TERT promoter mutations in human melanoma. Science. 2013 Feb 22;339(6122):957–9. https://doi.org/10.1126/science.1229259

510. Horn S, Figl A, Rachakonda PS, Fischer C, Sucker A, Gast A, et al. TERT promoter mutations in familial and sporadic melanoma. Science. 2013 Feb 22;339(6122):959–61. https://doi.org/10.1126/science.1230062

511. Griewank KG, Murali R, Puig-Butille JA, Schilling B, Livingstone E, Potrony M, et al. TERT promoter mutation status as an independent prognostic factor in cutaneous melanoma. J Natl Cancer Inst. 2014 Sep;106(9):dju246. https://doi.org/10.1093/jnci/dju246

512. Maldonado JL, Fridlyand J, Patel H, Jain AN, Busam K, Kageshita T, et al. Determinants of BRAF mutations in primary melanomas. J Natl Cancer Inst. 2003 Dec 17;95(24):1878–90. https://doi.org/10.1093/jnci/djg123

513. Menzies AM, Haydu LE, Visintin L, Carlino MS, Howle JR, Thompson JF, et al. Distinguishing clinicopathologic features of patients with V600E and V600K BRAF-mutant metastatic melanoma. Clin Cancer Res Off J Am Assoc Cancer Res. 2012 Jun 15;18(12):3242–9. https://doi.org/10.1158/1078-0432.CCR-12-0052

514. Shain AH, Yeh I, Kovalyshyn I, Sriharan A, Talevich E, Gagnon A, et al. The Genetic Evolution of Melanoma from Precursor Lesions. N Engl J Med. 2015 Nov 12;373(20):1926–36. https://doi.org/10.1056/NEJMoa1502583

515. Guo W, Wang H, Li C. Signal pathways of melanoma and targeted therapy. Signal Transduct Target Ther. 2021 Dec 20;6(1):424. https://doi.org/10.1038/s41392-021-00827-6

516. Davies H, Bignell GR, Cox C, Stephens P, Edkins S, Clegg S, et al. Mutations of the BRAF gene in human cancer. Nature. 2002 Jun 27;417(6892):949–54. https://doi.org/10.1038/nature00766

517. Pollock PM, Harper UL, Hansen KS, Yudt LM, Stark M, Robbins CM, et al. High frequency of BRAF mutations in nevi. Nat Genet. 2003 Jan;33(1):19–20. https://doi.org/10.1038/ng1054

518. Hingorani SR, Jacobetz MA, Robertson GP, Herlyn M, Tuveson DA. Suppression of BRAF(V599E) in human melanoma abrogates transformation. Cancer Res. 2003 Sep 1;63(17):5198–202.

519. Karasarides M, Chiloeches A, Hayward R, Niculescu-Duvaz D, Scanlon I, Friedlos F, et al. B-RAF is a therapeutic target in melanoma. Oncogene. 2004 Aug 19;23(37):6292–8. https://doi.org/10.1038/sj.onc.1207785

520. Randic T, Kozar I, Margue C, Utikal J, Kreis S. NRAS mutant melanoma: Towards better therapies. Cancer Treat Rev. 2021 Sep;99:102238. https://doi.org/10.1016/j.ctrv.2021.102238

521. Andersen LB, Fountain JW, Gutmann DH, Tarlé SA, Glover TW, Dracopoli NC, et al. Mutations in the neurofibromatosis 1 gene in sporadic malignant melanoma cell lines. Nat Genet. 1993 Feb;3(2):118–21. https://doi.org/10.1038/ng0293-118

522. Nissan MH, Pratilas CA, Jones AM, Ramirez R, Won H, Liu C, et al. Loss of NF1 in cutaneous melanoma is associated with RAS activation and MEK dependence. Cancer Res. 2014 Apr 15;74(8):2340–50. https://doi.org/10.1158/0008-5472.CAN-13-2625

523. Krauthammer M, Kong Y, Bacchiocchi A, Evans P, Pornputtapong N, Wu C, et al. Exome sequencing identifies recurrent mutations in NF1 and RASopathy genes in sun-exposed melanomas. Nat Genet. 2015 Sep;47(9):996–1002. https://doi.org/10.1038/ng.3361

524. Papp T, Pemsel H, Rollwitz I, Schipper H, Weiss DG, Schiffmann D, et al. Mutational analysis of N-ras, p53, CDKN2A (p16(INK4a)), p14(ARF), CDK4, and MC1R genes in human dysplastic melanocytic naevi. J Med Genet. 2003 Feb;40(2):E14. https://doi.org/10.1136/jmg.40.2.e14

525. Serrano M, Lee H, Chin L, Cordon-Cardo C, Beach D, DePinho RA. Role of the INK4a locus in tumor suppression and cell mortality. Cell. 1996 Apr 5;85(1):27–37. https://doi.org/10.1016/s0092-8674(00)81079-x

526. Wölfel T, Hauer M, Schneider J, Serrano M, Wölfel C, Klehmann-Hieb E, et al. A p16INK4a-insensitive CDK4 mutant targeted by cytolytic T lymphocytes in a human melanoma. Science. 1995 Sep 1;269(5228):1281–4. https://doi.org/10.1126/science.7652577

527. Sauter ER, Yeo U-C, von Stemm A, Zhu W, Litwin S, Tichansky DS, et al. Cyclin D1 is a candidate oncogene in cutaneous melanoma. Cancer Res. 2002 Jun 1;62(11):3200–6.

528. Stahl JM, Sharma A, Cheung M, Zimmerman M, Cheng JQ, Bosenberg MW, et al. Deregulated Akt3 activity promotes development of malignant melanoma. Cancer Res. 2004 Oct 1;64(19):7002–10. https://doi.org/10.1158/0008-5472.CAN-04-1399

529. Robertson GP. Functional and therapeutic significance of Akt deregulation in malignant melanoma. Cancer Metastasis Rev. 2005 Jun;24(2):273–85. https://doi.org/10.1007/s10555-005-1577-9

530. Scherer D, Kumar R. Genetics of pigmentation in skin cancer--a review. Mutat Res. 2010 Oct;705(2):141–53. https://doi.org/10.1016/j.mrrev.2010.06.002

531. American cancer society - Genetic Counseling & Testing for Melanoma | High Risk for Melanoma [Internet]. [cited 2022 Jan 27]. Available from: https://www.cancer.org/cancer/melanoma-skin-cancer/causes-risks-prevention/genetic-counseling-and-testing-for-people-at-high-risk-of-melanoma.html

532. Swetter SM, Tsao H, Bichakjian CK, Curiel-Lewandrowski C, Elder DE, Gershenwald JE, et al. Guidelines of care for the management of primary cutaneous melanoma. J Am Acad Dermatol. 2019 Jan;80(1):208–50. https://doi.org/10.1016/j.jaad.2018.08.055

533. Kalady MF, White RR, Johnson JL, Tyler DS, Seigler HF. Thin melanomas: predictive lethal characteristics from a 30-year clinical experience. Ann Surg. 2003 Oct;238(4):528–35; discussion 535-537. https://doi.org/10.1097/01.sla.0000090446.63327.40

534. Sandru A, Voinea S, Panaitescu E, Blidaru A. Survival rates of patients with metastatic malignant melanoma. J Med Life. 2014 Dec;7(4):572–6.

535. Melanoma Survival Rates [Internet]. Melanoma Research Alliance. [cited 2022 Jan 28]. Available from: https://www.curemelanoma.org/about-melanoma/melanoma-staging/melanoma-survival-rates/

536. Melanoma Survival Rates | Melanoma Survival Statistics [Internet]. [cited 2022 Jan 28]. Available from: https://www.cancer.org/cancer/melanoma-skin-cancer/detection-diagnosis-staging/survival-rates-for-melanoma-skin-cancer-by-stage.html

537. Burns D, George J, Aucoin D, Bower J, Burrell S, Gilbert R, et al. The Pathogenesis and Clinical Management of Cutaneous Melanoma: An Evidence-Based Review. J Med Imaging Radiat Sci. 2019 Sep;50(3):460-469.e1. https://doi.org/10.1016/j.jmir.2019.05.001

538. Canadian Cancer Society - Treatments for melanoma skin cancer [Internet]. Canadian Cancer Society. [cited 2022 Jan 28]. Available from: https://cancer.ca/en/cancer-information/cancer-types/skin-melanoma/treatment

539. American Society of Clinical Oncology - Systemic therapy for melanoma [Internet]. ASCO. [cited 2022 Jan 28]. Available from: https://www.asco.org/practice-patients/guidelines/melanoma

540. Giavazzi R, Garofalo A. Syngeneic murine metastasis models : b16 melanoma. Methods Mol Med. 2001;58:223–9. https://doi.org/10.1385/1-59259-137-X:223

541. Gregg RK. Model Systems for the Study of Malignant Melanoma. Methods Mol Biol Clifton NJ. 2021;2265:1–21. https://doi.org/10.1007/978-1-0716-1205-7_1

542. Overwijk WW, Restifo NP. B16 as a mouse model for human melanoma. Curr Protoc Immunol. 2001 May;Chapter 20:Unit 20.1. https://doi.org/10.1002/0471142735.im2001s39

543. Dankort D, Curley DP, Cartlidge RA, Nelson B, Karnezis AN, Damsky WE, et al. Braf(V600E) cooperates with Pten loss to induce metastatic melanoma. Nat Genet. 2009 May;41(5):544–52. https://doi.org/10.1038/ng.356

544. The Jackson Laboratory - 013590 - BRaf[CA], Pten[loxP], Tyr::CreER[T2] Strain Details [Internet]. [cited 2022 Jan 28]. Available from: https://www.jax.org/strain/013590

545. Hooijkaas AI, Gadiot J, van der Valk M, Mooi WJ, Blank CU. Targeting BRAFV600E in an inducible murine model of melanoma. Am J Pathol. 2012 Sep;181(3):785–94. https://doi.org/10.1016/j.ajpath.2012.06.002

546. Kowalewski DJ, Stevanović S. Biochemical large-scale identification of MHC class I ligands. Methods Mol Biol Clifton NJ. 2013;960:145–57. https://doi.org/10.1007/978-1-62703-218-6_12

547. Rappsilber J, Ishihama Y, Mann M. Stop and go extraction tips for matrix-assisted laser desorption/ionization, nanoelectrospray, and LC/MS sample pretreatment in proteomics. Anal Chem. 2003 Feb 1;75(3):663–70. https://doi.org/10.1021/ac026117i

548. Haas W, Faherty BK, Gerber SA, Elias JE, Beausoleil SA, Bakalarski CE, et al. Optimization and use of peptide mass measurement accuracy in shotgun proteomics. Mol Cell Proteomics MCP. 2006 Jul;5(7):1326–37. https://doi.org/10.1074/mcp.M500339-MCP200

549. Percolator [Internet]. [cited 2022 Apr 7]. Available from: http://percolator.ms/

550. Kennedy BE, Murphy JP, Clements DR, Konda P, Holay N, Kim Y, et al. Inhibition of Pyruvate Dehydrogenase Kinase Enhances the Antitumor Efficacy of Oncolytic Reovirus. Cancer Res. 2019 Aug 1;79(15):3824–36. https://doi.org/10.1158/0008-5472.CAN-18-2414

551. Caron E, Kowalewski DJ, Chiek Koh C, Sturm T, Schuster H, Aebersold R. Analysis of Major Histocompatibility Complex (MHC) Immunopeptidomes Using Mass Spectrometry. Mol Cell Proteomics MCP. 2015 Dec;14(12):3105–17. https://doi.org/10.1074/mcp.O115.052431

552. Yadav M, Jhunjhunwala S, Phung QT, Lupardus P, Tanguay J, Bumbaca S, et al. Predicting immunogenic tumour mutations by combining mass spectrometry and exome sequencing. Nature. 2014 Nov 27;515(7528):572–6. https://doi.org/10.1038/nature14001

553. Kowalewski DJ, Schuster H, Backert L, Berlin C, Kahn S, Kanz L, et al. HLA ligandome analysis identifies the underlying specificities of spontaneous antileukemia immune responses in chronic lymphocytic leukemia (CLL). Proc Natl Acad Sci U S A. 2015 Jan 13;112(2):E166-175. https://doi.org/10.1073/pnas.1416389112

554. Barnstable CJ, Bodmer WF, Brown G, Galfre G, Milstein C, Williams AF, et al. Production of monoclonal antibodies to group A erythrocytes, HLA and other human cell surface antigens-new tools for genetic analysis. Cell. 1978 May;14(1):9–20. https://doi.org/10.1016/0092-8674(78)90296-9

555. Laumont CM, Daouda T, Laverdure J-P, Bonneil É, Caron-Lizotte O, Hardy M-P, et al. Global proteogenomic analysis of human MHC class I-associated peptides derived from non-canonical reading frames. Nat Commun. 2016 Jan 5;7:10238. https://doi.org/10.1038/ncomms10238

556. Nagarajan NA, de Verteuil DA, Sriranganadane D, Yahyaoui W, Thibault P, Perreault C, et al. ERAAP Shapes the Peptidome Associated with Classical and Nonclassical MHC Class I Molecules. J Immunol Baltim Md 1950. 2016 Aug 15;197(4):1035–43. https://doi.org/10.4049/jimmunol.1500654

557. Noble WS. Mass spectrometrists should search only for peptides they care about. Nat Methods. 2015 Jul;12(7):605–8. https://doi.org/10.1038/nmeth.3450

558. Frewen BE, Merrihew GE, Wu CC, Noble WS, MacCoss MJ. Analysis of peptide MS/MS spectra from large-scale proteomics experiments using spectrum libraries. Anal Chem. 2006 Aug 15;78(16):5678–84. https://doi.org/10.1021/ac060279n

559. Schubert B, Brachvogel H-P, Jürges C, Kohlbacher O. EpiToolKit--a web-based workbench for vaccine design. Bioinforma Oxf Engl. 2015 Jul 1;31(13):2211–3. https://doi.org/10.1093/bioinformatics/btv116

560. Lundegaard C, Lund O, Nielsen M. Accurate approximation method for prediction of class I MHC affinities for peptides of length 8, 10 and 11 using prediction tools trained on 9mers. Bioinforma Oxf Engl. 2008 Jun 1;24(11):1397–8. https://doi.org/10.1093/bioinformatics/btn128

561. Vita R, Overton JA, Greenbaum JA, Ponomarenko J, Clark JD, Cantrell JR, et al. The immune epitope database (IEDB) 3.0. Nucleic Acids Res. 2015 Jan;43(Database issue):D405-412. https://doi.org/10.1093/nar/gku938

562. Rammensee H, Bachmann J, Emmerich NP, Bachor OA, Stevanović S. SYFPEITHI: database for MHC ligands and peptide motifs. Immunogenetics. 1999 Nov;50(3–4):213–9. https://doi.org/10.1007/s002510050595

563. Lin HH, Ray S, Tongchusak S, Reinherz EL, Brusic V. Evaluation of MHC class I peptide binding prediction servers: applications for vaccine research. BMC Immunol. 2008 Mar 16;9:8. https://doi.org/10.1186/1471-2172-9-8

564. Andreatta M, Nielsen M. Gapped sequence alignment using artificial neural networks: application to the MHC class I system. Bioinforma Oxf Engl. 2016 Feb 15;32(4):511–7. https://doi.org/10.1093/bioinformatics/btv639

565. Shanmugam AK, Nesvizhskii AI. Effective Leveraging of Targeted Search Spaces for Improving Peptide Identification in Tandem Mass Spectrometry Based Proteomics. J Proteome Res. 2015 Dec 4;14(12):5169–78. https://doi.org/10.1021/acs.jproteome.5b00504

566. Wang X, Slebos RJC, Wang D, Halvey PJ, Tabb DL, Liebler DC, et al. Protein identification using customized protein sequence databases derived from RNA-Seq data. J Proteome Res. 2012 Feb 3;11(2):1009–17. https://doi.org/10.1021/pr200766z

567. Hämmerling GJ, Hämmerling U, Lemke H. Isolation of twelve monoclonal antibodies against Ia and H-2 antigens. Serological characterization and reactivity with B and T lymphocytes. Immunogenetics. 1979 Dec 1;8(1):433–45. https://doi.org/10.1007/BF01561454

568. Hämmerling GJ, Rüsch E, Tada N, Kimura S, Hämmerling U. Localization of allodeterminants on H-2Kb antigens determined with monoclonal antibodies and H-2 mutant mice. Proc Natl Acad Sci U S A. 1982 Aug;79(15):4737–41. https://doi.org/10.1073/pnas.79.15.4737

569. Käll L, Canterbury JD, Weston J, Noble WS, MacCoss MJ. Semi-supervised learning for peptide identification from shotgun proteomics datasets. Nat Methods. 2007 Nov;4(11):923–5. https://doi.org/10.1038/nmeth1113

570. Elias JE, Gygi SP. Target-decoy search strategy for increased confidence in large-scale protein identifications by mass spectrometry. Nat Methods. 2007 Mar;4(3):207–14. https://doi.org/10.1038/nmeth1019

571. Caron E, Espona L, Kowalewski DJ, Schuster H, Ternette N, Alpízar A, et al. An open-source computational and data resource to analyze digital maps of immunopeptidomes. eLife. 2015 Jul 8;4. https://doi.org/10.7554/eLife.07661

572. Faridi P, Aebersold R, Caron E. A first dataset toward a standardized community-driven global mapping of the human immunopeptidome. Data Brief. 2016 Jun;7:201–5. https://doi.org/10.1016/j.dib.2016.02.016

573. Walz S, Stickel JS, Kowalewski DJ, Schuster H, Weisel K, Backert L, et al. The antigenic landscape of multiple myeloma: mass spectrometry (re)defines targets for T-cell-based immunotherapy. Blood. 2015 Sep 3;126(10):1203–13. https://doi.org/10.1182/blood-2015-04-640532

574. Eng JK, McCormack AL, Yates JR. An approach to correlate tandem mass spectral data of peptides with amino acid sequences in a protein database. J Am Soc Mass Spectrom. 1994 Nov;5(11):976–89. https://doi.org/10.1016/1044-0305(94)80016-2

575. Kertesz-Farkas A, Keich U, Noble WS. Tandem Mass Spectrum Identification via Cascaded Search. J Proteome Res. 2015 Aug 7;14(8):3027–38. https://doi.org/10.1021/pr501173s

576. Karosiene E, Lundegaard C, Lund O, Nielsen M. NetMHCcons: a consensus method for the major histocompatibility complex class I predictions. Immunogenetics. 2012 Mar;64(3):177–86. https://doi.org/10.1007/s00251-011-0579-8

577. Dougherty TJ, Gomer CJ, Henderson BW, Jori G, Kessel D, Korbelik M, et al. Photodynamic Therapy. JNCI J Natl Cancer Inst. 1998 Jun 17;90(12):889–905. https://doi.org/10.1093/jnci/90.12.889

578. Bonnett R. Chemical aspects of photodynamic therapy. Amsterdam, The Netherlands: Gordon and Breach Science Publishers; 2000. 305 p. (Advanced chemistry texts).

579. Hamblin MR, Mróz P, editors. Advances in photodynamic therapy: basic, translational, and clinical. Boston, Mass: Artech House; 2008. 559 p. (Artech House engineering in medicine & biology series).

580. Agostinis P, Berg K, Cengel KA, Foster TH, Girotti AW, Gollnick SO, et al. Photodynamic therapy of cancer: An update. CA Cancer J Clin. 2011 Jul;61(4):250–81. https://doi.org/10.3322/caac.20114

581. Allison RR. Photodynamic therapy: oncologic horizons. Future Oncol. 2014 Jan;10(1):123–4. https://doi.org/10.2217/fon.13.176

582. Benov L. Photodynamic Therapy: Current Status and Future Directions. Med Princ Pract. 2015;24(s1):14–28. https://doi.org/10.1159/000362416

583. Abrahamse H, Hamblin MR. New photosensitizers for photodynamic therapy. Biochem J. 2016 Feb 15;473(4):347–64. https://doi.org/10.1042/BJ20150942

584. Shafirstein G, Bellnier D, Oakley E, Hamilton S, Potasek M, Beeson K, et al. Interstitial Photodynamic Therapy—A Focused Review. Cancers. 2017 Jan 24;9(12):12. https://doi.org/10.3390/cancers9020012

585. Gollnick SO, Vaughan L, Henderson BW. Generation of effective antitumor vaccines using photodynamic therapy. Cancer Res. 2002 Mar;62(6):1604–8.

586. Gollnick SO. Photodynamic therapy and antitumor immunity. J Natl Compr Canc Netw. 2012 Oct;10 Suppl 2:S40-43.

587. Reginato E. Immune response after photodynamic therapy increases anti-cancer and anti-bacterial effects. World J Immunol. 2014;4(1):1–11. https://doi.org/10.5411/wji.v4.i1.1

588. Vatansever F, Hamblin MR. Photodynamic Therapy and Antitumor Immune Response. In: Rezaei N, editor. Cancer Immunology [Internet]. Berlin, Heidelberg: Springer Berlin Heidelberg; 2015 [cited 2020 Jun 8]. p. 383–99. Available from: http://link.springer.com/10.1007/978-3-662-44946-2_21https://doi.org/10.1007/978-3-662-44946-2_21

589. Yang Y, Hu Y, Wang H. Targeting Antitumor Immune Response for Enhancing the Efficacy of Photodynamic Therapy of Cancer: Recent Advances and Future Perspectives. Oxid Med Cell Longev. 2016;2016:1–11. https://doi.org/10.1155/2016/5274084

590. Hwang HS, Shin H, Han J, Na K. Combination of photodynamic therapy (PDT) and anti-tumor immunity in cancer therapy. J Pharm Investig. 2018 Mar;48(2):143–51. https://doi.org/10.1007/s40005-017-0377-x

591. Korbelik M. Role of cell stress signaling networks in cancer cell death and antitumor immune response following proteotoxic injury inflicted by photodynamic therapy: TUMOR AND HOST RESPONSE TO PDT AND BCG. Lasers Surg Med. 2018 Jul;50(5):491–8. https://doi.org/10.1002/lsm.22810

592. Kaleta-Richter M, Kawczyk-Krupka A, Aebisher D, Bartusik-Aebisher D, Czuba Z, Cieślar G. The capability and potential of new forms of personalized colon cancer treatment: Immunotherapy and Photodynamic Therapy. Photodiagnosis Photodyn Ther. 2019 Mar;25:253–8. https://doi.org/10.1016/j.pdpdt.2019.01.004

593. Nath S, Obaid G, Hasan T. The Course of Immune Stimulation by Photodynamic Therapy: Bridging Fundamentals of Photochemically Induced Immunogenic Cell Death to the Enrichment of T-Cell Repertoire. Photochem Photobiol. 2019 Nov;95(6):1288–305. https://doi.org/10.1111/php.13173

594. Falk-Mahapatra R, Gollnick SO. Photodynamic Therapy and Immunity: An Update. Photochem Photobiol. 2020 Apr 23;php.13253. https://doi.org/10.1111/php.13253

595. FDA. Highlights of prescribing information for Photofrin (porfimer sodium) injection [Internet]. FDA; 2011. Available from: https://www.accessdata.fda.gov/drugsatfda_docs/label/2011/020451s020lbl.pdf

596. Levy J, Levy E. Photofrin-PDT from Bench to Bedside: Some Lessons Learned. In: Pandey RK, Kessel D, Dougherty TJ, editors. Handbook of photodynamic therapy: updates on recent applications of porphyrin-based compounds. New Jersey: World Scientific; 2016.

597. Kessel D. Thomas J. Dougherty: An Appreciation. Photochem Photobiol. 2020 May;96(3):454–7. https://doi.org/10.1111/php.13144

598. Ormond A, Freeman H. Dye Sensitizers for Photodynamic Therapy. Materials. 2013 Mar 6;6(3):817–40. https://doi.org/10.3390/ma6030817

599. Rapozzi V, Jori G. Basic and Clinical Aspects of Photodynamic Therapy. In: Rapozzi V, Jori G, editors. Resistance to Photodynamic Therapy in Cancer [Internet]. Cham: Springer International Publishing; 2015 [cited 2020 Jun 22]. p. 3–26. (Resistance to Targeted Anti-Cancer Therapeutics; vol. 5). Available from: http://link.springer.com/10.1007/978-3-319-12730-9_1https://doi.org/10.1007/978-3-319-12730-9_1

600. McFarland SA, Mandel A, Dumoulin-White R, Gasser G. Metal-based photosensitizers for photodynamic therapy: the future of multimodal oncology? Curr Opin Chem Biol. 2020 Jun;56:23–7. https://doi.org/10.1016/j.cbpa.2019.10.004

601. Chou TM, Woodburn KW, Cheong W-F, Lacy SA, Sudhir K, Adelman DC, et al. Photodynamic therapy: Applications in atherosclerotic vascular disease with motexafin lutetium. Catheter Cardiovasc Interv. 2002 Nov;57(3):387–94. https://doi.org/10.1002/ccd.10336

602. Allison RR, Mang TS, Wilson BD, Vongtama V. Tin ethyl etiopurpurin—induced photodynamic therapy for the treatment of human immunodeficiency virus—associated kaposi's sarcoma. Curr Ther Res. 1998 Jan;59(1):23–7. https://doi.org/10.1016/S0011-393X(98)85020-0

603. Azzouzi A-R, Barret E, Moore CM, Villers A, Allen C, Scherz A, et al. TOOKAD ® Soluble vascular-targeted photodynamic (VTP) therapy: determination of optimal treatment conditions and assessment of effects in patients with localised prostate cancer: TOOKAD ® soluble vascular targeted photodynamic (VTP) therapy in patients with localised prostate cancer. BJU Int. 2013 Oct;112(6):766–74. https://doi.org/10.1111/bju.12265

604. Smith NA, Sadler PJ. Photoactivatable metal complexes: from theory to applications in biotechnology and medicine. Philos Trans R Soc Math Phys Eng Sci. 2013 Jul 28;371(1995):20120519. https://doi.org/10.1098/rsta.2012.0519

605. Bahreman A, Cuello-Garibo J-A, Bonnet S. Yellow-light sensitization of a ligand photosubstitution reaction in a ruthenium polypyridyl complex covalently bound to a rhodamine dye. Dalton Trans. 2014;43(11):4494–505. https://doi.org/10.1039/C3DT52643G

606. Knoll JD, Albani BA, Turro C. New Ru(II) Complexes for Dual Photoreactivity: Ligand Exchange and 1O2 Generation. Acc Chem Res. 2015 Aug 18;48(8):2280–7. https://doi.org/10.1021/acs.accounts.5b00227

607. Mari C, Huang H, Rubbiani R, Schulze M, Würthner F, Chao H, et al. Evaluation of Perylene Bisimide-Based Ru $^{II}$ and Ir $^{III}$ Complexes as Photosensitizers for Photodynamic Therapy: Evaluation of Perylene Bisimide-Based Ru $^{II}$ and Ir $^{III}$ Complexes as Photosensitizers for Photodynamic Therapy. Eur J Inorg Chem. 2017 Mar 27;2017(12):1745–52. https://doi.org/10.1002/ejic.201600516

608. Sun W, Li S, Häupler B, Liu J, Jin S, Steffen W, et al. An Amphiphilic Ruthenium Polymetallodrug for Combined Photodynamic Therapy and Photochemotherapy In Vivo. Adv Mater. 2017 Feb;29(6):1603702. https://doi.org/10.1002/adma.201603702

609. Poynton FE, Bright SA, Blasco S, Williams DC, Kelly JM, Gunnlaugsson T. The development of ruthenium( II ) polypyridyl complexes and conjugates for *in vitro* cellular and *in vivo* applications. Chem Soc Rev. 2017;46(24):7706–56. https://doi.org/10.1039/C7CS00680B

610. Heinemann F, Karges J, Gasser G. Critical Overview of the Use of Ru(II) Polypyridyl Complexes as Photosensitizers in One-Photon and Two-Photon Photodynamic Therapy. Acc Chem Res. 2017 Nov 21;50(11):2727–36. https://doi.org/10.1021/acs.accounts.7b00180

611. Liu J, Zhang C, Rees TW, Ke L, Ji L, Chao H. Harnessing ruthenium(II) as photodynamic agents: Encouraging advances in cancer therapy. Coord Chem Rev. 2018 May;363:17–28. https://doi.org/10.1016/j.ccr.2018.03.002

612. Havrylyuk D, Deshpande M, Parkin S, Glazer EC. Ru(II) complexes with diazine ligands: electronic modulation of the coordinating group is key to the design of “dual action” photoactivated agents. Chem Commun. 2018;54(88):12487–90. https://doi.org/10.1039/C8CC05809A

613. Loftus LM, Al-Afyouni KF, Rohrabaugh TN, Gallucci JC, Moore CE, Rack JJ, et al. Unexpected Role of Ru(II) Orbital and Spin Contribution on Photoinduced Ligand Exchange: New Mechanism To Access the Photodynamic Therapy Window. J Phys Chem C. 2019 Apr 25;123(16):10291–9. https://doi.org/10.1021/acs.jpcc.9b01576

614. Karges J, Blacque O, Jakubaszek M, Goud B, Goldner P, Gasser G. Systematic investigation of the antiproliferative activity of a series of ruthenium terpyridine complexes. J Inorg Biochem. 2019 Sep;198:110752. https://doi.org/10.1016/j.jinorgbio.2019.110752

615. van Rixel VHS, Ramu V, Auyeung AB, Beztsinna N, Leger DY, Lameijer LN, et al. Photo-Uncaging of a Microtubule-Targeted Rigidin Analogue in Hypoxic Cancer Cells and in a Xenograft Mouse Model. J Am Chem Soc. 2019 Nov 20;141(46):18444–54. https://doi.org/10.1021/jacs.9b07225

616. Havrylyuk D, Stevens K, Parkin S, Glazer EC. Toward Optimal Ru(II) Photocages: Balancing Photochemistry, Stability, and Biocompatibility Through Fine Tuning of Steric, Electronic, and Physiochemical Features. Inorg Chem. 2020 Jan 21;59(2):1006–13. https://doi.org/10.1021/acs.inorgchem.9b02065

617. Dixon IM, Lebon E, Sutra P, Igau A. Luminescent ruthenium–polypyridine complexes & phosphorus ligands: anything but a simple story. Chem Soc Rev. 2009;38(6):1621. https://doi.org/10.1039/b804763b

618. Breivogel A, Meister M, Förster C, Laquai F, Heinze K. Excited State Tuning of Bis(tridentate) Ruthenium(II) Polypyridine Chromophores by Push-Pull Effects and Bite Angle Optimization: A Comprehensive Experimental and Theoretical Study. Chem - Eur J. 2013 Oct 4;19(41):13745–60. https://doi.org/10.1002/chem.201302231

619. Bignozzi CA, Argazzi R, Boaretto R, Busatto E, Carli S, Ronconi F, et al. The role of transition metal complexes in dye sensitized solar devices. Coord Chem Rev. 2013 May;257(9–10):1472–92. https://doi.org/10.1016/j.ccr.2012.09.008

620. Chang K-C, Sun S-S, Odago MO, Lees AJ. Anion recognition and sensing by transition-metal complexes with polarized N H recognition motifs. Coord Chem Rev. 2015 Feb;284:111–23. https://doi.org/10.1016/j.ccr.2014.09.009

621. Sun Q, Mosquera-Vazquez S, Suffren Y, Hankache J, Amstutz N, Lawson Daku LM, et al. On the role of ligand-field states for the photophysical properties of ruthenium(II) polypyridyl complexes. Coord Chem Rev. 2015 Jan;282–283:87–99. https://doi.org/10.1016/j.ccr.2014.07.004

622. Li G, Sun L, Ji L, Chao H. Ruthenium( II ) complexes with dppz: from molecular photoswitch to biological applications. Dalton Trans. 2016;45(34):13261–76. https://doi.org/10.1039/C6DT01624C

623. Luo D, Carter KA, Miranda D, Lovell JF. Chemophototherapy: An Emerging Treatment Option for Solid Tumors. Adv Sci. 2017 Jan;4(1):1600106. https://doi.org/10.1002/advs.201600106

624. White JK, Schmehl RH, Turro C. An overview of photosubstitution reactions of Ru(II) imine complexes and their application in photobiology and photodynamic therapy. Inorganica Chim Acta. 2017 Jan;454:7–20. https://doi.org/10.1016/j.ica.2016.06.007

625. Keane PM, Kelly JM. Transient absorption and time-resolved vibrational studies of photophysical and photochemical processes in DNA-intercalating polypyridyl metal complexes or cationic porphyrins. Coord Chem Rev. 2018 Jun;364:137–54. https://doi.org/10.1016/j.ccr.2018.02.018

626. Aletti AB, Gillen DM, Gunnlaugsson T. Luminescent/colorimetric probes and (chemo-) sensors for detecting anions based on transition and lanthanide ion receptor/binding complexes. Coord Chem Rev. 2018 Jan;354:98–120. https://doi.org/10.1016/j.ccr.2017.06.020

627. Mede T, Jäger M, Schubert US. “Chemistry-on-the-complex”: functional Ru $^{II}$ polypyridyl-type sensitizers as divergent building blocks. Chem Soc Rev. 2018;47(20):7577–627. https://doi.org/10.1039/C8CS00096D

628. Juris A, Balzani V, Barigelletti F, Campagna S, Belser P, von Zelewsky A. Ru(II) polypyridine complexes: photophysics, photochemistry, eletrochemistry, and chemiluminescence. Coord Chem Rev. 1988 Mar;84:85–277. https://doi.org/10.1016/0010-8545(88)80032-8

629. Kalyanasundaram K. Photochemistry of polypyridine and pophyrin complexes. London: Acad. Pr; 1992. 626 p.

630. Balzani V, Juris A, Venturi M, Campagna S, Serroni S. Luminescent and Redox-Active Polynuclear Transition Metal Complexes †. Chem Rev. 1996 Jan;96(2):759–834. https://doi.org/10.1021/cr941154y

631. Balzani V, Credi A, Venturi M. Photochemistry and photophysics of coordination compounds: An extended view. Coord Chem Rev. 1998 Apr;171:3–16. https://doi.org/10.1016/S0010-8545(98)90005-4

632. Balzani V, Juris A. Photochemistry and photophysics of Ru(II)□polypyridine complexes in the Bologna group. From early studies to recent developments. Coord Chem Rev. 2001 Jan;211(1):97–115. https://doi.org/10.1016/S0010-8545(00)00274-5

633. McClenaghan ND, Leydet Y, Maubert B, Indelli MT, Campagna S. Excited-state equilibration: a process leading to long-lived metal-to-ligand charge transfer luminescence in supramolecular systems. Coord Chem Rev. 2005 Jul;249(13–14):1336–50. https://doi.org/10.1016/j.ccr.2004.12.017

634. Campagna S, Puntoriero F, Nastasi F, Bergamini G, Balzani V. Photochemistry and Photophysics of Coordination Compounds: Ruthenium. In: Balzani V, Campagna S, editors. Photochemistry and Photophysics of Coordination Compounds I [Internet]. Berlin, Heidelberg: Springer Berlin Heidelberg; 2007 [cited 2019 Jul 15]. p. 117–214. Available from: http://link.springer.com/10.1007/128_2007_133https://doi.org/10.1007/128_2007_133

635. Liu Y, Hammitt R, Lutterman DA, Joyce LE, Thummel RP, Turro C. Ru(II) Complexes of New Tridentate Ligands: Unexpected High Yield of Sensitized $^{1}O_{2}$. Inorg Chem. 2009 Jan 5;48(1):375–85. https://doi.org/10.1021/ic801636u

636. Sun Y, Joyce LE, Dickson NM, Turro C. Efficient DNA photocleavage by [Ru(bpy)2(dppn)]2+ with visible light. Chem Commun. 2010;46(14):2426. https://doi.org/10.1039/b925574e

637. Lincoln R, Kohler L, Monro S, Yin H, Stephenson M, Zong R, et al. Exploitation of Long-Lived $^{3}$IL Excited States for Metal–Organic Photodynamic Therapy: Verification in a Metastatic Melanoma Model. J Am Chem Soc. 2013 Nov 13;135(45):17161–75. https://doi.org/10.1021/ja408426z

638. Albani BA, Peña B, Leed NA, de Paula NABG, Pavani C, Baptista MS, et al. Marked Improvement in Photoinduced Cell Death by a New Tris-heteroleptic Complex with Dual Action: Singlet Oxygen Sensitization and Ligand Dissociation. J Am Chem Soc. 2014 Dec 10;136(49):17095–101. https://doi.org/10.1021/ja508272h

639. Shi G, Monro S, Hennigar R, Colpitts J, Fong J, Kasimova K, et al. Ru(II) dyads derived from α-oligothiophenes: A new class of potent and versatile photosensitizers for PDT. Coord Chem Rev. 2015 Jan;282–283:127–38. https://doi.org/10.1016/j.ccr.2014.04.012

640. Reichardt C, Monro S, Sobotta FH, Colón KL, Sainuddin T, Stephenson M, et al. Predictive Strength of Photophysical Measurements for in Vitro Photobiological Activity in a Series of Ru(II) Polypyridyl Complexes Derived from π-Extended Ligands. Inorg Chem. 2019 Mar 4;58(5):3156–66. https://doi.org/10.1021/acs.inorgchem.8b03223

641. Toupin NP, Nadella S, Steinke SJ, Turro C, Kodanko JJ. Dual-Action Ru(II) Complexes with Bulky π-Expansive Ligands: Phototoxicity without DNA Intercalation. Inorg Chem. 2020 Mar 16;59(6):3919–33. https://doi.org/10.1021/acs.inorgchem.9b03585

642. Yin H, Stephenson M, Gibson J, Sampson E, Shi G, Sainuddin T, et al. In vitro multiwavelength PDT with 3IL states: teaching old molecules new tricks. Inorg Chem. 2014;53(9):4548–59.

643. Foxon SP, Alamiry MAH, Walker MG, Meijer AJHM, Sazanovich IV, Weinstein JA, et al. Photophysical Properties and Singlet Oxygen Production by Ruthenium(II) Complexes of Benzo[ *i* ]dipyrido[3,2- *a* :2′,3′- *c* ]phenazine: Spectroscopic and TD-DFT Study. J Phys Chem A. 2009 Nov 19;113(46):12754–62. https://doi.org/10.1021/jp906716g

644. Mroz P, Huang Y-Y, Szokalska A, Zhiyentayev T, Janjua S, Nifli A-P, et al. Stable synthetic bacteriochlorins overcome the resistance of melanoma to photodynamic therapy. FASEB J. 2010 Sep;24(9):3160–70.

645. Baldea I, Filip AG. Photodynamic therapy in melanoma--an update. J Physiol Pharmacol Off J Pol Physiol Soc. 2012 Apr;63(2):109–18.

646. Zonios G, Dimou A, Bassukas I, Galaris D, Tsolakidis A, Kaxiras E. Melanin absorption spectroscopy: new method for noninvasive skin investigation and melanoma detection. J Biomed Opt. 2008;13(1):014017. https://doi.org/10.1117/1.2844710

647. Davids LM, Kleemann B. Combating melanoma: the use of photodynamic therapy as a novel, adjuvant therapeutic tool. Cancer Treat Rev. 2011 Oct;37(6):465–75. https://doi.org/10.1016/j.ctrv.2010.11.007

648. Tardivo JP, Del Giglio A, Paschoal LHC, Ito AS, Baptista MS. Treatment of melanoma lesions using methylene blue and RL50 light source. Photodiag Photodyn Ther. 2004 Dec;1(4):345–6. https://doi.org/10.1016/S1572-1000(05)00005-0

649. Huang Y-Y, Vecchio D, Avci P, Yin R, Garcia-Diaz M, Hamblin MR. Melanoma resistance to photodynamic therapy: new insights. Biol Chem. 2013 Feb;394(2):239–50. https://doi.org/10.1515/hsz-2012-0228

650. Nelson JS, McCullough JL, Berns MW. Photodynamic therapy of human malignant melanoma xenografts in athymic nude mice. J Natl Cancer Inst. 1988 Mar;80(1):56–60.

651. Zong R, Thummel RP. A new family of Ru complexes for water oxidation. J Am Chem Soc. 2005 Sep 21;127:12802–3. https://doi.org/10.1021/ja054791m

652. Wang C, Lystrom L, Yin H, Hetu M, Kilina S, McFarland SA, et al. Increasing the triplet lifetime and extending the ground-state absorption of biscyclometalated Ir( III ) complexes for reverse saturable absorption and photodynamic therapy applications. Dalton Trans. 2016;45(41):16366–78. https://doi.org/10.1039/C6DT02416E

653. Tong L, Inge AK, Duan L, Wang L, Zou X, Sun L. Catalytic Water Oxidation by Mononuclear Ru Complexes with an Anionic Ancillary Ligand. Inorg Chem. 2013 Mar 4;52(5):2505–18. https://doi.org/10.1021/ic302446h

654. Haberdar R. The Synthesis and Study of 4-Aza-Acridine Type Ligands and Their Ru(II) Complexes. [Houston, TX]: University of Houston; 2012.

655. Pazderski L, Pawlak T, Sitkowski J, Kozerski L, Szłyk E. $^{1}$H NMR assignment corrections and $^{1}$H, $^{13}$C, $^{15}$N NMR coordination shifts structural correlations in Fe(II), Ru(II) and Os(II) cationic complexes with 2,2′-bipyridine and 1,10-phenanthroline. Magn Reson Chem. 2010;48:450–7. https://doi.org/10.1002/mrc.2600

656. Kalyanasundaram K. Photochemistry of Polypyridine and Por- phyrin Complexes; London: Academic Press; 1992.

657. Campagna S, Puntoriero F, Nastasi F, Bergamini G, Balzani V. Photochemistry and Photophysics of Coordination Compounds: Ruthenium. In: Balzani V, Campagna S, editors. Photochemistry and Photophysics of Coordination Compounds I [Internet]. Springer Berlin Heidelberg; 2007 [cited 2015 Jul 21]. p. 117–214. (Topics in Current Chemistry). Available from: http://link.springer.com/chapter/10.1007/128_2007_133

658. Thummel RP, Lefoulon F. Polyaza cavity shaped molecules. 2. Annelated derivatives of 2,2’-biquinoline and the corresponding N-oxides. J Org Chem. 1985 Mar;50(5):666–70. https://doi.org/10.1021/jo00205a022

659. Thummel RP, Lefoulon F. Polyaza cavity shaped molecules. 11. Ruthenium complexes of annelated 2,2’-biquinoline and 2,2’-bi-1,8-naphthyridine. Inorg Chem. 1987 Mar;26(5):675–80. https://doi.org/10.1021/ic00252a009

660. Thummel RP, Hegde V. Polyaza-cavity shaped molecules. 14. Annelated 2-(2’-pyridyl)indoles, 2,2’-biindoles, and related systems. J Org Chem. 1989 Mar;54(7):1720–5. https://doi.org/10.1021/jo00268a040

661. Thummel RP, Jahng Y. Polyaza cavity-shaped molecules. 9. Ruthenium(II) complexes of annelated derivatives of 2,2’:6,2"-terpyridine and related systems: synthesis, properties, and structure. Inorg Chem. 1986 Jul;25(15):2527–34. https://doi.org/10.1021/ic00235a009

662. Zong R, Thummel RP. A New Family of Ru Complexes for Water Oxidation. J Am Chem Soc. 2005 Sep;127(37):12802–3. https://doi.org/10.1021/ja054791m

663. Kaveevivitchai N, Kohler L, Zong R, El Ojaimi M, Mehta N, Thummel RP. A Ru(II) Bis-terpyridine-like Complex that Catalyzes Water Oxidation: The Influence of Steric Strain. Inorg Chem. 2013 Sep 16;52(18):10615–22. https://doi.org/10.1021/ic4016383

664. Badiei YM, Polyansky DE, Muckerman JT, Szalda DJ, Haberdar R, Zong R, et al. Water Oxidation with Mononuclear Ruthenium(II) Polypyridine Complexes Involving a Direct Ru $^{IV}$ ═O Pathway in Neutral and Alkaline Media. Inorg Chem. 2013 Aug 5;52(15):8845–50. https://doi.org/10.1021/ic401023w

665. Chen KG, Leapman RD, Zhang G, Lai B, Valencia JC, Cardarelli CO, et al. Influence of Melanosome Dynamics on Melanoma Drug Sensitivity. JNCI J Natl Cancer Inst. 2009 Sep;101(18):1259–71. https://doi.org/10.1093/jnci/djp259

666. Rossi S, Cordella M, Tabolacci C, Nassa G, D'Arcangelo D, Senatore C, et al. TNF-alpha and metalloproteases as key players in melanoma cells aggressiveness. J Exp Clin Cancer Res. 2018 Dec;37(1):326. https://doi.org/10.1186/s13046-018-0982-1

667. Lazic S, Kaspler P, Shi G, Monro S, Sainuddin T, Forward S, et al. Novel Osmium-based Coordination Complexes as Photosensitizers for Panchromatic Photodynamic Therapy. Photochem Photobiol. 2017 Oct;93(5):1248–58. https://doi.org/10.1111/php.12767

668. Roque JA, Barrett PC, Cole HD, Lifshits LM, Shi G, Monro S, et al. Breaking the barrier: an osmium photosensitizer with unprecedented hypoxic phototoxicity for real world photodynamic therapy. Chem Sci. 2020;10.1039.D0SC03008B. https://doi.org/10.1039/D0SC03008B

669. Lucky SS, Soo KC, Zhang Y. Nanoparticles in Photodynamic Therapy. Chem Rev. 2015 Feb 25;115(4):1990–2042. https://doi.org/10.1021/cr5004198

670. Roque J, Havrylyuk D, Barrett PC, Sainuddin T, McCain J, Colón K, et al. Strained, Photoejecting Ru(II) Complexes that are Cytotoxic Under Hypoxic Conditions. Photochem Photobiol. 2020 Mar;96(2):327–39. https://doi.org/10.1111/php.13174

671. Sitnik T, Hampton J, Henderson B. Reduction of tumour oxygenation during and after photodynamic therapy in vivo: effects of fluence rate. Br J Cancer. 1998 May;77(9):1386–94. https://doi.org/10.1038/bjc.1998.231

672. Henderson BW, Busch TM, Snyder JW. Fluence rate as a modulator of PDT mechanisms. Lasers Surg Med. 2006 Jun;38(5):489–93. https://doi.org/10.1002/lsm.20327

673. Cottrell WJ, Paquette AD, Keymel KR, Foster TH, Oseroff AR. Irradiance-Dependent Photobleaching and Pain in -Aminolevulinic Acid-Photodynamic Therapy of Superficial Basal Cell Carcinomas. Clin Cancer Res. 2008 Jul 15;14(14):4475–83. https://doi.org/10.1158/1078-0432.CCR-07-5199

674. Rizvi I, Anbil S, Alagic N, Celli JP, Zheng LZ, Palanisami A, et al. PDT Dose Parameters Impact Tumoricidal Durability and Cell Death Pathways in a 3D Ovarian Cancer Model. Photochem Photobiol. 2013 Jul;89(4):942–52. https://doi.org/10.1111/php.12065

675. Lee J, Lee Y, Xu L, White R, Sullenger BA. Differential Induction of Immunogenic Cell Death and Interferon Expression in Cancer Cells by Structured ssRNAs. Mol Ther J Am Soc Gene Ther. 2017 07;25(6):1295–305. https://doi.org/10.1016/j.ymthe.2017.03.014

676. Budhwani M, Mazzieri R, Dolcetti R. Plasticity of Type I Interferon-Mediated Responses in Cancer Therapy: From Anti-tumor Immunity to Resistance. Front Oncol. 2018;8:322. https://doi.org/10.3389/fonc.2018.00322

677. Galluzzi L, Buqué A, Kepp O, Zitvogel L, Kroemer G. Immunogenic cell death in cancer and infectious disease. Nat Rev Immunol. 2017;17(2):97–111. https://doi.org/10.1038/nri.2016.107

678. Gujar S, Dielschneider R, Clements D, Helson E, Shmulevitz M, Marcato P, et al. Multifaceted therapeutic targeting of ovarian peritoneal carcinomatosis through virus-induced immunomodulation. Mol Ther J Am Soc Gene Ther. 2013 Feb;21(2):338–47. https://doi.org/10.1038/mt.2012.228

679. Kolarova H, Nevrelova P, Tomankova K, Kolar P, Bajgar R, Mosinger J. Production of reactive oxygen species after photodynamic therapy by porphyrin sensitizers. Gen Physiol Biophys. 2008 Jun;27(2):101–5.

680. Liang H, Zhou Z, Luo R, Sang M, Liu B, Sun M, et al. Tumor-specific activated photodynamic therapy with an oxidation-regulated strategy for enhancing anti-tumor efficacy. Theranostics. 2018;8(18):5059–71. https://doi.org/10.7150/thno.28344

681. Yuan M, Liu C, Li J, Ma W, Yu X, Zhang P, et al. The effects of photodynamic therapy on leukemia cells mediated by KillerRed, a genetically encoded fluorescent protein photosensitizer. BMC Cancer. 2019 Oct 7;19(1):934. https://doi.org/10.1186/s12885-019-6124-0

682. Garg AD, Krysko DV, Vandenabeele P, Agostinis P. DAMPs and PDT-mediated photo-oxidative stress: exploring the unknown. Photochem Photobiol Sci Off J Eur Photochem Assoc Eur Soc Photobiol. 2011 May;10(5):670–80. https://doi.org/10.1039/c0pp00294a

683. Wiersma VR, Michalak M, Abdullah TM, Bremer E, Eggleton P. Mechanisms of Translocation of ER Chaperones to the Cell Surface and Immunomodulatory Roles in Cancer and Autoimmunity. Front Oncol. 2015;5:7. https://doi.org/10.3389/fonc.2015.00007

684. Rufo N, Garg AD, Agostinis P. The Unfolded Protein Response in Immunogenic Cell Death and Cancer Immunotherapy. Trends Cancer. 2017;3(9):643–58. https://doi.org/10.1016/j.trecan.2017.07.002

685. McLellan AD, Starling GC, Williams LA, Hock BD, Hart DN. Activation of human peripheral blood dendritic cells induces the CD86 co-stimulatory molecule. Eur J Immunol. 1995 Jul;25(7):2064–8. https://doi.org/10.1002/eji.1830250739

686. Bak SP, Barnkob MS, Bai A, Higham EM, Wittrup KD, Chen J. Differential requirement for CD70 and CD80/CD86 in dendritic cell-mediated activation of tumor-tolerized CD8 T cells. J Immunol Baltim Md 1950. 2012 Aug 15;189(4):1708–16. https://doi.org/10.4049/jimmunol.1201271

687. Li Z, Ju X, Silveira PA, Abadir E, Hsu W-H, Hart DNJ, et al. CD83: Activation Marker for Antigen Presenting Cells and Its Therapeutic Potential. Front Immunol. 2019;10:1312. https://doi.org/10.3389/fimmu.2019.01312

688. Ma DY, Clark EA. The role of CD40 and CD154/CD40L in dendritic cells. Semin Immunol. 2009 Oct;21(5):265–72. https://doi.org/10.1016/j.smim.2009.05.010

689. Hochrein H, Shortman K, Vremec D, Scott B, Hertzog P, O'Keeffe M. Differential production of IL-12, IFN-alpha, and IFN-gamma by mouse dendritic cell subsets. J Immunol Baltim Md 1950. 2001 May 1;166(9):5448–55. https://doi.org/10.4049/jimmunol.166.9.5448

690. Henry CJ, Ornelles DA, Mitchell LM, Brzoza-Lewis KL, Hiltbold EM. IL-12 produced by dendritic cells augments CD8+ T cell activation through the production of the chemokines CCL1 and CCL17. J Immunol Baltim Md 1950. 2008 Dec 15;181(12):8576–84. https://doi.org/10.4049/jimmunol.181.12.8576

691. Daneshmandi S, Pourfathollah AA, Forouzandeh-Moghaddam M. Enhanced CD40 and ICOSL expression on dendritic cells surface improve anti-tumor immune responses; effectiveness of mRNA/chitosan nanoparticles. Immunopharmacol Immunotoxicol. 2018 Oct;40(5):375–86. https://doi.org/10.1080/08923973.2018.1510959

692. Peng Q, Qiu X, Zhang Z, Zhang S, Zhang Y, Liang Y, et al. PD-L1 on dendritic cells attenuates T cell activation and regulates response to immune checkpoint blockade. Nat Commun. 2020 Sep 24;11(1):4835. https://doi.org/10.1038/s41467-020-18570-x

693. Tsushima F, Yao S, Shin T, Flies A, Flies S, Xu H, et al. Interaction between B7-H1 and PD-1 determines initiation and reversal of T-cell anergy. Blood. 2007 Jul 1;110(1):180–5. https://doi.org/10.1182/blood-2006-11-060087

694. Patel J, Bozeman EN, Selvaraj P. Taming dendritic cells with TIM-3: another immunosuppressive strategy used by tumors. Immunotherapy. 2012 Dec;4(12):1795–8. https://doi.org/10.2217/imt.12.126

695. Wang XB, Fan ZZ, Anton D, Vollenhoven AV, Ni ZH, Chen XF, et al. CTLA4 is expressed on mature dendritic cells derived from human monocytes and influences their maturation and antigen presentation. BMC Immunol. 2011 Mar 18;12:21. https://doi.org/10.1186/1471-2172-12-21

696. Chen L. Co-inhibitory molecules of the B7-CD28 family in the control of T-cell immunity. Nat Rev Immunol. 2004 May;4(5):336–47. https://doi.org/10.1038/nri1349

697. Bronte V, Zanovello P. Regulation of immune responses by L-arginine metabolism. Nat Rev Immunol. 2005 Aug;5(8):641–54. https://doi.org/10.1038/nri1668

698. Klein SL, Flanagan KL. Sex differences in immune responses. Nat Rev Immunol. 2016;16(10):626–38. https://doi.org/10.1038/nri.2016.90

699. Gupta S, Artomov M, Goggins W, Daly M, Tsao H. Gender Disparity and Mutation Burden in Metastatic Melanoma. J Natl Cancer Inst. 2015 Nov;107(11). https://doi.org/10.1093/jnci/djv221

700. Scoggins CR, Ross MI, Reintgen DS, Noyes RD, Goydos JS, Beitsch PD, et al. Gender-related differences in outcome for melanoma patients. Ann Surg. 2006 May;243(5):693–8; discussion 698-700. https://doi.org/10.1097/01.sla.0000216771.81362.6b

701. Wallis CJD, Butaney M, Satkunasivam R, Freedland SJ, Patel SP, Hamid O, et al. Association of Patient Sex With Efficacy of Immune Checkpoint Inhibitors and Overall Survival in Advanced Cancers: A Systematic Review and Meta-analysis. JAMA Oncol. 2019 Apr 1;5(4):529–36. https://doi.org/10.1001/jamaoncol.2018.5904

702. Lin P-Y, Sun L, Thibodeaux SR, Ludwig SM, Vadlamudi RK, Hurez VJ, et al. B7-H1-dependent sex-related differences in tumor immunity and immunotherapy responses. J Immunol Baltim Md 1950. 2010 Sep 1;185(5):2747–53. https://doi.org/10.4049/jimmunol.1000496

703. Conforti F, Pala L, Bagnardi V, De Pas T, Martinetti M, Viale G, et al. Cancer immunotherapy efficacy and patients' sex: a systematic review and meta-analysis. Lancet Oncol. 2018;19(6):737–46. https://doi.org/10.1016/S1470-2045(18)30261-4

704. Grassadonia A, Sperduti I, Vici P, Iezzi L, Brocco D, Gamucci T, et al. Effect of Gender on the Outcome of Patients Receiving Immune Checkpoint Inhibitors for Advanced Cancer: A Systematic Review and Meta-Analysis of Phase III Randomized Clinical Trials. J Clin Med. 2018 Dec 12;7(12). https://doi.org/10.3390/jcm7120542

705. Joosse A, Collette S, Suciu S, Nijsten T, Patel PM, Keilholz U, et al. Sex is an independent prognostic indicator for survival and relapse/progression-free survival in metastasized stage III to IV melanoma: a pooled analysis of five European organisation for research and treatment of cancer randomized controlled trials. J Clin Oncol Off J Am Soc Clin Oncol. 2013 Jun 20;31(18):2337–46. https://doi.org/10.1200/JCO.2012.44.5031

706. Joosse A, Collette S, Suciu S, Nijsten T, Lejeune F, Kleeberg UR, et al. Superior outcome of women with stage I/II cutaneous melanoma: pooled analysis of four European Organisation for Research and Treatment of Cancer phase III trials. J Clin Oncol Off J Am Soc Clin Oncol. 2012 Jun 20;30(18):2240–7. https://doi.org/10.1200/JCO.2011.38.0584

707. Micheli A, Ciampichini R, Oberaigner W, Ciccolallo L, de Vries E, Izarzugaza I, et al. The advantage of women in cancer survival: an analysis of EUROCARE-4 data. Eur J Cancer Oxf Engl 1990. 2009 Apr;45(6):1017–27. https://doi.org/10.1016/j.ejca.2008.11.008

708. Duma N, Abdel-Ghani A, Yadav S, Hoversten KP, Reed CT, Sitek AN, et al. Sex Differences in Tolerability to Anti-Programmed Cell Death Protein 1 Therapy in Patients with Metastatic Melanoma and Non-Small Cell Lung Cancer: Are We All Equal? The Oncologist. 2019 Nov;24(11):e1148–55. https://doi.org/10.1634/theoncologist.2019-0094

709. Markle JG, Fish EN. SeXX matters in immunity. Trends Immunol. 2014 Mar;35(3):97–104. https://doi.org/10.1016/j.it.2013.10.006

710. Capone I, Marchetti P, Ascierto PA, Malorni W, Gabriele L. Sexual Dimorphism of Immune Responses: A New Perspective in Cancer Immunotherapy. Front Immunol. 2018;9:552. https://doi.org/10.3389/fimmu.2018.00552

711. Surcel M, Constantin C, Caruntu C, Zurac S, Neagu M. Inflammatory Cytokine Pattern Is Sex-Dependent in Mouse Cutaneous Melanoma Experimental Model. J Immunol Res. 2017;2017:9212134. https://doi.org/10.1155/2017/9212134

712. Hou J, Karin M, Sun B. Targeting cancer-promoting inflammation - have anti-inflammatory therapies come of age? Nat Rev Clin Oncol. 2021 May;18(5):261–79. https://doi.org/10.1038/s41571-020-00459-9

713. Hiam-Galvez KJ, Allen BM, Spitzer MH. Systemic immunity in cancer. Nat Rev Cancer. 2021 Jun;21(6):345–59. https://doi.org/10.1038/s41568-021-00347-z

714. Varadé J, Magadán S, González-Fernández Á. Human immunology and immunotherapy: main achievements and challenges. Cell Mol Immunol. 2021 Apr;18(4):805–28. https://doi.org/10.1038/s41423-020-00530-6

715. Trujillo JA, Sweis RF, Bao R, Luke JJ. T Cell-Inflamed versus Non-T Cell-Inflamed Tumors: A Conceptual Framework for Cancer Immunotherapy Drug Development and Combination Therapy Selection. Cancer Immunol Res. 2018 Sep;6(9):990–1000. https://doi.org/10.1158/2326-6066.CIR-18-0277

716. Zhang J, Endres S, Kobold S. Enhancing tumor T cell infiltration to enable cancer immunotherapy. Immunotherapy. 2019 Feb;11(3):201–13. https://doi.org/10.2217/imt-2018-0111

717. Li X, Gruosso T, Zuo D, Omeroglu A, Meterissian S, Guiot M-C, et al. Infiltration of CD8+ T cells into tumor cell clusters in triple-negative breast cancer. Proc Natl Acad Sci U S A. 2019 Feb 26;116(9):3678–87. https://doi.org/10.1073/pnas.1817652116

718. Wculek SK, Cueto FJ, Mujal AM, Melero I, Krummel MF, Sancho D. Dendritic cells in cancer immunology and immunotherapy. Nat Rev Immunol. 2020 Jan;20(1):7–24. https://doi.org/10.1038/s41577-019-0210-z

719. Green DR, Ferguson T, Zitvogel L, Kroemer G. Immunogenic and tolerogenic cell death. Nat Rev Immunol. 2009 May;9(5):353–63. https://doi.org/10.1038/nri2545

720. Yatim N, Cullen S, Albert ML. Dying cells actively regulate adaptive immune responses. Nat Rev Immunol. 2017 Apr;17(4):262–75. https://doi.org/10.1038/nri.2017.9

721. Edukulla R, Ramakrishna E, Woller N, Mundt B, Knocke S, Gürlevik E, et al. Antitumoral immune response by recruitment and expansion of dendritic cells in tumors infected with telomerase-dependent oncolytic viruses. Cancer Res. 2009 Feb 15;69(4):1448–58. https://doi.org/10.1158/0008-5472.CAN-08-1160

722. Embgenbroich M, Burgdorf S. Current Concepts of Antigen Cross-Presentation. Front Immunol. 2018;9:1643. https://doi.org/10.3389/fimmu.2018.01643

723. Galluzzi L, Senovilla L, Vacchelli E, Eggermont A, Fridman WH, Galon J, et al. Trial watch: Dendritic cell-based interventions for cancer therapy. Oncoimmunology. 2012 Oct 1;1(7):1111–34. https://doi.org/10.4161/onci.21494

724. Gu Y-Z, Zhao X, Song X-R. Ex vivo pulsed dendritic cell vaccination against cancer. Acta Pharmacol Sin. 2020 Jul;41(7):959–69. https://doi.org/10.1038/s41401-020-0415-5

725. Harari A, Graciotti M, Bassani-Sternberg M, Kandalaft LE. Antitumour dendritic cell vaccination in a priming and boosting approach. Nat Rev Drug Discov. 2020 Sep;19(9):635–52. https://doi.org/10.1038/s41573-020-0074-8

726. Fucikova J, Moserova I, Urbanova L, Bezu L, Kepp O, Cremer I, et al. Prognostic and Predictive Value of DAMPs and DAMP-Associated Processes in Cancer. Front Immunol. 2015;6:402. https://doi.org/10.3389/fimmu.2015.00402

727. Wang Q, Ju X, Wang J, Fan Y, Ren M, Zhang H. Immunogenic cell death in anticancer chemotherapy and its impact on clinical studies. Cancer Lett. 2018 Dec 1;438:17–23. https://doi.org/10.1016/j.canlet.2018.08.028

728. Sharman null, Allen null, van Lier JE null. Photodynamic therapeutics: basic principles and clinical applications. Drug Discov Today. 1999 Nov;4(11):507–17. https://doi.org/10.1016/s1359-6446(99)01412-9

729. Plaetzer K, Krammer B, Berlanda J, Berr F, Kiesslich T. Photophysics and photochemistry of photodynamic therapy: fundamental aspects. Lasers Med Sci. 2009 Mar;24(2):259–68. https://doi.org/10.1007/s10103-008-0539-1

730. Agostinis P, Berg K, Cengel KA, Foster TH, Girotti AW, Gollnick SO, et al. Photodynamic therapy of cancer: an update. CA Cancer J Clin. 2011 Aug;61(4):250–81. https://doi.org/10.3322/caac.20114

731. Benov L. Photodynamic therapy: current status and future directions. Med Princ Pract Int J Kuwait Univ Health Sci Cent. 2015;24 Suppl 1:14–28. https://doi.org/10.1159/000362416

732. Falk-Mahapatra R, Gollnick SO. Photodynamic Therapy and Immunity: An Update. Photochem Photobiol. 2020 May;96(3):550–9. https://doi.org/10.1111/php.13253

733. Beltrán Hernández I, Yu Y, Ossendorp F, Korbelik M, Oliveira S. Preclinical and Clinical Evidence of Immune Responses Triggered in Oncologic Photodynamic Therapy: Clinical Recommendations. J Clin Med. 2020 Jan 24;9(2):E333. https://doi.org/10.3390/jcm9020333

734. Gollnick SO, Brackett CM. Enhancement of anti-tumor immunity by photodynamic therapy. Immunol Res. 2010 Mar;46(1–3):216–26. https://doi.org/10.1007/s12026-009-8119-4

735. Gollnick SO, Owczarczak B, Maier P. Photodynamic therapy and anti-tumor immunity. Lasers Surg Med. 2006 Jun;38(5):509–15. https://doi.org/10.1002/lsm.20362

736. Galluzzi L, Kepp O, Kroemer G. Enlightening the impact of immunogenic cell death in photodynamic cancer therapy. EMBO J. 2012 Mar 7;31(5):1055–7. https://doi.org/10.1038/emboj.2012.2

737. M. Lifshits L, Iii JAR, Konda P, Monro S, D. Cole H, Dohlen D von, et al. Near-infrared absorbing Ru( ii ) complexes act as immunoprotective photodynamic therapy (PDT) agents against aggressive melanoma. Chem Sci. 2020;11(43):11740–62. https://doi.org/10.1039/D0SC03875J

738. Konda P, Lifshits LM, Roque JA, Cole HD, Cameron CG, McFarland SA, et al. Discovery of immunogenic cell death-inducing ruthenium-based photosensitizers for anticancer photodynamic therapy. Oncoimmunology. 2020 Dec 29;10(1):1863626. https://doi.org/10.1080/2162402X.2020.1863626

739. Juris A, Balzani V, Barigelletti F, Campagna S, Belser P, von Zelewsky A. Ru(II) polypyridine complexes: photophysics, photochemistry, eletrochemistry, and chemiluminescence. Coord Chem Rev. 1988 Mar;84:85–277. https://doi.org/10.1016/0010-8545(88)80032-8

740. Gaudino SJ, Kumar P. Cross-Talk Between Antigen Presenting Cells and T Cells Impacts Intestinal Homeostasis, Bacterial Infections, and Tumorigenesis. Front Immunol. 2019;10:360. https://doi.org/10.3389/fimmu.2019.00360

741. Rodríguez ME, Cogno IS, Milla Sanabria LS, Morán YS, Rivarola VA. Heat shock proteins in the context of photodynamic therapy: autophagy, apoptosis and immunogenic cell death. Photochem Photobiol Sci Off J Eur Photochem Assoc Eur Soc Photobiol. 2016 Aug 31;15(9):1090–102. https://doi.org/10.1039/c6pp00097e

742. Cerrato G, Liu P, Martins I, Kepp O, Kroemer G. Quantitative determination of phagocytosis by bone marrow-derived dendritic cells via imaging flow cytometry. Methods Enzymol. 2020;632:27–37. https://doi.org/10.1016/bs.mie.2019.07.021

743. Rubin JB, Lagas JS, Broestl L, Sponagel J, Rockwell N, Rhee G, et al. Sex differences in cancer mechanisms. Biol Sex Differ. 2020 Apr 15;11(1):17. https://doi.org/10.1186/s13293-020-00291-x

744. Ye Y, Jing Y, Li L, Mills GB, Diao L, Liu H, et al. Sex-associated molecular differences for cancer immunotherapy. Nat Commun. 2020 Apr 14;11(1):1779. https://doi.org/10.1038/s41467-020-15679-x

745. Massé D, Ebstein F, Bougras G, Harb J, Meflah K, Grégoire M. Increased expression of inducible HSP70 in apoptotic cells is correlated with their efficacy for antitumor vaccine therapy. Int J Cancer. 2004 Sep 10;111(4):575–83. https://doi.org/10.1002/ijc.20249

746. Chao MP, Jaiswal S, Weissman-Tsukamoto R, Alizadeh AA, Gentles AJ, Volkmer J, et al. Calreticulin is the dominant pro-phagocytic signal on multiple human cancers and is counterbalanced by CD47. Sci Transl Med. 2010 Dec 22;2(63):63ra94. https://doi.org/10.1126/scitranslmed.3001375

747. Schcolnik-Cabrera A, Oldak B, Juárez M, Cruz-Rivera M, Flisser A, Mendlovic F. Calreticulin in phagocytosis and cancer: opposite roles in immune response outcomes. Apoptosis Int J Program Cell Death. 2019 Apr;24(3–4):245–55. https://doi.org/10.1007/s10495-019-01532-0

748. Fucikova J, Kasikova L, Truxova I, Laco J, Skapa P, Ryska A, et al. Relevance of the chaperone-like protein calreticulin for the biological behavior and clinical outcome of cancer. Immunol Lett. 2018 Jan;193:25–34. https://doi.org/10.1016/j.imlet.2017.11.006

749. Dronca RS, Dong H. A gender factor in shaping T-cell immunity to melanoma. Front Oncol. 2015;5:8. https://doi.org/10.3389/fonc.2015.00008

750. Morgese F, Sampaolesi C, Torniai M, Conti A, Ranallo N, Giacchetti A, et al. Gender Differences and Outcomes in Melanoma Patients. Oncol Ther. 2020 Jun;8(1):103–14. https://doi.org/10.1007/s40487-020-00109-1

751. Bellenghi M, Puglisi R, Pontecorvi G, De Feo A, Carè A, Mattia G. Sex and Gender Disparities in Melanoma. Cancers. 2020 Jul 7;12(7):E1819. https://doi.org/10.3390/cancers12071819

752. Klein SL, Morgan R. The impact of sex and gender on immunotherapy outcomes. Biol Sex Differ. 2020 May 4;11(1):24. https://doi.org/10.1186/s13293-020-00301-y

753. Krysko O, Løve Aaes T, Bachert C, Vandenabeele P, Krysko DV. Many faces of DAMPs in cancer therapy. Cell Death Dis. 2013 May 16;4:e631. https://doi.org/10.1038/cddis.2013.156

754. Hangai S, Ao T, Kimura Y, Matsuki K, Kawamura T, Negishi H, et al. PGE2 induced in and released by dying cells functions as an inhibitory DAMP. Proc Natl Acad Sci U S A. 2016 Apr 5;113(14):3844–9. https://doi.org/10.1073/pnas.1602023113

755. Liu P, Zhao L, Loos F, Marty C, Xie W, Martins I, et al. Immunosuppression by Mutated Calreticulin Released from Malignant Cells. Mol Cell. 2020 Feb 20;77(4):748-760.e9. https://doi.org/10.1016/j.molcel.2019.11.004

756. Roh JS, Sohn DH. Damage-Associated Molecular Patterns in Inflammatory Diseases. Immune Netw. 2018 Aug;18(4):e27. https://doi.org/10.4110/in.2018.18.e27

757. Hernandez C, Huebener P, Schwabe RF. Damage-associated molecular patterns in cancer: a double-edged sword. Oncogene. 2016 Nov 17;35(46):5931–41. https://doi.org/10.1038/onc.2016.104

758. Oh SA, Wu D-C, Cheung J, Navarro A, Xiong H, Cubas R, et al. PD-L1 expression by dendritic cells is a key regulator of T-cell immunity in cancer. Nat Cancer. 2020 Jul;1(7):681–91. https://doi.org/10.1038/s43018-020-0075-x

759. Brunner-Weinzierl MC, Rudd CE. CTLA-4 and PD-1 Control of T-Cell Motility and Migration: Implications for Tumor Immunotherapy. Front Immunol. 2018;9:2737. https://doi.org/10.3389/fimmu.2018.02737

760. Hsu FJ, Komarovskaya M. CTLA4 blockade maximizes antitumor T-cell activation by dendritic cells presenting idiotype protein or opsonized anti-CD20 antibody-coated lymphoma cells. J Immunother Hagerstown Md 1997. 2002 Dec;25(6):455–68. https://doi.org/10.1097/00002371-200211000-00002

761. Laurent S, Carrega P, Saverino D, Piccioli P, Camoriano M, Morabito A, et al. CTLA-4 is expressed by human monocyte-derived dendritic cells and regulates their functions. Hum Immunol. 2010 Oct;71(10):934–41. https://doi.org/10.1016/j.humimm.2010.07.007

762. Mayoux M, Roller A, Pulko V, Sammicheli S, Chen S, Sum E, et al. Dendritic cells dictate responses to PD-L1 blockade cancer immunotherapy. Sci Transl Med. 2020 Mar 11;12(534):eaav7431. https://doi.org/10.1126/scitranslmed.aav7431

763. Konda P, Roque Iii JA, Lifshits LM, Alcos A, Azzam E, Shi G, et al. Photodynamic therapy of melanoma with new, structurally similar, NIR-absorbing ruthenium (II) complexes promotes tumor growth control via distinct hallmarks of immunogenic cell death. Am J Cancer Res. 2022;12(1):210–28.

764. Zhang X, Qi Y, Zhang Q, Liu W. Application of mass spectrometry-based MHC immunopeptidome profiling in neoantigen identification for tumor immunotherapy. Biomed Pharmacother Biomedecine Pharmacother. 2019 Dec;120:109542. https://doi.org/10.1016/j.biopha.2019.109542

765. Chong C, Müller M, Pak H, Harnett D, Huber F, Grun D, et al. Integrated proteogenomic deep sequencing and analytics accurately identify non-canonical peptides in tumor immunopeptidomes. Nat Commun. 2020 Mar 10;11(1):1293. https://doi.org/10.1038/s41467-020-14968-9

766. Andersen RS, Andersen SR, Hjortsø MD, Lyngaa R, Idorn M, Køllgård TM, et al. High frequency of T cells specific for cryptic epitopes in melanoma patients. Oncoimmunology. 2013 Jul 1;2(7):e25374. https://doi.org/10.4161/onci.25374

767. Lussier DM, Alspach E, Ward JP, Miceli AP, Runci D, White JM, et al. Radiation-induced neoantigens broaden the immunotherapeutic window of cancers with low mutational loads. Proc Natl Acad Sci U S A. 2021 Jun 15;118(24):e2102611118. https://doi.org/10.1073/pnas.2102611118

768. Klatt MG, Mun SS, Socci ND, Korontsvit T, Dao T, Scheinberg DA. Epigenetic Drug Treatment Induces Presentation of New Class of Non-Exonic, Cryptic Neoantigens in Acute Myeloid Leukemia Cells. Blood. 2018 Nov 29;132(Supplement 1):2717. https://doi.org/10.1182/blood-2018-99-113691

769. Grimaldi A, Cammarata I, Martire C, Focaccetti C, Piconese S, Buccilli M, et al. Combination of chemotherapy and PD-1 blockade induces T cell responses to tumor non-mutated neoantigens. Commun Biol. 2020 Feb 25;3(1):85. https://doi.org/10.1038/s42003-020-0811-x

770. Olsson N, Heberling ML, Zhang L, Jhunjhunwala S, Phung QT, Lin S, et al. An Integrated Genomic, Proteomic, and Immunopeptidomic Approach to Discover Treatment-Induced Neoantigens. Front Immunol. 2021;12:662443. https://doi.org/10.3389/fimmu.2021.662443

771. Weinschenk T, Gouttefangeas C, Schirle M, Obermayr F, Walter S, Schoor O, et al. Integrated functional genomics approach for the design of patient-individual antitumor vaccines. Cancer Res. 2002 Oct 15;62(20):5818–27.

772. Murciano-Goroff YR, Warner AB, Wolchok JD. The future of cancer immunotherapy: microenvironment-targeting combinations. Cell Res. 2020 Jun;30(6):507–19. https://doi.org/10.1038/s41422-020-0337-2

773. Svensson V, Vento-Tormo R, Teichmann SA. Exponential scaling of single-cell RNA-seq in the past decade. Nat Protoc. 2018 Apr;13(4):599–604. https://doi.org/10.1038/nprot.2017.149

774. Gohil SH, Iorgulescu JB, Braun DA, Keskin DB, Livak KJ. Applying high-dimensional single-cell technologies to the analysis of cancer immunotherapy. Nat Rev Clin Oncol. 2021 Apr;18(4):244–56. https://doi.org/10.1038/s41571-020-00449-x

775. Liu J, Qu S, Zhang T, Gao Y, Shi H, Song K, et al. Applications of Single-Cell Omics in Tumor Immunology. Front Immunol. 2021;12:697412. https://doi.org/10.3389/fimmu.2021.697412

776. Lin Z, Meng X, Wen J, Corral JM, Andreev D, Kachler K, et al. Intratumor Heterogeneity Correlates With Reduced Immune Activity and Worse Survival in Melanoma Patients. Front Oncol. 2020;10:596493. https://doi.org/10.3389/fonc.2020.596493

777. Ahmed F, Haass NK. Microenvironment-Driven Dynamic Heterogeneity and Phenotypic Plasticity as a Mechanism of Melanoma Therapy Resistance. Front Oncol. 2018;8:173. https://doi.org/10.3389/fonc.2018.00173

778. Fattore L, Ruggiero CF, Liguoro D, Mancini R, Ciliberto G. Single cell analysis to dissect molecular heterogeneity and disease evolution in metastatic melanoma. Cell Death Dis. 2019 Oct 31;10(11):827. https://doi.org/10.1038/s41419-019-2048-5

779. Hutchenreuther J, Leask A. Why target the tumor stroma in melanoma? J Cell Commun Signal. 2018 Mar;12(1):113–8. https://doi.org/10.1007/s12079-017-0419-1

780. Eom J, Park SM, Feisst V, Chen C-JJ, Mathy JE, McIntosh JD, et al. Distinctive Subpopulations of Stromal Cells Are Present in Human Lymph Nodes Infiltrated with Melanoma. Cancer Immunol Res. 2020 Aug;8(8):990–1003. https://doi.org/10.1158/2326-6066.CIR-19-0796

781. Galvani E, Mundra PA, Valpione S, Garcia-Martinez P, Smith M, Greenall J, et al. Stroma remodeling and reduced cell division define durable response to PD-1 blockade in melanoma. Nat Commun. 2020 Feb 12;11(1):853. https://doi.org/10.1038/s41467-020-14632-2

782. Davidson S, Efremova M, Riedel A, Mahata B, Pramanik J, Huuhtanen J, et al. Single-Cell RNA Sequencing Reveals a Dynamic Stromal Niche That Supports Tumor Growth. Cell Rep. 2020 May 19;31(7):107628. https://doi.org/10.1016/j.celrep.2020.107628

783. Yuan Z, Fan G, Wu H, Liu C, Zhan Y, Qiu Y, et al. Photodynamic therapy synergizes with PD-L1 checkpoint blockade for immunotherapy of CRC by multifunctional nanoparticles. Mol Ther J Am Soc Gene Ther. 2021 Oct 6;29(10):2931–48. https://doi.org/10.1016/j.ymthe.2021.05.017

784. Xu J, Xu L, Wang C, Yang R, Zhuang Q, Han X, et al. Near-Infrared-Triggered Photodynamic Therapy with Multitasking Upconversion Nanoparticles in Combination with Checkpoint Blockade for Immunotherapy of Colorectal Cancer. ACS Nano. 2017 May 23;11(5):4463–74. https://doi.org/10.1021/acsnano.7b00715

785. DeRosa MC, Crutchley RJ. Photosensitized singlet oxygen and its applications. Coord Chem Rev. 2002 Nov;233–234:351–71. https://doi.org/10.1016/S0010-8545(02)00034-6

786. Foxon SP, Metcalfe C, Adams H, Webb M, Thomas JA. Electrochemical and Photophysical Properties of DNA Metallo-intercalators Containing the Ruthenium(II) Tris(1-pyrazolyl)methane Unit. Inorg Chem. 2007 Jan;46:409–16. https://doi.org/10.1021/ic0607134

787. R Core Team. R: A Language and Environment for Statistical Computing [Internet]. Vienna, Austria: R Foundation for Statistical Computing; 2020. Available from: https://www.R-project.org/

788. Hughes SM. plater: Read, Tidy, and Display Data from Microtiter Plates. J Open Source Softw. 2016 Nov;1(7):106. https://doi.org/10.21105/joss.00106

789. Wickham H, François R, Henry L, Müller K. dplyr: A Grammar of Data Manipulation [Internet]. 2020. Available from: https://CRAN.R-project.org/package=dplyr

790. Wickham H, Bryan J. readxl: Read Excel Files [Internet]. 2019. Available from: https://CRAN.R-project.org/package=readxl

791. Schauberger P, Walker A. openxlsx: Read, Write and Edit xlsx Files [Internet]. 2019. Available from: https://CRAN.R-project.org/package=openxlsx

792. Wickham H, Henry L. tidyr: Tidy Messy Data [Internet]. 2020. Available from: https://CRAN.R-project.org/package=tidyr

793. Mcfarland S, Lifshits LM, Roque JA, Cole HD, Thummel RP, Cameron CG. NIR-absorbing Ru(II) Complexes Containing α-Oligothiophenes for Applications in Photodynamic Therapy. ChemBioChem. 2020 Aug 5;cbic.202000419. https://doi.org/10.1002/cbic.202000419

# APPENDIX A: COPYRIGHT PERMISSIONS

## Copyright I (Journal of Proteomics Research, American Chemical Society)



RE: Written permission request for thesis

Copyright <Copyright@ACS.org>
Mon 12/27/2021 12:37 PM
To: Prathyusha Konda <Prathyusha.Konda@Dal.Ca>; Copyright <Copyright@ACS.org>

CAUTION: The Sender of this email is not from within Dalhousie.

Dear **Prathyusha Konda**,

In reference to your message below, the following is from the **American Chemical Society's Policy on Theses and Dissertations:**
This policy addresses permission to include **your article(s)** or portions of text from **your article(s)** in your thesis.

**Reuse/Republication of the Entire Work in Theses or Collections**: Authors may reuse all or part of the Submitted, Accepted or Published Work in a thesis or dissertation that the author writes and is required to submit to satisfy the criteria of degree-granting institutions. Such reuse is permitted subject to the ACS' "Ethical Guidelines to Publication of Chemical Research". Appropriate citation of the Published Work must be made as follows:

"Reprinted with permission from [COMPLETE REFERENCE CITATION]. Copyright [YEAR] American Chemical Society." Insert the appropriate wording in place of the capitalized words. Citation information may be found after the "Cite this:" heading below the title of the online version and at the bottom of **the first page of the pdf or print version of your ACS journal article**.

If the thesis or dissertation to be published is in electronic format, a direct link to the Published Work must also be included using the ACS Articles on Request author-directed link.

If your university requires written permission and your manuscript has not yet received a DOI (published ASAP), send a request to copyright@acs.org that includes the manuscript number, the name of the ACS journal, and the date that you need to receive our reply.

If your university requires you to obtain permission for manuscripts in ASAP status or final published articles, you must use the RightsLink permission system. **See RightsLink instructions at http://pubs.acs.org/page/copyright/permissions.html and make requests at the "Rights & Permissions" link under the title of the online version of the article.**

**Submission to a Dissertation Distributor**: If you plan to submit your thesis to UMI or to another dissertation distributor, you should not include the unpublished ACS paper in your thesis if the thesis will be disseminated electronically, until ACS has published your paper. After publication of the paper by ACS, you may release the entire thesis (**not the individual ACS article by itself**) for electronic dissemination through the distributor; ACS's copyright credit line should be printed on the first page of the ACS paper.

I hope this information is helpful.

Sincerely,

Keri Travis
Copyright Specialist
Office of the Secretary & General Counsel
American Chemical Society
1155 Sixteenth Street, NW
Washington, DC 20036
202-604-2874

k_travis@acs.org

**From:** Prathyusha Konda <Prathyusha.Konda@Dal.Ca>
**Sent:** Sunday, December 26, 2021 8:07 PM
**To:** Copyright <Copyright@ACS.org>
**Subject:** [EXT] Written permission request for thesis

[Actual Sender is Prathyusha.Konda@dal.ca]

Hello,

I am one of the first authors of the manuscript titled "MHC-I Ligand Discovery Using Targeted Database Searches of Mass Spectrometry Data: Implications for T-Cell Immunotherapies" published in the Journal of Proteome Research (https://doi.org/10.1021/acs.jproteome.6b00971). I would like to request copyright permission and confirmation to use the material as a part of my doctoral thesis. Please let me know if you require any information from me.

Thank you very much,
Prathyusha

**Prathyusha Konda, BTech**
PhD Candidate
FACULTY OF MEDICINE | Microbiology & Immunology
Sir Charles Tupper Medical Building, Room 11J
Halifax, NS B3H 4R2 Canada
DALHOUSIE UNIVERSITY
https://scholar.google.ca/citations?user=LMu60kjth8EC&hl=en

## Copyright II (Chemical Science, Royal Society of Chemistry)



RE: Written permission request for thesis

CONTRACTS-COPYRIGHT (shared) <Contracts-Copyright@rsc.org>
Wed 1/5/2022 5:59 AM
To: Prathyusha Konda <Prathyusha.Konda@Dal.Ca>



Thank you for your enquiry.

The Royal Society of Chemistry (RSC) hereby grants permission for the use of your paper(s) specified below in the printed and microfilm version of your thesis. You may also make available the PDF version of your paper(s) that the RSC sent to the corresponding author(s) of your paper(s) upon publication of the paper(s) in the following ways: in your thesis via any website that your university may have for the deposition of theses, via your university's Intranet or via your own personal website. We are however unable to grant you permission to include the PDF version of the paper(s) on its own in your institutional repository. The Royal Society of Chemistry is a signatory to the STM Guidelines on Permissions (available on request).

Please note that if the material specified below or any part of it appears with credit or acknowledgement to a third party then you must also secure permission from that third party before reproducing that material.

Please ensure that the thesis includes the correct acknowledgement (see http://rsc.li/permissions for details) and a link is included to the paper on the Royal Society of Chemistry's website.

Please also ensure that your co-authors are aware that you are including the paper in your thesis.

Kind regards,

Matthew

Matthew Bailey
Licensing and Access Manager (interim)
Royal Society of Chemistry
Thomas Graham House
Science Park, Milton Road
Cambridge, CB4 0WF, UK
www.rsc.org

**From:** Prathyusha Konda <Prathyusha.Konda@Dal.Ca>
**Sent:** 27 December 2021 01:02
**To:** CONTRACTS-COPYRIGHT (shared) <Contracts-Copyright@rsc.org>
**Subject:** Written permission request for thesis

Hello,

I am one of the first authors of the manuscript titled "Near-infrared absorbing Ru(II) complexes act as immunoprotective photodynamic therapy (PDT) agents against aggressive melanoma" published in the journal Chemical Science (https://doi.org/10.1039/D0SC03875J). I would like to request copyright

permission and confirmation to use the material as a part of my doctoral thesis. Please let me know if you require any information from me.

Thank you very much,
Prathyusha

---

**Prathyusha Konda, BTech**
PhD Candidate
FACULTY OF MEDICINE | Microbiology & Immunology
Sir Charles Tupper Medical Building, Room 11J
Halifax, NS B3H 4R2 Canada
DALHOUSIE UNIVERSITY
https://scholar.google.ca/citations?user=LMu60kjth8EC&hl=en

**Copyright III (American Journal of Cancer Research)**

AJCR

e-Century Publishing Corporation

American Journal of Cancer Research

ISSN: 2156-6976

# AJCR: Infomation for Authors

The American Journal of Cancer Research (AJCR, ISSN 2156-6976) is an independent open access online journal dedicated to publication of original work in all areas of cancer research. AJCR is primarily devoted to original research papers (Main Research Articles and Brief Communications), and will also publish traditional Review articles. The goal of AJCR is to provide a forum for rapid dissemination of novel discoveries in basic and clinical studies of all human malignancies.

**SUBMISSION OF MANUSCRIPT** (Click to submit manuscript online)

**General Policy**

All manuscripts are submitted with the understanding that they have not been published elsewhere (except in the form of an abstract or as part of a published lecture or thesis) and are not currently under consideration for publication by another journal. It is the responsibility of the corresponding author to ensure that all authors have contributed to, read and approved the final manuscript for submission. The authors should keep a copy of manuscript submitted in case of revision, rejection, loss or damage. Receipt of manuscript will be acknowledged and a decision regarding acceptance made as soon as possible. Accepted manuscripts may be subject to editorial revision without notice.

## Copyright IV (Springer Nature, Bioinformatics for cancer immunotherapy)



SPRINGER NATURE LICENSE
TERMS AND CONDITIONS

Jan 23, 2022

This Agreement between Prathyusha Konda ("You") and Springer Nature ("Springer Nature") consists of your license details and the terms and conditions provided by Springer Nature and Copyright Clearance Center.

| | |
|---|---|
| License Number | 5235030665802 |
| License date | Jan 23, 2022 |
| Licensed Content Publisher | Springer Nature |
| Licensed Content Publication | Springer eBook |
| Licensed Content Title | Improving MHC-I Ligand Identification by Incorporating Targeted Searches of Mass Spectrometry Data |
| Licensed Content Author | Prathyusha Konda, J. Patrick Murphy, Shashi Gujar |
| Licensed Content Date | Jan 1, 2020 |
| Type of Use | Thesis/Dissertation |
| Requestor type | academic/university or research institute |
| Format | print and electronic |
| Portion | figures/tables/illustrations |
| Number of figures/tables/illustrations | 2 |

| | |
|---|---|
| Will you be translating? | no |
| Circulation/distribution | 1 - 29 |
| Author of this Springer Nature content | yes |
| Title | UNDERSTANDING THE ROLE OF T CELL MEDIATED IMMUNE RESPONSES IN CANCER IMMUNOTHERAPIES |
| Institution name | Dalhousie University |
| Expected presentation date | Apr 2022 |
| Portions | Figure 1 and Figure 2 |
| Requestor Location | Prathyusha Konda<br>Room 11J1, 5850 College Street<br>Sir Charles Tupper Medical Building<br><br>Halifax, NS B3H 4R2<br>Canada<br>Attn: Dalhousie University |
| Total | 0.00 CAD |

Terms and Conditions

**Springer Nature Customer Service Centre GmbH**
**Terms and Conditions**

This agreement sets out the terms and conditions of the licence (the **Licence**) between you and **Springer Nature Customer Service Centre GmbH** (the **Licensor**). By clicking 'accept' and completing the transaction for the material (**Licensed Material**), you also confirm your acceptance of these terms and conditions.

**1. Grant of License**

**1. 1.** The Licensor grants you a personal, non-exclusive, non-transferable, world-wide licence to reproduce the Licensed Material for the purpose specified in your order only. Licences are granted for the specific use requested in the order and for no other

use, subject to the conditions below.

**1. 2.** The Licensor warrants that it has, to the best of its knowledge, the rights to license reuse of the Licensed Material. However, you should ensure that the material you are requesting is original to the Licensor and does not carry the copyright of another entity (as credited in the published version).

**1. 3.** If the credit line on any part of the material you have requested indicates that it was reprinted or adapted with permission from another source, then you should also seek permission from that source to reuse the material.

**2. Scope of Licence**

**2. 1.** You may only use the Licensed Content in the manner and to the extent permitted by these Ts&Cs and any applicable laws.

**2. 2.** A separate licence may be required for any additional use of the Licensed Material, e.g. where a licence has been purchased for print only use, separate permission must be obtained for electronic re-use. Similarly, a licence is only valid in the language selected and does not apply for editions in other languages unless additional translation rights have been granted separately in the licence. Any content owned by third parties are expressly excluded from the licence.

**2. 3.** Similarly, rights for additional components such as custom editions and derivatives require additional permission and may be subject to an additional fee. Please apply to Journalpermissions@springernature.com/bookpermissions@springernature.com for these rights.

**2. 4.** Where permission has been granted **free of charge** for material in print, permission may also be granted for any electronic version of that work, provided that the material is incidental to your work as a whole and that the electronic version is essentially equivalent to, or substitutes for, the print version.

**2. 5.** An alternative scope of licence may apply to signatories of the STM Permissions Guidelines, as amended from time to time.

**3. Duration of Licence**

**3. 1.** A licence for is valid from the date of purchase ('Licence Date') at the end of the relevant period in the below table:

| Scope of Licence | Duration of Licence |
|---|---|
| Post on a website | 12 months |
| Presentations | 12 months |
| Books and journals | Lifetime of the edition in the language purchased |

**4. Acknowledgement**

**4. 1.** The Licensor's permission must be acknowledged next to the Licenced Material in print. In electronic form, this acknowledgement must be visible at the same time as the figures/tables/illustrations or abstract, and must be hyperlinked to the journal/book's homepage. Our required acknowledgement format is in the Appendix below.

**5. Restrictions on use**

**5. 1.** Use of the Licensed Material may be permitted for incidental promotional use and minor editing privileges e.g. minor adaptations of single figures, changes of format, colour and/or style where the adaptation is credited as set out in Appendix 1 below. Any other changes including but not limited to, cropping, adapting, omitting material that affect the meaning, intention or moral rights of the author are strictly prohibited.

**5. 2.** You must not use any Licensed Material as part of any design or trademark.

**5. 3.** Licensed Material may be used in Open Access Publications (OAP) before publication by Springer Nature, but any Licensed Material must be removed from OAP sites prior to final publication.

**6. Ownership of Rights**

**6. 1.** Licensed Material remains the property of either Licensor or the relevant third party and any rights not explicitly granted herein are expressly reserved.

**7. Warranty**

IN NO EVENT SHALL LICENSOR BE LIABLE TO YOU OR ANY OTHER PARTY OR ANY OTHER PERSON OR FOR ANY SPECIAL, CONSEQUENTIAL, INCIDENTAL OR INDIRECT DAMAGES, HOWEVER CAUSED, ARISING OUT OF OR IN CONNECTION WITH THE DOWNLOADING, VIEWING OR USE OF THE MATERIALS REGARDLESS OF THE FORM OF ACTION, WHETHER FOR BREACH OF CONTRACT, BREACH OF WARRANTY, TORT, NEGLIGENCE, INFRINGEMENT OR OTHERWISE (INCLUDING, WITHOUT LIMITATION, DAMAGES BASED ON LOSS OF PROFITS, DATA, FILES, USE, BUSINESS OPPORTUNITY OR CLAIMS OF THIRD PARTIES), AND
WHETHER OR NOT THE PARTY HAS BEEN ADVISED OF THE POSSIBILITY OF SUCH DAMAGES. THIS LIMITATION SHALL APPLY NOTWITHSTANDING ANY FAILURE OF ESSENTIAL PURPOSE OF ANY LIMITED REMEDY PROVIDED HEREIN.

**8. Limitations**

**8. 1.** ***BOOKS ONLY:*** Where **'reuse in a dissertation/thesis'** has been selected the following terms apply: Print rights of the final author's accepted manuscript (for clarity, NOT the published version) for up to 100 copies, electronic rights for use only on a personal website or institutional repository as defined by the Sherpa guideline

(www.sherpa.ac.uk/romeo/).

**8. 2.** For content reuse requests that qualify for permission under the STM Permissions Guidelines, which may be updated from time to time, the STM Permissions Guidelines supersede the terms and conditions contained in this licence.

**9. Termination and Cancellation**

**9. 1.** Licences will expire after the period shown in Clause 3 (above).

**9. 2.** Licensee reserves the right to terminate the Licence in the event that payment is not received in full or if there has been a breach of this agreement by you.

**Appendix 1 — Acknowledgements:**

**For Journal Content:**
Reprinted by permission from **[the Licensor]**: **[Journal Publisher** (e.g. Nature/Springer/Palgrave)] **[JOURNAL NAME] [REFERENCE CITATION** (Article name, Author(s) Name), **[COPYRIGHT]** (year of publication)

For **Advance Online Publication papers:**
Reprinted by permission from **[the Licensor]**: **[Journal Publisher** (e.g. Nature/Springer/Palgrave)] **[JOURNAL NAME] [REFERENCE CITATION** (Article name, Author(s) Name), **[COPYRIGHT]** (year of publication), advance online publication, day month year (doi: 10.1038/sj.[JOURNAL ACRONYM].)

**For Adaptations/Translations:**
Adapted/Translated by permission from **[the Licensor]**: **[Journal Publisher** (e.g. Nature/Springer/Palgrave)] **[JOURNAL NAME] [REFERENCE CITATION** (Article name, Author(s) Name), **[COPYRIGHT]** (year of publication)

**Note: For any republication from the British Journal of Cancer, the following credit line style applies:**

Reprinted/adapted/translated by permission from **[the Licensor]**: on behalf of Cancer Research UK: : **[Journal Publisher** (e.g. Nature/Springer/Palgrave)] **[JOURNAL NAME] [REFERENCE CITATION** (Article name, Author(s) Name), **[COPYRIGHT]** (year of publication)

For **Advance Online Publication** papers:
Reprinted by permission from The **[the Licensor]**: on behalf of Cancer Research UK: **[Journal Publisher** (e.g. Nature/Springer/Palgrave)] **[JOURNAL NAME] [REFERENCE CITATION** (Article name, Author(s) Name), **[COPYRIGHT]** (year of publication), advance online publication, day month year (doi: 10.1038/sj.[JOURNAL ACRONYM])

**For Book content:**
Reprinted/adapted by permission from **[the Licensor]**: **[Book Publisher** (e.g. Palgrave Macmillan, Springer etc) **[Book Title]** by **[Book author(s)] [COPYRIGHT]** (year of publication)

**Other Conditions:**

Version 1.3

**Questions? customercare@copyright.com or +1-855-239-3415 (toll free in the US) or +1-978-646-2777.**

## Copyright V (OncoImmunology, Taylor & Francis Group)



RE: koni20:Discovery of immunogenic cell death-inducing ruthenium-based photosensitizers for anticancer photodynamic therapy

Academic UK Non Rightslink <permissionrequest@tandf.co.uk>
Wed 2/2/2022 12:45 PM
To: Prathyusha Konda <Prathyusha.Konda@Dal.Ca>



Dear Sir/Madam

Thank you for your correspondence requesting permission to reproduce content from a Taylor & Francis Group content from our Journal in your thesis to be posted on your University's repository.

We will be pleased to grant the permission without fee on the condition that you acknowledge the original source of publication and insert a reference to the Journal's web site: www.tandfonline.com

**This permission does not cover any third party copyrighted work which may appear in the material requested. Please ensure you have checked all original source details for the rights holder.**

Please note that this licence **does not allow you to post our content on any third-party websites.**

Please note permission does not provide access to our article, if you are affiliated to an institution and your institution holds a subscription to the content you are requesting you will be able to view the article free of charge, if your institution does not hold a subscription or you are not affiliated to an institution that has a subscription then you will need to purchase this for your own personal use as we do not provide our articles free of charge for research.

Thank you for your interest in our Journal.

With best wishes,

Journal Permissions
**Journals, Taylor & Francis Group**
**Permissions e-mail:** permissionrequest@tandf.co.uk
**Web:** www.tandfonline.com

**4 Park Square, Milton Park, Abingdon, OX14 4RN**
**+44 (0)20 8052 0600**

Information Classification: General

**From:** Prathyusha Konda <prathyusha.konda@dal.ca>
**Sent:** 24 January 2022 00:31
**To:** Academic UK Non Rightslink <permissionrequest@tandf.co.uk>
**Subject:** koni20:Discovery of immunogenic cell death-inducing ruthenium-based photosensitizers for anticancer photodynamic therapy

Permissions Request

Type of use: Academic
Article title: Discovery of immunogenic cell death-inducing ruthenium-based photosensitizers for anticancer photodynamic therapy
Article DOI: 10.1080/2162402X.2020.1863626
Author name: Prathyusha Konda, Liubov M. Lifshits, John A. Roque III, Houston D. Cole, Colin G. Cameron, Sherri A. McFarland & Shashi Gujar
Journal title: OncoImmunology
Volume number: 10
Issue number: 1
Year of publication: 2021
Name: Prathyusha Konda
Street address: Room 11J1, 5850 College Street, Sir Charles Tupper Medical Building
Town: Halifax
Postcode/ZIP code: B3H 4R2
Country: Canada
Email: prathyusha.konda@dal.ca
Telephone: 9023294192
Intended use: To be used in your Thesis?
Are you requesting the full article?: No
Extract and number of words: Figures
Details of figure/table: Figure 1
Which University?: Dalhousie University
Title of your Thesis?: UNDERSTANDING THE ROLE OF T CELL MEDIATED IMMUNE RESPONSES IN CANCER IMMUNOTHERAPIES
University repository URL:
Is this a "Closed" or "Open" deposit?:
Additional comments:

# APPENDIX B: SUPPLEMENTAL CHEMISTRY METHODS AND FIGURES FOR CHAPTER 4

## 1. GENERAL METHODS

### 1.1. Instrumentation and Methods

Microwave reactions were performed in a CEM Discover microwave reactor. *Purifications:* neutral aluminum oxide, activated, Brockmann Grade I (58Å, −60 Mesh Powder, S.A. 150 $m^2 g^{-1}$) was used as a stationary phase for gravity column chromatography. Flash column chromatography was carried out on CombiFlash® EZ Prep from Teledyne ISCO (model: EZ Prep UV) using SILICYCLE SiliaSep™ Neutral Alumina cartridges. Sephadex® LH-20 was used for size-exclusion chromatography. The NMR spectra were recorded on JEOL ECA 500 NMR spectrometer, operating at 500 MHz for $^1$H experiments (University of North Carolina at Greensboro) and on Agilent 700 MHz spectrometer (The Joint School of Nanoscience and Nanoengineering at Greensboro) operating at 700 MHz for $^1$H experiments. The chemical shifts are reported in parts per million (ppm) and were referenced to the residual solvent peaks. ESI mass spectra were obtained using a Thermo Fisher Scientific LTQ Orbitrap XL at the Triad Mass Spectrometry Laboratory at University of North Carolina at Greensboro. HPLC analysis was carried out with 100 μM solutions in methanol using a Hypersil GOLD C18 reversed-phase column with an A–B gradient (98% → 5% A; A = 0.1% formic acid in $H_2O$, B = 0.1% formic acid in MeCN). Reported retention times are correct to within ±0.1 min.

### 1.2. Lipophilicity

Lipophilicity measurements were performed as done previously[670] but with 10 mM phosphate buffer at neutral pH (=7.4) in lieu of water. The log ($D_{o/w}$) was calculated as the log-transformed ratio of compound concentration in either phosphate buffer or 1-

octanol, with each solvent saturated with the other. Compounds with observed precipitate generally only had positive absorbance readings in 1-octanol and were assigned an estimated log ($D_{o/w}$) = −3 for majority lipophilicity. Any compound with observed precipitate was not used for correlation examples nor for in-text comparisons of their relative lipophilicities.

**1.3. Spectroscopy**

Spectroscopic and photophysical measurements of the complexes were carried out as dilute (5–20 μM) solutions of their chloride salts in spectroscopy-grade acetonitrile that had been distilled over $CaH_2$. UV-vis extinction coefficients ε were determined at spectral peaks from the slope of absorbance vs. concentration at five dilutions (20 μM serially diluted four times by 25%). Emission ($\Phi_{em}$) and singlet oxygen ($\Phi_{\Delta}$) quantum yields were determined by integrating the corresponding emission peak and applying the following equation:

$$\Phi = \Phi_s \left(\frac{I}{I_s}\right)\left(\frac{A_s}{A}\right)\left(\frac{\eta^2}{\eta_s^2}\right) \quad (1)$$

where *I* is the integrated emission, *A* is the UV-vis absorbance at the excitation wavelength, and η is the index of refraction of the solvent ($\eta^2/\eta_s^2$ = 1 in all cases here).

The subscript *s* denotes values under identical conditions from the reference compound, $Ru(bpy)_3(PF_6)_2$, for which $\Phi_{\Delta}$=0.56[785] and $\Phi_{em}$=0.012[786] in aerated acetonitrile. Oxygen was removed from the solution by sparging with Ar in a septum-capped cuvette for emission experiments, or by five freeze-pump-thaw cycles in a custom Schlenk-style cuvette for transient absorption measurements.

UV-vis spectra were measured on a Jasco V-730 spectrometer. Steady-state emission spectra were recorded with a PTI Quantamaster emission system with a

K170B PMT for measuring UV/visible spectra and a Hamamatsu R5509-42 NIR PMT for the near infrared (≲1400 nm). The emission and excitation spectra were corrected for nonlinear lamp and detector response.

Transient absorption (TA) lifetimes and spectra were determined with an Edinburgh Instruments LP-980 spectrometer equipped with a PMT-LP detector and a Continuum Minilite Nd:YAG excitation source set to 355 nm (7−9 mJ per pulse). This instrument was also used to measure emission lifetimes. An instrument response function was applied to correct short (<10 ns) signals.

## 1.4. Cell Culture

In general, cells were cultured using standard aseptic technique and no antibiotics.

### 1.4.1. A375

Female human melanoma cell line A-375 [A375] (ATCC CRL-1619) was subcultured in 75 $cm^2$ flasks (VWR, 10062-860) at split ratios of 1:4 to 1:8 (seeded approximately 200,00–400,000 cells $mL^{-1}$). A375 cells were split or fed every 2–3 days and used within 5–10 passages from receipt for reported assay results. Split steps included a rinse with 1× Dulbecco's Phosphate-Buffered Saline without $Ca^{2+}$ or $Mg^{2+}$ (DPBS; diluted and sterifiltered Corning 20-031-CV) and enzymatic dissociation using 0.25% w/v Trysin-EDTA. Culture media consisted of Dulbecco's Modified Eagle's Medium (DMEM; Hyclone SH30243.FS), which contained 4500 mg $L^{-1}$ glucose, 4 mM L-glutamine, 110 mg $L^{-1}$ sodium pyruvate, and was supplemented with 10% v/v FB essence (VWR, Avantor Seradigm, 10803-034). Cells were cultured at 10% USP-grade $CO_2$, ≥ 90% relative humidity, and 37°C in an air-jacketed incubator (VWR, 10810-902).

### 1.4.2. SKMEL28.

Male human melanoma cell line SK-MEL-28 [SKMEL28] (ATCC HTB-72) was subcultured as previously described at 5% USP-grade $CO_2$, ≥ 90% relative humidity, and

37°C in a water-jacketed incubator (ThermoFisher, Thermo Scientific 4110).[670] Split ratios were commonly performed between 1:2–1:5 (150,000–400,000 cells $mL^{-1}$). Cells were used within 5–10 passages from receipt at UTA and 10–15 passages at Acadia University.

### 1.5. Cellular Assays

There are two main categories of cellular assays, a) general dose-response screens on 384-well plate across multiple cell lines and b) specialized screens on 12- or 96-well plates. Cellular assays generally follow our previous works in 96-well plate format.[346,670] Regardless of well density, plates are only stacked 2-plates high in an incubator to facilitate temperature equilibrium. Our standard screen approach adapted to 384-well plates is described below, which had a total incubation time 1 day shorter than in 96-well plates due to observed edge effects. We describe light devices for photobiological evaluation following this procedure.

#### 1.5.1. Ru(II) compound solutions

Stock solutions of metal compounds were prepared at 5 mM in 10% v/v DMSO:water (type 1, ≥ 18.2 MΩ·cm). Stock solutions were stored in glass vials with PTFE-lined caps, protected from light with aluminum foil, and stored at −20°C when not in use. Cellular assays involved ≤ 0.6 % v/v DMSO at the highest compound concentration (300 μM).

#### 1.5.2. Cytotoxicity and photocytotoxicity

A miniaturized format for drug screening by hand. An electronic multichannel pipettor is strongly recommended for successful set-up by hand. Volumes of our standard assay in 96-well plates approximately decrease to 40%. Into 384-well plates (Greiner Bio-One, 781182), a DPBS perimeter of 100 μL $well^{-1}$ was installed into the outmost two wells (144 well count). After this, 10 μL $well^{-1}$ of DPBS was dispensed into all control wells (12 count). For sample and control wells (240 well count), 10 μL $well^{-1}$ of complete media

was added. An additional 20 µL well$^{-1}$ media was dispensed into negative cell controls. At this point, sample wells have 10 µL well$^{-1}$ complete media, positive controls 20 µL well$^{-1}$ media and DPBS, and negative controls 40 µL well$^{-1}$ of mainly media. It is optional to pre-equilibrate plates in a humidified incubator (37°C, 5% $CO_2$, ≥ 90% relative humidity - RH) to aid transfer of initial aliquots.

After media is dispensed, plates are equilibrated in the incubator for a minimum 15 mins before addition of cellular slurry. If seeding multiple cell lines, 2–4 different cell lines are a suggested limit for a single researcher. Plates were seeded 20 µL well$^{-1}$ across five plates at a time (i.e., per cell line) for sample and positive control wells. Cells were seeded at the following densities: A375 (5500 cells well$^{-1}$), B16F10 (4000 cells well$^{-1}$), and SKMEL28 (4000 cells well$^{-1}$).They were mixed twice (up, down, left, right tilting) in the biosafety cabinet and before placing inside the incubator and incubated 1–3 h.

During the incubation, compound dilutions were prepared in sterile 0.8 mL 96-deep well plates (Greiner Bio-One, 780261) using DPBS as solvent. Dilutions were prepared in serial across 9 concentrations ranging from 1200–4×10$^{-3}$ µM. Covered deep-well plates were incubated for 0.5–1 h before final dispensing ($d_f$ = 4) at 10 µL well$^{-1}$. All sample and control wells total 40 µL well$^{-1}$ at this point. Replicates are generally dispensed row-wise and spaced every 4 (triplicates) or 6 (duplicates) rows. The biosafety cabinet's lights were kept off while dispensing compound dilutions. Repeats across experiments change plate maps for compound and replicate locations. For a standard 12-channel pipettor, compounds are dispensed every other column. Therefore, it is important to plan liquid dispensing and an appropriate plate map ahead of time.

Following dark (sham) or light treatments (16–20 h drug-to-light interval, DLI), plates are further incubated overnight before final viability measurements. One day is removed from the post-PDT period of our standard 96-well plate assay to mitigate edge effects on

a 384-well plate. At this point, 10 µL well$^{-1}$ of 0.3 mM sterifiltered resazurin in 0.2 M phosphate buffer (pH = 7.4) is dispensed across all well plates. Generally, 4–6 plates are handled at a time in the biosafety cabinet. Resazurin dyed plates were incubated further for 4 h before reading fluorometrically on a Molecular Devices M2e (30 s shake, bottom-read, $\lambda_{exc}$ 530 nm, long-pass 570 nm, $\lambda_{em}$ 620 nm). Whereas unnecessary for a 96-well plate, it was found that assay S/N drastically improved if the reader's plate adaptor was removed prior to the read (shorter distance from well to detector).

**1.5.3. Hypoxia cytotoxicity and photocytotoxicity.**

Following our recent example, we probed activity of our lead compounds in hypoxia (1% $O_2$) for their oxygen dependence (PDT photosensitizer) relative to a compound highly oxygen-dependent for its activity $[Ru(bpy)_2(dppn)]Cl_2$.[670] This probe was conducted in parallel across normoxia (~18.5% $O_2$) and hypoxia for leads **2**, **6**, and **9** in 96-well plates and SKMEL28 cells. The results are shown in Appendix Table **S**.

**1.5.4. Light Devices and Protocols**

For photobiological evaluation, we used various visible and NIR light sources that we list by location. Standard screens treat at a fluence of 100 J cm$^{-2}$. Our location at Acadia University applied a broadband visible light 190 W BenQ S 510 overhead projector (400–700 nm, 40 mW cm$^{-2}$) and red light (625 nm, 35–40 mW$^{-2}$; LED array by Photodynamic Inc., Halifax, NS). Our location at Dalhousie University applied a cool white LED panel (SOLLA-CREE, 70 W, 25–30 mW$^{-2}$), a 633 nm UHP-LED (Prizmatix), and 733 nm laser (2 W, CivilLaser; (9–10 mW$^{-2}$) coupled to a 600 µm optical fiber with a 2 mm flat-cut diffuser (Medlight, FD1). Our location at UTA applied the same SOLLA-CREE cool white LED panel (18–22 mW$^{-2}$), 523 and 633 nm UHP-LEDs (Prizmatix; 20 mW$^{-2}$), and the same 733 nm laser (8–10 mW$^{-2}$).

For specialized irradiation protocols at UTA we restricted our in vitro model to the single cell line SKMEL28. Dosimetry work for both irradiance and fluence dependences, was conducted using clear 96-well plates and randomized plate maps limited to a 36-well quadrant of sample wells. We further explored the scope of our lead compounds with the Modulight ML8500 platform (37°C, 5% $CO_2$). With the ML8500, we applied lasers centered at 445 nm (25 J $cm^{-2}$, 100 $mW^{-2}$), 525 nm (100 J $cm^{-2}$, 300 $mW^{-2}$), 630 nm (200 J $cm^{-}2$, 300 $mW^{-2}$), 753 nm (200–400 J $cm^{-2}$, 300 $mW^{-2}$), 810 nm (400–600 J $cm^{-2}$, 400 $mW^{-2}$), and 976 nm (600 J $cm^{-2}$, 400 $mW^{-2}$). Different fluences were applied with the ML8500 in an attempt to match wavelength performance at clinically relevant irradiances (e.g., short illumination periods). These conditions were confirmed to exert no light-based toxicity in the absence of compounds **1**–**9** in our model cell line SKMEL28 [Appendix Figure S50]. Since the ML8500 is limited to a single well per treatment, it necessitates black well plates (96-well, Greiner Bio-One, 655090) to mitigate cross-talk between wells and randomized plate maps for studies > 1 h illumination to mitigate edge effects.

### 1.6. Maximum tolerated dose in mice

An 8-week old litter of female C57BL/6J mice, averaging 20 g per mouse, were treated by intraperitoneal injection of **2** in accordance with protocol A20-006 (approved by WFU Animal Care and Use Committee). Mice were incrementally dosed from 25–100 mg kg−1 with 200 µL injections and 10% DMSO in 0.9% saline as the vehicle. Solutions of **2** were immediately prepared with sonication prior to injection. Female mice were dosed by slow intraperitoneal injection (IP, the lower right abdominal quadrant) only after visible confirmation of complete compound dissolution. Animals were continuously monitored for 2 h, frequently over the next 6, and periodically for up to 2 weeks before being sacrificed. Mice were accordingly euthanized if (a) a combination of moderate severity

signs appeared, (b) a single severe sign appeared, or (c) the study period was complete, 2 weeks post-injection. The maximum tolerated dose (MTD) was defined as the dose that produces moderate signs of clinical toxicity in the final tested animal.

### 1.7. Data analysis and statistics

Data from 384-well plates was initially compiled and processed with custom R[(787)] scripts using the plater,[(788)] dplyr,[(789)] readxl,[(790)] openxlsx,[(791)] and tidyr[(792)] packages. All results from the endpoint-based resazurin assay are background subtracted with negative controls (media and DPBS) and normalized relative to positive cell controls. Any negative values are assumed to be a mismatch of background (i.e., fluorescence quenching) and assigned as zero values. Likewise, at high compound concentration, background fluorescence and/or quenching is often observed for this class of compounds. Zero values are assigned for these cases when indicated by several consecutive concentrations for a given treatment (dark or light). Additional verification is conducted via light microscopy before finalizing data corrections. Further discussion of assay limits for these compound types is provided in a recent review.[(346)]

Resazurin data over a wide concentration range was fit to both a three-parameter log-logistic and logistic models using GraphPad Prism 8.4.0 according to Equation S1Equation S2 (four-parameter shown) where bottom is constrained to equal zero and X is equal to concentration.

$$Y = \frac{Bottom + (Top - Bottom)}{(1 + (10^{Log(EC_{50} - X) * Hillslope})} \quad \text{Equation S1}$$

$$Y = \frac{Bottom + (Top - Bottom)}{\left(1 + (EC_{50}/X)^{Hillslope}\right)} \quad \text{Equation S2}$$

Experiments are typically done in triplicate with at least one repeat staggered by several days. Replicates are always plotted ± standard deviation (SD) on a plot.

Reported $EC_{50}$ values are ± SEM for a given experiment; these denote the effective concentration to reduce relative cell viability by 50% of the fitted curve ($EC_{50}$) ± standard error of the mean (SEM). Steep hill slopes with ambiguous confidence intervals are unable to determine the SEM and labelled as not determined (n.d.). Phototherapeutic indices (PI) are reported as the ratio of dark to light $EC_{50}$ values and used as a measure of light-induced potency. Summary activity plots used for quickly comparing compound potency (Log $EC_{50}$, PI, and Log PI) include SEM from log-logistic fits where applicable (Log $EC_{50}$). Correlation analyses for PI, lipophilicity, and $\Phi_{\Delta}$ were conducted using Pearson's correlation coefficients and two-tailed t-tests for discerning significance at $\alpha = 0.05$.

## 2. SYNTHESES OF RU(II) COMPLEXES 1–9

### 2.1. Materials

All solvents were purchased from commercial sources and used without further purification. Most of the solvents were purchased from Fisher Scientific or VWR and ethanol (200 proof) was purchased from Decon Laboratories. 1,10-Phenanthroline was purchased from Oakwood Chemical and ruthenium(III) trichloride trihydrate was purchased from Ark Pharm and Acros Organics. 4-Picoline was purchased from Alfa Aesar. Silver nitrate was purchased from Sigma-Aldrich. Triethylamine was purchased from Fisher Scientific. Deuterated solvents for NMR experiments were purchased from Cambridge Isotope Laboratories.

### 2.2. Synthetic Procedures

Complexes **1**–**9** were synthesized using conventional heating, and synthesis of several complexes of the series was adapted for microwave reactor, which significantly shortened reaction time while provided very similar reaction yield. Purification of the complexes **1**–**9** was performed with gravity column chromatography at first and then was

later replaced with flash column chromatography during synthesis optimization. The fastest way to afford the complexes **1**–**9** includes using microwave-assisted heating for synthesis and flash column chromatography for purification, but if those instrumentations are unavailable, conventional heating and gravity column chromatography could be used to afford complexes **1**–**9** in similar yields but would require longer time.

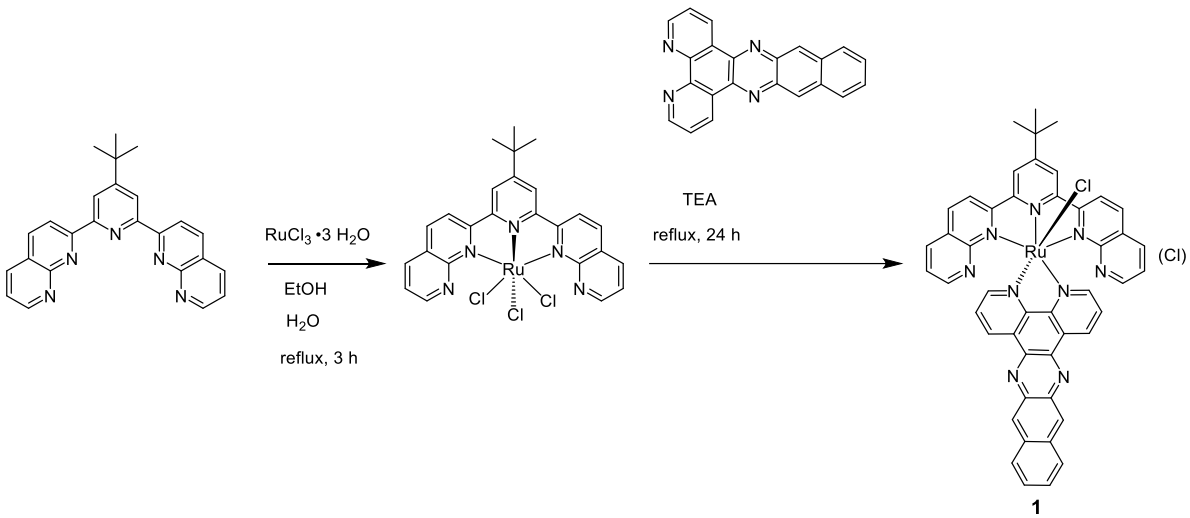


**Scheme S1.** Synthesis scheme for complex **1** [Ru(tpbn)(dppn)(Cl)]Cl (conventional heating method).

**Complex 1:** [Ru(tpbn)(dppn)(Cl)]Cl

Conventional heating method: A three-neck round-bottom flask, equipped with a nitrogen purge and a condenser, was charged with tpbn (0.100 g, 0.26 mmol) and EtOH (50 mL). Then, an aqueous solution of $RuCl_3$•$3H_2O$ was added (0.070 g, 0.27 mmol in 12 mL $H_2O$). The reaction mixture was well-stirred and refluxed for 3 h. Then, dppn (0.094 g, 0.28 mmol) and triethylamine (TEA) (1 mL) were added and the reaction mixture was refluxed for 24 h. The reaction mixture was concentrated under reduced pressure. The residue was treated with a few mL of $H_2O$ and the precipitate was isolated by filtration. The precipitate was washed with $H_2O$ and $Et_2O$ and dry-loaded on a column for purification. Column chromatography was performed on neutral alumina, using gradient

elution: 1) $CH_2Cl_2$ 2) 50% $CH_2Cl_2$ : 50% acetone 3) acetone 4) 97% acetone : 3% MeOH. The product fraction (deep-purple band) elutes the last with 97% acetone : 3% MeOH. The product fraction was concentrated under reduced pressure and the residue was treated with a few mL of $Et_2O$. The precipitate was isolated by filtration, washed with $Et_2O$ and dried. [Ru(tpbn)(dppn)(Cl)]Cl **1** was obtained as a dark-purple powder (0.095 g, 39% yield).

Microwave-assisted method: A microwave vial was filled with argon, and EtOH (2.00 mL) and $H_2O$ (0.48 mL) were added. The solvent mixture was degassed with argon for 10 minutes, and then tpbn (0.030 g, 0.076 mmol) and $RuCl_3$•$3H_2O$ (0.021 g, 0.080 mmol) were added to the reaction vial. The vial was capped, and the reaction mixture was exposed to microwave irradiation at 140°C for 15 min. After that, dppn (0.028 g, 0.084 mmol) and TEA (20 drops) were added to the reaction mixture. The reaction mixture was exposed to microwave irradiation at 140°C for another 15 min then concentrated under reduced pressure. The residue was treated with a few mL of $H_2O$ and the precipitate was isolated by filtration. The precipitate was washed with $H_2O$ and $Et_2O$ and dry-loaded on a column for purification. Column chromatography was performed on neutral alumina, using gradient elution: 1) $CH_2Cl_2$ 2) 50% $CH_2Cl_2$ : 50% acetone 3) acetone 4) 97% acetone : 3% MeOH. Product fraction (deep- purple band) elutes the last with 97% acetone : 3% MeOH. Product fraction was concentrated under reduced pressure and the residue was treated with a few mL of $Et_2O$. The precipitate was isolated by filtration, washed with $Et_2O$ and dried. [Ru(tpbn)(dppn)(Cl)]Cl **1** was obtained as a dark-purple powder (0.021 g, 30% yield).

$R_f$ = 0.61 (alumina; 8% $H_2O$ in acetonitrile).

$^1$H NMR (MeOD-$d_3$, 500 MHz): δ 10.73 (**d**, dd, $J_1$ = 5.5 Hz, $J_2$ = 1.5 Hz, 1H), 10.02 (**f**, dd, $J_1$ = 8.0 Hz, $J_2$ = 1.5 Hz, 1H), 9.16 (**g**, s, 1H), 9.16 (**c**, dd, $J_1$ = 8.0 Hz, $J_2$ = 1.5 Hz, 1H),

9.11 (**3**, s, 2H), 9.00 (**l**, s, 1H), 8.94 (**3′**, d, $J$ = 8.5 Hz, 2H), 8.54 (**4′**, d, $J$ = 8.5 Hz, 2H), 8.43 (**e**, dd, $J_1$ = 8.0 Hz, $J_2$ = 5.5 Hz, 1H), 8.30 (**h**, **k**, m, 2H), 8.27 (**5′**, dd, $J_1$ = 8.0 Hz, $J_2$ = 2.0 Hz, 2H), 7.99 (**7′**, dd, $J_1$ = 4.5 Hz, $J_2$ = 2.0 Hz, 2H), 7.89 (**a**, dd, $J_1$ = 5.5 Hz, $J_2$ = 1.5 Hz, 1H), 7.71 (**i**, **j**, m, 2H), 7.32 (**6′**, dd, $J_1$ = 8.0 Hz, $J_2$ = 4.5 Hz, 2H), 7.30 (**b**, dd, $J_1$ = 8.0 Hz, $J_2$ = 5.5 Hz, 1H), 1.80 (**4-tBu**, s, 9H).

HRMS (ESI$^+$) m/z: [M-Cl]$^+$ Calcd for $C_{47}H_{33}ClN_9Ru$ 860.1585; Found 860.1573.

HPLC retention time: 26.98 min.

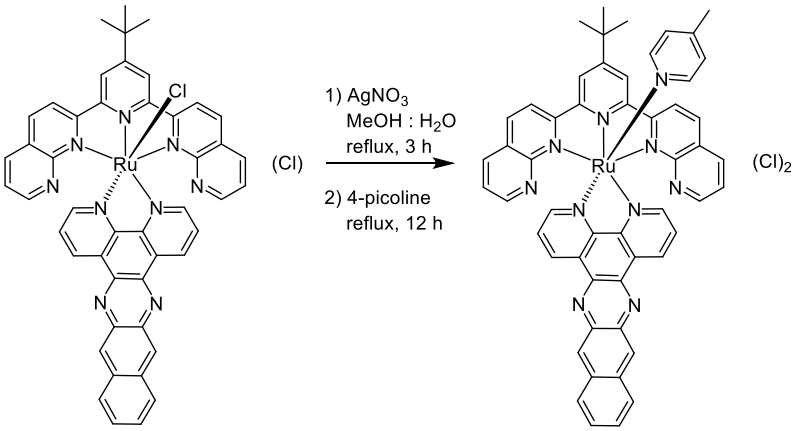


**Scheme S2.** Synthesis scheme for complex **2** [Ru(tpbn)(dppn)(4-pic)]$Cl_2$ (conventional heating method).

**Complex 2:** [Ru(tpbn)(dppn)(4-pic)]$Cl_2$

Conventional heating method: A round-bottom flask, equipped with a condenser, was charged with [Ru(tpbn)(dppn)(Cl)]Cl **1** (0.100 g, 0.11 mmol) and MeOH (8 mL). Then, aqueous solution of $AgNO_3$ (0.190 g, 1.10 mmol in 2 mL $H_2O$) was added dropwise. The reaction mixture was well-stirred and refluxed for 3 h. Then, 4-picoline (1.5 mL, 15.21 mmol) was added and the reaction mixture was refluxed for 12 h then concentrated under reduced pressure. The residue was treated with a few mL of $H_2O$ and the

precipitate was isolated by filtration. The precipitate was washed with $H_2O$ and $Et_2O$ and dry-loaded on a column for purification. Column chromatography was performed on neutral alumina, using gradient elution: 1) $CH_2Cl_2$ 2) 50% $CH_2Cl_2$ : 50% acetone 3) acetone 4) 95% acetone : 5% MeOH. The product fraction (maroon band) eluted last with 95% acetone : 5% MeOH. The product fraction was concentrated under reduced pressure and the residue was treated with a few mL of $Et_2O$. The precipitate was isolated by filtration, washed with $Et_2O$ and dried. [Ru(tpbn)(dppn)(4-pic)]$Cl_2$ **2** was obtained as a maroon powder (0.088 g, 81% yield).

Microwave-assisted method: The reaction was performed in 2 batches, then combined for workup and purification. *Batch 1*: A microwave vial was charged with [Ru(tpbn)(dppn)(Cl)]Cl **1** (0.017 g, 0.02 mmol), 4-picoline (0.2 mL, 2.02 mmol) and MeOH (1.5 mL). The vial was capped, and the reaction mixture was exposed to microwave irradiation at 150°C for 15 min. After that, $H_2O$ (0.4 mL) was added and the reaction mixture was exposed to microwave irradiation at 160°C for another 15 min. *Batch 2*: repeated procedure for batch 1. The reaction mixtures from batch 1 and batch 2 were combined and concentrated under reduced pressure. The residue was dried under high vacuum and purified with flash chromatography on alumina (eluent: gradient elution from 100% acetonitrile to 92% acetonitrile : 8% $H_2O$). The product fraction (maroon band, elutes with 92% acetonitrile : 8% $H_2O$) was concentrated under reduced pressure and further purified using size-exclusion chromatography on Sephadex LH-20 (eluent: MeOH). The main band (maroon) was collected and concentrated under reduced pressure. The residue was treated with a few mL of $Et_2O$, sonicated, and isolated by filtration. The precipitate was thoroughly washed with $Et_2O$ and dried. [Ru(tpbn)(dppn)(4-pic)]$Cl_2$ **2** was obtained as a maroon powder (0.027 g, 77% yield).

$R_f$ = 0.56 (alumina; 8% $H_2O$ in acetonitrile).

$^1$H NMR (MeOD-$d_3$, 500 MHz): δ 10.08 (**f**, dd, $J_1$ = 8.5 Hz, $J_2$ = 1.5 Hz, 1H), 9.47 (**d**, dd, $J_1$ = 5.5 Hz, $J_2$ = 1.5 Hz, 1H), 9.32 (**c**, dd, $J_1$ = 8.0 Hz, $J_2$ = 1.0 Hz, 1H), 9.20 (**g**, s, 1H), 9.17 (**3**, s, 2H), 9.05 (**3′**, d, $J$ = 8.5 Hz, 2H), 9.02 (**l**, s, 1H), 8.73 (**4′**, d, $J$ = 8.5 Hz, 2H), 8.43 (**e**, dd, $J_1$ = 8.5 Hz, $J_2$ = 5.5 Hz, 1H), 8.37 (**5′**, dd, $J_1$ = 8.0 Hz, $J_2$ = 2.0 Hz, 2H), 8.36 (**h**/**k**, d, $J$ = 8.0 Hz, 1H), 8.29 (**h**/**k**, d, $J$ = 8.0 Hz, 1H), 8.13 (**7′**, dd, $J_1$ = 4.0 Hz, $J_2$ = 2.0 Hz, 2H), 7.80 (**a**, dd, $J_1$ = 5.5 Hz, $J_2$ = 1.0 Hz, 1H), 7.72 (**i**, **j**, m, 2H), 7.65 (**2″**, d, $J$ = 7.0 Hz, 2H), 7.45 (**b**, dd, $J_1$ = 8.0 Hz, $J_2$ = 5.5 Hz, 1H), 7.43 (**6′**, dd, $J_1$ = 8.0 Hz, $J_2$ = 4.5 Hz, 2H), 7.00 (**3″**, d, $J$ = 6.0 Hz, 2H), 2.25 (**4″-Me**, s, 3H), 1.77 (**4-tBu**, s, 9H).

HRMS (ESI$^+$) m/z: $[M-2Cl]^{2+}$ Calcd for $C_{53}H_{40}N_{10}Ru$ 459.1235; Found 459.1229.

HPLC retention time: 23.44 min.

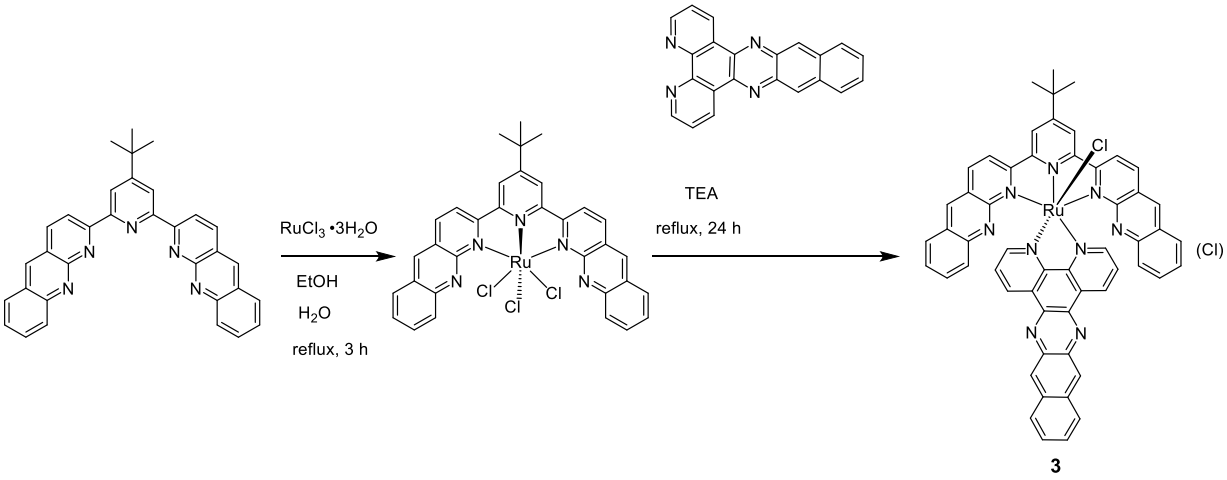


**3**

**Scheme S3.** Synthesis scheme for complex **3** [Ru(tpbbn)(dppn)(Cl)]Cl (conventional heating method).

**Complex 3:** [Ru(tpbbn)(dppn)(Cl)]Cl

Conventional heating method: A three-neck round-bottom flask, equipped with nitrogen purge and a condenser, was charged with tpbbn (0.200 g, 0.41 mmol) and EtOH (100 mL). Then, aqueous solution of $RuCl_3$•$3H_2O$ was added (0.112 g, 0.43 mmol in 24 mL $H_2O$). Reaction mixture was well-stirred and refluxed for 3 h. Then, dppn (0.150 g, 0.45

mmol) and TEA (2 mL) were added and the reaction mixture was refluxed for 24 h then concentrated under reduced pressure. The residue was treated with a few mL of $H_2O$ and the precipitate was isolated by filtration. The precipitate was washed with $H_2O$ and $Et_2O$ and dry-loaded on a column for purification. Column chromatography was performed on neutral alumina, using gradient elution: 1) $CH_2Cl_2$ 2) 50% $CH_2Cl_2$ : 50% acetone 3) acetone 4) 97% acetone : 3% MeOH. The product fraction (emerald-green band) eluted last with 97% acetone : 3% MeOH. The product fraction was concentrated under reduced pressure and the residue was treated with a few mL of $Et_2O$. The precipitate was isolated by filtration, washed with $Et_2O$ and dried. [Ru(tpbbn)(dppn)(Cl)]Cl **3** was obtained as a dark-green powder (0.130 g, 30% yield). Although not tested, it is highly likely that synthesis of **3** could also be performed using microwave-assisted heating and much shorter reaction times than conventional heating.

$R_f$ = 0.57 (alumina; 8% $H_2O$ in acetonitrile).

$^1$H NMR (DMSO-$d_6$, 700 MHz): δ 10.82 (**d**, dd, $J_1$ = 4.9 Hz, $J_2$ = 0.7 Hz, 1H), 10.32 (**f**, dd, $J_1$ = 8.4 Hz, $J_2$ = 0.7 Hz, 1H), 9.38 (**g**, s, 1H), 9.34 (**3**, s, 2H), 9.22 (**2′**, d, $J$ = 9.1 Hz, 2H), 9.17 (**9′**, s, 2H), 9.05 (**l**, s, 1H), 8.99 (**c**, dd, $J_1$ = 7.7 Hz, $J_2$ = 0.7 Hz, 1H), 8.88 (**1′**, d, $J$ = 9.1 Hz, 2H), 8.79 (**e**, dd, $J_1$ = 8.4 Hz, $J_2$ = 4.9 Hz, 1H), 8.44 (**h**/**k**, d, $J$ = 9.1 Hz, 1H), 8.35 (**h**/**k**, d, $J$ = 7.7 Hz, 1H), 8.06 (**5′**, d, $J$ = 8.4 Hz, 2H), 7.96 (**a**, dd, $J_1$ = 6.3 Hz, $J_2$ = 1.4 Hz, 1H), 7.77 (**i**/**j**, dd, $J_1$ = 8.4 Hz, $J_2$ = 7.0 Hz, 1H), 7.73 (**i**/**j**, dd, $J_1$ = 7.7 Hz, $J_2$ = 7.0 Hz, 1H), 7.69 (**7′**, dd, $J_1$ = 8.4 Hz, $J_2$ = 7.0 Hz, 2H), 7.50 (**6′**, dd, $J_1$ = 8.4 Hz, $J_2$ = 7.0 Hz, 2H), 7.39 (**b**, dd, $J_1$ = 7.7 Hz, $J_2$ = 6.3 Hz, 1H), 6.75 (**8′**, d, $J$ = 8.4 Hz, 2H), 1.80 (**4-tBu**, s, 9H).

HRMS (ESI$^+$) m/z: $[M\text{-}Cl]^+$ Calcd for $C_{55}H_{37}ClN_9Ru$ 960.1898; Found 960.1896.

HPLC retention time: 30.23 min.

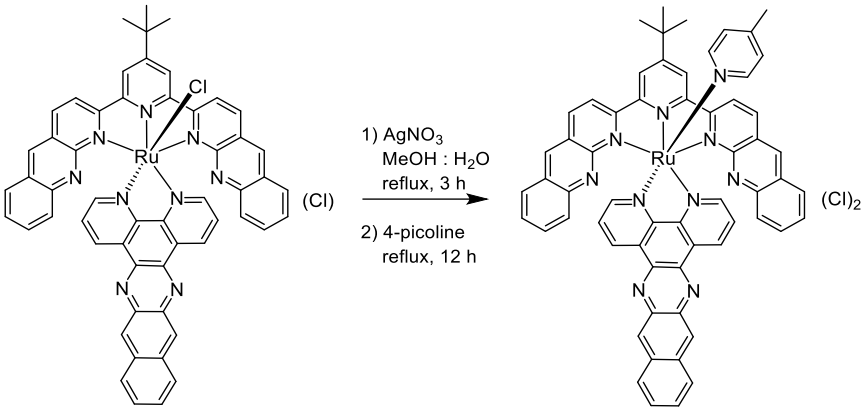


3 4

**Scheme S4.** Synthesis scheme for complex **4** [Ru(tpbbn)(dppn)(4-pic)]$Cl_2$ (conventional heating method).

**Complex 4:** [Ru(tpbbn)(dppn)(4-pic)]$Cl_2$

Conventional heating method: A round-bottom flask, equipped with a condenser, was charged with [Ru(tpbbn)(dppn)(Cl)]Cl **3** (0.070 g, 0.07 mmol) and MeOH (8 mL). Then, aqueous solution of $AgNO_3$ (0.120 g, 0.70 mmol in 2 mL $H_2O$) was added dropwise. The reaction mixture was well-stirred and refluxed for 3 h. Then, 4-picoline (1.5 mL, 15.21 mmol) was added and reaction mixture was refluxed for 12 h then concentrated under reduced pressure. The residue was treated with a few mL of $H_2O$ and the precipitate was isolated by filtration. The precipitate was washed with $H_2O$ and $Et_2O$ and dry-loaded on a column for purification. Column chromatography was performed on neutral alumina, using gradient elution: 1) $CH_2Cl_2$ 2) 50% $CH_2Cl_2$ : 50% acetone 3) acetone 4) 95% acetone : 5% MeOH. The product fraction (deep-purple band) eluted last with 95% acetone : 5% MeOH. The product fraction was concentrated under reduced pressure and the residue was treated with a few mL of $Et_2O$. The precipitate was isolated by filtration, washed with $Et_2O$ and dried. [Ru(tpbbn)(dppn)(4-pic)]$Cl_2$ **4** was obtained as a dark-purple powder (0.050 g, 66% yield).

Although not tested, it is highly likely that synthesis of **4** could also be performed using microwave-assisted heating and much shorter reaction times than conventional heating.

$R_f$ = 0.49 (alumina; 8% $H_2O$ in acetonitrile).

$^1$H NMR (MeOD-$d_3$, 700 MHz): δ 10.46 (**f**, d, $J$ = 8.4 Hz, 1H), 9.74 (**d**, d, $J$ = 4.9 Hz, 1H), 9.28 (**3**, s, 2H), 9.21 (**c**, d, $J$ = 7.7 Hz, 1H), 9.18 (**g**, s, 1H), 9.13 (**9′**, s, 2H), 9.05 (**2′**, d, $J$ = 8.4 Hz, 2H), 8.93 (**1′**, d, $J$ = 9.1 Hz, 2H), 8.91 (**l**, s, 1H), 8.83 (**e**, dd, $J_1$ = 8.4 Hz, $J_2$ = 5.6 Hz, 1H), 8.30 (**h/k**, d, $J$ = 8.4 Hz, 1H), 8.22 (**h/k**, d, $J$ = 7.7 Hz, 1H), 8.02 (**5′**, d, $J$ = 7.7 Hz, 2H), 7.88 (**a**, d, $J$ = 5.6 Hz, 1H), 7.79 (**2″**, d, $J$ = 7.0 Hz, 2H), 7.74 (**7′**, dd, $J_1$ = 8.4 Hz, $J_2$ = 7.0 Hz, 2H), 7.67 (**i**, **j**, m, 2H), 7.53 (**6′**, dd, $J_1$ = 7.7 Hz, $J_2$ = 7.0 Hz, 2H), 7.43 (**b**, dd, $J_1$ = 7.7 Hz, $J_2$ = 5.6 Hz, 1H), 7.01 (**8′**, d, $J$ = 8.4 Hz, 2H), 6.97 (**3″**, d, $J$ = 6.3 Hz, 2H), 2.22 (**4″-Me**, s, 3H), 1.81 (**4-tBu**, s, 9H).

HRMS (ESI$^+$) m/z: $[M-2Cl]^{2+}$ Calcd for $C_{61}H_{44}N_{10}Ru$ 509.1391; Found 509.1389.

HPLC retention time: 25.23 min.

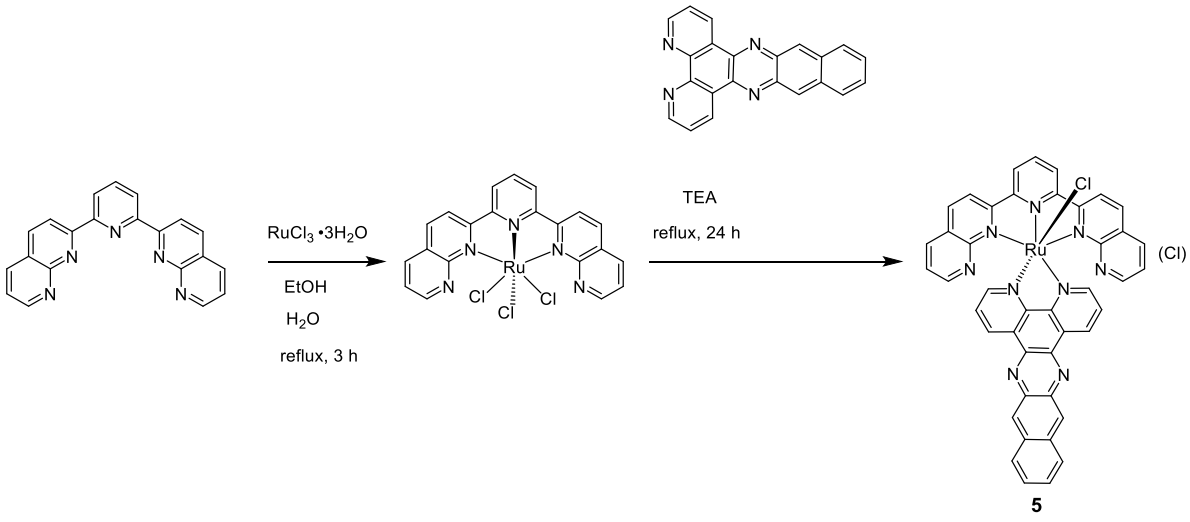


**Scheme S5.** Synthesis scheme for complex **5** [Ru(dnp)(dppn)(Cl)]Cl (conventional heating method).

**Complex 5:** [Ru(dnp)(dppn)(Cl)]Cl

Conventional heating method: A three-neck round-bottom flask, equipped with nitrogen purge and a condenser, was charged with dnp (0.100 g, 0.30 mmol) and EtOH (50 mL). Then, aqueous solution of $RuCl_3 \cdot 3H_2O$ was added (0.082 g, 0.32 mmol in 12 mL $H_2O$). The reaction mixture was well-stirred and refluxed for 3 h. Then, dppn (0.111 g, 0.33 mmol) and TEA (1 mL) were added and reaction mixture was refluxed for 24 h. The reaction mixture was concentrated under reduced pressure. The residue was treated with a few mL of $H_2O$ and the precipitate was isolated by filtration. The precipitate was washed with $H_2O$ and $Et_2O$ and dry-loaded on a column for purification. Column chromatography was performed on neutral alumina, using gradient elution: 1) $CH_2Cl_2$ 2) 50% $CH_2Cl_2$ : 50% acetone 3) acetone 4) 97% acetone : 3% MeOH 4) 95% acetone : 5% MeOH. The product fraction (plum-purple band) eluted last with 95% acetone : 5% MeOH. The product fraction was concentrated under reduced pressure and the residue was treated with a few mL of $Et_2O$. The precipitate was isolated by filtration, washed with $Et_2O$ and dried. [Ru(dnp)(dppn)(Cl)]Cl **5** was obtained as a dark-purple powder (0.080 g, 30% yield).

Microwave-assisted method: Reaction was performed in 2 batches, then combined for workup and purification. *Batch 1*: A microwave vial was filled with argon and EtOH (2.00 mL) and $H_2O$ (0.48 mL) were added. The solvent mixture was degassed with argon for 10 minutes, and then dnp (0.028 g, 0.084 mmol) and $RuCl_3 \cdot 3H_2O$ (0.023 g, 0.087 mmol) were added to the reaction vial. The vial was capped, and the reaction mixture was exposed to microwave irradiation at 100°C for 10 min and then at 120°C for 10 min. After that, dppn (0.030 g, 0.091 mmol) and TEA (20 drops) were added to the reaction mixture. The reaction mixture was exposed to microwave irradiation at 120°C for another 30 min. *Batch 2*: repeated procedure for batch 1. The reaction mixtures from batch 1 and

batch 2 were combined and concentrated under reduced pressure. The residue was treated with a few mL of $H_2O$ and the precipitate was isolated by filtration. The precipitate was washed with $H_2O$ and $Et_2O$ and dry-loaded on a gravity column for purification. Column chromatography was performed on neutral alumina, using gradient elution: 1) $CH_2Cl_2$ 2) 50% $CH_2Cl_2$ : 50% acetone 3) acetone 4) 98% acetone : 2% MeOH 5) 96.5% acetone : 3.5% MeOH. The product fraction (plum-purple band) eluted last with 96.5% acetone : 3.5% MeOH. The product fraction was concentrated under reduced pressure and the residue was treated with a few mL of $Et_2O$. The precipitate was isolated by filtration, washed with $Et_2O$ and dried. [Ru(dnp)(dppn)(Cl)]Cl **5** was obtained as a dark-purple powder (0.037 g, 26% yield).

$R_f$ = 0.57 (alumina; 8% $H_2O$ in acetonitrile).

$^1$H NMR (MeOD-$d_3$, 700 MHz): δ 10.74 (**d**, dd, $J_1$ = 4.9 Hz, $J_2$ = 1.4 Hz, 1H), 10.03 (**f**, dd, $J_1$ = 8.4 Hz, $J_2$ = 1.4 Hz, 1H), 9.15 (**c**, dd, $J_1$ = 7.7 Hz, $J_2$ = 0.7 Hz, 1H), 9.14 (**g**, s, 1H), 9.09 (**3**, d, $J$ = 8.4 Hz, 2H), 8.99 (**l**, s, 1H), 8.81 (**3′**, d, $J$ = 9.1 Hz, 2H), 8.54 (**4′**, d, $J$ = 8.4 Hz, 2H), 8.45 (**e**, dd, $J_1$ = 8.4 Hz, $J_2$ = 4.9 Hz, 1H), 8.38 (**4**, t, $J$ = 8.4 Hz, 1H), 8.29 (**h**,**k**, m, 2H), 8.27 (**5′**, dd, $J_1$ = 7.7 Hz, $J_2$ = 1.4 Hz, 2H), 8.01 (**7′**, dd, $J_1$ = 4.9 Hz, $J_2$ = 1.4 Hz, 2H), 7.87 (**a**, dd, $J_1$ = 5.6 Hz, $J_2$ = 0.7 Hz, 1H), 7.69 (**i**, **j**, m, 2H), 7.33 (**6′**, dd, $J_1$ = 7.7 Hz, $J_2$ = 4.9 Hz, 2H), 7.27 (**b**, dd, $J_1$ = 7.7 Hz, $J_2$ = 5.6 Hz, 1H).

HRMS (ESI$^+$) m/z: $[M\text{-}Cl]^+$ Calcd for $C_{43}H_{25}ClN_9Ru$ 804.0959; Found 804.0955.

HPLC retention time: 26.09 min.

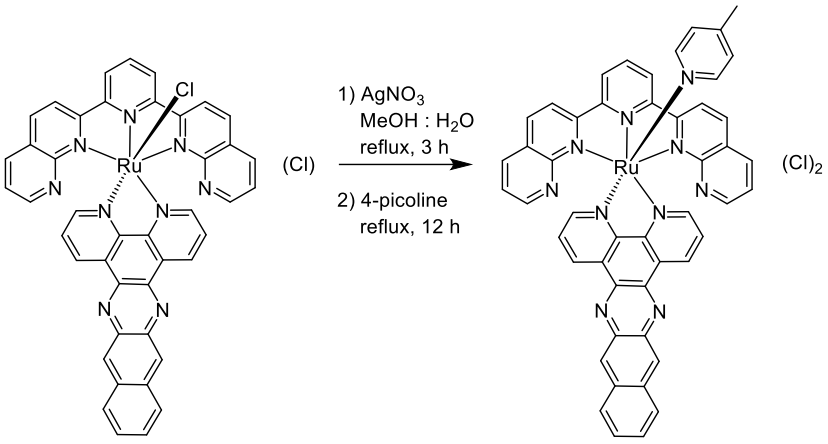


**5** **6**

**Scheme S6.** Synthesis scheme for complex **6** [Ru(dnp)(dppn)(4-pic)]$Cl_2$ (conventional heating method).

**Complex 6:** [Ru(dnp)(dppn)(4-pic)]$Cl_2$

Conventional heating method: A round-bottom flask, equipped with condenser, was charged with [Ru(dnp)(dppn)(Cl)]Cl **5** (0.040 g, 0.05 mmol) and MeOH (6 mL). Then, an aqueous solution of $AgNO_3$ (0.081 g, 0.48 mmol in 1.5 mL $H_2O$) was added dropwise. The reaction mixture was well-stirred and refluxed for 3 h. Then, 4-picoline (1.5 mL, 15.21 mmol) was added and the reaction mixture was refluxed for 12 h, then concentrated under reduced pressure. The residue was treated with a few mL of $H_2O$ and the precipitate was isolated by filtration. The precipitate was washed with $H_2O$ and $Et_2O$ and dry-loaded on a column for purification. Column chromatography was performed on neutral alumina, using gradient elution: 1) $CH_2Cl_2$ 2) 50% $CH_2Cl_2$ : 50% acetone 3) acetone 4) 95% acetone : 5% MeOH. The product fraction (red band) eluted last with 95% acetone : 5% MeOH. The product fraction was concentrated under reduced pressure and the residue was treated with a few mL of $Et_2O$. The precipitate was isolated by filtration, washed with $Et_2O$ and dried. [Ru(dnp)(dppn)(4-pic)]$Cl_2$ **6** was obtained as a maroon powder (0.035 g, 78% yield).

Microwave-assisted method: A microwave vial was charged with [Ru(dnp)(dppn)(Cl)]Cl **5** (0.037 g, 0.04 mmol), 4-picoline (0.4 mL, 4.12 mmol) and MeOH (2.8 mL). The vial was capped, and the reaction mixture was exposed to microwave irradiation at 150°C for 12 min. After that, $H_2O$ (0.8 mL) was added and the reaction mixture was exposed to microwave irradiation at 160°C for another 15 min. The reaction mixture was concentrated under reduced pressure and dried under high vacuum. The precipitate was purified with flash chromatography on alumina (eluent: gradient elution from 100% acetonitrile to 92% acetonitrile : 8% $H_2O$). The product fraction (maroon band, elutes with 92% acetonitrile : 8% $H_2O$) was concentrated under reduced pressure and further purified using size-exclusion chromatography on Sephadex LH-20 (eluent: MeOH). The main band (maroon) was collected and concentrated under reduced pressure. The residue was treated with a few mL of $Et_2O$, sonicated, and isolated by filtration. The precipitate was thoroughly washed with $Et_2O$ and dried. [Ru(dnp)(dppn)(4-pic)]$Cl_2$ **6** was obtained as a purple powder (0.021 g, 51% yield).

$R_f$ = 0.43 (alumina; 8% $H_2O$ in acetonitrile).

$^1$H NMR (MeOD-$d_3$, 500 MHz): δ 10.10 (**f**, dd, $J_1$ = 8.0 Hz, $J_2$ = 1.0 Hz, 1H), 9.50 (**d**, dd, $J_1$ = 5.5 Hz, $J_2$ = 1.5 Hz, 1H), 9.32 (**c**, dd, $J_1$ = 8.0 Hz, $J_2$ = 1.0 Hz, 1H), 9.19 (**g**, s, 1H), 9.18 (**3**, d, $J$ = 8.5 Hz, 2H), 9.02 (**l**, s, 1H), 8.91 (**3′**, d, $J$ = 8.5 Hz, 2H), 8.73 (**4′**, d, $J$ = 8.5 Hz, 2H), 8.51 (**4**, t, $J$ = 8.5 Hz, 1H), 8.44 (**e**, dd, $J_1$ = 8.5 Hz, $J_2$ = 5.5 Hz, 1H), 8.38 (**5′**, dd, $J_1$ = 8.5 Hz, $J_2$ = 2.0 Hz, 2H), 8.36 (**h**/**k**, d, $J$ = 8.0 Hz, 1H), 8.29 (**h**/**k**, d, $J$ = 8.0 Hz, 1H), 8.15 (**7′**, dd, $J_1$ = 4.5 Hz, $J_2$ = 2.0 Hz, 2H), 7.81 (**a**, dd, $J_1$ = 5.5 Hz, $J_2$ = 1.0 Hz, 1H), 7.72 (**i**, **j**, m, 2H), 7.65 (**2″**, d, $J$ = 6.5 Hz, 2H), 7.44 (**b**, dd, $J_1$ = 8.0 Hz, $J_2$ = 5.5 Hz, 1H), 7.44 (**6′**, dd, $J_1$ = 8.0 Hz, $J_2$ = 4.0 Hz, 2H), 7.00 (**3″**, d, $J$ = 6.0 Hz, 2H), 2.25 (**4″-Me**, s, 3H).

HRMS (ESI$^+$) m/z: $[M-2Cl]^{2+}$ Calcd for $C_{49}H_{32}N_{10}Ru$ 431.0922; Found 431.0913.

HPLC retention time: 22.91 min.

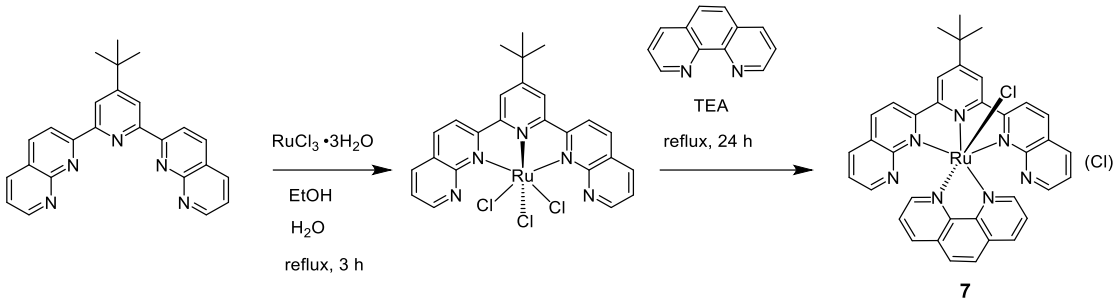


**Scheme S7.** Synthesis scheme for complex **7** [Ru(tpbn)(phen)(Cl)]Cl (conventional heating method).

**Complex 7:** [Ru(tpbn)(phen)(Cl)]Cl

Conventional heating method: A three-neck round-bottom flask, equipped with nitrogen purge and a condenser, was charged with tpbn (0.100 g, 0.26 mmol) and EtOH (50 mL). Then, an aqueous solution of $RuCl_3 \bullet 3H_2O$ was added (0.070 g, 0.27 mmol in 12 mL $H_2O$). The reaction mixture was well-stirred and refluxed for 3 h. Then, 1,10-phenanthroline (0.051 g, 0.28 mmol) and TEA (1 mL) were added and the reaction mixture was refluxed for 24 h, then concentrated under reduced pressure. The residue was treated with a few mL of $H_2O$ and the precipitate was isolated by filtration. The precipitate was washed with $H_2O$ and $Et_2O$ and dry-loaded on a column for purification. Column chromatography was performed on neutral alumina, using gradient elution: 1) $CH_2Cl_2$ 2) 50% $CH_2Cl_2$ : 50% acetone 3) acetone 4) 97% acetone : 3% MeOH. Product fraction (deep-purple band) eluted last with 97% acetone : 3% MeOH. The product fraction was concentrated under reduced pressure and the residue was treated with a few mL of $Et_2O$. The precipitate was isolated by filtration, washed with $Et_2O$ and dried. [Ru(tpbn)(phen)(Cl)]Cl **7** was obtained as a dark-purple powder (0.095 g, 48% yield).

Although it was not tested, it is highly likely that synthesis of **7** could also be performed using microwave-assisted heating using much shorter reaction times than conventional heating.

$R_f$ = 0.57 (alumina; 8% $H_2O$ in acetonitrile).

$^1$H NMR (MeOD-$d_3$, 500 MHz): δ 10.62 (**d**, dd, $J_1$ = 5.5 Hz, $J_2$ = 1.5 Hz, 1H), 9.08 (**3**, s, 2H), 8.90 (**3′**, d, $J$ = 8.5 Hz, 2H), 8.89 (**f**, dd, $J_1$ = 8.0 Hz, $J_2$ = 1.5 Hz, 1H), 8.49 (**4′**, d, $J$ = 8.5 Hz, 2H), 8.33 (**g**, d, $J$ = 9.0 Hz, 1H), 8.29 (**e**, dd, $J_1$ = 8.0 Hz, $J_2$ = 5.5 Hz, 1H), 8.23 (**5′**, dd, $J_1$ = 8.0 Hz, $J_2$ = 2.0 Hz, 2H), 8.07 (**c**, dd, $J_1$ = 8.0 Hz, $J_2$ = 1.0 Hz, 1H), 7.90 (**h**, d, $J$ = 9.0 Hz, 1H), 7.75 (**7′**, dd, $J_1$ = 4.5 Hz, $J_2$ = 2.0 Hz, 2H), 7.73 (**a**, dd, $J_1$ = 5.5 Hz, $J_2$ = 1.0 Hz, 1H), 7.31 (**6′**, dd, $J_1$ = 8.0 Hz, $J_2$ = 4.0 Hz, 2H), 7.15 (**b**, dd, $J_1$ = 8.0 Hz, $J_2$ = 5.5 Hz, 1H), 1.78 (**4-tBu**, s, 9H).

HRMS (ESI$^+$) m/z: [M-Cl]$^+$ Calcd for $C_{37}H_{29}ClN_7Ru$ 708.1211; Found 708.1201.

HPLC retention time: 22.74 min.

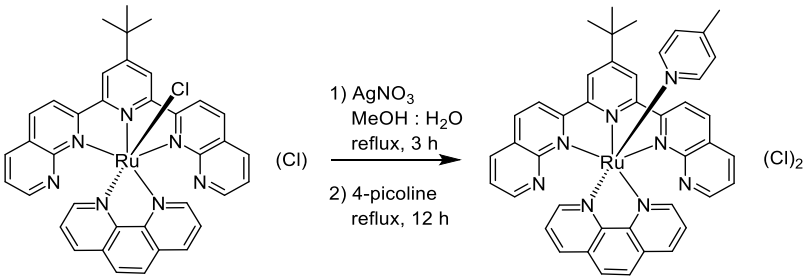


**7** **8**

**Scheme S8.** Synthesis scheme for complex **8** [Ru(tpbn)(phen)(4-pic)]$Cl_2$ (conventional heating method).

**Complex 8:** [Ru(tpbn)(phen)(4-pic)]$Cl_2$

Conventional heating method: A round-bottom flask, equipped with a condenser, was charged with [Ru(tpbn)(phen)(Cl)]Cl **7** (0.080 g, 0.11 mmol) and MeOH (7 mL). Then, an aqueous solution of $AgNO_3$ (0.190 g, 1.10 mmol in 2 mL $H_2O$) was added dropwise. The

reaction mixture was well-stirred and refluxed for 3 h. Then, 4-picoline (1.5 mL, 15.21 mmol) was added and the reaction mixture was refluxed for 12 h, then concentrated under reduced pressure. The residue was treated with a few mL of $H_2O$ and the precipitate was isolated by filtration. The precipitate was washed with $H_2O$ and $Et_2O$ and dry-loaded on a column for purification. Column chromatography was performed on neutral alumina, using gradient elution: 1) $CH_2Cl_2$ 2) 50% $CH_2Cl_2$ : 50% acetone 3) acetone 4) 95% acetone : 5% MeOH. The product fraction (deep-purple band) eluted last with 95% acetone : 5% MeOH. The product fraction was concentrated under reduced pressure and the residue was treated with a few mL of $Et_2O$. The precipitate was isolated by filtration, washed with $Et_2O$ and dried. [Ru(tpbn)(phen)(4-pic)]$Cl_2$ **8** was obtained as a dark-purple powder (0.070 g, 79% yield).

Microwave-assisted method: A microwave vial was charged with [Ru(tpbn)(phen)(Cl)]Cl **7** (0.044 g, 0.06 mmol), 4-picoline (0.4 mL, 4.12 mmol) and MeOH (2.8 mL). The vial was capped, and the reaction mixture was exposed to microwave irradiation at 150°C for 12 min. After that, $H_2O$ (0.8 mL) was added and the reaction mixture was exposed to microwave irradiation at 150°C for 12 min and then at 155°C for another 12 min. The reaction mixture was concentrated under reduced pressure and dried under high vacuum. The precipitate was purified with flash chromatography on alumina (eluent: gradient elution from 100% acetonitrile to 92% acetonitrile : 8% $H_2O$). The product fraction (deep-purple band, elutes with 92% acetonitrile : 8% $H_2O$) was concentrated under reduced pressure and further purified using size-exclusion chromatography on Sephadex LH-20 (eluent: MeOH). The main band (purple) was collected and concentrated under reduced pressure. The residue was treated with a few mL of $Et_2O$, sonicated, and isolated by filtration. The precipitate was thoroughly washed with $Et_2O$ and dried. [Ru(tpbn)(phen)(4-pic)]$Cl_2$ **8** was obtained as a dark-purple powder (0.034 g,

69% yield).

$R_f$ = 0.45 (alumina; 8% $H_2O$ in acetonitrile).

$^1$H NMR (MeOD-$d_3$, 500 MHz): δ 9.44 (**d**, dd, $J_1$ = 5.5 Hz, $J_2$ = 1.5 Hz, 1H), 9.14 (**3**, s, 2H), 9.01 (**3′**, d, $J$ = 8.5 Hz, 2H), 8.94 (**f**, dd, $J_1$ = 8.5 Hz, $J_2$ = 1.5 Hz, 1H), 8.68 (**4′**, d, $J$ = 8.5 Hz, 2H), 8.35 (**5′**, dd, $J_1$ = 8.5 Hz, $J_2$ = 2.0 Hz, 2H), 8.32 (**g**, d, $J$ = 9.0 Hz, 1H), 8.29 (**e**, dd, $J_1$ = 8.5 Hz, $J_2$ = 5.5 Hz, 1H), 8.19 (**c**, dd, $J_1$ = 8.5 Hz, $J_2$ = 1.5 Hz, 1H), 7.92 (**h**, d, $J$ = 9.0 Hz, 1H), 7.92 (**7′**, dd, $J_1$ = 4.5 Hz, $J_2$ = 2.0 Hz, 2H), 7.67 (**a**, dd, $J_1$ = 5.5 Hz, $J_2$ = 1.0 Hz, 1H), 7.66 (**2″**, d, $J$ = 6.5 Hz, 2H), 7.42 (**6′**, dd, $J_1$ = 8.0 Hz, $J_2$ = 4.5 Hz, 2H), 7.29 (**b**, dd, $J_1$ = 8.0 Hz, $J_2$ = 5.5 Hz, 1H), 6.97 (**3″**, d, $J$ = 6.5 Hz, 2H), 2.23 (**4″-Me**, s, 3H), 1.76 (**4-tBu**, s, 9H).

HRMS (ESI$^+$) m/z: [M-2Cl]$^{2+}$ Calcd for $C_{43}H_{36}N_8Ru$ 383.1047; Found 383.1041.

HPLC retention time: 18.39 min.

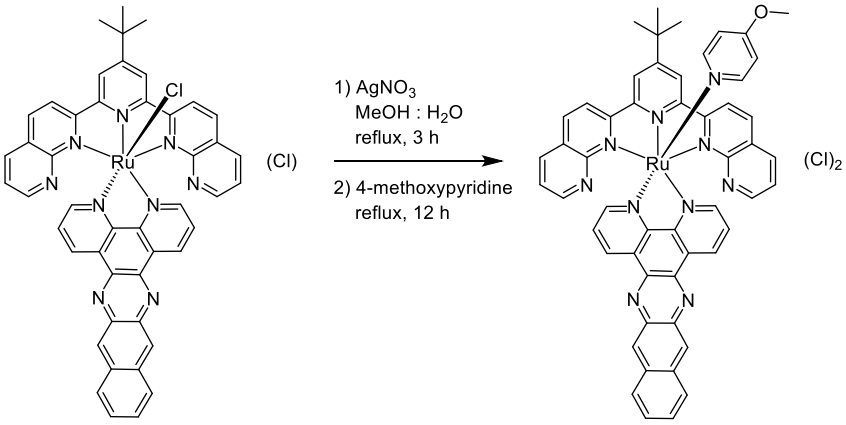


**1** **9**

**Scheme S9.** Synthesis scheme for complex **9** [Ru(tpbn)(dppn)(4-mp)]$Cl_2$ (conventional heating method).

**Complex 9:** [Ru(tpbn)(dppn)(4-mp)]$Cl_2$

Conventional heating method: A round-bottom flask, equipped with condenser, was

charged with [Ru(tpbn)(dppn)(Cl)]Cl **1** (0.050 g, 0.06 mmol) and MeOH (4 mL). Then, an aqueous solution of $AgNO_3$ (0.095 g, 0.56 mmol in 1 mL $H_2O$) was added dropwise. The reaction mixture was well-stirred and refluxed for 3 h. Then, 4-methoxypyridine (0.5 mL, 4.9 mmol) was added and reaction mixture was refluxed for 12 h, then concentrated under reduced pressure. The residue was treated with a few mL of $H_2O$ and the precipitate was isolated by filtration. The precipitate was washed with $H_2O$ and $Et_2O$ and dry-loaded on a column for purification. Column chromatography was performed on neutral alumina, using gradient elution: 1) $CH_2Cl_2$ 2) 50% $CH_2Cl_2$ : 50% acetone 3) acetone 4) 95% acetone : 5% MeOH. The product fraction (maroon band) eluted last with 95% acetone : 5% MeOH. The product fraction was concentrated under reduced pressure and the residue was treated with a few mL of $Et_2O$. The precipitate was isolated by filtration, washed with $Et_2O$ and dried. [Ru(tpbn)(dppn)(4-mp)]$Cl_2$ **9** was obtained as a maroon powder (0.016 g, 29% yield).

Microwave-assisted method: The reaction was performed in 2 batches, then combined for workup and purification. *Batch 1*: A microwave vial was charged with [Ru(tpbn)(dppn)(Cl)]Cl **1** (0.020 g, 0.02 mmol), 4-methoxypyridine (0.25 mL, 2.47 mmol) and MeOH (2.0 mL). The vial was capped, and the reaction mixture was exposed to microwave irradiation at 150°C for 12 min. After that, $H_2O$ (0.4 mL) was added and the reaction mixture was exposed to microwave irradiation at 160°C for 12 min. *Batch 2*: repeated the procedure for batch 1. The reaction mixtures from batches 1 and 2 were combined, concentrated under reduced pressure and dried under high vacuum. The residue was treated with a few mL of $Et_2O$, sonicated, and isolated by filtration. The precipitate was thoroughly washed with $Et_2O$ and dried. The precipitate was purified with flash chromatography on alumina (eluent: gradient elution from 100% acetonitrile to 92% acetonitrile : 8% $H_2O$). The product fraction (maroon band, elutes with 92% acetonitrile :

8% $H_2O$) was concentrated under reduced pressure and further purified using size-exclusion chromatography on Sephadex LH-20 (eluent: MeOH). The main band (maroon) was collected and concentrated under reduced pressure. The residue was treated with a few mL of $Et_2O$, sonicated, and isolated by filtration. The precipitate was thoroughly washed with $Et_2O$ and dried. [Ru(tpbn)(dppn)(4-mp)]$Cl_2$ **9** was obtained as a maroon powder (0.029 g, 66% yield).

$R_f$ = 0.54 (alumina; 8% $H_2O$ in acetonitrile).

$^1$H NMR (MeOD-$d_3$, 500 MHz): δ 10.08 (**f**, dd, $J_1$ = 8.0 Hz, $J_2$ = 1.0 Hz, 1H), 9.49 (**d**, dd, $J_1$ = 5.0 Hz, $J_2$ = 1.0 Hz, 1H), 9.28 (**c**, dd, $J_1$ = 8.5 Hz, $J_2$ = 2.0 Hz, 1H), 9.18 (**3**, s, 2H), 9.17 (**g**, s, 1H), 9.06 (**3′**, d, $J$ = 8.5 Hz, 2H), 9.01 (**l**, s, 1H), 8.73 (**4′**, d, $J$ = 8.5 Hz, 2H), 8.44 (**e**, dd, $J_1$ = 8.0 Hz, $J_2$ = 5.5 Hz, 1H), 8.37 (**5′**, dd, $J_1$ = 8.0 Hz, $J_2$ = 2.0 Hz, 2H), 8.32 (**h**/**k**, d, $J$ = 7.5 Hz, 1H), 8.28 (**h**/**k**, d, $J$ = 8.0 Hz, 1H), 8.14 (**7′**, dd, $J_1$ = 4.0 Hz, $J_2$ = 1.5 Hz, 2H), 7.79 (**a**, dd, $J_1$ = 6.0 Hz, $J_2$ = 1.5 Hz, 1H), 7.71 (**i**, **j**, m, 2H), 7.56 (**2″**, d, $J$ = 7.5 Hz, 2H), 7.43 (**6′**, **b**, m, 3H), 6.73 (**3″**, d, $J$ = 7.0 Hz, 2H), 3.75 (**4″-OMe**, s, 3H), 1.78 (**4-tBu**, s, 9H).

HRMS (ESI$^+$) m/z: $[M-2Cl]^{2+}$ Calcd for $C_{53}H_{40}N_{10}ORu$ 467.1209; Found 467.1199.

HPLC retention time: 23.58 min.

## 3. NMR SPECTRA OF RU(II) COMPLEXES 1–9

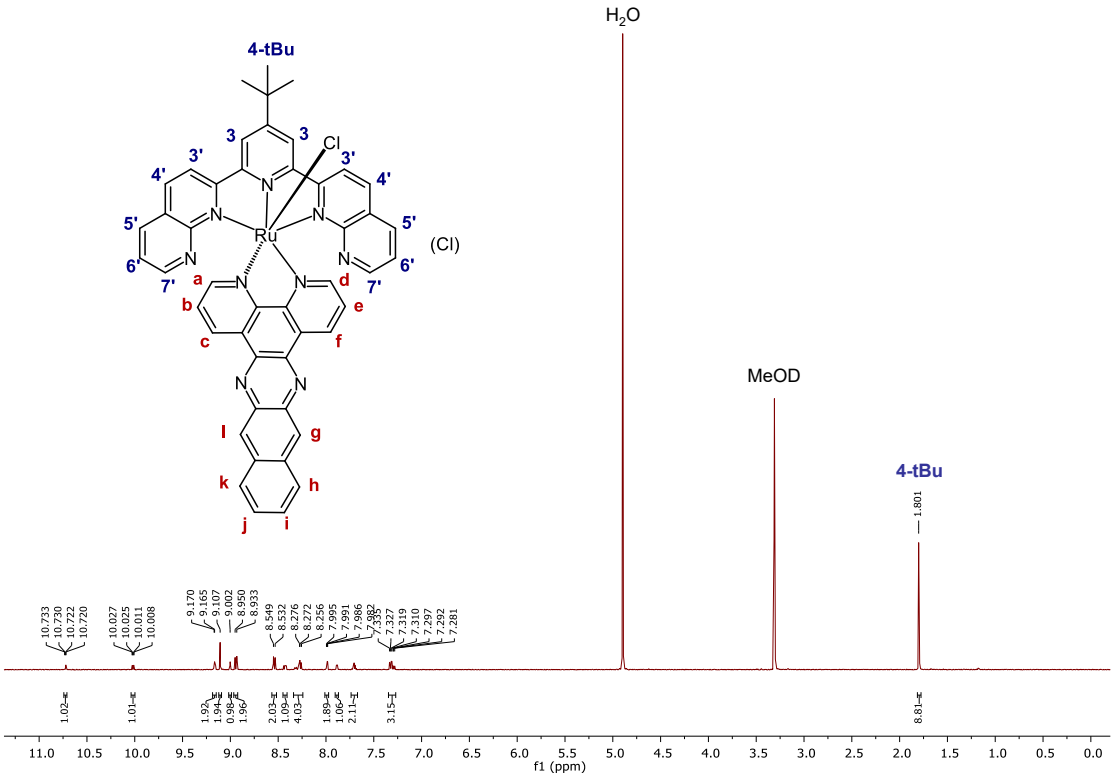


**Appendix Figure S1.** 500 MHz $^{1}$H NMR spectrum of **1** in MeOD-$d_3$ at 298 K.

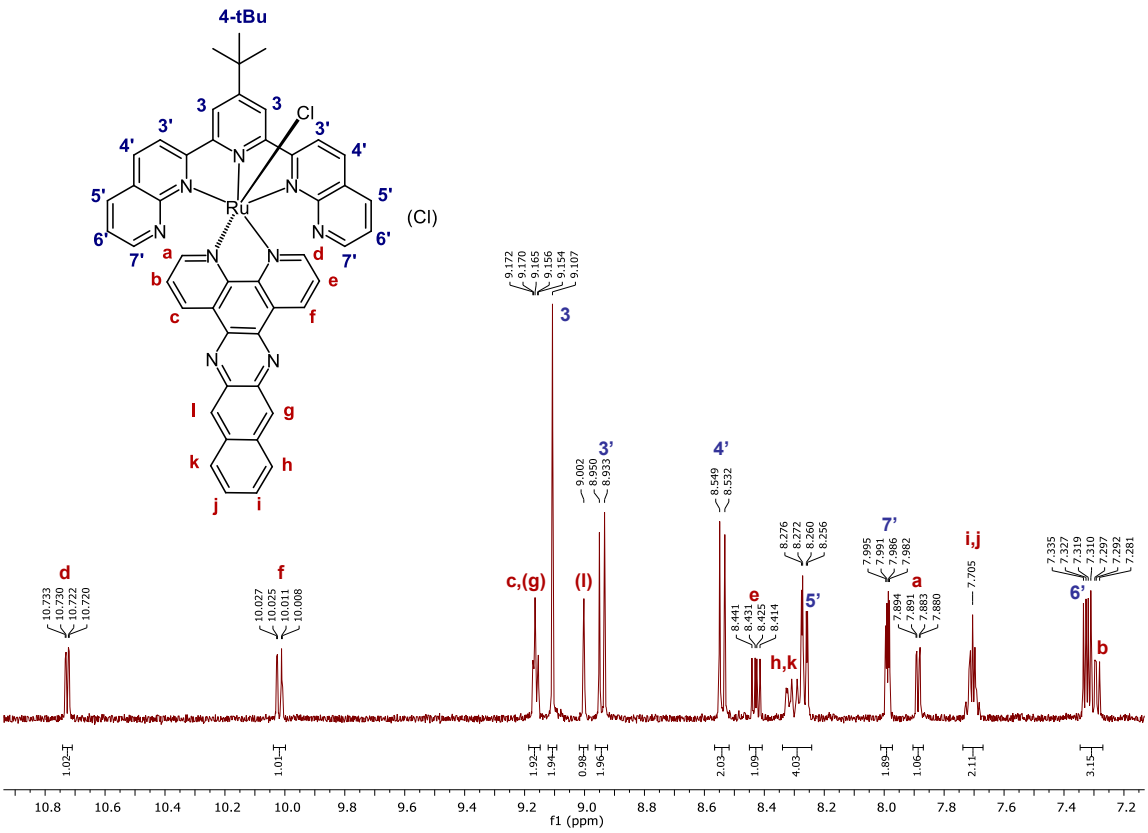


**Appendix Figure S2.** 500 MHz $^{1}$H NMR spectrum of **1** in MeOD-$d_3$ at 298 K, aromatic region.

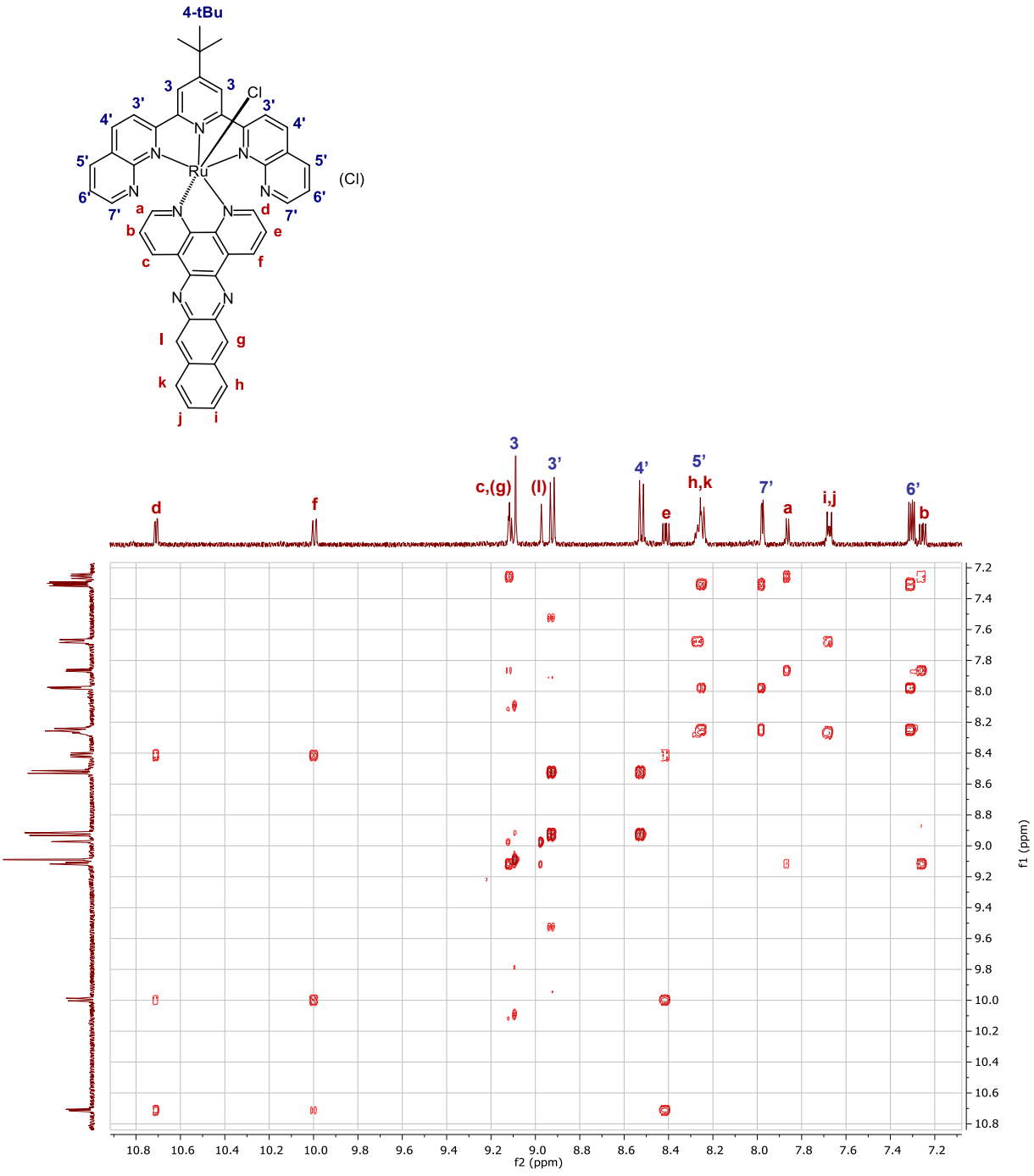


**Appendix Figure S3.** 500 MHz $^{1}$H–$^{1}$H COSY NMR spectrum of **1** in MeOD-$d_3$ at 298 K, aromatic region.

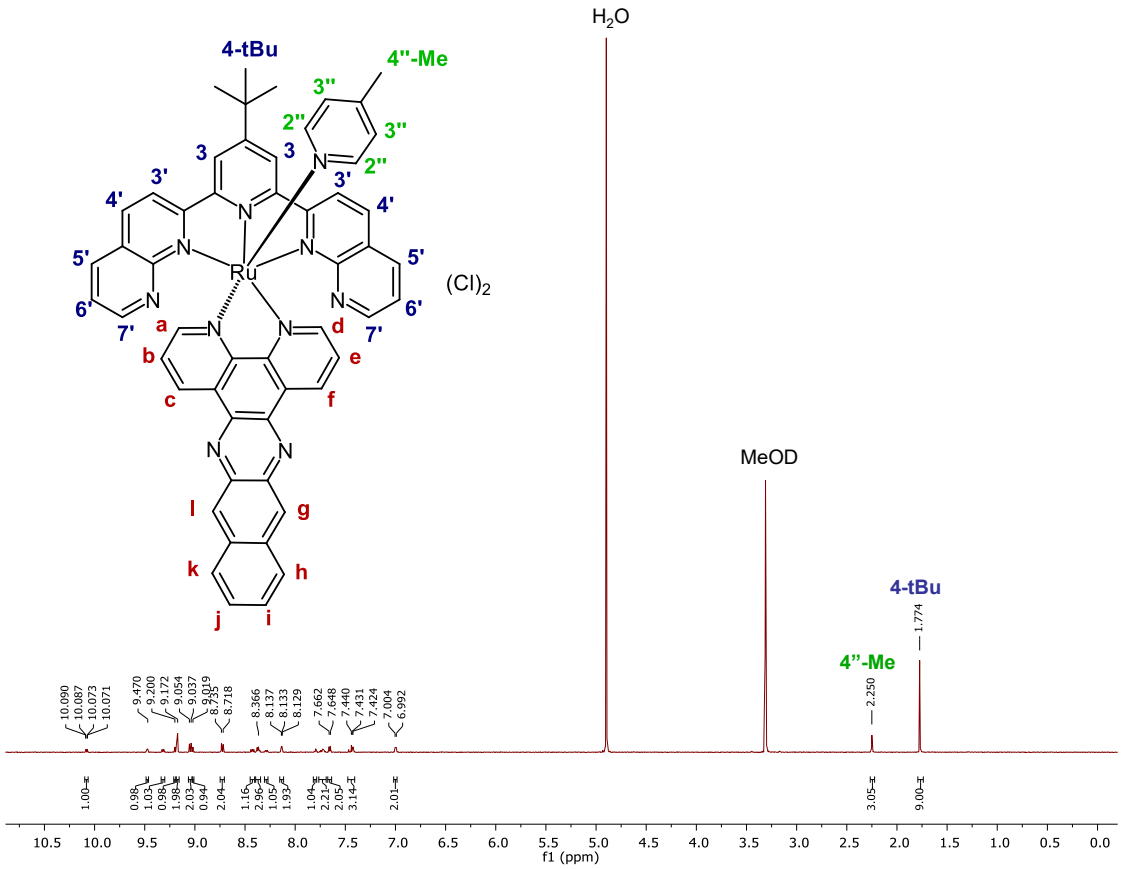


**Appendix Figure S4.** 500 MHz $^{1}$H NMR spectrum of **2** in MeOD-$d_3$ at 298 K.

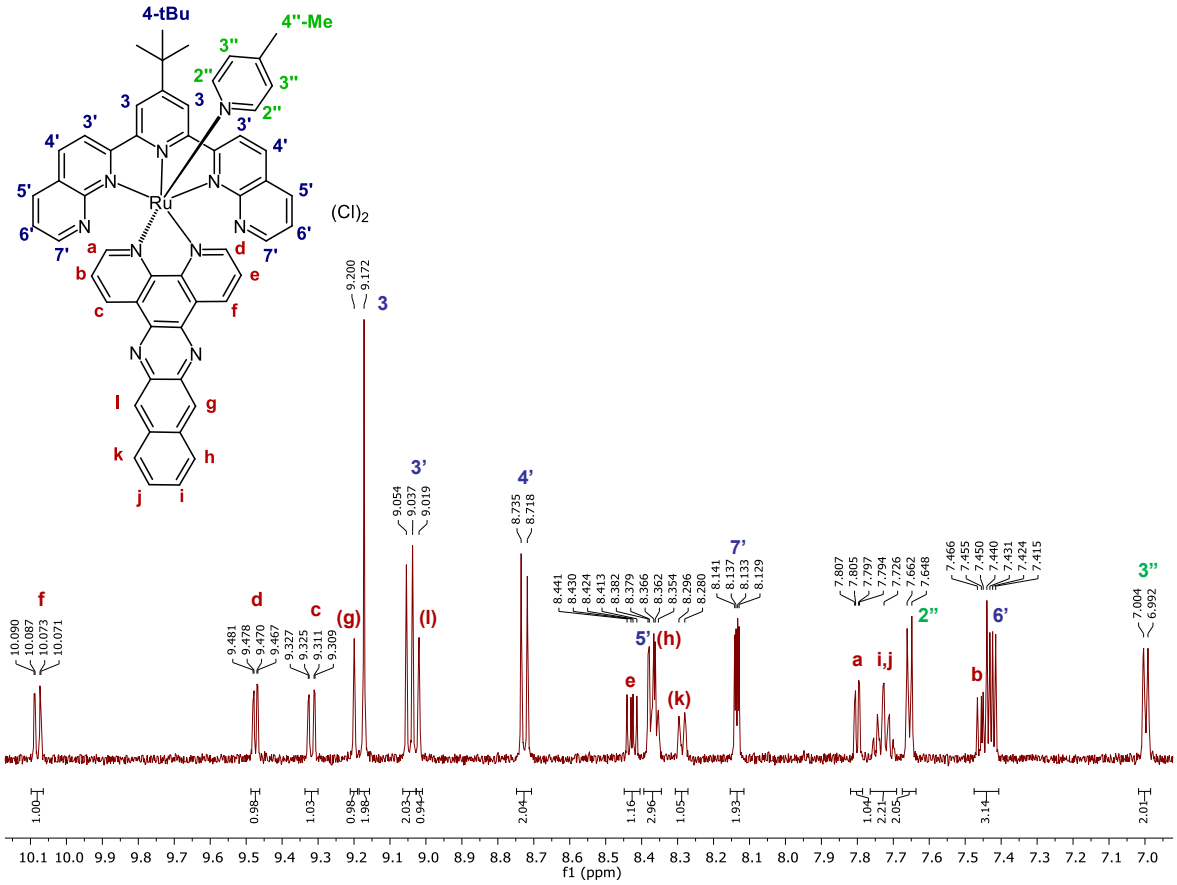


**Appendix Figure S5.** 500 MHz $^{1}$H NMR spectrum of **2** in MeOD-$d_3$ at 298 K, aromatic region.

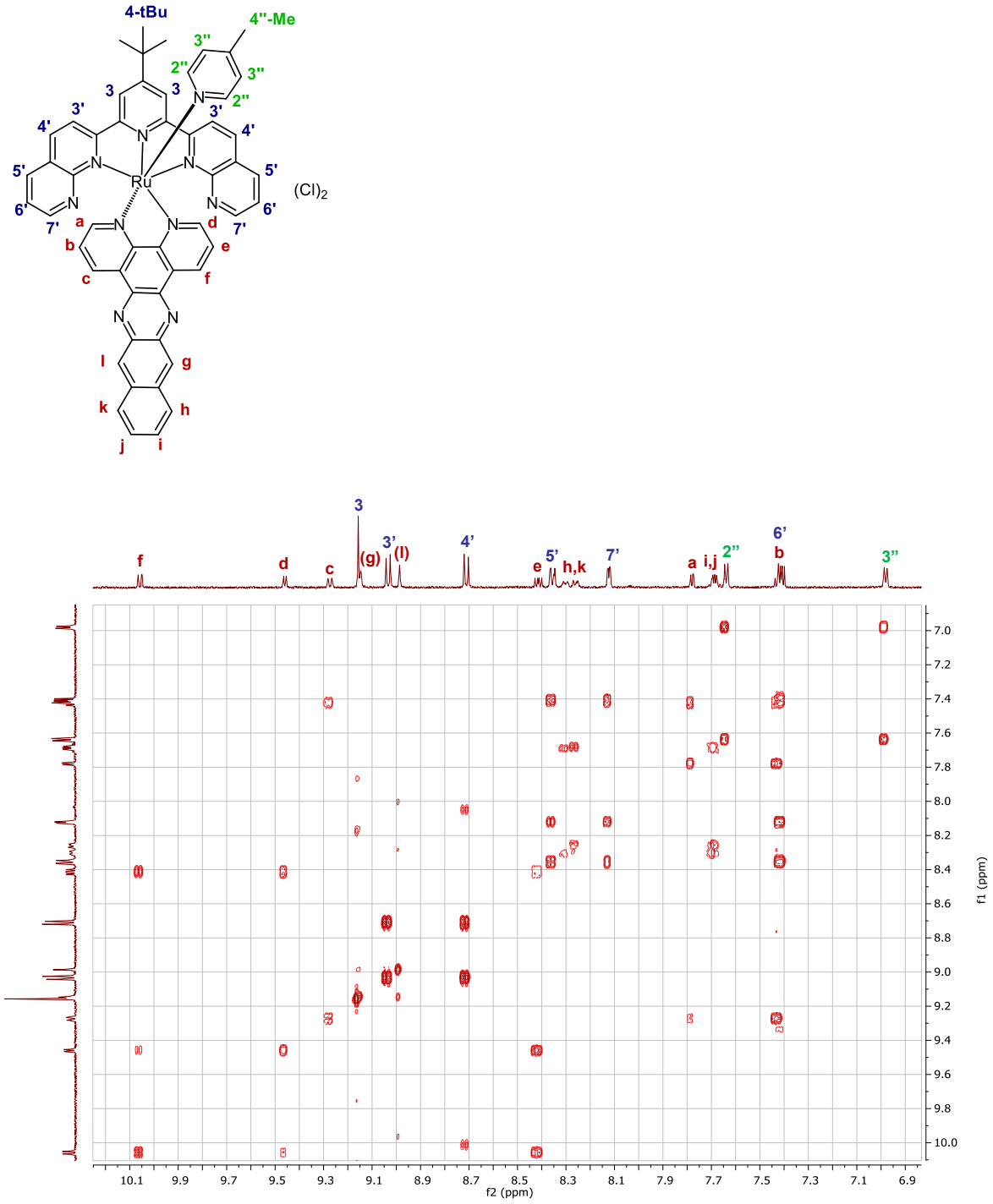


**Appendix Figure S6.** 500 MHz $^{1}$H–$^{1}$H COSY NMR spectrum of **2** in MeOD-$d_3$ at 298 K, aromatic region.

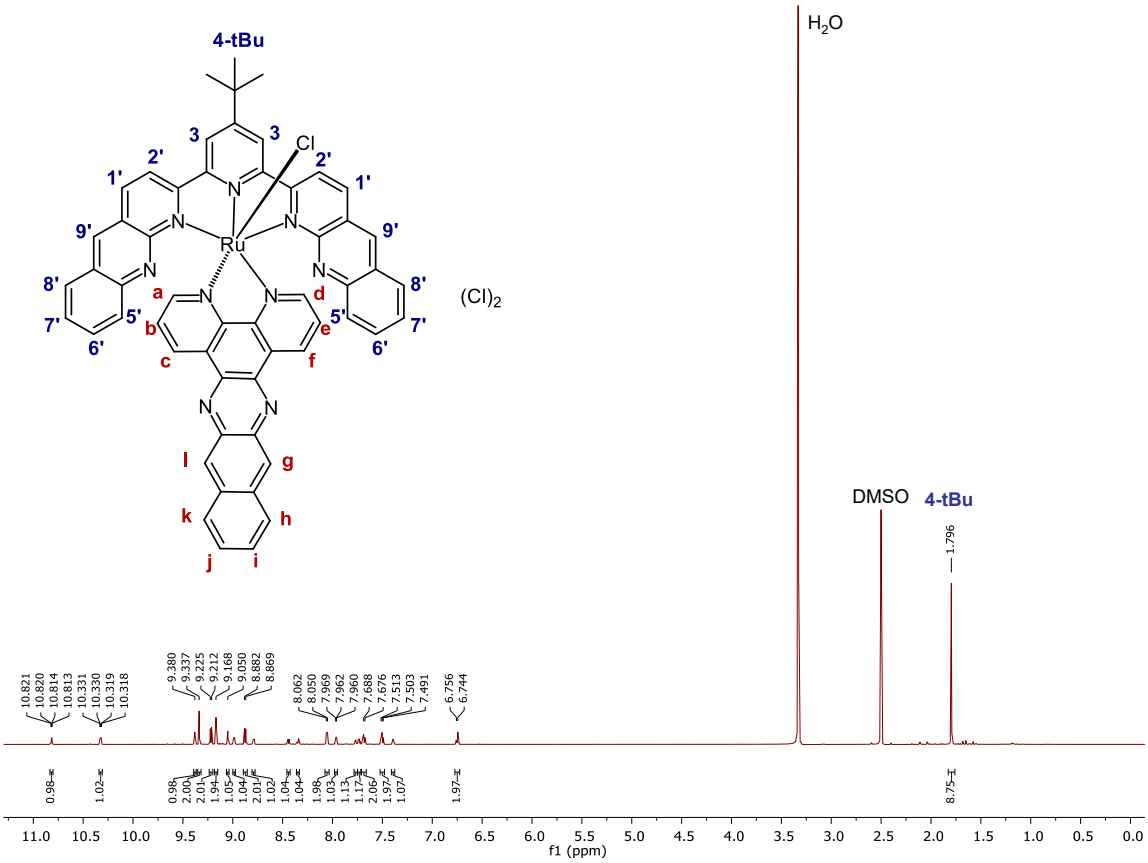


**Appendix Figure S7.** 700 MHz $^{1}$H NMR spectrum of **3** in DMSO-$d_6$ at 298 K.

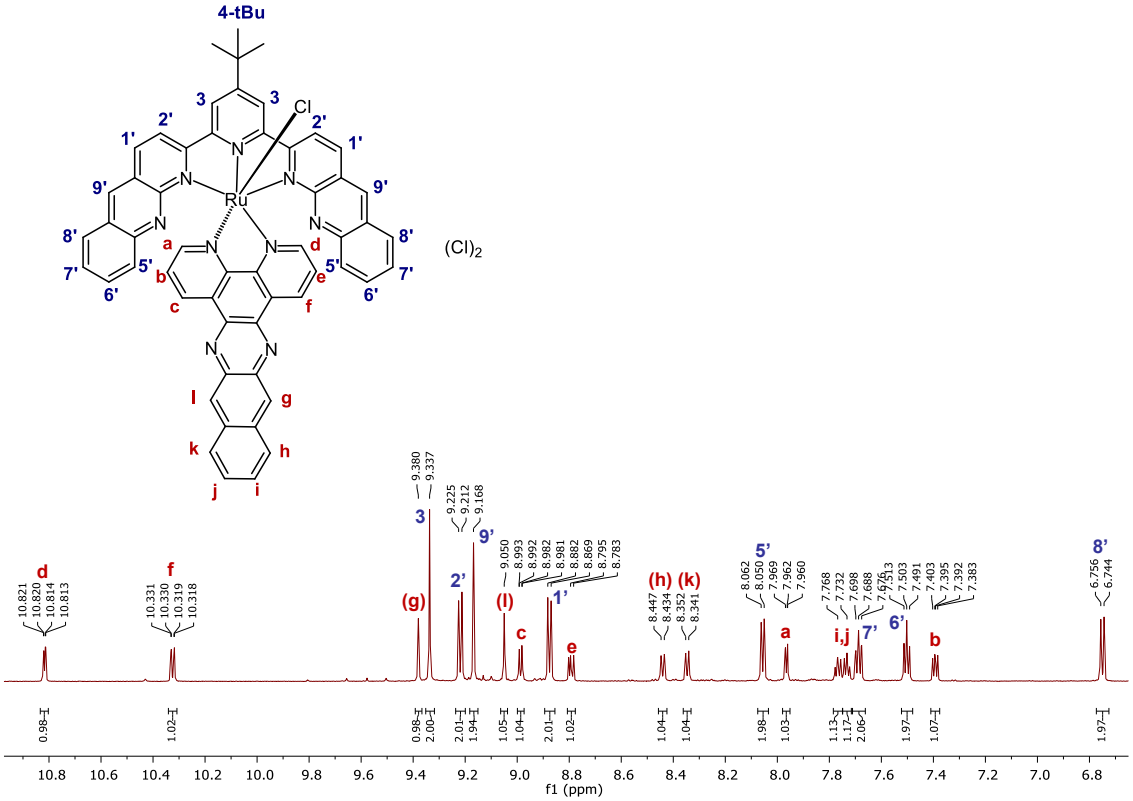


**Appendix Figure S8.** 700 MHz $^{1}$H NMR spectrum of **3** in DMSO-$d_6$ at 298 K, aromatic region.

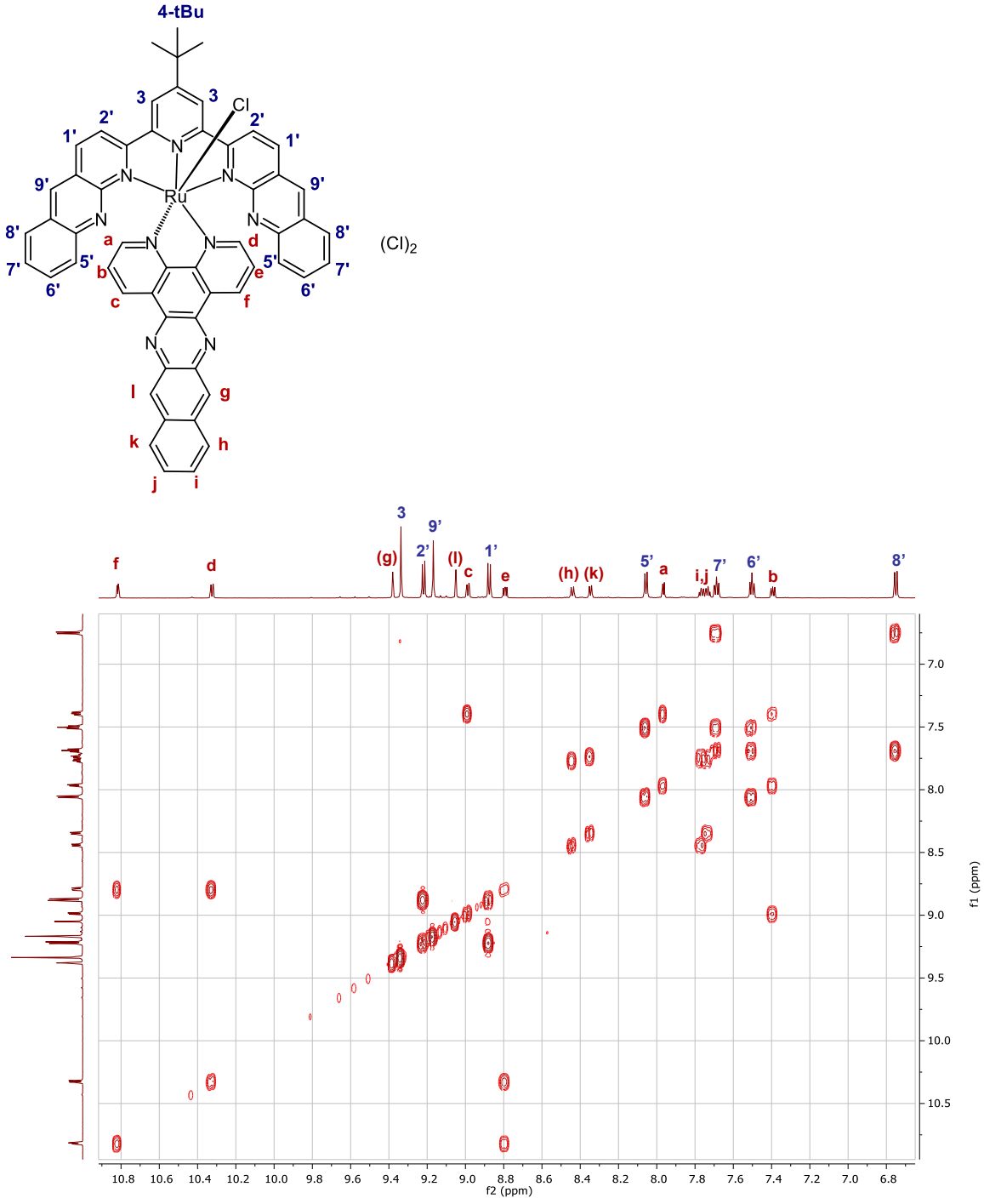


**Appendix Figure S9.** 700 MHz $^{1}$H–$^{1}$H COSY NMR spectrum of **3** in DMSO-$d_6$ at 298 K, aromatic region.

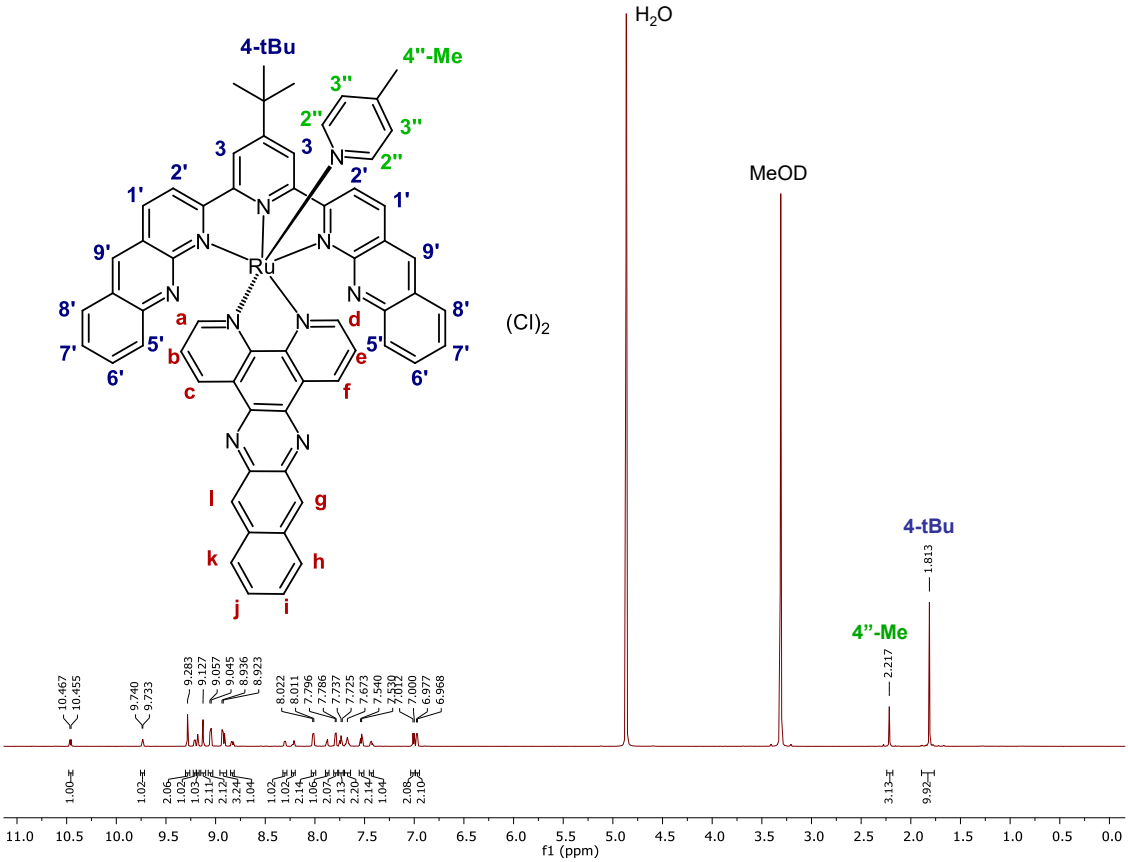


**Appendix Figure S10.** 700 MHz $^{1}$H NMR spectrum of **4** in MeOD-$d_3$ at 298 K.

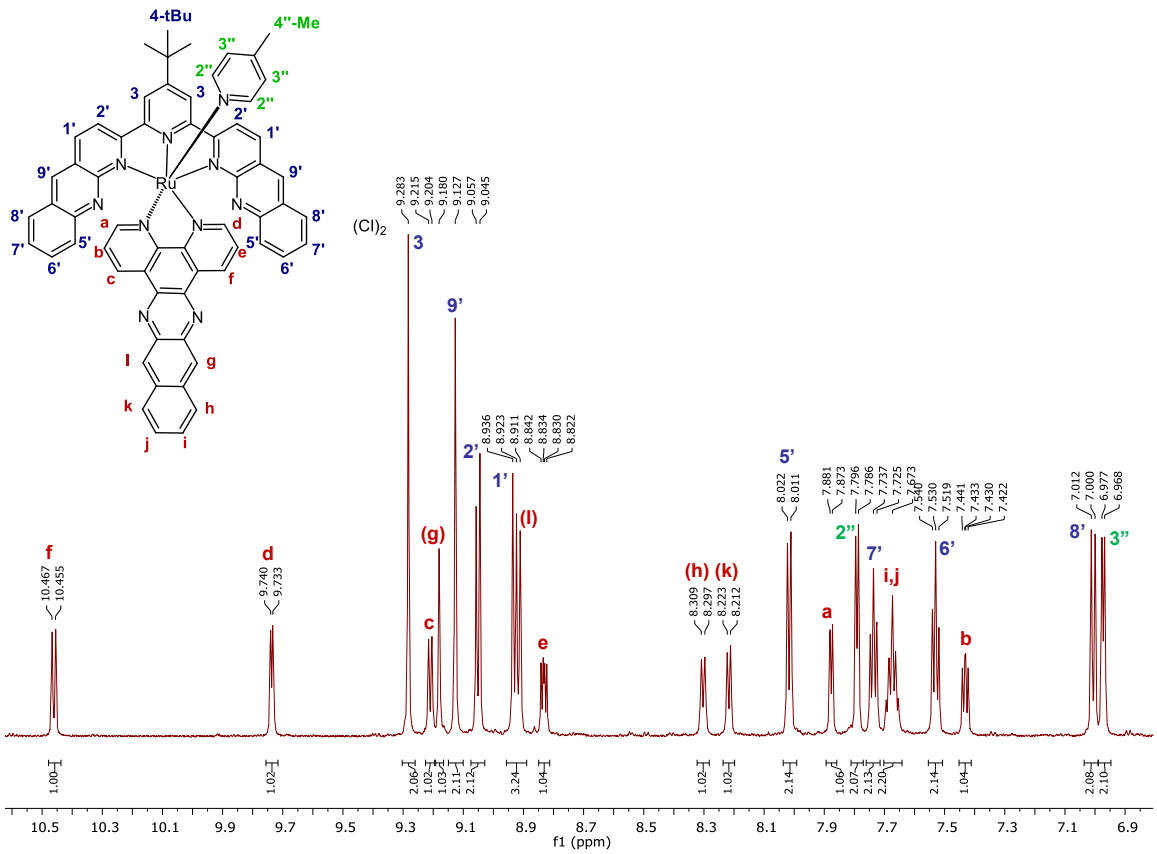


**Appendix Figure S11.** 700 MHz $^{1}$H NMR spectrum of **4** in MeOD-$d_3$ at 298 K, aromatic region.

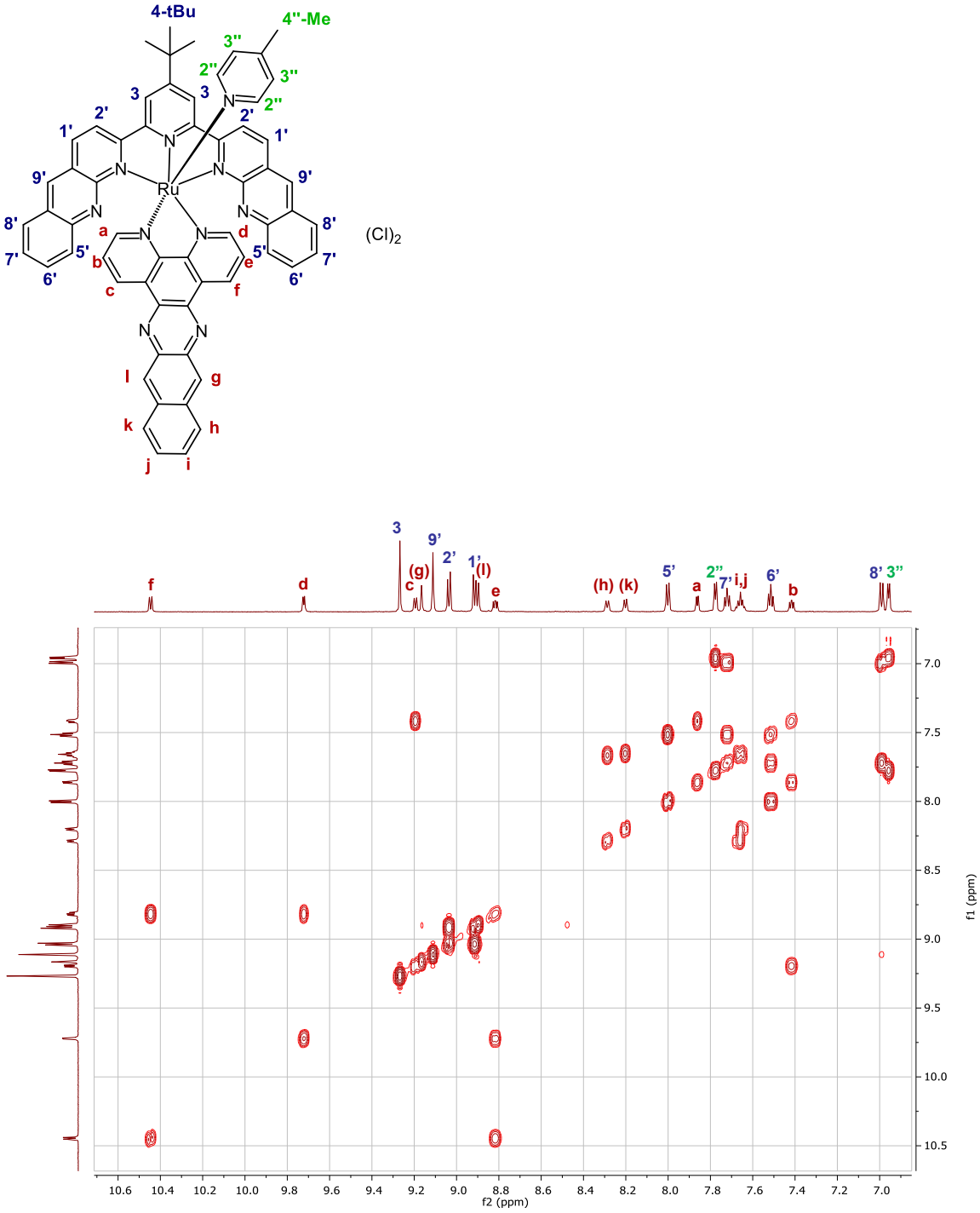


**Appendix Figure S121.** 700 MHz $^{1}$H–$^{1}$H COSY NMR spectrum of **4** in MeOD-$d_3$ at 298 K, aromatic region.

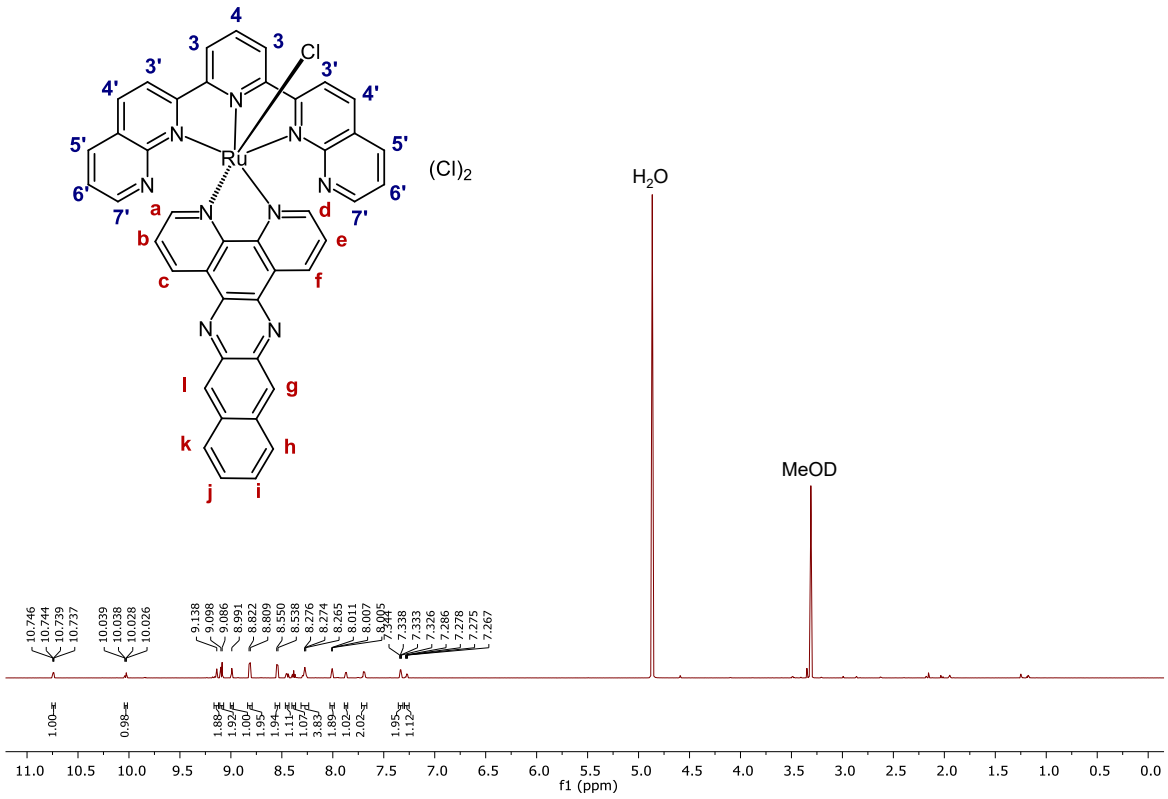


**Appendix Figure S13.** 700 MHz $^{1}$H NMR spectrum of 5 in MeOD-$d_3$ at 298 K.

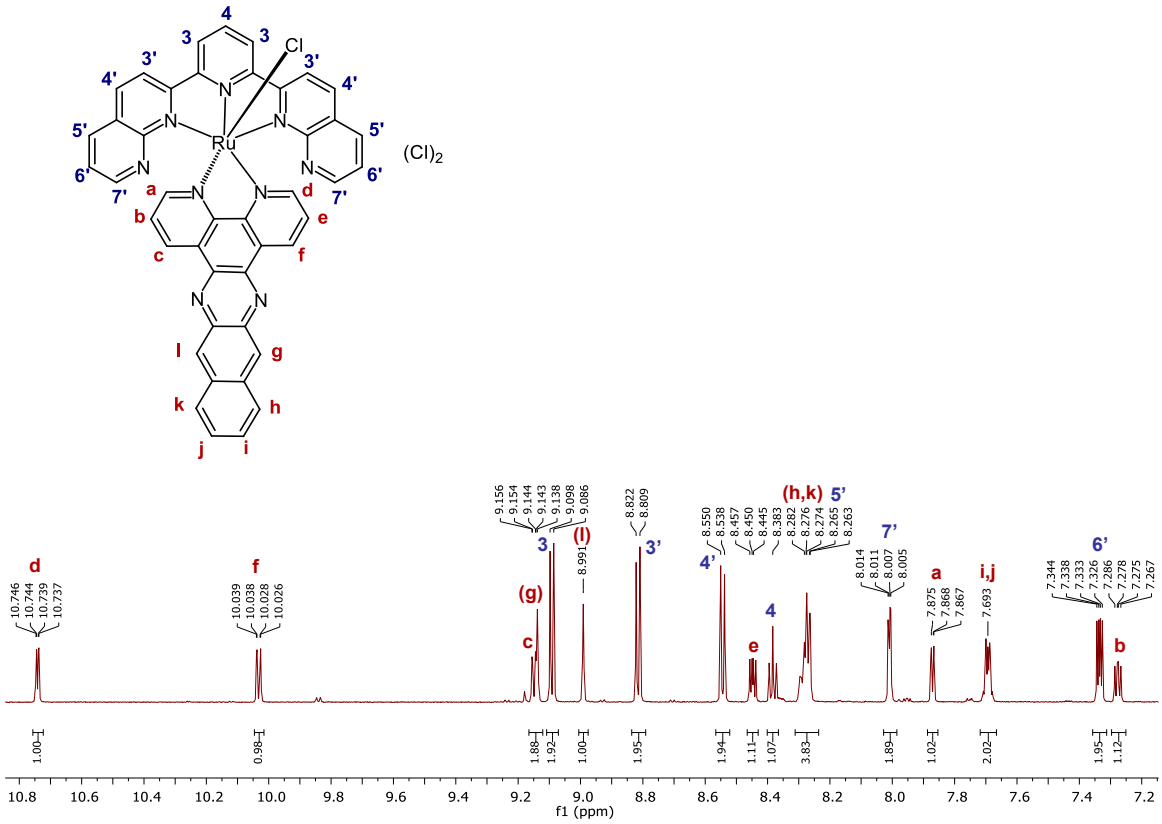


**Appendix Figure S14.** 700 MHz $^{1}$H NMR spectrum of **5** in MeOD-$d_3$ at 298 K, aromatic region.

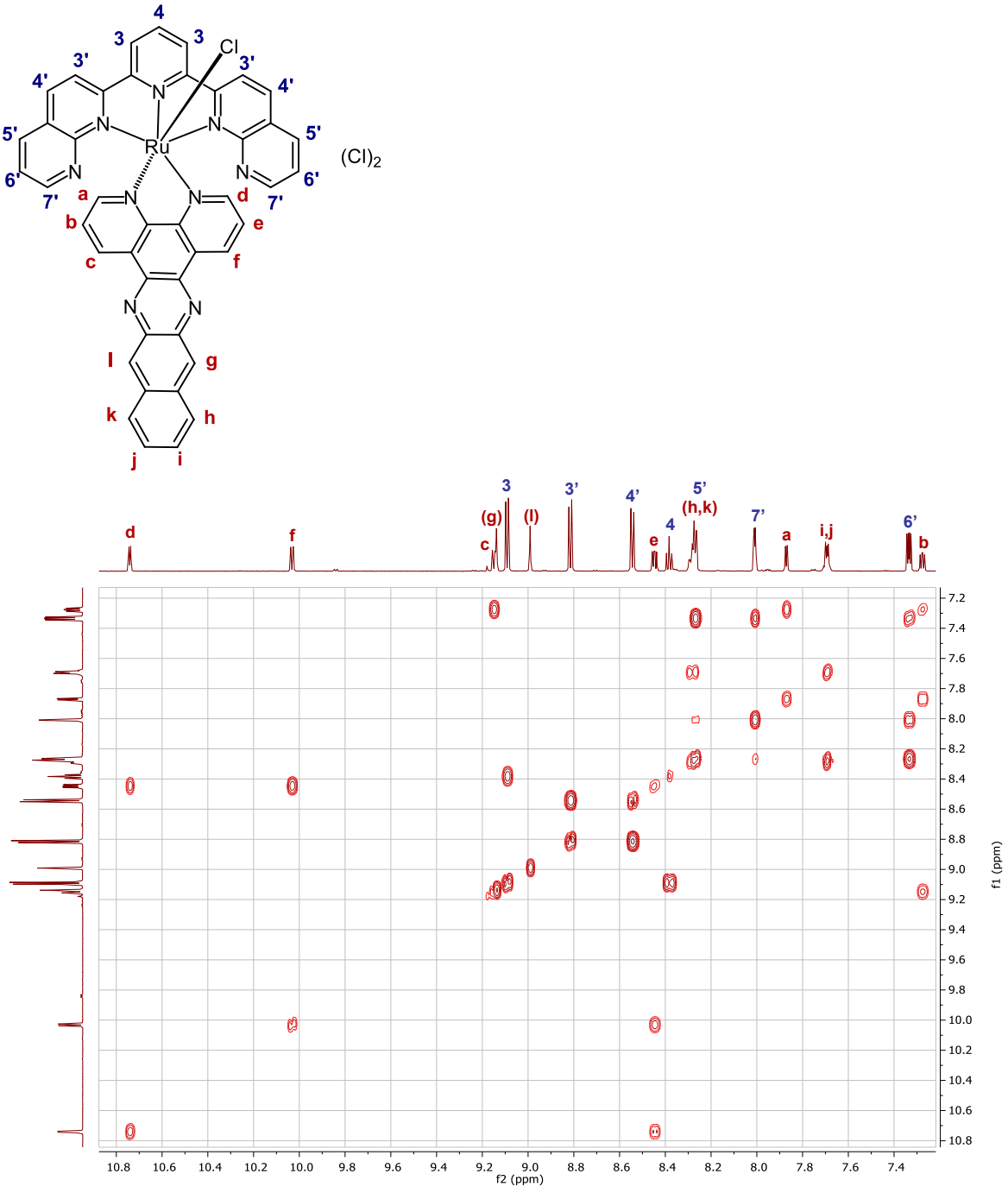


**Appendix Figure S15.** 700 MHz $^{1}$H–$^{1}$H COSY NMR spectrum of **5** in MeOD-$d_3$ at 298 K, aromatic region.

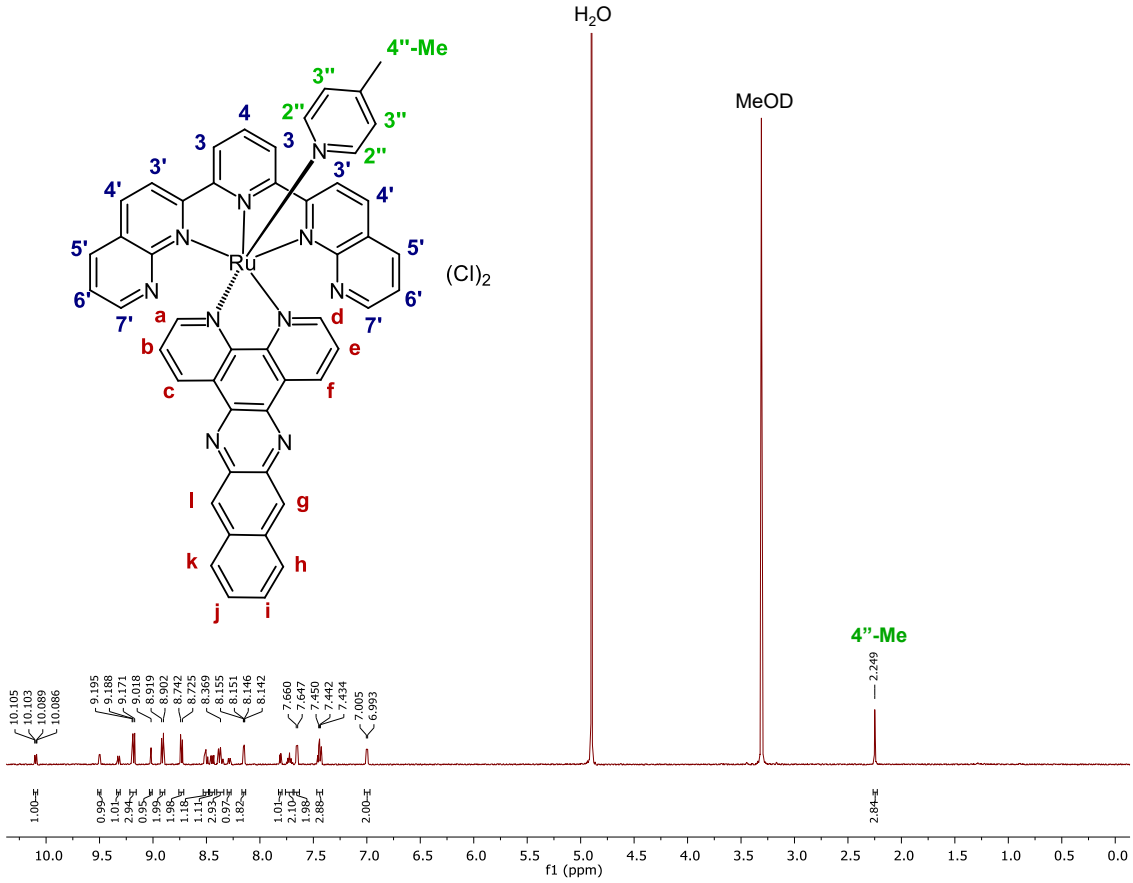


**Appendix Figure S16.** 500 MHz $^{1}$H NMR spectrum of **6** in MeOD-$d_3$ at 298 K.

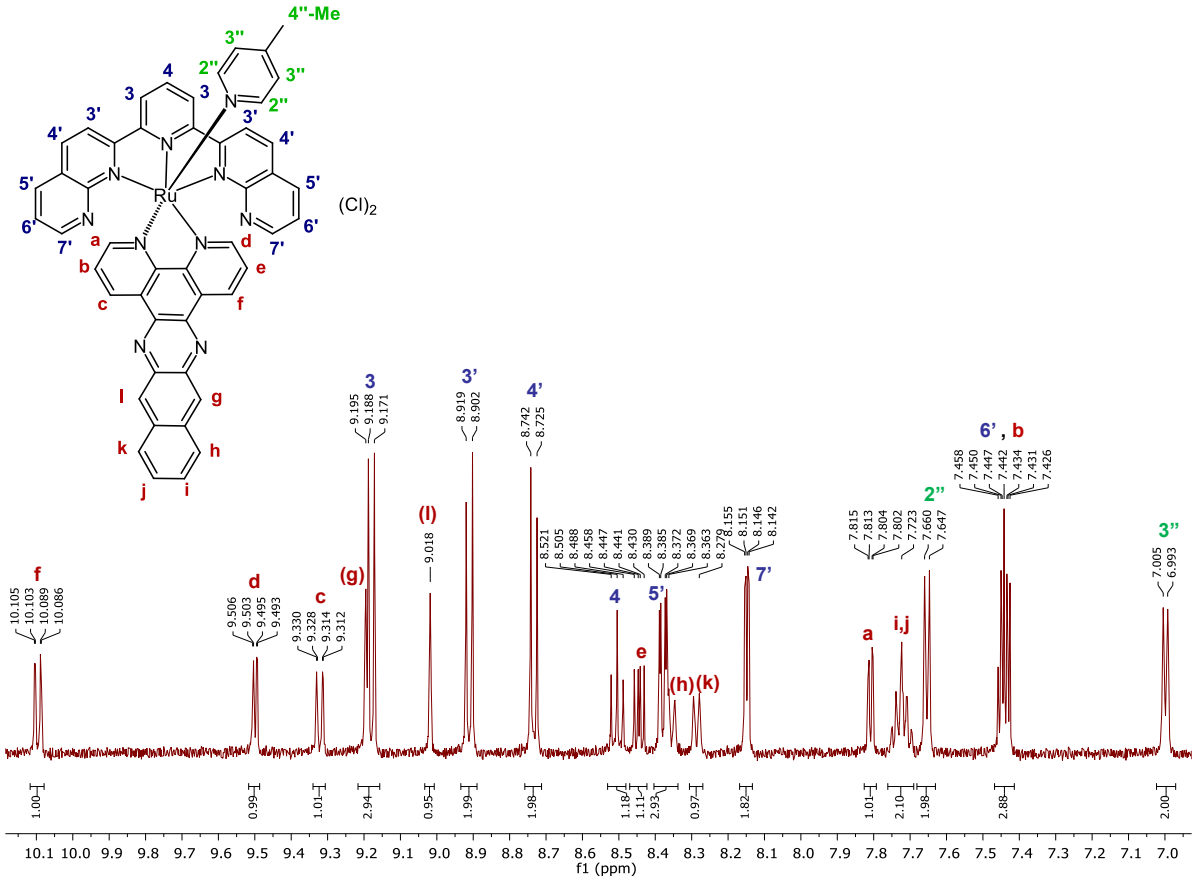


**Appendix Figure S17.** 500 MHz $^{1}$H NMR spectrum of **6** in MeOD-$d_3$ at 298 K, aromatic region.

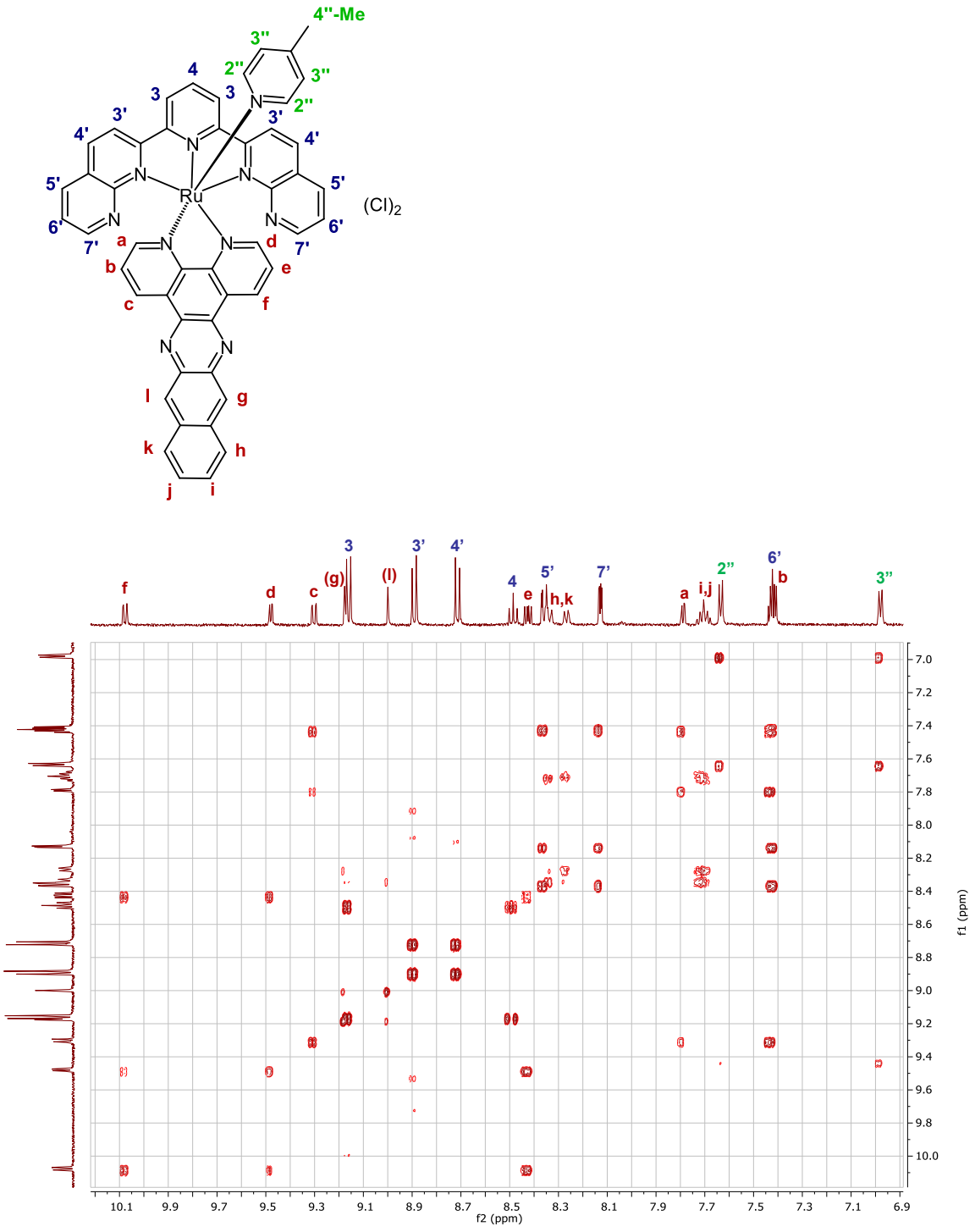


**Appendix Figure S18.** 500 MHz $^{1}$H–$^{1}$H COSY NMR spectrum of **6** in MeOD-$d_3$ at 298 K, aromatic region.

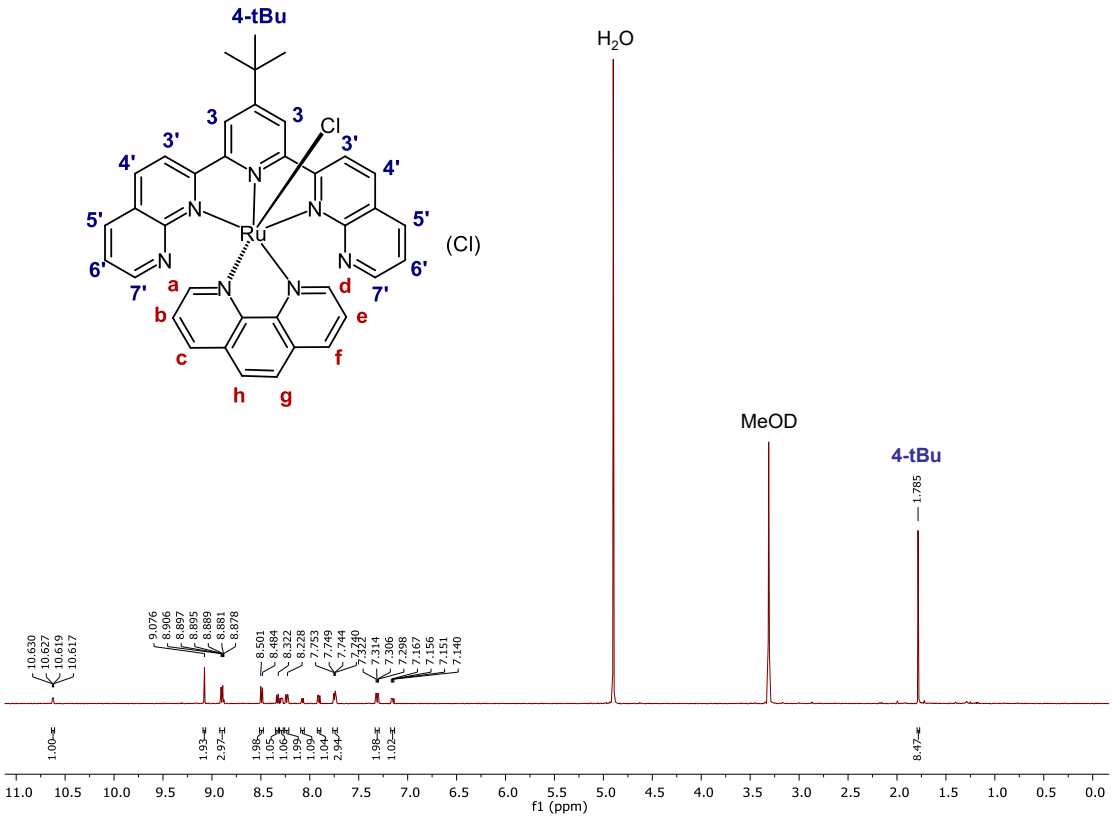


**Appendix Figure S19.** 500 MHz $^{1}$H NMR spectrum of **7** in MeOD-$d_3$ at 298 K.

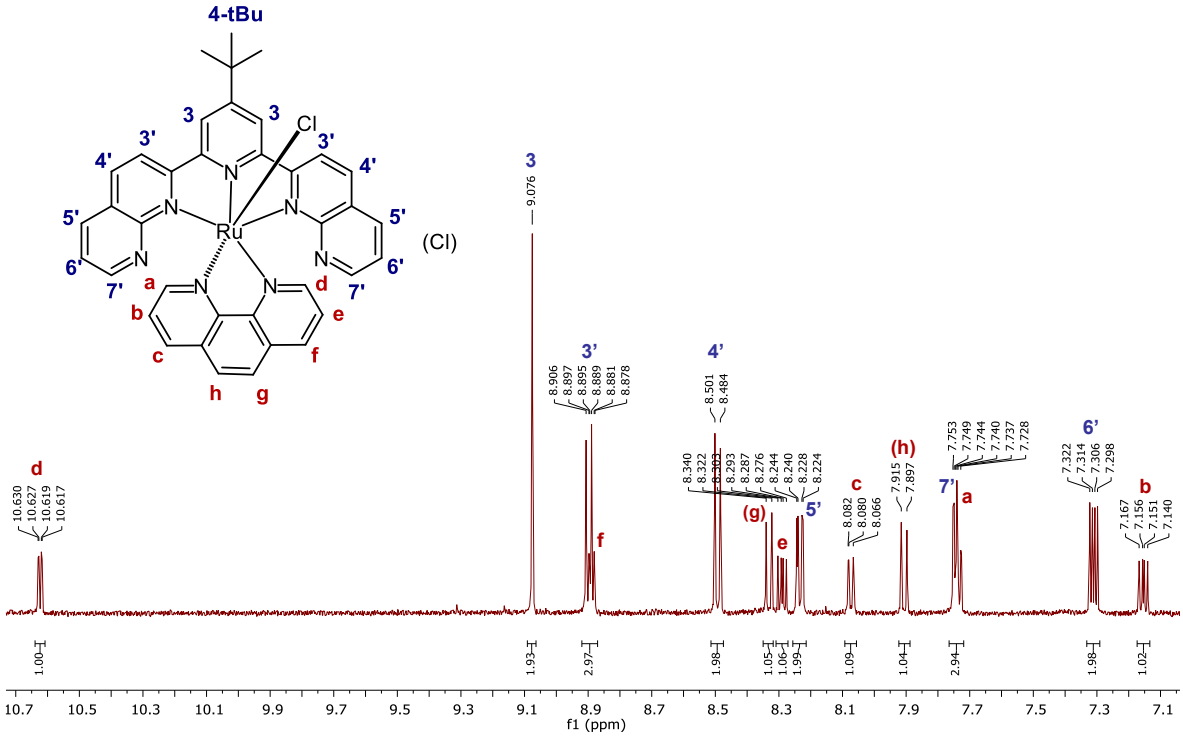


**Appendix Figure S20.** 500 MHz $^{1}$H NMR spectrum of **7** in MeOD-$d_3$ at 298 K, aromatic region.

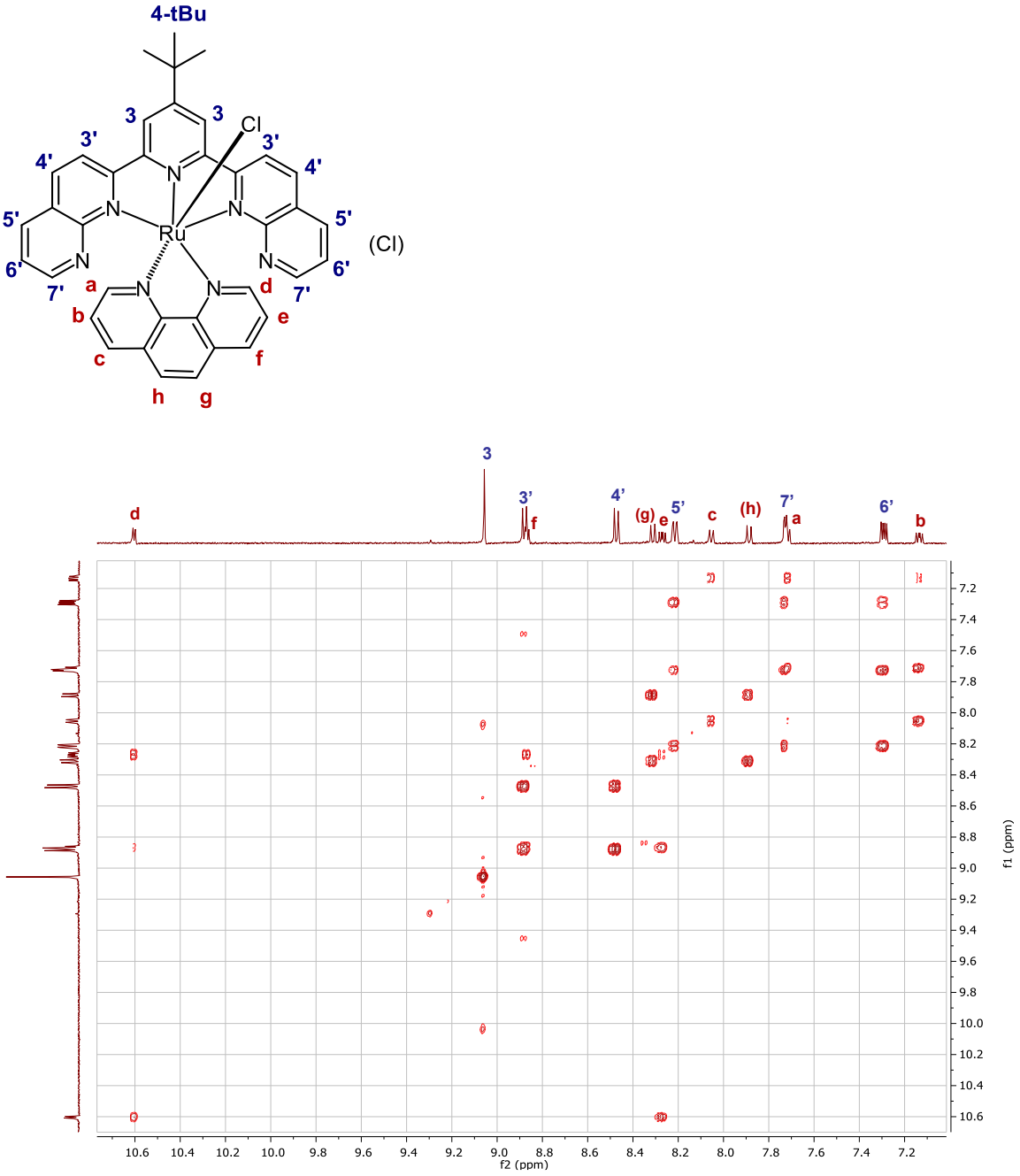


**Appendix Figure S21.** 500 MHz $^{1}$H–$^{1}$H COSY NMR spectrum of **7** in MeOD-$d_3$ at 298 K, aromatic region.

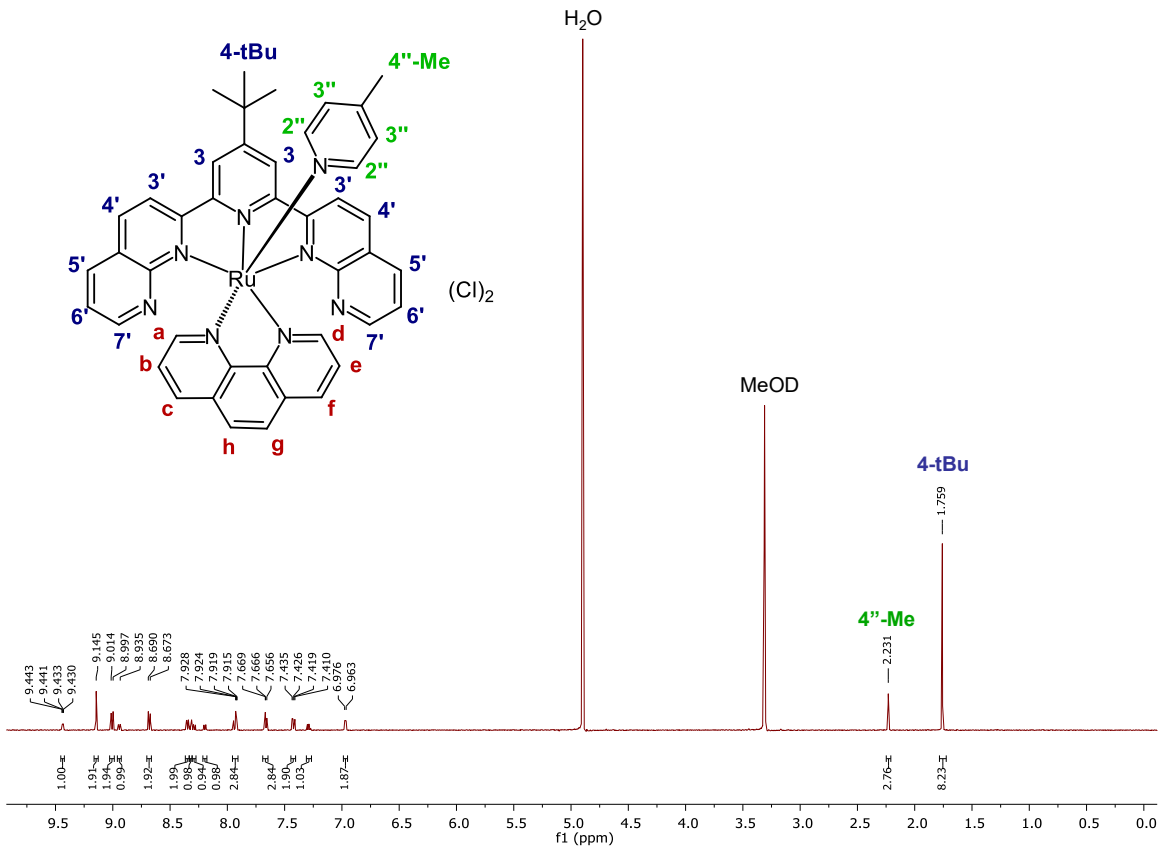


**Appendix Figure S22.** 500 MHz $^{1}$H NMR spectrum of **8** in MeOD-$d_3$ at 298 K.

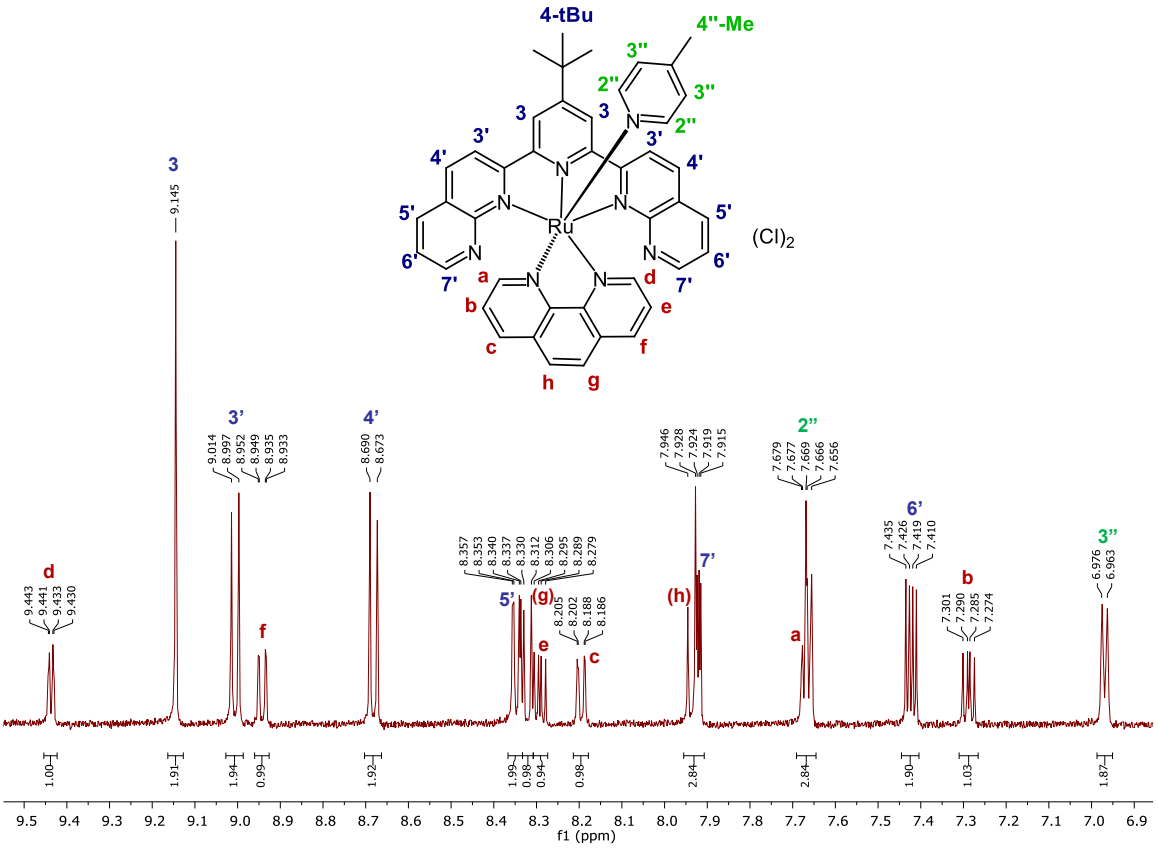


**Appendix Figure S23.** 500 MHz $^{1}$H NMR spectrum of **8** in MeOD-$d_3$ at 298 K, aromatic region.

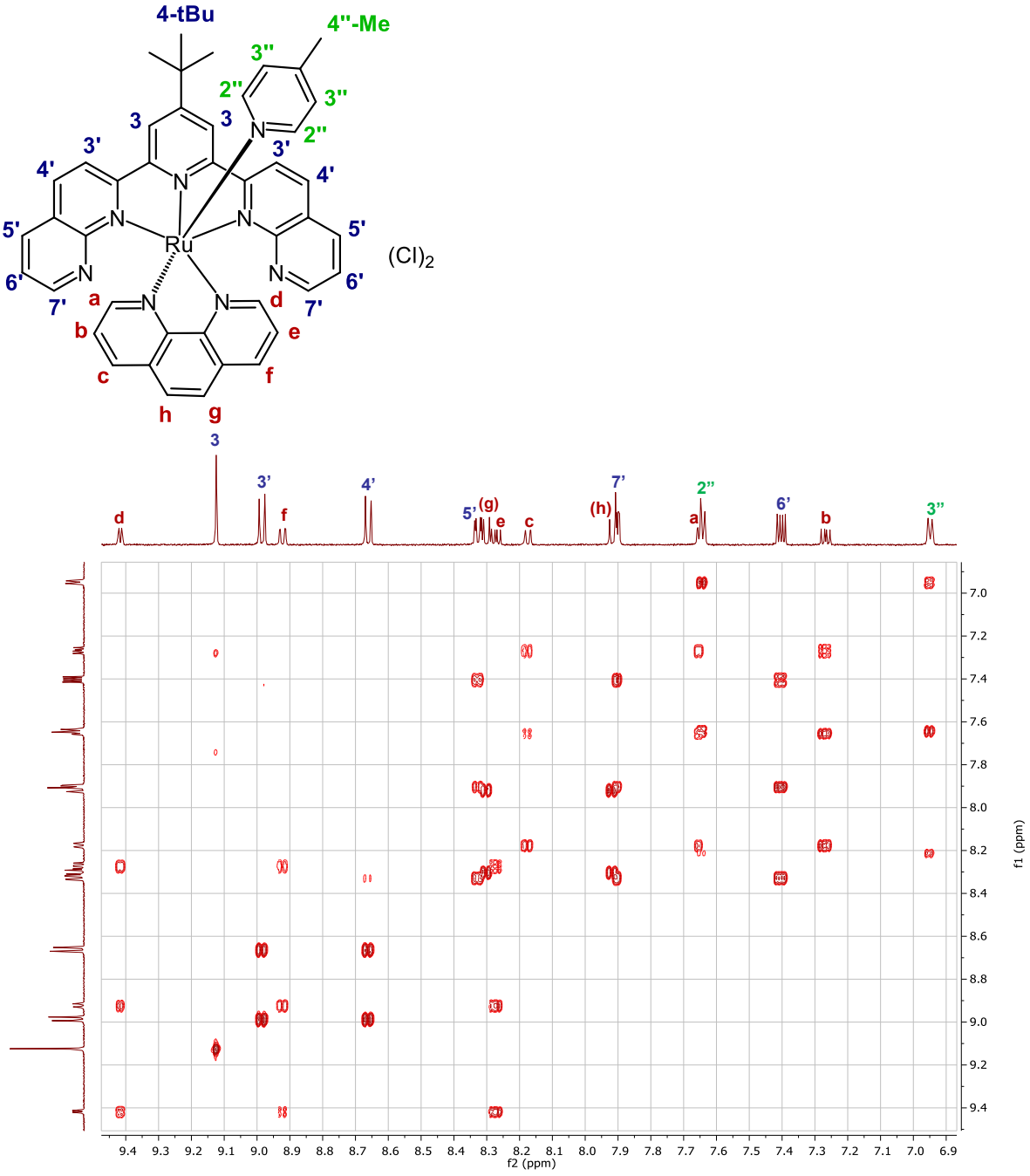


**Appendix Figure S24.** 500 MHz $^{1}$H–$^{1}$H COSY NMR spectrum of **8** in MeOD-$d_3$ at 298 K, aromatic region.

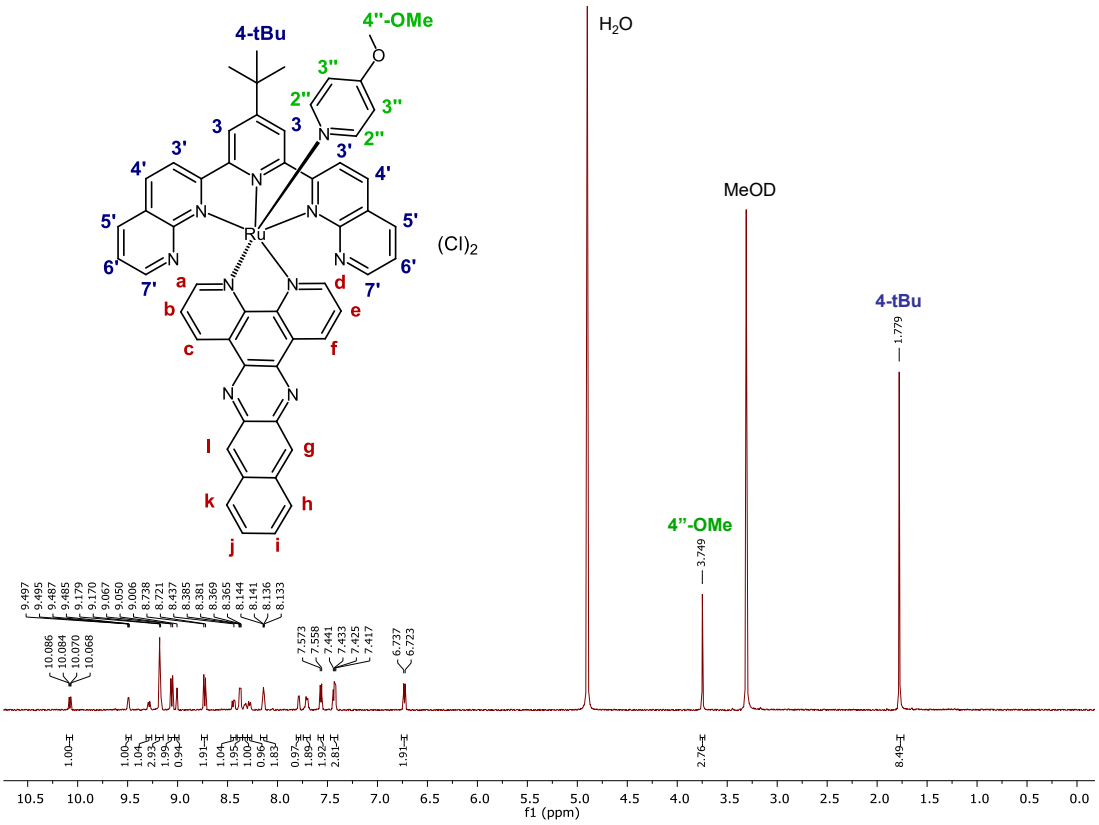


**Appendix Figure S25.** 500 MHz $^{1}$H NMR spectrum of **9** in MeOD-$d_3$ at 298 K.

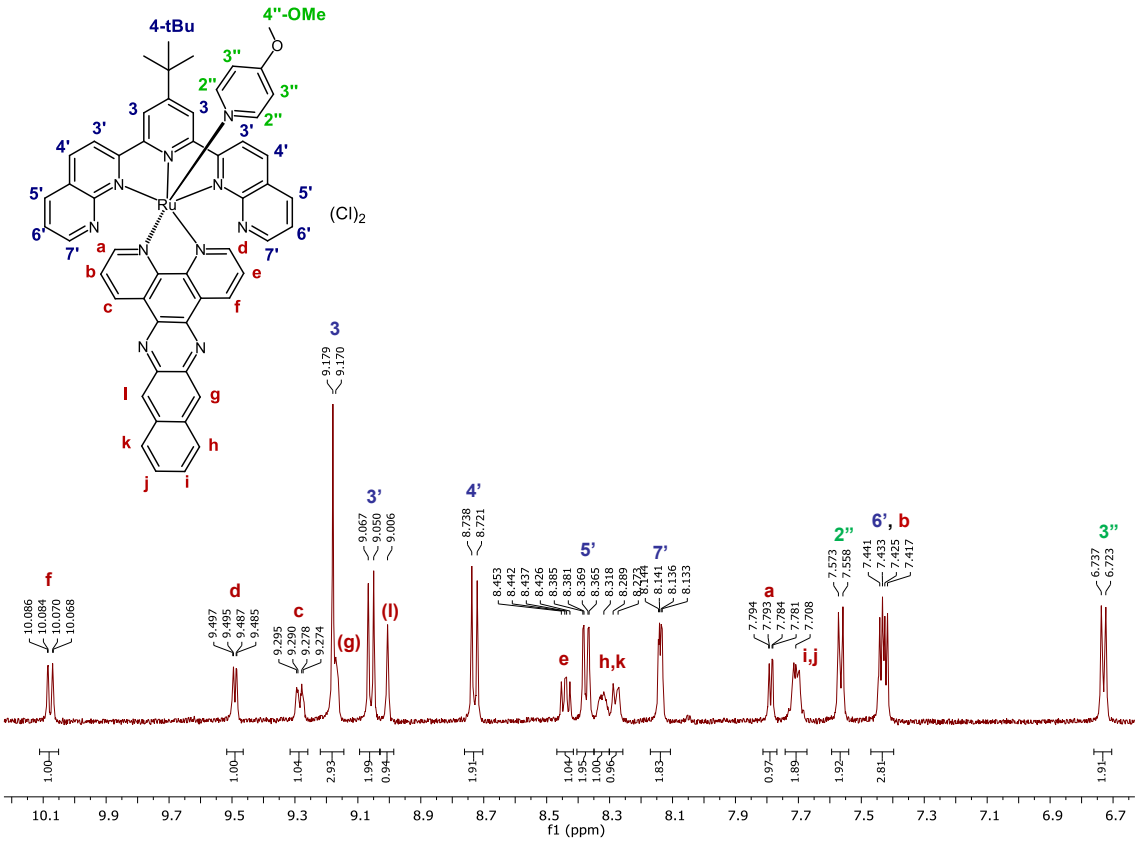


**Appendix Figure S26.** 500 MHz $^{1}$H NMR spectrum of **9** in MeOD-$d_3$ at 298 K, aromatic region.

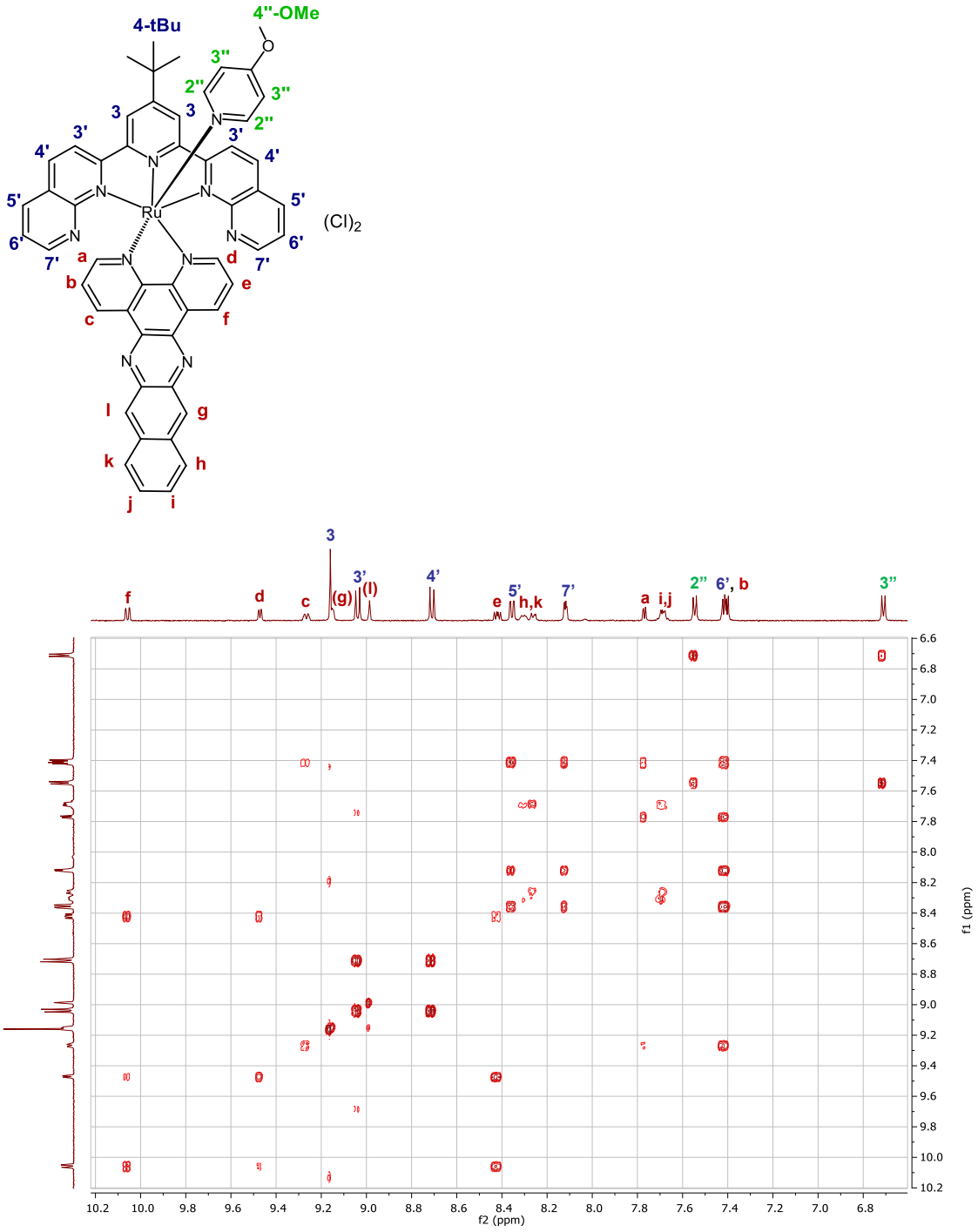


**Appendix Figure S27**2. 500 MHz 1H–1H COSY NMR spectrum of 9 in MeOD-d3 at 298 K, aromatic region.

## 4. DESCRIPTION OF 1H NMR ASSIGNMENTS OF RU(II) COMPLEXES 1–9

In addition to the reasoning described below, literature sources[654,655] were used to help with the assignments.

When two nonequivalent hydrogens are forming a single overlapping signal, they were denoted with a comma in between, for example: 7.43 (**6′**, **b**, m, 3H). When two nonequivalent, but very similar hydrogens, could be assigned to either of two signals, the two possible assignments were listed with a slash in between, for example: 8.36 (**h**/**k**, d, *J* = 8.0 Hz, 1H), 8.29 (**h**/**k**, d, *J* = 8.0 Hz, 1H). When two nonequivalent hydrogens in very similar electronic environments could be assigned to either of two signals but we have an assumption for which assignment is which, they were listed in parentheses, for example: see signals **(g)** and **(l)** at Figure S2.

Chart S1. Molecular Structures of Ru(II) Complexes 1–9 with labeling used for hydrogen assignments

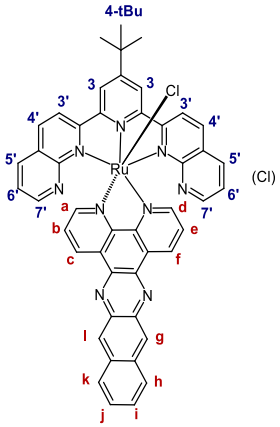


**1**

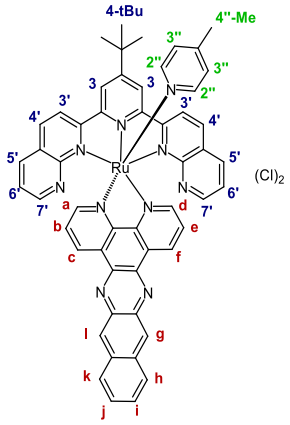


**2**

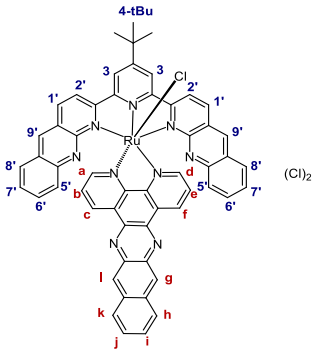


**3**

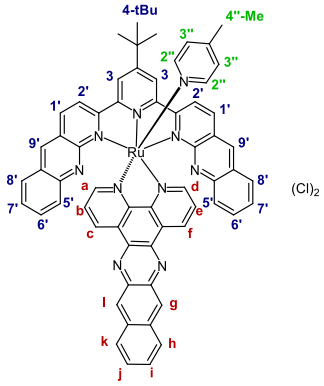


**4**

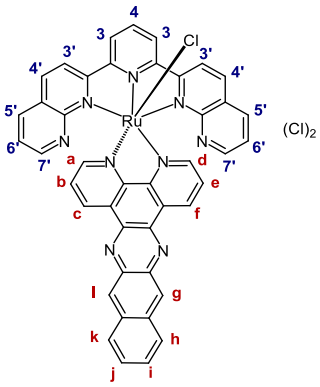


**5**

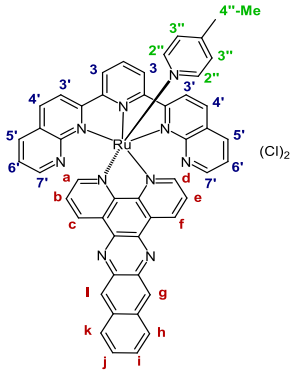


**6**

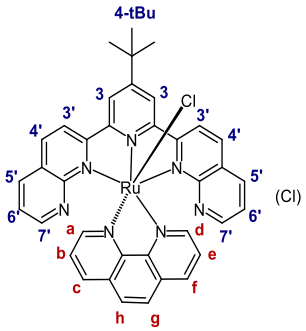


**7**

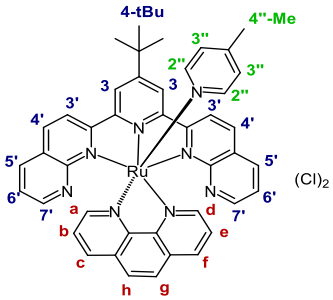


**8**

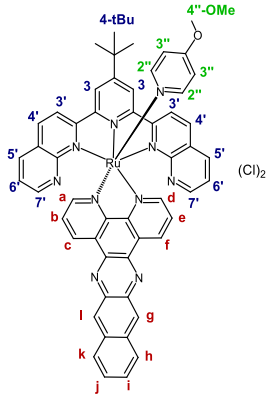


**9**

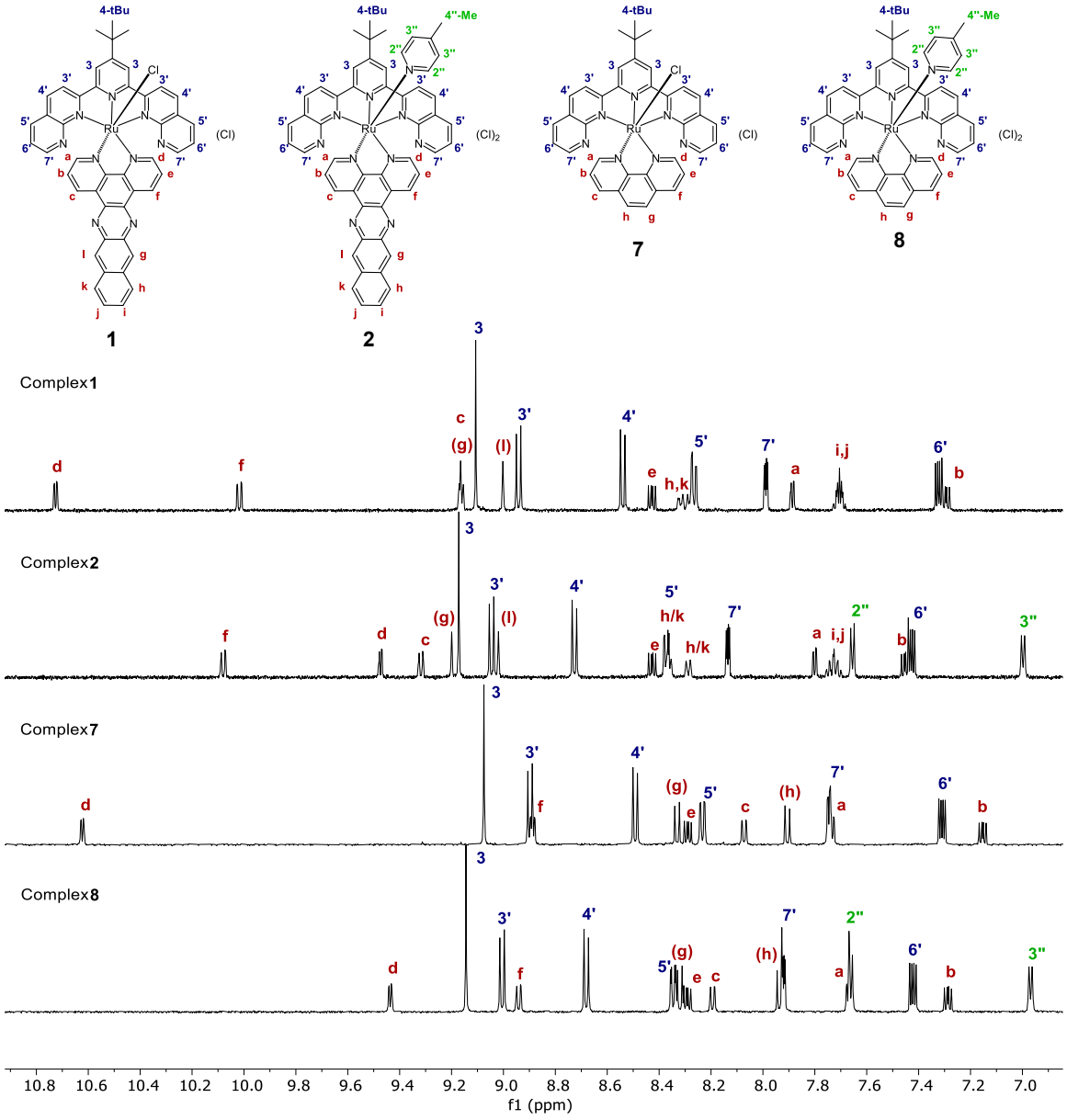


**Appendix Figure S28.** $^{1}$H NMR spectra of Ru(II) complexes **1**, **2**, **7**, and **8** in MeOD-$d_3$, aromatic region

## 5. GENERAL TRENDS

Several general trends could be derived from the assignments of $^1$H NMR signals from complexes **1**–**9**. All $^1$H signals from the chromophoric ligands (tpbn, tpbbn, dnp) integrated as 2 hydrogens each, which indicates that the chromophoric ligands were symmetrical relative to the other parts of the complex. The observed chemical shifts of the hydrogens were strongly influenced by the presence of both bonding and nonbonding electronegative nitrogens present in the ligand. The magnitude of the nitrogen's deshielding effect was based on its relative positioning to each hydrogen. For complexes with naphthyridine-based chromophoric ligands tpbn and dnp (complexes **1**, **2**, **5**–**9**), the relative chemical shifts for hydrogens followed the same pattern in each complex: **3** > **3′** > **4′** > **4** > **5′** > **7′** > **6′** in MeOD-$d_3$; hydrogen in position **4** was only present in complexes **5** and **6**, while for all other complexes this position was occupied by a ***t*-Bu** group. The most downfield hydrogen of all chromophoric ligand hydrogens was **3** (chemical shift ranging 9.08–9.18 ppm), which is positioned on the central pyridine ring of the ligand and appeared as a characteristic singlet (*s*) in complexes **1**, **2**, and **9**, or as a doublet (*d*) that coupled with **4** in complexes **5** and **6**. Hydrogens **3′** and **4′** were the next most downfield and occurred as doublets (*d*) that only coupled with each other. Based on the assumption that proton **3** (9.08–9.18 ppm) and **3′** have similar environments and would be closer in chemical shift than **3** and **4′**, hydrogen **3′** was assigned as the more downfield *d* of the two (8.81–9.06 ppm) and **4′** as the more upfield *d* of the two (8.49–8.73 ppm). When hydrogen **4** was present, it appeared as a characteristic triplet (*t*) at chemical shifts 8.38–8.51 ppm, upfield from **3**, **3′** and **4′** and downfield from **5′**, **6′**, and **7′**. The rest of the hydrogens from the chromophoric ligand (**5′**, **6′**, **7′**) appeared as doublets of doublets (*dd*) that coupled with each other. Hydrogen **6′** appeared as the most upfield *dd* in this spin system (7.31–7.44 ppm) and the most

upfield of the ligands. It was clearly distinguished from *dd* **5′** and **7′** as the one with the largest second *J*-value. Hydrogen **5′** was assigned as the most downfield *dd* of the **5′**-**6′**-**7′** spin system (8.23–8.37 ppm), and **7′** was assigned as a *dd* (7.75–8.15 ppm) in between **5′** and **6′**, based on the observed *J*-values and the assumption that $J_{5'6'} > J_{7'6'}$.

For complexes with the benzonaphthyridine-based chromophoric ligand tpbbn (complexes **3** and **4**), the relative chemical shifts for hydrogens of the tpbbn followed similar patterns: **3** > **2′** > **9′** > **1′** > **5′** > **7′** > **6′** > **8′** for **3** in DMSO-$d_6$ (relatively poor solubility in methanol) and **3** > **9′** > **2′** > **1′** > **5′** > **7′** > **6′** > **8′** for **4** in MeOD-$d_3$. As for the complexes with naphthyridine-based chromophoric ligands, the most downfield hydrogen was **3** (9.28–9.34 ppm), which is positioned on the central pyridine ring of the ligand. The most upfield hydrogens were **6′** (7.50–7.53 ppm) and **8′** (6.75–7.01 ppm), which are located on the distal phenyl ring of tpbbn (Figures S7–S12).

The monodentate ligand (L) that occupies the axial position in complexes **1**–**9** ($Cl^-$, 4-pic, or 4-mp) made all hydrogens from the NN ligand (dppn, phen) magnetically inequivalent, with one side of the bidentate ligand (NN) facing the same side as L and another pointing away from L. In all complexes (**1**–**9**) it was observed that hydrogens on the NN ligand that were facing the same side as L were typically positioned more downfield (deshielded by L) than similarly-positioned hydrogens on the side that was pointing away from L.

For all dppn-containing complexes (**1**–**6**, **9**), all $^1$H signals from the NN ligand dppn (**a**, **b**, **c**, **d**, **e**, **f**, **g**, **h**, **i**, **j**, **k**, **l**) were magnetically inequivalent due to the presence of L, with one side of dppn facing the same side as L (**d**, **e**, **f**, **g**, **h**, **i**) and the other pointing away from L (**a**, **b**, **c**, **l**, **k**, **j**). For all dppn-containing complexes (**1**–**6**, **9**), the relative chemical shifts for hydrogens on dppn followed very similar patterns: **d**, **f** > **c**, **g**, **l** > **e** > **h**, **k** > **a** >

**i**, **j** > **b**. Hydrogens **d**–**f**, which are spatially the closest to L, were affected the most by deshielding due to L. At closest proximity, the observed deshielding effect caused by L was strongest with $Cl^-$ (which is to be expected due to its electronegativity) and was attenuated, but still apparent, for 4-pic and 4-mp. Due to its close proximity to L, the chemical shift of hydrogen **d** was most strongly affected by the presence of L, ranging from 9.47-10.82 ppm across the **1**–**6**, **9** series. Hydrogen **d** was deshielded relative to **a** by almost 3 ppm when L was $Cl^-$, and by ~1.7–1.9 ppm when L was 4-pic or 4-mp. Hydrogens **e** and **f** are still relatively close to L and were deshielded by L as well, but less significantly than **d**; due their increased distance from L, the strength of the deshielding effect was approximately equal for $Cl^-$, 4-pic, or 4-mp. Hydrogen **e** was deshielded relative to **b** by ~1.1–1.4 ppm when L is $Cl^-$, and by ~1.0–1.4 ppm when L is 4-pic or 4-mp. Hydrogen **f** was deshielded relative to **c** by ~0.9–1.3 ppm when L is $Cl^-$, and by a similar ~0.8–1.2 ppm when L is 4-pic or 4-mp. As a result, in the complexes with $Cl^-$ in the axial position (**1**, **3**, **5**), hydrogen **d** appeared the most downfield (10.73–10.82) followed by hydrogen **f** (10.02–10.32). In the complexes with 4-pic (**2**, **4**, **6**) or 4-mp (**9**) in the axial position, hydrogen **f** appeared the most downfield (10.08–10.46), followed by hydrogen **d** (9.47–9.74).

Hydrogen **f** appeared more downfield than **e** due to it being in the *para*- position relative to the nitrogen coordinated to Ru and due to the spatial proximity of the non-coordinated nitrogen on dppn. Hydrogen **b**'s signal appeared very similar to that of proton **e** in terms of multiplicity and *J*-values (both are *dd* with $J_1$ = ~8 Hz and $J_2$ = ~5 Hz), but **b** (7.27–7.45 ppm) was much more upfield than **e** (8.43–8.83 ppm) due to the absence of deshielding effect from L. The assignments for hydrogens **a** and **c** were derived from their coupling to **b**, observed by $^1H$–$^1H$ COSY NMR. Hydrogens **b** and **e**, which are in the *meta*-position relative to the Ru-coordinated nitrogen, were the most

upfield among **a**-**b**-**c** and **d**-**e**-**f**, with **c** and **d** being the most downfield signals in their respective spin systems. In the absence of L's influence, proton **a** (7.79–7.96 ppm), which is in the *ortho*-position, was shielded by $Ru^{(655)}$ and appeared more upfield than **c** (8.99–9.32 ppm), which is in the *para*-position relative to the Ru-coordinated nitrogen and was consequently not shielded by Ru. While **d** was shielded by Ru as much as **a**, spatial proximity to L affected its chemical shift so that it appeared more downfield than **f** when L is $Cl^-$. However, once L is 4-pic or 4-mp, the chemical shift of **d** shifted less downfield than those by $Cl^-$. With the shielding effect of Ru on proton **d** still in place, proton **f** (*para*-position) appeared more downfield than proton **d** (*ortho*-position) just like proton **c** (*para*-position) appeared more downfield than proton **a** (*ortho*-position). Another factor influencing the chemical shift of **f** and **c** was spatial proximity to the non-coordinated nitrogen from dppn, which strongly exacerbated the deshielding effect. Hydrogens **g** and **l** appeared as singlets that integrated as 1 proton each. Because it is assumed that hydrogens on the side of dppn that are facing L (**d**–**i**) would be deshielded, **g** was assigned as being slightly more downfield (9.14–9.38 ppm) than **l** (8.91–9.05 ppm). Hydrogens on different sides of dppn that are more distant from L became more and more similar by chemical shifts, with **h** and **k** signals observed to be very close to each other around ~8.3 ppm and **i** & **j** overlapping to form one multiplet at ~7.7 ppm.

In the phen-containing complexes (**7**, **8**), all $^1H$ signals from the phen ligand (**a**–**g**) were magnetically inequivalent, as observed for the $^1H$ signals from the dppn ligand in the dppn-containing complexes (**1**–**6**, **9**). The chemical shifts for hydrogens of the phen ligand followed the same pattern in both complexes **7** (L = Cl) and **8** (L = 4-pic): **d** > **f** > **g** > **e** > **c** > **h** > **a** > **b**. Hydrogen **d** appeared the most downfield in complexes **7** (L = $Cl^-$) and **8** (L = 4-pic). Chemical shifts of hydrogen **d** in complex **7** (10.62 ppm) *vs.* in complex **8** (9.44 ppm) were significantly different due to a stronger deshielding of **d** in **7** by $Cl^-$

than **d** in **8** by 4-pic — similar to what was observed for dppn-containing complexes **1–6**, **9**. While hydrogen **d** appeared the most downfield in dppn-containing complexes with $Cl^-$ (**1**, **3**, **5**), hydrogen **f** is the one that appeared the most downfield in dppn-containing complexes with 4-pic or 4-mp (**2**, **4**, **6**, **9**). Hydrogen **f** appeared at ~8.9 ppm in complexes **7** and **8** (phen, L = $Cl^-$), which was significantly more upfield from 10.02–10.46 ppm where it appeared in dppn-containing complexes **1, 3, 5** (L = $Cl^-$) and **2**, **4**, **6**, **9** (L = 4-pic or 4-mp). This difference outlines the effect of spatial proximity of the non-coordinated nitrogen from dppn on hydrogen **f**, as the proximity to this nitrogen significantly deshielded **f**. Since phen does not have a non-coordinated nitrogen analogous to that of dppn, the chemical shift for **f** was moved upfield in phen-containing complexes **7** and **8** when compared to that of **f** in dppn-containing complexes **1–6**, **9**. The same effect was responsible for proton **c** appearing more upfield in complexes **7** and **8** (~8.1 ppm) than in complexes **1–6**, **9** (8.99–9.32 ppm). Protons **h** and **g** in complexes **7** and **8** formed a two-spin system, which was identified by correlations observed with $^1H$–$^1H$ COSY NMR, with **g** assigned as the more downfield of the two (~8.3 ppm) and **h** assigned as the more upfield of the two (~7.9 ppm) based on the assumption that protons from the side of phen facing L appear more downfield.

In the complexes with 4-pic or 4-mp (**2**, **4**, **6**, **8**, **9**), aromatic $^1H$ signals **2″** and **3″** from 4-pic or 4-mp were present. Both **2″** and **3″** integrated as 2 hydrogens each (due to the symmetry of the complex) and were picked out as a *d* that only coupled with each other. **2″** was assigned as the more downfield *d* of the two (7.56–7.79 ppm) and **3″** as the more upfield *d* of the two (6.73–7.00 ppm) based on the assumption that the one in *ortho*-position to nitrogen (**2″**) would appear more downfield. Overall, the spin system of **2″**-**3″** resembles the spin system **3′**-**4′**, as each appeared as a pair of doublets. However, it is characteristic of 4-pic protons such as **2″** and especially **3″** to appear

upfield relative to other polypyridyl protons, such as that of tpbn, tppbn, dnp and dppn, which makes **2″**-**3″** and **3′**-**4′** spin systems easy to distinguish.

The ***t*-Bu** group from tpbn and tpbbn (~1.8 ppm), the methyl group from 4-pic (~2.2 ppm) and the methoxy group from 4-mp (3.75 ppm) all gave rise to characteristic singlets (*s*) that are clearly observed in the aliphatic region of the spectra and are easily assigned (see Figures S1–S27).

A 2D $^{1}$H–$^{1}$H ROESY experiment was carried out for the related **4-pic**- and **tpbn**-containing Ru(II) complex, which revealed characteristic through-space couplings for the following hydrogens: **3** with **3′** ; **4’** with **5’** ; **3** with **4-tBu** ; **3″** with **4″-Me** ; and equivalent position of **d** with **2″**, and confirmed our assumptions for the assignments of **3′** *vs.* **4’**, **5′** *vs.* **7’**, and **2″** *vs.* **3″**.[793]

Complex **1**

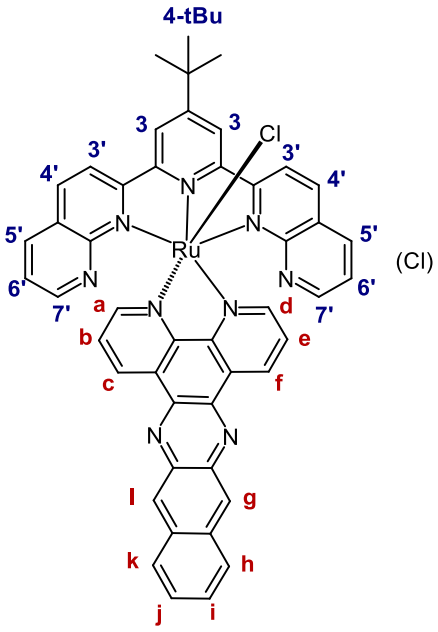


$^1$H NMR (MeOD-$d_3$, 500 MHz): δ 10.73 (**d**, dd, $J_1$ = 5.5 Hz, $J_2$ = 1.5 Hz, 1H), 10.02 (**f**, dd, $J_1$ = 8.0 Hz, $J_2$ = 1.5 Hz, 1H), 9.16 (**g**, s, 1H), 9.16 (**c**, dd, $J_1$ = 8.0 Hz, $J_2$ = 1.5 Hz, 1H), 9.11 (**3**, s, 2H), 9.00 (**l**, s, 1H), 8.94 (**3′**, d, $J$ = 8.5 Hz, 2H), 8.54 (**4′**, d, $J$ = 8.5 Hz, 2H), 8.43 (**e**, dd, $J_1$ = 8.0 Hz, $J_2$ = 5.5 Hz, 1H), 8.30 (**h**, **k**, m, 2H), 8.27 (**5′**, dd, $J_1$ = 8.0 Hz, $J_2$ = 2.0 Hz, 2H), 7.99 (**7′**, dd, $J_1$ = 4.5 Hz, $J_2$ = 2.0 Hz, 2H), 7.89 (**a**, dd, $J_1$ = 5.5 Hz, $J_2$ = 1.5 Hz, 1H), 7.71 (**i**, **j**, m, 2H), 7.32 (**6′**, dd, $J_1$ = 8.0 Hz, $J_2$ = 4.5 Hz, 2H), 7.30 (**b**, dd, $J_1$ = 8.0 Hz, $J_2$ = 5.5 Hz, 1H), 1.80 (**4-tBu**, s, 9H).

*Hydrogens from **tpbn***: All hydrogen signals from the chromophoric ligand **tpbn** (**3**, **3′**, **4′**, **5′**, **6′** and **7′**) integrate as 2 hydrogens each, since **tpbn** is positioned symmetrically relative to the other parts of the complex. As the only singlet (*s*) among **tpbn** hydrogens, **3** was assigned as a *s* at 9.11 ppm. Both **3′** and **4′** were picked out as doublets (*d*) that

only couple with each other (coupling observed at $^{1}$H–$^{1}$H COSY NMR). **3′** was assigned as the more downfield *d* of the two (8.94 ppm) and **4′** as a more upfield *d* of the two (8.54 ppm), based on the assumption that hydrogen **3** (9.11 ppm) and **3′** (8.94 ppm) have similar environments and would be closer by chemical shifts than **3** and **4′**. Among the spin system **5′**-**6′**-**7′** (correlations with each other observed with $^{1}$H–$^{1}$H COSY NMR), all three are *dd* but **6′** is distinguished as a *dd* with largest second *J*-value among the three (7.32 ppm, dd, $J_1$ = 8.0 Hz, $J_2$ = 4.5 Hz). **5′** is assigned as a more downfield *dd* at 8.27 ppm ($J_{5'6'}$ = 8.0 Hz, $J_{5'7'}$ = 2.0 Hz), and **7′** is assigned as a more upfield *dd* at 7.99 ppm ($J_{7'6'}$ = 4.5 Hz, $J_{7'5'}$ = 2.0 Hz), based on the observed *J*-values and the assumption that $J_{5'6'} > J_{7'6'}$. The singlet at 1.80 ppm integrates as 9 hydrogens and is assigned to the **4-tBu** group.

*Hydrogens from **dppn**:* The negatively-charged **chloride** ligand is occupying the axial position and makes all $^{1}$H from PDT ligand **dppn** (**a**, **b**, **c**, **d**, **e**, **f**, **g**, **h**, **i**, **j**, **k**, **l**) magnetically inequivalent, with one side of **dppn** facing the same side as **chloride** (**d**, **e**, **f**, **g**, **h**, **i**) and the other pointing away from the **chloride** (**a**, **b**, **c**, **l**, **k**, **j**). Hydrogens **d–f**, which are spatially closest to the **chloride**, are affected by it the most, causing chemical shifts that are significantly more downfield than they would be in the absence of **chloride**. Hydrogen **d** was assigned as the most downfield hydrogen at 10.73 ppm, because of its proximity to the **chloride**. Based on this assignment, $J_{de}$ is 5.5 Hz. Hydrogens **e** and **f** were derived from their coupling to **d**, observed with $^{1}$H–$^{1}$H COSY NMR. Both **e** and **f** appear as doublets of doublets (*dd*), with hydrogen **e** being assigned to the *dd* exhibiting a larger second *J*-value than **f** (**e**, dd, $J_{ef}$ = 8.0 Hz, $J_{ed}$ = 5.5 Hz; **f**, dd, $J_{ef}$ = 8.0 Hz, $J_{fd}$ = 1.5 Hz). With this assignment, $J_{ed}$ = 5.5 Hz which matches the observed $J_{de}$ from the hydrogen **d** assignment. Hydrogen **f** (10.02 ppm) appears more downfield than **e** (8.43 ppm), due to being in the *para*- position relative to the nitrogen

that is coordinated to Ru and due to the spatial proximity to the non-coordinated nitrogen on **dppn**. Hydrogen **b** was assigned as the signal that appears very similar to that of hydrogen **e** in terms of multiplicity and *J*-values (both are *dd* with $J_1$ = 8.0 Hz and $J_2$ = 5.5 Hz), but **b** (7.30 ppm) is much more upfield than **e** (8.43 ppm) due to the absence of **chloride** near **b**. Hydrogens **a** and **c** were derived from their coupling to **b**, observed by $^1$H–$^1$H COSY NMR. Both **a** and **c** appear as *dd*, and assignments were made based on the observed *J*-values and the assumption that $J_{ab} < J_{cb}$. Hence, **a** was assigned as a dd at 7.89 ppm (dd, $J_{ab}$ = 5.5 Hz, $J_{ac}$ = 1.5 Hz) and **c** as a *dd* at 9.16 ppm ($J_{cb}$ = 8.0 Hz, $J_{ca}$ = 1.5 Hz). After hydrogens **a**, **b**, **c**, **d**, **e**, and **f** were assigned, the following trends were observed: hydrogens **b** and **e**, which are in the *meta*-position relative to Ru-coordinated nitrogen, are the most upfield among **a**-**b**-**c** and **d**-**e**-**f**, with **c** and **d** being the most downfield signals in their respective spin systems. In the absence of **chloride** influence, hydrogen **a**, which is in the *ortho*-position, is shielded by Ru (see ref. 1) and appears more upfield than **c**, which is in the *para*-position relative to the coordinating nitrogen and is not shielded by Ru. While **d** is shielded by Ru as much as **a**, spatial proximity to **chloride** affects its chemical shift so that it appears more downfield than **f**. Hydrogens **g** and **l** were assigned as singlets that integrate as 1 hydrogen each, with the assumption that **g** appear slightly more downfield (9.16 ppm) than **l** (9.00 ppm), based on the assumption that hydrogens from the side of **dppn** that is facing **chloride** appear more downfield. Hydrogens on different sides of **dppn** that are further away from **chloride** become more similar by chemical shifts, with **h** and **k** observed very close to each other at 8.30 ppm and **i** & **j** overlapping to form one multiplet at 7.71 ppm.

Complex **2**

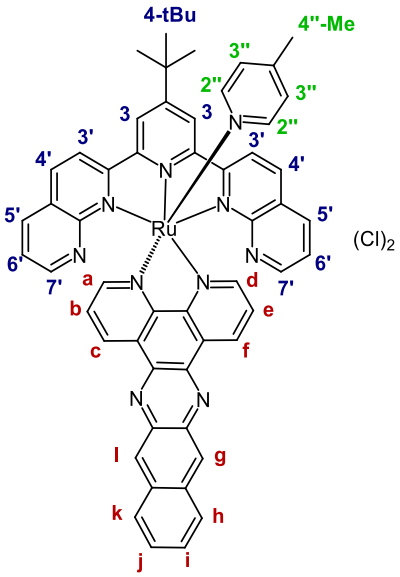


$^1$H NMR (MeOD-$d_3$, 500 MHz): δ 10.08 (**f**, dd, $J_1$ = 8.5 Hz, $J_2$ = 1.5 Hz, 1H), 9.47 (**d**, dd, $J_1$ = 5.5 Hz, $J_2$ = 1.5 Hz, 1H), 9.32 (**c**, dd, $J_1$ = 8.0 Hz, $J_2$ = 1.0 Hz, 1H), 9.20 (**g**, s, 1H), 9.17 (**3**, s, 2H), 9.05 (**3′**, d, $J$ = 8.5 Hz, 2H), 9.02 (**l**, s, 1H), 8.73 (**4′**, d, $J$ = 8.5 Hz, 2H), 8.43 (**e**, dd, $J_1$ = 8.5 Hz, $J_2$ = 5.5 Hz, 1H), 8.37 (**5′**, dd, $J_1$ = 8.0 Hz, $J_2$ = 2.0 Hz, 2H), 8.36 (**h**/**k**, d, $J$ = 8.0 Hz, 1H), 8.29 (**h**/**k**, d, $J$ = 8.0 Hz, 1H), 8.13 (**7′**, dd, $J_1$ = 4.0 Hz, $J_2$ = 2.0 Hz, 2H), 7.80 (**a**, dd, $J_1$ = 5.5 Hz, $J_2$ = 1.0 Hz, 1H), 7.72 (**i**, **j**, m, 2H), 7.65 (**2″**, d, $J$ = 7.0 Hz, 2H), 7.45 (**b**, dd, $J_1$ = 8.0 Hz, $J_2$ = 5.5 Hz, 1H), 7.43 (**6′**, dd, $J_1$ = 8.0 Hz, $J_2$ = 4.5 Hz, 2H), 7.00 (**3″**, d, $J$ = 6.0 Hz, 2H), 2.25 (**4″-Me**, s, 3H), 1.77 (**4-tBu**, s, 9H).

In complex **2,** all hydrogens follow the same trends as described in the $^1$H assignments of complex **1**, except for the hydrogens **d** and **f**. In complex **1**, **d** is the most downfield hydrogen, while **f** is the most downfield hydrogen in complex **2**. Once the **chloride** ligand in the axial position is substituted with 4-picoline (**4-pic**), the chemical shift of

hydrogen **d** is shifted less downfield, and with the shielding effect of Ru on hydrogen **d** still in place, hydrogen **f** (*para*-position) appears more downfield than hydrogen **d** (*ortho*-position) just like hydrogen **c** (*para*-position) appears more downfield than hydrogen **a** (*ortho*-position). When chemical shifts of hydrogen **f** in complex **1** and hydrogen **f** in complex **2** are compared, they are found to be very similar (10.02 ppm in **1** and 10.08 ppm in **2**), meanwhile the chemical shifts of hydrogen **d** are significantly different (10.73 ppm in **1** and 9.47 ppm in **2**). This confirms the assumption that the chemical shift of hydrogen **d**, which is spatially closest to the axial ligand, is significantly affected by the type of the axial ligand, while hydrogen **f**, which is further away from the axial ligand, is not very affected by the presence of the axial ligand.

In complex **2**, in addition to hydrogens from **tpbn** and $^{1}$H from **dppn**, hydrogens from **4-pic** are present: **2″**, **3″**, and **4″-Me**. Both **2″** and **3″** integrate as 2 hydrogens each and were picked out as *d* that only couple with each other (coupling observed at $^{1}$H–$^{1}$H COSY NMR). **2″** was assigned as the more downfield *d* of the two (7.65 ppm) and **3″** as the more upfield *d* of the two (7.00 ppm), based on the assumption that the hydrogen in the *ortho*-position relative to nitrogen (**2″**) appears more downfield. Overall, spin system of **2″**-**3″** resembles spin system **3′**-**4′**, as each appear as a pair of doublets. However, it is characteristic of **4-pic** hydrogens such as **2″** and especially **3″** to appear upfield relative to other pyridyl hydrogens, such as that of **tpbn** and **dppn**, which makes the **2″**-**3″** and **3′**-**4′** spin systems easy to distinguish. The singlet at 2.25 ppm integrates as 3 hydrogens and is assigned to the **4″-Me** group.

Complex **3**

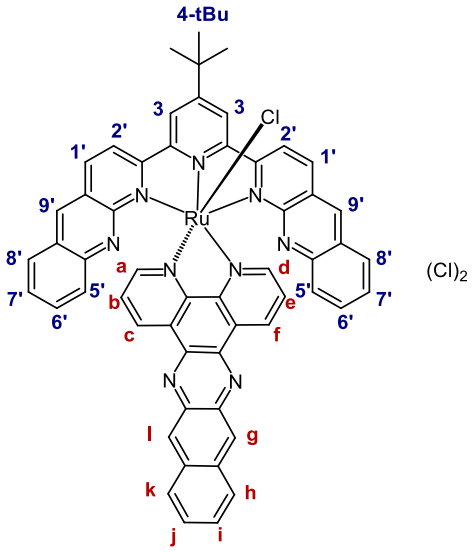


$^1$H NMR (DMSO-$d_6$, 700 MHz): δ 10.82 (**d**, dd, $J_1$ = 4.9 Hz, $J_2$ = 0.7 Hz, 1H), 10.32 (**f**, dd, $J_1$ = 8.4 Hz, $J_2$ = 0.7 Hz, 1H), 9.38 (**g**, s, 1H), 9.34 (**3**, s, 2H), 9.22 (**2′**, d, $J$ = 9.1 Hz, 2H), 9.17 (**9′**, s, 2H), 9.05 (**l**, s, 1H), 8.99 (**c**, dd, $J_1$ = 7.7 Hz, $J_2$ = 0.7 Hz, 1H), 8.88 (**1′**, d, $J$ = 9.1 Hz, 2H), 8.79 (**e**, dd, $J_1$ = 8.4 Hz, $J_2$ = 4.9 Hz, 1H), 8.44 (**h**/**k**, d, $J$ = 9.1 Hz, 1H), 8.35 (**h**/**k**, d, $J$ = 7.7 Hz, 1H), 8.06 (**5′**, d, $J$ = 8.4 Hz, 2H), 7.96 (**a**, dd, $J_1$ = 6.3 Hz, $J_2$ = 1.4 Hz, 1H), 7.77 (**i**/**j**, dd, $J_1$ = 8.4 Hz, $J_2$ = 7.0 Hz, 1H), 7.73 (**i**/**j**, dd, $J_1$ = 7.7 Hz, $J_2$ = 7.0 Hz, 1H), 7.69 (**7′**, dd, $J_1$ = 8.4 Hz, $J_2$ = 7.0 Hz, 2H), 7.50 (**6′**, dd, $J_1$ = 8.4 Hz, $J_2$ = 7.0 Hz, 2H), 7.39 (**b**, dd, $J_1$ = 7.7 Hz, $J_2$ = 6.3 Hz, 1H), 6.75 (**8′**, d, $J$ = 8.4 Hz, 2H), 1.80 (**4-tBu**, s, 9H).

In complex **3,** all hydrogens from **dppn** follow the same trends as described in the hydrogen assignments of complex **1**. Chromophoric ligand **tpbbn** has hydrogens that are similar to that of the ligand **tpbn,** with a few additional aromatic hydrogens. Hydrogens from **tpbbn** that are similar to the hydrogens from **tpbn** were assigned in a similar manner as described for complex **1** (**3** as a singlet at 9.34 ppm, **2′** and **1′** as a

pair of doublets, with **2′** more downfield of the two at 9.22 ppm, and **1′** more upfield of the two at 8.88 ppm). **9′** is assigned to the singlet that integrates as 2 hydrogens (9.17 ppm) and that is not assigned as **3**. Spin system **5′**-**6′**-**7′**-**8′** is identified by correlations observed through $^{1}$H–$^{1}$H COSY NMR. **5′** and **8′** are both doublets with identical *J*-values of 8.4 Hz; **5′** was assigned as the more downfield doublet of the two (8.06 ppm),[(654)] with **8′** appearing at 6.75 ppm. Hydrogens **6′** and **7′** are both doublets of doublets, and the assignments were made based on the correlations to **5′** and **8′** observed with $^{1}$H–$^{1}$H COSY NMR. **6′** was assigned as the hydrogen at 7.50 ppm (dd, $J_{5'6'}$ = 8.4 Hz, $J_{7'6'}$ = 7.0 Hz), and **7′** was assigned as the hydrogen at 7.69 ppm (dd, $J_{8'7'}$ = 8.4 Hz, $J_{6'7'}$ = 7.0 Hz). The singlet at 1.80 ppm integrates as 9 hydrogens and is assigned to the **4-tBu** group.

Complex **4**

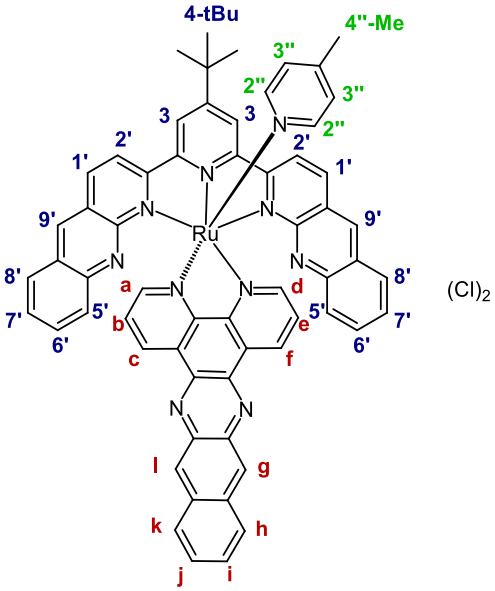


$^{1}$H NMR (MeOD-$d_3$, 700 MHz): δ 10.46 (**f**, d, *J* = 8.4 Hz, 1H), 9.74 (**d**, d, *J* = 4.9 Hz, 1H), 9.28 (**3**, s, 2H), 9.21 (**c**, d, *J* = 7.7 Hz, 1H), 9.18 (**g**, s, 1H), 9.13 (**9′**, s, 2H), 9.05 (**2′**, d, *J* = 8.4 Hz, 2H), 8.93 (**1′**, d, *J* = 9.1 Hz, 2H), 8.91 (**l**, s, 1H), 8.83 (**e**, dd, $J_1$ = 8.4 Hz, $J_2$ =

5.6 Hz, 1H), 8.30 (**h/k**, d, *J* = 8.4 Hz, 1H), 8.22 (**h/k**, d, *J* = 7.7 Hz, 1H), 8.02 (**5′**, d, *J* = 7.7 Hz, 2H), 7.88 (**a**, d, *J* = 5.6 Hz, 1H), 7.79 (**2″**, d, *J* = 7.0 Hz, 2H), 7.74 (**7′**, dd, $J_1$ = 8.4 Hz, $J_2$ = 7.0 Hz, 2H), 7.67 (**i**, **j**, m, 2H), 7.53 (**6′**, dd, $J_1$ = 7.7 Hz, $J_2$ = 7.0 Hz, 2H), 7.43 (**b**, dd, $J_1$ = 7.7 Hz, $J_2$ = 5.6 Hz, 1H), 7.01 (**8′**, d, *J* = 8.4 Hz, 2H), 6.97 (**3″**, d, *J* = 6.3 Hz, 2H), 2.22 (**4″-Me**, s, 3H), 1.81 (**4-tBu**, s, 9H).

Hydrogens in complex **4** were assigned based off of the $^1$H assignments for complex **3**, except for the hydrogens **d** and **f**. Like in complex **2**, in complex **4** hydrogen **f** (*para*-position) appears more downfield than hydrogen **d** (*ortho*-position). In complex **4**, in addition to hydrogens from **tpbbn** and **dppn**, hydrogens from **4-pic** are present: **2″**, **3″**, and **4″-Me**. Similar to complex **2**, **2″** was assigned as a doublet at 7.79 ppm and **3″** as a doublet at 6.97 ppm. The singlet at 2.22 ppm integrates as 3 hydrogens and is assigned to the **4″-Me** group.

Complex **5**

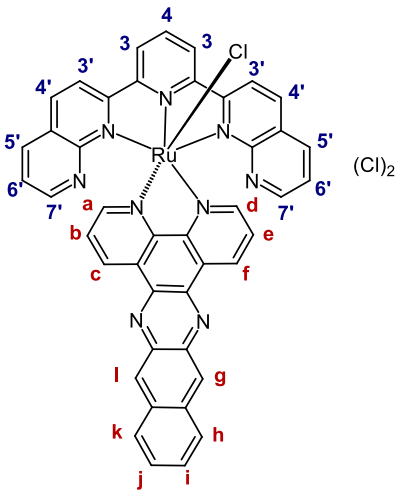

$^1$H NMR (MeOD-$d_3$, 700 MHz): δ 10.74 (**d**, dd, $J_1$ = 4.9 Hz, $J_2$ = 1.4 Hz, 1H), 10.03 (**f**, dd, $J_1$ = 8.4 Hz, $J_2$ = 1.4 Hz, 1H), 9.15 (**c**, dd, $J_1$ = 7.7 Hz, $J_2$ = 0.7 Hz, 1H), 9.14 (**g**, s, 1H), 9.09 (**3**, d, $J$ = 8.4 Hz, 2H), 8.99 (**l**, s, 1H), 8.81 (**3′**, d, $J$ = 9.1 Hz, 2H), 8.54 (**4′**, d, $J$ = 8.4 Hz, 2H), 8.45 (**e**, dd, $J_1$ = 8.4 Hz, $J_2$ = 4.9 Hz, 1H), 8.38 (**4**, t, $J$ = 8.4 Hz, 1H), 8.29 (**h**,**k**, m, 2H), 8.27 (**5′**, dd, $J_1$ = 7.7 Hz, $J_2$ = 1.4 Hz, 2H), 8.01 (**7′**, dd, $J_1$ = 4.9 Hz, $J_2$ = 1.4 Hz, 2H), 7.87 (**a**, dd, $J_1$ = 5.6 Hz, $J_2$ = 0.7 Hz, 1H), 7.69 (**i**, **j**, m, 2H), 7.33 (**6′**, dd, $J_1$ = 7.7 Hz, $J_2$ = 4.9 Hz, 2H), 7.27 (**b**, dd, $J_1$ = 7.7 Hz, $J_2$ = 5.6 Hz, 1H).

Hydrogens in complex **5** were assigned based off of the $^1$H assignments for complex **1**. Since the **4-tBu** group is absent in complex **5**, hydrogen **3** that was a singlet in complex **1** appears as the doublet at 9.09 ppm ($J$ = 8.4 Hz), and hydrogen **4** appears as the triplet at 8.38 ppm ($J$ = 8.4 Hz).

Complex **6**

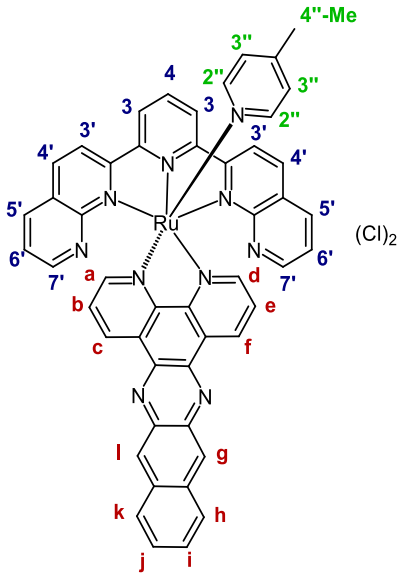


$^1$H NMR (MeOD-$d_3$, 500 MHz): δ 10.10 (**f**, dd, $J_1$ = 8.0 Hz, $J_2$ = 1.0 Hz, 1H), 9.50 (**d**, dd, $J_1$ = 5.5 Hz, $J_2$ = 1.5 Hz, 1H), 9.32 (**c**, dd, $J_1$ = 8.0 Hz, $J_2$ = 1.0 Hz, 1H), 9.19 (**g**, s, 1H), 9.18 (**3**, d, $J$ = 8.5 Hz, 2H), 9.02 (**l**, s, 1H), 8.91 (**3′**, d, $J$ = 8.5 Hz, 2H), 8.73 (**4′**, d, $J$ = 8.5 Hz, 2H), 8.51 (**4**, t, $J$ = 8.5 Hz, 1H), 8.44 (**e**, dd, $J_1$ = 8.5 Hz, $J_2$ = 5.5 Hz, 1H), 8.38 (**5′**, dd, $J_1$ = 8.5 Hz, $J_2$ = 2.0 Hz, 2H), 8.36 (**h**/**k**, d, $J$ = 8.0 Hz, 1H), 8.29 (**h**/**k**, d, $J$ = 8.0 Hz, 1H), 8.15 (**7′**, dd, $J_1$ = 4.5 Hz, $J_2$ = 2.0 Hz, 2H), 7.81 (**a**, dd, $J_1$ = 5.5 Hz, $J_2$ = 1.0 Hz, 1H), 7.72 (**i**, **j**, m, 2H), 7.65 (**2″**, d, $J$ = 6.5 Hz, 2H), 7.44 (**b**, dd, $J_1$ = 8.0 Hz, $J_2$ = 5.5 Hz, 1H), 7.44 (**6′**, dd, $J_1$ = 8.0 Hz, $J_2$ = 4.0 Hz, 2H), 7.00 (**3″**, d, $J$ = 6.0 Hz, 2H), 2.25 (**4″-Me**, s, 3H).

Hydrogens in complex **6** were assigned based off the $^1$H assignments of complex **5**, except for the hydrogens **d** and **f**. Like in complex **2**, in complex **6** hydrogen **f** (*para*-position) appears more downfield than hydrogen **d** (*ortho*-position). In complex **6**, in

addition to $^1$H from **dnp** and **dppn**, $^1$H from **4-pic** are present: **2″**, **3″**, and **4″-Me**. Similar to complex **2**, **2″** was assigned as a doublet at 7.65 ppm and **3″** as a doublet at 7.00 ppm. The singlet at 2.25 ppm integrates as 3 hydrogens and is assigned to the **4″-Me** group.

Complex **7**

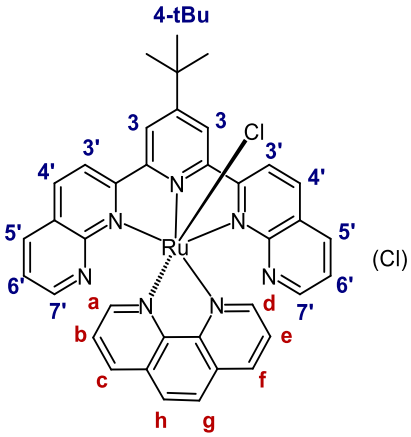


$^1$H NMR (MeOD-$d_3$, 500 MHz): δ 10.62 (**d**, dd, $J_1$ = 5.5 Hz, $J_2$ = 1.5 Hz, 1H), 9.08 (**3**, s, 2H), 8.90 (**3′**, d, $J$ = 8.5 Hz, 2H), 8.89 (**f**, dd, $J_1$ = 8.0 Hz, $J_2$ = 1.5 Hz, 1H), 8.49 (**4′**, d, $J$ = 8.5 Hz, 2H), 8.33 (**g**, d, $J$ = 9.0 Hz, 1H), 8.29 (**e**, dd, $J_1$ = 8.0 Hz, $J_2$ = 5.5 Hz, 1H), 8.23 (**5′**, dd, $J_1$ = 8.0 Hz, $J_2$ = 2.0 Hz, 2H), 8.07 (**c**, dd, $J_1$ = 8.0 Hz, $J_2$ = 1.0 Hz, 1H), 7.90 (**h**, d, $J$ = 9.0 Hz, 1H), 7.75 (**7′**, dd, $J_1$ = 4.5 Hz, $J_2$ = 2.0 Hz, 2H), 7.73 (**a**, dd, $J_1$ = 5.5 Hz, $J_2$ = 1.0 Hz, 1H), 7.31 (**6′**, dd, $J_1$ = 8.0 Hz, $J_2$ = 4.0 Hz, 2H), 7.15 (**b**, dd, $J_1$ = 8.0 Hz, $J_2$ = 5.5 Hz, 1H), 1.78 (**4-tBu**, s, 9H).

In complex **7**, hydrogens from **tpbn** were assigned based off the $^1$H assignments of complex **1**. Since **dppn** is replaced with **phen** in complex **7**, there are less magnetically

inequivalent hydrogens than in complex **1** (only **a-g** in complex **7**, while there are **a-l** in complex **1**). Hydrogens **d-e-f** and **a-b-c** were assigned following the same strategy as was used for the assignment of hydrogens **d-e-f** and **a-b-c** in complex **1**. When chemical shifts of hydrogen **f** in complex **1** and hydrogen **f** in complex **7** are compared, they are found to be quite different (10.02 ppm in **1** and 8.89 ppm in **7**). This outlines the effect of the spatial proximity of the non-coordinated nitrogen from **dppn** on hydrogen **f**, as the proximity to this nitrogen moves chemical shift of **f** downfield. Since **phen** does not have a non-coordinated nitrogen analogous to that of **dppn**, the chemical shift of **f** is moved upfield in complex **7** when compared to chemical shift of **f** in complex **1**. The same effect is responsible for hydrogen **c** being more upfield in complex **7** than in complex **1** (9.16 ppm in **1** and 8.07 ppm in **7**). Hydrogens **h** and **g** form a two-spin system, which is identified by correlations observed with $^{1}H–^{1}H$ COSY NMR, with **g** assigned as the more downfield of the two (8.33 ppm) and **h** assigned as the more upfield of the two (7.90 ppm) based on the assumption that hydrogens on the side of **phen** that is facing **chloride** appear more downfield.

Complex **8**

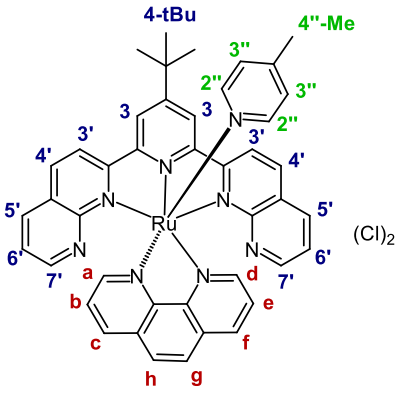

$^1$H NMR (MeOD-$d_3$, 500 MHz): δ 9.44 (**d**, dd, $J_1$ = 5.5 Hz, $J_2$ = 1.5 Hz, 1H), 9.14 (**3**, s, 2H), 9.01 (**3′**, d, $J$ = 8.5 Hz, 2H), 8.94 (**f**, dd, $J_1$ = 8.5 Hz, $J_2$ = 1.5 Hz, 1H), 8.68 (**4′**, d, $J$ = 8.5 Hz, 2H), 8.35 (**5′**, dd, $J_1$ = 8.5 Hz, $J_2$ = 2.0 Hz, 2H), 8.32 (**g**, d, $J$ = 9.0 Hz, 1H), 8.29 (**e**, dd, $J_1$ = 8.5 Hz, $J_2$ = 5.5 Hz, 1H), 8.19 (**c**, dd, $J_1$ = 8.5 Hz, $J_2$ = 1.5 Hz, 1H), 7.92 (**h**, d, $J$ = 9.0 Hz, 1H), 7.92 (**7′**, dd, $J_1$ = 4.5 Hz, $J_2$ = 2.0 Hz, 2H), 7.67 (**a**, dd, $J_1$ = 5.5 Hz, $J_2$ = 1.0 Hz, 1H), 7.66 (**2″**, d, $J$ = 6.5 Hz, 2H), 7.42 (**6′**, dd, $J_1$ = 8.0 Hz, $J_2$ = 4.5 Hz, 2H), 7.29 (**b**, dd, $J_1$ = 8.0 Hz, $J_2$ = 5.5 Hz, 1H), 6.97 (**3″**, d, $J$ = 6.5 Hz, 2H), 2.23 (**4″-Me**, s, 3H), 1.76 (**4-tBu**, s, 9H).

The hydrogens of complex **8** were assigned following based on the $^1$H assignments of complex **7**. Unlike what was observed in other complexes containing the **4-pic** axial ligand (complexes **2**, **4**, and **6**), hydrogen **d** is still assigned as the most downfield, not hydrogen **f**. This assignment is based on the observed *J*-values of coupling with hydrogen **e** and the assumption that $J_{fe} > J_{de}$. Hydrogen **d** is assigned as the doublet of doublets at 9.44 ppm ($J_{de}$ = 5.5 Hz, $J_{df}$ = 1.5 Hz), and hydrogen **f** is assigned as the doublet of doublets at 8.94 ppm ($J_{fe}$ = 8.5 Hz, $J_{fd}$ = 1.5 Hz). When chemical shifts of hydrogen **d** in complex **7** and hydrogen **d** in complex **8** are compared, they are found to be significantly different (10.62 ppm in **7** and 9.44 ppm in **8**), just like in complex **1** *vs.* complex **2**. However, even with the upfield shift of hydrogen **d** caused by the absence of **chloride**, hydrogen **d** still stays the most downfield hydrogen in complex **8** because hydrogen **f** from **phen** (~9 ppm) is noticeably more upfield than hydrogen **f** from **dppn** (~10 ppm). In complex **8**, in addition to $^1$H from **tpbn** and **phen**, $^1$H from **4-pic** are present: **2″**, **3″**, and **4″-Me**. Similar to complex **2**, **2″** was assigned as a doublet at 7.66 ppm and **3″** as a doublet at 6.97 ppm. The singlet at 2.23 ppm integrates as 3 hydrogens and is assigned to the **4″-Me** group.

Complex **9**

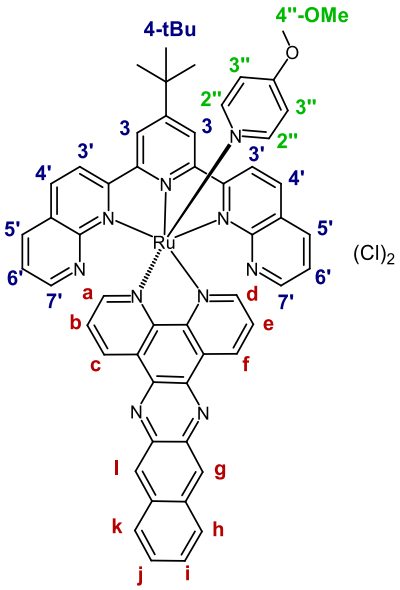


$^1$H NMR (MeOD-$d_3$, 500 MHz): δ 10.08 (**f**, dd, $J_1$ = 8.0 Hz, $J_2$ = 1.0 Hz, 1H), 9.49 (**d**, dd, $J_1$ = 5.0 Hz, $J_2$ = 1.0 Hz, 1H), 9.28 (**c**, dd, $J_1$ = 8.5 Hz, $J_2$ = 2.0 Hz, 1H), 9.18 (**3**, s, 2H), 9.17 (**g**, s, 1H), 9.06 (**3′**, d, $J$ = 8.5 Hz, 2H), 9.01 (**l**, s, 1H), 8.73 (**4′**, d, $J$ = 8.5 Hz, 2H), 8.44 (**e**, dd, $J_1$ = 8.0 Hz, $J_2$ = 5.5 Hz, 1H), 8.37 (**5′**, dd, $J_1$ = 8.0 Hz, $J_2$ = 2.0 Hz, 2H), 8.32 (**h**/**k**, d, $J$ = 7.5 Hz, 1H), 8.28 (**h**/**k**, d, $J$ = 8.0 Hz, 1H), 8.14 (**7′**, dd, $J_1$ = 4.0 Hz, $J_2$ = 1.5 Hz, 2H), 7.79 (**a**, dd, $J_1$ = 6.0 Hz, $J_2$ = 1.5 Hz, 1H), 7.71 (**i**, **j**, m, 2H), 7.56 (**2″**, d, $J$ = 7.5 Hz, 2H), 7.43 (**6′**, **b**, m, 3H), 6.73 (**3″**, d, $J$ = 7.0 Hz, 2H), 3.75 (**4″-OMe**, s, 3H), 1.78 (**4-tBu**, s, 9H).

Hydrogens in complex **9** were assigned based off the $^1$H assignments of complex **2**, and overall follow the same trend as in complex **2**. As expected, the methyl group signal from the axial ligand **4-mp** in complex **9** (**4″-OMe** at 3.75 ppm) is moved significantly downfield relative to the methyl group signal from the axial ligand **4-pic** in complex **2** (**4″-Me** at 2.25 ppm).

## 6. ESI⁺ MASS SPECTRA OF RU(II) COMPLEXES 1–9

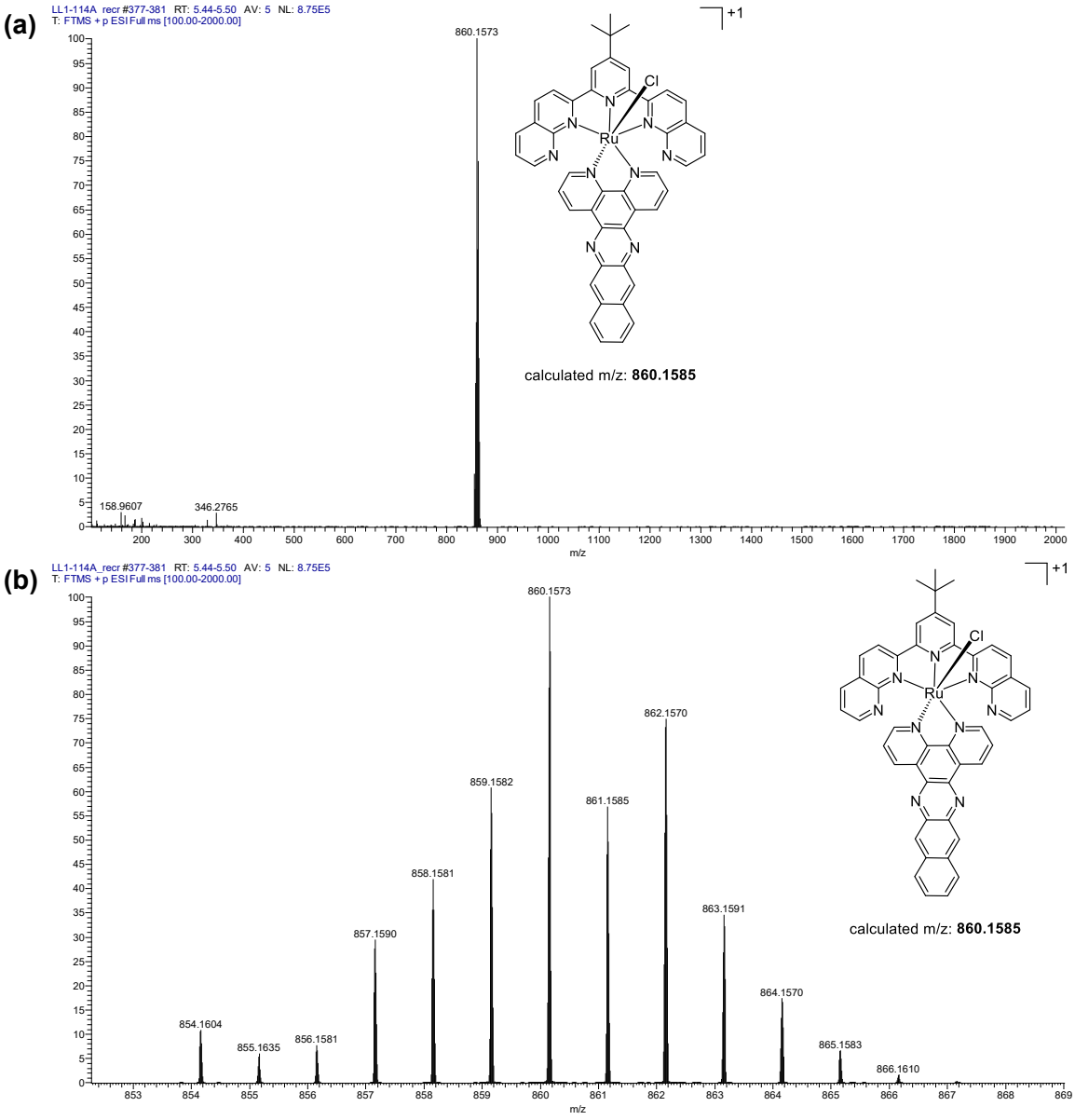


**Appendix Figure S29.** (a) High resolution ESI⁺ mass spectrum for complex **1**. (b) Zoom of 860.1573 peak showing isotopic distribution.

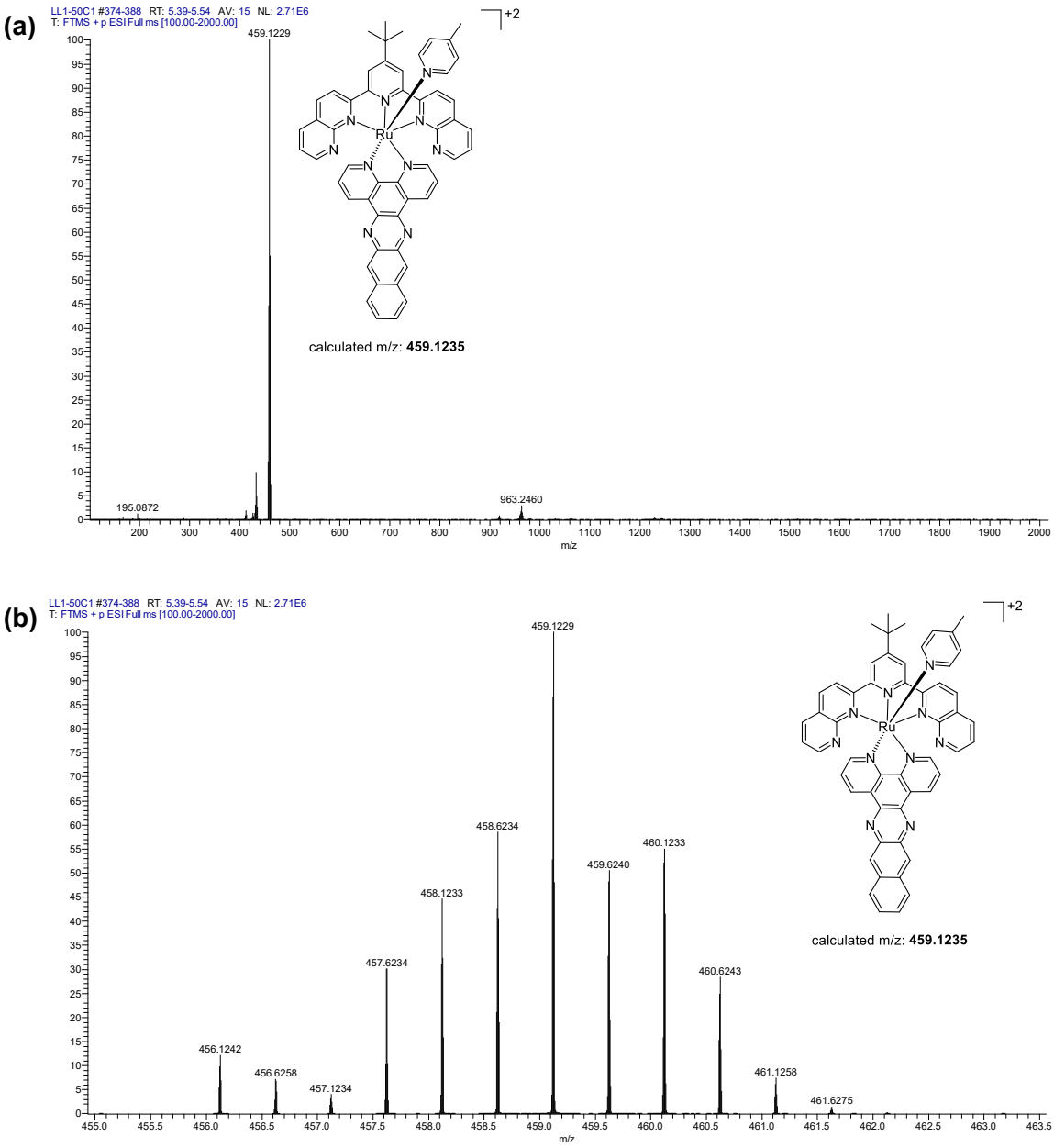


**Appendix Figure S30.** (a) High resolution ESI$^+$ mass spectrum for complex **2**. (b) Zoom of 459.1229 peak showing isotopic distribution.

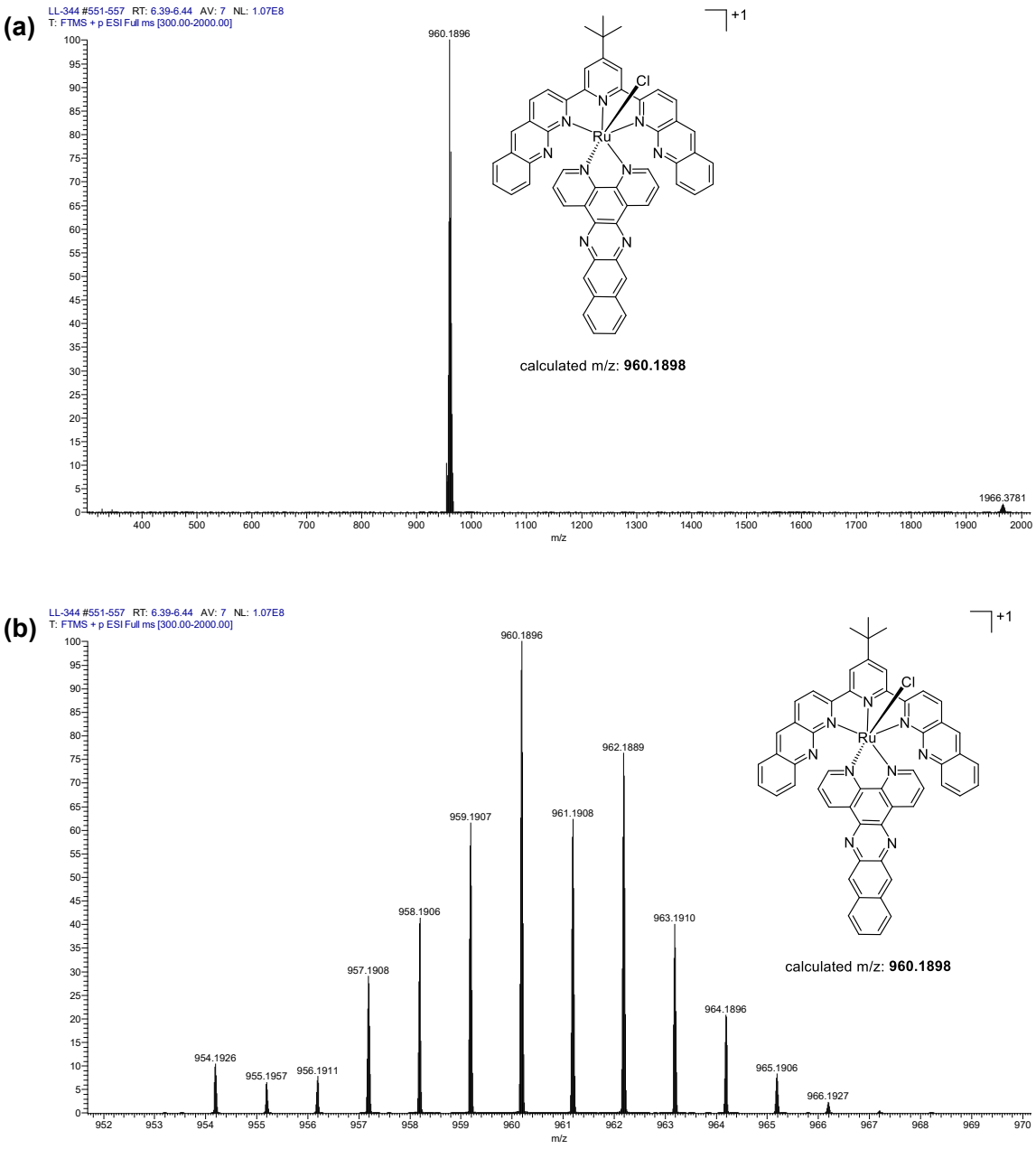


**Appendix Figure S31.** (a) High resolution ESI$^+$ mass spectrum for complex **3**. (b) Zoom of 960.1896 peak showing isotopic distribution

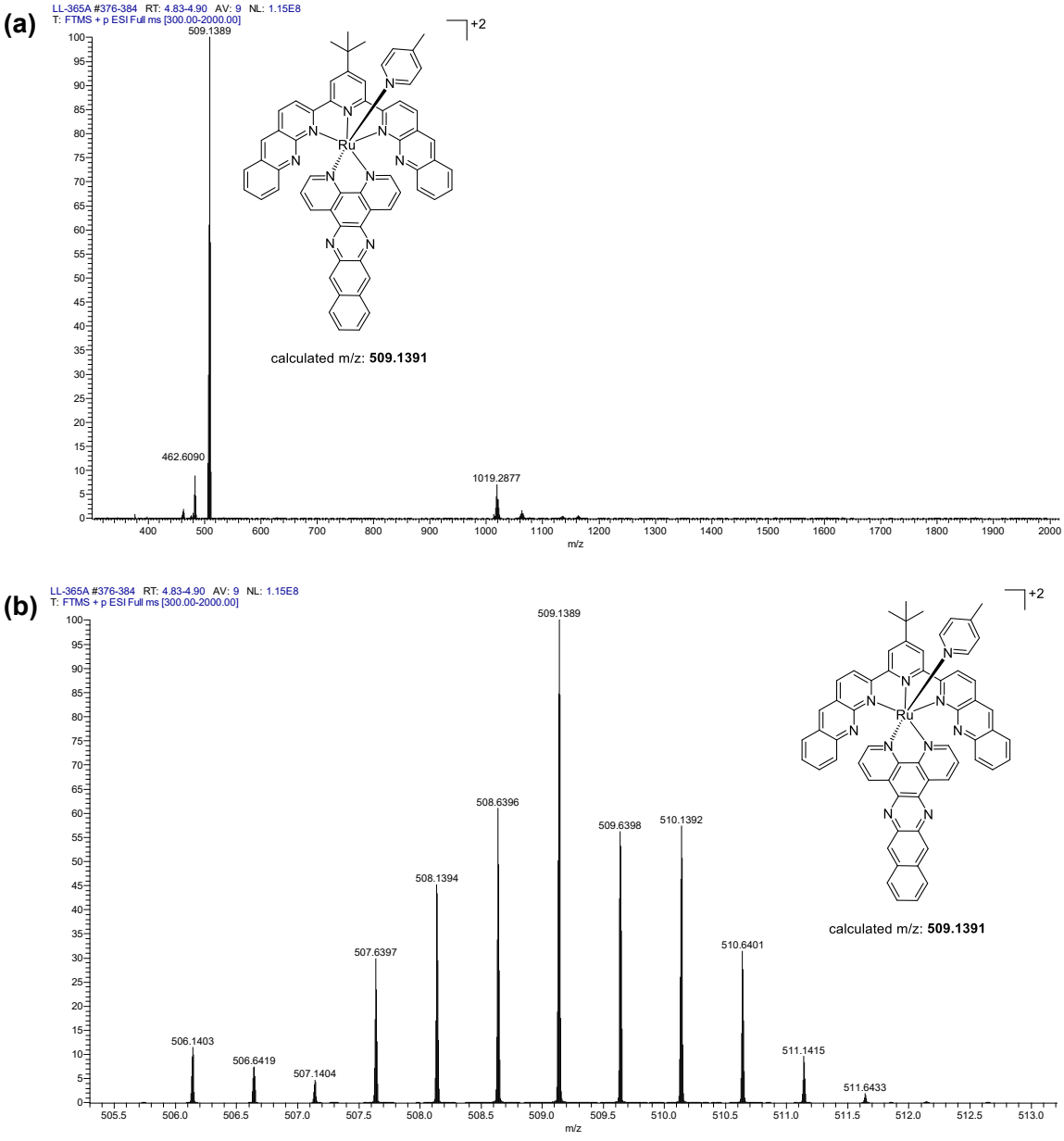


**Appendix Figure S32.** (a) High resolution ESI$^+$ mass spectrum for complex **4**. (b) Zoom of 509.1389 peak showing isotopic distribution.

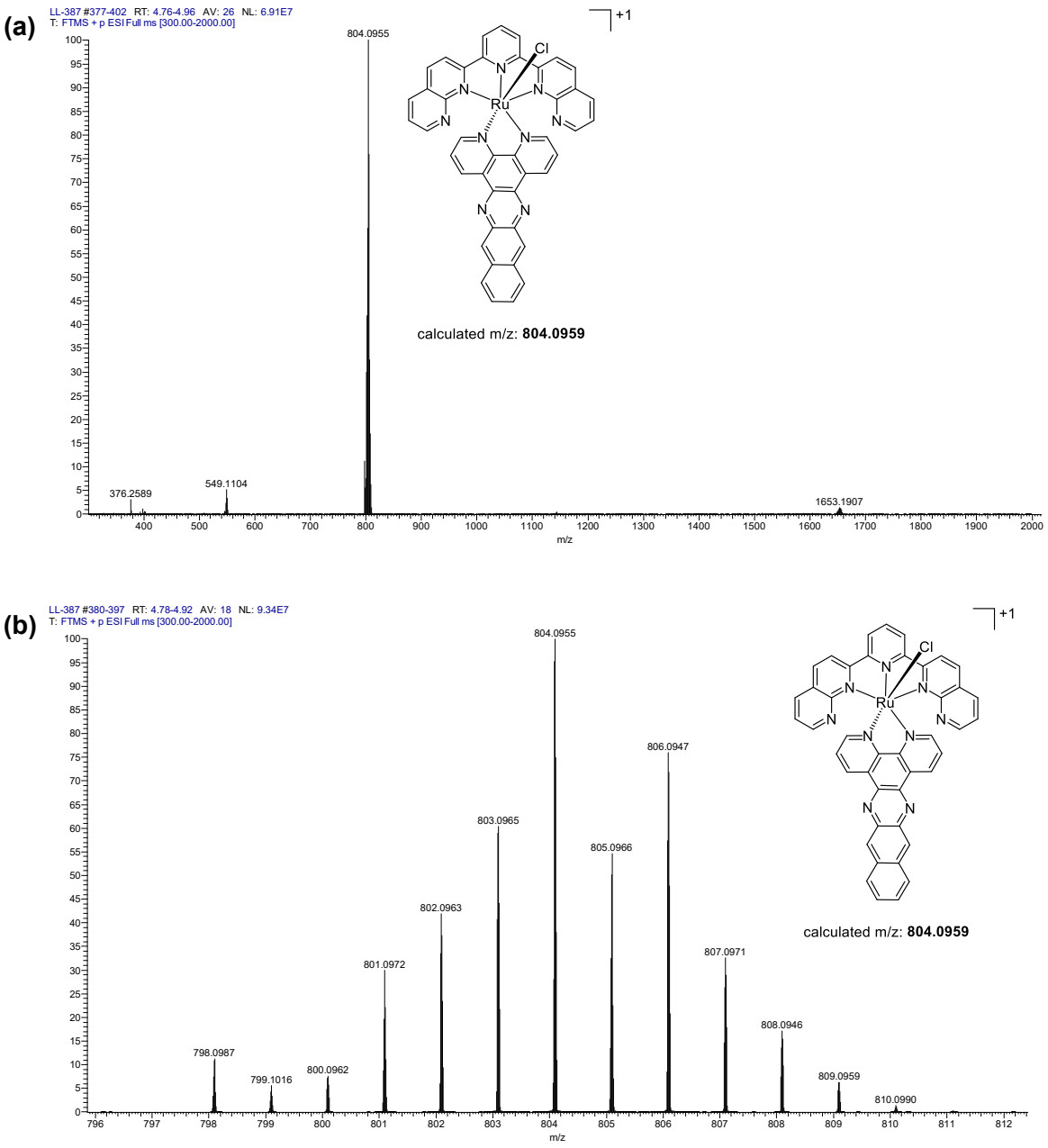


**Appendix Figure S33.** (a) High resolution ESI$^+$ mass spectrum for complex **5**. (b) Zoom of 804.0955 peak showing isotopic distribution.

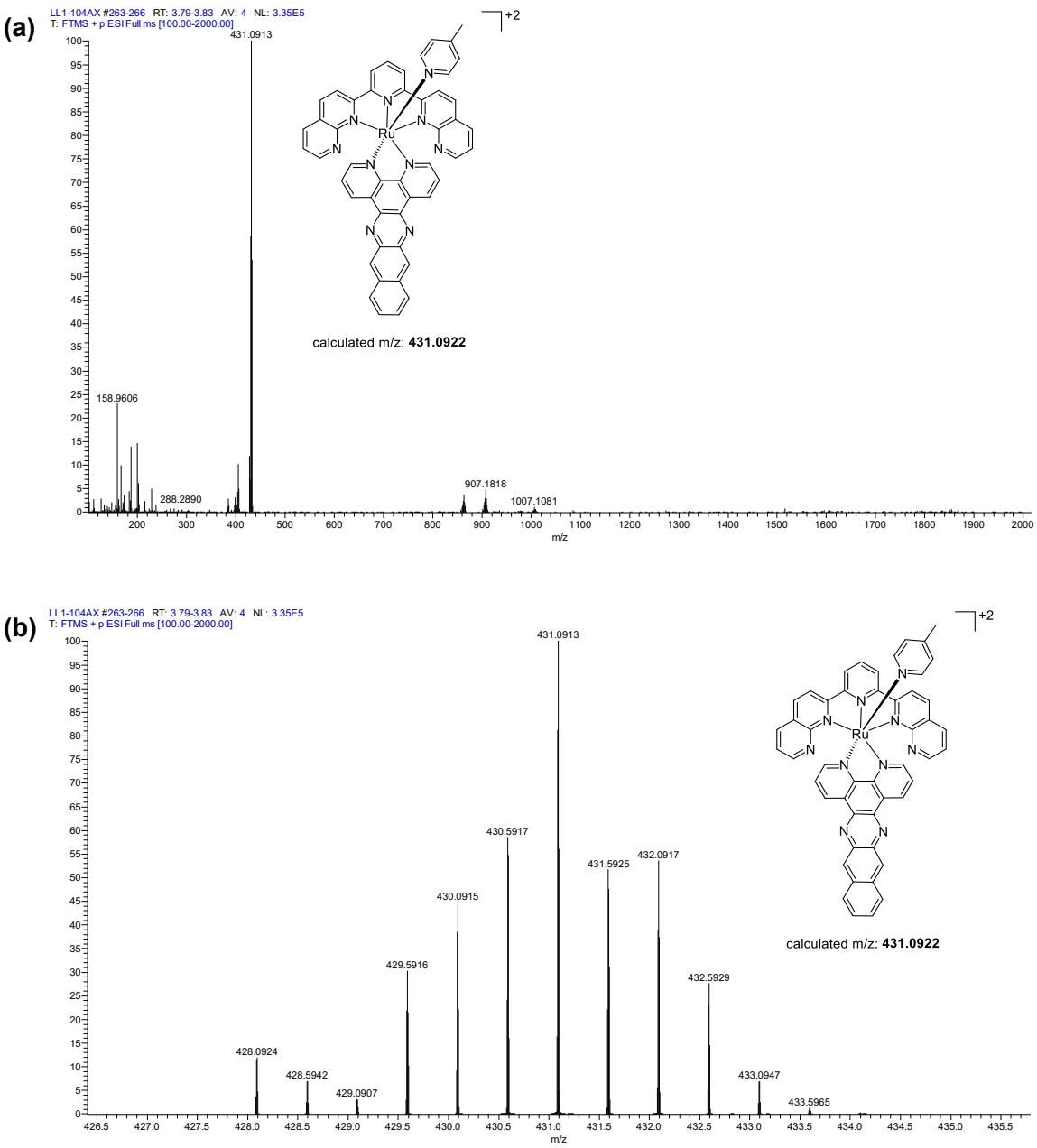


**Appendix Figure S34.** (a) High resolution ESI$^+$ mass spectrum for complex **6**. (b) Zoom of 431.0913 peak showing isotopic distribution.

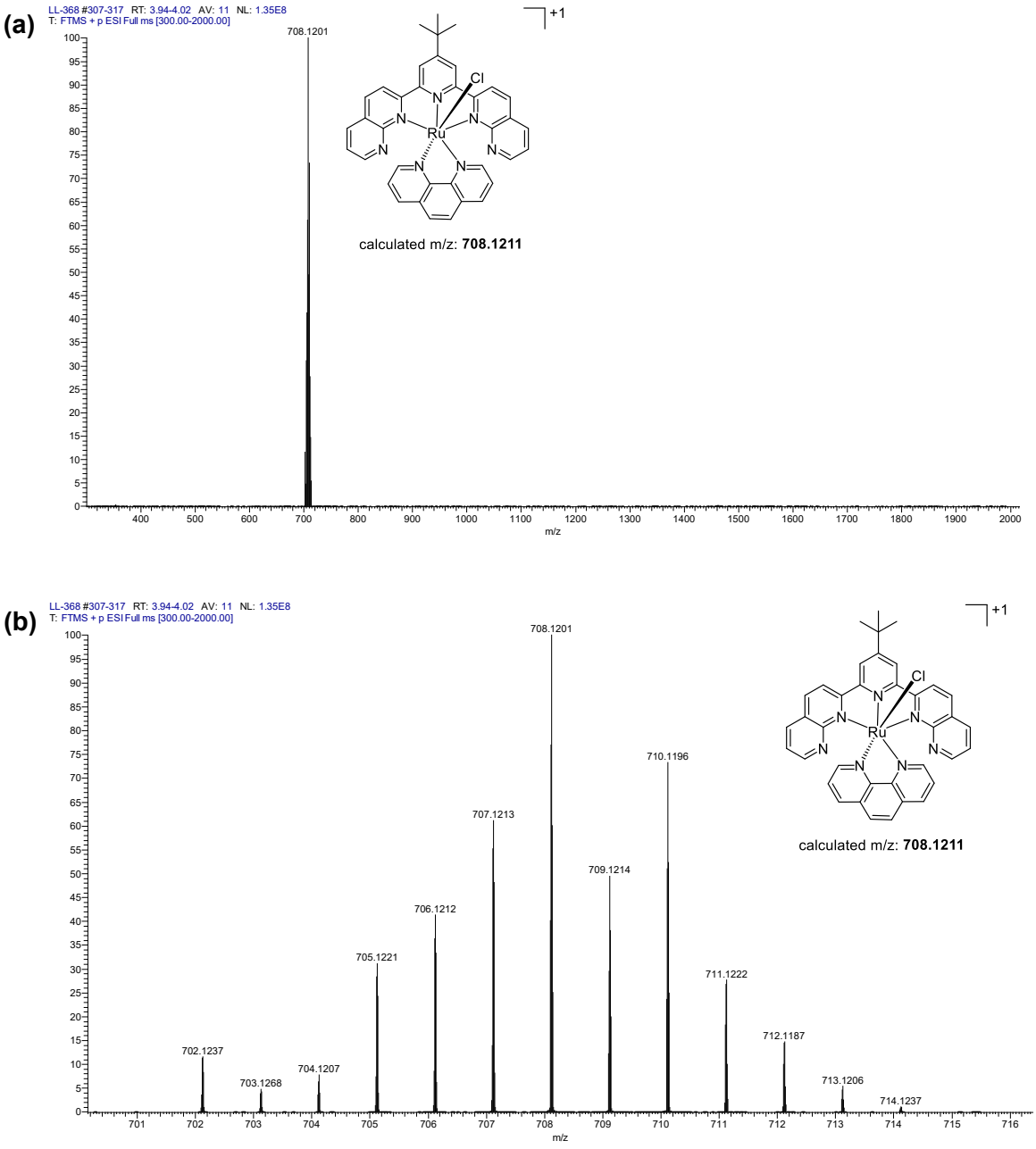


**Appendix Figure S35.** (a) High resolution ESI$^+$ mass spectrum for complex **7**. (b) Zoom of 708.1201 peak showing isotopic distribution.

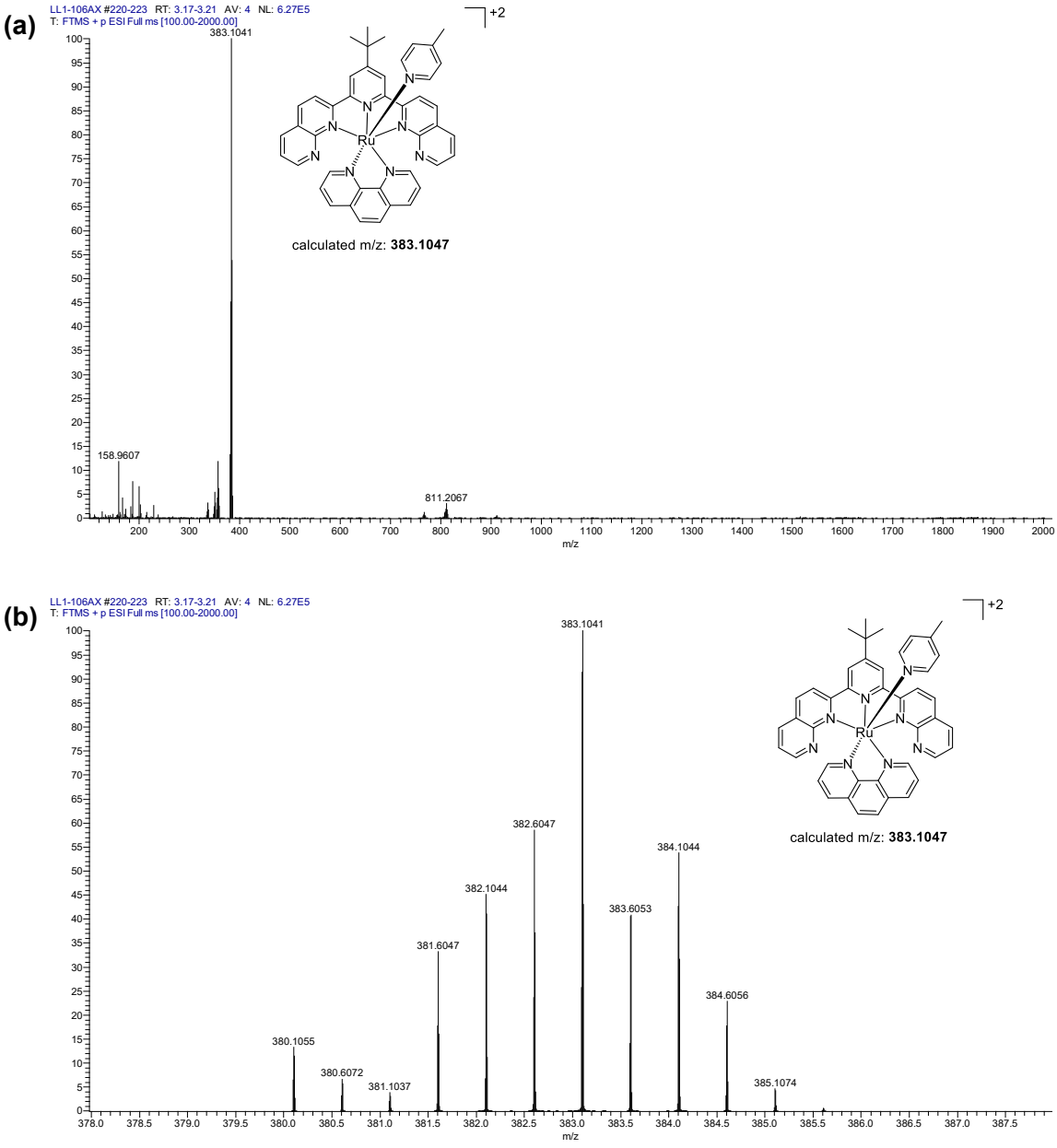


**Appendix Figure S36.** (a) High resolution ESI$^+$ mass spectrum for complex **8**. (b) Zoom of 383.1041 peak showing isotopic distribution.

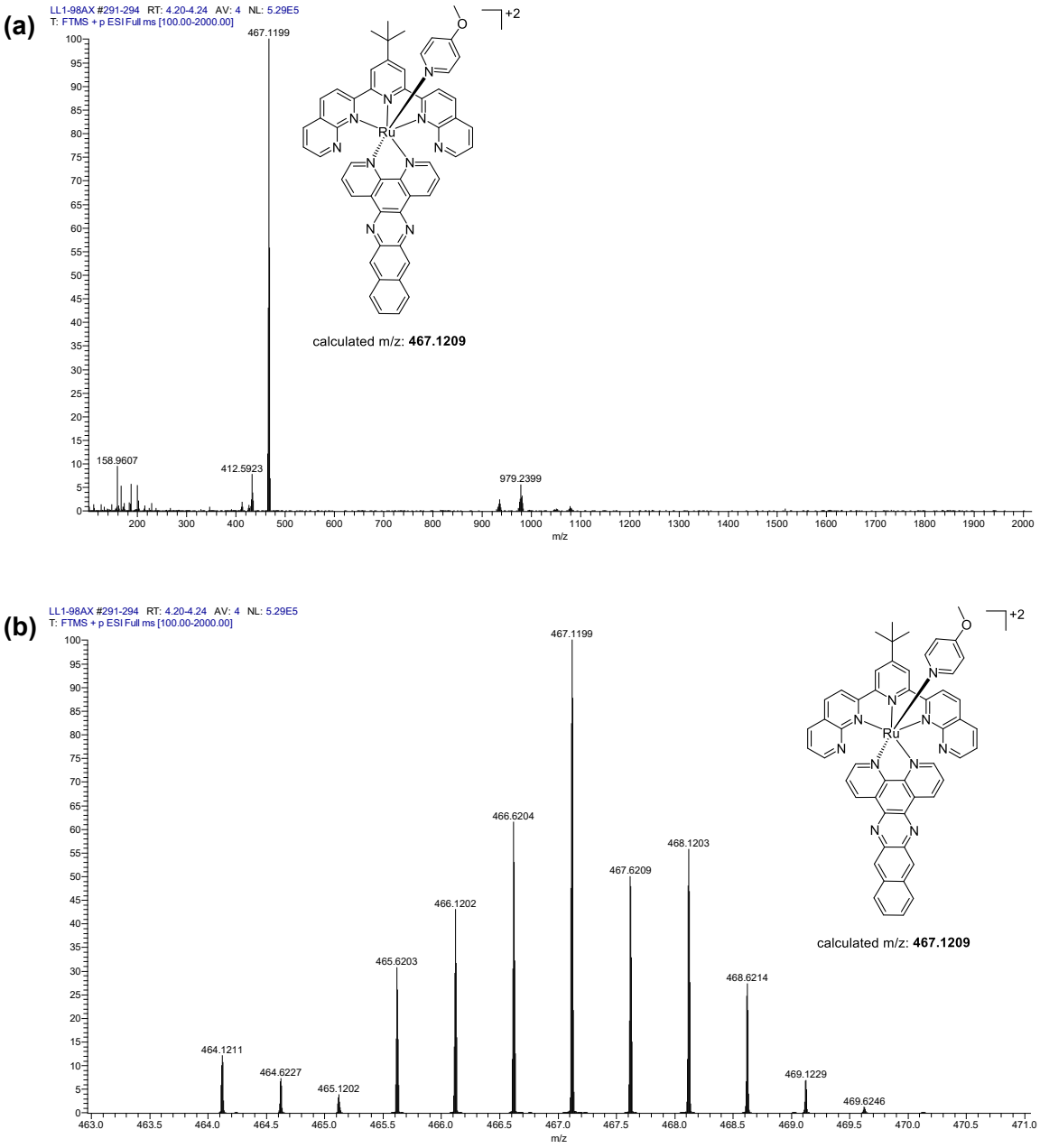


**Appendix Figure S37.** (a) High resolution ESI$^+$ mass spectrum for complex **9**. (b) Zoom of 467.1199 peak showing isotopic distribution.

## 7. HPLC CHROMATOGRAMS OF RU(II) COMPLEXES 1–9

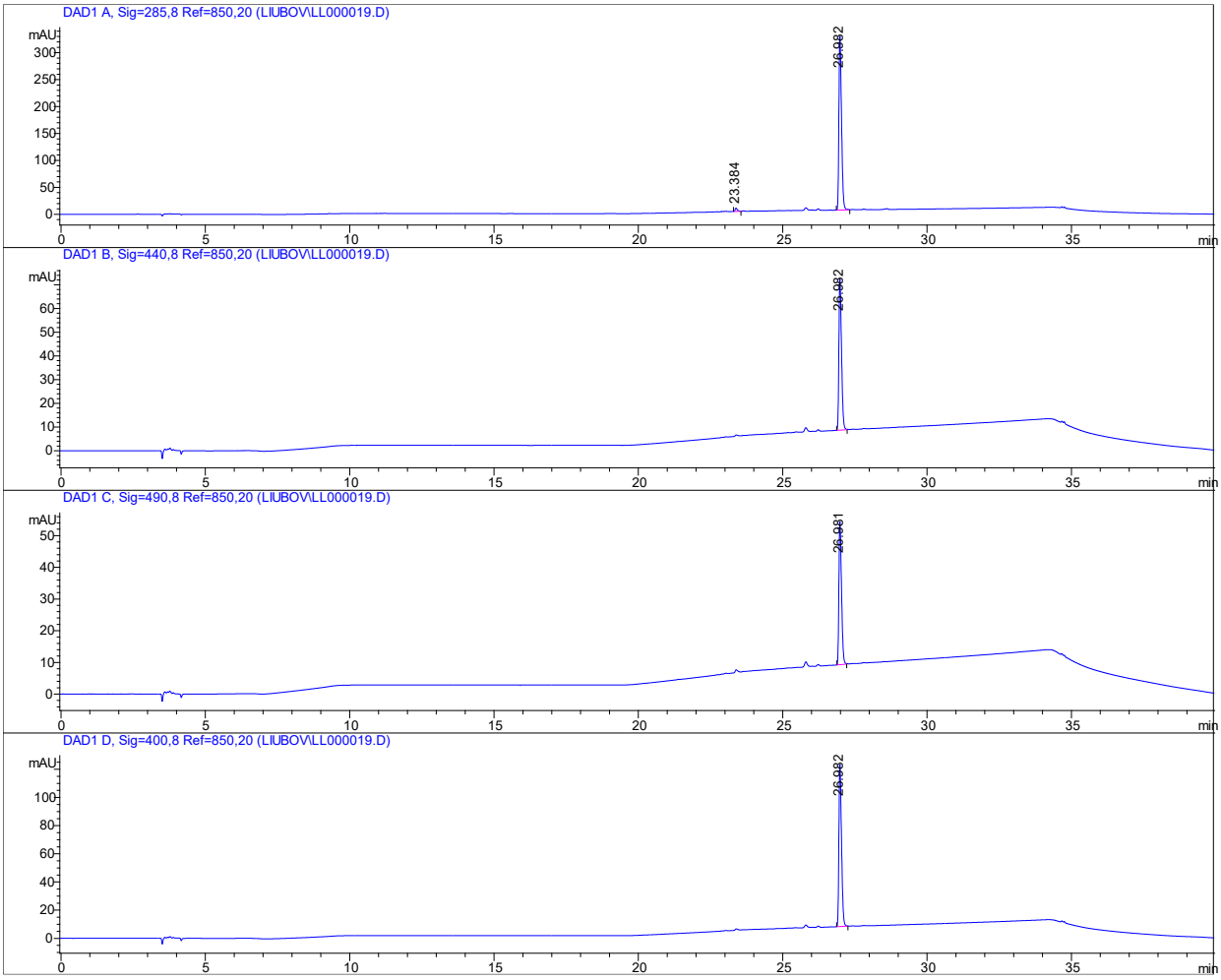


**Appendix Figure S38.** HPLC chromatogram of complex **1** collected at the following wavelengths: 285, 440, 490, 400 nm (98.3% purity by peak area).

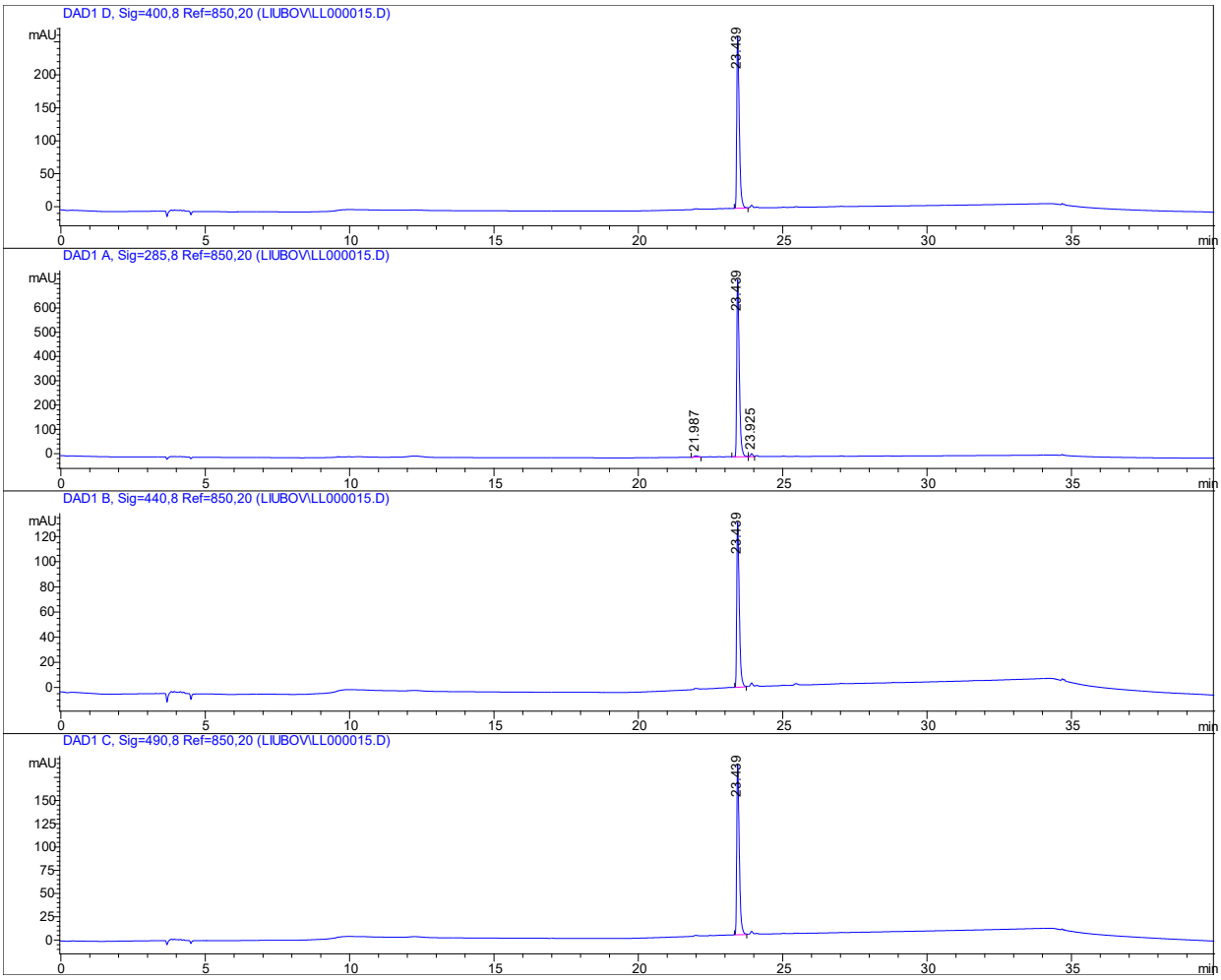


**Appendix Figure S39.** HPLC chromatogram of complex **2** collected at the following wavelengths: 400, 285, 440, 490 nm (97.2% purity by peak area).

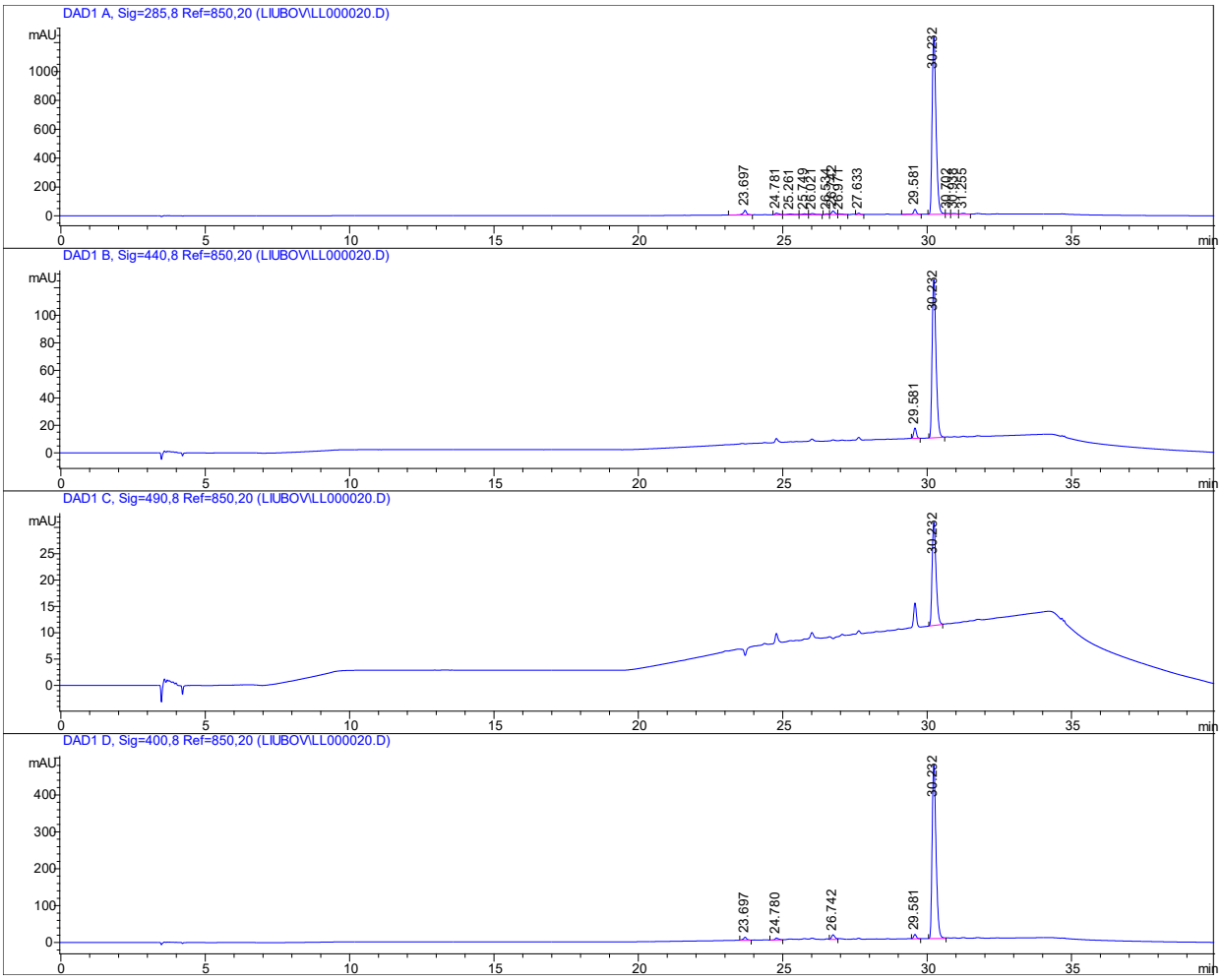


**Appendix Figure S40.** HPLC chromatogram of complex **3** collected at the following wavelengths: 285, 440, 490, 400 nm (94.2% purity by peak area).

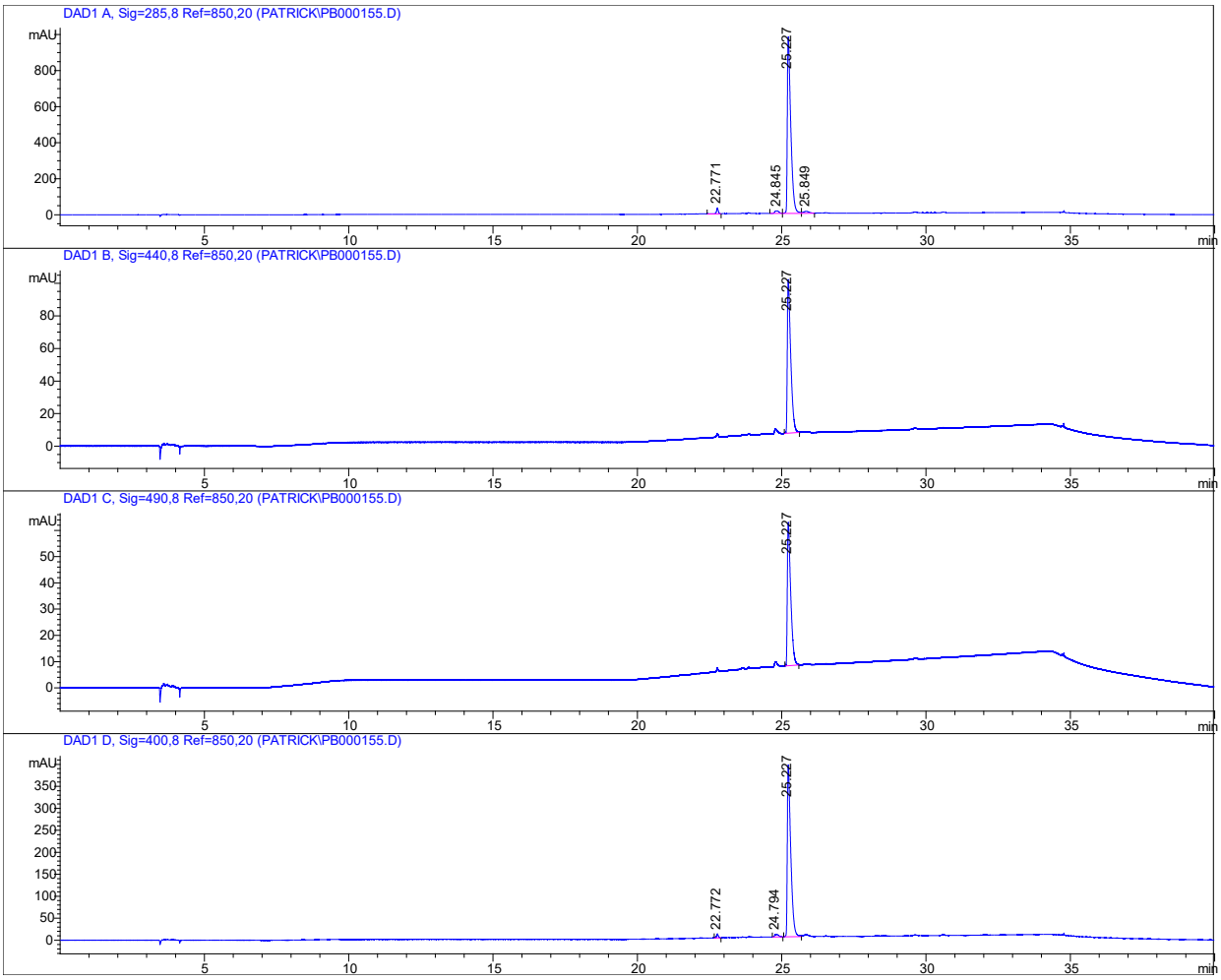


**Appendix Figure S41.** HPLC chromatogram of complex **4** collected at the following wavelengths: 285, 440, 490, 400 nm (94.8% purity by peak area).

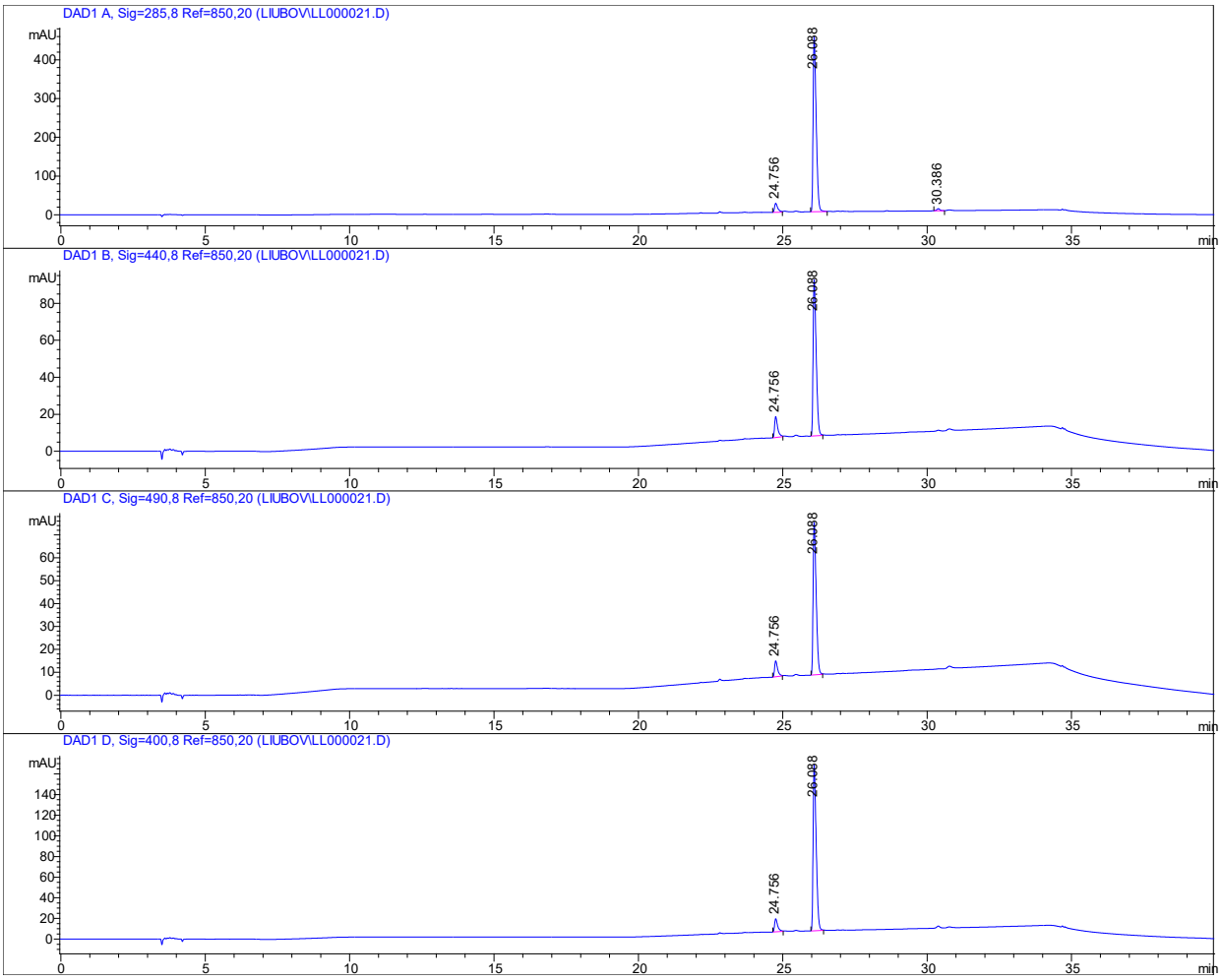


**Appendix Figure S42.** HPLC chromatogram of complex **5** collected at the following wavelengths: 285, 440, 490, 400 nm (88.3% purity by peak area).

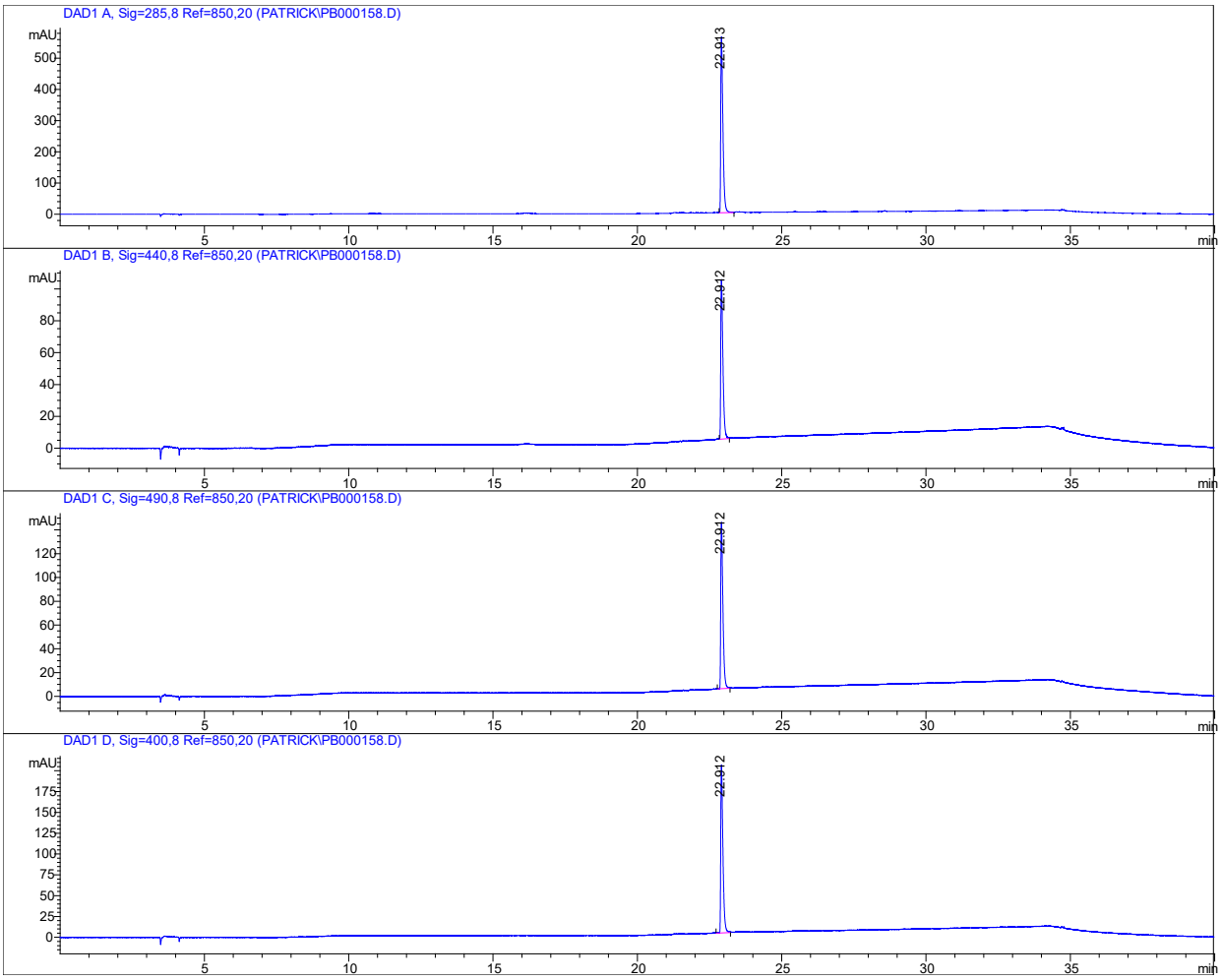


**Appendix Figure S43.** HPLC chromatogram of complex **6** collected at the following wavelengths: 285, 440, 490, 400 nm (100% purity by peak area).

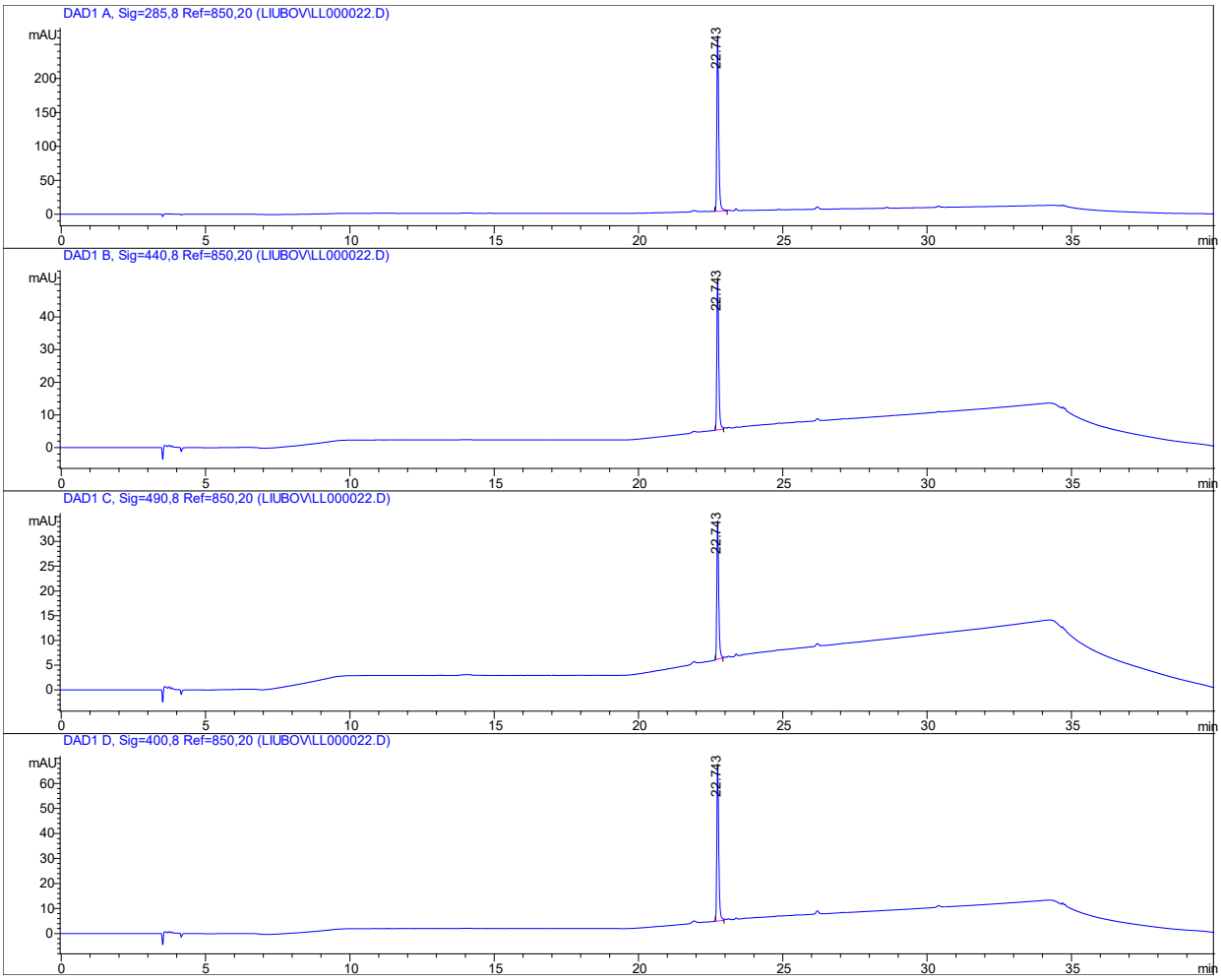


**Appendix Figure S44.** HPLC chromatogram of complex **7** collected at the following wavelengths: 285, 440, 490, 400 nm (100% purity by peak area).

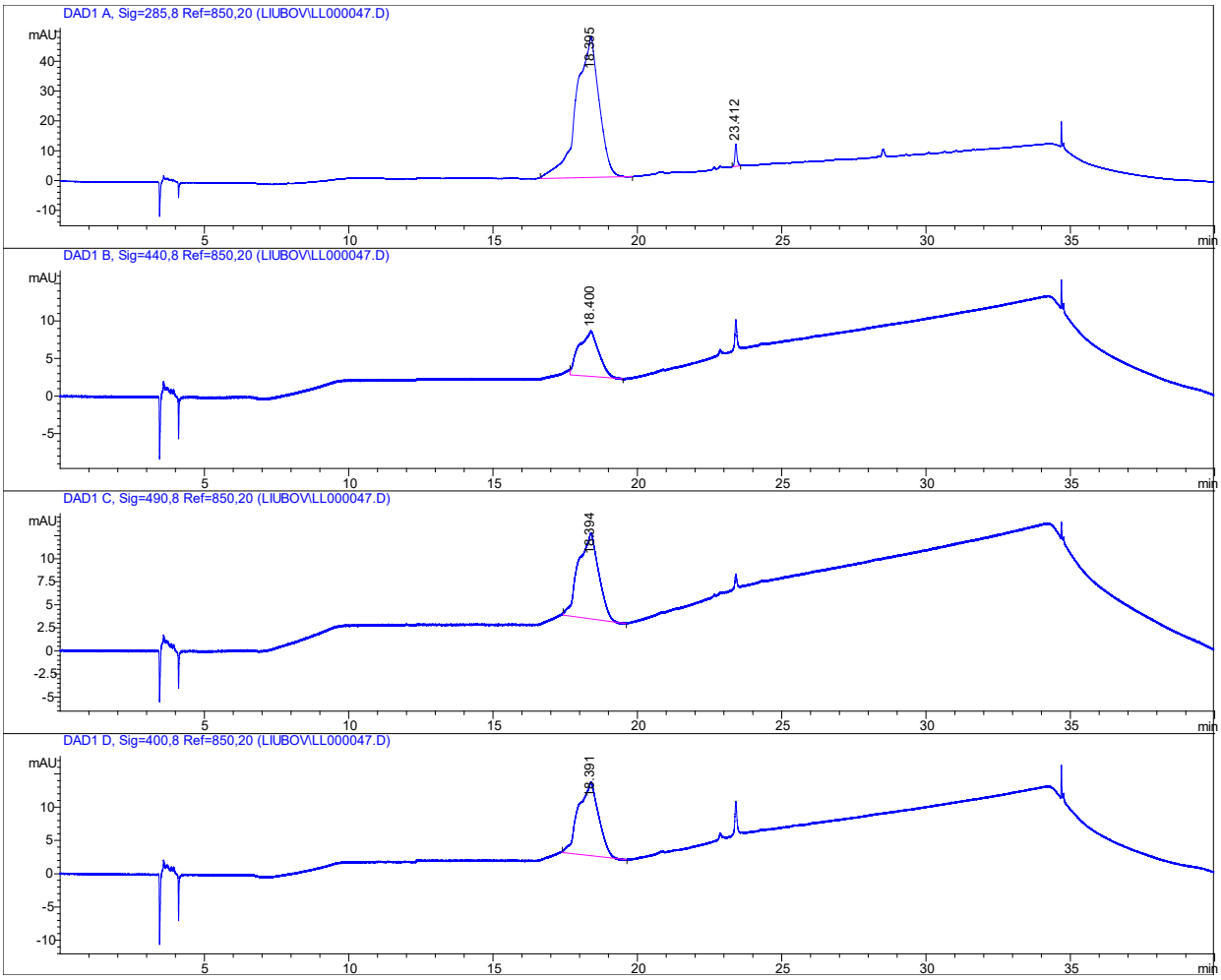


**Appendix Figure S45.** HPLC chromatogram of complex **8** collected at the following wavelengths: 285, 440, 490, 400 nm (98.5% purity by peak area).

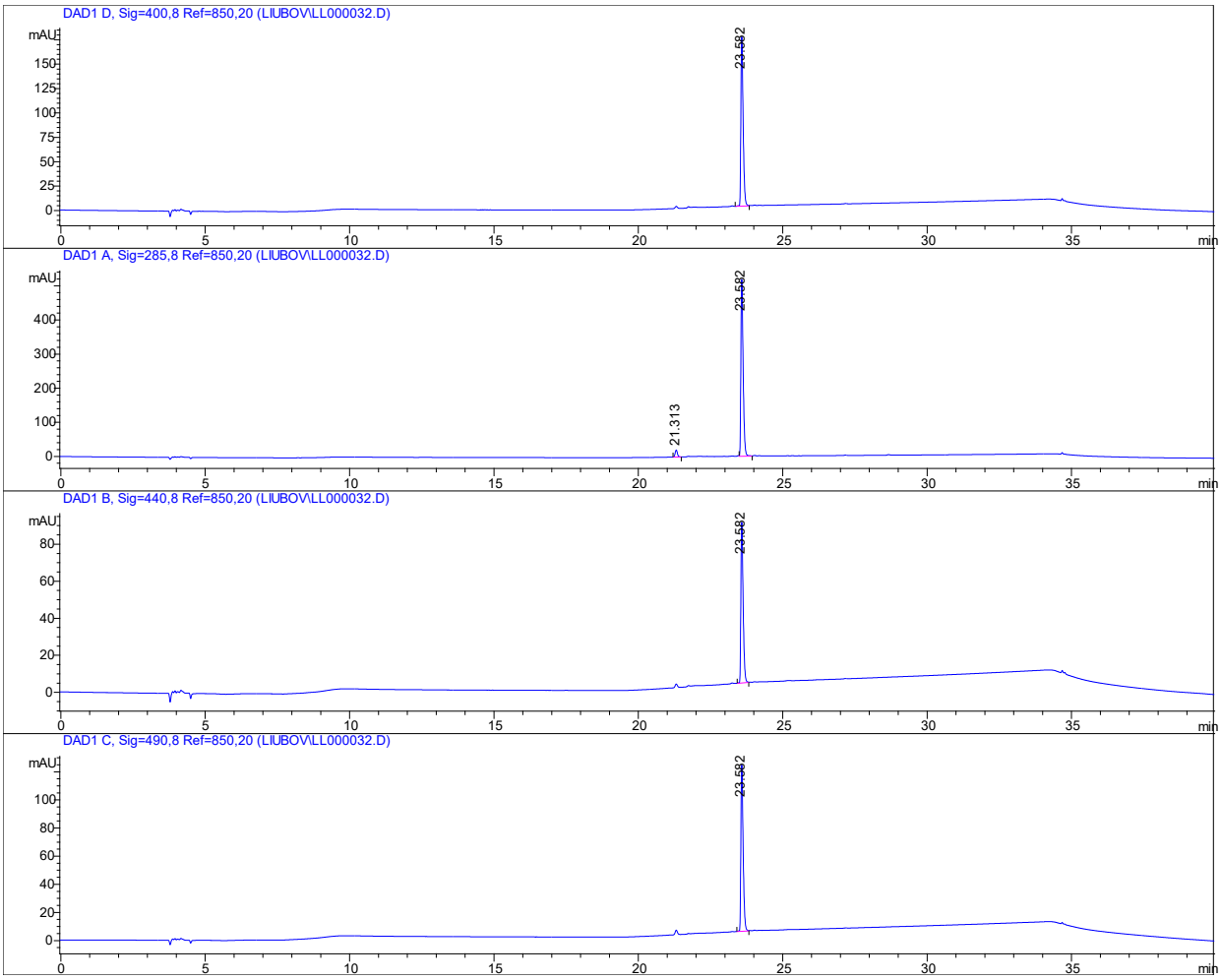


**Appendix Figure S46.** HPLC chromatogram of complex **9** collected at the following wavelengths: 400, 285, 440, 490 nm (96.1% purity by peak area).

## 8. PHOTOBIOLOGY

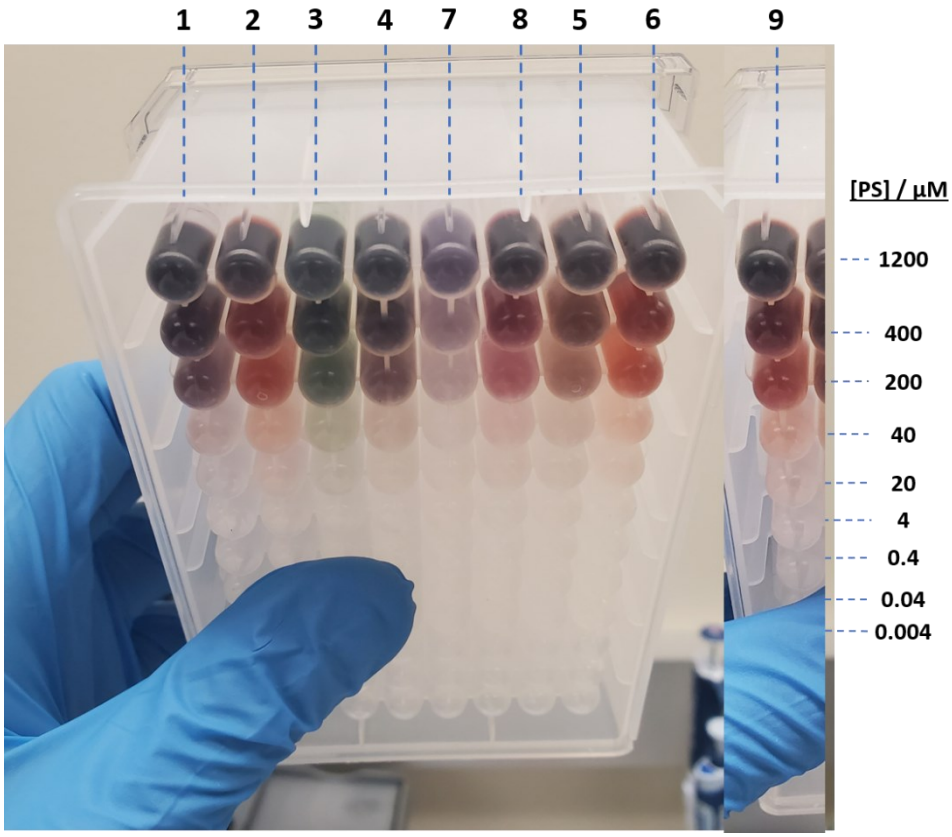


**Appendix Figure S47**. Freshly prepared serial dilutions of compounds 1–9 in 1× DPBS.

**Appendix Table S1**. Correlation parameters for Log ($D_{o/w}$) versus Log (Dark $EC_{50}$)

| Cell line | A375 | B16F10 | SKMEL28 |
|---|---|---|---|
| Pearson r coefficient | −0.6649 | −0.8665 | −0.9041 |
| 95% CI | −0.9751 to 0.5259 | −0.9911 to 0.06677 | −0.9937 to -0.1078 |
| $R^2$ | 0.4421 | 0.7509 | 0.8174 |
| p-value (α=0.05)[a] | 0.2208 | 0.0573 | 0.0351 |

Only soluble compounds included. n=5 since compounds **1**,**3**,**5**,**7** precipitated to some extent during experimentation. [a]two-tailed p-test, $p<0.05$ = statistically significant

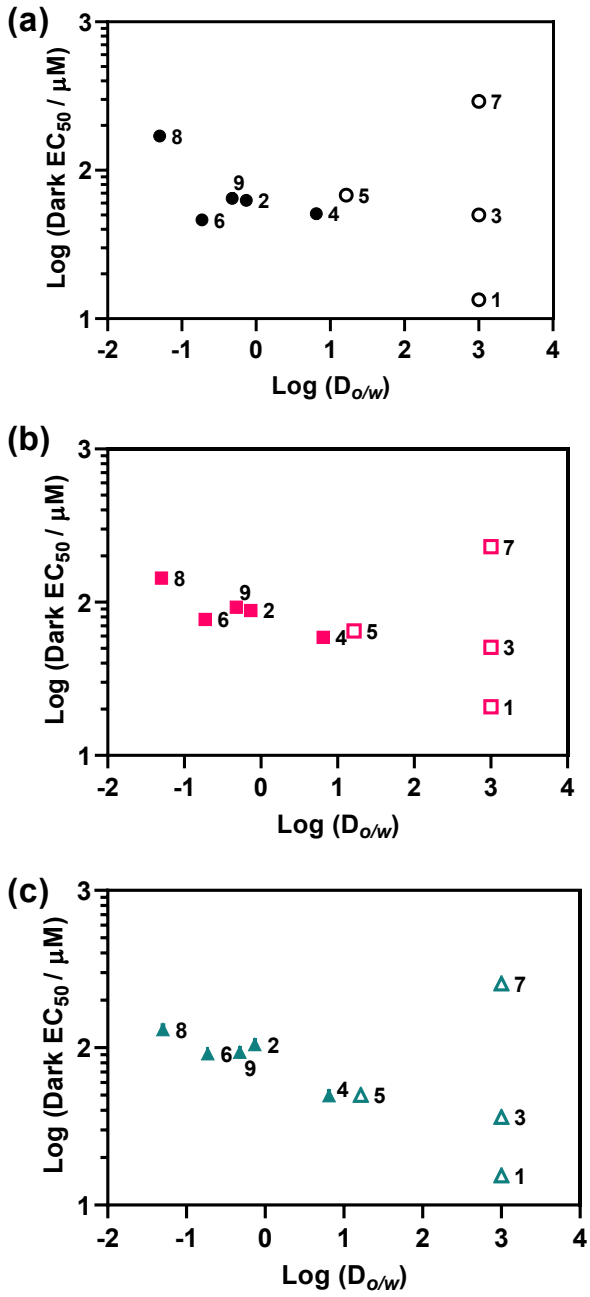


**Appendix Figure S48.** Log-Log scatter plot of distribution coefficient (± SD) versus Dark $EC_{50}$ (± SEM) in (a) A375, (b) B16F10, and (c) SKMEL28 cell lines. Open symbols designate ambiguous Log ($D_{o/w}$) values where precipitation occurred in either the aqueous or organic partitions. Tabulated Log ($D_{o/w}$) are included in Table S2.

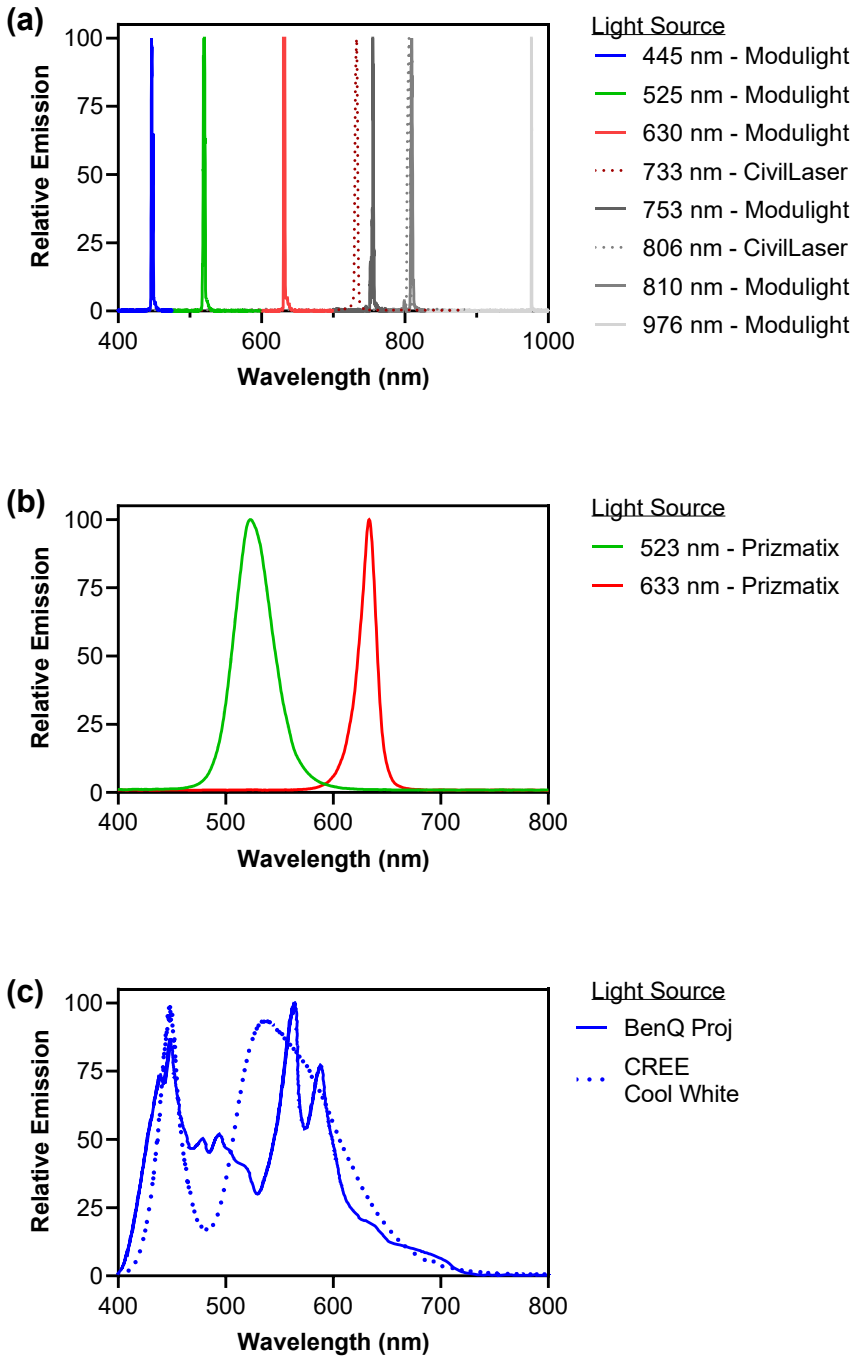


**Appendix Figure S49.** Normalized emission from the light sources used in the photobiological studies: (a) lasers, (b) monochromatic LEDs, and (c) broadband visible projector lamp or broadband visible CREE LEDs.

**Appendix Table S2.** Log distribution coefficient ($LogD_{o/w}$) of **1**–**9** in 1-octanol and PBS (pH=7.4). [a]value not determined due to precipitation.

| cmpd | $Log(D_{o/w} \pm SD)$ |
|---|---|
| **1** | 3[a] |
| **2** | −0.131 ± 0.009 |
| **3** | 3[a] |
| **4** | 0.813 ± 0.016 |
| **5** | 1.215 ± 0.055 |
| **6** | −0.730 ± 0.007 |
| **7** | 3[a] |
| **8** | −1.298 ± 0.021 |
| **9** | −0.32 ± 0.017 |

**Appendix Table S3.** Comparison of (photo)cytotoxicities in different cell lines across the three laboratories performed by three different researchers.

| | | | $EC_{50}$ ± SEM[1] (μM) | | | PI[2] | |
|---|---|---|---|---|---|---|---|
| PS# | Cell Line | Location | Dark[3] | 633 nm[4] | Visible[4,5] | 633 nm[4] | Visible[4,5] |
| **2** | B16F10 | UTA | 88.2 ± 5.5 | 1.89 ± 0.03 | 1.74 ± 0.14 | 47 | 51 |
| **2** | B16F10 | Dal | 52.3 ± 1.5 | 1.44 ± 0.04 | - | 36 | - |
| **2** | SKMEL28 | UTA | 105 ± 6 | 0.798 ± 0.097 | 0.292 ± 0.016 | 132 | 360 |
| **2** | SKMEL28 | AU | 70.9 ± 1.9 | 0.63 ± 0.013 | 0.329 ± 0.008 | 113 | 216 |
| **6** | B16F10 | UTA | 77.0 ± 4.3 | 1.97 ± 0.09 | 0.940 ± 0.090 | 39 | 82 |
| **6** | B16F10 | Dal | 63.2 ± 1.0 | 2.12 ± 0.08 | - | 30 | - |
| **6** | SKMEL28 | UTA | 91.9 ± 5.9 | 1.37 ± 0.10 | 0.359 ± 0.026 | 67 | 256 |
| **6** | SKMEL28 | AU | 79.6 ± 2.5 | 0.521 ± 0.012 | 0.333 ± 0.033 | 153 | 239 |
| **9** | B16F10 | UTA | 92.8 ± 6.0 | 2.12 ± 0.10 | 0.87 ± 0.12 | 44 | 107 |
| **9** | B16F10 | Dal | 29.2 ± 1.6 | 1.22 ± 0.01 | - | 24 | - |
| **9** | SKMEL28 | UTA | 94.0 ± 7.5 | 1.52 ± 0.04 | 0.602 ± n.d. | 62 | 156 |
| **9** | SKMEL28 | AU | 56.7 ± 1.5 | 0.396 ± 0.017 | 0.286 ± 0.017 | 143 | 198 |

[1]Effective concentration to reduce cell viability to 50% ($EC_{50}$) and standard error of the mean (SEM), [2]phototherapeutic index (PI) provides the ratio of dark (sham) to light treatment, [3]dark treatment or absence of light during treatment, [4]light treatment uses 20–30 mW $cm^{-2}$ and 100 J $cm^{-2}$, [5]cool white visible (400–700 nm), [6]n.d. = not determined due to a steep hill slope, "-" = treatment not performed.

**Appendix Table S4.** Comparison of (photo)cytotoxicities of **1**–**9** under four different conditions in female melanoma A375 cells at UTA.

| cmpd | $EC_{50}$ ± SEM (μM) | | | | | PI | | | |
|---|---|---|---|---|---|---|---|---|---|
| | Dark[3] | 733 nm[4] | 633 nm[5] | 523 nm[5] | Visible[5,6] | 733 nm[4] | 633 nm[4] | 523 nm[5] | Visible[5,6] |
| **1** | 13.4 ± 0.4 | 5.35 ± 0.09 | 4.78 ± 0.05 | 4.87 ± 0.08 | 1.94 ± 0.08 | 3 | 3 | 3 | 7 |
| **2** | 62.6 ± 0.9 | 1.77 ± 0.12 | 1.45 ± 0.02 | 1.28 ± 0.05 | 1.21 ± 0.07 | 35 | 43 | 49 | 52 |
| **3** | 50.0 ± n.d.[7] | 49.6 ± n.d.[7] | 24.3 ± 1.0 | 15.6 ± 0.8 | 1.97 ± 0.22 | 1 | 2 | 3 | 25 |
| **4** | 51.1 ± n.d.[7] | 13.9 ± 2.1 | 12.7 ± 0.4 | 12.1 ± 0.3 | 6.53 ± 0.06 | 4 | 4 | 4 | 8 |
| **5** | 68.1 ± 2.0 | 26.4 ± 1.6 | 20.1 ± 0.8 | 14.0 ± 0.8 | 4.87 ± 0.41 | 3 | 3 | 5 | 14 |
| **6** | 46.3 ± 1.2 | 1.62 ± 0.12 | 1.48 ± 0.03 | 1.10 ± 0.02 | 1.04 ± 0.07 | 29 | 31 | 42 | 45 |
| **7** | 292 ± 9 | 214 ± 6 | 152 ± 3 | 170 ± 4 | 116 ± 4 | 1 | 2 | 2 | 3 |
| **8** | 170 ± 7 | 191 ± 7 | 187 ± 7 | 198 ± 7 | 179 ± 15 | 1 | 1 | 1 | 1 |
| **9** | 64.6 ± 1.0 | 2.00 ± 0.05 | 1.59 ± 0.05 | 1.43 ± 0.03 | 0.867 ± 0.079 | 32 | 41 | 45 | 75 |

[1]Effective concentration to reduce cell viability to 50% ($EC_{50}$) and standard error of the mean (SEM), [2]phototherapeutic index (PI) provides the ratio of dark (sham) to light treatment, [3]dark treatment or absence of light during treatment, [4]light treatment uses 9 mW $cm^{-2}$ and 100 J $cm^{-2}$, [5]light treatment uses 20 mW $cm^{-2}$ and 100 J $cm^{-2}$, [6]cool white visible (400–700 nm), [7]n.d. = not determined due to a steep hill slope.

**Appendix Table S5.** Comparison of (photo)cytotoxicities of **1**–**9** under four different conditions in murine melanoma B16F10 cells at UTA

| cmpd | $EC_{50}$ ± SEM (μM) | | | | | PI | | | |
|---|---|---|---|---|---|---|---|---|---|
| | Dark[3] | 733 nm[4] | 633 nm[5] | 523 nm[5] | Visible[5,6] | 733 nm[4] | 633 nm[4] | 523 nm[5] | Visible[5,6] |
| **1** | 20.8 ± 1.6 | 5.09 ± 0.07 | 4.85 ± n.d.[7] | 2.17 ± 0.08 | 1.65 ± 0.05 | 4 | 4 | 10 | 13 |
| **2** | 88.2 ± 5.5 | 2.57 ± 0.16 | 1.89 ± 0.03 | 1.46 ± 0.09 | 1.74 ± 0.14 | 34 | 47 | 60 | 51 |
| **3** | 50.7 ± 1.7 | 53.4 ± 1.0 | 49.9 ± n.d.[7] | 16.3 ± 1.6 | 1.92 ± 0.05 | 1 | 1 | 3 | 26 |
| **4** | 58.8 ± 2.0 | 15.0 ± 2.0 | 13.7 ± 0.8 | 13.7 ± 0.7 | 6.77 ± 0.15 | 4 | 4 | 4 | 9 |
| **5** | 65.0 ± 2.5 | 54.1 ± 1.5 | 50.3 ± n.d.[7] | 27.4 ± 2.4 | 7.58 ± 0.99 | 1 | 1 | 2 | 9 |
| **6** | 77.0 ± 4.3 | 2.14 ± 0.03 | 1.97 ± 0.09 | 1.31 ± 0.07 | 0.939 ± 0.092 | 36 | 39 | 59 | 82 |
| **7** | 231 ± 9 | 217 ± 8 | 166 ± 5 | 168 ± 4 | 121 ± 5 | 1 | 1 | 1 | 2 |
| **8** | 144 ± 4 | 171 ± 12 | 176 ± 8 | 182 ± 9 | 113 ± 12 | 1 | 1 | 1 | 1 |
| **9** | 92.8 ± 6.0 | 2.41 ± 0.04 | 2.12 ± 0.10 | 1.47 ± 0.05 | 0.871 ± 0.115 | 39 | 44 | 63 | 107 |

[1]Effective concentration to reduce cell viability to 50% ($EC_{50}$) and standard error of the mean (SEM), [2]phototherapeutic index (PI) provides the ratio of dark (sham) to light treatment, [3]dark treatment or absence of light during treatment, [4]light treatment uses 9 mW $cm^{-2}$ and 100 J $cm^{-2}$, [5]light treatment uses 20 mW $cm^{-2}$ and 100 J $cm^{-2}$, [6]cool white visible (400–700 nm), [7]n.d. = not determined due to a steep hill slope.

**Appendix Table S6.** Comparison of (photo)cytotoxicities of **1**–**9** under four different conditions in male melanoma SKMEL28 cells at UTA

| cmpd | $EC_{50}$ ± SEM (μM) | | | | | PI | | | |
|---|---|---|---|---|---|---|---|---|---|
| | Dark[3] | 733 nm[4] | 633 nm[5] | 523 nm[5] | Visible[5,6] | 733 nm[4] | 633 nm[4] | 523 nm[5] | Visible[5,6] |
| **1** | 15.4 ± 1.1 | 1.83 ± 0.07 | 1.43 ± 0.11 | 1.02 ± 0.23 | 0.702 ± n.d.[7] | 8 | 11 | 15 | 22 |
| **2** | 105 ± 6 | 1.56 ± 0.04 | 0.798 ± 0.097 | 0.424 ± 0.073 | 0.292 ± 0.016 | 67 | 132 | 248 | 360 |
| **3** | 36.2 ± 3.0 | 49.5 ± n.d.[7] | 16.2 ± 1.2 | 13.7 ± 0.5 | 1.14 ± n.d.[7] | 1 | 2 | 3 | 32 |
| **4** | 49.7 ± n.d.[7] | 12.6 ± 2.5 | 7.61 ± 0.06 | 5.95 ± 0.22 | 3.29 ± 0.16 | 4 | 7 | 8 | 15 |
| **5** | 50.0 ± 3.3 | 16.0 ± 1.1 | 14.9 ± 0.9 | 6.09 ± 0.28 | 1.27 ± 0.21 | 3 | 3 | 8 | 39 |
| **6** | 91.9 ± 5.9 | 1.29 ± 0.18 | 1.37 ± 0.10 | 0.407 ± 0.084 | 0.359 ± 0.026 | 71 | 67 | 226 | 256 |
| **7** | 256 ± 8 | 167 ± 6 | 127 ± 7 | 122 ± 6 | 67.3 ± 1.7 | 2 | 2 | 2 | 4 |
| **8** | 131 ± 3 | 112 ± 5 | 96.8 ± 4.3 | 61.5 ± 1.3 | 41.7 ± n.d.[7] | 1 | 1 | 2 | 3 |
| **9** | 94.0 ± 7.5 | 1.56 ± 0.18 | 1.52 ± 0.04 | 0.720 ± n.d.[7] | 0.602 ± n.d.[7] | 60 | 62 | 131 | 156 |

[1]Effective concentration to reduce cell viability to 50% ($EC_{50}$) and standard error of the mean (SEM), [2]phototherapeutic index (PI) provides the ratio of dark (sham) to light treatment, [3]dark treatment or absence of light during treatment, [4]light treatment uses 9 mW $cm^{-2}$ and 100 J $cm^{-2}$, [5]light treatment uses 20 mW $cm^{-2}$ and 100 J $cm^{-2}$, [6]cool white visible (400–700 nm), [7]n.d. = not determined due to a steep hill slope.

**Appendix Table S7.** Comparison of leads **1**, **6**, and **9** for (photo)cytotoxicity in normoxia vs. hypoxia in 96-well plates

| | | | $EC_{50}$ ± SEM[1] (μM) | | | PI[2] | |
|---|---|---|---|---|---|---|---|
| cmpd | Cell Line | Oxygen % | Dark[3] | 633 nm[4] | Visible[4,5] | 633 nm[4] | Visible[4,5] |
| **2** | SKMEL28 | 18.5 | 63.3 ± 1.4 | 0.520 ± 0.015 | 0.543 ± 0.009 | 122 | 116 |
| **6** | SKMEL28 | 18.5 | 69.4 ± 0.6 | 0.605 ± 0.021 | 0.595 ± 0.005 | 115 | 117 |
| **9** | SKMEL28 | 18.5 | 103 ± 3 | 0.654 ± 0.013 | 0.591 ± 0.006 | 157 | 174 |
| **$R_1$**[6] | SKMEL28 | 18.5 | 135 ± 5 | 0.612 ± 0.014 | 0.083 ± 0.001 | 221 | 1631 |
| **2** | SKMEL28 | 1 | 42.0 ± 1.1 | 21.4 ± 2.3 | 37.6 ± 1.9 | 2 | 1 |
| **6** | SKMEL28 | 1 | 67.9 ± 0.8 | 67.1 ± 2.2 | 78.2 ± 0.9 | 1 | 1 |
| **9** | SKMEL28 | 1 | 90.9 ± 2.0 | 33.4 ± 5.8 | 71.0 ± 3.5 | 3 | 1 |
| **$R_1$**[6] | SKMEL28 | 1 | 136 ± 3 | 133 ± 6 | 117 ± 2 | 1 | 1 |

[1]Effective concentration to reduce cell viability to 50% ($EC_{50}$) and standard error of the mean (SEM), [2]phototherapeutic index (PI) provides the ratio of dark (sham) to light treatment, [3]dark treatment or absence of light during treatment, [4]light treatment uses 20–30 mW $cm^{-2}$ and 100 J $cm^{-2}$,[5]cool white broadband visible source (400–700 nm), [6]reference $R_1$ = oxygen sensitive PDT agent $[Ru(bpy)_2(dppn)]Cl_2$.

**Appendix Table S8.** Correlation parameters for Log ($\Phi_{\Delta}$) versus Log (PI)

| Cell line | A375 | B16F10 | SKMEL28 |
|---|---|---|---|
| Pearson r coefficient | 0.9540 | 0.9860 | 0.9773 |
| 95% CI | 0.7910 to 0.9905 | 0.9327 to 0.9972 | 0.8923 to 0.9954 |
| $R^2$ | 0.9101 | 0.9723 | 0.9551 |
| p-value (α=0.05)[a] | <0.0001 | <0.0001 | <0.0001 |

[a]two-tailed p-test, p<0.05 = statistically significant

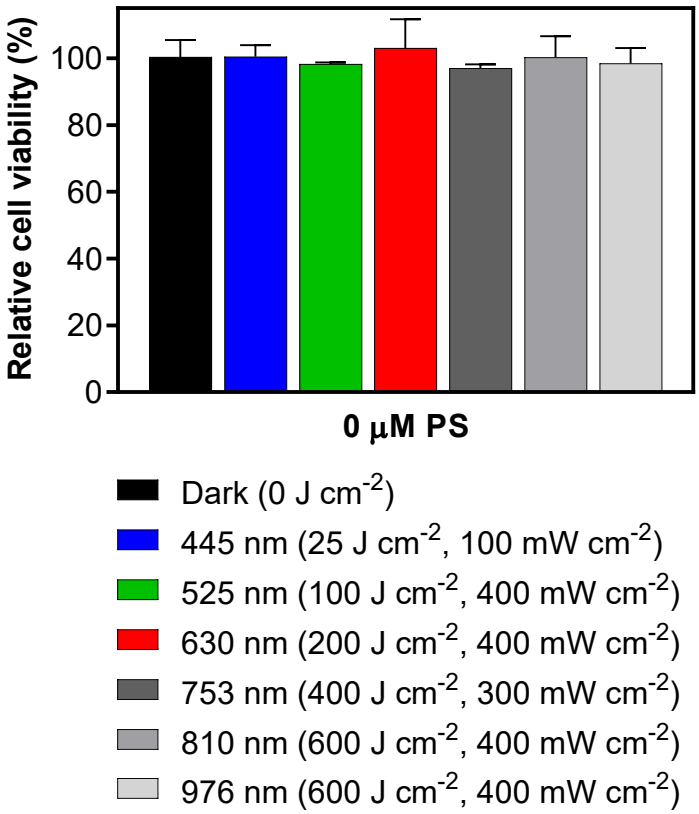


**Appendix Figure S50.** Light controls on ML8500 with SKMEL28 cells at tested treatments with higher fluence and wavelength included for 753, 810, and 976 nm.

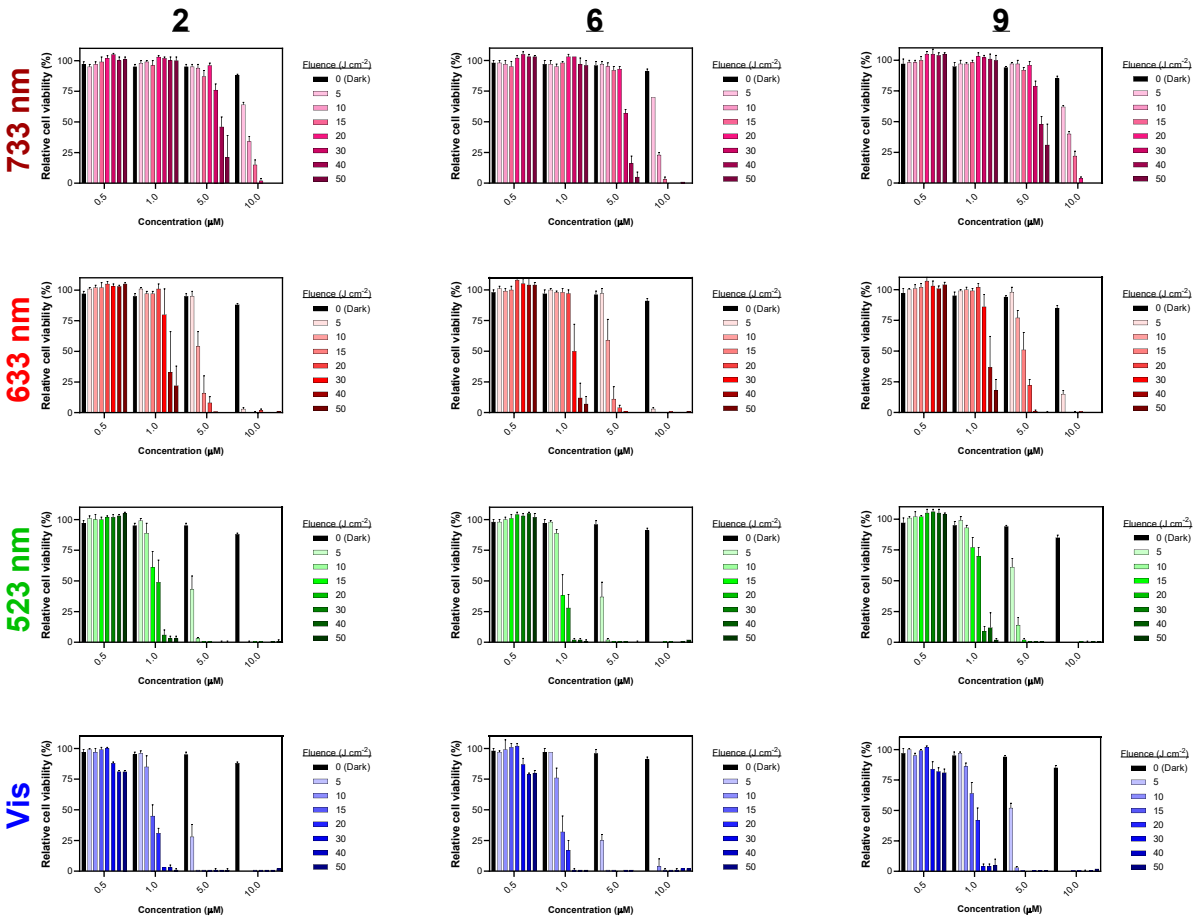


**Appendix Figure S51.** Fluence dependence (± SD) of compounds (left) **2**, (middle) **6**, and (right) **9** against SKMEL28 cells with row-wise 733 nm, 633 nm, 523 nm, and cool white vis treatments at 10 mW cm$^{-2}$ and fluences ranging from 0–50 J cm$^{-2}$.

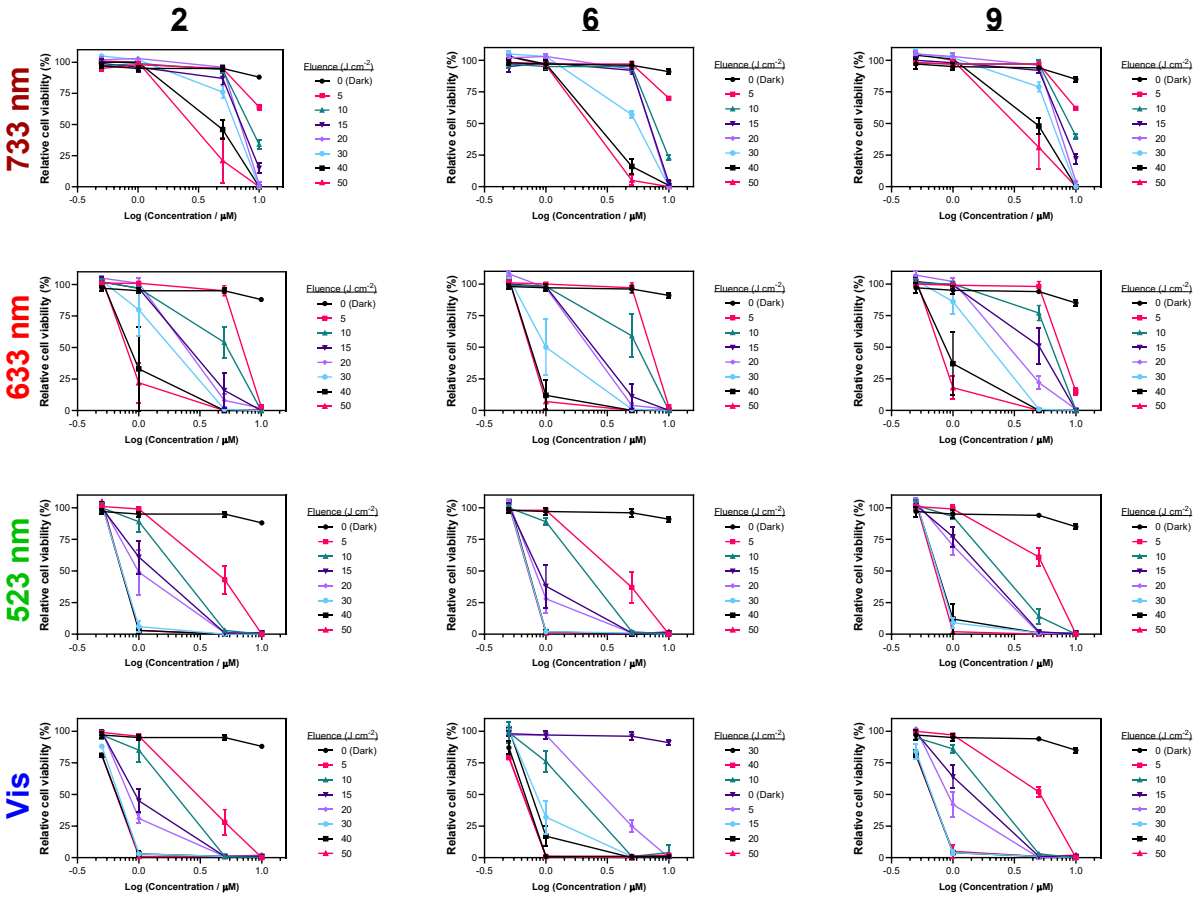


**Appendix Figure S52.** Alternate plotting for the fluence dependence (± SD) of compounds (left) **2**, (middle) **6**, and (right) **9** against SKMEL28 cells with row-wise 733 nm, 633 nm, 523 nm, and cool white vis treatments at 10 mW cm$^{-2}$ and fluences ranging from 0–50 J cm$^{-2}$.

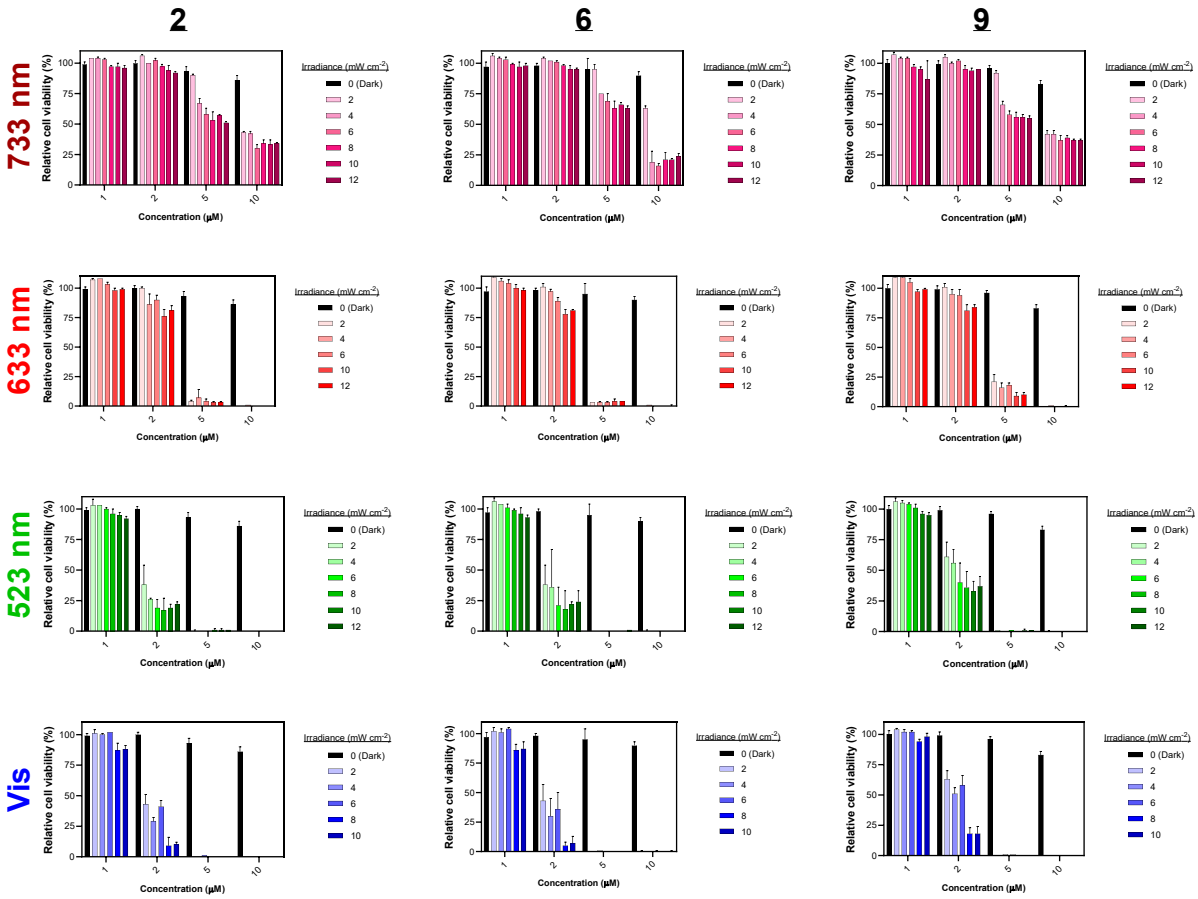


**Appendix Figure S533.** Irradiance dependence (± SD) of compounds (left) **2**, (middle) **6**, and (right) **9** against SKMEL28 cells with row-wise 733 nm, 633 nm, 523 nm, and cool white vis treatments at 10 J cm$^{-2}$ (0 J cm$^{-}$2, Dark) and irradiances ranging from 2–10 mW cm$^{-2}$.

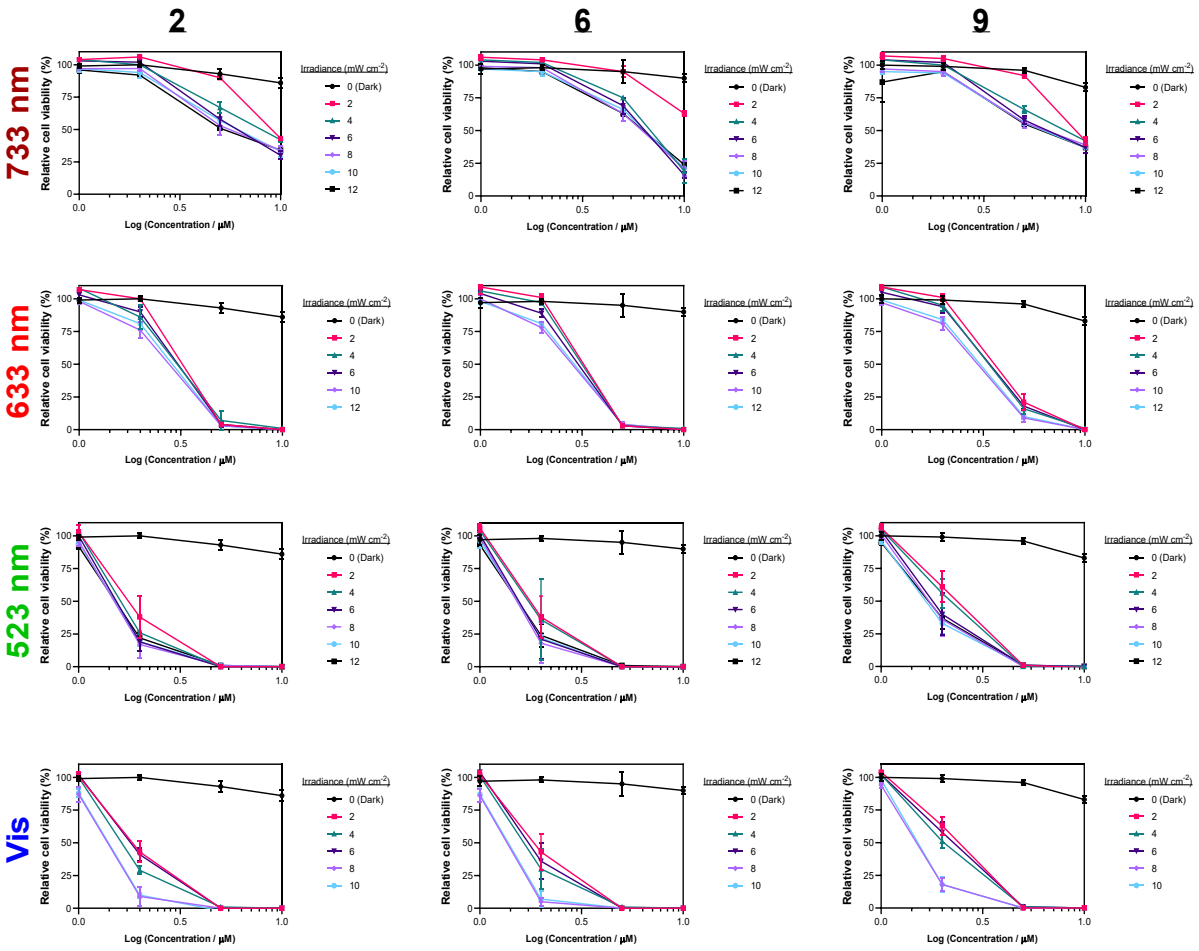


**Appendix Figure S54.** Alternate plotting for the irradiance dependence (± SD) of compounds (left) **2**, (middle) **6**, and (right) **9** against SKMEL28 cells with row-wise 733 nm, 633 nm, 523 nm, and cool white vis treatments at 10 J $cm^{-2}$ (0 J $cm^{-2}$, Dark) and irradiances ranging from 2–10 mW $cm^{-2}$.